Numerical Ship Hydrodynamics

Lars Larsson • Frederick Stern • Michel Visonneau
Editors

Numerical Ship Hydrodynamics

An assessment of the Gothenburg 2010 Workshop

Springer

Editors
Lars Larsson
Dept. of Shipping and Marine Technology
Chalmers University of Technology
Gothenburg
Sweden

Frederick Stern
IIHR-Hydroscience & Engineering
University of Iowa
Iowa City
USA

Michel Visonneau
Fluid Mechanics Laboratory
Ecole Centrale de Nantes
Nantes Cedex 3
France

ISBN 978-94-024-0085-4 ISBN 978-94-007-7189-5 (eBook)
DOI 10.1007/978-94-007-7189-5
Springer Dordrecht Heidelberg London New York

© Springer Science+Business Media Dordrecht 2014
Softcover reprint of the hardcover 1st edition 2014
No part of this work may be reproduced, stored in a retrieval system, or transmitted in any form or by any means, electronic, mechanical, photocopying, microfilming, recording or otherwise, without written permission from the Publisher, with the exception of any material supplied specifically for the purpose of being entered and executed on a computer system, for exclusive use by the purchaser of the work.

Printed on acid-free paper

Springer is part of Springer Science+Business Media (www.springer.com)

Preface

The Gothenburg 2010 Workshop on CFD in Ship Hydrodynamics was the sixth in a series starting in 1980. The purpose of the Workshops is to assess the state of the art in CFD for hydrodynamic applications. Active researchers in the field worldwide are invited to provide computed results for a number of well specified test cases, and the organizers collect and present the results such that comparisons between different methods can be made easily. Detailed information about each method is also reported via a questionnaire provided by the organizers. All results are discussed at a meeting, and a final assessment of the workshop is made by the organizers.

The present workshop attracted 33 groups from all over the world, and different types of computations were carried out for three hulls. It was by far the largest of the workshops in the series so far. All computed results were compiled in a volume, called Proceedings II, and distributed at the meeting, which was held in Gothenburg 8–12 December 2010. Unlike previous workshops, there was no presentation of submitted papers. Instead, the three main organizers gave reviews of the submitted results at the meeting, and most of the time was spent on discussions of these reviews.

In this book, updated versions of the reviews are presented, together with a verification and validation study of the submitted resistance predictions, as well as new measurement data obtained after the workshop and a comprehensive set of additional computations carried out by the organizers to investigate topics of particular interest found at the meeting. The book has been written by the three main organizers and their co-workers. Together with supplementary information on the web site extras.springer.com the book constitutes the final documentation of the Gothenburg 2010 Workshop and gives a state-of-the-art assessment of the CFD capabilities within the area of Ship Hydrodynamics.

Gothenburg, Iowa City and Nantes
March 2013

Lars Larsson, Frederick Stern and Michel Visonneau

Contents

1 Introduction, Conclusions and Recommendations 1
Lars Larsson, Frederick Stern and Michel Visonneau

2 Evaluation of Resistance, Sinkage and Trim, Self Propulsion and Wave Pattern Predictions 17
Lars Larsson and Lu Zou

3 Evaluation of Local Flow Predictions 65
Michel Visonneau

4 Evaluation of Seakeeping Predictions 141
Frederick Stern, Hamid Sadat-Hosseini, Maysam Mousaviraad and Shanti Bhushan

5 A Verification and Validation Study Based on Resistance Submissions 203
Lu Zou and Lars Larsson

6 Additional Data for Resistance, Sinkage and Trim 255
Lu Zou and Lars Larsson

7 Post Workshop Computations and Analysis for KVLCC2 and 5415 . . 265
Shanti Bhushan, Tao Xing, Michel Visonneau, Jeroen Wackers, Ganbo Deng, Frederick Stern and Lars Larsson

Contributors

Shanti Bhushan Mississippi State University, Starkville, MS, USA

Ganbo Deng CNRS/Centrale Nantes, Nantes, France

Lars Larsson Chalmers University of Technology, Gothenburg, Sweden

Maysam Mousaviraad University of Iowa and Iowa Institute of Hydraulic Research (IIHR), Iowa City, IA, USA

Hamid Sadat-Hosseini University of Iowa and Iowa Institute of Hydraulic Research (IIHR), Iowa City, IA, USA

Frederick Stern University of Iowa and Iowa Institute of Hydraulic Research (IIHR), Iowa City, USA

Michel Visonneau CNRS/Centrale Nantes, Nantes, France

Tao Xing University of Idaho, Moscow, ID, USA

Jeroen Wackers CNRS/Centrale Nantes, Nantes, France

Lu Zou Shanghai Jiao Tong University, Shanghai, China
Chalmers University of Technology, Gothenburg, Sweden

Chapter 1
Introduction, Conclusions and Recommendations

Lars Larsson, Frederick Stern and Michel Visonneau

Abstract The Gothenburg 2010 Workshop on CFD in Hydrodynamics was the sixth in a series started in 1980. The purpose of the Workshops is to regularly assess the state of the art in Numerical Hydrodynamics and to provide guidelines for further developments in the area. The 2010 Workshop was by far the largest one so far, with 33 participating groups of CFD specialists and a larger number of test cases than before. All participants submitted their computed results during the fall of 2010. The results were compiled by the organizers and discussed at a meeting in Gothenburg in December 2010. In Chap. 1 the background and development of the Workshops since the start are presented. The three hulls used in the 2010 Workshop are introduced and the computations requested from the participants are specified. Based on a questionnaire sent to all participants the details of their CFD methods are listed, and finally the general conclusions and recommendation for future Workshops are presented. The detailed results of the computations are discussed in subsequent Chapters.

1 Background

In 1980 an international workshop on the numerical prediction of ship viscous flow was held in Gothenburg (Larsson 1981). The objective was to assess the state-of-the-art and to find directions for the future developments in the field. Participants in the workshop had been invited long before and had delivered results for two well specified test cases to the organizers. Detailed information on the features of each participating method had also been submitted and compiled in a table. By comparing the computed results on the one hand, and the details of the methods on the other, the most promising approaches could be sorted out.

L. Larsson (✉)
Chalmers University of Technology, Gothenburg, Sweden
e-mail: lars.larsson@chalmers.se

M. Visonneau
CNRS/Centrale Nantes, Nantes, France
e-mail: michel.visonneau@ec-nantes.fr

F. Stern
University of Iowa and Iowa Institute of Hydraulic Research (IIHR), Iowa City, USA
e-mail: frstern@engineering.uiowa.edu

L. Larsson et al. (eds.), *Numerical Ship Hydrodynamics,*
DOI 10.1007/978-94-007-7189-5_1, © Springer Science+Business Media Dordrecht 2014

Now, more than 30 years have passed since this first workshop and the event has been repeated a number of times. In 1990 the second workshop was held, again in Gothenburg (Larsson et al. 1991). While practically all methods participating in the 1980 workshop had been of the boundary layer type, now all but one were of the Reynolds-Averaged Navier-Stokes (RANS) type. A huge improvement in the prediction of the flow around the stern was noted. The workshop idea was picked up in Japan and the third workshop was held in Tokyo in 1994 (Kodama et al. 1994). Notable from this workshop is that free-surface capabilities had become available in many of the RANS methods. The fourth workshop in the series was held in Gothenburg in 2000 (Larsson et al. 2002; 2003). Now, three modern hull forms—a VLCC, a container ship and a frigate—were introduced as test cases, and these hulls have been kept ever since. At this time, formal verification and validation (V&V) procedures were introduced. While in the previous workshops the emphasis had been on the wake and waves of a towed hull, self-propulsion was introduced in 2000. This was kept in the fifth workshop in Tokyo in 2005 (Hino 2005), where some seakeeping and manoeuvring cases were introduced as well. Even though the same three hulls were used, this increased the number of test cases significantly.

This book deals with the sixth workshop in the series, held in Gothenburg in December 2010. Again, the three previous hulls were used and the areas covered were resistance and local flow, self-propulsion and seakeeping. The reason for not including manoeuvring was that this area is covered well within the SIMMAN Workshops (Stern et al. 2011, www.simman2013.dk). Like in all previous workshops, participants were asked to provide computed results, information about the method used and a paper summarizing the computations. To allow more time for discussion no papers were presented, however. Instead, the three main organizers presented evaluations of the results within all areas. Each day of the three-day Workshop commenced with a report by one of the organizers, covering the areas to be discussed during the day.

The present chapter gives a background to the Workshop, specifies the hulls and test cases and summarizes the methods used. General conclusions and recommendations for future work are also included. Chapters 2, 3 and 4 are the evaluation reports by the three main organizers. The first versions of these reports were presented at the Workshop, but considerable revisions have been made afterwards. It should be noted that these reports are based solely on results submitted for evaluation at the Workshop. No results from submitted papers or from computations carried out afterwards are included. Since verification and validation were emphasized in the present Workshop, a separate chapter on V&V of all submitted resistance predictions is included as Chap. 5. The two final chapters contain additional information. Chapter 6 presents relevant experimental data collected after the Workshop and in Chap. 7 new computations (including those of submitted papers) are reported. The additional computations highlight some particularly interesting features of the test cases.

This book replaces Proceedings, Part 1 of the Workshop. The detailed results and papers by all participants are presented in the Proceedings, Part 2, distributed at the Workshop. These Proceedings can be downloaded from the web site

extras.springer.com (see the book cover) together with much other supplementary information, such as the spreadsheet with detailed information about all methods, discussions at the Workshop and some photos.

2 Hulls

The three hulls used in the Workshop were:

1. The KVLCC2, a second variant of a Korean VLCC
2. The KCS, a Korean container ship
3. The DTMB 5415, a surface combatant

The KVLCC2 was designed at the Korea Research Institute for Ships and Ocean Engineering (now MOERI) around 1997 to be used as a test case for CFD predictions. Extensive towing tank tests were carried out, providing data for resistance, sinkage and trim, wave pattern and nominal wake at several cross-planes near the stern (Van et al. 1998a, b; Kim et al. 2001). Mean velocity and turbulence data were obtained by Postech (Lee et al. 2003) in a wind tunnel. At the CFD Tokyo Workshop in 2005 (Hino 2005) there was a slight modification of the stern contour of this ship and it was therefore renamed as KVLCC2M. The modification is explained in Hino (Hino 2005). In the present workshop the original design was used. Data for pitch, heave, and added resistance are available from Osaka University, INSEAN and NTNU measurements (Sadat-Hosseini et al. 2012 and Bingjie and Steen 2010).

Also the KCS was designed by MOERI for the same purpose as the KVLCC2, and similar tests were carried out for this hull (Van et al. 1998b; Kim et al. 2001). Self-propulsion tests were carried out at the Ship Research Institute (now NMRI) in Tokyo and are reported in Hino (2005). Data for pitch, heave, and added resistance are also available from Force/DMI measurements (Simonsen et al. 2008).

Model 5415 was conceived as a preliminary design for a Navy surface combatant around 1980. The hull geometry includes both a sonar dome and transom stern. Propulsion is provided through twin open-water propellers driven by shafts supported by struts.

The model test data for the 5415 includes:

- Local flow measurements (Mean velocity and cross flow vectors) (Olivieri et al. 2001).
- PIV-measured nominal wake in regular head waves (Mean velocity, turbulent kinetic energy, and Reynolds stresses). (Longo et al. 2007)
- Resistance, sinkage, trim, and wave profiles (Olivieri et al. 2001).
- Wave diffraction (Waves, 1st harmonic amplitude of mean velocities, turbulent kinetic energy, and Reynolds stresses) (Longo et al. 2007; Hino 2005).
- Roll decay (Motion, free surface, mean velocities) (Irvine et al. 2004).

Side views of the three hulls are seen in Fig. 1.1 and the main particulars are given in Table 1.1. No full scale ships exist.

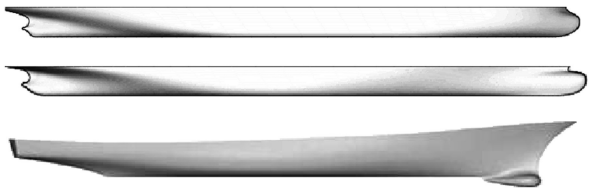


Fig. 1.1 The three ships used in the workshop. (*upper*: KVLCC2, *middle*: KCS, *bottom*: 5415)

The Cartesian coordinate system adopted in the workshop has its origin at the forward perpendicular, x is backwards, y to starboard and z vertically upwards, as shown in Fig. 1.2.

3 Test Cases

Several types of computations were requested, namely:

1. Local flow at fixed condition, either at zero sinkage and trim (denoted FX_0) or dynamic sinkage and trim ($FX_{\sigma\tau}$). In some cases FX_0 is simulated by pre-ballasting the hull to obtain zero sinkage and trim in the free condition at the correct Froude number (FR_0).
2. Resistance, sinkage and trim either at FX_0 or at heave- and pitch-free condition ($FR_{z\theta}$)
3. Self-propulsion at FX_0 or $FR_{z\theta}$
4. Heave and pitch in waves either at $FR_{z\theta}$ or with free surge ($FR_{xz\theta}$)
5. Forward speed diffraction at $FX_{\sigma\tau}$
6. Free roll decay at $FX_{\sigma\tau}$ and free to roll (FR_{φ})

Table 1.1 Main particulars of the three ships

Main particulars (Full Scale)			KVLCC2	KCS	DTMB 5415
Length between perpendiculars		L_{PP} (m)	320.0	230.0	142.0
Maximum beam of waterline		B (m)	58.0	32.2	19.06
Draft		T (m)	20.8	10.8	6.15
Displacement		Δ (m^3)	312622	52030	8424.4
Wetted area w/o rudder		S_W (m^2)	27194	9424	2972.6
Wetted surface area of rudder		S_R (m^2)	273.3	115.0	30.8
Block coefficient (C_B)		$\Delta/(L_{PP}{\cdot}B{\cdot}T)$	0.8098	0.6505	0.507
Propeller center, long. location (from FP)		x/L_{PP}	0.9825	0.9825	0.9453
Propeller center, vert. location (below WL)		$-z/L_{PP}$	0.04688	0.02913	–
LCB ($\%L_{PP}$), fwd +		–	3.48	−1.48	−0.683
Vertical Center of Gravity (from keel)		KG (m)	18.6	7.28	7.5473
Metacentric height		GM (m)	5.71	0.60	1.95
Moment of Inertia		K_{xx}/B	0.40	0.40	0.37
Moment of Inertia		K_{yy}/L_{PP}, K_{zz}/L_{PP}	0.25	0.25	0.25
Service speed	Speed	U (knots)	15.5	24.0	18.0, 30.0
	Froude number	Fr	0.142	0.26	0.248, 0.413

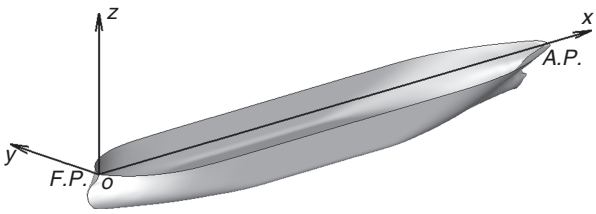


Fig. 1.2 Cartesian coordinate system

All test cases for the three hulls are listed in Table 1.2. The measurements were taken at the organizations within brackets. See the references above. There are altogether 18 cases and the participants were free to select which cases to compute.

4 Participants and Methods

The workshop participants are listed in Table 1.3 together with the main features of their methods. In the first column the acronym of the participating group is given. This is used in combination with the code name of column three to identify each submission. The cases computed are given in column two. In the remaining columns the features of each method are given.

The majority of methods use two-equation turbulence models, $k-\varepsilon$ or $k-\omega$. There are also some one-equation models, either Spalart-Allmaras or Menter. The

Table 1.2 Test cases

Case number	Hull	Attitude	Measured quantity
1.1a	KVLCC2	FX_0	Mean velocity, Reynolds stresses (Postech WT)
1.1b		FR_0	Wave pattern (MOERI)
1.2a		FR_0	Resistance (MOERI)
1.2b		$FR_{z\theta}$	Resistance, sinkage and trim (MOERI)
1.4a		$FR_{z\theta}$	Pitch, heave, added resistance (INSEAN)
1.4b		$FR_{z\theta}$	Pitch, heave, added resistance (NTNU)
1.4c		$FR_{xz\theta}$	Surge, Pitch, heave, added resistance (Osaka Univ)
2.1	KCS	FR_0	Wave pattern, mean velocities (MOERI)
2.2a		FR_0	Resistance (MOERI)
2.2b		$FR_{z\theta}$	Resistance, sinkage and trim (MOERI)
2.3a		FX_0	Self-propulsion at ship point (thrust, torque, force balance or RPM, mean velocity), local flow (NMRI)
2.3b		$FR_{z\theta}$	Self-propulsion at model point (thrust, torque, force balance or RPM), sinkage and trim (FORCE)
2.4		$FR_{z\theta}$	Pitch, heave, added resistance (FORCE)
3.1a	DTMB 5415	$FX_{\sigma\tau}$	Mean velocity, resistance, wave pattern (INSEAN)
3.1b		$FX_{\sigma\tau}$	Mean velocity, resistance, wave pattern, Reynolds stresses (IIHR)
3.2		$FR_{z\theta}$	Resistance, sinkage and trim (INSEAN)
3.5		$FX_{\sigma\tau}$	Wave diffraction, Mean velocity (IIHR)
3.6		FR_{φ}	Roll decay (IIHR)

Table 1.3 Workshop participants and methods

Organization	Cases Submitted	Code	Turbulence (incl. non-RANS)	Wall Model	Free Surface	Propeller	Discretization		Grid Type	Velocity Pressure
							Type	Order		
CD-Adapco	2.2a, 2.2b	STAR-CCM+	Standard $k-\varepsilon$	N	VOF	–	FV	2	U	PR
CEHINAV TU Madrid	3.1a	STAR-CCM+	$k-\omega$ SST	N	VOF	–	FV	1	MU	PR SIMPLE
Chalmers	1.1a	SHIPFLOW4.3	$k-\omega$ SST EASM	N	–	–	FV	2	S	A
CSSRC	2.1, 2.2a, 2.2b, 2.3a, 3.1a, 3.2	FLUENT 6.3	$k-\omega$ SST RNG k-ε	N	VOF	Actual	FV	2	MS	PR SIMPLE
CTO	2.3a	STAR-CCM+	$k-\varepsilon$	N WO	VOF	Actual	FV	2	U	PR SIMPLE
ECN/CNRS	1.1b, 1.4a, 1.4b, 3.6	ISISCFD	$k-\omega$, EASM	WO	VOF	Body force	FV	2	U	PR SIMPLE
ECN/HOE	1.1a, 1.1b, 1.4a, 1.4b, 2.1, 3.1a, 3.1b, 3.5, 3.6	ICARE	Wilcox $k-\omega$ $k-\omega$ SST	N WO	Nonlin. track	Body force	FD	2	S	D
FLOWTECH	2.1	SHIPFLOW-VOF-4.3	$k-\omega$ SST	N	VOF	–	FV	2	MS	A
FOI	3.1a	OpenFOAM	LES	WO	VOF	–	FV	2	U	PR
FORCE	2.4	CFDShip-Iowa	$k-\omega$ SST	N	Level set	–	FD	2	OS	PR PISO
GL&UDE Univ. Duisburg	1.4a, 1.4b, 1.4c, 2.2a, 2.2b, 2.4, 3.6	Comet OpenFOAM	$k-\varepsilon$	N WO	VOF	–	FV	Mixed	U	PR SIMPLE
HSVA	1.1a, 1.2a	FreSCo+	2E $k-\omega$	N	VOF	–	FV	3	U	PR
IHI/Univ. Tokyo	2.4	WISDAM-UTokyo	Baldwin-Lomax and DSGS	N	Density function ρ	–	FV	3	OS	PR MAC
IIHR	1.1a, 1.4a, 1.4c, 2.1, 2.3a, 2.3b, 2.4, 3.1a, 3.1b, 3.5, 3.6	CFDShip-Iowa V4, V4.5, V6	Hybrid $k-\varepsilon/k-\omega$ based DES Hybrid ARS based DES	WO N	Level set	Actual Body force	FD	2∼4	S, OS	PR Fractional step

Table 1.3 (continued)

Organization	Cases Submitted	Code	Turb. model (incl. non-RANS)	Wall Model	Free Surface	Propeller	Discretization		Grid Type	Velocity Pressure
							Type	Order		
IIHR-SJTU	2.1, 2.3a	FLUENT12.0.16	Realizable $k-\varepsilon$	N, W	VOF	Body force	FV	3	MS	PR
IST	1.1a	PARNASSOS	$k-\omega$ SST	N	–	–	FD	2	S	D
Kyushu University	1.4b	RIAM-CMEN	DNS	N	THINC	–	FD	3	S	PR
MARIC	1.1a, 1.1b, 1.2a,2.1, 2.2a, 2.3a, 3.1a, 3.1b, 3.2	FLUENT	Realizable $k-\varepsilon$	N	VOF	Actual	FV	2	MS	PR SIMPLE
MARIN	2.1, 2.3a, 3.1a, 3.2	PARNASSOS	1E Menter	N	Free-surface fitting	–	FD	2	MS	D
MOERI	1.1b, 1.2a, 1.2b,2.1, 2.2a, 2.2b, 2.3a, 2.3b	WAVIS	Realizable $k-\varepsilon$	WO	Level set	Body force	FV	3	MS	PR SIMPLEC
NavyFOAM (NSWC/P S ARL)	1.1a, 3.1a, 3.1b, 3.2	NavyFOAM	Wilcox $k-\omega$	WO	VOF	–	FV	2, 3	MS MU	PR
NMRI	1.1a, 2.1, 2.3a, 3.1b, 3.5	SURF	1E Modified Spalart-Allmaras	N	Level set	Body force	FV	2	S, U	A
NSWC-PC ARL	3.2	CFDShip-Iowa V4.5	DES Hybrid $k-\varepsilon/k-\omega$	N	Level set	–	FD	4	S, OS	PR
NTNU	1.1a, 1.1b, 1.2a	FLUENT	$k-\omega$ SST	N	VOF	–	FV	2	MU	PR SIMPLE
SNUTT	2.1, 2.3a	FLUENT6.3	$k-\varepsilon$	W	VOF	Actual	FV	2	MU	D
Southampton Univ. QinetiQ	2.1, 2.2b, 2.3a	CFX 12	$k-\omega$ SST	W	VOF	Body force	FV	2	MS	D
SSPA	2.3a, 2.3b	SHIPFLOW4.3	EASM	N	–	Body force	FV	2	OS	A
SSRC Univ. Strathclyde	2.1, 2.3a, 3.1b, 3.5, 3.6	FLUENT12.1	$k-\omega$ SST	N	VOF	Actual	FV	2	MS	PR

Table 1.3 (continued)

Organization	Cases Submitted	Code	Turb. model (incl. non-RANS)	Wall Model	Free Surface	Propeller	Discretization		Grid Type	Velocity Pressure
							Type	Order		
SVA Potsdam	2.1, 2.2a	ANSYS-CFX12	$k-\omega$ SST	N	VOF	–	FV	2	MU	D
TUHH	1.1b, 2.4	FreSCo+	$k-\omega$ SST	N	VOF	–	FV	3	U	PR SIMPLE
TUHH ANSYS	2.1, 2.2a, 2.3a,	CFX12.1	$k-\omega$ SST	N WO	VOF	Actual	FV	2	MS	Fully coupled $w-p$, SIMPLER p-equation
Univ. Genova	3.1a, 3.2	StarCCM+	Realizable $k-\varepsilon$	N	VOF	–	FV	2	U	PR SIMPLE
VTT	1.1a, 1.1b, 1.2a, 2.1	FINFLO	$k-\omega$ SST	N	Nonlin. track	–	FV FD	3	MS OS	A, PR

A Artificial Compressibility; *D* Direct Method; *FD* Finite Difference; *FV* Finite Volume; *MS* Multiblock Structured; *MU* Multiblock Unstructured; *N* No Slip; *OS* Overlapping Structured; *PR* Pressure Correction; *S* Single Block Structured; *U* Unstructured; *W/WO* Wall Functions With/Without Pressure Gradient Correction

anisotropic models are either of the algebraic stress or Reynolds stress type. Note that there are also some LES/DES methods and even a DNS method.

Most of the participants use no-slip wall boundary conditions, but there are also several methods with wall functions, both with and without pressure gradient corrections. The Volume of Fluid (VOF) technique is the most popular one for the free-surface modeling, but there are also several level set methods. There are only three entries with surface tracking. The propeller is represented either as an actual rotating propeller or through a body force approximation. Simulations were performed using both finite difference and finite volume codes, but there was no finite element method. 2nd or 3rd order accurate schemes were used and limited studies used 4th order schemes. The grids used were either single- or multi-block structured ones (butt-joined or overlapping) or unstructured ones. Most methods are pressure based but there are also several solving the equations directly or with an artificial compressibility.

A complete specification of each method and application is given on the web site extras.springer.com, based on the replies to a questionnaire answered by all participating groups.

5 Conclusions

The Gothenburg 2010 Workshop on numerical Ship Hydrodynamics was a huge effort by a large number of people. 33 groups participated and computed one or more of the 18 test cases for the three hulls. The results represent the state-of-the-art in computational hydrodynamics at present. The main conclusions are:

Chapter 2 (Evaluation of Resistance, Sinkage and Trim, Self Propulsion and Wave Pattern Predictions)

1. The mean comparison error, defined as the difference between the measured value (D) and the computed value (S), for all computed resistance cases is practically zero; only—0.1 %D, and the mean standard deviation is 2.1 %D. The latter represents a considerable improvement since 2005, where the mean standard deviation was 4.7 %D. Among the hulls the KVLCC2 has the largest mean error, -2.0 %, i.e. an over prediction of the resistance, while 5415 has the largest mean standard deviation, 3.2 %. This is for the towed cases. The self-propelled KCS has a considerably larger error and standard deviation (3.7 and 3.2 %, resp,) than the towed hull (-0.3 and 1.3 %, resp.).
2. Excluding the self-propulsion results there is no discernible improvement in the resistance prediction for grid sizes above 3 million cells. All results for towing in this range are within ± 4 % of the measured data. For smaller grid sizes the error is within ± 8 %.
3. There is no visible improvement in accuracy of the resistance prediction for turbulence models more advanced that the two-equation models. However, the statistical basis for this conclusion is weak, due to few predictions with advanced models.

4. Systematic grid variations were reported for slightly less than half of the submissions. An interesting finding is that almost all variations of structured grids were convergent, while this was the case for only one of the seven submissions with unstructured grids. The order of accuracy, determined by either one of the two established methods, is often very different from the theoretical one. In particular, the very large order of accuracy obtained in many submissions is a matter of concern, since the statistical base for the uncertainty estimation is limited to accuracies smaller than twice the theoretical one.
5. The comparison errors and standard deviations of the sinkage and trim are larger than for the resistance, particularly at low speed. Since there is no fundamental reason for this to be the case, the problems are likely to be due to the difficulties of measuring the two quantities at low speed. This conjecture is supported by a subsequent investigation for 5415 where measurement errors as large as 100 % were noted for a Froude number of 0.1. Additional computations for KVLCC2, presented in Chap. 7, also support the conjecture. It should be stressed, however, that the comparison errors are smaller in the speed range $Fr > 0.2$, where the average errors are around 4 % for both quantities.
6. Self-propulsion results are available only for KCS, in fixed and free conditions. For K_T and K_Q the mean comparison errors are 0.6 and -2.6 % resp. The standard deviations are 7.0 and 6.0 % resp.; considerably larger than for resistance. Comparing actual and modeled propellers it is seen that the actual propeller has a much smaller mean standard deviation. For K_T it is half, and for K_Q it is only 1/3 of that of the modeled propeller. There is no clear advantage when it comes to comparison error, however.
7. In general, the wave contours on the hull and at the wave cut closest to the hull are well predicted. Further away from the hull the results differ considerably between the methods. The best submissions for all three hulls capture all the features of the waves out to the edge of the measured region. For KVLCC2 this holds only for a few methods, while most submissions exhibit a far too rapid decay of the wave pattern away from the hull. More methods manage to keep the waves rather well out to the edge of the measured region for KCS, and particularly for 5415. At the higher speeds for these hulls the waves are longer, and a sufficient number of grid points per wave length can be used.

Chapter 3 (Evaluation of Local Flow Predictions)

1. Compared to the results obtained in 2000 and 2005, the study of the flow around the KVLCC2 has shown that much progress has been made towards consistent and more reliable computations of after body flows for U shaped hulls. The intense bilge vortex and its related action on the velocity field is accurately reproduced by a majority of contributors employing very similar turbulence models implemented in different solvers and on various grids in terms of number of points or topology. The turbulence data confirm that the turbulence anisotropy is large in the propeller disk and more specifically in the core of the bilge vortex. For the first time, hybrid LES turbulence models have been introduced to compute model scale ship flows with a globally satisfactory performance on the mean flow-field. However,

one has noticed that these models, in their current state of development, tend to predict ship wake composed of somewhat too intense longitudinal vortices. Explicit Algebraic Reynolds Stress Models reproduce satisfactorily the measured structure of the turbulence and appear to be the best answer in terms of robustness and computational cost for this specific flow field, compared to RSTM or DES based strategies, as long as one is interested in time-averaged quantities although difference persist in the total wake fraction distribution in the main vortical region.

2. The study of the flow around the KCS gave us the opportunity to assess the best available methods to predict hull/propeller coupling in self propulsion conditions. Considering the complexity of this exercise, the results obtained by most of the participants are in good agreement with the experiments. This may be due to the use of very fine grids but the major factor explaining this observation is probably the accuracy of the propeller model. Surprisingly, flow computations based on RANSE everywhere (actual propeller) do not appear significantly better than the best hybrid formulations based on simplified physics for the propeller (modelled propeller, cf. conclusion for K_T and K_Q above). However, a simple body force formulation is not suited, which is not astonishing. In the same order of idea, the turbulence model does not seem to play a crucial role. Here again, hybrid LES computations have been presented for the first time in the framework of self-propelled model-scale flows. The performance of this unsteady turbulence modeling strategy is already very promising despite the fact that it does not outperform the best computations based on Reynolds-averaged statistical turbulence closures.
3. Compared to the results obtained during the last workshop held in 2005 in Tokyo, the level of agreement between computations and experiments for the flow around the DTMB 5415 (case 3.1a) has been much improved. This is probably due to a mix of several reasons involving modeling and discretization errors. Undoubtedly, the grids used in 2010 are finer, which reduce significantly the sources of discretization errors. It is also the first time that one can evaluate the time accurate LES or DES solution methods for these high Reynolds number flows. LES and DES solution methods brought new answers to stimulate the discussion and clarify the complex topology of a flow for which experiments provided only very sparse information.
4. The cases 3.5 and 3.6 are devoted to unsteady flow configurations, either due to the diffraction in waves or to the roll decay. The test case 3.5 illustrates the far better behavior of the solution provided by IIHR/CFDShip-IowaV4. This clear superiority is probably due to the use of a very fine grid, which is two orders of magnitude larger than the mesh used by the other participants. Although based on a theoretically more reliable turbulence model and a relatively fine grid, NMRI/SURF results are still polluted by too high a level of numerical diffusion. Although 100's M of grid points are not necessary to accurately predict such flows using URANS, more reliable turbulence models, such as anisotropic models, and a relatively finer grid than that used by the submissions would help reduce the numerical and modeling diffusion and dissipation, thereby improving numerical predictions. The same conclusions seem to hold for the test case 3.6 although the

small number of participants precludes any general and consistent analysis on the reasons of disagreement between computations and experiments.

Chapter 4 (Evaluation of Seakeeping Predictions)

1. Test cases related to seakeeping are studied in this chapter including heave and pitch with or without surge motions in regular head waves for KVLCC2 and KCS, wave diffraction for DTMB 5415, and roll-decay with forward speed for DTMB 5415. For seakeeping, the total average error is 23 %D, comparable to the average error for previous seakeeping predictions. The errors of the CFD predictions are similar for the different geometries, different wavelengths, the linear and steep waves, and for the cases with and without surge motion. The errors are larger for the cases with zero forward speed. For wave diffraction submissions, the large grid size DES simulation has achieved an average error value of less than 10 %D, while for the small grid size URANS simulations the average error is 28 %D. For roll decay submissions, the average error values are 10 %D for resistance and less than 1 %D for roll motions.
2. For steady calm water resistance, the average error is 7 %D for submissions corresponding to the seakeeping conditions, compared to 2.25 %D for submissions reported in Chap. 2 and 3 %D for previous studies. The larger errors are due to both the smaller number of calm water submissions in this chapter and possibly the data since the seakeeping experimental setup is used to measure the calm water resistance. The 0th harmonic of resistance and the 1st harmonic amplitude and phase are predicted by 18 and 34 %D, respectively. Therefore, for resistance, the largest error values are observed for the 1st harmonic amplitude and phase, followed by 0th harmonic amplitude and then steady.
3. For motions, the average error is 9 %D for steady calm water submissions corresponding to the seakeeping conditions, comparable to the errors for G 2010 Chap. 2 submissions and previous studies. The average error is 54 %D for 0th harmonic while it is around 13 %D for 1st harmonic amplitude and phase. Therefore, the largest error values for motions are observed for the 0th harmonic amplitudes followed by 1st harmonic amplitude and phase and then steady.
4. Comparing the average errors of the URANS predictions with those for the potential flow for seakeeping shows that the 1st harmonics of motions are predicted within 14 %D error for URANS while the potential flow shows an average error of 20 %D. The URANS predictions of motions show similar order of error for short, mid-range and long wavelengths and small and large wave amplitudes while for the potential flow the average error for both heave and pitch reduces to 3.7 %D by excluding the large errors for small motions at short wavelength ($\lambda/L \leq 0.8$). It should be noted that H/λ values were also large for short wavelengths The 0th harmonic of the resistance (and added resistance) is predicted by about 18 %D for URANS compared to 24 % for potential flow for all the wavelengths. Therefore, URANS showed capability for a wide range of head wave conditions covering short, medium and long waves, small and large amplitude waves and including global and local flow variables; however, with larger errors compared to the potential flow for the motions for medium and long wavelengths and with larger computational cost.

5. There are several issues that need to be resolved for further assessment of CFD predictions for seakeeping: (1) additional experimental uncertainty analysis is required, including multiple facilities; (2) consensuses are needed on the best normalization and averaging for the errors for small values such as sinkage and trim and motions in short waves, e.g., %D vs. %DR and mean error vs. E_{RSS}; (3) verification studies are needed to estimate numerical uncertainties, including comparisons between currently used verification procedures; (4) experimental measurements require additional care for the head wave resistance, small sinkage and trim values, and Fourier coefficient analysis; and (5) more studies are required for zero forward speed issues and under resolved peaks of motions. Also, the capability of URANS codes for seakeeping applications should be investigated in future for the self-propelled ship, irregular waves, oblique waves, large wave amplitudes, zero forward speed, and for more mid-range wavelength (frequency) conditions to better define the ship motions curve.

Chapter 5 (A Verification and Validation Study Based on Resistance Submissions)

1. The Factor of Safety (FS) Method and the Least Squares Root (LSR) method produce rather similar V&V results in the vicinity of the asymptotic range, while the CGI method typically gives a smaller uncertainty. The results are quite different far from this range, which is not surprising, since none of the methods was developed for such cases. This is an issue for further studies.
2. The iterative convergence U_I may influence the determination of the discretization uncertainty U_G. Computed results indicate that U_I has a significant influence on U_G for U_I % $\varepsilon_{12} > 0.1$, where ε_{12} is the solution change between the two finest grids. The same holds if U_I %$U_G > 0.1$. U_I can thus be compared with either ε_{12} or U_G.
3. The grid convergence study depends on many factors, such as grid type, grid size, grid refinement ratio, convergence state, convergence rate (order of accuracy). From the present investigations the following conclusions can be drawn:
   a. Unstructured grids more seldom achieve monotonic convergence than the structured grids.
   b. 2 to 10 million grid points and a refinement ratio $r_G = 1.2$ were most common among the research groups. The observed order of accuracy indicates no clear dependence on the grid size or refinement ratio.
   c. Most submissions achieved monotonic convergence (77 % from the FS/GCI method, 91 % from the LSR method) and most solutions are in the vicinity of the asymptotic range ($0.5 < P < 1.5$) for both the FS/GCI (55 of 77 %) and LSR (64 of 91 %) methods. P is the ratio of the achieved and theoretical order of accuracy. An issue in the grid convergence study is the scatter in solutions, which complicates the study and has been shown to significantly affect the determination of the grid convergence and the order of accuracy. Although the LSR method takes the scatter into account, more investigations are needed to further improve the determination of grid convergence for solutions with scatter.
4. The numerical uncertainty U_{SN} is mostly larger than the experimental uncertainty U_D.

5. Most resistance solutions are estimated to have a lower comparison error E than validation error U_{val}, i.e. $|E| < U_{val}$, burying the modeling error in the numerical and experimental noise. On the other hand, for the cases with $|E| > U_{val}$, modeling errors are significant, and reducing E is an objective of the model improvement. As a source of modeling errors, the turbulence models are investigated. The most common ones, k-ε and k-ω, are shown to produce larger $|E|$ and U_{val} than the other models (1E and EASM), especially the k-ω model. However, the small number of entries with models other than the two-equation models makes it difficult to draw firm conclusions.

Chapter 6 (Additional Data for Resistance, Sinkage and Trim)

1. In this Chapter, additional resistance, sinkage and trim data for the three Workshop hulls are presented and compared with data used at the workshop. The comparison enables an estimate of facility bias errors.
2. For KVLCC2 and KCS one additional set of data is added to that used at the Workshop. The estimated bias errors in residuary resistance are very small, around 0.2 % of the mean total resistance, while those of sinkage and trim are considerably larger: 6–11 % of the mean values across the Froude number range.
3. For 5415 new data from three organizations are presented. Bias errors in residuary resistance are here estimated to 0.9–1.6 % of the mean total resistance. Sinkage errors are in the range 3–6 % of the mean value and trim errors are around 0.01.

Chapter 7 (Post Workshop Computations and Analysis for KVLCC2 and 5415)

1. The submissions for the local flow predictions for KVLCC2 and 5415 ranged from URANS on 615 K to 305 M grids and hybrid RANS/LES (HRLES) with DES on 13 to 305 M grids. The large disparity in the grid sizes made it difficult to draw concrete conclusions regarding the most reliable turbulence model, appropriate numerical method and grid resolution requirements for such simulations. In this chapter additional analysis is performed for KVLCC2 and 5415 on intermediate grids to shed more light on these issues.
2. Second order TVD or bounded central difference schemes are found to be sufficient for URANS even on 10s M grids, whereas fourth or higher order schemes are required for HRLES. Resistance predictions show grid uncertainties ≤ 2.2 % for URANS on 50 M grid and HRLES on 300 M grid, which suggests that these grids are approaching asymptotic range.
3. URANS with anisotropic turbulence model perform better than URANS with isotropic turbulence model. Grid with 3 M points are found to be sufficient for resistance predictions, however, finer grid with up to 10s M points are required for local flow predictions. Adaptive grid refinement is helpful in generating optimal grids for URANS simulations, and allows accurate prediction of the onset of the longitudinal vortices from the sonar dome surface. However available grid refinement technique based on the Hessian of pressure, fails to refine the grid further downstream along the hull.
4. Hybrid RANS/LES models are promising in providing the details of the flow topology. However, they show limitations for flows with limited separation, such

as grid induced separation for bluff bodies and inability to trigger turbulence for slender bodies. Implementation of improved delayed DES and/or physics based RANS/LES transition is required to address these limitations. Grid resolution of 300 M shows resolved turbulence levels of $> 95\,\%$ for bluff bodies, thus such grids seem sufficiently fine for HRLES.

5. The free-surface predictions do not show significant dependence on boundary layer predictions, and accurate prediction for 5415 at $Fr = 0.28$ is obtained using just 2 M grid points. However, larger grid requirements have been reported for KVLCC2. The free-surface reduces pressure gradients on the sonar dome, causing weaker vortical structures than single phase.
6. Flow over 5415 shows three primary vortices, and all of them originate from the sonar dome surface. Onset analysis shows that all the three vortices have open-type separation, and separate from the surface due to cross flow.
7. Further investigation of KVLCC2 blockage in the wind tunnel as reported by CFD submissions, eliminates blockage as the cause of difference in CFD submissions and experimental data. It is pointed out that the differences could be due to different stern geometries used in CFD and experiments, in particular sharpness of the stern.

6 Future Workshops

The Gothenburg 2010 Workshop was the sixth in a series started in 1980. Since 1990 the workshops have been held essentially every 5 years. This is a period long enough to allow significant progress to take place, but short enough to enable an evaluation of the new developments without undue delay. Therefore, the 5-year period should be maintained. In order to ascertain timely and efficient workshops in the future a Steering Committee for the CFD Workshops in Ship Hydrodynamics was formed in December 2011. Its primary responsibilities are to select the organizer and venue of the next workshop, to define the test cases and to coordinate campaigns to obtain more data. Support will also be given to the local Organizing Committee in the organization of each workshop. The members of the Steering Committee are the organizers of the previous and next workshops (presently Prof. Lars Larsson, Chalmers and Dr. Nobuyuki Hirata, NMRI, resp.), area representatives of the USA (presently Prof. Frederick Stern, IIHR), Europe (presently Dr. Michel Visonneau, ECN/CNRS) and Asia (presently Dr. Jin Kim, MOERI), as well as the chairman of the ITTC CFD Committee (presently Prof. Takanori Hino, YNU). The present Steering Committee is jointly chaired by Profs. Larsson and Stern.

The date and venue of the next workshop are tentatively set to 2–4 December 2015 at the National Maritime Institute, Tokyo, Japan. Some test cases of the previous workshop will remain, but there will be a greater emphasis on captive and free running self-propulsion and advanced seakeeping cases along with local flow including appendages and propulsors with focus on turbulence variables. A possible new test case is the waterjet driven Delft catamaran tested in many conditions, including static drift, and oblique incoming waves.

Acknowledgements The workshop was organized by a committee of six members: the authors and Dr. Emilio Campana, Dr. Suak Ho Van and Prof. Yasuyuki Toda, who significantly contributed to the success of the workshop. Important contributions were also made by Dr. Alessandro Iafrati, who developed and maintained the web site, as well as Prof. Rickard Bensow and Andreas Feymark, who prepared and compiled the questionnaire. Finally, the great efforts by all workshop participants in the preparation and delivery of all computed results shall not be forgotten. The financial support by the Office of Naval Research Global, Grant N62909-11-1-1011, is gratefully acknowledged.

References

Bingjie G, Steen S (2010) "Added resistance of a VLCC in short waves", 29th International Conference on Ocean offshore and Arctic Engineering, OMAE, Shanghai

Hino T (Ed.) (2005) "Proceedings of CFD workshop Tokyo 2005", NMRI report

Irvine M, Longo J, Stern F (2004) "Towing tank tests for surface combatant for free roll decay and coupled pitch and heave motions". Proc. 25th ONR Symposium on Naval Hydrodynamics. St Johns, Canada

Kim WJ, Van DH, Kim DH (2001) Measurement of flows around modern commercial ship models". Exp Fluids 31:567–578

Kodama Y, Takeshi H, Hinatsu M, Hino T, Uto S, Hirata N, Murashige S (1994) "Proceedings, CFD workshop". Ship Research Institute, Tokyo

Larsson L (Ed.) (1981) "SSPA-ITTC workshop on ship boundary layers", SSPA Report 90, Gothenburg

Larsson L, Patel VC, Dyne G (Eds.) (1991) "SSPA-CTH-IIHR workshop on viscous flow", Flowtech Research Report 2, Flowtech Int. AB, Gothenburg

Larsson L, Stern F, Bertram V (Eds.) (2002) "Gothenburg 2000-A Workshop on Numerical Hydrodynamics", Department of Naval Architecture and Ocean Engineering. Chalmers University of Technology, Gothenburg

Larsson L, Stern F, Bertram V (2003) Benchmarking of computational fluid dynamics for ship flow: the Gothenburg 2000 Workshop". J Ship Res 47:63–81

Lee SJ, Kim HR, Kim WJ, Van SH (2003) Wind tunnel tests on flow characteristics of the KRISO 3600 TEU Containership and 300 K VLCC Double-deck Ship Models". J Ship Res 47(1):24–38

Longo J, Shao J, Irvine M, Stern F (2007) "Phase-Averaged PIV for the nominal wake of a surface ship in regular head waves" ASME J Fluids Eng 129:524–540

Olivieri A, Pistani F, Avanaini A, Stern F, Penna R (2001) towing tank experiments of resistance, sinkage and trim, boundary layer, wake, and free surface flow around a naval combatant INSEAN 2340 model", Iowa institute of hydraulic research. The University of Iowa. IIHR Report No 421:pp 56

Sadat-Hosseini H, Wu PC, Carrica PM, Kim H, Toda Y, Stern F (2012) CFD Verification and validation of added resistance and motions of KVLCC2 with fixed and free surge in short and long head waves". Ocean Engineering 59:240–273

Simonsen C, Otzen J, Stern F (2008) "EFD and CFD for KCS Heaving and pitching in regular head waves", Proc. 27th Symp. Naval Hydrodynamics. Seoul

Stern F, Agdrup K, Kim SY, Hochbaum AC, Rhee KP, Quadvlieg F, Perdon P, Hino T, Broglia R, Gorski J (2011) Experience from SIMMAN 2008: the first workshop on verification and validation of ship maneuvering simulation methods". J Ship Res 55(2):135–147

Van SH, Kim WJ, Yim DH, Kim GT, Lee CJ, Eom JY (1998a) "Flow Measurement around a 300 K VLCC Model", proceedings of the Annual Spring Meeting, SNAK, Ulsan, pp 185–188

Van SH, Kim WJ, Yim GT, Kim DH, Lee CJ (1998b) "Experimental Investigation of the Flow Characteristics around Practical Hull Forms", Proceedings 3rd Osaka Colloquium on advanced CFD applications to ship flow and hull form design, Osaka

Chapter 2
Evaluation of Resistance, Sinkage and Trim, Self Propulsion and Wave Pattern Predictions

Lars Larsson and Lu Zou

Abstract In Chap. 2 results in several areas are discussed. Resistance predictions were requested for all three hulls and there is a large number of submissions. It is found that for grid sizes larger than 3M cells all submissions are within 4 % of the measured data. The mean comparison error (data-simulation) is only −0.1 % and the mean standard deviation is 2.1 % of the data value, excluding self-propelled cases for which the error is larger. There is no discernible effect of the turbulence model; two equation models work as well as the more advanced ones. Sinkage and trim exhibit large comparison errors for the smallest Froude numbers, but this is likely to be due to measurement inaccuracies. For Froude numbers above 0.2 the mean comparison error is around 4 % and the standard deviation 8–10 %. Self-propulsion results are reported with real operating propellers as well as modeled ones. For K_T and K_Q the mean comparison errors are 0.6 and −2.6 % resp. The standard deviations are 7.0 and 6.0 % resp. Comparing actual and modeled propellers it is seen that the actual propeller has a much smaller mean standard deviation. For K_T it is half, and for K_Q it is only 1/3 of that of the modeled propeller. There is no clear advantage when it comes to comparison error, however. In general, the wave contour on the hull and at the wave cut closest to the hull is well predicted. Further away from the hull the results differ considerably between the methods. The best submissions for all three hulls capture all the features of the waves out to the edge of the measured region.

L. Larsson (✉)
Chalmers University of Technology, Gothenburg, Sweden
e-mail: lars.larsson@chalmers.se

L. Zou
Shanghai Jiao Tong University, Shanghai, China
e-mail: luzou@sjtu.edu.cn

L. Larsson et al. (eds.), *Numerical Ship Hydrodynamics,*
DOI 10.1007/978-94-007-7189-5_2, © Springer Science+Business Media Dordrecht 2014

1 Resistance

1.1 Statistics

One of the most important questions in computational hydrodynamics is how well resistance can be predicted. Resistance is the primary parameter when designing a ship, and virtually all new designs are tank tested to find its resistance characteristics. Together with the propulsive efficiency the resistance determines the required power and this is the most important quality of the ship from an economical and environmental point of view.

The present Workshop received 89 predictions of resistance for three different ship types at several Froude numbers, both in fixed and free conditions, and with and without an operating propeller. Therefore there is a reasonably large statistical basis for answering the question:

- *How accurately can the resistance of a ship be predicted today?*

A related question is how computational accuracy compares with experimental accuracy. How close is CFD to towing tank accuracy? Also, it is of considerable interest to evaluate the increase in computational accuracy compared with previous Workshops in the series.

Apart from that, the data base of computed results may be used to look into an equally important question, namely:

- *How can we learn from the data base to set up the most accurate computations?*

By relating the achieved accuracy to the features of the computations, as described in detail in the answers to the Questionnaire (see the web site extras.springer.com and the summary in Chap. 1), in principle the most promising approach could be found. This is not an easy task, however, since the methods and computations constitute an extremely complex combination of features, and evaluating the influence of each of them would require a much larger set of results than that available here. Therefore the statistical evaluation is restricted to the two main parameters which determine the accuracy of a CFD prediction, namely the grid density and the turbulence model.

In Table 2.1 a statistical analysis of all computed total resistance coefficients is presented. Cases which include such coefficients are 1.2a&b, 2.2a&b, 2.3a&b, 3.1a&b and 3.2. For KVLCC2 and KCS cases, “a” means fixed in sinkage and trim, while “b” means free to sink and trim. For 5415 3.1a&b are with the sinkage and trim fixed to the dynamic values at the corresponding Froude number, while the model is free in 3.2. The fixed computations for Cases 1 and 2 are for only one Froude number, while the free computations are for a range of speeds. 2.3a&b are self-propulsion cases where the resistance is equal to the sum of the propeller trust and the applied towing force.

In column 4 of Table 2.1 the mean comparison error E_{mean} is given in per cent of the measured data value, D. According to the sign convention of the Workshop E_{mean} is defined as $D - S_{mean}$, where S_{mean} is the mean of all simulated values for

Table 2.1 Resistance statistics, all cases

Hull	Case No.	*Fr*	$E_{mean}\%D$	$\sigma_{SD}\%D$	$U_D\%D$	No. of entries
KVLCC2	1.2a (fixed)	0.1423	−1.7 (0.0)	1.3 (6.2)	1.0 (0.7)	5 (13)
	1.2b (free)	0.1010	−0.3	–	1.0	1
		0.1194	−1.3	–	1.0	1
		0.1377	−2.3	–	1.0	1
		0.1423	−2.9	–	1.0	1
		0.1369	−2.8	–	1.0	1
		0.1515	−2.8	–	1.0	1
	Mean of KVLCC2		*−2.0*	–		
KCS	2.2a (fixed)	0.26	−1.3 (−1.1)	1.2 (4.2)	1.0	8(11)
	2.2b (free)	0.1083	+1.6	1.4	1.0	4
		0.1516	−0.1	1.1	1.0	3
		0.1949	−0.9	1.7	1.0	4
		0.2274	−1.0	1.4	1.0	6
		0.2599	−0.3	1.2	1.0	4
		0.2816	−0.4	0.8	1.0	6
	2.3a (fixed, prop.)	0.26	−0.3[a] (−0.9)	3.1(1.0)	–	14[a] (4)
	2.3b (free, prop.)	0.26	7.2	3.3	–	3
	Mean of KCS (w/o prop.)		*−0.3*	*1.3*		
	Mean of KCS (prop.)		*3.7*	*3.2*		
5415	3.1a (fixed σ&τ)	0.28	2.5 (1.6)	3.8 (5.3)	0.6 (2.2)	5 (11)
	3.1b (fixed σ&τ)	0.28	−2.6	4.4	0.6	5
	3.2 (free)	0.138	−2.8	4.4	1.3	5
		0.28	0.1 (−1.9)	2.1 (−)	0.6 (2.2)	6(1)
		0.41	4.3	1.4	0.6	5
	Mean of 5415		*0.3*	*3.2*		
Mean of cases with $Fn < 0.2$			$E_{mean,\,Fn<0.2} = -1.2\,\%D$	$\sigma_{SD\,mean,\,Fn<0.2} = 2.0\,\%D$		27
Mean of cases with $Fn > 0.2$			$E_{mean,\,Fn>0.2} = -0.3\,\%D$	$\sigma_{SD\,mean,\,Fn>0.2} = 2.3\,\%D$		62
Mean of all cases			$E_{mean,\,all\,cases} = -0.1\,\%D$	$\sigma_{SD\,mean} = 2.1\,\%D$		89 (40)

[a] Results from MARIC with a hub cap are excluded

the particular case and Froude number. The standard deviation, σ_{SD}, is given in column 5 in per cent of the data value, and in column 6 the estimated data uncertainty is presented. Finally, in the last column the number of entries for the case is seen. Values within brackets are from the 2005 Workshop (Hino 2005).

A very surprising conclusion from the 2005 Workshop was that the mean comparison error E_{mean} was so small for the five different cases that included resistance predictions. These cases correspond to 1.2a, 2.2a, 2.3a, 3.1a and 3.2 in the present notation. For these cases E_{mean} was 0.0, −1.1, −0.4, 1.6 and −1.9 % of the data, respectively. The standard deviation in the predictions was however quite large for 1.2a, 2.2a and 3.1a, namely 6.2, 4.2 and 5.3 %, respectively, of the data. For 2.3a it was quite low, and for 3.2 there was only one entry.

Table 2.1 reveals a substantial reduction in the standard deviation (*%D*) for the towed KVLCC2 and KCS cases, from 6.2 to 1.3 and from 4.2 to 1.2 respectively in the fixed condition. Also, $|E_{mean}|$ for these conditions is well below 2 %, which indicates

that all predictions for this condition are quite accurate, although still not within the experimental accuracy. There is only one submission for the free KVLCC2 condition and it has a somewhat higher $|E_{mean}|$ in the upper Froude number range, about 3 %. The free KCS condition has however several submissions and very small comparison errors and standard deviations, around 1 % for both. The total comparison error for KVLCC2 (including fixed and free conditions) is -2.0 %, while for the towed KCS cases it is -0.3 %. The mean standard deviation of the latter is 1.3 %.

The self-propelled KCS has standard deviations around 3 % and the comparison error is very small for the fixed case. However, for the free case $|E_{mean}|$ is quite high: 7.2 %. All three submissions under predict the resistance significantly. It should be noted that the fixed KCS in self-propulsion is the only case for which the standard deviation has increased compared to 2005. The mean comparison error and standard deviation for the self-propelled cases is 3.7 and 3.2 %, respectively, considerably larger than for the towed cases.

5415 with sinkage and trim fixed to the dynamic values have comparison errors below 3 % and standard deviations around 4 %. In view of the fact that the only difference between 3.1a and b is the Reynolds number (apart from a very small difference in sinkage and trim), the difference is large, but the statistical basis is too small for a comparison. For the free 5415 in 3.2 both the mean error and the standard deviation seem to depend strongly on the Froude number. The best results is obtained at $Fr = 0.28$, where the water just clears the transom. For this condition the mean error is practically zero and the standard deviation among the 6 submissions is about 2 %. The mean comparison error for 5415 is quite small, 0.3 %, while the mean standard deviation is larger than for the other towed cases: 3.2 %.

Table 2.1 shows the statistics for all cases, and indicates the accuracy obtainable for each case. Even more interesting is however the information found on the last line: the mean error and the mean standard deviation (weighted by number of entries) for all cases. The mean error for all computed cases is practically zero; only -0.1 %, while the mean standard deviation is 2.1 %; a surprisingly small value. In the 2005 workshop the mean error of all 40 submissions was in fact equally small: 0.1 %, while the mean standard deviation was 4.7 %. While the distribution between "simple" and "difficult" cases is not the same in the two workshops, it seems safe to conclude that the scatter has been reduced considerably. In fact, even the largest standard deviation in the present computations (cases 3.1b and 3.2) is smaller than the mean standard deviation in 2005.

In the table a split has also been made between high and low Froude numbers. As will be seen below, the accuracy in these two regions differs considerably when it comes to sinkage and trim, but for resistance this difference it not significant.

We will now turn to the second question above: how to learn from the computed results. The first question is: *how dependent are the results on the grid size*? Note that this is a comparison of completely unsystematically varied grids and methods, as opposed to the systematically varied grids for each method to be described in the next section. In Fig. 2.1 the error of all computed results is plotted versus grid size. There is also a coding of the points where filled symbols represent fixed cases and open ones cases free to sink and trim. Each hull has a symbol, except KCS which has one symbol for towing and one for self-propulsion. Note that the largest grid

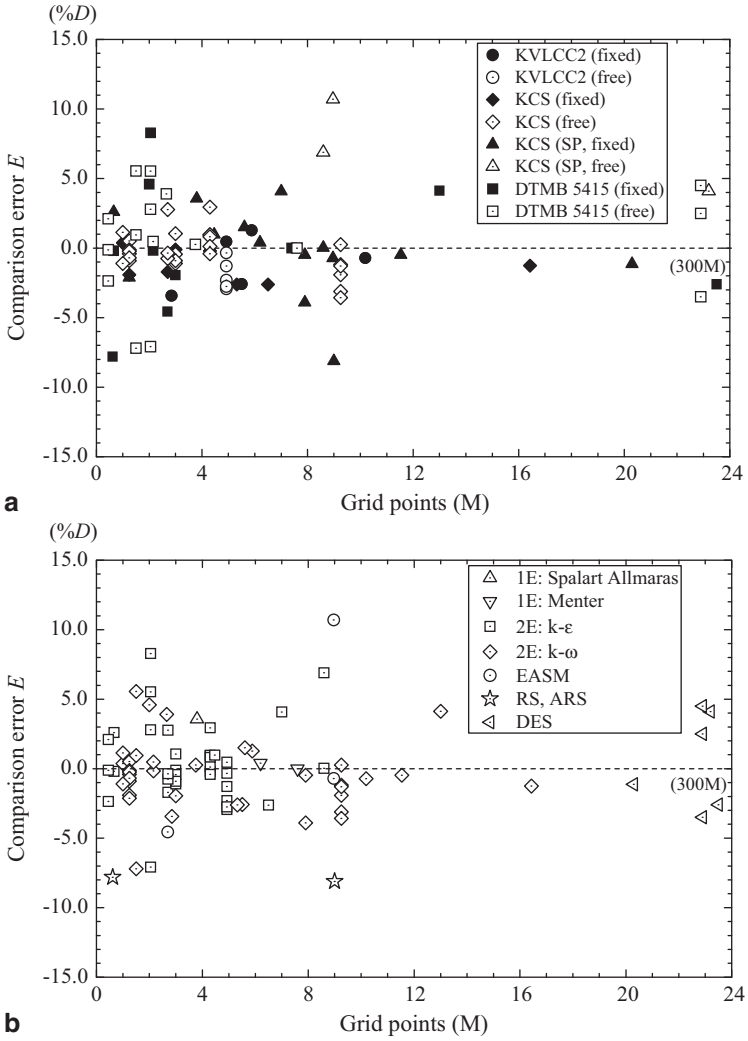


Fig. 2.1 **a** Comparison error for all resistance submissions versus grid size. **b** Comparison error for all resistance submissions versus grid size

is much larger than the others (300 M cells) and has been moved into the plot and marked 300 M.

Analyzing Fig. 2.1a it is seen that about 90 % of all computations are made with grids smaller than 10 M cells. The scatter within this range seems to be significantly larger than for the larger grids. However, this is mainly caused by the large scatter of the self-propulsion submissions (triangle symbols), so if these are excluded, and only towed resistance is considered, there is no error decrease above 3 M grid points. All points seem to be within approximately ± 4 %. Not even the very large grid at

300 M cells shows any significant improvement; it is slightly below 3 %. However, below 3 M cells the maximum errors increase to about 8 %.

The second lesson to learn from the computed results is: *how dependent are the results of the turbulence model?* In Fig. 2.1b the same points as in Fig. 2.1a are plotted, but with a different symbol coding. Each symbol represents a turbulence model. Up-triangle symbol means 1-equation Spalart-Allmaras models, down-triangle symbol means 1-equation Menter models, square symbol means 2-equation k-ε models, diamond symbol represents 2-equation k-ω models, circle symbol represents Explicit Algebraic Stress Models (EASM), star symbol Reynolds stress models and left-triangle Detached Eddy Simulation models (DES). There is a large number of entries for the 2-equation models so for them the statistical basis is rather good. For the others there are rather few entries, but a reasonable conclusion is that a more advanced model is not a guarantee for a good result, even with a large number of grid points.

Table 2.2 gives the statistics for the different models. Note again that there are very few entries for some of them. The relatively poor result for the more advanced methods is apparent, while the simpler 2-equation models seem to do a good job. EASM and RS, ARS suffer from one bad point for a very coarse grid and two bad points computed for the self-propulsion cases, which may be more difficult than the towed cases, while the three very good results for the Menter model were obtained with the same code and user.

1.2 Grid Dependence and Uncertainty

In this Section a brief analysis of the uncertainty of the computed resistance will be presented. A more comprehensive discussion is found in Chap. 5.

According to standard procedures (see e.g. ITTC 2008) the comparison error $E = D\text{-}S$ is to be compared with the validation uncertainty U_{val}, defined as $U_{val^2} = U_{SN^2} + U_{D^2}$, where the numerical uncertainty $U_{SN^2} = U_{G^2} + U_{I^2}$ and U_D is the data uncertainty specified in Table 2.1. U_G and U_I are the grid and iterative uncertainties, resp. In the ITTC vocabulary, if $|E| \leq U_{val}$, validation has been achieved at the U_{val} level, meaning that the error is within the "noise level". If on the other hand $|E| \gg U_{val}$, validation has not been achieved and the sign and magnitude of E could be used to improve the CFD modeling.

Thus, to compute the numerical uncertainty U_{SN} we need the grid uncertainty U_G and the iterative uncertainty U_I. Information about both quantities was requested by the organizers. To obtain $U_{G,}$ participants were asked to provide solutions for at least three grids and the estimated U_I was to be compared with the difference between the solutions on the two finest grids, ε_{12}. For $|U_I/\varepsilon_{12}| \ll 1$ the effect of the iterative error may be neglected. Unfortunately these instructions were not well followed and more than half of the submissions were with only one grid. This is a pity, since for the first time a large scale test could have been made of the proposals made in the literature for estimating the grid uncertainty U_G through systematic grid variations.

There are essentially two such procedures in use: the ITTC procedure (ITTC 2008) based on the work at the Iowa University (for the most recent development

Table 2.2 Mean comparison errors for the turbulence models

Turbulence model	E_{mean}	$\|E\|_{mean}$	No. of entries
1-E Spalart Allmaras	3.6	3.6	1
1-E Menter	0.1	0.1	3
2-E k-ε	0.3	2.1	37
2-E k-ω	−0.5	1.8	37
EASM	1.8	5.9	3
RS, ARS	−8.0	−8.0	2
DES	0.6	3.1	6

along this line, see Xing and Stern 2010) and the procedure stemming from the three Workshops on CFD Uncertainty held in Lisbon during the last decade (for the most recent development of this procedure, see Eça et al. 2010). Both procedures are based on systematic grid variations for a number of simple test cases. There is however very little information in the literature of how well the procedures can be applied to cases of industrial interest. As pointed out in Eça et al. (2010) such cases are prone to include perturbations of the solutions for various reasons, such as not exactly scaled grids (aspect ratio, skewness, etc), limiters of different kinds in turbulence models and numerical schemes, and post processing errors. Even more important is perhaps also the fact that iterative convergence may be so slow in real applications, particularly for fine grids, that the iterations are stopped prematurely with an iterative error too large to be neglected. Any perturbation of this kind will affect the difference between the successively refined solutions, which is the basis for all methods for uncertainty estimation based on grid sequencing.

Although many grid variations are missing we have a substantial number of submissions with such variations. There is in fact a large difference between the cases. For KVLCC2 *all* resistance submissions include grid variations, while for 5415 this is so for less than 25 % of the submissions. For KCS the number is around 40 %. The reported results will be used below to shed some light on the most important question:

- *How useful is grid sequencing for numerical uncertainty estimates in cases of industrial relevance?*

It will be hard to give a strict answer to this question, but some indications may be found, as will be seen below. A relevant question is however what happened to the submissions which did not report grid variations. Was that due to failure to apply proposed procedures or were variations not tried?

To start with, the reported iterative convergence U_I may be analyzed. As stated, this must be small enough not to affect the solution differences significantly, and as a practical limit U_I may be set to 10 % of the difference between the two finest grid solutions, ε_{12}. It should be stated that this limit is not substantiated by systematic investigations, and it is not a very strict requirement. Nevertheless 25 % of the reported grid convergence studies do not satisfy this criterion and in some cases U_I is of the same order as $\varepsilon_{12.}$ This is a source of scatter in the reported results. It should be pointed out that even the determination of U_I is not unambiguous. In most cases it is determined as the amplitude of the resistance fluctuation over one or more wave lengths at the end of the iterations.

Methods for estimating the discretization error U_G from systematic grid variations are based on the fact that the error of the numerical solution can be expressed as a series expansion in the typical step size of the grid, h. The order of accuracy of the method, p, is determined by the first term in the series, proportional to h^p. As h is reduced the importance of this term increases and for sufficiently small h the influence of all other terms may be neglected. h is then said to be in the "asymptotic range". Since the error is proportional to h^p it may be computed if the constant of proportionality (α) is known, and the solution S_0 at zero step size may be obtained from the formula $S_0 = S_1 - \alpha h^p$, where S_1 is a known solution. To determine α, another solution S_2 is required. This technique is known as Richardson extrapolation. If p is not known a priori a third solution S_3 is required. From the three known solutions S_1, S_2 and S_3 the three unknowns S_0, α and p are computed.

Richardson extrapolation in its original form is of limited practical value since h is seldom in the asymptotic range, at least not for cases of interest in hydrodynamics. However, the equation for S_0 is still used. The power p will then be influenced by the neglected higher order terms in the error expansion and will thus be different from the theoretical order of magnitude p_{th} of the method. The difference between p and p_{th}, or the ratio p/p_{th} is then used as a measure of the "distance" to the asymptotic range.

In Richardson extrapolation methods the error in the solution S_1, i.e. $S_1 - S_0$ is denoted δ_{RE}. This quantity is taken as a metric for the numerical uncertainty. In the original approach by Roache (1998) δ_{RE} was multiplied by a safety factor FS to estimate the numerical (grid) uncertainty U_G. The factor was either 1.25 or 3, depending on conditions. In the most recent developments of the Iowa method (Xing and Stern 2010) FS is computed from p/p_{th} using two empirical formulas; one for values above unity and one for smaller values. The original Iowa method, endorsed by the ITTC (ITTC 2008) is slightly more complicated but the basic idea is the same. Eça and Hoekstra (see Eça et al. 2010) use different formulas for U_G in different ranges of p. For most conditions these formulas are based on δ_{RE}. The exact formulas for both methods are given in Chap. 5.

In Fig. 2.2 all grid variation studies submitted to the Workshop (for resistance) are presented, case by case. The comparison error E is plotted against grid density represented by the non-dimensional step size h_i/h_1, where h_i is the step size of grid i and h_1 refers to the finest grid. In the legend the submitting organization is given, followed by the type of grid used. The notations for the grids are S, MS, OS, U and MU, which stand for single block structured, multi-block structured, overlapping structured, single block unstructured and multi-block unstructured, respectively. Within the round brackets the step ratio, r_G between successive computations is given first, followed by the ratio of the observed and theoretical order of accuracy. There are altogether 40 grid variations in Fig. 2.2. Surprisingly enough 33 of these are for structured grids. In general, the grid convergence is quite good for these grids. Visual inspection yields that almost all converge monotonically, i.e. $0 < R < 1$, where $R = (S_1 - S_2)/(S_2 - S_3)$ and S_n represents the solution on the n:th grid. Only one seems to be divergent ($R > 1$) and one oscillatory ($-1 > R > 0$). The convergence characteristics are confirmed by the given p, but this has not been computed for all cases.

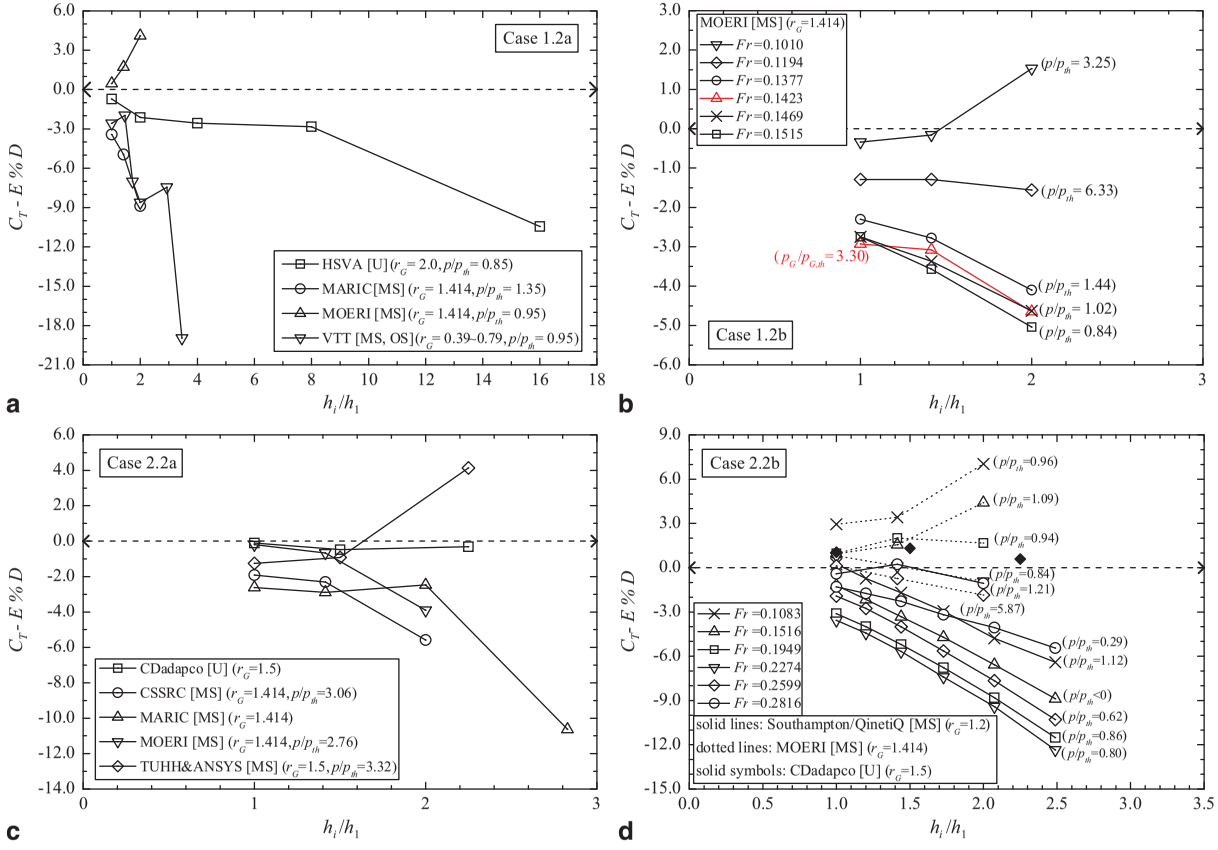


Fig. 2.2 **a** Grid dependence of C_T comparison error E in Case 1.2a. **b** Grid dependence of C_T comparison error E in Case 1.2b. **c** Grid dependence of C_T comparison error E in Case 2.2a. **d** Grid dependence of C_T comparison error E in Case 2.2b. **e** Grid dependence of C_T comparison error E in Case 2.3a. **f** Grid dependence of C_T comparison error E in Case 2.3b. **g** Grid dependence of C_T comparison error E in Case 3.1a and 3.1b. **h** Grid dependence of C_T comparison error E in Case 3.2

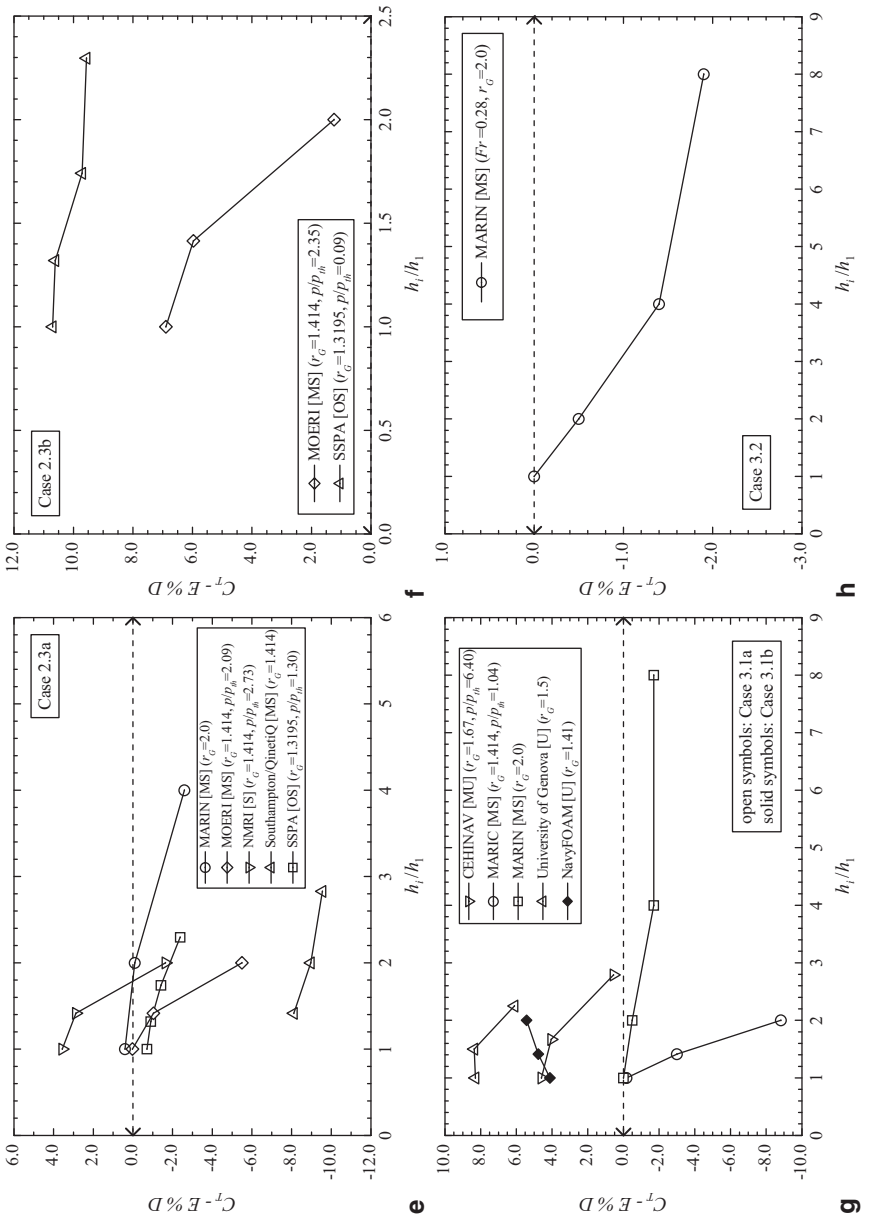


Fig. 2.2 (continued)

As expected, the situation is considerably worse for the unstructured grids, for which only one exhibits monotonic convergence, while two are divergent and four are oscillatory. This is most likely due to the inherent variation in cell geometry during the refinement process. There must be a larger scatter than for the structured grids, but nevertheless a very small dependence on grid density is demonstrated for several of the unstructured methods, notably that of CDadapco (2.2a, 2.2b) and MARIC (2.2a, for smaller step sizes).

Very few of the structured grids have more than three step sizes, the requested minimum. This makes it difficult to investigate the scatter. The largest grid variation was carried out by VTT with 9 grids in Case 1.2a. (only six are shown in Fig. 2.2a, since the others are outside the range of errors.) The grids were obtained from three original grids, and each one was refined twice by a factor of two. From the results it seems as though each one of the original grids has its own smooth convergence line, but taken together the convergence is quite irregular. This has to be further investigated. The most instructive variation is that of Southampton/Qinetiq in 2.2b. Six systematically varied grids were used for all Froude numbers and the variation is surprisingly smooth. Four grids were used by MARIN in 3.a and 3.2, and by SSPA in 2.3a and b, but it is hard to draw conclusions from so few grids.

So, for the structured grids monotonic convergence is obtained for the vast majority of cases, which indicates that grid convergence studies may be useful in the estimation of the discretization error. The question is how well the proposed quantitative techniques work. As mentioned the achieved p is used to determine the distance to the asymptotic range and thereby the numerical uncertainty. Therefore the distribution of the values of p reported by the participants is of interest. It turns out that of the reported 29 values of p 18 are larger than the theoretical value and 11 smaller. The mean value of p/p_{th} for those below 1 is 0.74, while the mean for those above in 2.7.

The values below 1 could be explained by deviations from the theoretical order of certain elements in the numerical method. Such elements may the turbulence model, an improper implementation of a boundary condition or a limiter for reducing the numerical order of accuracy in regions of large gradients. As the step size tends to zero the total order of the method tends towards the lowest order of any element of the method. For the step sizes used in the present calculations this may well mean an order of accuracy 74 % of the nominal one. It should be noted that improper convergence rates may be detected through code verification studies (see e.g. Eça et al. 2010). It is not known to what extent such studies have been carried out for the codes used in the present computations.

While at least part of the low order convergences might be explained by deficiencies in the method this is not possible for the convergence rates above the nominal one. The many large values of p/p_{th} (up to 6), and the mean value of 2.7 is a matter of concern. Such large values are clearly outside the statistical base for the empirical uncertainty methods (Xing and Stern 2010; Eça et al. 2010). In fact the Iowa method predicts a very large safety factor for $p/p_{th} = 2.7$, namely 28.7! Eca & Hoekstra specify a safety factor of 3, but with δ_{RE} computed using the theoretical p and a curve fit to the data. The difference between the two methods is considerably smaller than it looks, however, as the nominal δ_{RE} in the Eca and Hoekstra method is considerably

Table 2.3 Sinkage statistics, all free cases

Hull	Case No.	*Fr*	$E_{mean}\%D$	$\sigma_{SD}\%D$	$U_D\%D$	No. of Entries
KVLCC2	1.2b	0.1010	−90.1	–	–	1
		0.1194	−26.1	–	–	1
		0.1377	−20.9	–	–	1
		0.1423	−18.2	–	–	1
		0.1369	−23.3	–	–	1
		0.1515	−21.3	–	–	1
	Mean of KVLCC2		*−33.3*	–		
KCS	2.2b	0.1083	−67.1	8.2	–	4
		0.1516	−44.1	15.1	–	3
		0.1949	−12.9	6.6	–	4
		0.2274	−4.2	4.1	–	6
		0.2599	1.5	4.8	–	4
		0.2816	−2.1	5.6	–	6
	2.3b	0.26	−24.3	25.1	–	2
	Mean of KCS		*−21.9*	*9.9*	–	
5415	3.2	0.138	31.4	17.7	–	5
		0.28	3.1 (8.1)	10.3 (−)	11.2 (1.4)	6(1)
		0.41	6.5	13.8	4.4	5
	Mean of 5415		*13.7*	*13.9*		
Mean of cases with $Fn < 0.2$		$E_{mean,\,Fn<0.2} = -29.3\,\%D$		$\sigma_{SD\,mean,\,Fn<0.2} = 11.9\,\%D$		22
Mean of cases with $Fn > 0.2$		$E_{mean,\,Fn>0.2} = -4.5\,\%D$		$\sigma_{SD\,mean,\,Fn>0.2} = 10.7\,\%D$		29
Mean of all cases		$E_{mean,\,all\ cases} = -21.0\,\%D$		$\sigma_{SD\,mean} = 11.2\,\%D$		51

larger than the real δ_{RE} computed with the achieved (very high) p. On the other hand, it is not very useful to base the uncertainty formulas on statistics from simple cases with large p:s since the large values here are likely to be due to scatter, rather than a strong influence from higher order error terms due to a too coarse grid. In any case these computations indicate that a large emphasis should be placed on p values very different from the theoretical one; p/p_{th} close to 1 is an exception!

The good news learnt from this section is that practically all methods using structured grids seem to converge monotonically with grid refinement. There is good hope for uncertainty assessment methods, but emphasis should be placed on convergence rates quite different from the theoretical one. A final remark will close this Section: we have seen the good convergence for systematically varied grid densities in a given grid and CFD solver, but as seen in the previous Section there was not even a tendency of improving solutions with grid refinement for different grids and solvers. Why?

2 Sinkage and Trim

A statistical evaluation of the sinkage for all free cases is presented in Table 2.3. The same quantities as for resistance are given. There is however no information of the experimental uncertainty for KVLCC2 and KCS, and for 5415 it is available only for the two highest Froude numbers, see Appendix.

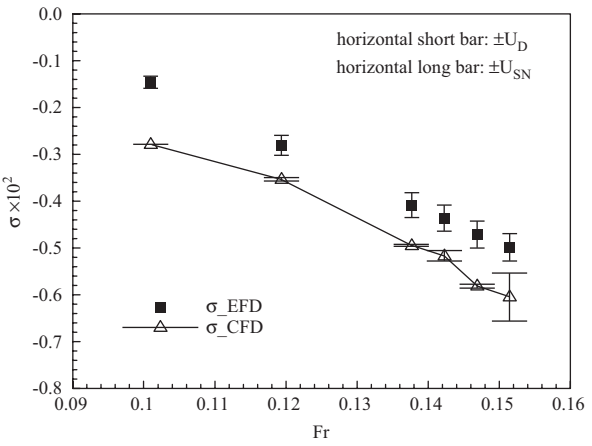


Fig. 2.3 Sinkage (σ) versus *Fr*, with error bars, Case 1.2b (MOERI-WAVIS)

It is seen immediately that the mean comparison errors are considerably larger than for the resistance. This is so particularly at the lowest Froude numbers for KVLCC2 and KCS, which are 90 and 67 % over predicted, respectively. At the higher Froude numbers the error drops to about 20 % for KVLCC2, while it goes down to almost zero for KCS. The mean error is quite large also for 5415 at the lowest Froude number, but it drops to rather small values for the higher Froude numbers. The only case computed in 2005 is the intermediate Froude number 0.28, and there is an apparent improvement in accuracy, but the statistical basis is too small to draw any conclusion. Comparing the hulls, it is seen that the slowest hull, the KVLCC2 has the largest errors, while both the error and standard deviation are reduced for the other two hulls. The mean values for all cases are reported on the last row, and in the second and third row from the bottom a split has been made between high and low Froude numbers. As expected there is a clear reduction in error in the high Froude number range.

Fig. 2.3 shows the predicted and measured sinkage versus Froude number for the only submission for Case 1.2b, MOERI-WAVIS. It is seen that there is a more or less constant shift of computed values below the measured ones. The shift is considerably larger than the stated numerical and measurement accuracy, but in absolute terms it is only about 1 mm.

The generally smaller comparison errors of Case 2.2b are clearly displayed in Fig. 2.4, where there is an apparently very good fit to the data over the whole speed range. There seems to be a consistent under prediction of the sinkage at the lower speeds, but again it is very small in absolute terms, about 1 mm. In spite of this the relative error becomes very large at these speeds.

There is no reason why sinkage should be more difficult to compute than resistance. Sinkage is almost entirely due to pressure forces which add up to a relatively large vertical force. In Fig. 2.5 the top part shows a vertical view of the pressure on the KVLCC2 as computed for the double model case (Zou et al. 2010). It is seen that practically the whole surface in this view has a negative pressure coefficient contributing to a downward force. In the other two views, from the bow and stern, there are

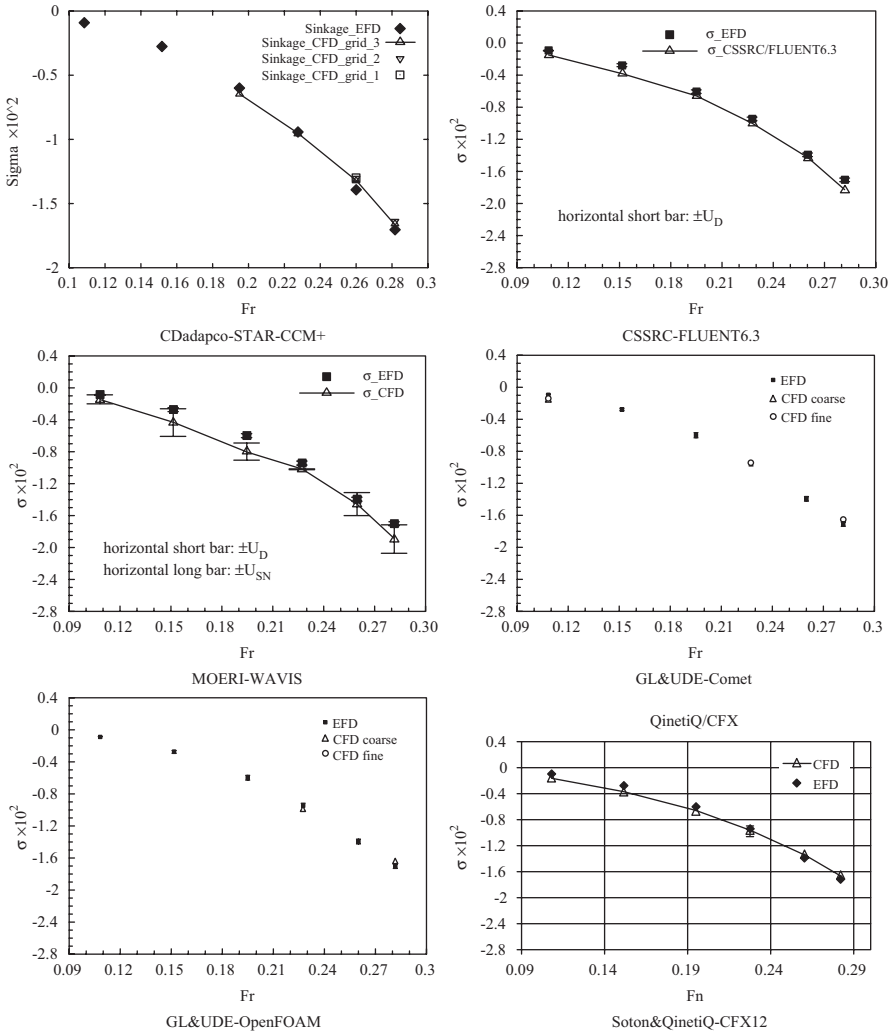


Fig. 2.4 Sinkage (σ) versus *Fr*, Case 2.2b (All six submissions)

regions of very large pressure coefficients, both positive and negative. These opposing contributions to the longitudinal force practically cancel, and the small difference is the pressure resistance. The ratio of vertical and longitudinal pressure forces in this case is about 20! If friction is added the ratio becomes approximately 5. Therefore it should be easier to compute the sinkage force than the resistance. However, the sinkage is more dependent on the deformation of the free surface than the resistance. Around the hull the water surface is generally lowered due to the slight under-pressure caused by the over-velocities due to the displacement effect of the hull. The accuracy in the predicted water level thus influences the sinkage

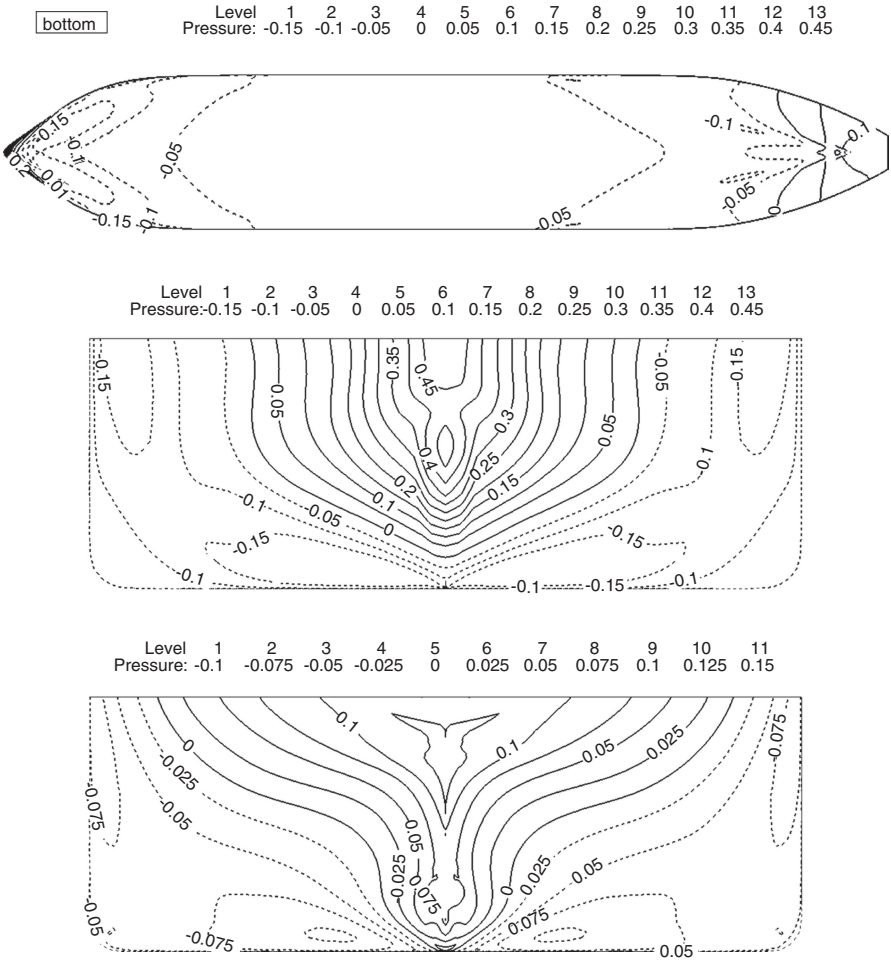


Fig. 2.5 Pressure distribution on the KVLCC2 *Top*: vertical view; *middle*: bow view; *bottom*: stern view. Negative pressure: *dotted line*

prediction. This accuracy can be evaluated from the wave plots. Since the largest sinkage errors were found in Case 1.2b, where MOERI-WAVIS was the only contributor (Fig. 2.3) it is of interest to see how accurately the free surface waves were predicted by this code.

In Fig. 2.6 the wave cut closest to the hull at $Fr = 0.142$ is shown. There is a remarkable correspondence between the simulations and the data. Every detail of the wave is accurately represented. If the code can predict the very difficult wave this accurately it must be able to compute the much simpler general lowering of the surface (sometimes called the Bernoulli wave) at any Froude number with a very high accuracy. This leads to the conclusion that the large comparison errors in the low speed range of Table 2.3 are rather due to difficulties of measuring the very small sinkage accurately than to inaccuracy in the numerical prediction. This

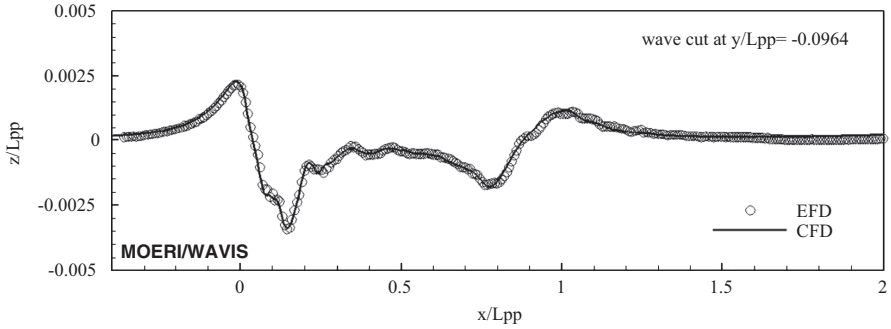


Fig. 2.6 Wave cut at $y/L_{PP} = -0.0964$. Predictions by MOERI-WAVIS

Table 2.4 Trim statistics, all free cases

Hull	Case No.	*Fr*	$E_{mean}\%D$	$\sigma_{SD}\%D$	$U_D\%D$	No. of Entries
KVLCC2	1.2b	0.1010	17.1	–	10.1	1
		0.1194	12.7	–	8.8	1
		0.1377	4.8	–	7.6	1
		0.1423	3.2	–	7.4	1
		0.1369	0.8	–	7.1	1
		0.1515	5.9	–	6.8	1
	Mean of KVLCC2		*7.4*	–		
KCS	2.2b	0.1083	−60.3	38.6	9.6	4
		0.1516	0.7	4.9	6.8	3
		0.1949	1.6	3.8	4.6	4
		0.2274	−3.2	4.6	3.3	6
		0.2599	−3.1	3.0	2.3	4
		0.2816	3.6	4.2	1.8	6
	2.3b	0.26	−6.6	19.3	–	2
	Mean of KCS		*−9.6*	*11.2*		
5415	3.2	0.138	164.6	243.6	7.6	5
		0.28	36.6 (2.1)	−56.4 (−)	4.7 (1.8)	6(1)
		0.41	−9.0	10.5	0.9	5
	Mean of 5415		*64.1*	*65.9*		
Mean of cases with $Fn < 0.2$		$E_{mean,\,Fn<0.2} = 15.1\,\%D$		$\sigma_{SD\,mean,\,Fn<0.2} = 72.7\,\%D$		22
Mean of cases with $Fn > 0.2$		$E_{mean,\,Fn>0.2} = -3.7\,\%D$		$\sigma_{SD\,mean,\,Fn>0.2} = 8.3\,\%D$		29
Mean of all cases		$E_{mean,\,all\,cases} = 8.9\,\%D$		$\sigma_{SD\,mean} = 36.9\,\%D$		51

conclusion is supported by the sinkage and trim uncertainty analysis reported in the Appendix. Although results are presented only for one facility and one hull, a general conclusion is that it is very difficult to measure sinkage of the order of 1 mm due to the extreme requirements on the levelness of the rails for such cases. Further support for the conclusion is also found in the additional computations presented in Chap. 7.5, where results from Chalmers and ECN-CNRS are shown to coincide very well with those of MOERI, in spite of different ways to treat the free surface.

In Table 2.4 a statistical evaluation is shown for the predicted trim of all free cases. It is seen that the mean comparison error is relatively small for most Froude numbers

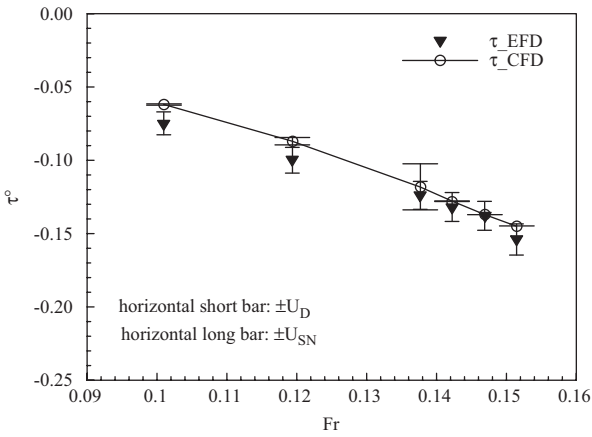


Fig. 2.7 Trim (τ) versus *Fr*, with error bars, Case 1.2b. (MOERI-WAVIS)

in the KVLCC2 and KCS cases. Again there is a problem at the lowest speeds, where the trim is very small. For Case 2.2b the measured trim is 0.017 degrees at Froude number 0.1083. This corresponds to a difference in sinkage of 2 mm between bow and stern for the 7.3 m model.

The errors for 5415 in Table 2.4 are extremely large, at least for the lowest Froude number 0.138. Looking at the individual contributions it turns out that the large E and σ are due to two submissions, while the error for the other three is about 20 %. The reason for the large errors is not discussed in the paper for one of these submissions and the paper is missing for the other. At the intermediate Froude number 0.28 the errors are still very large for these submissions, while the mean error for the other four it is around 10 %. At the highest Froude number, 0.41 all are in the range 6–20 %.

As expected, the last rows of Table 2.4 show that the mean comparison errors in the high speed range are much smaller than those in the low speed range, considering all cases.

Looking at Fig. 2.5 it is seen that there are forces at the bow and stern that cooperate to generate a trim: the strong suction at the forward bilges and the high pressure at the aft end, which both tend to generate a bow down trim. However, there is also a significant area aft of midship where the forces tend to generate a bow up trim. Therefore it should be somewhat more difficult to predict the trim than the sinkage, but more simple than the resistance, provided there is no problem predicting the slope of the disturbed surface around the ship. Again referring to Fig. 2.6 this is not the case for MOERI-WAVIS, the only contributor to 1.2b. Their results could be expected to be very accurate, so the relatively large comparison error for the lowest Froude number is likely to be due to difficulties measuring the very small trim (again, see Appendix). The results are displayed in Fig. 2.7. As expected the error bars overlap at the four higher Froude numbers, but not at the lowest ones.

The results of all predictions for 2.2b are shown in Fig. 2.8. There is a very good correspondence between data and computations. Even the sharp rise in the curve at the highest Froude number is predicted well. At the lowest speed (not computed by all) there is however a systematic under prediction relative to the measured value.

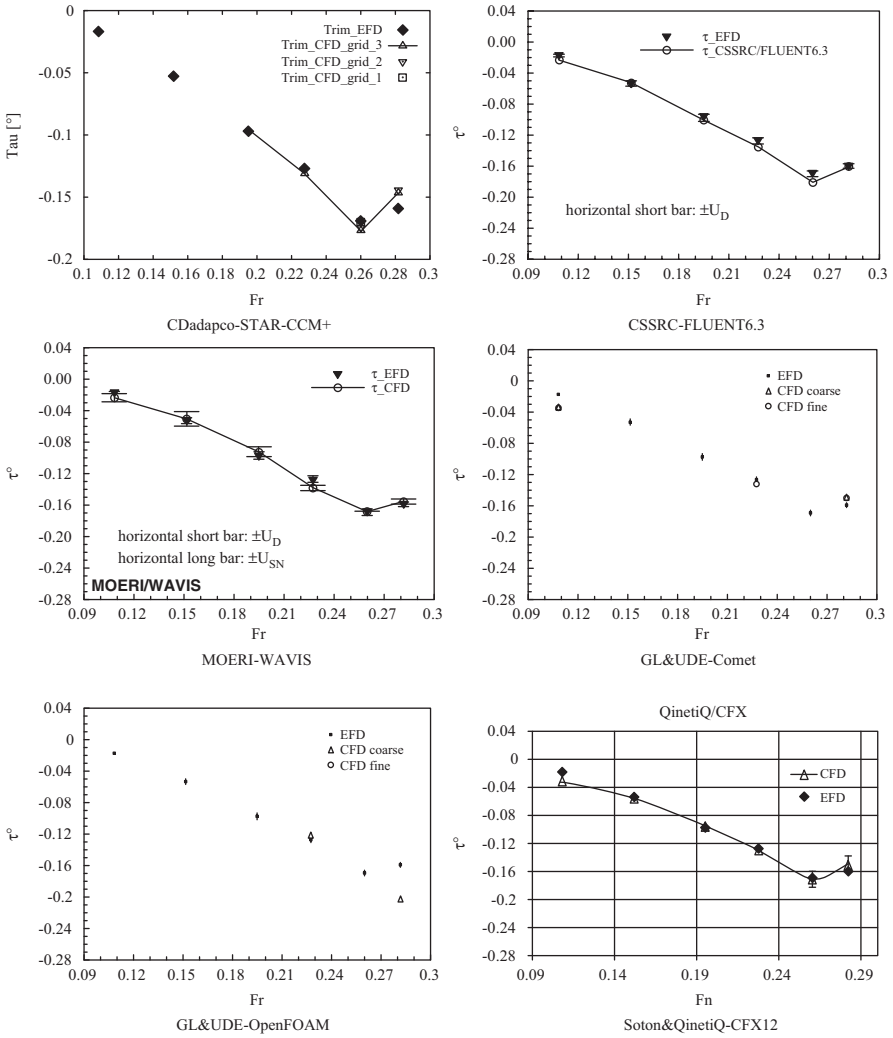


Fig. 2.8 Trim (τ) versus *Fr*, Case 2.2b. (All six submissions)

3 Self-Propulsion

Self-propulsion results were requested only for the KCS hull and only at one Froude number: 0.26. In Case 2.3a the hull was kept fixed in the zero speed attitude, while in 2.3b the hull was free to sink and trim. Experimental data are available from NMRI for a 7.3 m hull in 2.3a and from FORCE for a 4.4 m hull in 2.3b. The NMRI hull was without a rudder, while a rudder was fitted to the FORCE hull.

In 2.3a computations were requested for the model at the *ship point*, i.e. the hull was towed to account for the larger skin friction at model scale compared to full scale.

Table 2.5 Summary of self-propulsion computations. (KCS hull)

Case no.	Classification	Group	Prop. model	*E%D*			
				K_T	K_Q	n	$R_{T(SP)} - T$
2.3a	Given n, actual propeller	CSSRC	A	0.06	−1.39	–	−8.03
		MARIC	A	4.12	−2.88	–	−4.12
		SNUTT	A	−1.94	−7.99	–	−3.43
		SSRC(1)	A	3.35	−0.35	–	−8.89
		TUHH-FDS&ANSYS	A	6.47	−0.42	–	−14.38
	Given *SFC*, actual propeller	CTO	A	11.65	1.77	−3.16	–
		IIHR	A	0.65	−2.81	−1.27	–
		SSRC(2)	A	−1.59	−3.82	−2.11	–
	Given *SFC*, modeled propeller	IIHR/SJTU	BP	2.4	1	0.7	–
		MARIN	BE	−4.7	−7.3	2.6	–
		MOERI	BS	1.76	0.66	−1.11	–
		NMRI	BX	−6.53	−16.32	5.68	–
		South/QinetiQ	BP	−18.92	−17.99	1.49	–
		SSPA	BL	−5.34	−6.26	2.34	–
2.3b	Given *SFC*, act. or mod. propeller	IIHR	A	6.7	5.1	−2	–
		MOERI	BS	12.13	12.55	−3.87	–
		SSPA	BL	−0.18	2.45	4.98	–

A actual propeller, *BP* prescribed body force, *BL* lifting line, *BS* lifting surface, *BE* boundary element, *BX* other body force

This force, the skin friction correction, *SFC*, was pre-computed and was the same as in the measurements. In the experiments the thrust T, was adjusted by varying the rpm, n, such that $T = R_{T(SP)} - SFC$, where $R_{T(SP)}$ is the resistance in self-propulsion. Most of the participants did the simulations in this way, i.e. the force balancing was automatically achieved by the flow code. An alternative was to avoid the balancing and use the measured rpm in the simulation. In the first case the achieved n was requested, while in the second case the resulting towing force $R_{T(SP)} - T$ was to be reported. In 2.3b computations were carried out for the *model point*, so no towing force was applied, but the balancing was carried out in the same way as in 2.3a.

The flow codes may thus be classified with respect to the way the rpm was handled: either adjusted to achieve the given *SFC* or fixed to the given n. Another classification is to split between methods with a real rotating propeller (*actual propeller*) and a propeller modeled is some way. Several such models were used, as is seen in Table 2.5, which summarizes all self-propulsion results in 2.3a and b. It is seen that altogether there were 5 groups using the given n and 12 groups with force balancing to achieve the given *SFC*. Of the 17 submissions 9 used a real rotating propeller, while 8 used a model, which is specified in column four. The comparison errors are given in the

Table 2.6 Error statistics, Cases 2.3a and b

Items (No. Entries/Total)	K_T		K_Q		n		$R_T(SP) - T$	
	E%D mean	σ_{SD}*%D mean*	*E%D mean*	σ_{SD}*%D mean*	*E%D mean*	σ_{SD}*%D mean*	*E%D mean*	σ_{SD}*%D mean*
Actual prop. (9/17)	3.3	4.1	−1.4	2.6	−2.1	0.8	−7.8	3.9
Modeled prop. (8/17)	−2.4	8.0	−3.9	7.9	1.6	3.3	–	–
Given SFC (12/17)	−0.2	7.8	−2.6	6.7	0.4	3.3	–	–
Given *n* (5/17)	2.4	3.3	−2.6	3.2	–	–	−7.8	4.4
Case2.3a (14/17)	−0.6	7.2	−4.6	6.1	0.6	2.8	−7.8	4.4
Case2.3b (3/17)	6.2	6.2	6.7	5.2	−0.3	4.7	–	–
Mean Case 2.3a&b	0.6	7.0	−2.6	6.0	0.4	3.1	−7.8	3.6

four rightmost columns, for K_T, K_Q, n and the towing force $R_{T(SP)} - T$. For cases with a given n the computed towing force is given and vice versa.

We may use the computed results to try to answer the following questions related to the prediction of K_T, K_Q, n and $R_{T(SP)} - T$:

- *How strong is the relation between grid size and accuracy?*
- *Is there a difference in accuracy between actual propeller simulations and simulations with a modeled propeller?*
- *Are the more advanced propeller models better than the simpler ones?*
- *Is there a difference in accuracy between predictions with force balancing (given SFC) and with given rpm?*
- *Are the errors smaller for a fixed model than for a model free to sink and trim?*

To better display the errors similar plots as for the resistance are given in Figs. 2.9a–d. Again, the vast majority of grids have less than 10 M cells, 14 out of 17. (These computations are a subset of those for the resistance). There is a clear difference in scatter between the three predictions in the range 10–24 M cells and those below 10 M. For K_T, K_Q and n the maximum scatter in the upper range is around ± 7, 5 and 2 %, respectively, while in the lower range it is within 19, 18 and 6 %. For the towing force $R_{T(SP)} - T$ there are very few entries and the largest error is for an 11.5 M grid. All quantities but n have considerably larger errors than resistance.

Of more interest is perhaps the difference between the actual and modeled propellers and between the force-balanced and fixed rpm cases. Difficulties of handling the free-to-sink-and-trim case may be revealed by comparing 2.3a and b, so the available set of results may be cut in different directions. In the following we will look at these different aspects, and to get a more quantitative base for the comparisons Table 2.6 has been prepared. Here actual propeller results may be compared with those from modeled propellers, computations with a given *SFC* with those with a given n, and the fixed attitude results from 2.3a with the free attitude results from 2.3b. The comparisons are made in terms of the mean error E_{mean} and the mean standard deviation σ_{SDmean}, both in per cent of the experimental data.

In Figs. 2.9a–d actual propellers are displayed as triangles and diamonds, while modeled ones are represented by circles. There is a clear trend of smaller scatter for the actual propellers in the K_T, K_Q and n plots (for $R_{T(SP)} - T$ there are only actual propellers represented). These findings are confirmed in Table 2.5. All three

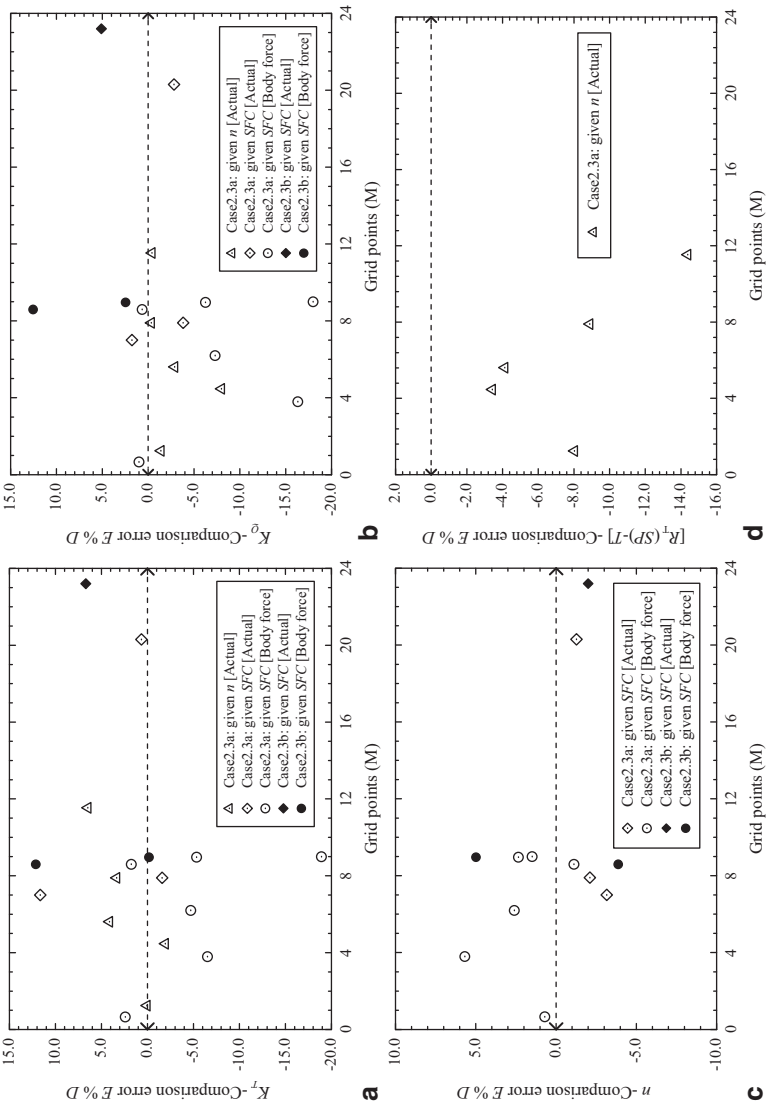


Fig. 2.9 **a** Comparison error for K_T versus grid size. **b** Comparison error for K_Q versus grid size. **c** Comparison error for n versus grid size. Given towing force: $R_{T(SP)} - T = SFC$. **d** Comparison error for $R_{T(SP)} - T$ versus grid size. Given n

quantities have a smaller σ_{SDmean} for the actual propellers than for the modeled ones, and the difference is particularly large K_Q. For the mean error E_{mean} there is no clear trend.

Since there are so few submissions in each category of propeller models, it is difficult to draw conclusions on the accuracy of the different models. The simplest model, a prescribed body force is used in two submissions, one of which (IIHR/SJTU) with very good results. For the other submission (South/QinetiQ) the errors are very large. The situation is similar for the lifting surface methods; one very good (MOERI, 2.3a) and one rather bad (MOERI, 2.3b) submission. On the average, the theoretically much simpler lifting line method (SSPA 2.3a and b) seems to be at least as accurate, and the single submission with a BEM method (MARIN) is no better than the lifting line method.

Computations with force balancing are represented by diamond and circle symbols in Figs. 2.9a–d, while those with given rpm are shown by triangle symbols. There is an obvious difference in scatter of the K_T and K_Q results between the two cases and this is confirmed in Table 2.6. σ_{SDmean} for given n is less than half of that for given towing force, while the mean error E_{mean} is somewhat larger for K_T. The most surprising result here is the large over prediction of the towing force for given rpm shown in Fig. 2.9c and confirmed in Table 2.6. If n is given, the towing force is significantly over predicted, while if SFC is given (and the forces balanced) the rpm is computed very well (see the relatively small values of E_{mean} and σ_{SDmean} for n). If the propeller is relatively lightly loaded a small (percentage) change in n may correspond to a relatively large (percentage) change in thrust and a corresponding large change in towing force to acquire force balance.

In Figs. 2.9a–d results for Case 2.3a are represented by open symbols, while filled symbols represent Case 2.3b. It is seen immediately that the small number of results for 2.3b (only 3) makes it very difficult to draw conclusions concerning the differences in accuracy between the two cases. E_{mean} and σ_{SDmean} for all quantities have been computed and presented in Table 2.6, but we will refrain from drawing any conclusions.

The last line of Table 2.6 is perhaps the most interesting one. Here we have the mean values of all self-propulsion submissions. These numbers may give a general indication of the accuracy obtainable in self-propulsion predictions. For K_T the mean error is 0.6 $\%D$ and the mean standard deviation 7 $\%D$ and the corresponding values for K_Q are $-2.6\,\%D$ and 6 $\%D$, respectively. The predicted n for a given SFC has a mean error of 0.4 $\%D$ and a standard deviation of 3.1 $\%D$, while the numbers are larger for the towing force for given n: $-7.8\,\%D$ and 3.6 $\%D$, respectively.

4 Wave Pattern

Wave pattern predictions in the Workshop are reported for Cases 1.1b (KVLCC2), 2.1 (KCS) and 3.1a and b (5415). The hulls represent completely different ship types and Froude numbers, so the capability of the codes to predict the free surface is tested over a wide range of possibilities. Workshop participants provided several different graphs to enable an evaluation of the codes. A general overview is provided in the

wave contour plots, where the wave height is given in a region surrounding the hull. For KCS close-ups of the regions in front of and behind the hull are also presented and there is a plot of the wave profile along the hull. Wave cuts at three distances from the center plane are presented for all hulls. These cuts enable a very detailed comparison between computed and measured waves, since the measured data are presented in every plot.

The computed results will be presented case by case below, and the submissions for each particular case listed in a table. In the tables the methods are also classified with respect to type of free surface treatment employed, either surface tracking (T) or surface capturing. In the latter case there is a distinction between Volume of Fluid (VOF) and Level Set (LS). The type of grid and the total number of cells are given as well. Now, the total grid number is not a very relevant measure of the grid density of importance for the wave prediction, so the participants were asked to provide the following grid information: number of grid points per fundamental wave length along the waterline, number of grid points in the transverse direction on the surface at midship and step size in the vertical direction near the hull at midship. This information was plotted in a graph that is presented after the wave figures for each case in Volume 2 of the Proceedings. In the following, examples of good results will be presented. For a better understanding of the review, reference should be made to the complete collection of figures in Volume 2, found on the web site extras.springer.com.

4.1 KVLCC2

The Froude number for KVLCC2 is quite low, 0.142, which means that the fundamental wave length $2\pi Fr^2$ is only 1/8 L_{PP}, so a large number of cells are required to get a sufficient number of cells per wave length. Small cells are also required in the vertical direction, since the maximum wave height is less than 1 % of L_{PP}. This case is a challenging task for most methods.

The wave contours for KVLCC2, measured at MOERI, are presented in Fig. 2.10. A complex wave pattern is seen with very short waves essentially located at the edge of the Kelvin wedge. For a hull of this type with pronounced shoulders four wave systems should be expected: one from the high pressure regions at each end of the hull and one for each shoulder. However, the speed is so low in this case that no waves seem to be generated near the stern. The dominating wave system is that from the bow, but close inspection also reveals a more weak system originating at the forward shoulder and merging with the bow system after a short distance.

All submissions for KVLCC2 are listed in Table 2.7. Excellent results are exhibited by ECN/CNRS-ISISCFD, which is an unstructured grid solver with surface capturing and the VOF technique. The wave pattern, as displayed in Fig. 2.11, reveals all the details of the waves seen in Fig. 2.10. In fact, the predicted wave pattern displays the generated shoulder wave system more clearly than the experiments. It is seen inside the main system from the bow and merges with the latter around $x/L_{PP} = 0.75$. There is also a very good correspondence between the measured and computed wave cuts, as seen in Fig. 2.12.

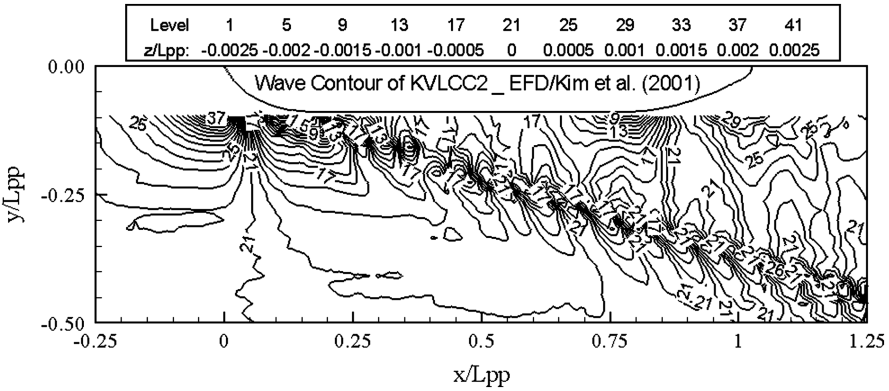


Fig. 2.10 Wave elevation contours ($\Delta z/L_{PP} = 0.000125$): experiment. (MOERI, Kim et al. 2001)

Table 2.7 Submissions in Case 1.1b

Code identifier	Free surface method	Grid type	No. of grid points (M)
ECN/BEC/HO-Icare	T	S	1.1
ECN/CNRS-ISISCFD	V	U	5.5
MARIC-Fluent V.6.3.26	V	MS	2.2
MOERI-WAVIS	LS	MS	4.3
NTNU-FLUENT	V	U	5.9
TUHH-FreSCo+	V	MS, OS	3.4
VTT-FINFLO	T	U	5.5

T tracking, *V* volume of fluid, *LS* level set, *S* structured, *U* unstructured, *MS* multi block structured, *MU* multi block unstructured, *OS* overlapping structured

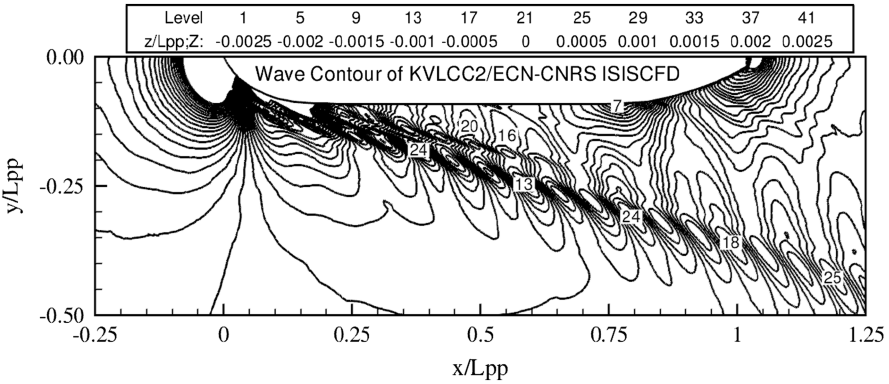


Fig. 2.11 Wave elevation contours ($\Delta z/L_{PP} = 0.000125$): ECN/CNRS-ISISCFD

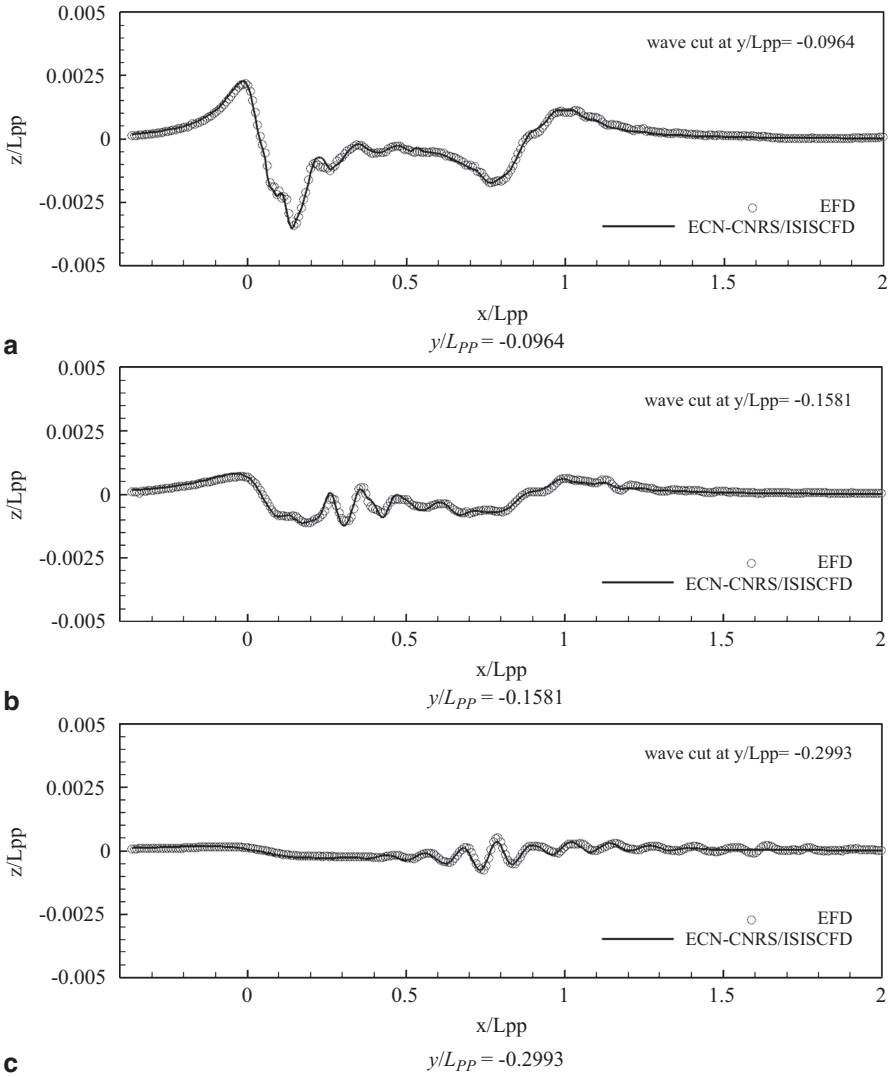


Fig. 2.12 Longitudinal wave cuts: ECN/CNRS-ISISCFD (CFD: *solid line*; EFD: *open circles*)

ISISCFD has a newly implemented grid adaptation technique where the original grid is refined in several steps and concentrated in regions where a large grid density is required. The total number of grid points is 5.5 M, but it is stated in the paper that grid convergence is achieved with 2.7 M grid points. In Fig. 2.13 the grid density distribution is displayed. The full line represents the grid density in the longitudinal direction along the hull, and the unit is points per fundamental wave length, ppwl. The grid density in the transverse direction at midship is represented by the dashed line, using the same scale. To the right in the figure the step size in the vertical direction

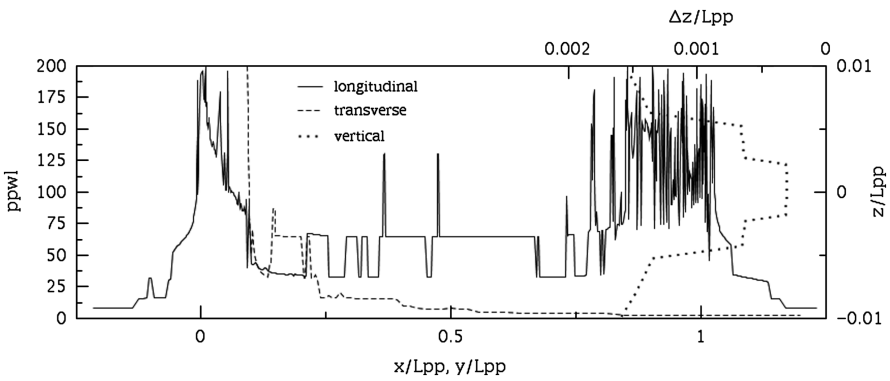


Fig. 2.13 Grid density distribution along the waterline (*solid*), and in transverse (*dashed*) and vertical (*dotted*) directions at mid-ship: ECN/CNRS-ISISCFD

on the hull at midship is shown. The scale for the step size is shown at the top of the figure. The spikes in the full line are due to the fact that this is an unstructured grid, where it is difficult to display the cell size in one direction. If a ray is sent through the grid in one direction it will cut the cells randomly, and if this happens close to a cell corner a very short cell size is recorded. Therefore the distribution becomes very irregular in an unstructured grid. However, the lower envelope of the curve may be assumed to represent the main dimensions of the cells rather well.

The longitudinal grid density has peaks at the ends of the hull, somewhat below 200 ppwl at the bow, but probably considerably less at the stern (hard to see due to the fluctuations). Along the hull the density is in the range 40–70 ppwl. There is a plateau-like distribution of the transverse density at around 70 ppwl in the region $0.15 < y/L_{PP} < 0.20$, which covers the Kelvin wedge. A similar distribution is used in TUHH-FreSCo, which also exhibits very good results. For other methods the grid density drops off more gradually in the transverse direction. The vertical step size is quite small close to the surface but increases rapidly with distance from the surface. A likely reason for the good results is an efficient distribution of the cells.

It should be pointed out that all submissions exhibit very good results at the innermost wave cut. The resolution is good enough to compute the flow close to the hull. However, all submissions but the two mentioned above deteriorate considerably away from the hull. This is clearly seen in the wave contours and in the outermost wave cut. An interesting submission is NTNU-FLUENT, also using VOF, which exhibits a fairly well resolved wave pattern over the major part of the hull, but with a very low longitudinal grid density, only 20–25 ppwl even at the ends of the hull. The transverse grid density is reasonable, however, as well as the vertical step size. The total grid size is large, so the small longitudinal density is difficult to explain.

Table 2.8 Submissions in Case 2.1

Code identifier	Free surface method	Grid type	No. of grid points (M)
CSSRC-Fluent6.3	V	MS	1.3
ECN/BEC/HO-Icare	T	S	1.0
FLOWTECH-SHIPFLOW-VOF-4.3	V	OS	4.3
IIHR-CFDShipIowaV4.0 (DES)	LS	OS	6.9
IIHR-CFDShipIowaV4.0 (RANS)	LS	OS	6.9
IIHR/SJTU-FLUENT12.0.16	V	MS	0.7
MARIC-FLUENT6.3	V	MS	6.5
MARIN-PARNASSOS	T	S	3.1
MOERI-WAVIS	LS	MS	4.3
NMRI-SURF	LS	S	4.9
SNUTT-FLUENT6.3	V	MU	1.8
Southampton-CFX (BSL)	V	MS	9.2
Southampton-CFX (SST)	V	MS	9.2
SSRC-FLUENT12.1	V	MS	2.5
SVA-CFX12	V	MU	5.3
TUHH&ANSYS-CFX12.1	V	U	5.0
VTT-FINFLO	T	T	4.1

T tracking, *V* volume of fluid, *LS* level set, *S* structured, *U* unstructured, *MS* multi-block structured, *MU* multi-block unstructured, *OS* overlapping structured

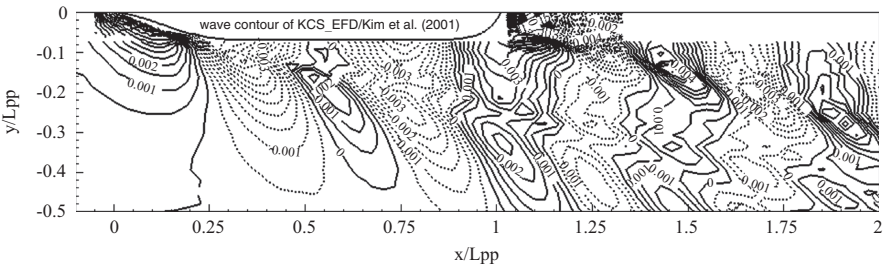


Fig. 2.14 Wave elevation contours (global wave field) ($\Delta z = 0.0005$): MARIN-PARNASSOS (*Solid lines*: positive (+) values; *Dashed lines*: negative (−) values)

4.2 KCS

This is the most popular test case for wave pattern predictions with 17 submissions presented in Table 2.8. The Froude number for this container ship is 0.26, which yields approximately 2 fundamental wave lengths along the hull. Measured wave contours are presented in Fig. 2.14. It is seen that all four wave systems show up to a smaller or larger extent. The most pronounced ones are those from the bow and stern but there are systems originating with wave troughs also at the two shoulders. The weakest one is that from the aft shoulder and it may be hard to detect. There are however some small islands in the contours, particularly far downstream that indicate the existence of this system. Note that the free surface is much longer in this case as compared with the previous one. Here the region back to $x/L_{PP} = 2$ is covered, while for KVLCC2 the region is cut at $x/L_{PP} = 1.25$.

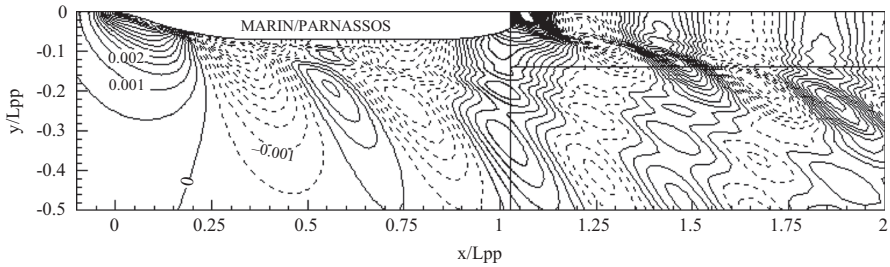


Fig. 2.15 Wave elevation contours (global wave field) ($\Delta z = 0.0005$): experiment. (MOERI, Kim et al. 2001) (*Solid lines*: positive (+) values; *Dashed lines*: negative (−) values)

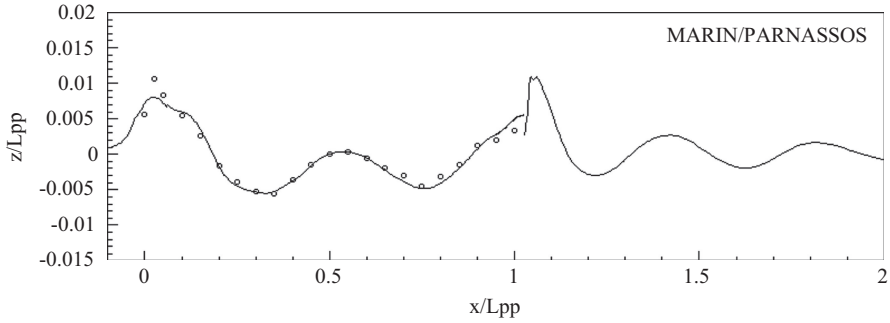


Fig. 2.16 Wave profile on the hull (CFD: *solid line*; EFD: *open circles*): MARIN-PARNASSOS

Several methods predict the wave contours very accurately. This holds for CSSRC-Fluent6.3, IIHR-CFDShipIowaV4.0 (DES), IIHR-CFDShipIowaV4.0 (RANS), MARIN-PARNASSOS and Southampton-CFX (BSL), as well as MOERI-WAVIS and SVA-CFX12, if the aftermost region on the free surface is neglected. For the latter two the reported grid density shows a rapid drop where the results deteriorate. Predictions by MARIN-PARNASSOS are shown in Fig. 2.15.

The wave profile in is surprisingly similar for all methods. As an example, the MARIN-PARNASSOS results are given in Fig. 2.16. There is a consistent slight over prediction of the stern wave crest and an under prediction (for all but TUHH&ANSYS-CFX12.1) of the bow crest, but over the main part of the hull almost all methods predict a wave profile in very good correspondence with the measured data. The under prediction at the bow could be due to difficulties of modeling the thin sheet of water often found on the hull surface at the wave crest.

There is a very wide variation in longitudinal grid density between the methods, from around 700 ppwl down to about 100 ppwl in the bow peak, without any significant effect on the under prediction, so the grid density in this region should not be responsible for the difference between the measured and computed wave height. On the other hand, the difference might well be due to difficulties of measuring the wave profile in this region due to the thin water sheet.

With only one exception (a submission with a very small grid), the innermost wave cut at $y/L_{PP} = -0.0741$ is well predicted along the length of the hull. This is in spite of the fact that the longitudinal grid density varies considerably, from around 25–100 ppwl at midship and from around 100–700 ppwl at the stern. Aft of the hull the accuracy deteriorates more or less rapidly. MARIN-PARNASSOS (Fig. 2.17a), NMRI-SURF and the two Southampton-CFX results exhibit an excellent correspondence with the data all the way to the end of the cut, and the grid density plots show that these submissions have a relatively large grid density, typically 20–40 ppwl, all the way to the end of the cut. In most other submissions the density drops off more rapidly. Exceptions are the two IIHR-CFDShipIowa results which are cut at $x/L_{PP} = 1.5$, just after a significant deviation from the data. This is in spite of a relatively large grid density, around 40 ppwl, in the region.

There is only a very small deterioration of the results at the next cut at $y/L_{PP} = -0.1509$ and the changes at the outermost cut at -0.4224 are also relatively small. Very good results are again found for MARIN-PARNASSOS (Fig. 2.17b, c), NMRI-SURF and the two Southampton-CFX submissions. A puzzling result is that of SVA-CFX12, which is almost as accurate as that of the four best ones in all cuts, in spite of the fact that there is an obvious drop in resolution in the wave contours behind $x/L_{PP} = 1.5$, where the grid density drops off suddenly from a very high value, about 100 ppwl to about 15.

Analyzing the three submissions with the best overall results it is seen that they are rather different. MARIN's code PARNASSOS is perhaps the most unique method. It is a surface tracking method, where a combined kinetic and dynamic boundary condition is solved in an iterative manner, as opposed to most other tracking methods where two separate conditions are satisfied and the solution obtained through time stepping. A large emphasis has also been put on the numerical accuracy, with a very small damping and dispersion as a result. The good predictions of this method were obtained with a relatively small number of cells: 3.1 M.

The code SURF, developed at NMRI, is an unstructured solver with surface capturing based on a single phase Level Set method, while the code used by Southampton is the commercial CFX method with a multi-block structured grid and a Volume of Fluid representation of the free surface. The grid used in SURF was of medium size, 4.9 M, while that in CFX was large, 9.2 M. It should be mentioned that the good results from CFX were obtained with a Reynolds stress turbulence model. Less accurate results were obtained using a two-equation model. This influence of the turbulence model on the free surface is somewhat surprising.

4.3 5415

Wave pattern predictions for smooth water conditions are presented in Cases 3.1a and b. Experiments for 3.1a were carried out at INSEAN with a 7.3 m model, while the 3.1b experiments were made at IIHR with a 3 m long model. The Froude number was the same in both experiments: 0.28, which resulted in a difference in Reynolds number, 11.9×10^6 resp. 5.1×10^6. In both cases the hull was kept fixed at the

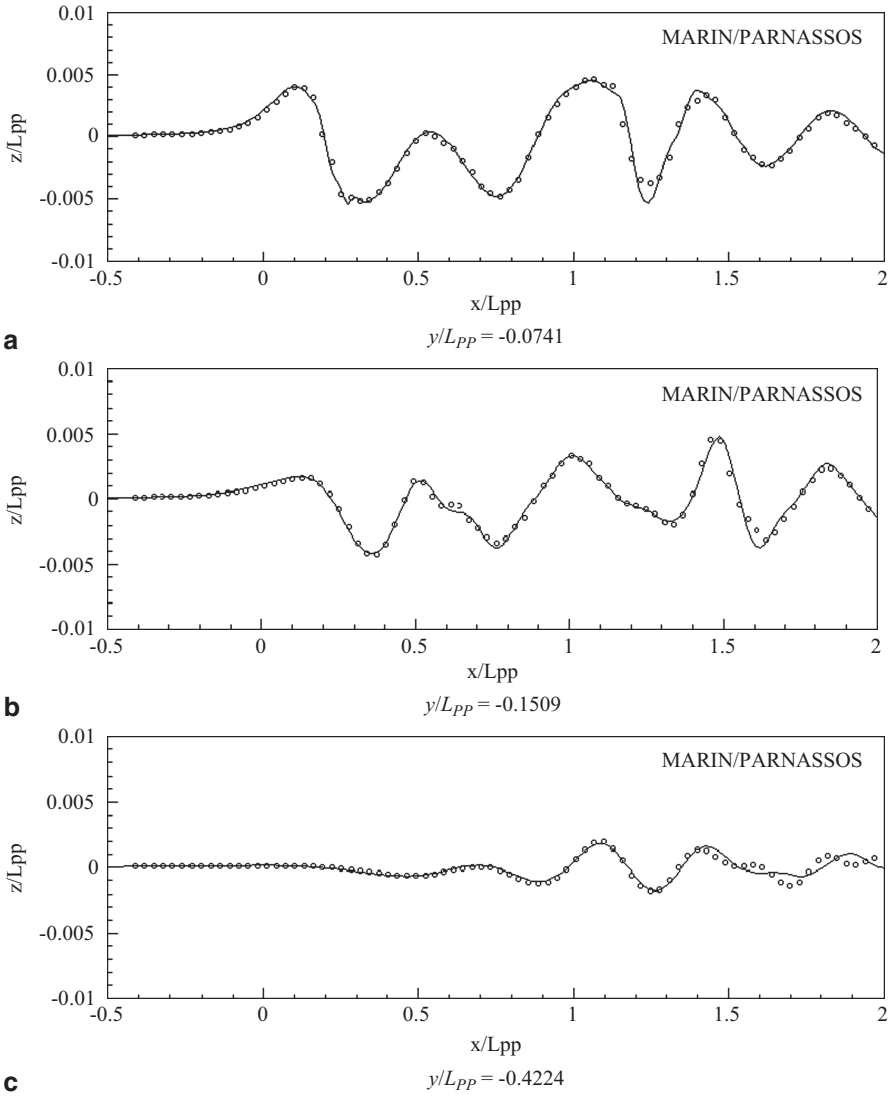


Fig. 2.17 Longitudinal wave cuts: MARIN-PARNASSOS (CFD: *solid line*; EFD: *open circles*)

dynamic sinkage and trim, but there was a small difference between the cases. The sinkage was $-1.82 \times 10^{-3}\ L_{PP}$ in 3.1a and $-1.92 \times 10^{-3}\ L_{PP}$ in 3.1b, and the trim was -0.108 and -0.136 degrees, respectively in the two cases.

The measured wave patterns are shown in Figs. 2.18 and 2.19. A strong bow wave with rather elongated crests and troughs along the edge of the Kelvin wave system is seen. No other waves are visible in the experimental data of 3.1a, which do not cover

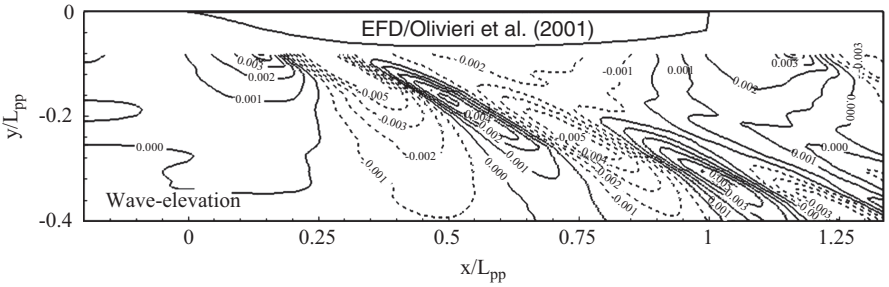


Fig. 2.18 Case 3.1a. Wave elevation contours ($\Delta z/L_{PP} = 0.001$): experiment (INSEAN, Olivieri et al. 2001) (*Solid lines*: positive (+) values; *Dashed lines*: negative (−) values)

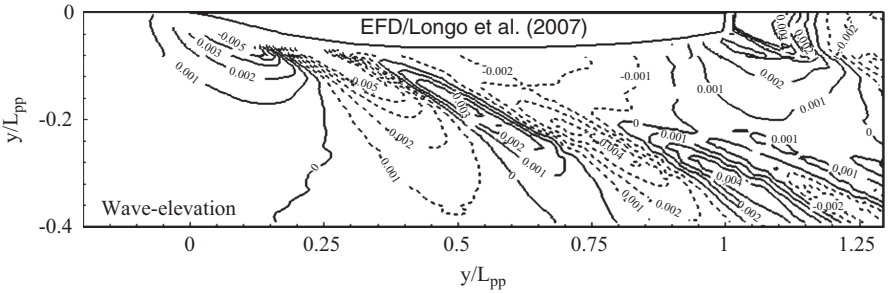


Fig. 2.19 Case 3.1b. Wave elevation contours ($\Delta z/L_{PP} = 0.001$): experiment (IIHR, Longo et al. 2007) (*Solid lines*: positive (+) values; *Dashed lines*: negative (−) values)

the region behind the transom. However, the 3.1b data, as well as all predicted wave patterns, have a more or less pronounced stern wave system with a steep slope down from the side to the trough behind the dry transom. This steep slope is manifested as a concentration of contours originating at the lower corner of the transom in the figures and continuing backwards at an angle similar to that of the Kelvin wedge.

In Table 2.9 all submissions for Cases 3.1a and b are presented. Several groups computed both cases as seen in the table. Note the very large variation in number of grid points.

Many submissions capture all the main features of the global wave pattern. This holds for CEHINAV-CCM+, FOI-OF, IIHR-CFDShipIowaV4.0 (DES), MARIN-PARNASSOS, Navy FOAM, NMRI-SURF and UoGe-STARCCM+. Although the number of grid points is not very large for some of these submissions, down to 2 M, the wave pattern is well predicted. This is in sharp contrast to the KVLCC2 case, where most methods failed to predict the outer region of the wave field. Obviously the present case is simpler, due to the much higher Froude number and the corresponding much larger wave length. The CEHINAV-CCM+ results are given as an example in Fig. 2.20.

Table 2.9 Submissions in Cases 3.1a and b

Code identifier	Case 3.1a or 3.1b	Free surface method	Grid type	No. of grid points (M)
CEHINAV-StarCCM+	A	V	MU	2.0
CSSRC-Fluent6.3	A	V	MS	1.3
ECN/BEC/HO-Icare	a, b	T	S	0.8
FOI-OF	A	V	U	57.6
IIHR-CFDShipIowaV4.0 (DES)	a, b	LS	OS	300
IIHR-CFDShipIowaV4.0 (RANS)	a, b	LS	OS	0.6
IIHR-CFDShip-IowaV6	a, b	LS	S (Cart.)	276
MARIC-FLUENT6.3.26	a, b	V	MS	2.2
MARIN-PARNASSOS	A	T	MS	7.6
NavyFOAM-NavyFOAM	a, b	V	U	13
NMRI-SURF	B	LS	U	2.7
SSRC-FLUENT12.1	B	V	MS	?
UoGe-STARCCM+	A	V	U	2.0

T tracking, *V* volume of fluid, *LS* level set, *S* structured, *U* unstructured, *MS* multi-block structured, *MU* multi-block unstructured, *OS* overlapping structured

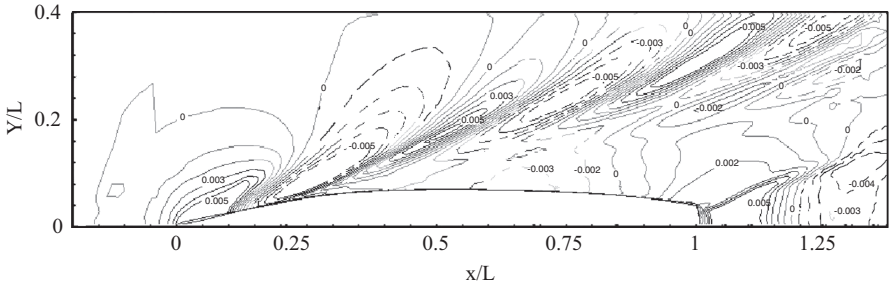


Fig. 2.20 Case 3.1a. Wave elevation contours ($\Delta z/L_{PP} = 0.001$): CEHINAV-STAR-CCM+ (*Solid lines*: positive (+) values; *Dashed lines*: negative (−) values)

A more detailed comparison with the measured waves can be made in the wave cuts for the two cases. At the innermost cut ($y/L_{PP} = 0.082$) only CEHINAV-CCM+ (Fig. 2.21a), CSSRC-Fluent6.3, IIHR-CFDShip-IowaV6 and Navy FOAM capture both the crest and the trough in the first wave. The stern wave height is captured by only the first of these codes. This is a very surprising result! While the results for the other two hulls seemed rather well correlated with the grid density in the three directions this does not seem to be the case here. CEHINAV-CCM+ has a constant distribution of the longitudinal grid density equal to 75 ppwl, a small density in the transverse direction of about 10 ppwl in the region outside the boundary layer, but inside the Kelvin wave, and an extremely large step size in the vertical direction. The latter is likely to be a mistake by an order of magnitude in the plotting, since the step size given is approximately as large as the entire wave height. However, even with a ten times smaller vertical step size the CEHINAV-CCM+ grid is very coarse, particularly compared with the excessively fine grids used by IIHR in two of their submissions. Here the peaks in grid density at the bow and stern are 1600

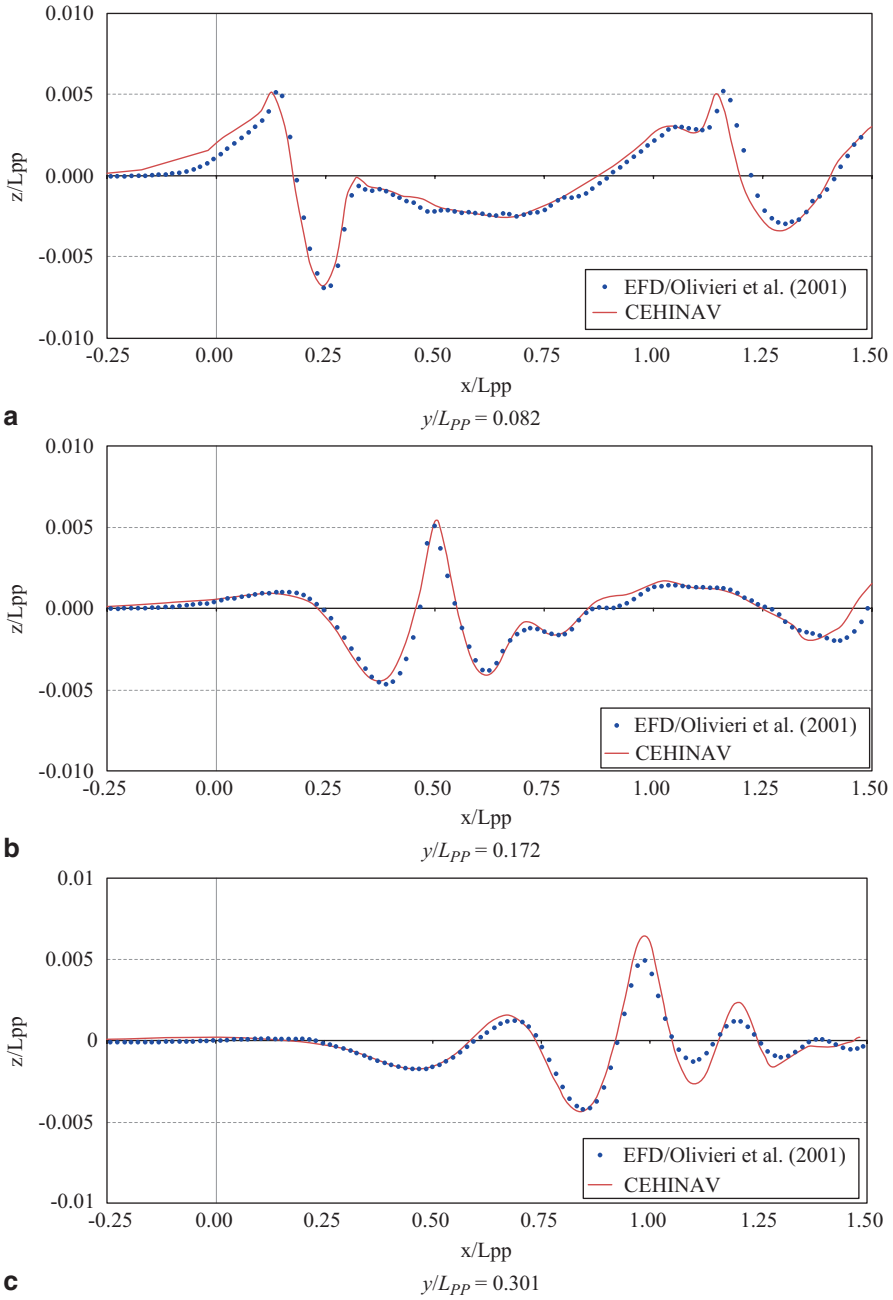


Fig. 2.21 Case 3.1a. Longitudinal wave cuts: CEHINAV-STAR-CCM+ (CFD: *solid line*; EFD: *circles*)

and 1000 ppwl, respectively and the vertical step $0.0003L_{PP}$, a very small value. The transverse grid density is also very large for the DES computations, but similar to that of most other methods for the V6 computations.

It is in fact interesting to compare the two IIHR submissions with the same code, CFDShipIowaV4.0. In the DES computations 300 M cells were used, while in the RANS computations an extremely coarse grid of only 0.6 M cells was employed. Nevertheless it is hard to say that the DES results are better at the innermost wave cut.

Several submitted results deteriorate at the next wave cut at $y/L_{PP} = 0.172$. However, again CEHINAV-CCM+ (Fig. 2.21b) exhibits excellent results. Good predictions are also presented by FOI-OF and SSRC-FLUENT12.1. FOI used a very large number of cells, 57.6 M, while the number of cells used by SSRC is unknown (it was presented neither in the questionnaire reply nor in the papers). No cell distribution is given for FOI-OF but it is presented for SSRC and the density appears to be medium compared to other submissions.

At the outermost wave cut the best results are presented by SSRC-FLUENT12.1 and Navy-FOAM, while those by CEHINAV-CCM+ (Fig. 2.21c) and MARIN-PARNASSOS are quite accurate as well.

Combining the ratings for the wave contours and all three wave cuts the best performance is seen for FOI-OF, CEHINAV-StarCCM+, Navy-FOAM (Fig. 2.22a–c, Case 3.1b), SSRC-FLUENT12.1 and MARIN-PARNASSOS. The good performance of FOI-OF and to some extent also Navy-FOAM might be explained by a large grid density (but they also use the same code OpenFOAM) and, as we have seen above, MARIN's results can be due to the efficient technique for handling the free surface explained above, while all the other methods use VOF. In view of the small number of grid points, only 2 M, the consistently good results for CEHINAV-CCM+ are surprising. The distribution of grid points in the longitudinal direction is also unusual, since it is constant at 75 ppwl, entirely without peaks. The vertical cell size must be smaller than the given one, $0.01L_{PP}$, so this value should be checked. SSRC-FLUENT12.1 has a medium grid density with around 50 ppwl along the hull, rising to 3–400 ppwl at the ends, a gradually dropping transverse density with around 20 ppwl at $y/L_{PP} = 0.5$ and a vertical step size of $0.001L_{PP}$.

Comparing the different types of free surface modeling in the submissions for all cases, it is seen that the VOF technique is by far the most popular one. 21 submissions employed this technique, while the Level Set approach was used in 8 submissions. Surface tracking was used in 7 cases. Checking the best results of for all hulls it is seen that, with one exception, they were obtained with the VOF technique. The exception is MARIN-PARNASSOS, which is a tracking method with several unique features, as described above. Although the successful results of the VOF method are clear it would be premature to rank the Level Set method as inferior. It had many fewer submissions and was very close in several cases. Further, the accuracy in the predictions seems to be mainly determined by another parameter: the grid density.

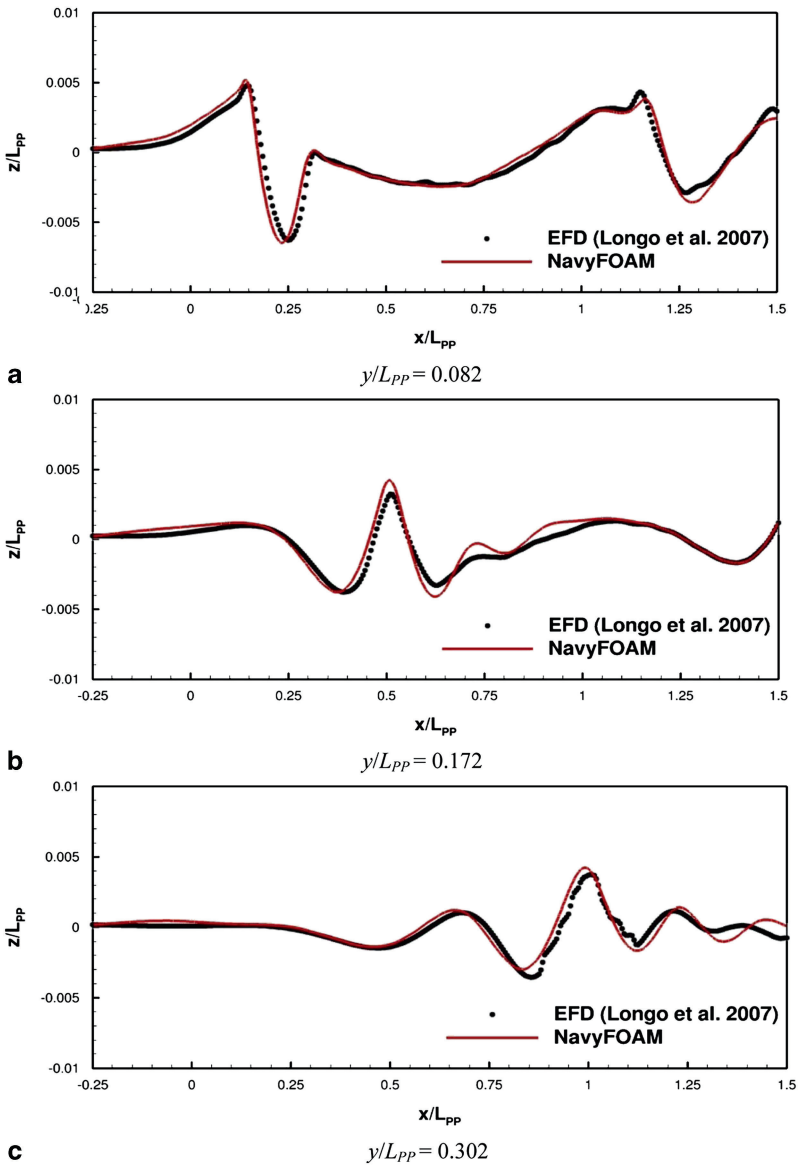


Fig. 2.22 Case 3.1b. Longitudinal wave cuts: NavyFOAM-NavyFOAM (CFD: *solid line*; EFD: *circles*)

5 Conclusions

- The mean comparison error for all computed resistance cases is practically zero; only $-0.1\,\%D$, and the mean standard deviation is $2.1\,\%D$. The latter represents a considerable improvement since 2005, where the mean standard deviation was $4.7\,\%D$. Among the hulls the KVLCC2 has the largest mean error, $-2.0\,\%$, i.e. an over prediction of the resistance, while 5415 has the largest mean standard deviation, $3.2\,\%$. This is for the towed cases. The self-propelled KCS has a considerably larger error and standard deviation (3.7 and $3.2\,\%$, resp.) than the towed hull (-0.3 and $1.3\,\%$, resp.).
- Excluding the self-propulsion results there is no discernible improvement in the resistance prediction for grid sizes above 3 million cells. All results for towing in this range are within $\pm 4\,\%$ of the measured data. For smaller grid sizes the error is within $\pm 8\,\%$.
- There is no visible improvement in accuracy of the resistance prediction for turbulence models more advanced that the two-equation models. However, the statistical basis for this conclusion is weak, due to few predictions with advanced models.
- Systematic grid variations were reported for slightly less than half of the submissions. An interesting finding is that almost all variations of structured grids were convergent, while this was the case for only one of the seven submissions with unstructured grids. The order of accuracy, determined by either one of the two established methods, is often very different from the theoretical one. In particular, the very large order of accuracy obtained in many submissions is a matter of concern, since the statistical base for the uncertainty estimation is limited to accuracies smaller than twice the theoretical one.
- The comparison errors and standard deviations of the sinkage and trim are much larger than for the resistance. Since there is no fundamental reason for this to be the case, the problems are likely to be due to the difficulties of measuring the two quantities at low speed. This conjecture is supported by the investigation reported in the Appendix, and the fact that the comparison errors are considerably smaller in a speed range above $Fr = 0.2$ than below this limit.
- Self-propulsion results are available only for KCS, in fixed and free conditions. For K_T and K_Q the mean comparison errors are 0.6 and $-2.6\,\%$ resp. The standard deviations are 7.0 and $6.0\,\%$ resp.; considerably larger than for resistance. Comparing actual and modeled propellers it is seen that the actual propeller has a much smaller mean standard deviation. For K_T it is half, and for K_Q it is only 1/3 of that of the modeled propeller. There is no clear advantage when it comes to comparison error, however.
- In general, the wave contour on the hull and at the wave cut closest to the hull is well predicted. Further away from the hull the results differ considerably between the methods. The best submissions for all three hulls capture all the features of the waves out to the edge of the measured region. For KVLCC2 this holds only for a few methods, while most submissions exhibit a far too rapid decay of the

wave pattern away from the hull. More methods manage to keep the waves rather well out to the edge of the measured region for KCS, and particularly for 5415. At the higher speeds for these hulls the waves are longer, and a sufficient number of grid points per wave length can be used.

Appendix: Revised Uncertainty Analysis for Sinkage and Trim Measurements in Longo and Stern (2005)

Hyunse Yoon, Joe Longo and Frederick Stern

Introduction

One issue raised at the Gothenburg 2010 Workshop on CFD in Ship Hydrodynamics is the unrealistically small error estimates for IIHR sinkage and trim data for the DTMB model 5512 (a 3.048 m geosim model of DTMB 5415). Bias error from the towing tank rail levelness was identified as an important missing error source in the original analysis. Therefore, an investigation has been undertaken to examine rail levelness at the IIHR towing tank facility and its effect on sinkage and trim uncertainty analysis (UA). The results are used to update previously published sinkage and trim UA for model 5512 (Longo and Stern 2005) and recast the original data and UA with alternate sinkage and trim data reduction equations (DRE's).

Overview of Original Sinkage and Trim UA

In the original experiments, displacements of the model at the fore ΔFP and aft ΔAP perpendicular are measured at a range of Fr ($Fr = 0.05 - 0.45$; $\Delta Fr = 0.01$) with a potentiometer-based measurement system. The original DRE's were following the 18th ITTC (ITTC 1987) for sinkage and trim coefficients respectively as

$$\sigma = \frac{2}{Fr^2}\frac{\Delta FP + \Delta AP}{2L_{pp}} \tag{2.1}$$

$$\tau = \frac{2}{Fr^2}\frac{\Delta AP - \Delta FP}{L_{pp}} \tag{2.2}$$

where L_{pp} is the length between perpendiculars. These sinkage and trim DRE's in functional form are written

$$\sigma,\ \tau = \sigma,\ \tau(\Delta FP,\ \Delta AP,\ L_{pp},\ Fr) \tag{2.3}$$

and the UA equations are written

$$B^2_{\Delta FP} = B^2_{\Delta FP1} + B^2_{\Delta FP2} + B^2_{\Delta FP3}, B^2_{\Delta AP} = B^2_{\Delta AP1} + B^2_{\Delta AP2} + B^3_{\Delta AP3} \tag{2.4}$$

Table 2.10 Original uncertainty estimates using Eqs. (2.1) and (2.2) for sinkage and trim tests with model 5512. Rail levelness bias is *not* included in this analysis

Sinkage						
Term	*Fr* = 0.10		*Fr* = 0.28		*Fr* = 0.41	
	(-)	(%)	(-)	(%)	(-)	(%)
$(B_{\Delta FP}\theta_{\Delta FP})^2$	(1.994E-03)^2	71.5	(2.525E-04)^2	47.4	(1.181E-04)^2	27.2
$(B_{\Delta AP}\theta_{\Delta AP})^2$	(1.201E-03)^2	25.9	(1.520E-04)^2	17.2	(7.112E-05)^2	9.9
$(B_{Uc}\theta_{Uc}$	(3.828E-04)^2	2.6	(2.184E-04)^2	35.5	(1.796E-04)^2	62.9
$(B_\sigma$	(2.359E-03)^2	83.8	(3.668E-04)^2	32.7	(2.264E-04)^2	45.3
$(P_\sigma)^2$	(1.038E-03)^2	16.2	(5.260E-04)^2	67.3	(2.486E-04)^2	54.7
U_σ	2.577E-03	***8.7***	6.413E-04	***1.4***	3.362E-04	***0.6***
D_σ	2.978E-02		4.738E-02		5.633E-02	
U_σ (mm)	*0.040*		*0.078*		*0.087*	
D_σ (mm)	*0.459*		*5.765*		*14.652*	
Trim						
Term	*Fr* = 0.10		*Fr* = 0.28		*Fr* = 0.41	
	(-)	(%)	(-)	(%)	(-)	(%)
$(B_{\Delta FP}\theta_{\Delta FP})^2$	(3.988E-03)^2	71.1	(5.049E-04)^2	60.6	(2.362E-04)^2	40.7
$(B_{\Delta AP}\theta_{\Delta AP})^2$	(2.401E-03)^2	25.8	(3.040E-04)^2	22.0	(1.422E-04)^2	14.7
$(B_{Uc}\theta_{Uc})^2$	(8.330E-04)^2	3.1	(2.712E-04)^2	17.5	(2.473E-04)^2	44.6
$(B_\tau)^2$	(4.729E-03)^2	53.6	(4.209E-07)^2	38.6	(3.704E-04)^2	7.8
$(P_\tau)^2$	(4.403E-03)^2	46.4	(8.180E-04)^2	61.4	(1.272E-03)^2	92.2
U_τ	6.461E-03	***10.0***	1.044E-03	***1.8***	1.325E-03	***1.7***
D_τ	6.480E-02		5.881E-02		7.757E-02	
U_τ (°)	*0.002*		*0.002*		*0.006*	
D_τ (°)	*0.019*		*0.135*		*0.379*	

$$B^2_{\sigma,\tau} = \theta^2_{\Delta FP} B^2_{\Delta FP} + \theta^2_{\Delta AP} B^2_{\Delta AP} + \theta^2_{L_{pp}} B^2_{L_{pp}} + \theta^2_{Fr} B^2_{Fr} \tag{2.5}$$

$$P_{\overline{\sigma,\tau}} = t S_{\overline{\sigma,\tau}} / \sqrt{M} \tag{2.6}$$

$$U^2_{\sigma,\tau} = B^2_{\sigma,\tau} + P^2_{\overline{\sigma,\tau}} \tag{2.7}$$

Eq. (2.4) is the combined effect of ΔFP, ΔAP elemental bias errors. Eq. (2.5) is the bias uncertainty of the sinkage and trim coefficients σ and τ. The sensitivity coefficients θ's are evaluated analytically with derivatives of eqs. (2.1) and (2.2). Eq. (2.6) is the precision uncertainty of the mean sinkage and trim from $\mathrm{M} = 10$ repeat tests, and Eq. (2.7) is the total uncertainty of σ and τ. $B_{L_{PP}}$ is assumed to be zero.

In Eq. (2.4), the elemental error sources are: (1) calibration standard ($B_{\Delta FP1,\Delta AP1}$), (2) potentiometer misalignment ($B_{\Delta FP2,\Delta AP2}$), and (3) scatter in the potentiometer calibration data ($B_{\Delta FP3,\Delta AP3}$) which are combined with a root sum square to form $B_{\Delta FP,\Delta AP}$. The original analysis did not include an error source associated with towing tank rail deviation from the level condition. This error source was overlooked but important as dips and humps in the rails retract or extend the potentiometers, respectively, during a test and register errors in the ΔFP, ΔAP measurements.

Table 2.10 is a revision the original sinkage and trim UA results published in Longo and Stern 2005 (Table 3, p. 61). Table 2.10 uses a clearer expression for the squared terms than in the original publication where the values before squaring

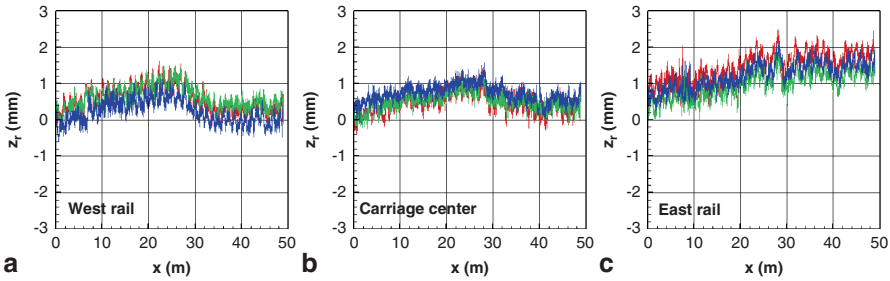


Fig. 2.23 Rail inspection measurement (before rail correction) results of the west rail (**a**), center of the carriage (**b**), and east rail (**c**)

were used. From Table 2.10, results show that bias uncertainty is a dominant error source contributing about 70–80 % of total uncertainty for the lowest *Fr* but decreases in importance with increasing *Fr* because the dynamic range of the measurement increases with increasing *Fr*. Therefore, it is expected that inclusion of the rail bias in the bias uncertainty will have the largest effect on low-*Fr* uncertainties. Total uncertainties are about 10 %, 1.5–2 %, 0.5–2 % for sinkage and trim for $Fr = 0.10$, 0.28, 0.41, respectively.

Table 2.10 also provides additional information than its original version in Longo and Stern (2005), which are dimensional values of the sinkage and trim values $D_{\sigma,\tau}$ and UA $U_{\sigma,\tau}$. From the original sinkage and trim UA without inclusion of rail bias, $U_\sigma = 0.04 - 0.09$ mm and $U_\tau = 0.002 - 0.006$. These are not realistic values as it is practically not possible for typical towing tank facilities to achieve such accuracy in leveling their towing carriage rails. An unevenness of an order of ± 0.5 mm is expected at best.

IIHR Towing Tank Rail Inspection

Rail Inspection Before Rail Correction

An initial rail inspection was made during April 2011. Relative rail elevations were measured by using an ultrasonic distance sensor (Senix TS-30S) with referenced to the towing tank calm water surface. The sensor was attached to the carriage at three different locations including at the northwest carriage wheel, carriage center, and northeast carriage wheel. The measurements were made while the carriage was running at a slow speed ($U_C = 0.25$ m/s) over a tank length of approximately 50 m. Data were acquired as time-histories sampled at 100 Hz and for 240 s. Statistical analysis of the rail elevation time history data includes mean value $z_{r,ave}$, standard deviation $z_{r,stdev}$, root-mean-square (rms) $z_{r,rms}$, maximum value $z_{r,\max}$, minimum value $z_{r,\min}$, and (max-min)/2 $z_{r,(\max-\min)/2}$.

Fig. 2.23 shows that the west rail is inclined upward for the first 25 m, then dips and plateaus in the last 25 m; the center of the carriage generally follows the trends

Table 2.11 Summary of rail inspection measurement results (Before rail correction)

No	$z_{r,ave}$ (mm)	$z_{r,stdev}$ (mm)	$z_{r,rms}$ (mm)	$z_{r,max}$ (mm)	$z_{r,min}$ (mm)	$z_{r,(max\text{-}min)/2}$ (mm)
			West rail			
1	0.499	0.351	0.610	1.610	-0.379	0.994
2	0.552	0.310	0.633	1.490	-0.221	0.855
3	0.151	0.319	0.353	1.142	-0.577	0.859
Ave	**0.401**	**0.327**	**0.532**	**1.414**	**-0.392**	**0.903**
			Center of carriage			
1	0.426	0.276	0.508	1.444	-0.401	0.922
2	0.488	0.245	0.546	1.312	-0.278	0.795
3	0.702	0.261	0.749	1.573	-0.404	0.989
Ave	**0.539**	**0.261**	**0.601**	**1.443**	**-0.361**	**0.902**
			East rail			
1	1.485	0.525	1.575	2.471	-0.601	1.536
2	1.010	0.467	1.113	1.918	-0.633	1.276
3	1.230	0.426	1.302	2.121	0.000	1.060
Ave	**1.242**	**0.473**	**1.330**	**2.170**	**-0.411**	**1.291**

of the west rail, but appears a little flatter; the east rail is inclined upward through 50 m and exhibits the poorest overall levelness. This is confirmed in Table 2.11 where $z_{r,rms}$ is 0.53, 0.60, and 1.33 mm for the west rail, center of carriage, and east rail, respectively.

Rail Inspection After Rail Correction

Rail corrections were made at the IIHR towing tank during August 2011. The corrections were made at a 72 rail-support locations for each of the west and east rails, a total of 144 locations. The spacing between the adjacent supports is about 30 inches (762 mm). For the rail correction, first the west and east rails were leveled against each other at one location ($x \approx 13$ m) and then rail support heights were adjusted to bring the rail elevation within a ± 0.5 mm range from the level through the rail length.

Subsequently, an after-correction rail inspection was made during September 2011. A similar measurement technique was used as for the before-correction rail inspection, but this time two servo-type (Kenek SWT-10) wave gauges were used instead of ultrasonic distance sensor. One gauge was fixed near at the northwest wheel and the other near at the northeast wheel of the IIHR PMM carriage. Three carriage runs were made with $Uc = 0.1$ m/s. Data acquisition occurred at 100 Hz and for 560 s.

Rail elevation measurement results are shown in Fig. 2.24 and Table 2.12 with the same format and entries as Fig. 2.23 and Table 2.11, respectively. Fig. 2.24 shows the improved levelness of the rails after correction. From Table 2.12, $z_{r,ave}$ is very small, -0.052 and -0.037 mm for the west and east rail, respectively, which indicates that both rails are well leveled each other through the length. $z_{r,rms}$ is

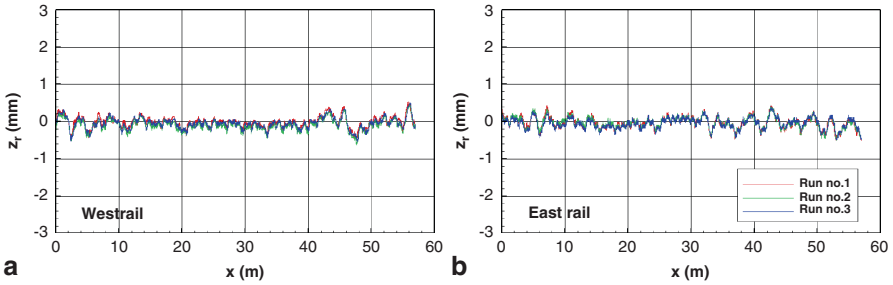


Fig. 2.24 Rail inspection measurement (after rail correction) results of the west rail (**a**), and east rail (**b**)

Table 2.12 Summary of rail inspection measurement results (After rail correction)

No	$z_{r,ave}$ (mm)	$z_{r,stdev}$ (mm)	$z_{r,rms}$ (mm)	$z_{r,max}$ (mm)	$z_{r,min}$ (mm)	$z_{r,(max\text{-}min)/2}$ (mm)
			West rail			
1	-0.016	0.153	0.154	0.529	-0.507	0.518
2	-0.092	0.153	0.178	0.466	-0.619	0.543
3	-0.048	0.153	0.160	0.498	-0.542	0.520
Ave	**-0.052**	**0.153**	**0.162**	**0.498**	**-0.556**	**0.527**
			East rail			
1	-0.027	0.162	0.164	0.422	-0.508	0.465
2	-0.034	0.154	0.158	0.436	-0.493	0.465
3	-0.051	0.150	0.159	0.428	-0.486	0.457
Ave	**-0.037**	**0.155**	**0.160**	**0.428**	**-0.496**	**0.462**

0.162 and 0.160 mm for the west and east rail, respectively, which are just 30 and 12 %, respectively, of those values before rail correction.

Revised Sinkage and Trim UA

Rail Levelness Bias

The original sinkage and trim UA in Longo and Stern (2005) is revised by including the rail levelness bias as the fourth elemental bias error $B_{\Delta FP4,\Delta AP4}$ in the analysis. The rail bias is defined in two different ways for the before and after rail correction cases. For the former case, the rails are not only undulating but also inclined along the length (Fig. 2.23), thus either $z_{r,ave}$ or $z_{r,stdev}$ (or their root-sum-square, $z_{r,rms}$) may not serve well as the rail un-levelness standard. For this case, the carriage center average $r_{z,(\max-\min)/2}$ value is used as the rail levelness bias. On the other hand, for the latter after-correction case, the $\overline{z_{r,stdev}}$ value with multiplied by four (i.e., $\pm 2\overline{z_{r,stdev}}$) is used as the rail levelness bias, where $\overline{z_{r,stdev}}$ is an average of the west and east rail $\overline{z_{r,stdev}}$ values.

Table 2.13 Elemental trim and sinkage bias errors

Trim and sinkage measurement data						
Term	*Fr* = 0.10		*Fr* = 0.28		*Fr* = 0.41	
ΔFP (mm)	0.958		9.343		4.562	
ΔAP (mm)	-0.040		2.187		24.742	
Bias error without rail levelness bias						
Term	*Fr* = 0.10		*Fr* = 0.28		*Fr* = 0.41	
	(mm)	(%ΔFP,ΔAP)	(mm)	(%ΔFP,ΔAP)	(mm)	(%ΔFP,ΔAP)
$B_{\Delta FP}$	0.061	***6.4***	0.061	***0.7***	0.061	***1.3***
$B_{\Delta AP}$	0.037	***92.5***	0.037	***1.7***	0.037	***0.1***
*Bias error with rail levelness bias (**before** rail correction)*						
Term	*Fr* = 0.10		*Fr* = 0.28		*Fr* = 0.41	
	(mm)	(%ΔFP,ΔAP)	(mm)	(%ΔFP,ΔAP)	(mm)	(%ΔFP,ΔAP)
$B_{\Delta FP}$	0.904	***94.4***	0.904	***9.7***	0.904	***19.8***
$B_{\Delta AP}$	0.903	***2257.5***	0.903	***41.3***	0.903	***3.6***
*Bias error with rail levelness bias (**after** rail correction)*						
Term	*Fr* = 0.10		*Fr* = 0.28		*Fr* = 0.41	
	(mm)	(%ΔFP,ΔAP)	(mm)	(%ΔFP,ΔAP)	(mm)	(%ΔFP,ΔAP)
$B_{\Delta FP}$	0.619	***64.6***	0.619	***6.6***	0.619	***13.6***
$B_{\Delta AP}$	0.617	***1542.5***	0.617	***28.2***	0.617	***2.5***

Table 2.13 presents the elemental bias errors $B_{\Delta FP}$ and $B_{\Delta AP}$ values as per Eq. (2.4) with and without including the rail levelness bias $B_{\Delta FP4,\Delta AP4}$ component. For the without rail bias case (as for the original sinkage and trim UA), $B_{\Delta FP}$ and $B_{\Delta AP}$ values are quite small, 0.061 and 0.037 mm, respectively, for all *Fr*'s. Compared to the actual dimensional sinkage and trim measurements, these $B_{\Delta FP}$ and $B_{\Delta AP}$ values correspond to only about 1–2 % of ΔFP and ΔAP (ranging from approximately 0 mm and up to about 25 mm), except for the low *Fr* case where ΔFP, $\Delta AP \approx 0$. By including the rail bias, $B_{\Delta FP}$ and $B_{\Delta AP}$ values increase to about 4−40 % of ΔFP and ΔAP for the case before rail correction and about 3−30 % after rail correction, again expect for the low *Fr* case.

ITTC Equations

The UA is recomputed by using the rail bias before rail correction and summarized in Table 2.14 with the same format and entries as Table 2.10. Now $B_{\Delta FP,\Delta AP}$ accounts for about 99–100 % of the total bias uncertainty. B_σ and B_τ contribute to U_σ and U_τ, respectively, at the 99 % level for all *Fr* except for $Fr = 0.41$ where B_τ is a 94 % contributor to U_τ. U_σ is increased a factor of 16, 8, 7 for $Fr = 0.10$, 0.28, 0.41, respectively. U_τ is increased a factor of 13, 10, 4 for $Fr = 0.10$, 0.28, 0.41, respectively. The UA for the case after rail correction is summarized in Table 2.15, where the factors are relatively small; 11, 6, 5 for U_σ, respectively, and 9, 7, 3 for U_τ, respectively.

Sinkage and trim coefficients are plotted in Fig. 2.25 versus *Fr* per Eqs. (2.1) and (2.2) with original and revised UA results as error bars. The error bars highlight improvements in the uncertainty estimates with inclusion of the rail bias. Low-*Fr*

Table 2.14 Revised sinkage and trim UA results using Eqs. (2.1) and (2.2). Rail level bias *before* rail correction is included in this analysis

Sinkage						
Term	*Fr* = 0.10		*Fr* = 0.28		*Fr* = 0.41	
	(-)	(%)	(-)	(%)	(-)	(%)
$(B_{\Delta FP}\theta_{\Delta FP})^2$	$(2.934E\text{-}02)^2$	50.1	$(3.715E\text{-}03)^2$	50.0	$(1.738E\text{-}03)^2$	49.8
$(B_{\Delta AP}\theta_{\Delta AP})^2$	$(2.930E\text{-}02)^2$	49.9	$(3.710E\text{-}03)^2$	49.8	$(1.736E\text{-}03)^2$	49.7
$(B_{Uc}\theta_{Uc})^2$	$(3.828E\text{-}04)^2$	0.0	$(2.184E\text{-}04)^2$	0.2	$(1.796E\text{-}04)^2$	0.5
$(B_\sigma)^2$	$(4.147E\text{-}02)^2$	99.9	$(5.255E\text{-}03)^2$	99.0	$(2.463E\text{-}03)^2$	99.0
$(P_\sigma)^2$	$(1.038E\text{-}03)^2$	0.1	$(5.260E\text{-}04)^2$	1.0	$(2.486E\text{-}04)^2$	1.0
U_σ	4.148E-02	***139.3***	5.281E-03	***11.1***	2.475E-03	***4.4***
D_σ	2.978E-02		4.738E-02		5.633E-02	
U_σ (mm)	*0.639*		*0.643*		*0.644*	
D_σ (mm)	*0.459*		*5.765*		*14.652*	
Trim						
Term	*Fr* = 0.10		*Fr* = 0.28		*Fr* = 0.41	
	(-)	(%)	(-)	(%)	(-)	(%)
$(B_{\Delta FP}\theta_{\Delta FP})^2$	$(5.869E\text{-}02)^2$	50.1	$(7.431E\text{-}03)^2$	50.0	$(3.476E\text{-}03)^2$	49.9
$(B_{\Delta AP}\theta_{\Delta AP})^2$	$(5.860E\text{-}02)^2$	49.9	$(7.420E\text{-}03)^2$	49.9	$(3.471E\text{-}03)^2$	49.8
$(B_{Uc}\theta_{Uc})^2$	$(8.330E\text{-}04)^2$	0.0	$(2.712E\text{-}04)^2$	0.1	$(2.473E\text{-}04)^2$	0.3
$(B_\tau)^2$	$(8.294E\text{-}02)^2$	99.7	$(1.103E\text{-}04)^2$	99.4	$(4.919E\text{-}03)^2$	93.7
$(P_\tau)^2$	$(4.403E\text{-}03)^2$	0.3	$(8.180E\text{-}04)^2$	0.6	$(1.272E\text{-}03)^2$	6.3
U_τ	8.306E-02	***128.2***	1.054E-02	***17.9***	5.080E-03	***6.5***
D_τ	6.480E-02		5.881E-02		7.757E-02	
U_τ (°)	*0.024*		*0.024*		*0.025*	
D_τ (°)	*0.019*		*0.135*		*0.379*	

Table 2.15 Revised sinkage and trim UA results using Eqs. (2.1) and (2.2). Rail level bias *after* rail correction is included in this analysis

Sinkage						
Term	*Fr* = 0.10		*Fr* = 0.28		*Fr* = 0.41	
	(-)	(%)	(-)	(%)	(-)	(%)
$(B_{\Delta FP}\theta_{\Delta FP})^2$	$(2.009E\text{-}02)^2$	50.1	$(2.544E\text{-}03)^2$	50.0	$(1.190E\text{-}03)^2$	49.6
$(B_{\Delta AP}\theta_{\Delta AP})^2$	$(2.003E\text{-}02)^2$	49.8	$(2.536E\text{-}03)^2$	49.7	$(1.186E\text{-}03)^2$	49.3
$(B_{Uc}\theta_{Uc})^2$	$(3.828E\text{-}04)^2$	0.0	$(2.184E\text{-}04)^2$	0.4	$(1.796E\text{-}04)^2$	1.1
$(B_\sigma)^2$	$(2.837E\text{-}02)^2$	99.9	$(3.599E\text{-}03)^2$	97.9	$(1.690E\text{-}03)^2$	97.9
$(P_\sigma)^2$	$(1.038E\text{-}03)^2$	0.1	$(5.260E\text{-}04)^2$	2.1	$(2.486E\text{-}04)^2$	2.1
U_σ	2.839E-02	***95.4***	3.637E-03	***7.7***	1.708E-03	***3.0***
D_σ	2.978E-02		4.738E-02		5.633E-02	
U_σ (mm)	*0.437*		*0.443*		*0.444*	
D_σ (mm)	*0.459*		*5.765*		*14.652*	
Trim						
Term	*Fr* = 0.10		*Fr* = 0.28		*Fr* = 0.41	
	(-)	(%)	(-)	(%)	(-)	(%)
$(B_{\Delta FP}\theta_{\Delta FP})^2$	$(4.019E\text{-}02)^2$	50.1	$(5.088E\text{-}03)^2$	50.1	$(2.380E\text{-}03)^2$	49.9
$(B_{\Delta AP}\theta_{\Delta AP})^2$	$(4.006E\text{-}02)^2$	49.8	$(5.072E\text{-}03)^2$	49.8	$(2.373E\text{-}03)^2$	49.6
$(B_{Uc}\theta_{Uc})^2$	$(8.330E\text{-}04)^2$	0.0	$(2.712E\text{-}04)^2$	0.1	$(2.473E\text{-}04)^2$	0.5
$(B_\tau)^2$	$(5.675E\text{-}02)^2$	99.4	$(5.169E\text{-}05)^2$	98.7	$(3.370E\text{-}03)^2$	87.5
$(P_\tau)^2$	$(4.403E\text{-}03)^2$	0.6	$(8.180E\text{-}04)^2$	1.3	$(1.272E\text{-}03)^2$	12.5
U_τ	5.692E-02	***87.8***	7.236E-03	***12.3***	3.602E-03	***4.6***
D_τ	6.480E-02		5.881E-02		7.757E-02	
U_τ (°)	*0.016*		*0.017*		*0.018*	
D_τ (°)	*0.019*		*0.135*		*0.379*	

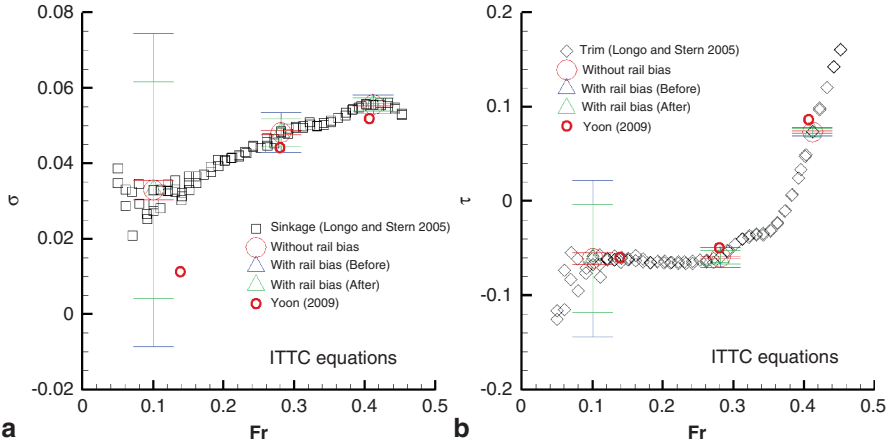


Fig. 2.25 Sinkage and trim measurement results using Eqs. (2.1) and (2.2) for model 5512. *Red* is for the case without inclusion of rail bias in the UA and *blue* and *green* for the cases with the rail bias values before and after rail correction, respectively

error bars have better coverage of the data where there is increase scatter. Yoon (2009) also confirms that the revised sinkage and trim UA is more realistic as the independently measured trim and sinkage data approximately fall into the revised UA bounds. It should be noted that the original σ and τ plots presented in the Fig. 4 of Longo and Stern (2005) are mistakenly showing the values of $4z/L_{PP}$ and 2θ, which should be replaced with the present Fig. 2.25.

Alternate equations

The alternate presentation and current standard for sinkage and trim results is with the equations below

$$\frac{z}{L_{PP}} = \frac{\Delta FP + \Delta AP}{2L_{PP}} \tag{2.8}$$

$$\theta = \frac{\Delta AP - \Delta FP}{L_{PP}} \tag{2.9}$$

where z is the displacement midway between FP and AP and θ is the trim angle in radian. Rail bias effects on sinkage and trim UA results are also applied to DRE's (8) and (9). In functional form, Eqs. (2.8) and (2.9) are written

$$z/L_{PP} = z/L_{PP}(\Delta FP, \Delta AP, L_{PP}) \tag{2.10}$$

$$\theta = \theta(\Delta FP, \Delta AP, L_{PP}) \tag{2.11}$$

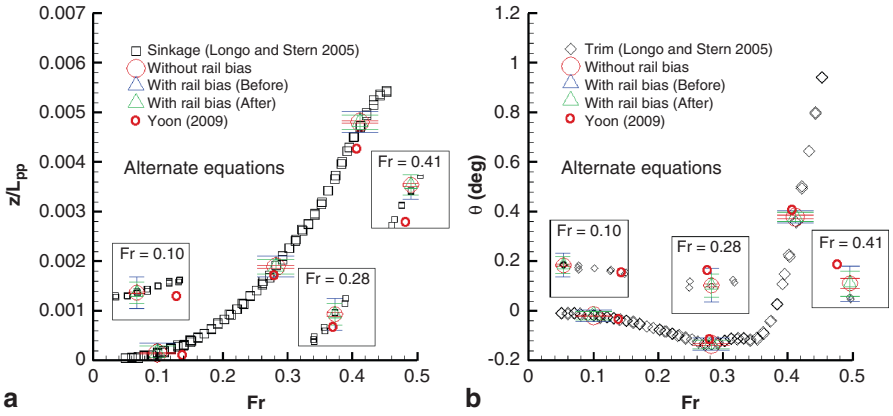


Fig. 2.26 Sinkage and trim measurement results using Eqs. (2.8) and (2.9) for model 5512. *Red* is for the case without inclusion of rail bias in the UA and *blue* and *green* for the cases with rail biases before and after rail correction, respectively. The small-boxed insertion windows show a magnified view of the UA comparison

and the UA equations are written similarly as for Eqs. (2.4), (2.5), (2.6), (2.7),

$$B^2_{\Delta FP} = B^2_{\Delta FP1} + B^2_{\Delta FP2} + B^2_{\Delta FP3}, B^2_{\Delta AP} = B^2_{\Delta AP1} + B^2_{\Delta AP2} + B^3_{\Delta AP3} \tag{2.12}$$

$$B^2_{z/L_{PP},\theta} = \theta^2_{\Delta FP} B^2_{\Delta FP} + \theta^2_{\Delta AP} B^2_{\Delta AP} + \theta^2_{L_{PP}} B^2_{L_{PP}} \tag{2.13}$$

$$P_{\overline{z/L_{PP},\theta}} = t S_{\overline{z/L_{PP},\theta}} / \sqrt{M} \tag{2.14}$$

$$U^2_{z/L_{PP},\theta} = B^2_{z/L_{PP},\theta} + P^2_{\overline{z/L_{PP},\theta}} \tag{2.15}$$

The original sinkage and trim data is recomputed using Eqs. (2.8) and (2.9) and plotted with error bars in Fig. 2.26. New UA is done for cases without and with the rail bias, similarly as done previously for the ITTC equations. The UA is summarized in Table 2.16 for the case without rail bias and in Tables 2.17 and 2.18 for the cases with rail bias before and after rail correction, respectively. Data in Fig. 2.26 exhibit much less low-Fr scatter than in Fig. 2.25 due to the absence of the Fr^2 term in Eqs. (2.8) and (2.9). In Tables 2.16, 2.17, 2.18, overall UA are not much different than those in Tables 2.10, 2.14, and 2.15.

Conclusions

An investigation of rail levelness and its effect on sinkage and trim uncertainty analysis (UA) is done for the IIHR towing tank facility. The results are used to update previously published sinkage and trim UA for model 5512 sinkage and trim

Table 2.16 Sinkage and trim UA results using Eqs. (2.8) and (2.9). Rail level bias is *not* included in this analysis

Sinkage						
Term	*Fr* = 0.10		*Fr* = 0.28		*Fr* = 0.41	
	(-)	(%)	(-)	(%)	(-)	(%)
$(B_{\Delta FP}\theta_{\Delta FP})^2$	$(1.008E\text{-}05)^2$	73.4	$(1.008E\text{-}05)^2$	73.4	$(1.008E\text{-}05)^2$	73.4
$(B_{\Delta AP}\theta_{\Delta AP})^2$	$(6.068E\text{-}06)^2$	26.6	$(6.068E\text{-}06)^2$	26.6	$(6.068E\text{-}06)^2$	26.6
$(B_{z/Lpp})^2$	$(1.176E\text{-}05)^2$	82.8	$(1.176E\text{-}05)^2$	18.9	$(1.176E\text{-}05)^2$	32.2
$(P_{z/Lpp})^2$	$(5.362E\text{-}06)^2$	17.2	$(2.435E\text{-}05)^2$	81.1	$(1.708E\text{-}05)^2$	67.8
$U_{z/Lpp}$	1.293E-05	***8.6***	2.704E-05	***1.4***	2.074E-05	***0.4***
$D_{z/Lpp}$	1.505E-04		1.891E-03		4.807E-03	
U_σ *(mm)*	*0.039*		*0.082*		*0.063*	
D_σ *(mm)*	*0.459*		*5.765*		*14.652*	
Trim						
Term	*Fr* = 0.10		*Fr* = 0.28		*Fr* = 0.41	
	(-)	(%)	(-)	(%)	(-)	(%)
$(B_{\Delta FP}\theta_{\Delta FP})^2$	$(2.016E\text{-}05)^2$	73.4	$(2.016E\text{-}05)^2$	73.4	$(2.016E\text{-}05)^2$	73.4
$(B_{\Delta AP}\theta_{\Delta AP})^2$	$(1.214E\text{-}05)^2$	26.6	$(1.214E\text{-}05)^2$	26.6	$(1.214E\text{-}05)^2$	26.6
$(B_\theta)^2$	$(2.353E\text{-}05)^2$	52.7	$(2.353E\text{-}05)^2$	34.8	$(2.353E\text{-}05)^2$	3.4
$(P_\theta)^2$	$(2.231E\text{-}05)^2$	47.3	$(3.222E\text{-}05)^2$	65.2	$(1.247E\text{-}04)^2$	96.6
U_θ	3.242E-05	***9.9***	3.990E-05	***1.7***	1.269E-04	***1.9***
D_θ	3.274E-04		2.348E-03		6.621E-03	
U_τ *(°)*	*0.002*		*0.002*		*0.007*	
D_τ *(°)*	*0.019*		*0.135*		*0.379*	

Table 2.17 Sinkage and trim UA results using Eqs. (2.8) and (2.9). Rail level bias *before* rail correction is included in this analysis

Sinkage						
Term	*Fr* = 0.10		*Fr* = 0.28		*Fr* = 0.41	
	(-)	(%)	(-)	(%)	(-)	(%)
$(B_{\Delta FP}\theta_{\Delta FP})^2$	$(1.483E\text{-}04)^2$	50.1	$(1.483E\text{-}04)^2$	50.1	$(1.483E\text{-}04)^2$	50.1
$(B_{\Delta AP}\theta_{\Delta AP})^2$	$(1.481E\text{-}04)^2$	49.9	$(1.481E\text{-}04)^2$	49.9	$(1.481E\text{-}04)^2$	49.9
$(B_{z/Lpp})^2$	$(2.096E\text{-}04)^2$	99.9	$(2.096E\text{-}04)^2$	98.7	$(2.096E\text{-}04)^2$	99.3
$(P_{z/Lpp})^2$	$(5.362E\text{-}06)^2$	0.1	$(2.435E\text{-}05)^2$	1.3	$(1.708E\text{-}05)^2$	0.7
$U_{z/Lpp}$	2.097E-04	***139.3***	2.110E-04	***11.2***	2.103E-04	***4.4***
$D_{z/Lpp}$	1.505E-04		1.891E-03		4.807E-03	
U_σ *(mm)*	*0.639*		*0.643*		*0.641*	
D_σ *(mm)*	*0.459*		*5.765*		*14.652*	
Trim						
Term	*Fr* = 0.10		*Fr* = 0.28		*Fr* = 0.41	
	(-)	(%)	(-)	(%)	(-)	(%)
$(B_{\Delta FP}\theta_{\Delta FP})^2$	$(2.966E\text{-}04)^2$	50.1	$(2.966E\text{-}04)^2$	50.1	$(2.966E\text{-}04)^2$	50.1
$(B_{\Delta AP}\theta_{\Delta AP})^2$	$(2.962E\text{-}04)^2$	49.9	$(2.962E\text{-}04)^2$	49.9	$(2.962E\text{-}04)^2$	49.9
$(B_\theta)^2$	$(4.192E\text{-}04)^2$	99.7	$(4.192E\text{-}04)^2$	99.4	$(4.192E\text{-}04)^2$	91.9
$(P_\theta)^2$	$(2.231E\text{-}05)^2$	0.3	$(3.222E\text{-}05)^2$	0.6	$(1.247E\text{-}04)^2$	8.1
U_θ	4.198E-04	***128.2***	4.204E-04	***17.9***	4.373E-04	***6.6***
D_θ	3.274E-04		2.348E-03		6.621E-03	
U_τ *(°)*	*0.024*		*0.024*		*0.025*	
D_τ *(°)*	*0.019*		*0.135*		*0.379*	

Table 2.18 Sinkage and trim UA results using Eqs. (2.8) and (2.9). Rail level bias *after* rail correction is included in this analysis

Sinkage						
Term	*Fr* = 0.10		*Fr* = 0.28		*Fr* = 0.41	
	(-)	(%)	(-)	(%)	(-)	(%)
$(B_{\Delta FP}\theta_{\Delta FP})^2$	$(1.016E\text{-}04)^2$	50.2	$(1.016E\text{-}04)^2$	50.2	$(1.016E\text{-}04)^2$	50.2
$(B_{\Delta AP}\theta_{\Delta AP})^2$	$(1.012E\text{-}04)^2$	49.8	$(1.012E\text{-}04)^2$	49.8	$(1.012E\text{-}04)^2$	49.8
$(B_{z/Lpp})^2$	$(1.434E\text{-}04)^2$	99.9	$(1.434E\text{-}04)^2$	97.2	$(1.434E\text{-}04)^2$	98.6
$(P_{z/Lpp})^2$	$(5.362E\text{-}06)^2$	0.1	$(2.435E\text{-}05)^2$	2.8	$(1.708E\text{-}05)^2$	1.4
$U_{z/Lpp}$	1.435E-04	***95.4***	1.454E-04	***7.7***	1.444E-04	***3.0***
$D_{z/Lpp}$	1.505E-04		1.891E-03		4.807E-03	
U_σ *(mm)*	*0.437*		*0.443*		*0.440*	
D_σ *(mm)*	*0.459*		*5.765*		*14.652*	
Trim						
Term	*Fr* = 0.10		*Fr* = 0.28		*Fr* = 0.41	
	(-)	(%)	(-)	(%)	(-)	(%)
$(B_{\Delta FP}\theta_{\Delta FP})^2$	$(2.031E\text{-}04)^2$	50.2	$(2.031E\text{-}04)^2$	50.2	$(2.031E\text{-}04)^2$	50.2
$(B_{\Delta AP}\theta_{\Delta AP})^2$	$(2.025E\text{-}04)^2$	49.8	$(2.025E\text{-}04)^2$	49.8	$(2.025E\text{-}04)^2$	49.8
$(B_\theta)^2$	$(2.868E\text{-}04)^2$	99.4	$(2.868E\text{-}04)^2$	98.8	$(2.868E\text{-}04)^2$	84.1
$(P_\theta)^2$	$(2.231E\text{-}05)^2$	0.6	$(3.222E\text{-}05)^2$	1.2	$(1.247E\text{-}04)^2$	15.9
U_θ	2.876E-04	***87.9***	2.886E-04	***12.3***	3.127E-04	***4.7***
D_θ	3.274E-04		2.348E-03		6.621E-03	
U_τ *(°)*	*0.016*		*0.017*		*0.018*	
D_τ *(°)*	*0.019*		*0.135*		*0.379*	

measurements (Longo and Stern 2005). Rail bias is measured and shown to be significant in comparison with other sinkage and trim bias error sources such as those with associated with the trim and sinkage measurement devices and sensors. Accordingly, a rail levelness correction work has been done at the IIHR towing tank followed by another rail bias measurement after the rail correction. Based on the coverage of error bars on σ and τ coefficient data, revised UA results with inclusion of rail bias are more realistic uncertainty estimates. UA for alternate sinkage and trim variables $(z/L_{PP}, \theta)$ demonstrates that rail bias improves uncertainty coverage from unrealistically small to realistic. Consequently, inclusion of rail bias in sinkage and trim UA is important to provide a more comprehensive accounting of error sources for this measurement.

References

Eça L, Vaz G, Hoekstra M (2010) Code verification, solution verification and validation in RANS solvers. OMAE2010, Shanghai, China

Hino T (ed) (2005) Proceedings of CFD Workshop Tokyo 2005. NMRI report

Irvine M, Longo J, Stern F (2004) Towing tank tests for surface combatant for free roll decay and coupled pitch and heave motions. Proc. 25th ONR Symposium on Naval Hydrodynamics, St Johns, Canada

ITTC (1987) Report of the resistance and flow committee. Kobe, Japan

ITTC (2008) ITTC recommended procedures and guidelines. Uncertainty analysis in CFD Verification and Validation. Methodology and procedures. International Towing Tank Conference, document 7.5-03-01-01

Kim WJ, Van DH, Kim DH (2001) Measurement of flows around modern commercial ship models. Exp Fluid 31:567–578

Kodama Y, Takeshi H, Hinatsu M, Hino T, Uto S, Hirata N, Murashige S (1994) Proceedings, CFD Workshop. Ship Research Institute, Tokyo, Japan

Larsson L (ed) (1981) SSPA-ITTC Workshop on Ship Boundary Layers. SSPA Report 90, Gothenburg, Sweden

Larsson L, Patel VC, Dyne G (eds) (1991) SSPA-CTH-IIHR Workshop on Viscous Flow. Flowtech Research Report 2, Flowtech Int. AB, Gothenburg, Sweden

Larsson L, Stern F, Bertram V (eds) (2002) Gothenburg 2000-A Workshop on Numerical Hydrodynamics. Department of Naval Architecture and Ocean Engineering, Chalmers University of Technology, Gothenburg, Sweden

Larsson L, Stern F, Bertram V (2003) Benchmarking of computational fluid dynamics for ship flow: the Gothenburg 2000 Workshop. J Ship Res 47:63–81

Lee SJ, Kim HR, Kim WJ, Van SH (2003) Wind tunnel tests on flow characteristics of the KRISO 3600 TEU Containership and 300 K VLCC Double-deck Ship Models. J Ship Res 47(1):24–38

Longo J, Stern F (2005) Uncertainty assessment for towing tank tests with examples for surface combatant DTBM model 5415. J Ship Res 49(1):55–68

Longo J, Shao J, Irvine M, Stern F (2007) Phase-averaged PIV for the nominal wake of a surface ship in regular head waves, ASME. J Fluids Eng 129:524–540

Olivieri A, Pistani F, Avanaini A, Stern F, Penna R (2001) Towing tank experiments of resistance, sinkage and trim, boundary layer, wake, and free surface flow around a naval combatant INSEAN 2340 model. Iowa Institute of Hydraulic Research, The University of Iowa. IIHR Report No 421:pp 56

Roache PJ (1998) Verification and validation in computational science and engineering. Hermosa Publishers, Albuquerque

Simonsen C, Otzen J, Stern F (2008) EFD and CFD for KCS heaving and pitching in regular head waves. Proc. 27th Symp. Naval Hydrodynamics, Seoul, Korea

Stern F, Agdrup K, Kim SY, Hochbaum AC, Rhee KP, Quadvlieg F, Perdon P, Hino T, Broglia R, Gorski J (inpress) Experience from SIMMAN 2008: The first workshop on verification and validation of ship maneuvering simulation methods. J Ship Res

Van SH, Kim WJ, Yim DH, Kim GT, Lee CJ, Eom JY (1998a) Flow measurement around a 300 K VLCC model. Proceedings of the Annual Spring Meeting, SNAK, Ulsan, pp. 185–188

Van SH, Kim WJ, Yim GT, Kim DH, Lee CJ (1998b) Experimental investigation of the flow characteristics around practical hull forms. Proceedings 3rd Osaka Colloquium on Advanced CFD Applications to Ship Flow and Hull Form Design, Osaka, Japan

Xing T, Stern F (2010) Factors of safety for Richardson extrapolation. J Fluids Eng 132(6):061403-061403-13. doi:10.1115/1.4001771

Yoon H (2009) Phase-Averaged stereo-PIV flow field and force/moment/motion measurements for surface combatant in PMM maneuvers. Ph.D. thesis, University of Iowa

Zou L, Larsson L, Orych M (2010) Verification and validation of CFD predictions for a manoeuvring tanker. ICHD2010, Shanghai, China

Chapter 3
Evaluation of Local Flow Predictions

Michel Visonneau

Abstract In this Chapter, the computations performed by all the contributors are analyzed from the point of view of the local flow analysis in order to assess the level of agreement between computations and local flow measurements and identify the sources of errors. Pure resistance with or without free-surface, hull/propeller coupling, wave diffraction or roll decay configurations are reviewed in detail. One observes a general improvement of the agreement between simulations and measurements and a strong consistency of the simulations, compared to the previous editions of this workshop. When a reasonably fine grid is employed, similar turbulence models provide similar results, independently of the code used, which illustrates the state of maturity of modern CFD methodologies. For resistance and hull/propeller coupling configurations, a detailed comparison of the best statistical turbulence models and LES or hybrid LES turbulence closures, introduced for the first time in this workshop, is conducted to identify their respective impact on local flow simulations.

1 Introduction

In this Chapter, we will review from the point of view of the local flow analysis the computations provided by the contributors to the Gothenburg G2010 workshop and reported in Volume II of the Gothenburg 2010 proceedings. Although it is not possible to conduct such a local analysis for all the test cases since local flow measurements are not available for every case, we will be able to perform this exercise for the three ships involved in this workshop. The viscous flow around the KVLCC2 without free-surface and propeller (Case 1.1a) will be studied in great detail thanks to the availability of local velocity and Reynolds stress measurements at various sections including the propeller disk. The study will be focused on the respective influence of discretization and modeling errors in the wake flow and we will examine new solutions provided by promising new turbulence closures (hybrid LES) compared to different classes of more established isotropic or anisotropic statistical closures. Then, the flow around the KCS with and without propeller will be examined (cases 2.1 and 2.3a). The objective here will be to compare the various propeller modeling and

M. Visonneau (✉)
CNRS/Centrale Nantes, Nantes, France
e-mail: michel.visonneau@ec-nantes.fr

L. Larsson et al. (eds.), *Numerical Ship Hydrodynamics,*
DOI 10.1007/978-94-007-7189-5_3, © Springer Science+Business Media Dordrecht 2014



Fig. 3.1 KVLCC2—Hull geometry

to try to provide recommendations for future studies. Finally, the flow around the US Navy combatant DTMB5415 will be analyzed for three different flow configurations. Case 3.1a will be devoted to the study of the global flow around the ship with a focus on the flow topology, the details of the flow at the bow and the relative influence of discretization and modeling errors. While all the previous test cases are not strongly influenced by the presence of the free-surface, the two last test cases (cases 3.5 and 3.6) will make possible a study of the influence of the free-surface on the local flow through the analysis of wave diffraction and roll-decay for the same ship.

By studying and comparing the contributions of various teams with different numerical methods and physical models, the general objective of this study is to draw information of general interest for the numerical ship hydrodynamics community. However, in some cases, it will be difficult to conclude on the basis of the available computations. This will open the way to additional studies described in Chap. 7 which will aim at clarifying some fundamental interrogations left open at the end of this Chapter.

2 KVLCC2–Case 1.1-a

KVLCC2, shown in Fig. 3.1, is the second variant of the MOERI tanker with more U-shaped stern frame-lines (Van et al 1998a, b; Kim et al 2001). As explained in Hino (2005), it differs from the KVLCC2M used in the CFD Workshop Tokyo in 2005, mainly at the stern contour near the propeller shaft. Since turbulence data are required, the original hull (KVLCC2) is used in the present Workshop. The flow over the double-body hull, without rudder, was measured in a wind-tunnel at POSTECH. Turbulence data were also obtained at POSTECH, see Lee et al. (2003). Towing tank tests were also performed at KRISO for the same Reynolds number ($Re = 4.6 \times 10^6$) at a Froude number ($Fr = 0.142$) small enough to eliminate any additional free-surface effects. The axial velocity contours and cross-flow vectors are available at the following cross-sections $x/L_{pp} = 0.85$; 0.9825 (propeller plane); 1.1. The total wake fraction at propeller plane determined from wind-tunnel and towing tank's experiments at several radii ($r/R = 0.4$; 0.6; 0.8; 1.0) can also be used to perform a more detailed assessment of the computations. Then, the transversal evolution of the three velocity components at $x/L_{pp} = 0.9825$ and $z/L_{pp} = -0.05075$ can also be checked. Last but not least, the turbulent kinetic energy and five Reynolds stress components ($\overline{uu}$, $\overline{vv}$, $\overline{ww}$, $\overline{uv}$, $\overline{uw}$) are also available at the propeller plane ($x/L_{pp} = 0.9825$) to make possible a more detailed assessment of the results.

It is well known that turbulence anisotropy is an additional source of longitudinal vorticity production. In fact the turbulence anisotropy acts as a direct source term

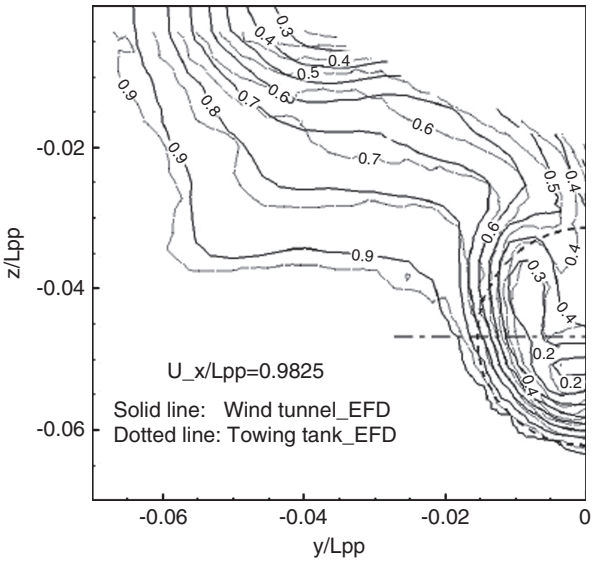


Fig. 3.2 KVLCC2—Comparison between towing tank and wind tunnel measurements at $X/L_{pp} = 0.9825$

in the transport equation of the longitudinal vorticity. Having the normal Reynolds stresses available at the propeller plane will make possible a detailed verification of the amount of measured anisotropy in the propeller plane.

2.1 Description of the Experimental Results

The flow at model scale around the KVLCC2 is characterized by the gradual development of an intense stern bilge vortex which creates a strong distortion of the axial velocity iso-contours at the propeller plane. This distortion is due to the transport of low momentum fluid from the vicinity of the hull to the center of the flow field under the action of an intense longitudinal vortex. Under the main vortex, one can guess the existence of a secondary counter-rotating vortex close to the vertical plane of symmetry. This leads to the so-called hook-shape of the iso-wakes which is clearly visible in the towing tank and wind tunnel experiments. It is interesting to compare these experiments which are almost identical but differ in the vicinity of the vertical plane of symmetry (see the level $U = 0.4$ in Fig. 3.2). These local differences may be attributed to blockage effects, the tunnel blockage being more than 6 % while the towing tank blockage is only 0.3 %. On the other hand, it seems easier to control the quality of the measurements (in terms of flow symmetry for instance) in a wind tunnel than in a towing tank where small free-surface deformations may create perturbations. These various sources of experimental errors will have to be considered during the comparisons with computations which were performed without any blockage effect and free-surface deformation. However, the quantification of the influence of blockage effect on the detailed flow map is a question which has to be left open in this

Table 3.1 Main characteristics of the computations

Organization/Code name	Turbulence models	Wall model	Discretization characteristics
CHALMERS/ SHIPFLOW4.3	EASM	Low Re near wall turbulence model, no slip	Structured grid, 3.2 million points
ECN-BEC/ICARE	k-ω model	Low Re near wall turbulence model, no slip	Structured grid, 1,1 million points
HSVA/FreSCo$^+$	k-ω model	Low Re near wall turbulence model, no slip	Unstructured grid, 3.4 million points
IIHR/CFDShip-Iowa-V4.5 (ARS)	ARS	Low Re near wall turbulence model, no slip	Over-set structured grids, 305 million points (Grid G0) and 13 million points (Grid G1)
IIHR/CFDShip-Iowa-V4.5 (ARS-DES)	ARS based DES	Low Re near wall turbulence model, no slip	Over-set structured grids, 13 million points (Grid G1)
IST-MARIN/ PARNASSOS (RCKSKL)	k sqrt(kl)	Low Re near wall turbulence model, no slip	Structured grid, 6.3 million points
IST-MARIN/ PARNASSOS (RCSST)	SST with rotation correction	Low Re near wall turbulence model, no slip	Structured grid, 6.3 million points
IST-MARIN/ PARNASSOS (SST)	SST	Low Re near wall turbulence model, no slip	Structured grid, 6.3 million points
NSWCCD-ARL-UM/ NavyFOAM	k-ω	Wall function	Multi-block unstructured, 8 million points
NMRI/SURF	EASM	Low Re near wall turbulence model, no slip	Unstructured grid, 3.8 million points
NTNU/FLUENT	RSM, SST k-ω, k-ω	Low Re near wall turbulence model, no slip	Multi-block structured grid, 4.2 million points
MARIC/FLUENT6.3	RSM	Low Re near wall turbulence model, no slip	Structured grid, 2.8 million points

Chapter. Additional studies performed by CHALMERS and ECN-CNRS to assess the role played by the blockage effects will be described in Chap. 7.

2.2 Review of Contributions

Twelve contributions from nine organizations were uploaded for the test case 1.1a. The names of organizations and codes used are recalled in Table 3.1 with the main characteristics of their computations grouped in terms of relevant categories based on physical modeling (i.e. turbulence models), wall models, discretization characteristics (grid topology, mesh density, time step, etc. . .). In addition to the cases listed in Table 1, IIHR (Xing et al. 2010) also performed a verification of ARS-DES using Grids 1, 2, 3, 4 where grids 2–4 are obtained by systematically coarsening Grid G1 using a grid refinement ratio square root of 2.

It is widely accepted that the prediction for the nominal velocity at the propeller plane for U shaped hull such as the KVLCC2 tanker depends strongly on turbulence modeling, as soon as a reasonably fine grid is used. Turbulence models employed by different participants can be classified into three groups: (i) Unsteady hybrid LES model (IIHR/CFDShip-Iowa_DES which is the ARS-DES previously mentioned), (ii) anisotropic non-linear statistical turbulence modeling: Reynolds stress transport model (NTNU/FLUENT, MARIC/FLUENT6.3), algebraic Reynolds stress model (IIHR/CFDShip-Iowa_ARS, NMRI/SURF, CHALMERS/SHIPFLOW4.3) and (iii) isotropic linear eddy-viscosity model (ECN-BEC/ICARE, HSVA/FreSCo$^+$, IST-MARIN/PARNASSOS, NSWCCD-ARL-UM/NavyFOAM, NTNU/FLUENT). One participant introduces *ad hoc* rotation correction to a linear eddy-viscosity model (IST-MARIN/PARNASSOS). To be complete, one should mention that IIHR also performed computations with a blended k-ε-k-ω DES (BKW-DES) and Delayed DES (BKW-DDES). These results were not uploaded to the Gothenburg 2010 ftp site before the deadline and have not been reported in the section "Part 2: Computed results" of Volume II of the Proceedings. Consequently, they will not be discussed in this Chap. 3 but more detailed analysis and further comparisons between several versions of the Detached Eddy-Simulation closures will be provided in Chap. 7 specifically devoted to additional computations aimed at clarifying some points emerging from the analysis conducted in this Chapter.

All the discretization methods are formally second order accurate and are based on multi-block structured or unstructured grids which are all body fitted. However, the code CFDShip-Iowa also uses an hybrid 2nd/4th order discretization scheme in its version V4.5. The average size of mesh is around 4 million points for most of the methods with the noticeable exceptions of IIHR/CFDShip-Iowa-V4.5 (ARS-DES) using an extremely fine mesh (305 million points) and ECN-BEC/ICARE which employs a somewhat coarser grid (1.1 million points). Based on previous studies performed by the author, one can consider that, except for ECN-BEC, the grids used in this workshop are such that, for the statistical turbulence closures, the modeling error should dominate over the discretization error, which means that it should be meaningful to analyze the results according to the above-mentioned categories.

2.3 Analysis of Axial Velocity Contours at $X/L_{pp} = 0.85$

Most of the results are very similar at this cross-section where one can see the development of the stern bilge vortex. However, one can estimate the amount of vorticity already present at this section through the distortion of the levels $U = 0.9$ and 1.0. Some results (IIHR/CFDShip-Iowa-V4 (ARS-DES), MARIC/FLUENT6.3, NMRI/SURF, for instance) already exhibit a significant distortion. IIHR results showed that different turbulence models, numerical schemes and grid resolutions have negligible effects at this section since flow is in steady state (Fig. 3.3).

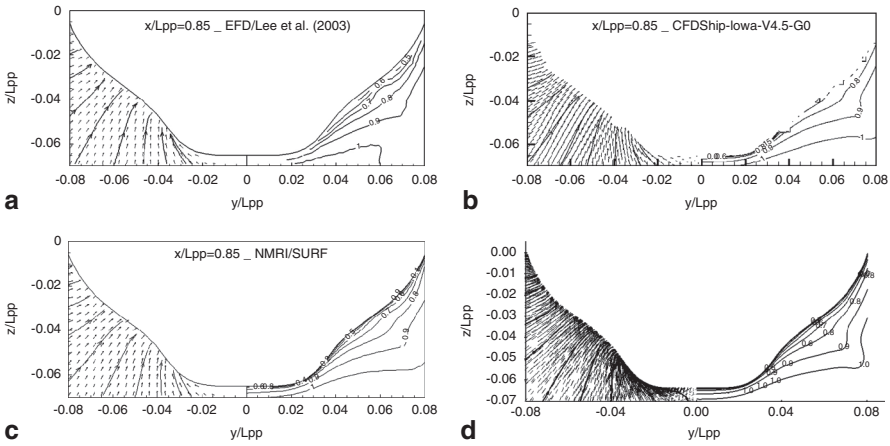


Fig. 3.3 Isowake contours at $x/L_{pp} = 0.85$. **a** Experiments, **b** IIHR-CFDSHIP-IOWA-V4.5, **c** NMRI/SURF **d** VTT/FINFLO

2.4 Analysis of Axial Velocity Contours at $X/L_{pp} = 0.9825$

At this section, the bilge vortex has developed and its impact on the iso-wakes is very large. A first group of results is in very good agreement with experiments, namely IIHR/CFDShip-Iowa-V4 (ARS-DES), NTNU/FLUENT, NMRI/SURF, CHALMERS/SHIPFLOW4.3, MARIC/FLUENT6.3 and NSWCCD-ARL-UM/NavyFOAM. Except NSWCCD-ARL-UM/NavyFOAM which uses a k-ω model (original version of 1998), all other results are based on various anisotropic turbulence models. IIHR/CFDShip-Iowa-V4 used both an algebraic Reynolds Stress model (ARS) and an ARS based DES (ARS-DES) version while both CHALMERS/SHIPFLOW4.3 and NMRI/SURF utilizes the Explicit Algebraic Stress Model developed by ECN-CNRS some years ago (Deng et al. 2005). Computations performed with FLUENT (NTNU/FLUENT and MARIC/FLUENT6.3) are based on a more complex Reynolds Stress Transport Model which solves additional transport equations for the Reynolds Stress components. It is interesting to notice that all these results agree better with the towing tank measurements than with the wind-tunnel experiments since all the computations predict an iso-wake contour of 0.4 which does not cross the vertical plane of symmetry but remains parallel to it. The main stern bilge vortex is very accurately captured and the hook-shape of the iso-axial velocity contours is very well reproduced. A second counter-rotating vortex below the first one, hardly visible in the experiments is present in all these computations. In that region which is in the wake of the propeller hub, the agreement between the best solutions and the experiments is less good. Let us recall that this is a region where the flow is probably influenced by the shape of the hub which is slightly different because of the presence of the hub cap in the computations. One can also notice that the ARS based DES solution contains more intense longitudinal vortices, a characteristic on which we will come back in the next sections. Comparison between ARS-G1 and

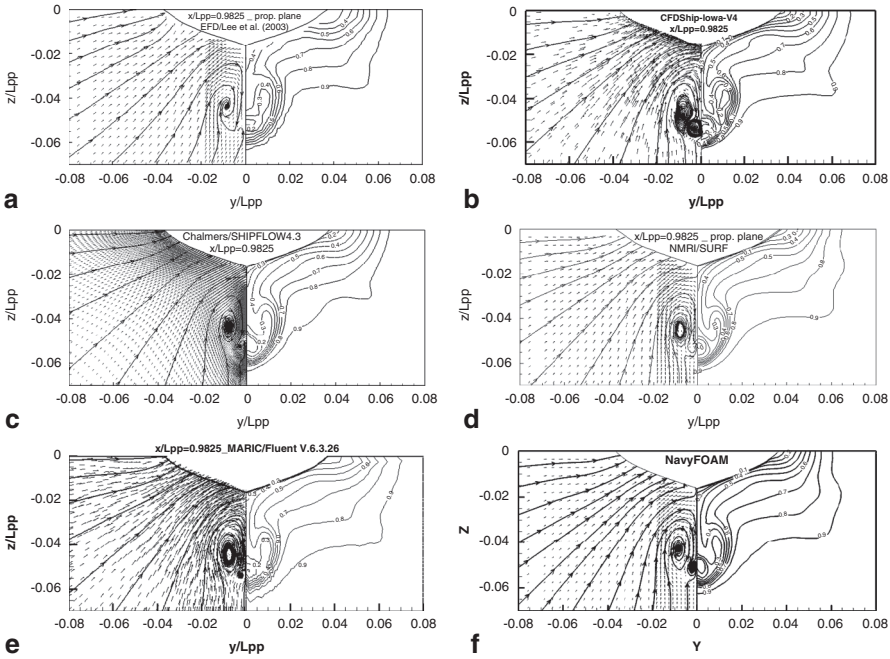


Fig. 3.4 Isowake contours at $x/L_{pp} = 0.9825$. **a** Experiments, **b** IIHR/CFDSHIP-IOWA-V4, **c** CHALMERS/SHIPFLOW4.3, **d** NMRI/SURF, **e** MARIC/FLUENT6.3.26, **f** NSWCCD-ARL-UM/NavyFOAM

ARS-G0 shows that grid refinement has little effects on the flow pattern for ARS. ARS-DES-G1 shows more vortical structures than ARS-G1 and agree better with EFD. The issue of grid induced separation for DES models, is probably due to the fact that LES is activated inside the boundary layer on the very fine 305M grid. According to the authors, this grid induced separation was resolved using Delayed DES (DDES) simulation on the same grid and these new results will be described in Chap. 7. Figure 3.4 provides a set of representative examples illustrating this analysis.

On the other hand, linear eddy viscosity models without ad-hoc rotation correction under estimate the intensity of the bilge vortex (ECN-BEC/ICARE, HSVA/FreSCo$^+$, IST-MARIN/PARNASSOS-SST, VTT/FINFLO). A noticeable exception is Navy-FOAM which uses Wilcox's k-ω 1998 model which gives a prediction similar to that obtained with algebraic Reynolds stress model. As this original model is not as widely used as the SST model for example since it was modified by Wilcox some years later, this performance needs to be further validated by other flow solvers. IST/MARIN presents some good prediction for the nominal velocity obtained with linear eddy-viscosity model with rotation correction or with a linear turbulence model (see Fig. 3.6). The improvement brought by those *ad-hoc* modifications seems to be limited to the mean velocity field at the propeller plane. In particular, the recirculation region in the stern region appears to be extended more upstream (see Fig. 3.18 in the section devoted to the wall streamlines), which is not in agreement with the experiments.

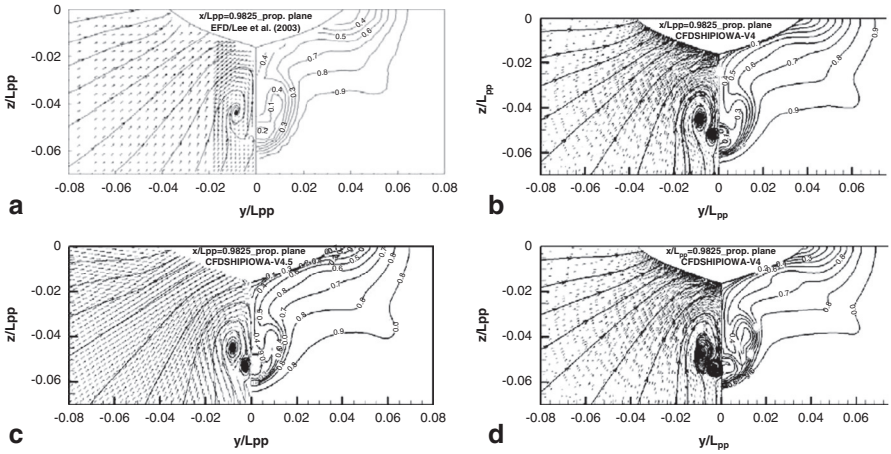


Fig. 3.5 U contours (*right* panel), cross flow vectors and streamlines (*left* panel) at x/Lpp = 0.9825: **a** EFD, **b** ARS-G1, **c** ARS-G0, **d** ARS-DES-G1 (computations from IIHR)

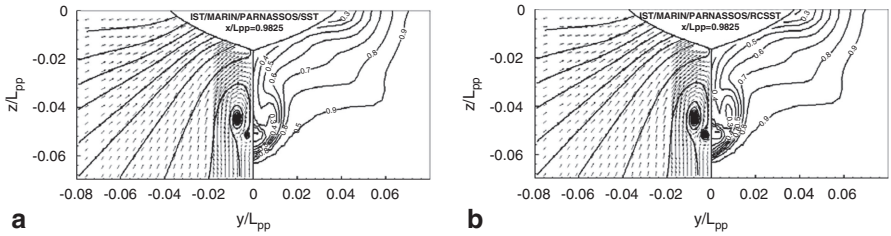


Fig. 3.6 Results from IST-MARIN/PARNASSOS. Role of the rotation correction (a) SST k-ω model (b) SST k-ω model with rotation correction

Figure 3.5 shows results obtained by IIHR at the propeller plane. One can observe that grid refinement has little effects on the flow pattern for ARS (see sub-figures (b) and (c)). On the other hand, large differences can be observed between ARS and ARS-DES results computed on the same grid G1 (see sub-figures (b) and (d)). Much stronger vortices are simulated with the help of the unsteady ARS-DES turbulence closure. An iso-wake contour U = 0.2 is even visible in the core of the main longitudinal vortex when simulated with ARS-DES, which indicates that the main predicted vortical structure is more intense than what is observed in the experiments (see sub-figure (a)) (Fig. 3.6).

2.5 Analysis of Axial Velocity Contours at X/L_{pp} = 1.1

Only one strong vortex is now visible close to the vertical plane of symmetry while a secondary vortex develops in the vicinity of the horizontal plane of symmetry. The bilge vortex captured by the contributors using anisotropic turbulence closures or

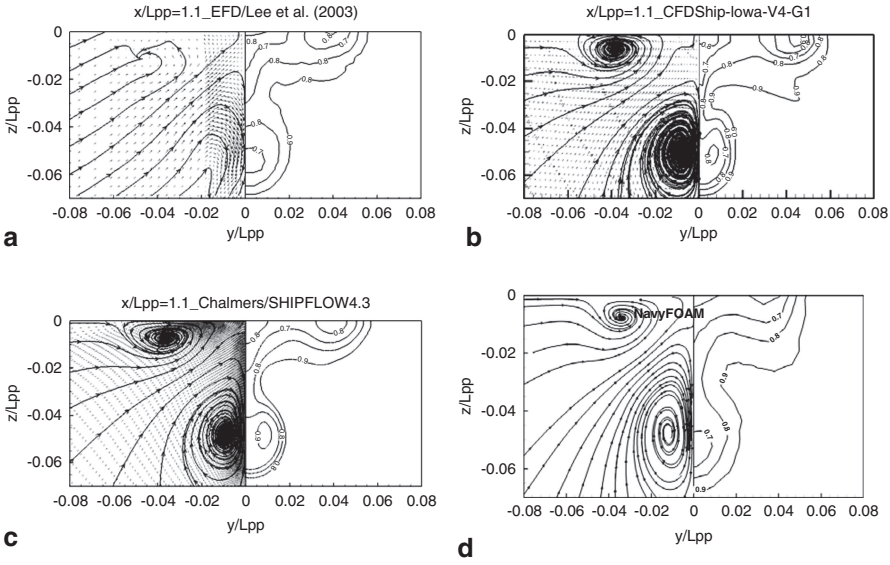


Fig. 3.7 Isowake contours at $x/L_{pp} = 1.1$. **a** Experiments **b** IIHR/CFDSHIP-IOWA-V4 **c** CHALMERS/SHIPFLOW4.3 **d** NSWCCD-ARL-UM/NavyFOAM

hybrid LES modeling is convected in the wake without losing too much intensity, which means that the analysis made for $X/L_{pp} = 0.9825$ remains valid for this section, in terms of longitudinal vorticity intensity (see Fig. 3.7).

2.6 Total Wake Fraction on the Propeller Plane

Figure 3.8 shows the total wake fraction, $w_T = 1\text{-}u/U$, u being the total local velocity and U the ship speed with respect to ϕ, the circumferential angle, counterclockwise from 0° (top) to 360°. This quantity is measured in the towing tank (lines) and wind tunnel (symbols) at four radial locations (r/R = 04, 0.6, 0.8 and 1.0), R being the propeller radius, R = 0.0425 m.

The shaft centerline O is at $z/L_{pp} = -0.04688$. One observes here again some differences between POSTECH and KRISO's experiments for ϕ between 120° and 240° and r/R = 0.6, 0.8, particularly. One notices here a more marked circumferential variation in the towing tank's experiments at the bottom of the core of the main longitudinal vortex. Differences in the vicinity of the vertical plane of symmetry are also reflected in the total wake fraction behavior.

To be consistent with the choice made before, it was decided to compare the computations with the wind tunnel experiments. These comparisons are shown in Fig. 3.9.

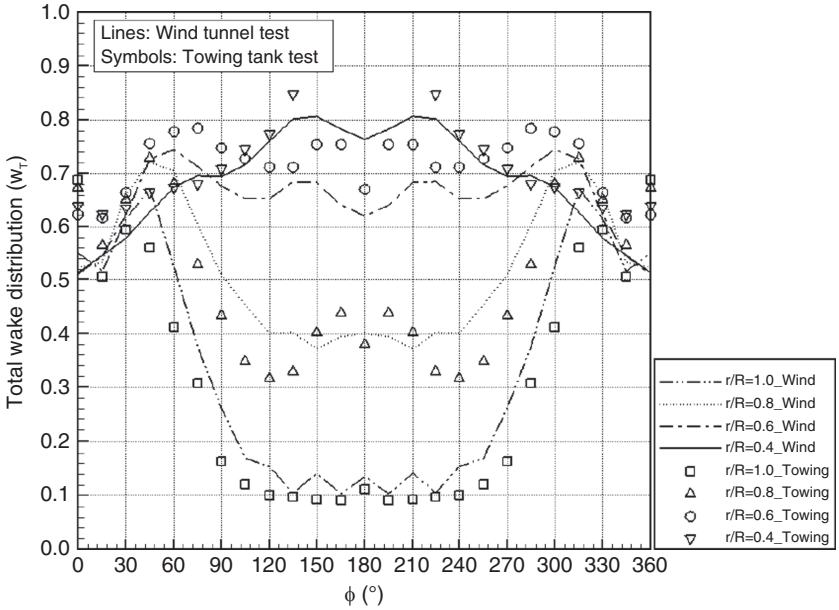


Fig. 3.8 Comparison between the total wake fraction w_T measured in the wind tunnel by POSTECH (*lines*) and by KRISO in the towing tank (*symbols*)

The Fig. 3.9 shows a comparison between the afore-mentioned experiments and computations from contributors using turbulence models belonging to three distinct categories. CHALMERS and NMRI use the same non-linear anisotropic statistical turbulence model and IIHR with the use of a non-linear algebraic Reynolds Stress statistical model (ARS). In the second category, we find IST-MARIN employing a linear isotropic turbulence model with or without correction rotation. The third category is composed of IIHR's contribution which proposes a radically different modeling approach based on an unsteady hybrid LES turbulence model (DES). First of all, all the computations predict accurately the circumferential variation of the total wake fraction at r/R = 1.0. At r/R = 0.8 and for ϕ outside of the critical interval (120 and 240°), most of the computations using non-linear anisotropic turbulence models agree reasonably well with the computations, the best answer being given by CHALMERS/SHIPFLOW4.3. On the other hand, computations based on linear turbulence model seem to underestimate the total wake fraction in the same region, while the rotation correction improves a bit the agreement with experiments. The DES computations are not perfectly symmetric with respect to the vertical plane of symmetry, which indicates a lack of convergence in terms of averaged flow quantities. This model tends to over-estimate the maximum of the total wake, providing a less regular circumferential variation than what is observed in the experiments. At the same radial location but for ϕ inside of the critical interval (120 and 240°), all the computations are far from the measurements. When the wind tunnel's experiments

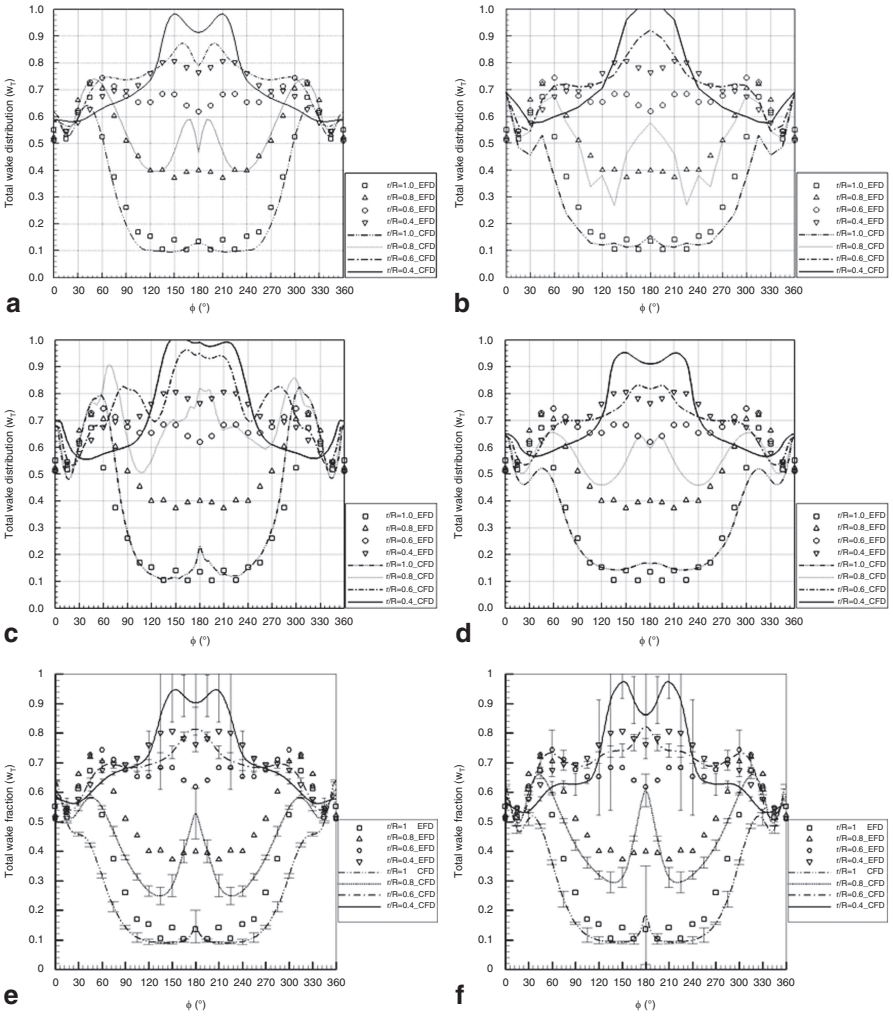


Fig. 3.9 Comparison between the total wake fraction w_T measured in the wind tunnel by POSTECH (symbols) and computations from various contributors (lines). **a** CHALMERS/SHIPFLOW4.3, **b** NMRI/SURF, **c** IIHR/CFDSHIP-IOWA-V4 (DES), **d** IIHR/CFDSHIP-IOWA-V4 (ARS), **e** IST-MARIN/PARNASSOS(SST), **f** IST-MARIN/PARNASSOS(RCSST)

show a plateau in this region, the anisotropic models implemented by CHALMERS and IIHR predict a double maximum configuration with a rapid increase of w_T and a decay more or less marked in the plane of symmetry while the linear models and the DES formulation provide a prediction with one maximum reached at the vertical plane of symmetry. It is very difficult to conclude since this region is also characterized by a high level of experimental uncertainty, if one compares the wind-tunnel's experiments to the towing tank's measurements. It is interesting however

to notice that this double maximum configuration is clearly observed in the towing tank's experiments although shifted vertically to the bottom by comparison with most of the computations predicting the same global behavior. At r/R = 0.6 and 0.4, the agreement between computations and measurements is again not very satisfactory since all the methods tend to over-estimate w_T by about 15 to 20 % in the vicinity of the plane of symmetry. Here again, the computations seem to be in better agreement with the towing tank's experiments. As shown in Xing et al. 2010, compared with ARS-G1, total wake fraction on the propeller plane predicted by ARS-G0 agrees much better with the data than ARS-G1 at all the four radial locations, especially for ϕ values between 90° and 270°. Compared with ARS-G1, ARS-DES-G1 over-predicts the velocity fluctuations at almost all ϕ.

2.7 Velocity Profiles and Cross-flow Vectors at Propeller Plane ($x/L_{pp} = 0.9825$, $z/L_{pp} = -0.05075$)

The analysis made in terms of global axial velocity contours in the propeller plane can be cross-checked with the lateral evolution of the local velocity profiles at particular vertical locations which are located in the core of the main bilge vortex. Contrary to what was often written in the past by some authors (who claimed, some years ago, that there was more consistency between results obtained by the same code using different turbulence closures than between different codes using the same turbulence model), one can observe a very strong coherence between groups using different codes run on similar grids and same turbulence models. This fact illustrates the maturity of modern RANSE solvers. Figure 3.10 shows the results obtained by codes representative of the three groups already mentioned, the hybrid LES modeling (ARS/DES from IIHR), the anisotropic non-linear statistical turbulence closures (contributions from NMRI and MARIC) and the isotropic linear turbulence closures (result from IST-MARIN).

IST-MARIN is the only one to report vertical bars corresponding to its evaluation of the range of uncertainty of their computations obtained from the modified procedure proposed in Eça et al. 2010. The large uncertainty range reported by these authors in the core of the vortex is likely to be attributed to the methodology used to evaluate the interval of confidence. Actually, this method uses a normalized data range on several grids when one does not observe a monotonic convergence from a Richardson's extrapolation analysis, which, according to the author of this review, provides a pessimistic estimate of the numerical reliability of these computations. The fact that so many codes used by different persons utilizing different but similar structured or unstructured grids, provide almost identical results when the same turbulence closures are used, seem to indicate indirectly that the numerical uncertainty is not that large.

Up to now, we have noticed that the turbulence modeling error played a crucial role in the ability of simulating accurately the stern flow at the propeller plane. Globally, one observes that the most sophisticated turbulence closures (i.e. time-accurate hybrid LES or anisotropic statistical closures) are able to capture turbulence

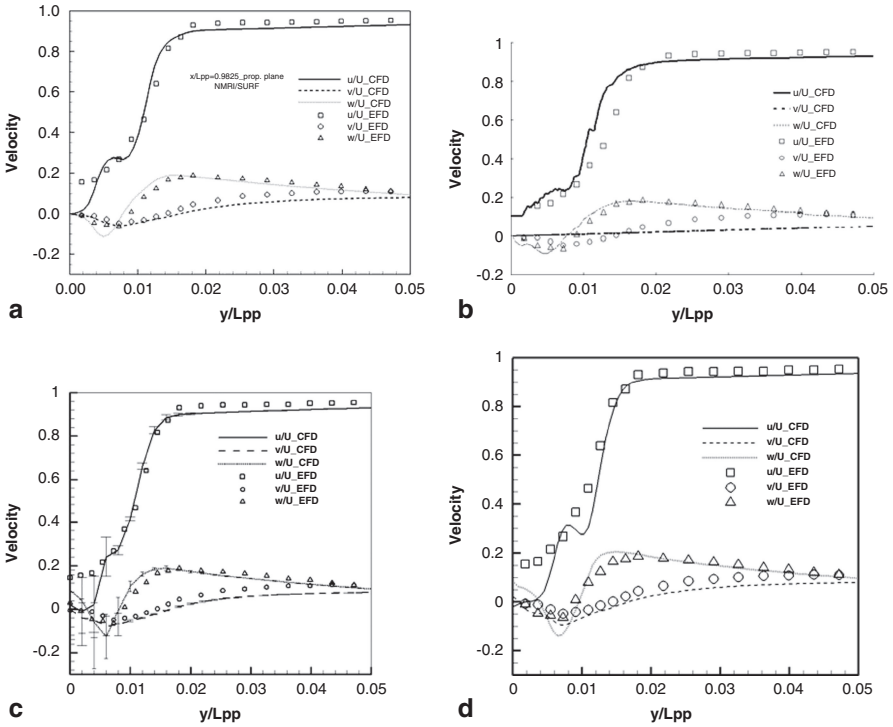


Fig. 3.10 Velocity profiles at $x/L_{pp} = 0.9825$, $z/L_{pp} = -0.0575$. **a** NMRI/SURF, **b** MARIC/FLUENT6.3.26, **c** IST-MARIN/PARNASSOS, **d** IIHR/CFDSHIP-IOWA-V4.5

anisotropy. They behave better than the simpler linear isotropic models, except if one modifies them by activating *ad hoc* corrections. The detailed analysis of the turbulence structure in the propeller plane should enable us to relate this observed numerical behavior to the accuracy of the prediction of shear and normal Reynolds stresses.

2.8 Turbulence Data at Propeller Plane ($x/L_{pp} = 0.9825$)

The exact transport equation for the longitudinal component of the vorticity reads:

$$\frac{D\omega_x}{Dt} - \nu\Delta\omega_x = \omega_x\frac{\partial U}{\partial x} + \omega_y\frac{\partial U}{\partial y} + \omega_z\frac{\partial U}{\partial z} - \frac{\partial^2(\overline{uw})}{\partial x\partial y} + \frac{\partial^2(\overline{uv})}{\partial x\partial z} + \left(\frac{\partial^2}{\partial z^2} - \frac{\partial^2}{\partial y^2}\right)(\overline{uw}) + \frac{\partial^2}{\partial y\partial z}(\overline{v^2} - \overline{w^2})$$

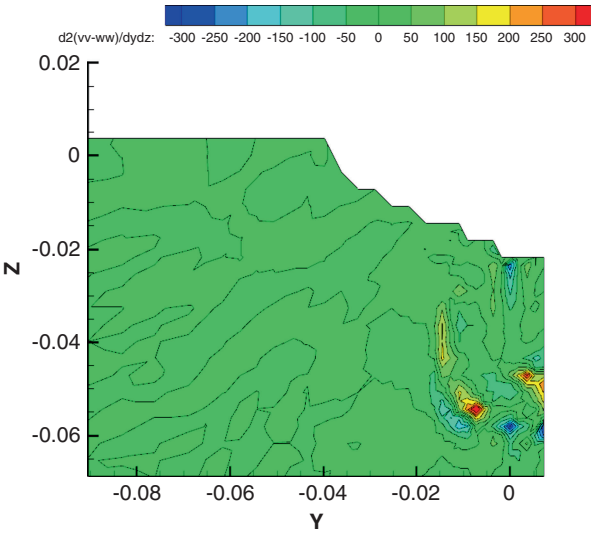


Fig. 3.11 Source term of the transport equation of longitudinal vorticity involving turbulence anisotropy recomputed from POSTECH's experiments

where the last term relates directly to the influence of the turbulence anisotropy on the production of longitudinal vorticity. It is therefore interesting to try to evaluate this source term from the available measurements of the normal Reynolds stresses. Figure 3.11 shows this source term directly evaluated from POSTECH's experiments. One can observe that the maximum values are actually reached in the core of the longitudinal vortices. Although this evaluation of a double cross-derivative on such a coarse experimental grid is obviously not accurate enough, this provides us with a valuable starting point for the analysis of the turbulence structure in the wake of the KVLCC2.

Let us start this analysis by the turbulence anisotropy at the propeller disk which will be in that case, represented by the differences between $\overline{uu}$, $\overline{vv}$ and $\overline{ww}$. Actually, this is the difference between $\overline{vv}$ and $\overline{ww}$ which is relevant in our case. If one compares the relative values of the normal turbulent stresses in POSTECH's measurements (see Fig. 3.12), one can notice a strong anisotropy inside the so-called hook shape characterizing the iso axial velocity contours. For instance, one finds $\max(\overline{uu}) = 0.016$, $\max(\overline{vv}) = 0.007$ and $\max(\overline{ww}) = 0.008$ while $\max(k) = 0.016$. Most of the codes using explicit anisotropic turbulent closures are able to predict with a reasonable agreement the turbulence structure at this cross-section. For instance, NMRI/SURF finds $\max(\overline{uu}) = 0.014$, $\max(\overline{vv}) = 0.008$ and $\max(\overline{ww}) = 0.009$ (see Fig. 3.13) while CHALMERS/SHIPFLOW4.3, using the same turbulence model finds roughly the same values i.e. $\max(\overline{uu}) = 0.014$, $\max(\overline{vv}) = 0.008$ and $\max(\overline{ww}) = 0.009$ (see Fig. 3.14). One can however notice that the extent of the zone where $\overline{vv}$ and $\overline{ww}$ are significant is slightly underestimated by both contributors (see for instance the location of the contour 0.003).

Moreover, in these hook-shaped structures, they both found one maximum, a topology which is not in agreement with the measurements which report a structure

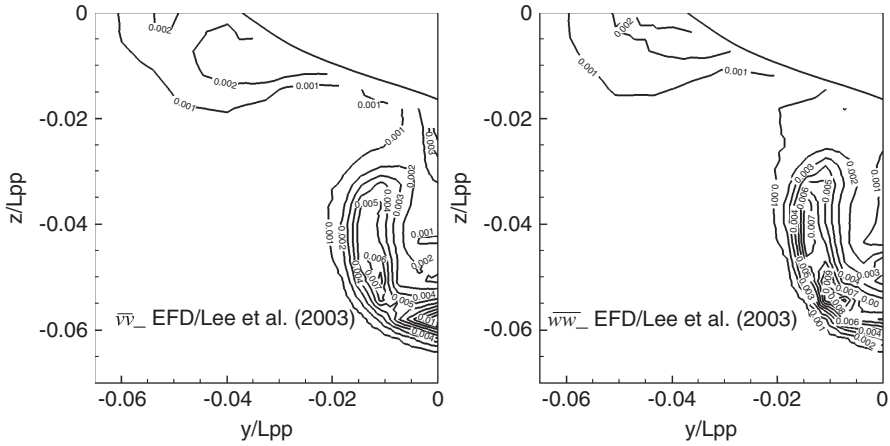


Fig. 3.12 Normal turbulent stresses $\overline{vv}$ and $\overline{ww}$ measured by POSTECH at section $X/L_{pp} = 1.1$

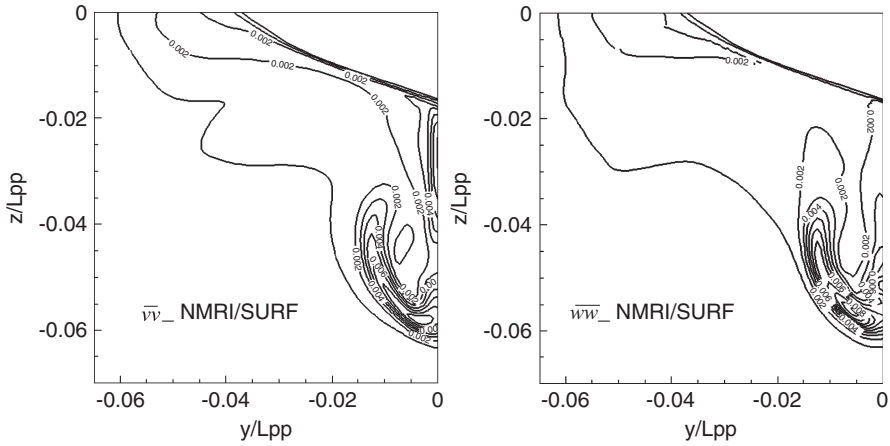


Fig. 3.13 Normal turbulent stresses $\overline{vv}$ and $\overline{ww}$ computed by NMRI/SURF at section $X/L_{pp} = 1.1$

with two extrema. It is interesting to notice here that this two-extrema configuration is well captured by IIHR with their hybrid LES model (Fig. 3.15). However, the values of these extrema are strongly underestimated in their computations since $\max(\overline{vv}) = 0.003$ and $\max(\overline{ww}) = 0.004$. The turbulence anisotropy is therefore more pronounced than what is observed with the anisotropic non-linear turbulence closures. This should probably be related with the more pronounced longitudinal vorticity which is found in the DES computations.

MARIC/FLUENT6.3.26, using a full Reynolds Stress Transport closure which is *a priori* more complete than the explicit algebraic stress model used by NMRI and CHALMERS, captures also the turbulence anisotropy but underestimates the maximum values of $\overline{vv}$ and $\overline{ww}$ (see Fig. 3.16). It is also worthwhile to underline a

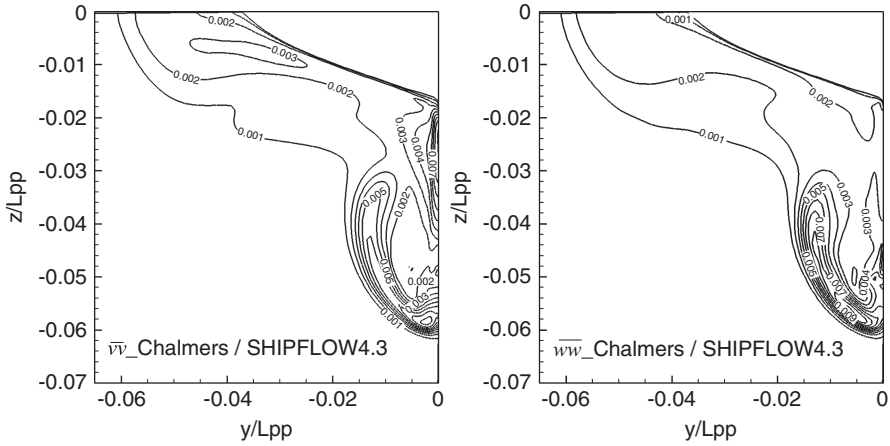


Fig. 3.14 Normal turbulent stresses $\overline{vv}$ and $\overline{ww}$ computed by CHALMERS/SHIPFLOWV4.3 at section $X/L_{pp} = 1.1$

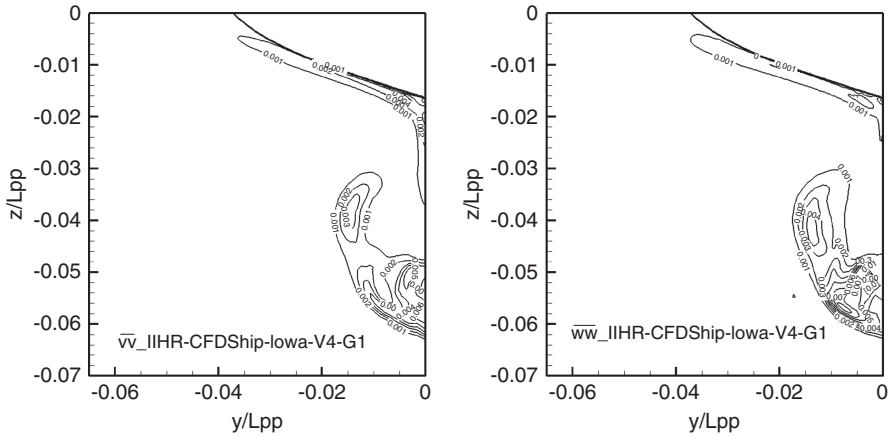


Fig. 3.15 Normal turbulent stresses $\overline{vv}$ and $\overline{ww}$ computed by IIHR:CFDSHIP-IOWA-V4.5 at section $X/L_{pp} = 1.1$

remarkable agreement between NTNU/FLUENT and MARIC/FLUENT6.3. Both organizations, using the same turbulence model, found max($\overline{uu}$) around 0.01, max($\overline{vv}$) around 0.004 and max($\overline{ww}$) around 0.005, results which are consistently smaller than the measurements, as explained before. This is again an illustration of a consistent trend associated to a specific turbulence modeling, independently from the grid (which has to be fine enough) and from the user of the solver (who has to be experienced enough . . .).

On the other hand, the linear isotropic closures fail to reproduce the correct turbulence anisotropy as expected. Therefore, instead of using the correct physical mechanism to enhance the longitudinal vorticity production, a correction factor is

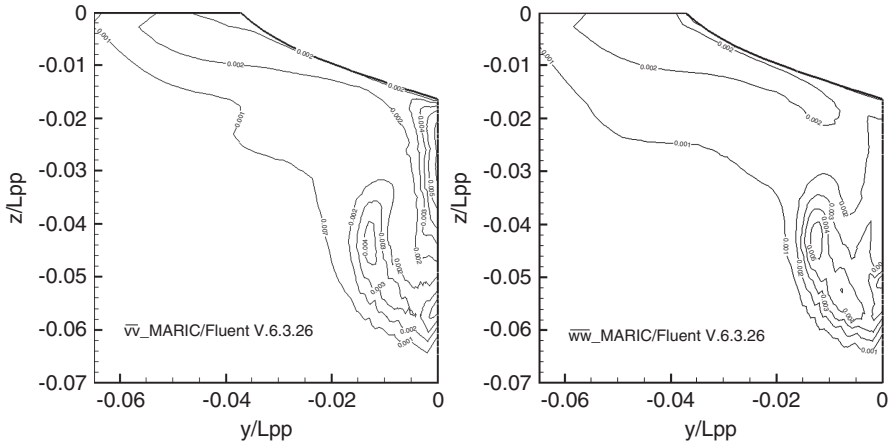


Fig. 3.16 Normal turbulent stresses $\overline{vv}$ and $\overline{ww}$ computed by MARIC/FLUENT6.3.26 at section $X/L_{pp} = 1.1$

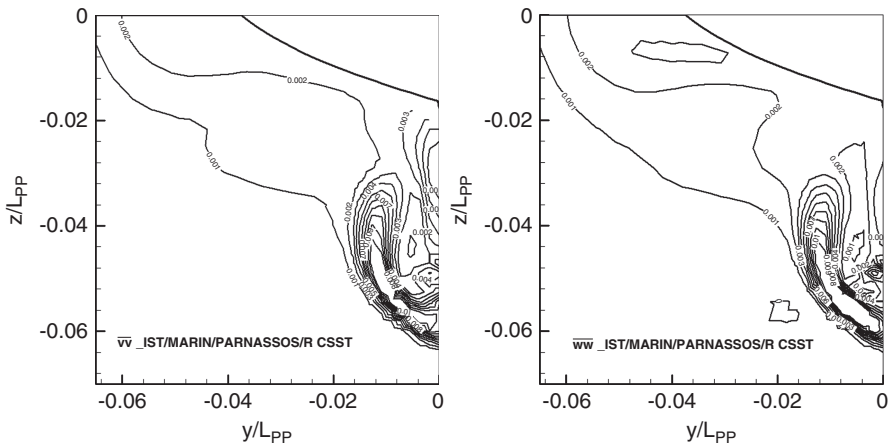


Fig. 3.17 Normal turbulent stresses $\overline{vv}$ and $\overline{ww}$ computed by IST-MARIN/PARNASSOS/RCSST at section $X/L_{pp} = 1.1$

used to limit the production of turbulence and consequently, to reduce locally the level of turbulent viscosity.

This is illustrated by the normal turbulent stresses computed by IST-MARIN in Fig. 3.17 for instance. One cannot see any significant difference between $\overline{vv}$ and $\overline{ww}$ in their results obtained with SST or RCSST although the iso-axial velocity contours are significantly modified by this rotation correction.

The turbulent shear stresses $\overline{uv}$ and $\overline{uw}$ are also measured and can be used to perform a detailed assessment of the computations. The agreement of all the computations with measurements is reasonable on $\overline{uv}$ except for the IIHR/DES computations which again do not reproduce the measured spatial distribution. For $\overline{uw}$, all the

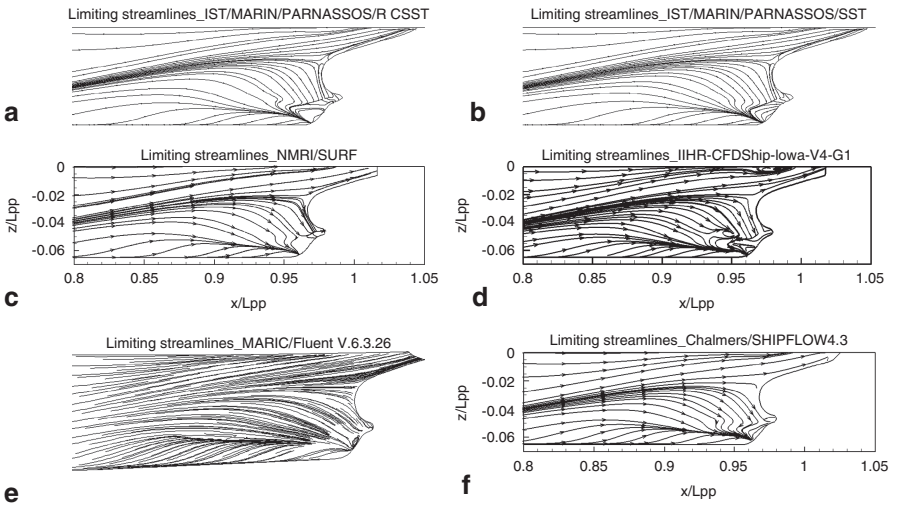


Fig. 3.18 KVLCC2—Wall streamlines computed by different participants. (a) IST-MARIN/PARNASSOS (RCSST) (b) ST-MARIN/PARNASSOS (SST) (c) IIHR-CFDSHIP-IOWA-V4 (ARS-DES) (d) NMRI/SURF (e) MARIC/FLUENT6.3.26 (f) CHALMERS/SHIPFLOW4.3

contributors find a zone of $\overline{uw} > 0.002$ which is consistently smaller than what is observed in the experiments. Only IIHR/CFDShip-Iowa-V4.5 simulations predict the region near the vertical symmetry plane where $\overline{uw}$ of EFD shows negative value at -0.002. This may be also related to the use of a much finer grid, compared to the other contributors. One can also notice that the global agreement on $\overline{uw}$ is far better when the ARS-DES model is used, compared to the results of the computations performed with ARS.

Compared to RANSE, DES computations on Grid 0 exhibit model Reynolds stress depletion (MSD) i.e. modeled Reynolds stress inside the boundary layer is very small due to a very low value of turbulent eddy viscosity. This issue is less apparent on a coarser grids (see ARS-DES-G1).

2.9 Limiting Wall Streamlines

The limiting wall streamlines (Fig. 3.18) provide a complementary view of the flow through the print of the flow on the hull.

By examining the extent of the line of convergence of wall streamlines and the extent of the recirculation zone, one can get very useful information on the behavior of the flow close to the hull. CHALMERS/SHIPFLOW4.3, NMRI/SURF, IIHR/CFDShip-Iowa-V4(ARS) and NSWCCD-ARL-UM/NavyFOAM produce very similar results according to these two criteria, which confirms the global similarity of their computations. On the other hand, VTT/FINFLO and IST-MARIN/PARNASSOS(SST) computations are characterized by a line of convergence which

is not enough extended upstream. This indicates that the longitudinal vortex is less intense. This picture is not fundamentally modified by the use of rotation correction factors (RCSST) or alternative turbulence models (RCKSKL). However, for these computations performed by IST/MARIN, one may notice a more extended zone of recirculation at the extremity of the hull, which is not confirmed by other contributors. In absence of any experimental visualization, it is difficult to conclude on that point. Results obtained with the RSTM model by MARIC/Fluent6.3.26 are somewhat singular in that they show a very extended line of convergence and almost no zone of recirculation at the extremity of the hull. The picture provided by the DES formulation implemented by IIHR confirm the fact that the flow is dominated by a very (too much) intense bilge vortex. Two focal points associated with two additional vortices are visible close to the hull and close to the horizontal plane of symmetry.

2.10 Discussion

Compared to the results obtained in 2000 and 2005, one can notice that much progress has been made towards consistent and more reliable computations of after body flows for U shaped hulls. The intense bilge vortex and its related action on the velocity field is accurately reproduced by a majority of contributors employing very similar turbulence models implemented in different solvers and on different grids in terms of number of points or topology. The debate on the relative importance of discretization *vs*. modeling errors opened in the mid-nineties should now be closed by the acknowledged prominent role played by turbulence anisotropy as long as a reasonable grid is used. From that point of view, around three million points are enough to assess a steady statistical turbulence closure without any significant pollution from discretization errors (for a flow domain bounded by two planes of symmetry) although local improvements can be brought on the total wake fraction for instance by using a finer grid. The turbulence data confirm that the turbulence anisotropy is large in the propeller disk and more specifically in the core of the bilge vortex. For the first time, hybrid LES turbulence models have been introduced to compute model scale ship flows with a globally satisfactory performance. However, one has noticed that these models, in their current state of development, tend to predict too low levels of turbulence, which lead to ship wake composed of somewhat too intense longitudinal vortices. For DES, grid induced separation inside the boundary layer and modeled stress depletion are observed for very fine grids inside the boundary layer. Improved DDES should be implemented in the future to remedy these issues. Explicit Algebraic Reynolds Stress Models reproduce satisfactorily the measured structure of the turbulence and appear to be the best answer in terms of robustness and computational cost for this specific flow field, compared to RSTM or unsteady DES based strategies, as long as one is interested in time-averaged quantities. However, difference persist in the total wake fraction distribution in the main vortical region indicating that progress in terms of turbulence models and/or control of the local discretization error are still necessary to improve the local quality of the flow field.



Fig. 3.19 KCS hull geometry

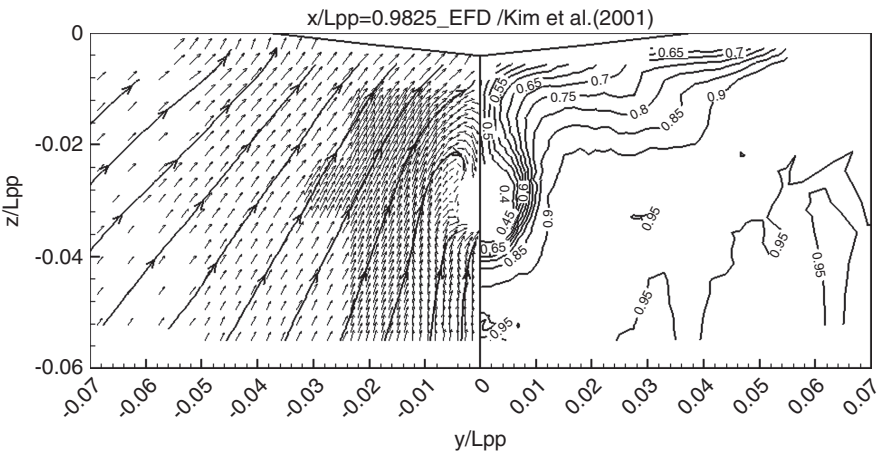


Fig. 3.20 Secondary velocities and isowake contours at $x/L_{pp} = 0.9825$

However, it will be difficult to perform such a local flow assessment without the help of very reliable local flow measurements.

3 KCS—Case 2.1

The KCS, shown in Fig. 3.19, was conceived to provide data for both explanation of flow physics and CFD validation for a modern container ship with a bulbous bow. The ship is towed in calm water conditions ($Fr = 0.26$, $Re = 1.4 \times 10^7$). Measurements of the flow field made at MOERI in 2001 give the cross-flow vectors, secondary streamlines and axial velocity contours at $x/L_{pp} = 0.9825$.

3.1 Description of the Experimental Results

At the experimental cross-section ($x/L_{pp} = 0.9825$) shown in Fig. 3.20, one can recognize the trace of the bilge vortex close to the vertical plane of symmetry. The intensity of this vortex is moderate since it does not create any significant distortion of the axial velocity contours (no hook shape is visible there up to the axial velocity contour $U = 0.4$). Therefore, the challenge posed by this test case consists in proving that one is able to simulate accurately the flow field at the propeller plane, which means being able to compute accurately the intensity of the main bilge vortex. Since

the measurements do not explore the core of the bilge vortex, it is difficult to determine the exact intensity of the stern bilge vortex and to conclude on the existence of an additional small counter-rotating vortex located below the main bilge vortex as it was observed for the KVLCC2.

3.2 Review of Contributions

Sixteen contributions were uploaded for the test case 2.1. The names of the organizations and the code used are recalled in Table 3.2 with the main characteristics of their computations grouped in terms of relevant categories based on physical modeling (i.e. turbulence models), wall models, discretization characteristics (mesh density, time discretization, etc. . .).

Only one hybrid LES model is used here by IIHR on a grid of moderate size, compared to the one used for Case 1.1-a. The other group of turbulence models is composed of classical isotropic linear turbulence models with or without *ad hoc* corrections.

All the discretization methods are formally second order accurate and are based on structured or unstructured grids which are all body fitted. Wall function (4 over 16) or low Re near wall formulations (12 over 16) are used. All these characteristics are listed in Table 3.2.

When RANS equations are solved with statistical turbulence models, the computations are performed on body fitted grids having an average number of 3 to 4 million points. Another group of computations is made on much coarser grids composed of less or around 1 million points (ECN-BEC/ICARE, IIHR-SJTU/Fluent12.0). This is understandable for ECN-BEC which uses a mono-fluid free-surface fitting strategy but seems to be very coarse for IIHR-SJTU/Fluent which employs a free-surface capturing methodology.

3.3 Analysis of Results

To try to compare the various computations, one can analyze the location of the axial velocity iso-contour $U = 0.4$ at $x/L_{pp} = 0.9825$ which gives an indirect measure of the vorticity strength and position. The maximum lateral distance is $y_{max}/L_{pp} = 0.0003$ while the minimum vertical location is $z_{min}/L_{pp} = -0.038$. Based on this criteria, the results provided by CSSRC/Fluent6.3, IIHR/CFDShip-IowaV4(DES), MARIC/FLUENT6.3, MARIN/PARNASSOS, MOERI/WAVIS and NMRI/SURF are in excellent agreement with the experiments (see Fig. 3.21). It is interesting to notice that the DES model provides once again a more intense bilge vortex and a visible secondary counter-rotating vortex, thanks to a probable local reduction of the computed turbulent viscosity. This is confirmed by the velocity profiles at $x/L_{pp} = 0.9825$, and $z/L_{pp} = -0.0302$ which indicate, for all these computations,

Table 3.2 Main characteristics of the computations

Organization/Code name	Turbulence model	Wall model	Discretization characteristics
ECN-BEC/ICARE	k-ω model	Low-Re turbulence model + no slip	Structured grid, 1 million points
MARIN/ PARNASSOS	Menter 1 equation (Dacles-Mariani (DM) correction)	Low-Re turbulence model + no slip	Structured grid, 3.1 million points
MARIC/Fluent6.3	k-ω SST	Low-Re turbulence model + no slip	Multi-block structured grid, 5.6 million points
CSSRC/Fluent6.3	RNG k-ε/k-ω SST	Low-Re turbulence model + no slip	Multi-block structured grid, 786 000 points
IIHR/CFDShip-IowaV4(DES)	DES model	Low-Re turbulence model + no slip	Multi-block overlapping grid, 6.87 million points
IIHR/CFDShip-IowaV4(RANSE)	Hybrid k-ε/k-ω	Low-Re turbulence model + no slip	Multi-block overlapping grid, 6.87 million points
IIHR-SJTU/ Fluent12.0	RNG k-ε	Mixed no-slip + wall function	Multi-block structured, 660 000 points
NMRI/SURF	1 equation Spalart Allmaras	Low-Re turbulence model + no slip	Structured grids, 4.9 million points
FLOWTECH/ SHIPFLOW-VOF-4.3	k-ω SST	Low-Re turbulence model + no slip	Multi-block structured, 4.3 million points
MOERI/WAVIS	RNG k-ε	Wall function	Multi-block structured, 8.6 million points
SNUTT/ FLUENT6.3	1 equation Spalart-Allmaras	Wall function	Multi-block unstructured, 1.8 million points
Southampton/CFX	BSL, SST	No slip and Wall function	Multi-block structured, 9 to 10 million points
SSRC/FLUENT12.1	k-ω SST	Low-Re turbulence model + no slip	Multi-block structured, 3 million points
SVA/CFX12	k-ω SST	Low-Re turbulence model + no slip	Multi-block unstructured, 5.3 million points
TUHH/CFX12.1	k-ω SST	Low-Re turbulence model + no slip	Multi-block structured, 16.5 million points
VTT/FINFLO	k-ω SST	Low-Re turbulence model + no slip	Multi-block overlapping structured, 4.15 million points

that the boundary layer thickness is accurately captured, like the maximum value of the vertical component of the velocity. For other contributors like ECN-BEC/ICARE, FLOWTECH/SHIPFLOW-VOF, the boundary layer is too thick and the velocity gradients at the edge of the boundary layer are not correctly captured, indicating too large a numerical diffusion in that region. This is also visible on the vertical component of the velocity which is underestimated. On the contrary, for SNUTT/FLUENT6.3, Southampton/CFX(SST) or VTT/FINFLO, the boundary layer appears to be too thin at this particular location. By comparing the DES and RANSE models implemented in CFDShip-Iowa (see Fig. 3.22) on the velocity profiles, one clearly sees that the stronger vorticity modeled by the DES version tends to shift the axial velocity profile away from the vertical plane of symmetry, in agreement with the experiments.

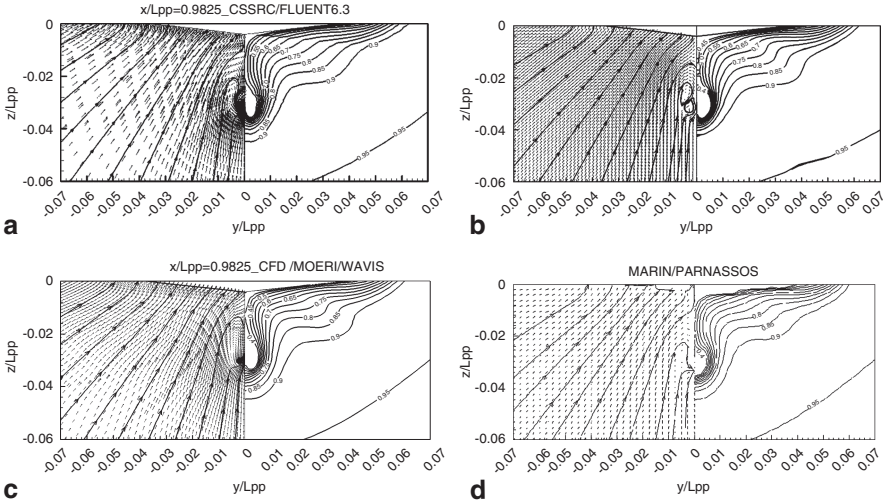


Fig. 3.21 KCS—Isowake contours at $x/L_{pp} = 0.9825$. **a** CSSRC/Fluent6.3, **b** IIHR-CFDSHIP-IOWA-V4 (DES), **c** MOERI-WAVIS, **d** MARIN/PARNASSOS

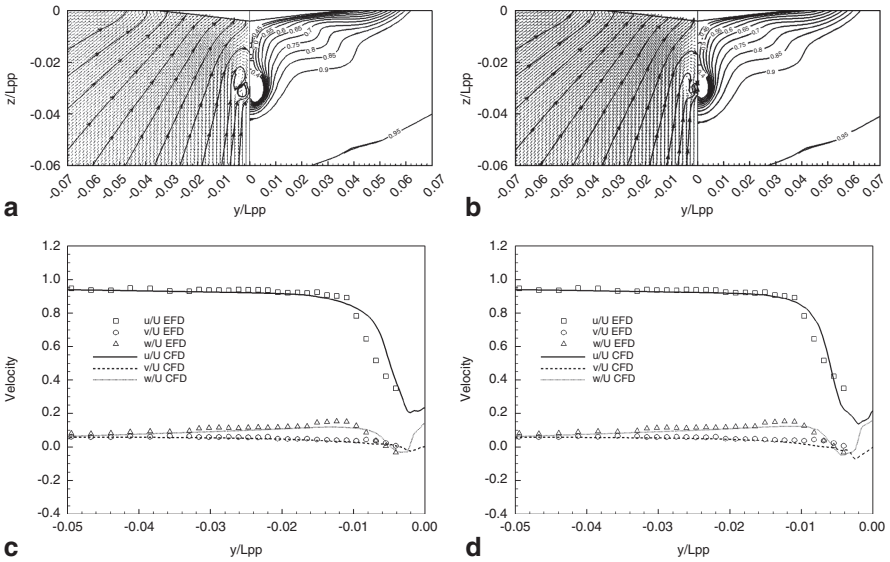


Fig. 3.22 KCS–IIHR—Comparison between DES and RANSE turbulence modeling. **a** DES, **b** RANSE, **c** RANSE, **d** LES

3.4 Discussion

The global agreement between computations and experiments in terms of local velocity profiles is very satisfactory. As previously noted, it seems that the DES model tends to predict more intense vortices. It is difficult to relate this characteristic to the modeled turbulence structure since we have no experimental information on turbulent quantities. It would also be very interesting to locate the critical gray zone where both RANSE and LES formulations are used in order to determine the real domain of influence of pure LES formulation. The linear isotropic turbulence models do their job correctly since this flow is not critical in terms of longitudinal vorticity content. One also should underline the use of relatively fine grids (around 3 million points) by most of the contributors, which reduces the amount of local numerical diffusion, leading globally to a more accurate flow simulation.

4 KCS—Case 2.3-a

The KCS was conceived to provide data for both explanation of flow physics and CFD validation for a modern container ship with a bulbous bow.

In addition to the towing tank experiments performed by MOERI in 2001, NMRI carried out self-propulsion tests which were reported in the proceedings of the Tokyo workshop in 2005. These flow measurements are used in this test case to evaluate the performance of up-to-date computation methods in self-propulsion conditions. The self-propulsion test is conducted at ship point, which means that one should adjust the rate of rotation of the propeller to get a force equilibrium taking into account the additional towing force (Skin Friction Correction) applied in the experiments.

4.1 Description of the Experimental Results

The axial velocity contours and cross-flow vectors are available downstream of the propeller at $x/L_{pp} = 0.991$ and provide a global view of the axial flow shown in Fig. 3.23. A more detailed analysis on the transversal evolution of the three components of the velocity is also possible thanks to detailed measurements performed at $x/L_{PP} = 0.9911$, $z/L_{PP} = -0.03$. The axial velocity contours are characterized by two regions inside and outside the propeller disk. Inside the propeller disk, one notices a characteristic asymmetric behavior with a moon crescent-like region of high velocity ($U = 1.1$). The analysis of the cross-flow vectors reveals the existence of a strong main vortex obviously due to flow induced by the propeller but one can also guess the presence of a smaller counter-rotating vortex located in right upper part of the propeller disk.

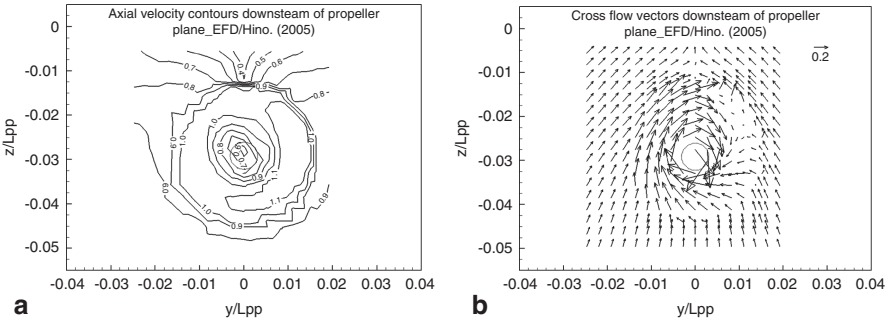


Fig. 3.23 KCS—Measured axial velocity contours and cross flow vectors at $x/L_{pp} = 0.9911$

4.2 Review of Contributions

Thirteen contributions were uploaded for the test case 2.3-a. The names of the organizations and the code used are recalled in Table 3.3 with the main characteristics of their computations grouped in terms of relevant categories based on physical modeling (i.e. turbulence models), wall models, discretization characteristics (mesh density, time discretization, etc. . .).

Only one hybrid LES model is used here by IIHR on a dense grid comprised of 20.3 million points. The other group of turbulence models is composed of classical isotropic linear turbulence models with or without *ad hoc* corrections.

A first group of organizations compute the flow around the actual propeller by solving the RANS equations in a rotating block communicating with the fixed mesh around the ship through a sliding interface while a second group resorts to a body force specification based on various physical formulations (lifting line, lifting surface, or actuator disk).

All the discretization methods are formally second order accurate and based on multi-block structured or unstructured grids which are body fitted. However, the code CFDShip-Iowa also uses an hybrid 2nd/4th order discretization scheme in its version V4.5.

Since there is no more vertical plane of symmetry, the average size of mesh is around 9 million points for the methods which compute the actual propeller. The use of simplified theory leads to a strong reduction in terms of grid density with the extreme case of IIHR-SJTU/Fluent12.0 which uses a grid composed of only 660 000 points. Other contributors use larger grids like, for instance, SSPA/SHIPFLOWv4.3 with a grid comprised of 8.9 million points, MARIN/PARNASSOS-PROCAL and MARIC/FLUENT6.3 with 6.2 and 5.6 million points, respectively.

Table 3.3 Main characteristics of the computations

Organization/Code name	Turbulence and propeller models	Propeller	Discretization characteristics
CTO/StarCCM +	k-ε	Actual propeller + RANSE, RP 9.8 rps	Unstructured grid, 7 million points
MARIN/PARNASSOS-PROCAL	Menter 1 equation (DM correction)	Actual propeller + BEM	Structured grid, 6.2 million points
MARIC/Fluent6.3	k-ω SST	Simplified propeller theory (body force), thrust balanced	Multi-block structured grid, 5.6 million points
CSSRC/Fluent6.3	RNG k-ε/k-ω SST	Actual propeller, thrust balanced	Multi-block structured grid, 1,247 million points
IIHR/CFDShip-IowaV4(DES)	DES	Actual propeller, thrust balanced	Multi-block structured grid, 20.3 million points
IIHR-SJTU/Fluent12.0	RNG k-ε	Prescribed body force	Multi-block structured, 660 000 points
NMRI/SURF	1 Eq. Spalart Allmaras	Simplified propeller theory (body force), thrust balanced	Structured grids, 3.8 million points
SSPA/SHIPFLOW-VOF-4.3	k-ω SST	Body force (lift. line), thrust balanced	Multi-block structured, 8.9 million points
MOERI/WAVIS	RNG k-ε	Body force (lift. Surface), RB, JB	Multi-block structured, 8.6 million points
SNUTT/FLUENT6.3	1 Eq. Spalart-Allmaras	Actual propeller, RP	Multi-block unstructured, 4.5 million points
SouthamptonQinetiQ/CFX	k-ω BSL, SST	Body force, RB, JB, TB, QB	Multi-block structured, 9 to 10 million points
SSRC/FLUENT12.1	k-ω SST	Actual propeller, RB	Multi-block structured, 3 million points
TUHH-FDS/CFX12.1	k-ω SST	Actual propeller	Multi-block structured, 6 to 10 million points

4.3 Cross-section $x/L_{pp} = 0.9911$

The analysis of the global axial velocity contours immediately suggests that the codes using too simplified a body force theory cannot model accurately the flow distribution inside the propeller disk. For instance, Southampton/CFX and IIHR-SJTU/Fluent predict an almost symmetric distribution of axial velocity contours which is clearly related to the body-force theory they used for these computations. Less simplified propeller modeling, although based on potential approximation, strongly improves the quality of the simulations, with the noticeable exception of MARIN/PARNASSOS-PROCAL which fails to reproduce the level of asymmetry in the propeller disk. Otherwise, approximations based on the lifting line (SSPA/SHIPFLOWv4.3) or lifting surface (MOERI/WAVIS) or other simplified theory (Moriyama's model) (NMRI/SURF) provide cheap and accurate formulations in view of their results for this test case. When the entire flow around the rotating propeller is computed by

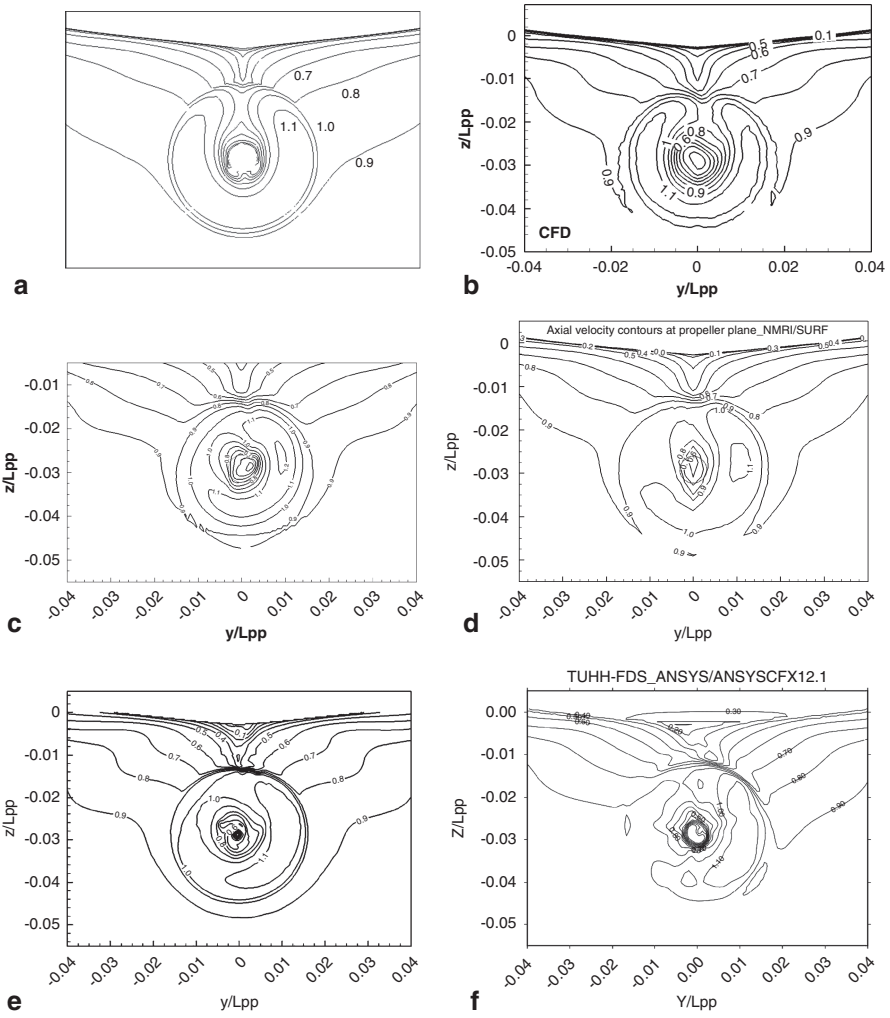


Fig. 3.24 Iso axial velocity contours computed by participants, (a) and (b) using a body-force theory, (c) and (d) an inviscid propeller model, (e) and (f) a full DES or RANSE model for the propeller. **a** SOUTHAMPTON/CFX. **b** IIHR-SJTU/FLUENT. **c** SSPA/SHIPFLOWV4.3. **d** NMRI/SURF. **e** IIHR/CFDSHIP-IOWA-V4 **f** TUHH-FDS/CFX12.1

solving RANS or DES equations on overlapping or sliding grids, the global agreement on the axial velocity contours is excellent but not necessarily better than what is observed for the hybrid formulations mentioned above. However, IIHR/DES computations appear to be able to capture correctly the counter-rotating vortex located in the right upper part of the propeller disk (see Fig. 3.24). Globally, this seems to indicate that, at this level of detail (which is actually very coarse), viscous effects on the propeller do not play a significant role.

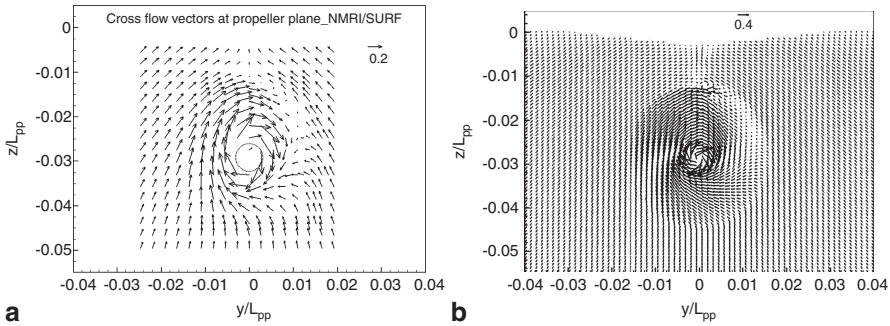


Fig. 3.25 Cross-flow velocities at section $x/L_{pp} = 0.9911$. **a** NMRI/SURF, **b** IIHR/CFDSHIP-IOWA-V4

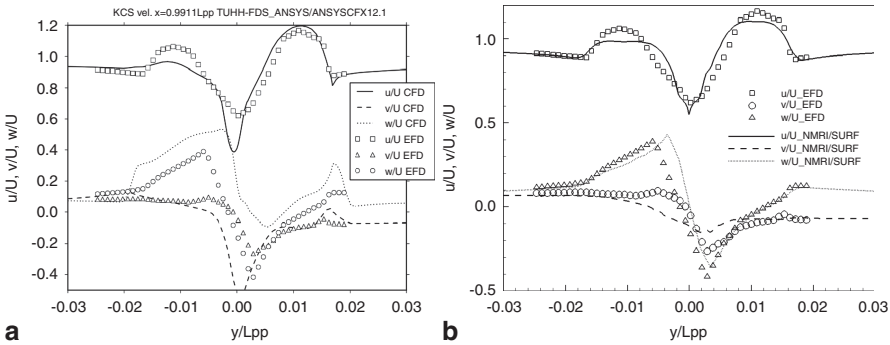


Fig. 3.26 Velocity profiles on the propeller plane ($x/L_{pp} = 0.9825$, $z/L_{pp} = -0.0302$). **a** TUHH-FDS/CFX12.1, **b** NMRI/SURF

4.4 Velocity Profiles on the Propeller Plane ($x/L_{pp} = 0.9825$, $z/L_{pp} = -0.0302$)

The availability of local velocity profiles at $x/L_{pp} = 0.9825$, $z/L_{pp} = -0.0302$ makes it possible a more detailed assessment of the computations. The first disagreement which is shared by almost all the computations is the too low value of U close to the plane of symmetry below $U = 0.4$ while the experimental value is around $U = 0.7$.

Only NMRI's results are not affected by this recurrent default. It is also worthwhile to notice that the results from MARIC/FLUENT6.3 seem to be strongly dependent on the presence of the hub cap in this particular region. Outside this region, the agreement on the axial velocity component asymmetry is very good for the methods which successfully predicted the global flow field.

The same remarks hold for the vertical and transverse velocity components. Except NMRI/SURF (see Fig. 3.26), no other group is able to capture the measured evolution of V and W, the change from positive to negative values across the vertical plane being too abrupt in the computations which take into account the actual propeller.

4.5 Discussion

Considering the complexity of this exercise, the results obtained by most of the participants are in good agreement with the experiments. This may be due to the use of very fine grids but the major factor explaining this observation is probably the accuracy of the propeller model. Surprisingly, computations based on RANSE everywhere do not appear significantly better than the best hybrid formulations based on simplified physics for the propeller. However, a too simplified actuator disk formulation is not suited, which is not astonishing. In the same order of idea, the turbulence model does not seem to play a crucial role. To enter a more detailed evaluation of velocity profiles, one needs to be sure that the computations are performed with the exact experimental geometry of the hub, especially for the location chosen in this validation exercise. Here again, hybrid LES computations have been presented for the first time in the framework of self-propelled model-scale flows. The performance of this unsteady turbulence modeling strategy is already very promising despite the fact that they do not out-perform the best computations based on Reynolds-averaged statistical turbulence closures. These hybrid LES approaches are very expensive in terms of CPU time but they are the only ones able to provide reliable informations on unsteadiness, an output which is particularly useful in the framework of marine propulsion.

5 DTMB5415—Cases 3.1-a & b

The model DTMB5415 shown in Fig. 3.27, was conceived as a preliminary design of a Navy Surface combatant. The hull geometry includes both a sonar dome and transom stern. In the test case 3.1-a and 3.1-b, only the bare hull in calm water conditions is considered. The Froude number for the computations is 0.28 and the hull is positioned in the basin at its dynamic sinkage and trim. Two series of experiments are available for this test case. The first one was performed at INSEAN by Olivieri et al. in 2001 for a model of 5.82 m long ($\mathrm{Re} = 1.19 \times 10^7$, sinkage $= -1.82\ 10^{-3} \mathrm{L_{pp}}$, trim $= -0.108°$) while a second set of experiments was done at IIHR by Longo et al. in 2007 at the same Froude number ($\mathrm{Fr} = 0.28$) with a smaller model of 3.048 m long ($\mathrm{Re} = 5.13 \times 10^6$, sinkage $= -1.92\ 10^{-3} \mathrm{L_{pp}}$, trim $= -0.136°$).

These two experiments provide complementary informations on the local flow. Measurements made at INSEAN give the contours of the longitudinal component of the velocity, cross-flow vectors and secondary streamlines in the following transversal cuts ($\mathrm{x/L_{pp}} = 0.1$; 0.2; 0.6; 0.8; 0.9346 (propeller plane) and 1.1) while those performed at IIHR provide streamwise velocity contours at $\mathrm{x/L_{pp}} = 0.9346$ but also informations on the Reynolds stress components ($\overline{uu}$, $\overline{vv}$, $\overline{ww}$, $\overline{uv}$ and $\overline{uw}$) and the turbulent kinetic energy at the same station.



Fig. 3.27 DTMB5415 hull geometry

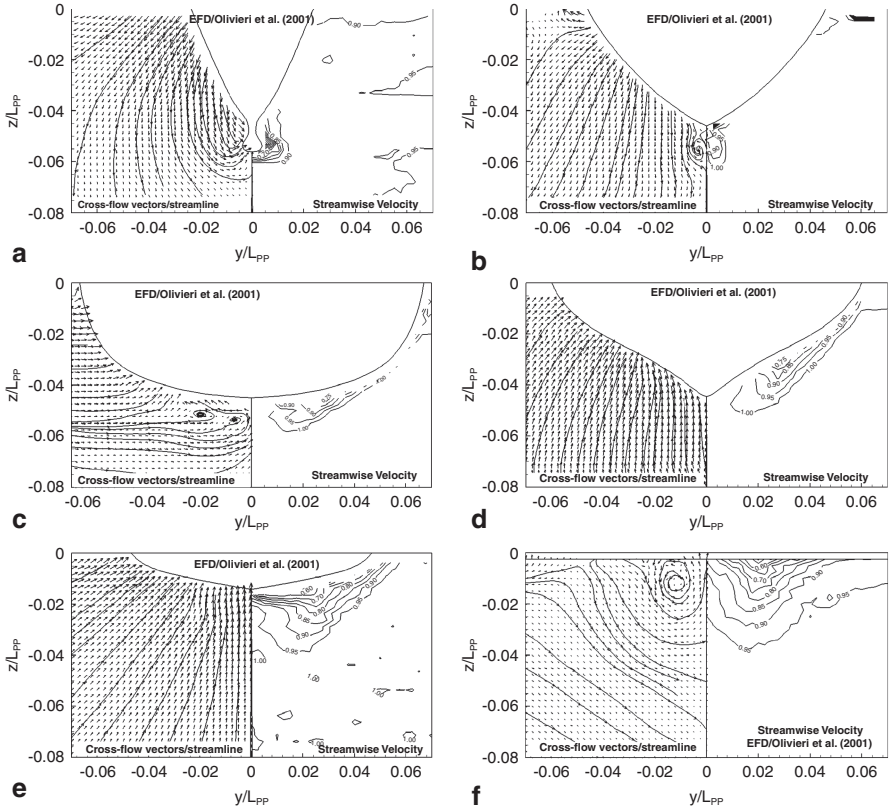


Fig. 3.28 DTMB5415—Measured cross-flow vectors and streamwise velocity contours at various sections. **a** $x/L_{pp} = 0.1$, **b** $x/L_{pp} = 0.2$, **c** $x/L_{pp} = 0.6$, **d** $x/L_{pp} = 0.8$, **e** $x/L_{pp} = 0.935$, **f** $x/L_{pp} = 1.1$

5.1 Brief Analysis of Experimental Results

Based on the available local flow measurements, it is possible to focus the analysis on two prominent characteristics, the generation and convection of the sonar dome and stern vortices and the related evolution of the hull boundary layer. Figure 3.28 shows the measured cross-flow vectors and streamwise velocity contours at several sections. It is very difficult on the basis of these incomplete experimental informations to propose a complete and consistent description of the three-dimensional topology of the flow from bow to stern. However, we may try to propose a first interpretation based

on these experiments, interpretation which will be completed later on by a detailed analysis of the computational results. Due to the particular shape of the bow which is caused by the presence of the sonar dome, at least one intense bow vortex is generated close to the vertical plane of symmetry and convected along the ship hull. The traces of this bow bilge vortex and the related secondary components of the velocity can be seen in the cross-section $x/L_{pp} = 0.2$ and further downstream at $x/L_{pp} = 0.6$ where a second vortex having the same sign as the first one can be observed.

According to the experimental report written by INSEAN in 2001, this second vortex is a stern bilge vortex which is created by the convergence of the wall streamlines in the afterbody flow due to the adverse pressure gradient. We will see that the computations seem to provide a somewhat different explanation. These two vortical structures are no more visible in the next two cross-sections ($x/L_{pp} = 0.8$ and 0.9436) showing only the secondary vectors but their trace would be visible when using iso-vorticity contours. In the wake of the hull, a large vortex is visible which is may be due to the coalescence of the two previous so-called "bow and stern bilge vortices", although EFD does not show explicitly the coalescence. The main action of these vortices on the hull boundary layer is to transport high momentum fluid towards the hull center-plane thinning the boundary layer, and convect low momentum fluid from the vicinity of the wall to the core of the flow, which creates this well-known pronounced bulge on the streamwise velocity contours (see sections $x/L_{pp} = 0.6$; 0.8 and 0.9436 (propeller plane)).

A last uncertain point concerns the analysis of the flow topology very close to the sonar dome. Although not clearly visible in the experiments, one wonders if there is one or several additional counter-rotating vortices located between the first bow bilge vortex mentioned earlier by INSEAN and the wall (see the cross-sections $x/L_{pp} = 0.2$ for instance). We are therefore in front of a test case where computations can actually be used to understand the flow topology where measurements provide only an incomplete description of the real physics.

5.2 Review of the Contributions

Eleven contributions were sent for the test case 3.1-a and only eight for the test case 3.1-b which will be considered below. The names of the organizations and the code used are recalled in Table 3.4 with the main characteristics of their computations.

It is possible to group the contributions in terms of relevant categories based on physical modeling (i.e. turbulence models), wall models, discretization characteristics (mesh density, time discretization, etc. . .).

Two Large Eddy Simulation (LES) models are employed in these comparisons, which will make possible cross-comparisons within this turbulence modeling category. FOI/OF uses a pure LES model (a Mixed Model based on a scale similarity term and a subgrid viscosity term) implemented in Open/FOAM while IIHR employs an hybrid DES modeling implemented in the version 4 of CFDShip-Iowa. It will be therefore very interesting to compare the solutions provided by these two time-accurate simulation methods which provide *a priori* more informations than

Table 3.4 Main characteristics of the computations

Organization/Code name	Turbulence model	Wall model	Discretization characteristics
ECN-BEC/ICARE	k-ωWilcox	Low-Re turbulence model + no slip	Structured grid, 800 000 points
FOI/OpenFOAM	LES Mixed model	Wall model	Multi-block structured grid, 58 million points, dt = ?,? flow times
MARIN/PARNASSOS	Menter one equation	Low-Re turbulence model + no slip	Structured grid, 7.4 million cells
MARIC/Fluent6.3	k-ω SST	Low-Re turbulence model + no slip	Multi-block structured grid, 2.15 million cells
University of Genoa/Star CCM +	RNG k-ε	Low-Re turbulence model + no slip	2 million cells
CSSRC/Fluent6.3	RNG k-ε	Wall function	Multi-block structured grid, 650 000 points
CEHINAV/StarCCM +	k-ω SST	Low-Re turbulence model + no slip	Unstructured grid, 2 million cells
IIHR/CFDShip-IowaV4(DES)	DES model	Low-Re turbulence model + no slip	Multi-block overlapping grid, 300 million points, dt = 510^{-4}, 4 flow times
IIHR/CFDShip-IowaV4(ARS)	Algebraic Reynolds Stress	Low-Re turbulence model + no slip	615 000 points
IIHR/CFDShip-IowaV6	DES model	Wall function + immersed boundary conditions	Cartesian grid, 276 million points
NSWCCD-ARL-UM/NavyFOAM	k-ω Wilcox	Low-Re turbulence model + no slip	6 million cells
NMRI/SURF	EASM	Low-Re turbulence model + no slip	2.7 million cells

the time-averaged statistical turbulence models. Among the statistical turbulence models, the available anisotropic formulations are the Algebraic Reynolds Stress implemented by IIHR in CFDShip-Iowa-V4 and the Explicit Algebraic Stress Model developed by Deng et al. (2005), and implemented in SURF by NMRI during a research collaboration between NMRI and ECN-CNRS. All other contributions are based on variants of isotropic turbulence models (RNG k-ε and k-ω variants).

All the discretization methods are formally second order accurate and based on structured or unstructured grids which are body-fitted, with the noticeable exception of IIHR which also proposed a solution based on the version 6 of its code CFDShip-Iowa which employs a Cartesian grid composed of 276 million points and immersed boundary conditions (wall function). From that point of view, it may also be interesting to distinguish between the codes employing low Re near wall turbulence models and the contributions using a wall function boundary condition on the hull. In this second category, one can also put the LES formulation employed by FOI which does not resolve the viscous sublayer but employs a wall model based on *ad hoc* modifications of the sub-grid model when the wall is approached. All these characteristics are listed in Table 3.4.

When RANS equations are solved with statistical turbulence models, the computations are performed on body fitted grids having an average number of points of 4 million points, except the approach based on Cartesian grid with immersed boundary conditions (version 6 of CFDShip-Iowa) which uses a grid comprised of 276 million points. IIHR carries out their DES computations on a grid composed of 300 million points with a dimensionless time step of 5×10^{-4}. Four flow times are computed to get a statistically converged solution. FOI employs a multi-block structured grid made of 58 million points, while the number and value of time steps are not reported.

5.3 Analysis of the Results

Cross-section $x/L_{pp} = 0.1$

The velocity contours shown in Fig. 3.29 illustrate already a non-uniform boundary layer development along the surface of the sonar dome. Close to the keel, the boundary layer is already much thinner than around the major part of sonar dome, a first characteristic which is already well captured by most of the participants except ECN-BEC-HO/ICARE, MARIN/PARNASSOS and IIHR/CFDShip-IowaV6 which predict a thicker boundary layer. This first inaccuracy in a region where the boundary layer is thin and where large gradients exist in the vicinity of the stagnation point in the fore part of the bow, may be attributed to the use of Immersed Boundary Condition in the case of IIHR and to too coarse a discretization for the other contributors.

Cross-section $x/L_{pp} = 0.2$

This section is located after the trailing edge of the sonar dome. From the experiments, one can see the trace of a first vortex located close to the vertical plane of symmetry and one can guess the existence of a second one located between the hull and the first one. All the computations capture the first vortex but it is interesting to notice that FOI/OF, NSWCCD-ARL-UM/NavyFOAM, CSSRC/Fluent6.3, IIHR/CFDShip-IowaV4(DES) are able to capture a second vortex. The reason why these contributors can capture this additional vortex has to be determined. It may indicate that the discretization is locally fine enough to reduce the amount of numerical dissipation and that the turbulence model provides the right amount of turbulent viscosity. However, such a behavior may also occur because of too coarse a discretization which fails to capture the flow gradients and the related turbulence production, leading to a quasi-laminar flow, more prone to destabilize and give birth to intense longitudinal vortices. It is also interesting to compare the location of the iso-contour 1.0 which gives an idea of the computed boundary layer thickness in the symmetry plane. Some computations suffer already from the fact that the vortex close to the keel plane is not intense enough to convect high momentum fluid from outside toward the wall (see the results from University of Genoa/STAR-CCM$^+$ or from ECN-BEC-HO/ICARE (for instance). IIHR/CFDShip-IowaV6 is based on the use of a Cartesian grid and immersed boundary formulation (wall function for the hull). The less accurate fore body vortex prediction seems to indicate that the wall region is not correctly computed, probably due to immersed boundary conditions limitations.

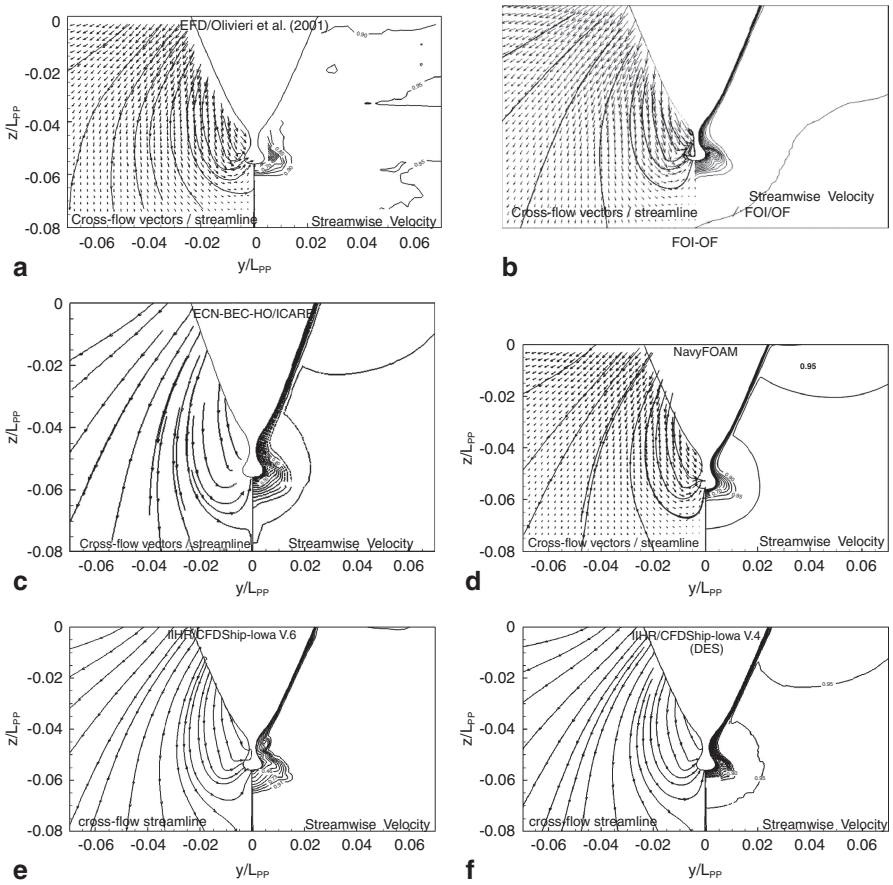


Fig. 3.29 Cross-flow vectors and streamwise velocity contours at $x/L_{pp} = 0.1$. **a** Experiments from INSEAN, **b** FOI/OF, **c** ECN-BEC-HO/ICARE, **d** NSWCCD-ARL-UM/NavyFOAM, **e** IIHR/CFDSHIP-IOWA-V6, **f** IIHR/CFDSHIP-IOWA-V4

Cross-section $x/L_{pp} = 0.6$

This section is located after mid-ship and one can clearly distinguish two co-rotating vortices in the INSEAN's experiments. According to the experimental report written by INSEAN, the vortex located close to the symmetry plane comes from the sonar dome and corresponds to the most intense one visible at $x/L_{pp} = 0.2$ while the other one is a stern bilge vortex created by the adverse pressure gradient taking place because of the geometric variations of the afterbody. The influence of these vortices contribute to the development of a bulge on the streamwise velocity contours. The first one convects high momentum toward the hull in the symmetry plane, making the boundary layer thinner while the second co-rotating stern bilge vortex extracts low momentum fluid from the wall, These two vortical structures are not captured by the computations which appear to be affected by too much diffusion at various levels. Here again, the most reliable computations in terms of isowakes are

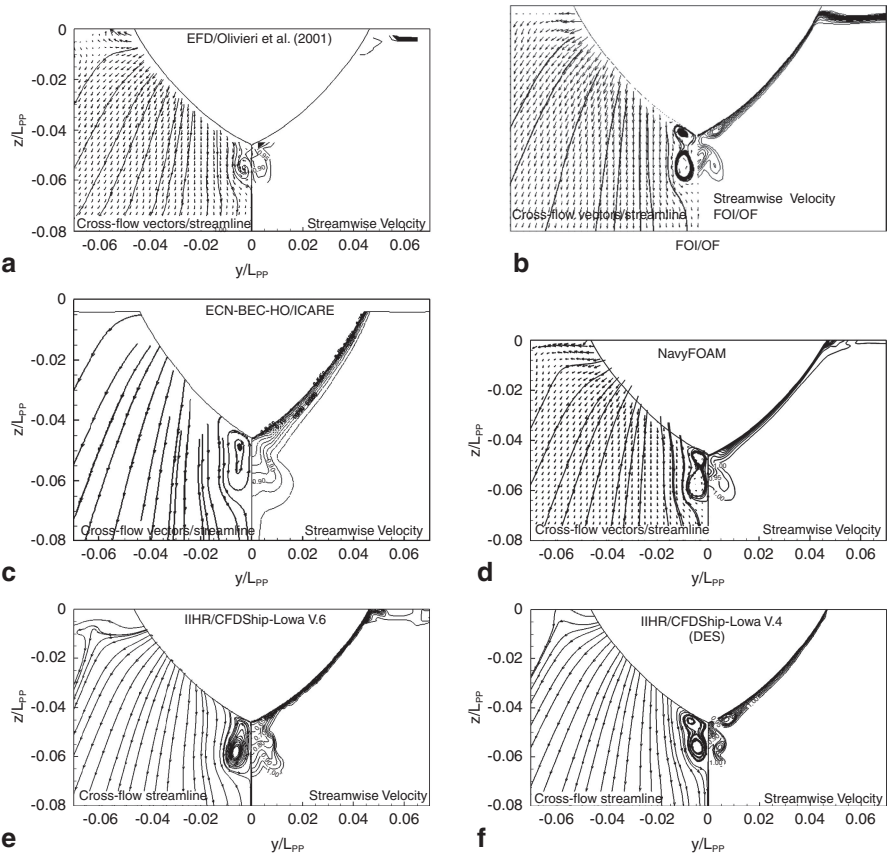


Fig. 3.30 Cross-flow vectors and streamwise velocity contours at $x/L_{pp} = 0.2$. **a** Experiments from INSEAN, **b** FOI/OF, **c** ECN-BEC-HO/ICARE, **d** NSWCCD-ARL-UM/NavyFOAM, **e** IIHR/CFDSHIP-IOWA-V6, **f** IIHR/CFDShip-Iowa-V4(DES)

provided by NSWCCD-ARL-UM/NavyFOAM, FOI/OF and CSSRC/FLUENT6.3 at a lesser degree. Among the other contributors, MARIN/PARNASSOS and MARIC/FLUENT6.3.26 are also able to produce a pronounced bulge on the streamwise contours. Once again, the results obtained with the DES formulation by IIHR/CFDShip-IowaV4 are interesting. Because of the too low level of computed turbulence (see the cross-section $x/L_{pp} = 0.9346$ for the analysis of the turbulence intensity), the flow is less viscous and lets survive two intense vortices located at the same position as the experiments (Fig. 3.29–3.31).

Cross-section $x/L_{pp} = 0.8$

No more trace of the main vortex is visible in the experiments if one examines the cross-flow components of the velocity. However, the characteristic bulge of the boundary layer and the very thin boundary layer thickness in the vertical plane of symmetry illustrates the action of vorticity on the flow. Contributions of SSRC/Fluent,

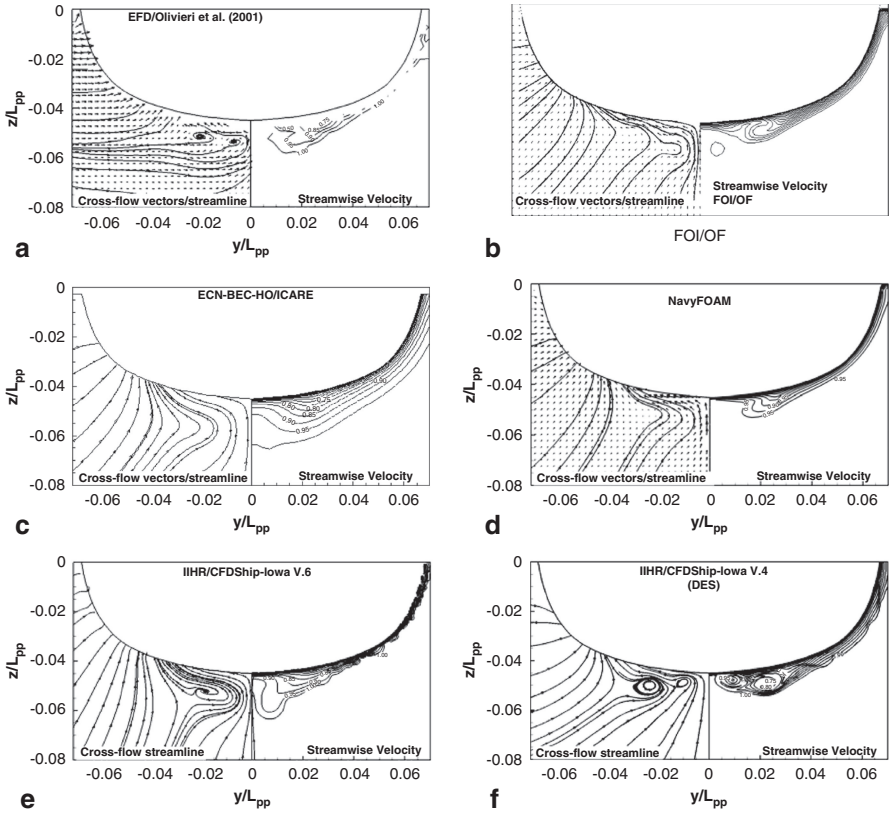


Fig. 3.31 Cross-flow vectors and streamwise velocity contours at $x/L_{pp} = 0.6$. **a** Experiments from INSEAN, **b** FOI/OF, **c** ECN-BEC-HO/ICARE, **d** NSWCCD-ARL-UM/NavyFOAM, **e** IIHR/CFDSHIP-IOWA-V6, **f** IIHR/CFDShip-Iowa-V4(DES)

MARIC/Fluent, NSWCCD-ARL-UM/NavyFOAM and MARIN are in good agreement with these experiments. On the other hand, ECN-BEC-HO/ICARE results exhibit far too thick a boundary layer. CEHINAV/STARCCM$^+$ and IIHR-CFDShip-IowaV4(ARS model) do not accurately capture the bulge of the boundary layer, probably due to grid discretization effects. IIHR/CFDShip-IowaV6 results show a very pronounced bulge in the iso wakes. This prediction is probably affected by the wall formulation of their immersed boundary conditions and the related lack of viscous effects. LES and DES simulation provided by FOI and IIHR, respectively, are both characterized by a high level of vorticity in the boundary layer which is not in agreement with what was measured by INSEAN. For FOI, we can see here the trace of a longitudinal vortex which emanates from the upper side of the sonar dome. Although the flow topology described by FOI's LES simulation, and at a lesser extent by IIHR DES computations, seem plausible, it is not entirely confirmed by the measurements at this specific station (Fig. 3.32).

Cross-section $x/L_{pp} = 0.9346$

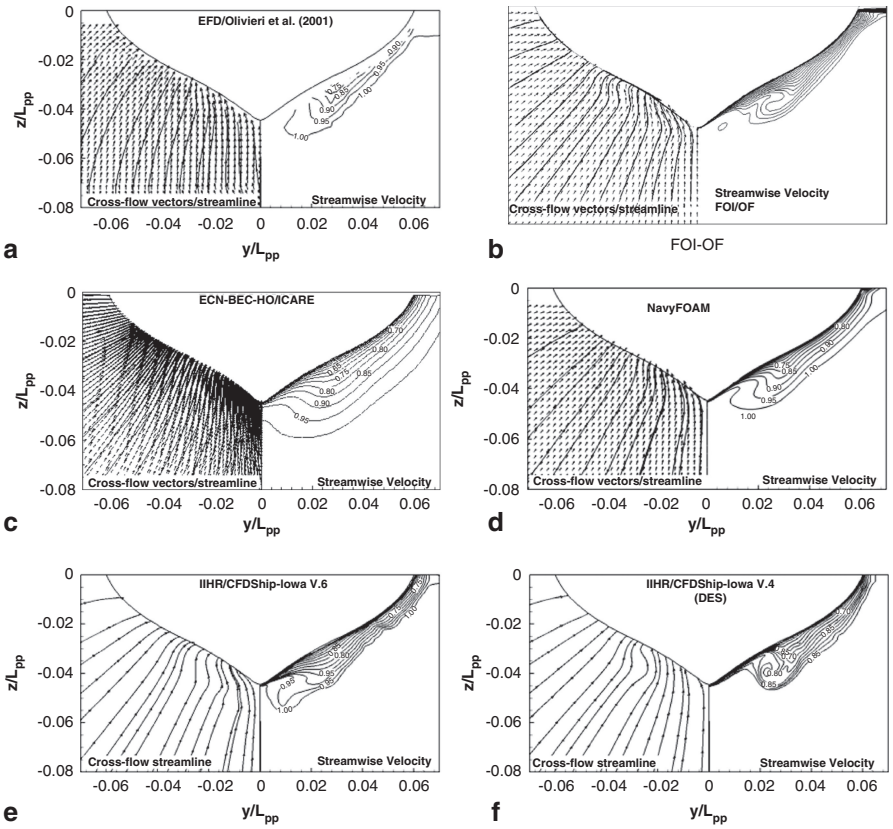


Fig. 3.32 Cross-flow vectors and streamwise velocity contours at $x/L_{pp} = 0.8$. **a** Experiments from INSEAN, **b** FOI/OF, **c** ECN-BEC-HO/ICARE, **d** NSWCCD-ARL-UM/NavyFOAM, **e** IIHR/CFDSHIP-IOWA-V6, **f** IIHR/CFDship-Iowa-V4(DES)

This section is of great interest since it is located at the propeller plane. Thanks to additional experiments made by Longo et al. (2007), we have also access to the distributions of the turbulent kinetic energy and five Reynolds stress components. The classification and analysis proposed for the previous cross-section can be repeated here. Contrary to the statistical models, LES and DES iso wake contours show a distortion related to a large amount of longitudinal vorticity, more or less in agreement with experiments for FOI/OF but clearly exaggerated for IIHR/CFDShip-IowaV4. This analysis is confirmed by the comparison on the turbulent kinetic energy and Reynolds stresses. While the methods based on statistical turbulence models are in reasonable agreement with measurements, the DES computations provided by IIHR show that the amount of computed turbulence is way too small 1.8×10^{-3} instead of 6×10^{-3} with a spatial distribution of iso contours which is not in agreement with experiments. This explains why the longitudinal vortices emanating from the sonar dome are not enough damped in the propeller plane. Unfortunately, we do not

have turbulence data from FOI to check if all the LES-like simulations are affected by the same flaws. ECN-BEC-HO/ICARE predicts a maximum value 6×10^{-3} for the turbulent kinetic energy which is about two times superior to the measurements, confirming the high level of effective viscosity present in their computations. Most of the other RANSE based solvers predict a somewhat lower value around 4×10^{-3} in reasonable agreement with the measurements. For these statistical turbulence models, one also notice a second peak of turbulent kinetic energy close the free-surface hardly visible in the measurements but predicted by ECN-BEC-HO/ICARE, IIHR/CFDShip-IowaV6, MARIC/FLUENT6.3.26. The same secondary turbulent kinetic energy peak but less intense and located closer to the wall is also visible in the simulations of NSWCCD-ARL-UM/NavyFOAM, SSRC/FLUENT, IIHR/CFDShip-IowaV4(ARS) and NMRI/SURF, these last results being in closer agreement with what can be guessed from Longo et al's experiments. The measurements of normal Reynolds stress components reveal also an expected strong anisotropy with $\max(\overline{uu}) = 2.8 \times 10^{-3}$, $\max(\overline{vv}) = 1.4 \times 10^{-3}$ and $\max(\overline{ww}) = 1.2 \times 10^{-3}$, all these maximum values occurring almost at the same location. The DES computations from IIHR contain almost no computed turbulence (with levels around 10^{-5}). On the other hand, NMRI ($\max(\overline{uu}) = 4.0 \times 10^{-3}$, $\max(\overline{vv}) = 2.6 \times 10^{-3}$, $\max(\overline{ww}) = 2.4 \times 10^{-3}$) predicts values of the normal Reynolds stresses which show a strong anisotropy but with values twice higher than the measurements. SSRC results ($\max(\overline{uu}) = 2.2 \times 10^{-3}$, $\max(\overline{vv}) = 2.6 \times 10^{-3}$, $\max(\overline{ww}) = 2.4 \times 10^{-3}$) show almost no anisotropy, which is expected since the RNG k-ε model is isotropic and the maximum values of the normal turbulence stresses are in good agreement with NMRI. Longo's measurements exhibit also a noticeable anisotropy but the maximum level of turbulence ($\max(\overline{uu}) = 2.8 \times 10^{-3}$ $\max(\overline{vv}) = 1.4 \times 10^{-3}$, $\max(\overline{ww}) = 1.2 \times 10^{-3}$) is twice smaller than what is computed by RANSE solvers.

The same conclusions concerning the DES computations hold for the Reynolds shear stresses $\overline{uw}$ and $\overline{uv}$. The maximum values measured by Longo are $\min(\overline{uv}) = -3.0 \times 10^{-3}$, $\max(\overline{uv}) = 5.0 \times 10^{-3}$ and $\max(\overline{uw}) = 10^{-3}$ while the DES computations predict generally levels around 10^{-5}. Predictions by RANSE solvers are in very good agreement with, for instance, the following similar min and max values for NMRI ($\min(\overline{uv}) = -4.0 \times 10^{-3}$, $\max(\overline{uv}) = 5.0 \times 10^{-3}$ and $\max(\overline{uw}) = 1.6 \times 10^{-3}$) and SSRC ($\min(\overline{uv}) = -4.0 \times 10^{-3}$, $\max(\overline{uv}) = 6.0 \times 10^{-3}$ and $\max(\overline{uw}) = 1.3 \times 10^{-3}$) (Fig. 3.33–3.39).

Cross-section $x/L_{pp} = 1.1$

In this section located in the wake of the ship, one notices a strong round vortex located close to the vertical plane of symmetry and, perhaps the trace of a secondary tiny structure close to the free-surface. FOI/OF and IIHR-CFDShip-IowaV4(DES) provide similar results characterized by two intense vortices correctly located. However, it seems that their intensity is over-estimated if one considers the very large distortion of isowakes which is not in agreement with the measurements. For the DES simulation, we know that this drawback is due to the lack of computed turbulent damping and one can suspect that the same explanation holds for the LES simulations provided by FOI. RANSE results provided by CSSRC/FLUENT6.3, MARIN/PARNASSOS, MARIC/FLUENT6.3.26 and NSWCCD-ARL-UM/NavyFOAM appear to be closer to the measurements.

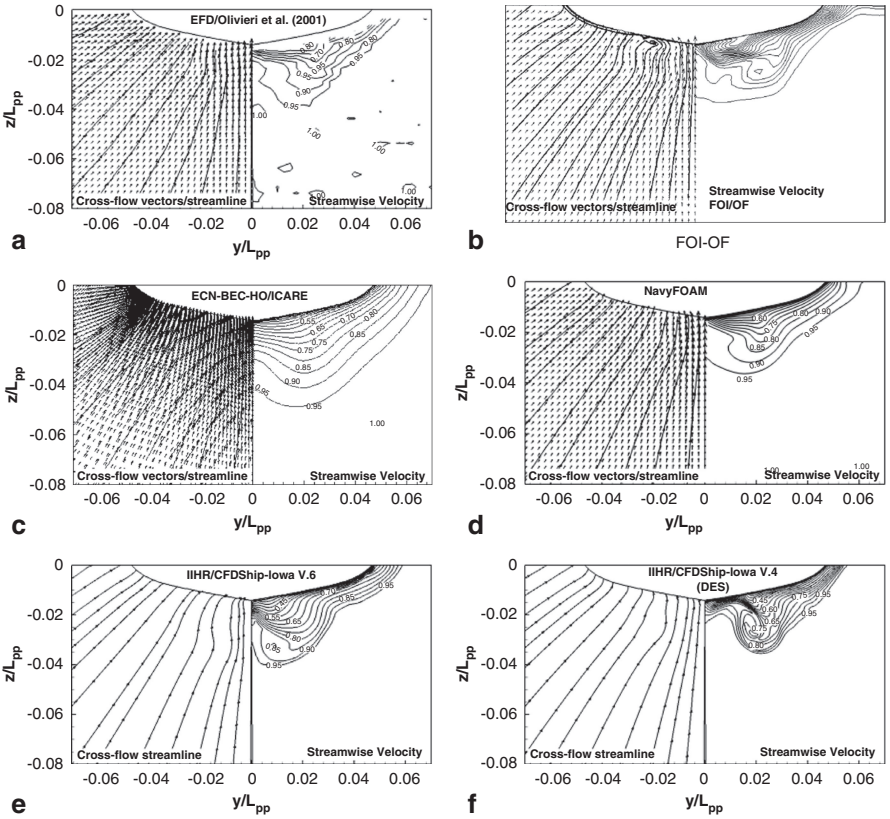


Fig. 3.33 Cross-flow vectors and streamwise velocity contours at $x/L_{pp} = 0.9346$. **a** Experiments from INSEAN, **b** FOI/OF, **c** ECN-BEC-HO/ICARE, **d** NSWCCD-ARL-UM/NavyFOAM, **e** IIHR/CFDShip-IowaV6, **f** IIHR/CFDShip-IowaV4(DES)

5.4 Comparative Analysis of the Flow Topology Based on Experiments and Computations

Based on the DES computations of IIHR performed on a very fine grid comprised of 300 M points, one can propose a plausible three-dimensional flow topology described in Fig. 3.41 taken from IIHR's paper (Bhushan et al. 2010). These vortical structures are shown in Fig. 3.41 using iso-surfaces of normalized helicity $Q = 100$ on the starboard side. A first longitudinal vortex called by IIHR the "sonar dome vortex" originates from the side of the sonar dome. This vortex is convected downwind, deviated towards the keel plane of symmetry and survives up to and after the stern. A second vortex named by IIHR "fore body vortex" initiates from the junction between the sonar dome trailing edge and the keel. It is also convected downwind, deviated outwards and is not significantly diffused by viscosity. Then, close to the section $X/L_{pp} = 0.800$, the sonar dome vortex wraps around the fore body vortex, which

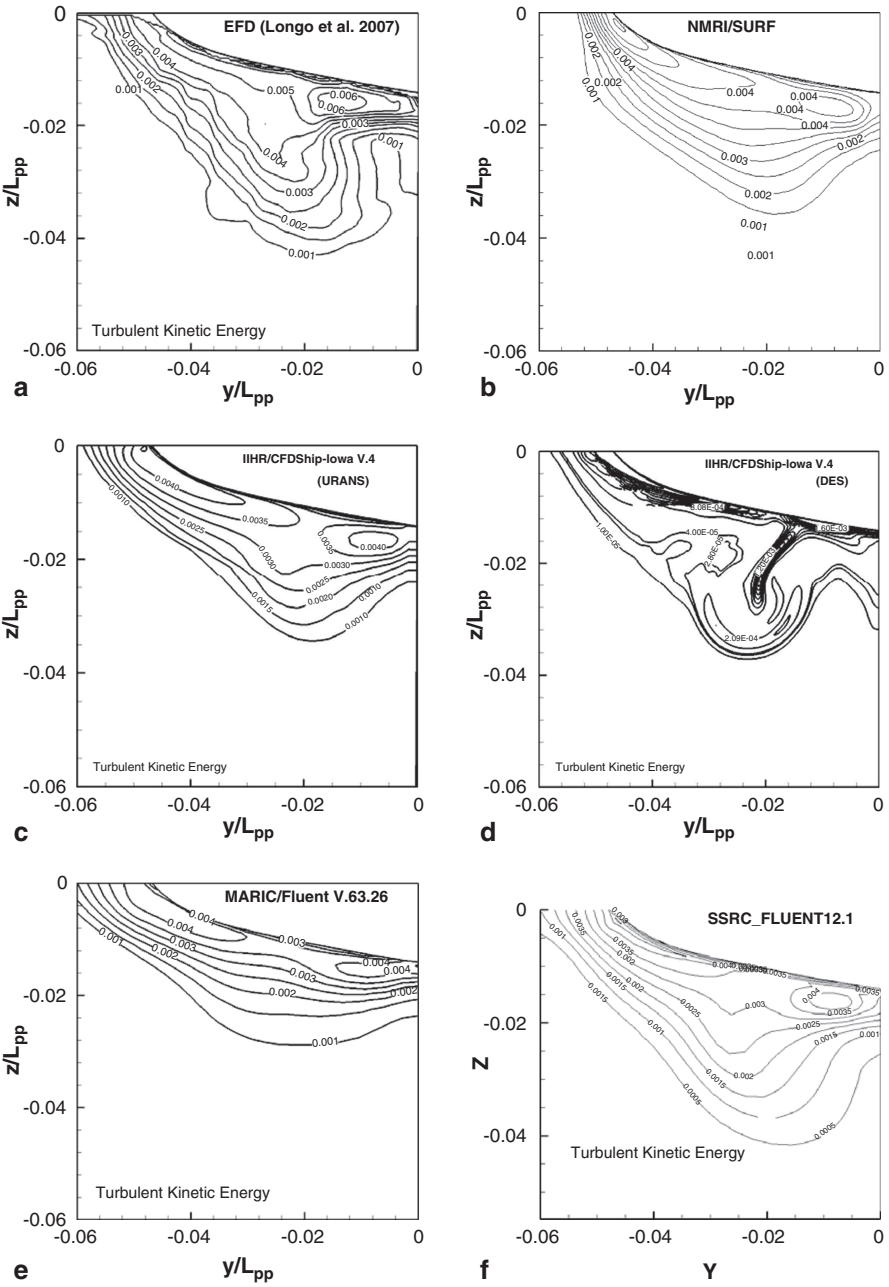


Fig. 3.34 Turbulent kinetic energy contours at $x/L_{pp} = 0.9346$. **a** Experiments from INSEAN, **b** NMRI/SURF, **c** IIHR-CFDSHIP-IOWA-V4(ARS), **d** IIHR-CFDSHIP-IOWA-V4(DES), **e** MARIC/FLUENT6.3.26, **f** SSRC/FLUENT12.1

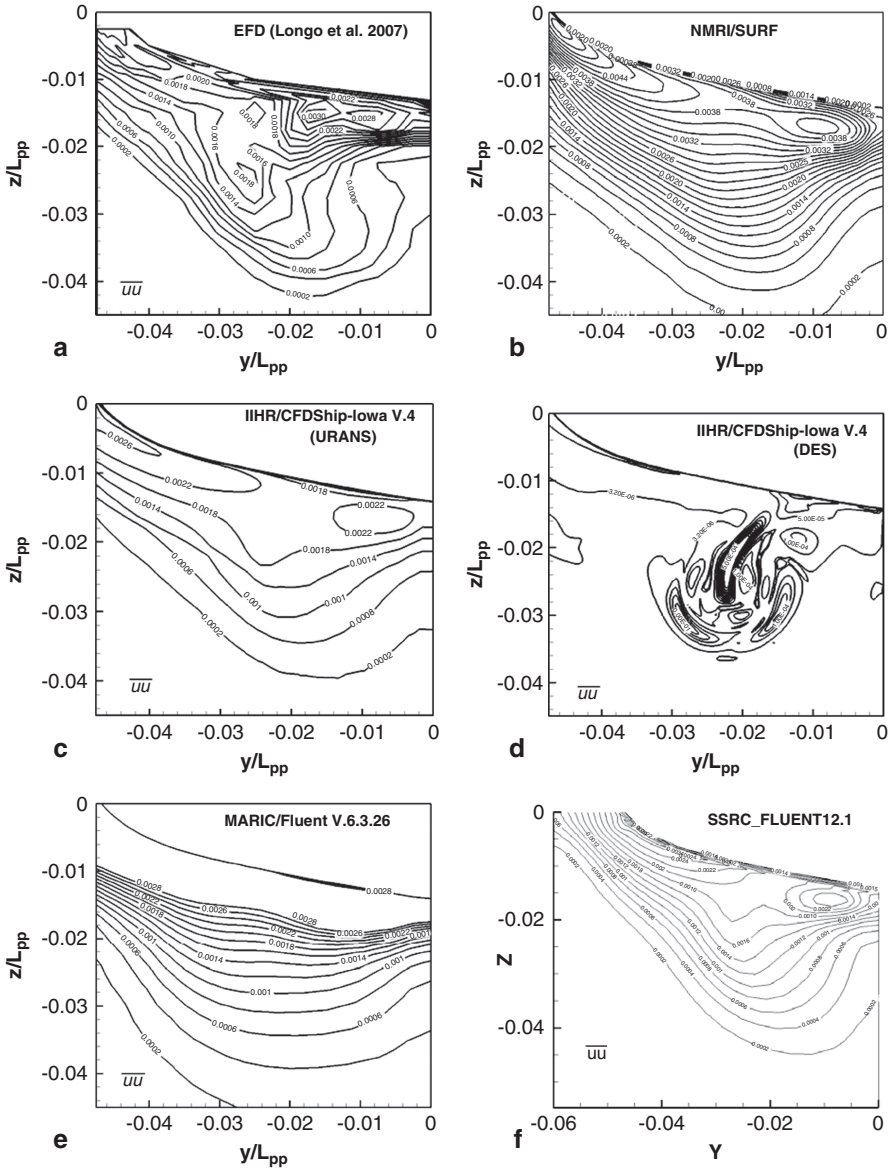


Fig. 3.35 $\overline{uu}$ contours at $x/L_{pp} = 0.9346$. **a** Experiments from INSEAN, **b** NMRI/SURF, **c** IIHR-CFDSHIP-IOWA-V4(ARS), **d** IIHR-CFDSHIP-IOWA-V4(DES), **e** MARIC/FLUENT6.3.26, **f** SSRC/FLUENT12.1

generates the after-body counter-rotating vortex. This interpretation is supported by the study of the wall streamlines in the fore part of the ship (see Fig. 3.42). One can clearly see two lines of convergence which correspond to the print on the wall of these two afore-mentioned longitudinal vortices. Based on these computations, one can now reject the interpretation given by INSEAN on the origin of this second

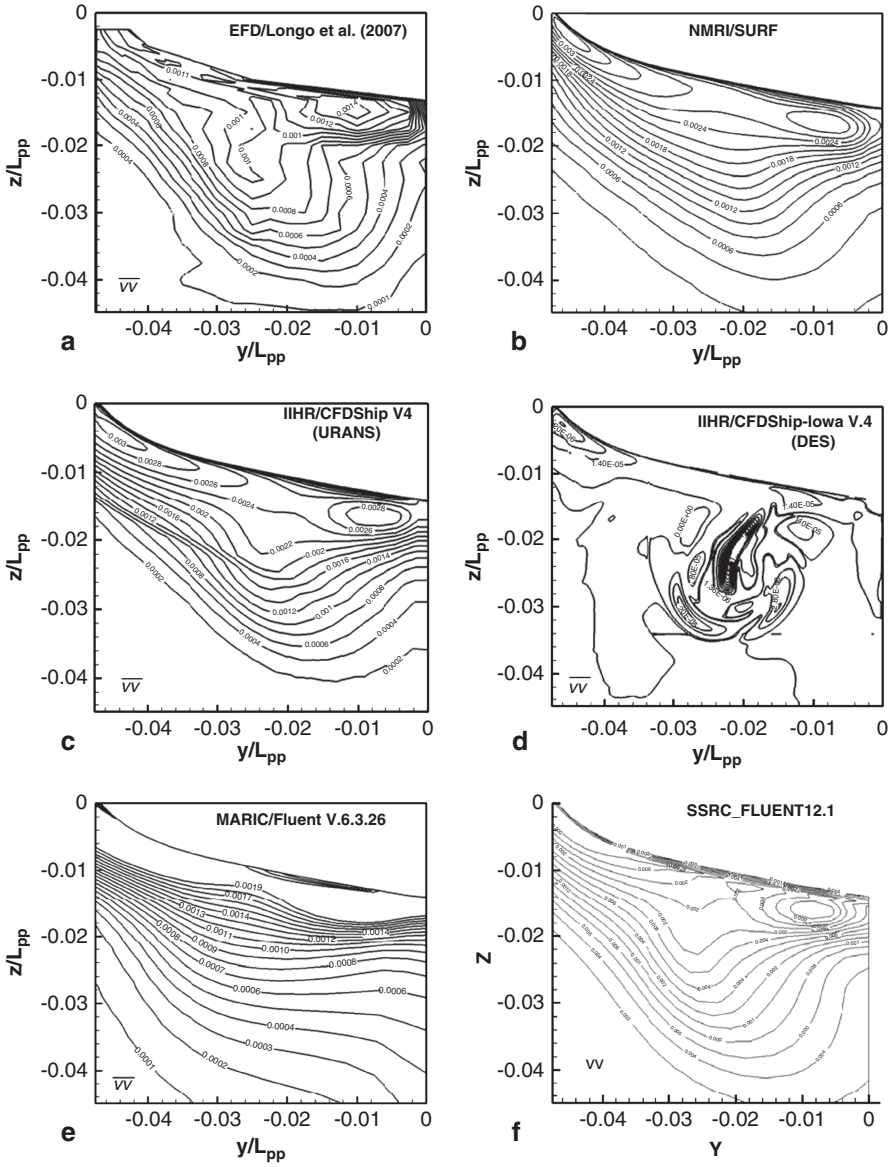


Fig. 3.36 $\overline{vv}$ contours at $x/L_{pp} = 0.9346$. **a** Experiments from INSEAN, **b** NMRI/SURF, **c** IIHR-CFDSHIP-IOWA-V4(ARS), **d** IIHR-CFDSHIP-IOWA-V4(DES), **e** MARIC/FLUENT6.3.26, **f** SSRC/FLUENT12.1

vortex called "fore body vortex", explanation which was provided on the basis of very sparse experimental informations. Instead of an hypothetical stern bilge vortex, this second vortical structure, called now "fore body vortex" is generated in the bow region, close to the intersection between the sonar dome trailing edge and the keel and is convected downwards without being significantly diffused.

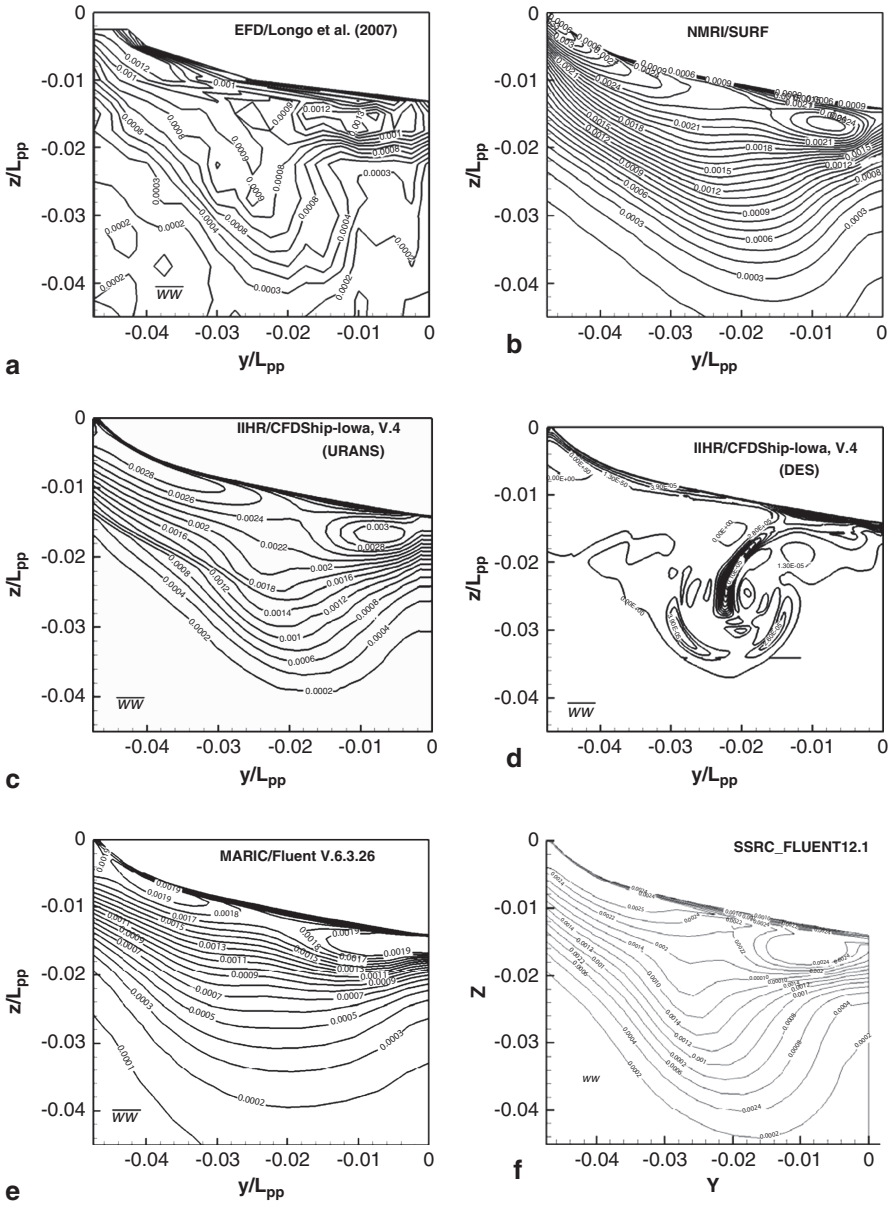


Fig. 3.37 $\overline{ww}$ contours at $x/L_{pp} = 0.9346$. **a** Experiments from INSEAN, **b** NMRI/SURF, **c** IIHR-CFDSHIP-IOWA-V4(ARS), **d** IIHR-CFDSHIP-IOWA-V4(DES), **e** MARIC/FLUENT6.3.26, **f** SSRC/FLUENT12.1

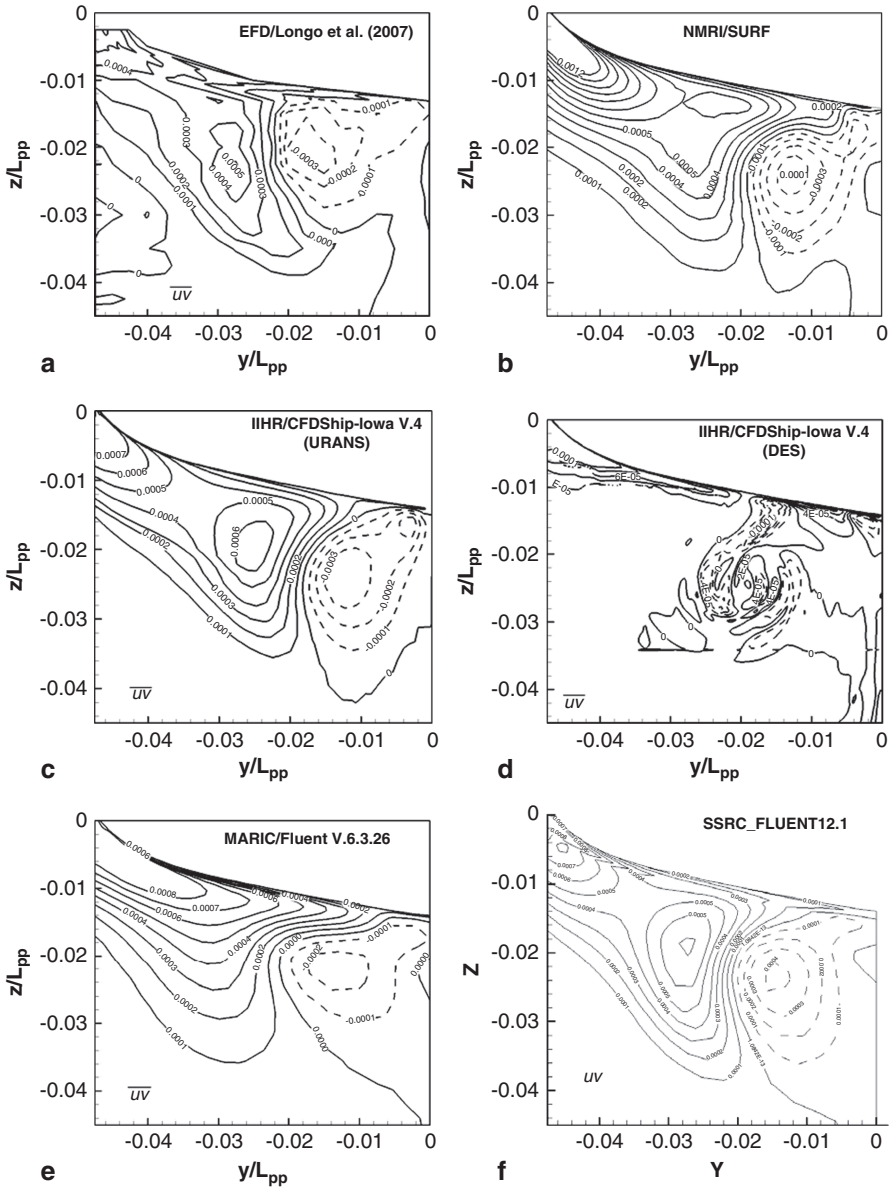


Fig. 3.38 $\overline{uv}$ contours at $x/L_{pp} = 0.9346$. **a** Experiments from INSEAN, **b** NMRI/SURF, **c** IIHR-CFDSHIP-IOWA-V4(ARS), **d** IIHR-CFDSHIP-IOWA-V4(DES), **e** MARIC/FLUENT6.3.26, **f** SSRC/FLUENT12.1

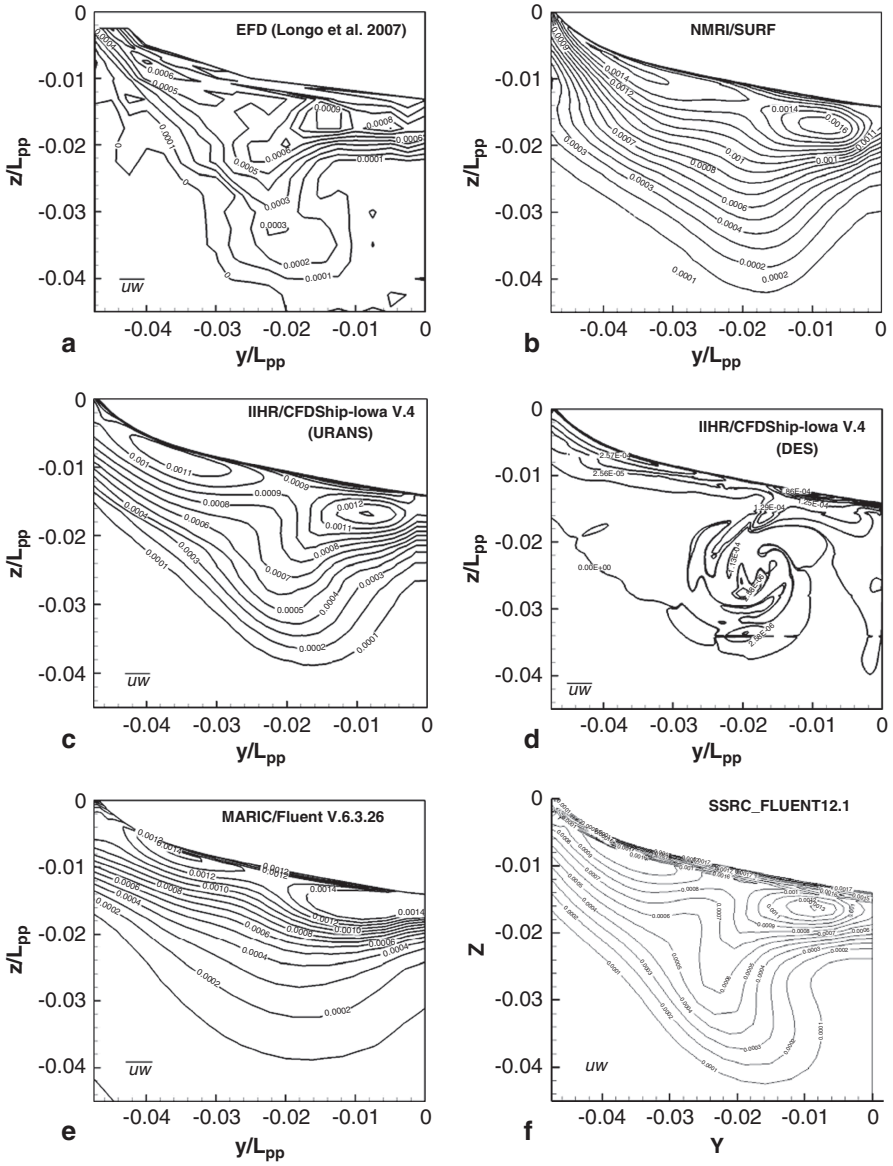


Fig. 3.39 $\overline{uw}$ contours at $x/L_{pp} = 0.9346$. **a** Experiments from INSEAN, **b** NMRI/SURF, **c** IIHR-CFDSHIP-IOWA-V4(ARS), **d** IIHR-CFDSHIP-IOWA-V4(DES), **e** MARIC/FLUENT6.3.26, **f** SSRC/FLUENT12.1

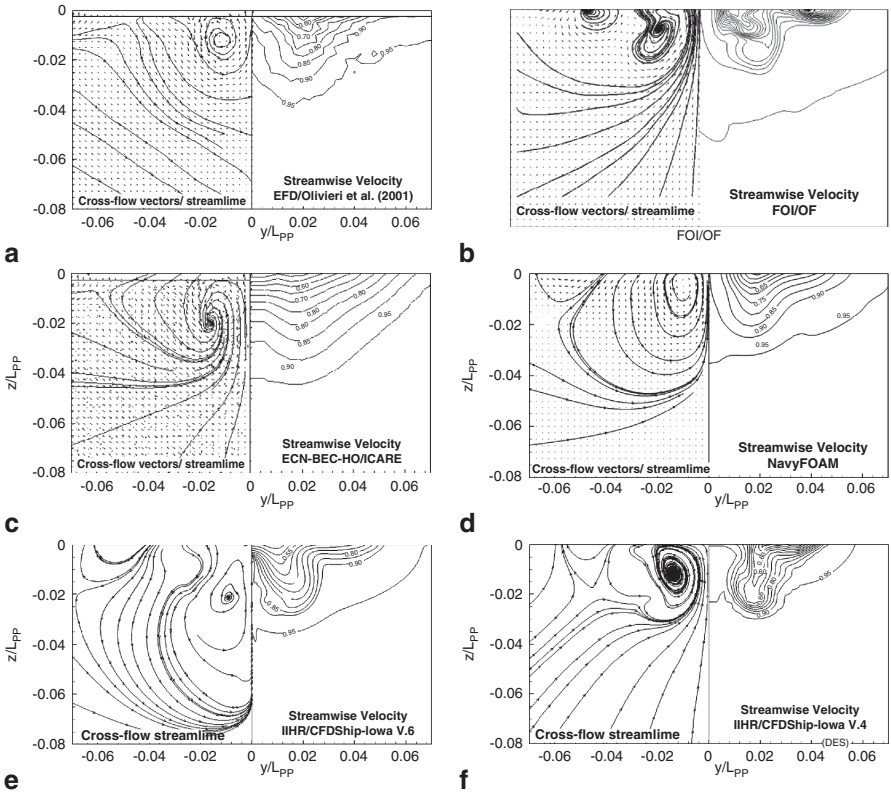


Fig. 3.40 Cross-flow vectors and streamwise velocity contours at $x/L_{pp} = 1.1$. **a** Experiments from INSEAN, **b** FOI/OF, **c** ECN-BEC-HO/ICARE, **d** NSWCCD-ARL-UM/NavyFOAM, **e** IIHR/CFDShip-IowaV6, **f** IIHR/CFDShip-IowaV4(DES)

5.5 Discussion and Tentative Conclusions Drawn from these Comparisons

Compared to the results obtained during the last workshop held in 2005 in Tokyo, the level of agreement between computations and experiments has been much improved. This is probably due to a mix of several reasons involving modeling and discretization errors. Undoubtedly, the grids used in 2010 are finer, which reduce significantly the sources of discretization errors. However, in five years, not much progress has been made on higher order discretization schemes for complex geometries since a majority of discretization schemes are formally second order accurate. Let us however point out the noticeable exception of IIHR/CFDSHIP-IOWA-V4 (DES) which uses hybrid discretization schemes for the convection which are formally 2nd/4th order accurate and IIHR/CFDSHIP-IOWA-V6 which uses 5th order accurate discretization schemes for the convection terms.

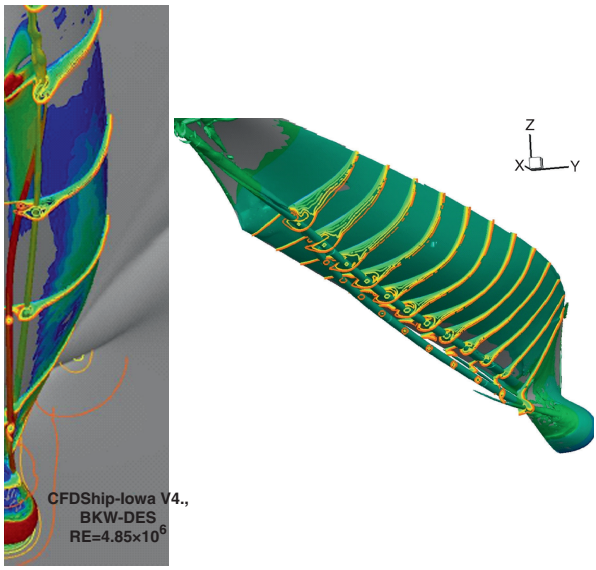


Fig. 3.41 Isosurface of normalized helicity Q = 100 obtained using CFDShip-Iowa-V4(DES)

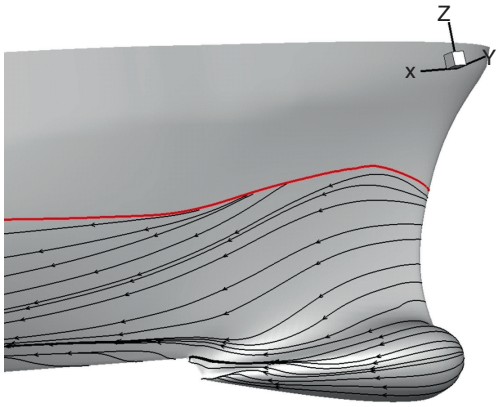


Fig. 3.42 Wall streamlines on the sonar dome using CFDShip-Iowa-V4(DES)

It is also the first time that one can evaluate the time accurate LES or DES solution methods for this high Reynolds number flows. If one puts aside the penalties in terms of computational power needed (one to two orders of magnitude more in terms of grid size), LES solution methods bring new answers to stimulate the discussion.

The points which have to be elucidated are: (i) what is the plausible flow topology on the sonar dome? and (ii) What is its downward influence on the development of the boundary layer along the hull? If one considers the results at section $x/L_{pp} = 0.1$, we have results with one, two or three vortices on each side of the ship. Unfortunately, the experiments are not detailed enough to clarify this point. LES-like solution provided by FOI and IIHR plead in favor of a pair of co-rotating longitudinal vortices generated around the trailing edge of the sonar dome and located close to the keel plane of symmetry, a configuration which is also found by several RANSE

based solution methods (NavyFOAM). Contrary to IIHR/CFDShip-IowaV4(DES), FOI/OF mentions the generation of a third vortex emanating from the upper side of the sonar dome, the so-called bilge vortex, which is less stable and partially located within the hull boundary layer and further away from the keel It also contributes to the formation of the bulge in the boundary layer iso-wake contours. IIHR also captures this vortex but it appears very quickly damped in their computations. According to their computations, this is one of the pair of vortices generated at the trailing edge of the sonar dome which causes the bulge in the boundary layer profile at the nominal wake plane. Without any other information, it is difficult to conclude.

It is however wise to consider these first LES or hybrid LES results with extreme caution. Thanks to the measurements of the turbulent kinetic energy and Reynolds stresses components in the propeller plane, we know that the amount of turbulence predicted by the DES model is far too small, which leads to a flow dominated by too intense vortical structures which do not correspond to the real physics. What is true for this specific cross-section should be also true for the whole flow domain. Let us remember that, fifteen years ago, the use of isotropic turbulence models on very coarse grids (20 000 points) led us to compute almost perfect hook-shape iso-velocity contours at the HSVA tanker propeller plane just because the grid was too coarse to create any significant turbulence production, which reduced fortunately the local level of turbulent viscosity. Once finer grids were used, the isotropic turbulence models played their noxious role and the hook disappeared for ever (until rotation correction was later introduced). With the DES results, we may be in face of a more sophisticated expression of the same disease for which under-resolved turbulence lead to a more intense longitudinal vorticity and an apparent better agreement with the experiments. Since FOI did not provide any information on the turbulence data, it is difficult to conclude but one can notice that the agreement between LES/DES computations and experiments deteriorates as one progresses towards the stern of the hull, the boundary layer appearing to be too much distorted by too intense longitudinal vortices.

Experiments provided a very sparse view of the flow. More resolved experiments may capture the vortices, and describe the interaction of sonar dome and fore-body keel vortices. Computations helped us to understand the flow topology, especially LES and DES. Now, are we able to conclude that the use of DES or LES turbulence models is mandatory to get the right flow topology? In other words, did LES or DES find the right topology for the right reasons? Once again, we have to reassess the respective role of discretization vs modeling errors. This is the reason why additional computations with statistical closures on very fine grids in the vicinity of the sonar dome will be presented in Chap. 7 with additional DES studies.

6 DTMB5415—Case 3.5

In the test case 3.5, the bare hull is towed in incoming head waves of moderate skewness ($\lambda = 1.5L_{pp}$, $A_k = 0.025$). The Froude number for the computations is 0.28 and the hull is positioned in the basin at its dynamic sinkage and trim as before.

Table 3.5 Main characteristics of the computations

Organization/code name	Turbulence model	Wall model	Discretization characteristics
ECN/ICARE	k-ω model	Low-Re turbulence model + no slip	Structured grid, 800 000 points
CSSRC/Fluent6.3	RNG k-ε	Wall function	Multi-block structured grid, 2 million cells
IIHR/CFDShip-IowaV4	DES	Low-Re turbulence model + no slip	114 million points
NMRI/SURF	EASM	Low-Re turbulence model + no slip	1.7 million cells

This experiment provides information on the three components of the velocity at the propeller plane for four different temporal phases equi-distributed on the wave period. 0th and 1st harmonic amplitudes and the 1st harmonic phase are also provided.

6.1 Review of Contributions

Four contributions have been uploaded for the test case 3.5. The names of the organizations and the code used are recalled in Table 3.5 with the main characteristics of their computations.

Contrary to test case 3.1, all the computations are based on RANS equations complemented by statistical turbulence models. We are therefore in face of contributors using a priori very similar methodologies and the differences should be attributed to discretization errors coming from too diffusive discretization schemes or too coarse grids/large time steps.

For this test case, all the turbulence models used by ECN/ICARE, CSSRC/Fluent6.3 and IIHR/CFDShip-IowaV4 are based on isotropic closures. As previously, NMRI/SURF employs the non-linear and anisotropic explicit algebraic stress model (EASM).

All the discretization methods are formally second order accurate and used on mono or multi-block structured body-fitted grids. However, ECN/ICARE uses their original SWENSE decomposition which consists in solving a modified viscous differential model close to the hull which govern the difference between the real viscous flow and the incident wavy flow modeled by a potential theory with non-linear free-surface boundary conditions. This strategy has been developed to reduce the number of discretization points for the viscous operator by solving a correction of the viscous flow field which is supposed to be more regular than the original one, the wavy component of the flow field being contained by the inviscid solution. All these characteristics are listed in Table 3.5.

Based on their defect-correction SWENSE formulation, ECN/ICARE used a coarse grid comprised of about 650 000 points while NMRI/SURF built a denser grid made of 1.7 million hexaedric cells. IIHR/CFDShip-Iowa decided to rely on a very fine grid made of 114 million points. The large grid simulation was performed on 500 processors which required 180 K CPU hours.

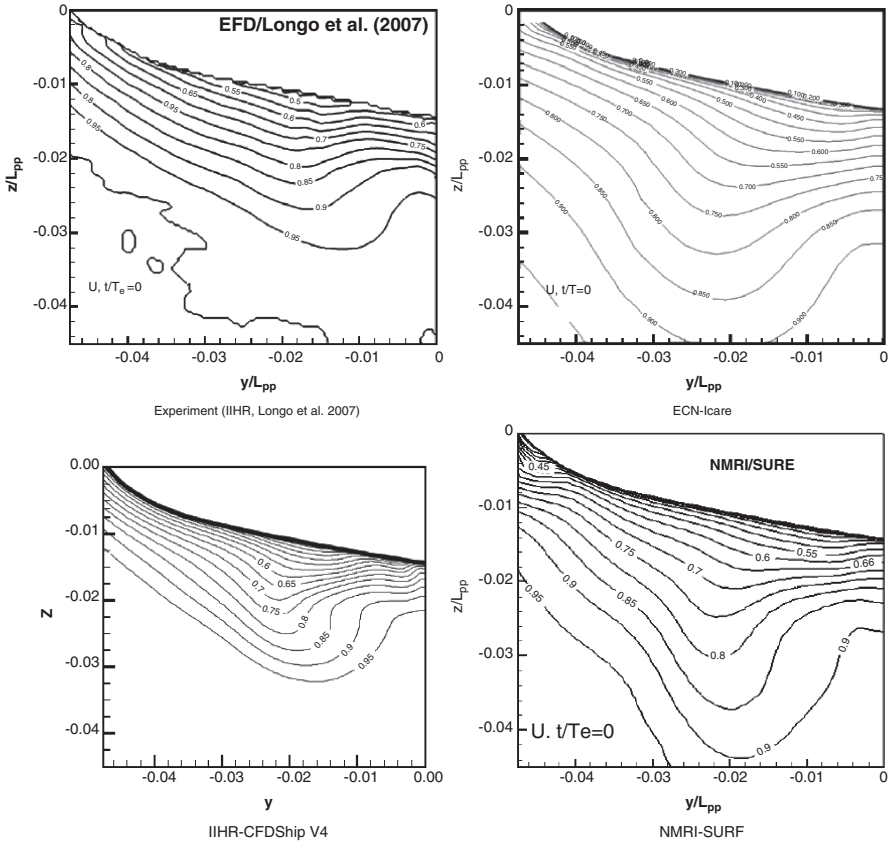


Fig. 3.43 U contours at x/Lpp = 0.935, t/Te = 0 (ΔU = 0.05)

6.2 Description of the Experimental Results

Figures 3.43–3.54 show the unsteady nominal wake boundary layer and cross flow pattern corresponding to steady streaming motion induced by the incident wave superimposed on the steady-flow pattern. The steady velocity contours correlate with the steady axial vorticity which induces a boundary layer bulge outboard of the vortex center and thinning of the boundary layer towards the center plane. The regular head wave induces three primary effects: (1) the wave-induced pressure gradients cause accelerations/decelerations of the axial and vertical velocities; (2) the unsteady wave elevation transports fluid axially and vertically with amplitude in phase with the wave elevation; and (3) the wave induces a time varying $\pm 2.8°$ angle of attack on the sonar dome resulting in unsteady sonar dome vortices with wavelength $U_c/f_e = 0.54$. As the wave crest passes the nominal wake plane, i.e., t/Te = 0, the boundary layer bulge contracts and the boundary layer towards the center plane expands, and an opposite trend is observed during the passage of the wave trough, t/Te = 1/2. The

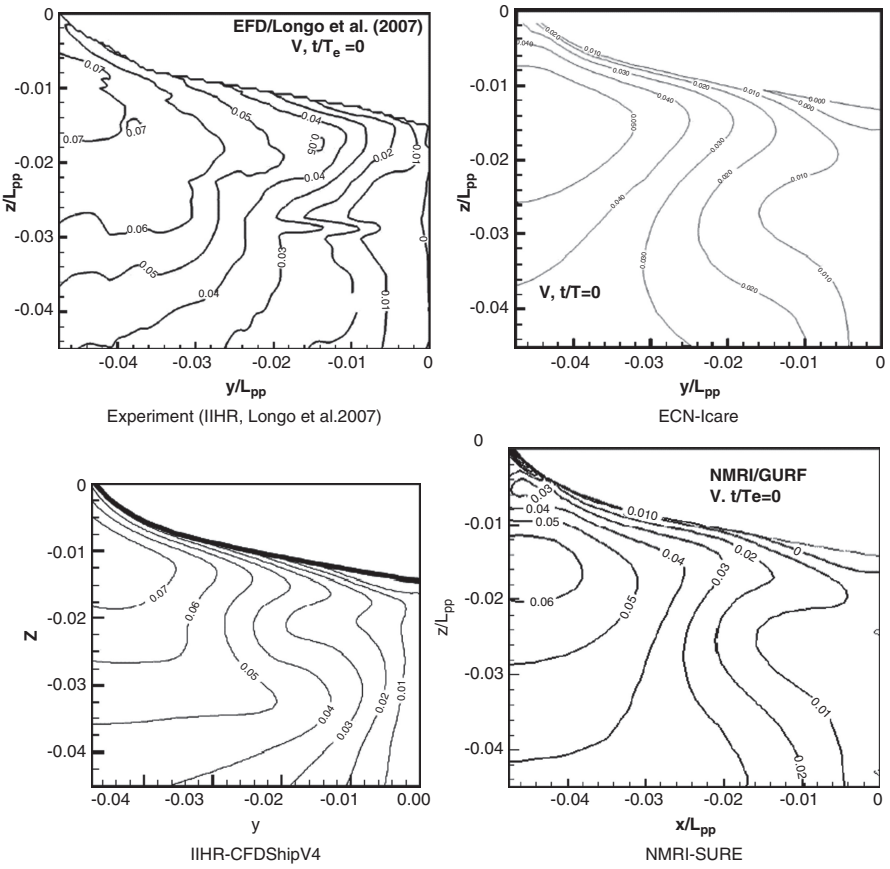


Fig. 3.44 V contours at x/Lpp = 0.935, t/Te = 0 (ΔV = 0.01)

transverse velocity shows small increases towards the center plane and decreases outboard of the vortex center, respectively.

The axial velocity 1st harmonic amplitude shows very large amplitudes in the bulge and thin boundary layer regions (see Fig. 3.56). The former is in phase and the latter −Π out of phase with the incident wave. These large amplitudes are attributed to the wave-induced vertical transport of fluid. The transverse velocity 1st harmonic amplitude shows fairly small response in the boundary layer bulge and thin boundary layer regions, but fairly large response at the hull shoulder near the free surface where the phase is Π/3. Near the steady vortex center, the phase abruptly changes from −Π to Π. The vertical velocity 1st harmonic amplitude shows small response everywhere indicating the hull and boundary layer has a significant damping effect on the wave-induced vertical velocities (see Fig. 3.62). The phase is the same as of the regular head wave vertical velocity, i.e., −Π/2, except in the bulge and thin boundary layer region where it is in phase with the wave.

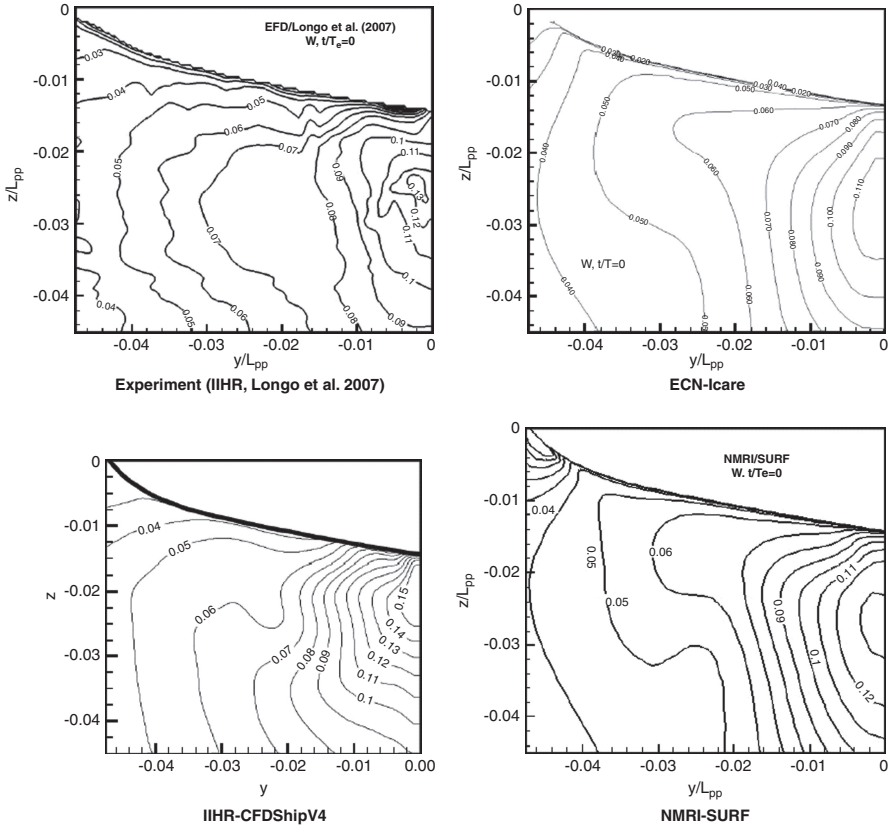


Fig. 3.45 W contours at x/Lpp = 0.935, t/Te = 0 (ΔW = 0.01)

6.3 Analysis of Results—Time t/Te = 0

The results provided by ECN/ICARE are characterized by a boundary layer which is 1.5 times too thick, a flaw which was also observed in their results for test case 3.1a. This overestimation of the boundary layer thickness is observed at a lesser degree in NMRI's results. IIHR/CFDShip-IowaV4 results are in good agreement with the measurements for this time.

V component is one order of magnitude smaller compared to U component and comparisons are more challenging. The global agreement is good for all the contributions. Some details like the pronounced distortion of the contours in the center of this plane is not captured by any computation.

All the participants are able to capture the peak on the vertical W component close to the keel plane although its experimental value (max(W) = 0.13) is underestimated by ECN/ICARE (max(W) = 0.11) and overestimated by IIHR/CFDShip-IowaV4 (max(W) = 0.15).

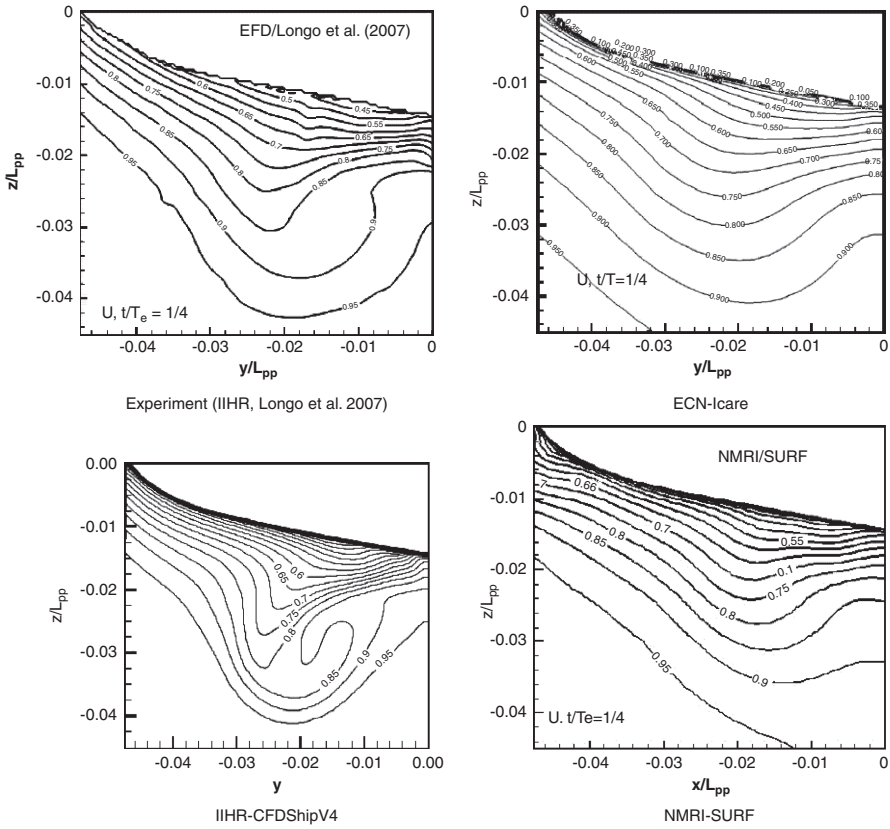


Fig. 3.46 U contours at x/Lpp = 0.935, t/Te = 1/4 (ΔU = 0.05)

6.4 Time t/Te = 1/4

For the longitudinal velocity component, the same problem noted above affects results from ECN/ICARE and NMRI/SURF for the next temporal phase. One notices a too thick boundary layer in the vertical plane of symmetry which is related with a too low of vorticity in this region. IIHR/ CFDShip-IowaV4 seems, on the contrary, to predict a flow in better agreement with the experiments, the level of vorticity close to the plane being probably slightly overestimated.

At this time, the best result on the V component is provided by IIHR which captures most of the details of the complex spatial distribution of V. ECN/ICARE and NMRI/SURF results seem to be far more diffused.

The measurements show a complicated spatial distribution of W component with a pronounced bulge on the iso contours W = 0.05. This behavior is perfectly reproduced by IIHR/CFDShip-IowaV4 and missed by the other participants.

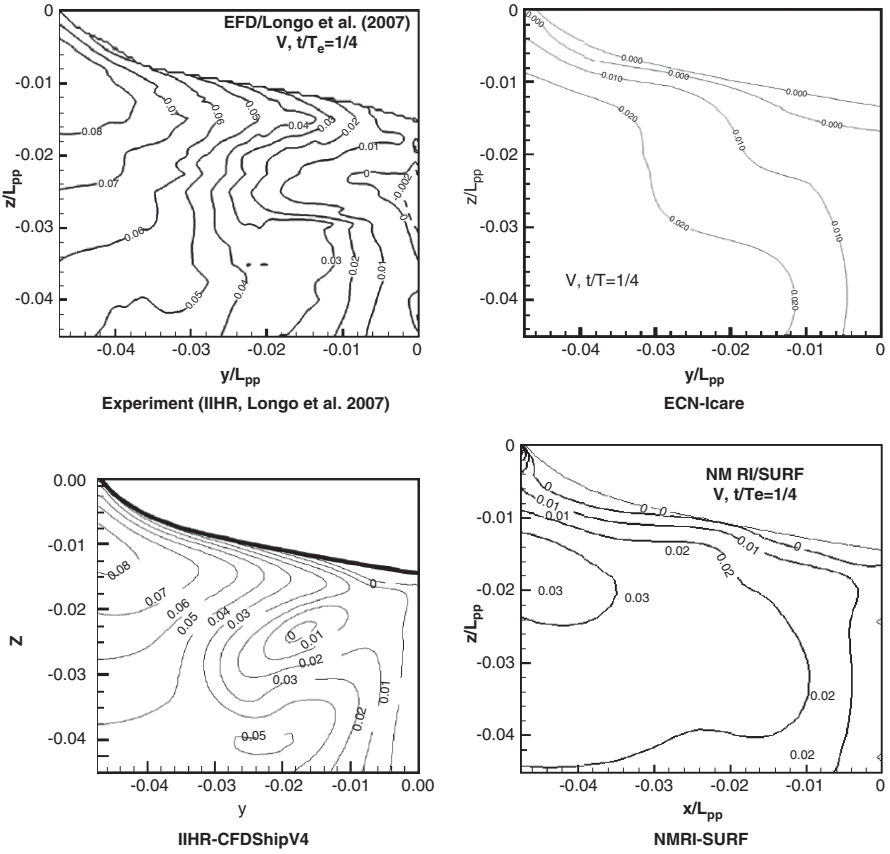


Fig. 3.47 V contours at x/Lpp = 0.935, t/Te = 1/4 (V = 0.01)

6.5 Time t/Te = 1/2

Globally, the analysis made previously for U and V components remains valid for this specific time. IIHR/CFDShip-IowaV4 results are in remarkable agreement with the experiments. ECN/ICARE and NMRI/SURF computations seem to be affected by too high a level of numerical diffusion.

Here again, the results provided by IIHR/CFDShip-IowaV4 on the vertical W velocity component are far better than the others which seem to be polluted by a high level of numerical diffusion. For instance, the iso-contour W = 0.06 is almost perfectly reproduced by IIHR/CFDShip-IowaV4.

6.6 Time t/Te = 3/4

Again, the analysis made previously for U and V components remains valid for this specific time. The best results are provided by IIHR/CFDShip-IowaV4 although

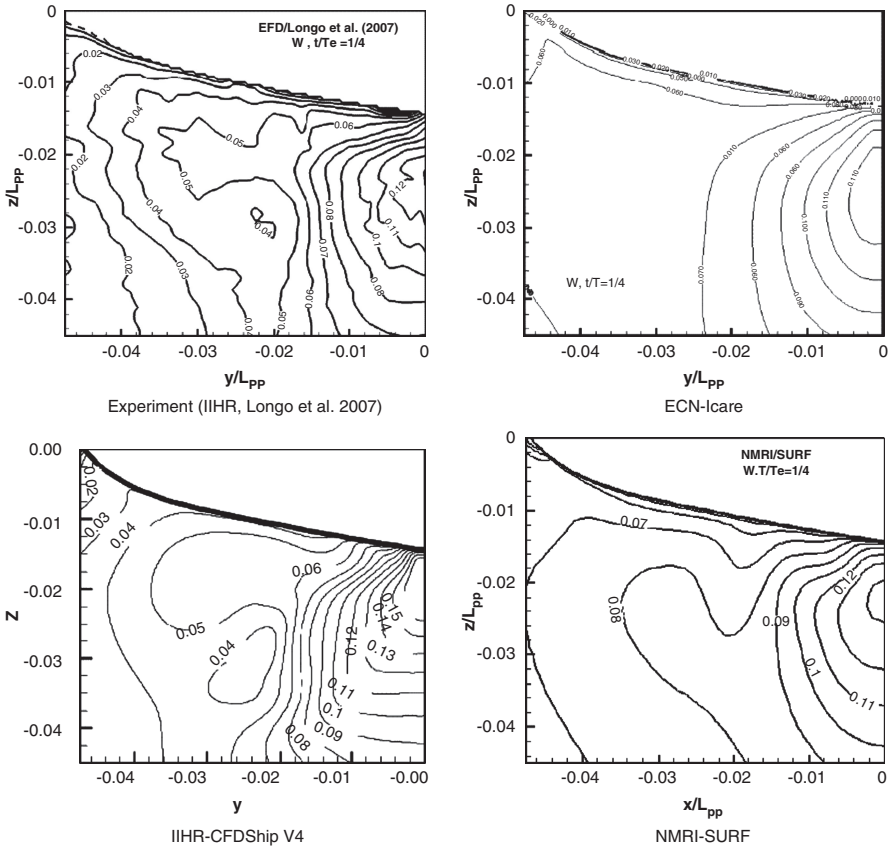


Fig. 3.48 W contours at x/Lpp = 0.935, t/Te = 1/4 (ΔW = 0.01)

the amount of vorticity close to the vertical plane of symmetry seems to be overestimated.

Concerning the V component SSRC/FLUENT12.1 results are slightly better than those provided by ECN/ICARE and NMRI/SURF.

Here again, SSRC/FLUENT12.1 results on the vertical W component are slightly better than those provided by ECN/ICARE and NMRI/SURF.

6.7 0th and 1st Harmonic Amplitudes and 1st Harmonic Phase

The far better results provided by IIHR/CFDShip-IowaV4 in terms of phase-averaged behavior are fully confirmed by the study of 0th and 1st harmonic amplitudes and 1st harmonic phase (see Figs. 3.55–3.63). Although NMRI/SURF results are in good agreement with the measurements for the 0th harmonic amplitude, the computations

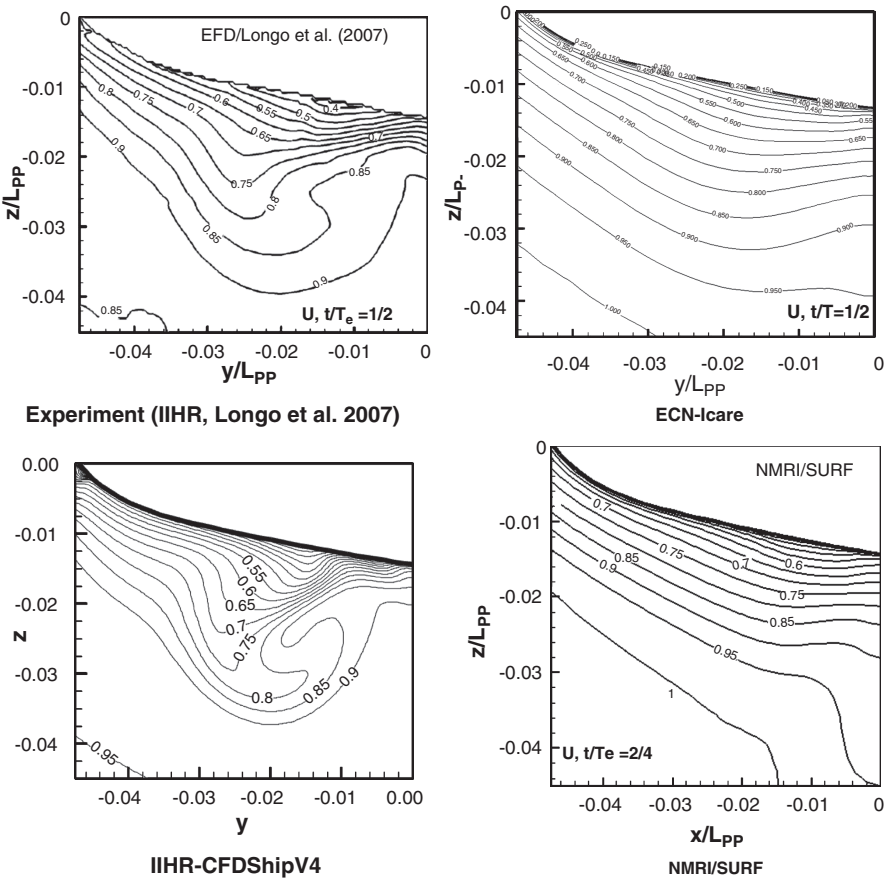


Fig. 3.49 U contours at x/Lpp = 0.935, t/Te = 1/2 (ΔU = 0.05)

of IIHR/CFDShip-IowaV4 are systematically better for the 1st harmonic amplitude. It is not possible to compare the various contributions for the 1st harmonic phase since only NMRI/SURF sent these informations which are in reasonable agreement with the experiments.

6.8 Comparison with Previous CFD Workshops

In the previous Tokyo (2005) workshop, four organizations (ECN/ICARE, France; ECN-CNRS/ISIS-CFD, France; IIHR/CFDShip-IowaV4, US and SVA/nep III, Germany) contributed for this test case. All the submissions used in-house research solvers based on either finite-volume or finite-difference methods on collocated grids. The submissions were for URANS using standard k-w or blended k-ε/k-w SST models. For the free-surface treatment level-set, interface tracking or multi-domain

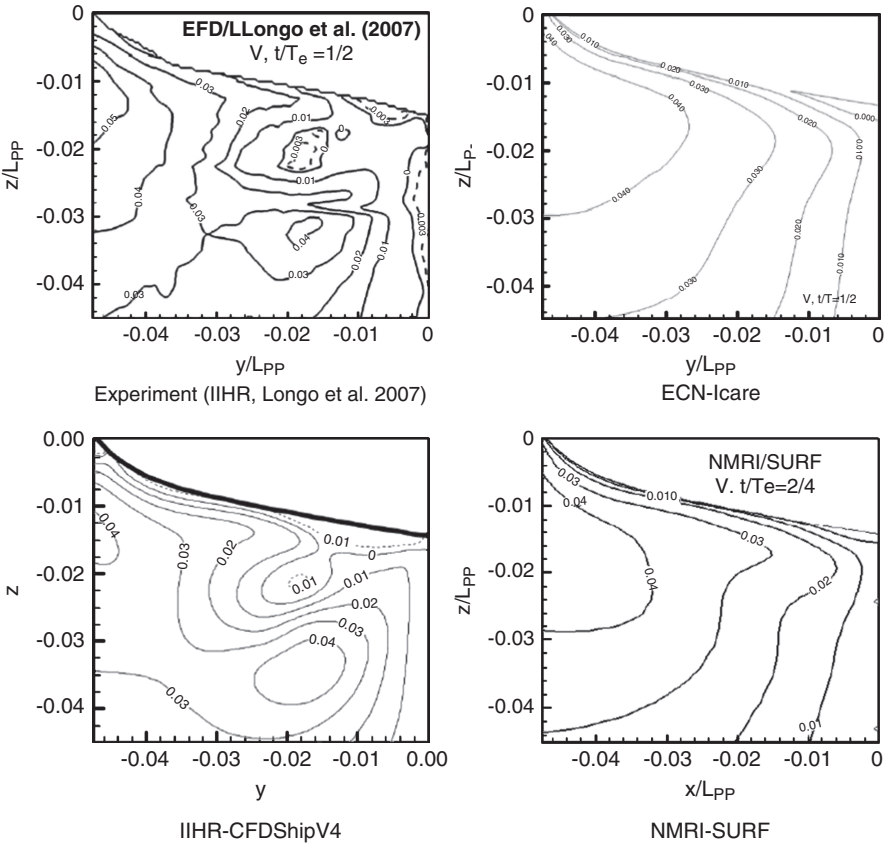


Fig. 3.50 V contours at x/Lpp = 0.935, t/Te = 1/2 (ΔV = 0.01)

formulation based on mass/volume fraction transport equations were used. Simulations were performed using 2nd order implicit schemes. The grid sizes varied from 0.9 to 3M points. SVA/nep III used unstructured grid, whereas other submissions used structured grid.

The expansion and contraction of the boundary layer bulge with the passage of the wave was predicted well, but the boundary layer thickness was over-predicted by 20–30 %D. The boundary layer thickness towards the center plane expanded at the wave trough, which is opposite to the experimental data trend. ECN-CNRS/ISIS-CFD on 2.2M grid performed best among the submissions and predicted the decrease of the transverse velocity below the vortex center and decrease of vertical velocity outboard of the vortex center. However, the mean transverse and vertical velocity contours were diffused and dissipated compared to EFD.

All the simulations predicted the axial velocity 1st harmonic amplitude well in the boundary layer bulge region, but with 10 %D lower peaks. The large amplitudes towards the center plane were not predicted well. Similarly, the 1st harmonic phases are predicted well in the boundary layer bulge, but not in the thin boundary layer

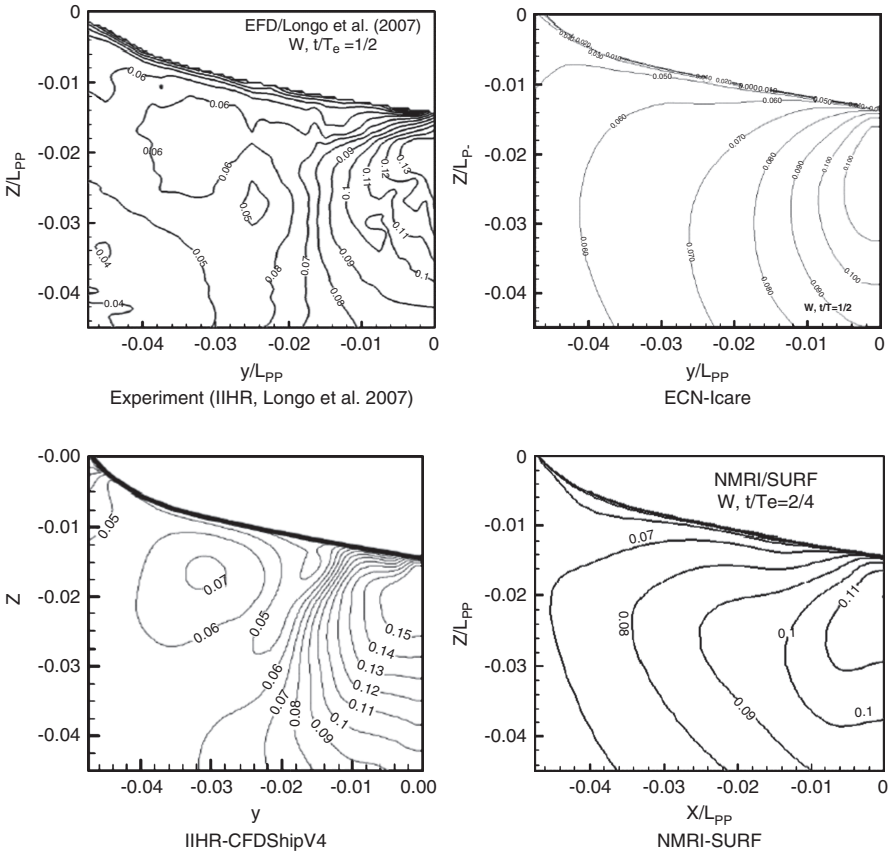


Fig. 3.51 W contours at x/Lpp = 0.935, t/Te = 1/2 ($\Delta W = 0.01$)

region. The transverse velocity 1st harmonic amplitudes in the shoulder region were over-predicted by 10 %D. The phase near the shoulder region was not predicted accurately, but the abrupt change of phase in near the steady vortex center was predicted well. All the submissions predicted the vertical velocity 1st harmonic amplitude well, but only ECN-CNRS/ISIS-CFD predicted the phase well.

6.9 Discussion

This test case illustrates the far better behavior of the solution provided by IIHR/CFDShip-IowaV4. This clear superiority is very probably due to the use of a very fine grid which is two orders of magnitude larger than the mesh used by the other participants. However, the boundary layer is 9 % thinner and the cross-flow velocities are 9 % higher than the EFD, suggesting the vortex strength is over-predicted.

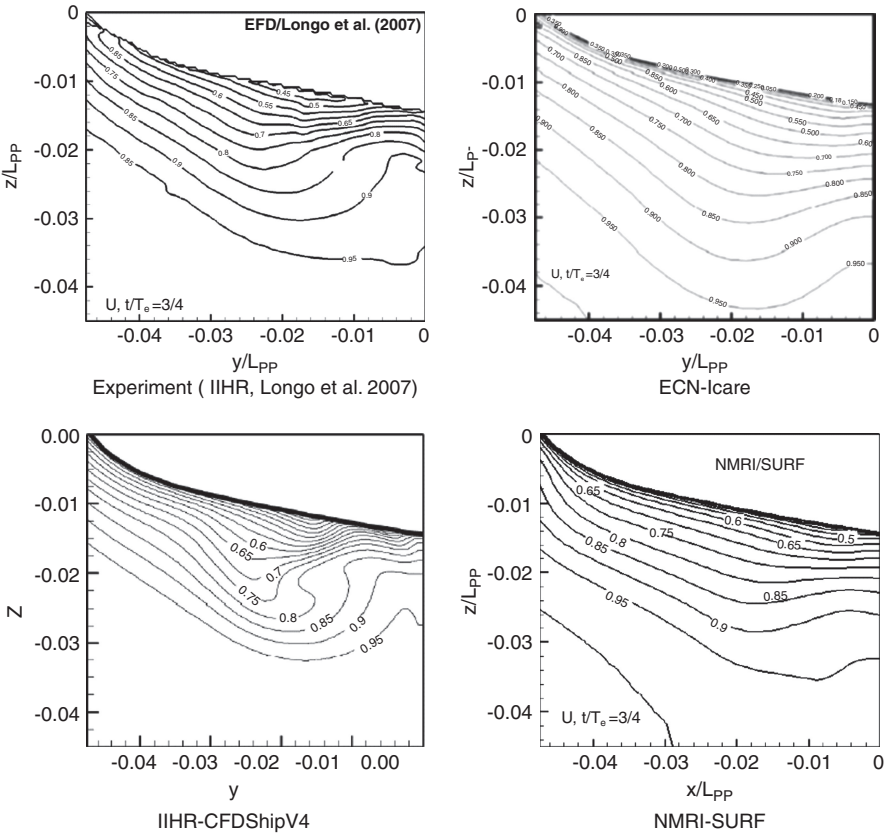


Fig. 3.52 U contours at x/Lpp = 0.935, t/Te = 3/4 (ΔU = 0.05)

The coarse grid simulations over-predict the boundary layer bulge at nominal wake plane and predict diffused cross flow contours, but predict the 1st amplitude and phase well. This suggests that, even though the vortices are diffused and dissipated, their evolution which is governed by the head waves are predicted reasonably well.

Overall, the large grid simulations significantly improve resistance and moment predictions as observed for the sea-keeping cases. The grid resolutions are also an important factor for improved wave elevation and flow predictions. The coarse grid simulations suffer from excessive numerical diffusion and dissipation. Although based on a theoretically more reliable turbulence model and a relatively fine grid, NMRI/SURF results are still polluted by too high a level of numerical diffusion. The innovative SWENSE defect correction employed by ECN/ICARE does not bring any improvement since their results are too much damped with a boundary layer thickness strongly over-estimated as it was already noticed in test case 3.1-a. Here again, the discretization errors are still very large, even if a modified viscous formulation is solved. SSRC/FLUENT12.1 results are in reasonable agreement with

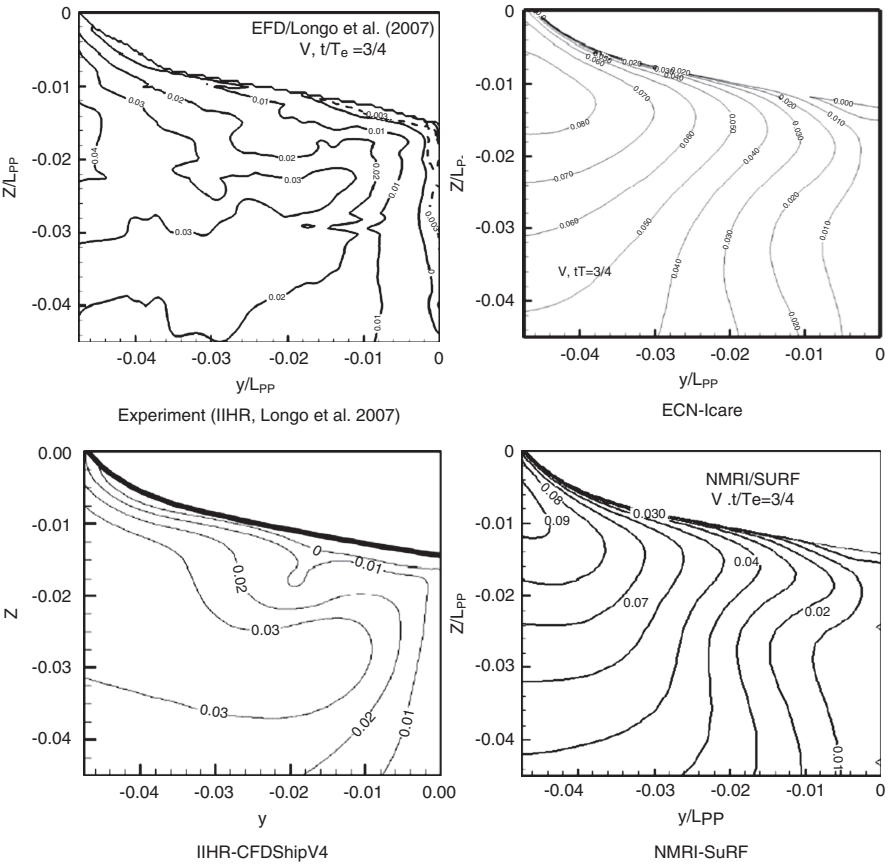


Fig. 3.53 V contours at x/Lpp = 0.935, t/Te = 3/4 ($\Delta V = 0.01$)

the experiments but the agreement is less good than what is demonstrated by IIHR. Although 100's M of grid points are not necessary to accurately predict such flows using URANS, more reliable turbulence models, such as anisotropic models, and a relatively finer grid than that used by the submissions would help reduce the numerical diffusion and dissipation, thereby improving numerical predictions. However, for advanced LES/DES models 100's M of grid points are required to achieve expected 80-90 % resolved turbulence levels.

7 DTMB5415—Case 3.6

The model-scale test for 1/46.6 scale 5415 bare hull with bilge keels free to roll-decay advancing in calm water was performed in the IIHR towing tank (Irvine et al., 2004). The flow conditions were $Re = 2.56 \times 10^6$, $Fr = 0.138$, $\sigma = 2.93 \times 10^{-4}$,

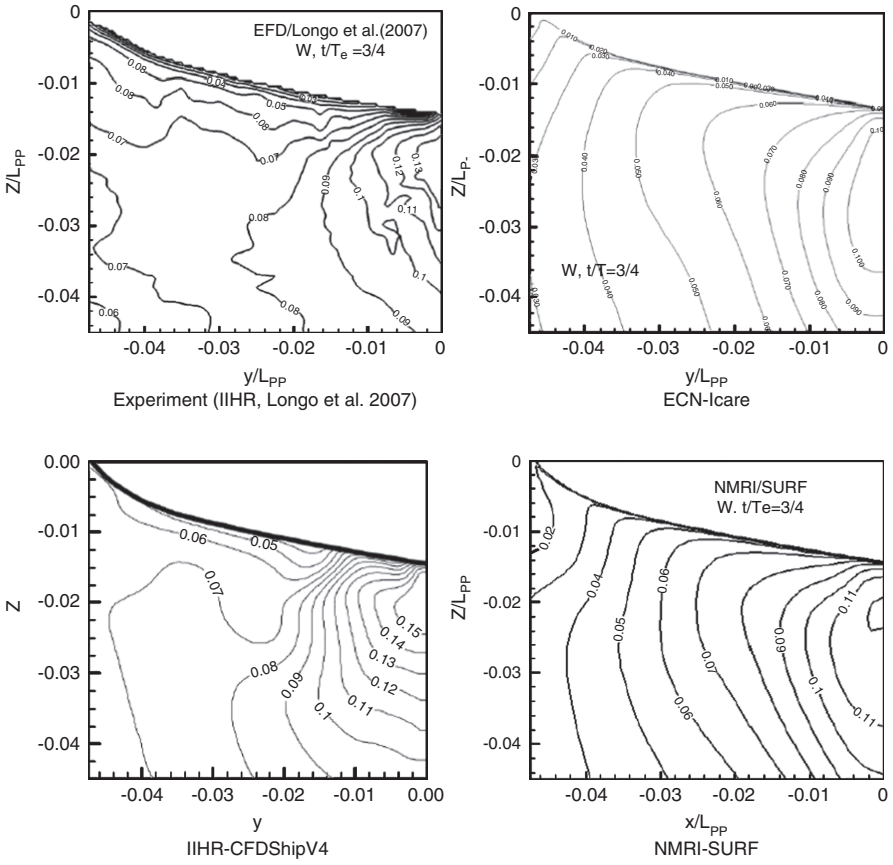


Fig. 3.54 W contours at x/Lpp = 0.935, t/Te = 3/4 ($\Delta W = 0.01$)

$\tau = -3.47 \times 10^{-2\circ}$ and initial roll angle $\varphi = 10°$. Data were procured for the forces and moments using strain gage load cell, the unsteady ship roll motion using a Krypton Motion Tracker, the unsteady wave elevation on the starboard side using four servo wave probes. Using 2D PIV system, this experiment provides also informations on the three components of the velocity at cross-section $x/L_{pp} = 0.675$ where the bilge keels are located for four different temporal phases equi-distributed on the second cycle of roll. 0th and 1st harmonic amplitudes and the 1st harmonic phase are also provided.

7.1 Review of the Contributions

Only three organizations (two teams from Ecole Centrale de Nantes using their respective codes, ICARE and ISIS-CFD and SSRC using FLUENT 12.1) uploaded

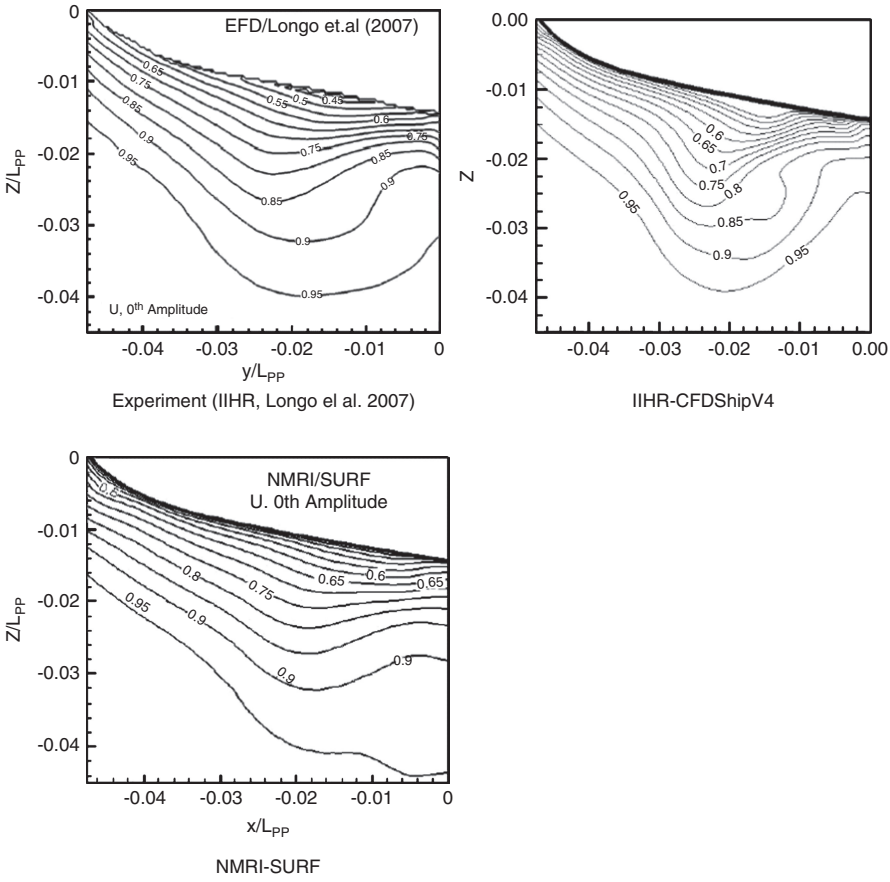


Fig. 3.55 U contours of 0th harmonic amplitude at x/Lpp = 0.935 ($\Delta U = 0.05$)

volume solution for the test case 3.6. The names of the organizations and the code used are recalled in Table 3.6 with the main characteristics of their computations.

For this test case, ECN-BEC-HO/ICARE and CSSRC/Fluent6.3 employed isotropic turbulence closures. ECN-CNRS/ISIS-CFD used both a SST k-ω model and the anisotropic EASM but reported minor differences between these two turbulence closures. It should be recalled that the vortex generation is imposed by the geometry of the bilge keels, which explains the reduced influence of the turbulence models on the flow fields compared to the KVLCC2 test case 1.1-a. All the discretization methods are formally second order accurate and used on mono, multi-block structured body-fitted grids or fully unstructured grids. For instance, ECN-BEC-HO/ICARE used a relatively coarse grid comprised of about 650,000 points while ECN-CNRS/ISIS-CFD produced, thanks to the automatic grid refinement, an unstructured grid made of 4,886,000 points which included 3 to 4 levels of local refinement. SSRC/FLUENT12.1 used a grid comprised of 3 million cells. The simulations were performed on 16 to 32 CPU and the averaged CPU time was 700 hours.

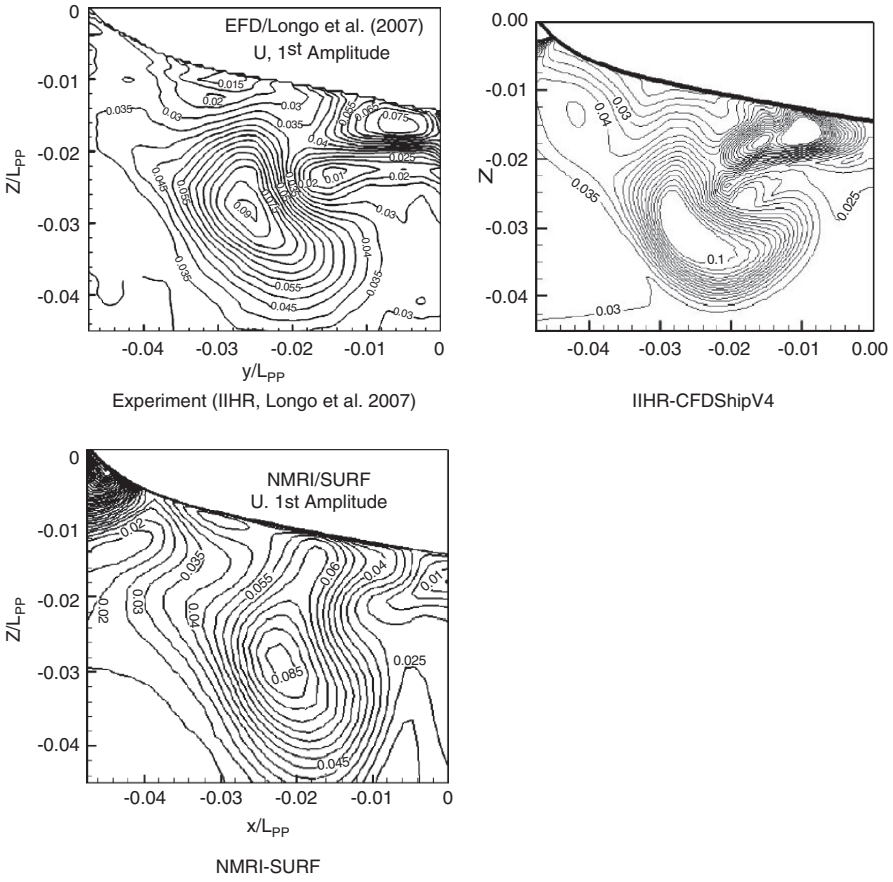


Fig. 3.56 U contours of 1st harmonic amplitude at x/Lpp = 0.935 ($\Delta U = 0.005$)

7.2 Description of the Experimental Results

The axial velocity contours in Fig. 3.64 shows development of a low velocity region outboard of the bilge keel when the model starts to roll to the port side from the fully rolled starboard position, $t/T_e = 0$. As the model continues to roll, the low velocity region is convected away from the bilge keel and higher momentum fluid moves towards the bilge keel. When the model is fully rolled to the port side, $t/T_e = 1/2$, the low velocity region is observed inboard of the bilge keel, and moves away from the bilge keel as the model continues to roll from the port to starboard side. The low velocity region indicates the presence of the vortex core. The transverse velocity contours in Fig. 3.65 show positive velocity near the hull outboard of the bilge keel and negative velocity below that, when the model rolls from the starboard to port side, t/Te = 1/4. The reverse trend is observed, i.e., negative velocities near the hull inboard of the bilge keel and positive velocity below that, when the model rolls from

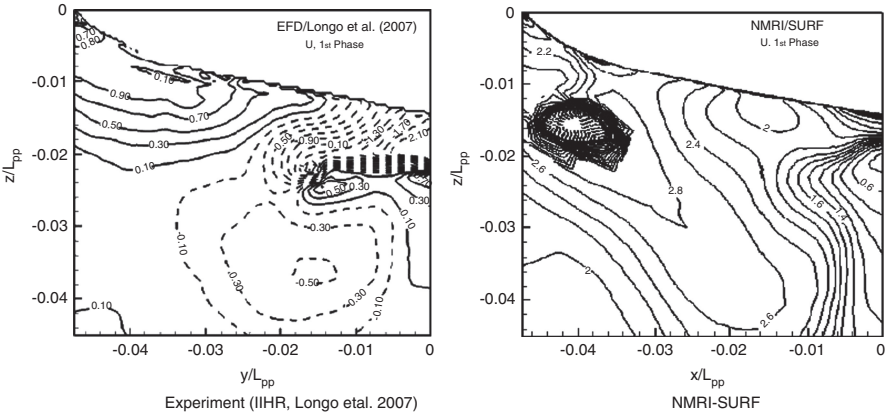


Fig. 3.57 U contours of 1st harmonic phase at x/Lpp = 0.935 (ΔGU = 0.2). Solid lines positive (+) values, Dashed lines negative (–) values

the port to starboard side. The vertical velocity contours in Fig. 3.66 show down-flow near the bilge keel tip and up-flow outboard of the down-flow, when the model starts to roll from starboard to port. As the model continues to roll, the down-flow increases in size and magnitude and moves outboard of the bilge keel. A similar flow pattern inboard of the bilge keel with enlarged up-flow is observed when the model starts to roll from port to starboard. The transverse and vertical velocities contour indicates a change in vortex circulation sign with the change in roll direction. Wilson et al. (2006) explained this flow pattern due to the formation of bilge keel vortices with opposite circulation and convection of the vortices depending on the phase of the roll.

7.3 Analysis of the Results

Three velocity components are provided at $x/L_{pp} = 0.675$ for four temporal phases equi-distributed over the second cycle of roll decay. Only ECN-BEC-HO/ICARE and ECN-CNRS/ISIS-CFD have produced results for all the phases, SSRC results being restricted to the phase 3Te/4.

The coarse grid ECN-BEC-HO/ICARE predictions in Figs. 3.64–3.66 capture the overall trends in the boundary layer and cross flow pattern. But the minimum and maximum values are over-predicted by 30 %D. Checking the distribution of the longitudinal velocity component U, the results provided by ECN-BEC-HO/ICARE are characterized by a boundary layer which is 1.5 times too thick, a flaw which was also observed in their results for test case 3.1a and 3.5. The boundary layer thickness is correctly reproduced by ECN-CNRS/ISIS-CFD. Some details like the localized small vortex (contour U = 0.82) are, however, not captured or slightly diffused. Globally, ECN-CNRS/ISIS-CFD predictions on finer grid compare very well with the experiments, where the minimum and maximum velocities compare within 6 %D of the EFD. The cross-flow predictions are slightly better than the axial

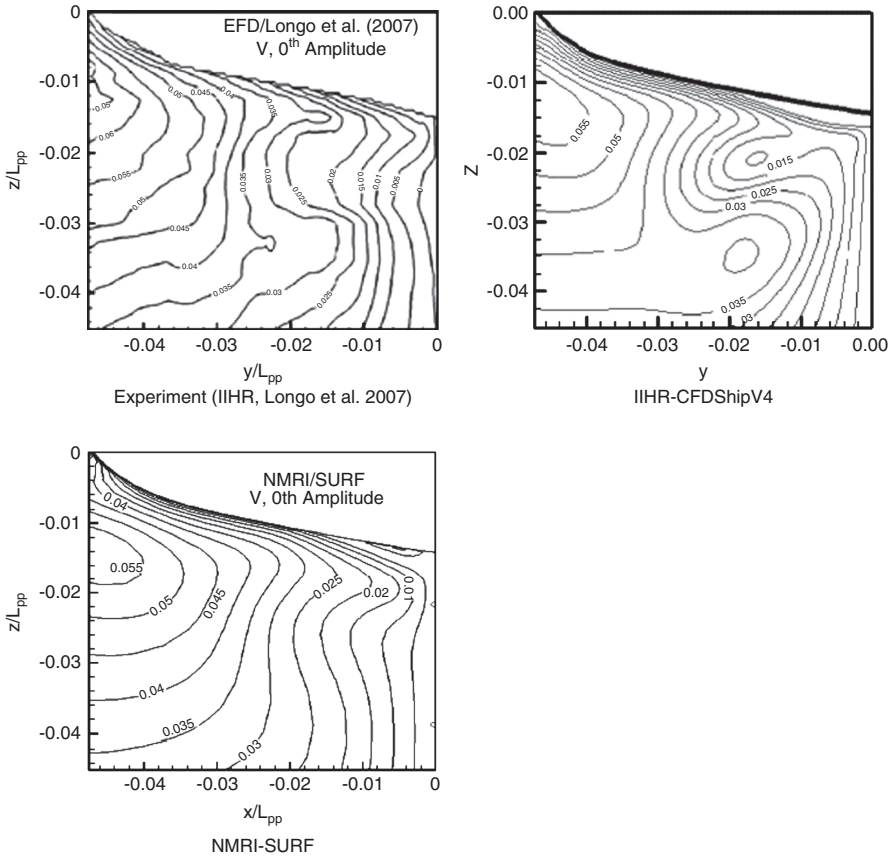


Fig. 3.58 V contours of 0th harmonic amplitude at x/Lpp = 0.935 ($\Delta V = 0.005$)

velocity, where latter shows over-prediction of the transport of low momentum fluid away from the bilge keel. This suggests that the vortex convection due to roll motion is predicted well, but the bilge keel vortex inception is not predicted accurately. Even finer grids near the bilge keel are required to capture the vortex inception accurately.

The V component is one order of magnitude smaller compared to U and comparisons are more challenging. The global agreement is good for all the contributions. Some details like the pronounced distortion of the contours in the center of this plane are not captured by any computation.

7.4 Comparison with Previous CFD

Wilson et al. (2006) performed URANS verification and validation studies using CFDShip-Iowa V3, which uses surface tracking method for free-surface modeling,

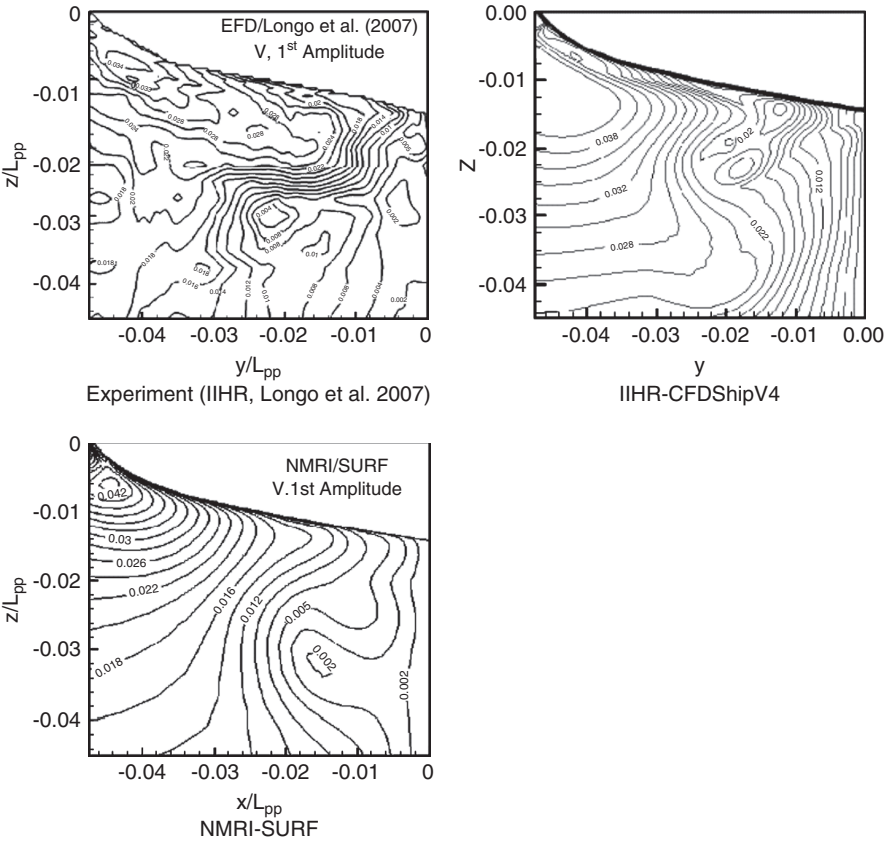


Fig. 3.59 V contours of 1st harmonic amplitude at x/Lpp = 0.935 (ΔV = 0.002)

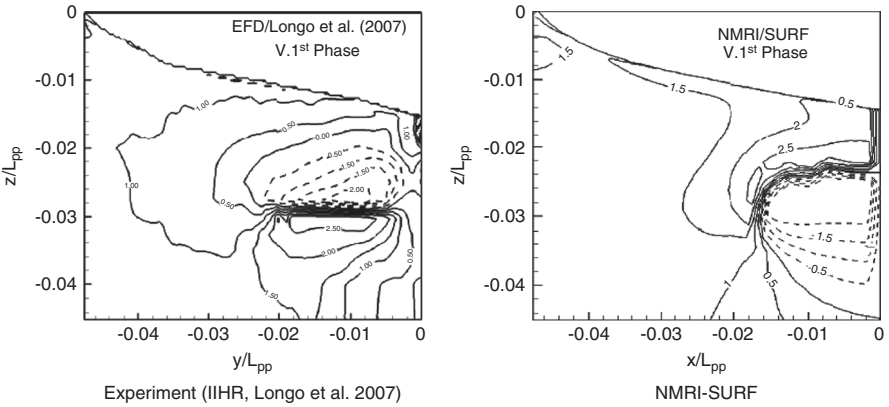


Fig. 3.60 V contours of 1st harmonic phase at x/Lpp = 0.935 (ΔGV = 0.5) Solid lines positive (+) values, Dashed lines negative (–) values

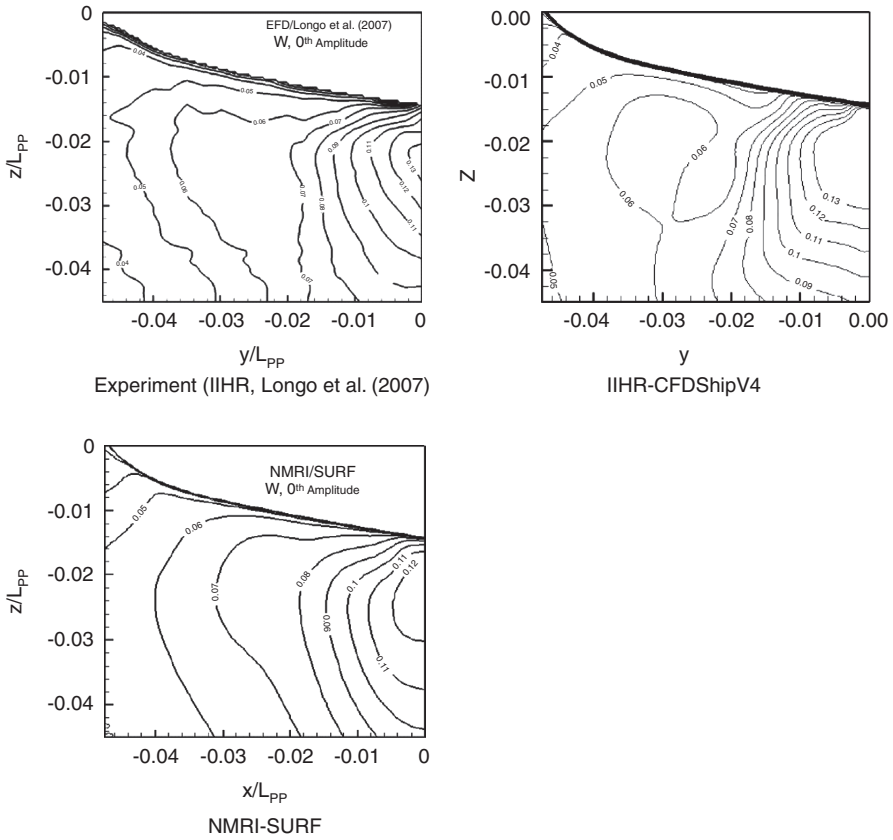


Fig. 3.61 W contours of 0th harmonic amplitude at x/Lpp = 0.935 ($\Delta W = 0.03$)

on 2.3M grid to understand the source of free oscillations and identify the vortical structures for this case. Time step and grid verification studies were performed for roll-decay using refinement ratio $r = 2^1/4$ following methodology and procedure proposed by Stern et al. (2001). The time step size varied from 0.00841 to 0.01189 and grid sizes from 0.86M to 2.3M. As summarized in Table 2 of Chap. 4, the uncertainties are UT, UG and USN are 0.63 %S1, 0.54 %S1 and 0.83 %S1, respectively. The roll motion was predicted well and validated at UV = 1.71 %D interval.

The results showed that the roll motion induces an oscillating angle of attack for the sonar dome producing a sinuous motion of the sonar dome vortices. The alternating angle of attack results in a serpentine motion of the sonar dome vortices leading to an unsteady asymmetric axial velocity contours. Two primary vortices are shed from the sonar dome on each side, one from the side of the sonar dome and other from the intersection of sonar dome and the keel. When the model rolls from starboard to port, the starboard side vortices strengthens and the port side vortices weaken, and vice versa. The vortices on each side split into two segments at the axial location

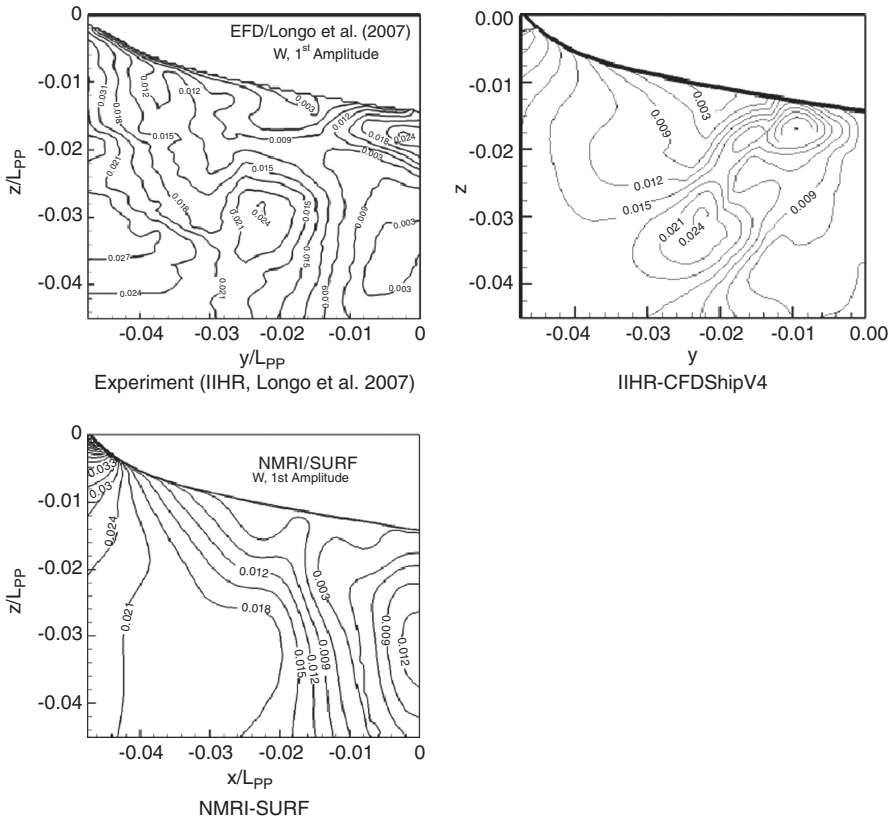


Fig. 3.62 W contours of 1st harmonic amplitude at x/Lpp = 0.935 ($\Delta W = 0.03$)

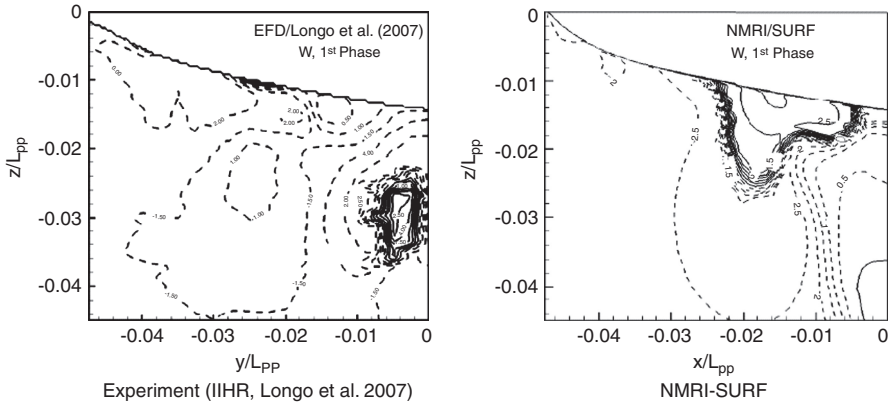


Fig. 3.63 W contours of 1st harmonic phase at x/Lpp = 0.935 ($\Delta GW = 0.5$). Solid lines positive (+) values, Dashed lines negative (–) values

Table 3.6 Main characteristics of the computations

Organization/Code name	Turbulence model	Wall model	Discretization characteristics
ECN-BEC-HO/ICARE	k-ω SST	Low-Re turbulence model + no slip	Structured grid, 650,000 points
ECN-CNRS/ISIS-CFD	k-ω SST, EASM	Wall function	Unstructured grid with automatic grid refinement, 4,886,000 points
SSRC/FLUENT12.1	RNG k-ε	Wall function	Unstructured grid, 3 million points

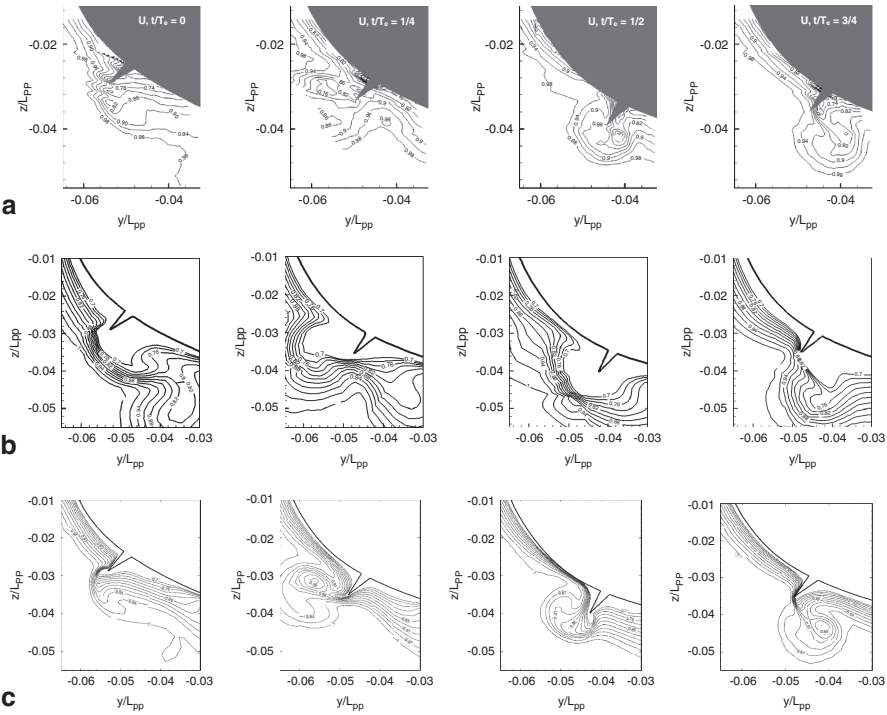


Fig. 3.64 Contours of U velocity at x/Lpp = 0.675 during second cycle of roll decay (ΔU = 0.03) for phases t/Te = 0, t/Te = 1/4, t/Te = 1/2 and t/Te = 3/4. **a** EFD, **b** ECN-BEC-HO/ICARE, **c** ECN-CNRS/ISIS-CFD

with maximum curvature. Further downstream the vortices are stretched and flatted normal to the hull. The bilge keel generates two additional sets of vortices from the tip. One set is generated with negative axial vorticity for the clockwise roll which is advected towards the starboard side, and another set with positive axial vorticity for the anti-clockwise roll which is advected towards the port side. The formation of bilge keel vortices with opposite circulation and advection of the vortices depending on the phase of the roll explains the EFD observations.

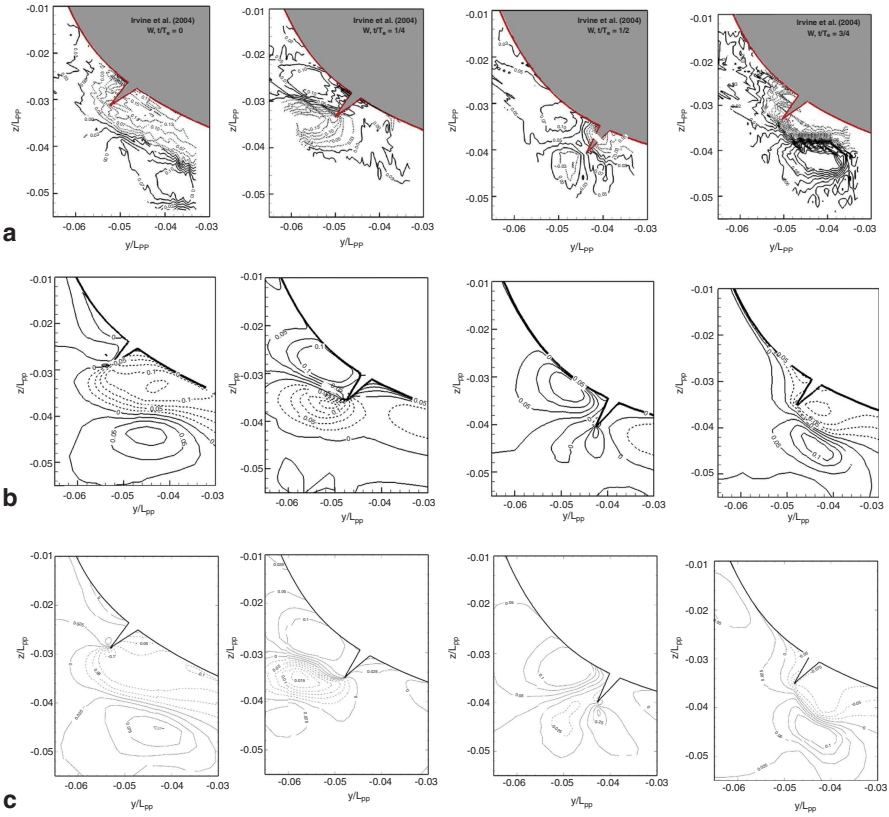


Fig. 3.65 Contours of V velocity at x/Lpp = 0.675 during second cycle of roll decay (ΔV = 0.025) for phases t/Te = 0, t/Te = 1/4, t/Te = 1/2 and t/Te = 3/4. **a** EFD, **b** ECN-BEC-HO/ICARE, **c** ECN-CNRS/ISIS-CFD

The overall agreement between the CFD and EFD predictions were good. However, the axial velocity contours showed over-prediction of the transport of low momentum fluid away from the bilge keel compared to EFD. It was concluded that the difference could be due to the difference in vortex strength, location or transport predictions, and are probably caused by insufficient grid resolution.

The roll-decay predictions reported in G2010 are comparable to IIHR/CFDShip-Iowa V3 predictions. ECN-CNRS/ISIS-CFD wave elevation predictions on 4.9M grid are similar to IIHR/CFDShip-Iowa V3 predictions, where both show dissipated Kelvin waves away from the hull. Similarly, ECN-BEC-HO/ICARE, ECN-CNRS/ISIS-CFD and IIHR/CFDShip-Iowa V3 compared well for the bilge keel boundary layer and cross flow predictions, and both showed deficiency in bilge keel vortex inception prediction.

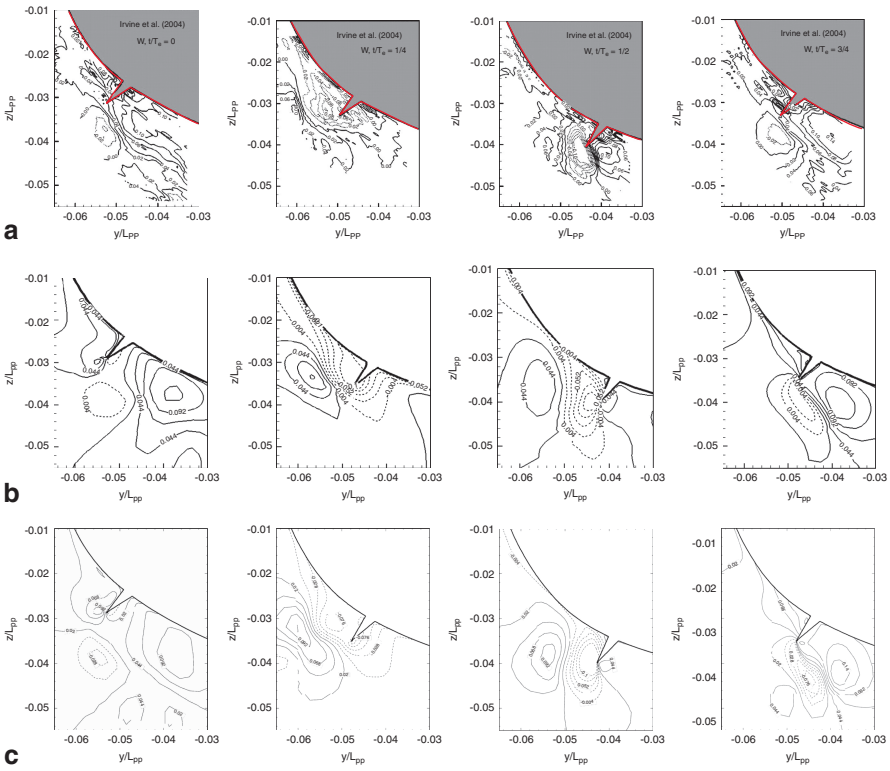


Fig. 3.66 Contours of W velocity at x/Lpp = 0.675 during second cycle of roll decay ($\Delta W = 0.024$) for phases t/Te = 0, t/Te = 1/4, t/Te = 1/2 and t/Te = 3/4. **a** EFD, **b** ECN-BEC-HO/ICARE, **c** ECN-CNRS/ISIS-CFD

7.5 Discussion

The unsteady velocities near the bilge keel are predicted within 6 %D of EFD. The results show good predictions for the vortex advection, but suggest slight deficiency at vortex inception.

One can notice that the anisotropic models do not show significant improvement over the isotropic model for the global variable predictions. This is because the vortex generation is imposed by the geometry of the bilge keels thus the turbulence models do not influence the flow predictions. On the other hand for KVLCC2 test case 1.1-a or 5415 test case 3.1 or 3.5 the vortices are advected, thus the anisotropic turbulence models show improved predictions.

8 Conclusion and Open Questions

In this Chapter, we have reviewed the computations provided by the contributors to the Gothenburg G2010 workshop from the point of view of the local flow analysis. This detailed analysis was conducted for the three ships concerned by the workshop, namely the KVLCC2 (case 1.1-a), the KCS (cases 2.1 and 2.3-a) and the DTMB5415 (cases 3.1, 3.5 and 3.6). We tried to assess the progress achieved in numerical ship hydrodynamics during the last five years separating the Gothenburg workshop from the Tokyo workshop held in 2005, to underline general trends and provide useful recommendations.

This exercise was dominated by the following recurrent fundamental question: if one wants to improve the reliability of our computations, what should be improved? Should we only build denser grids to capture details which are hidden by the numerical dissipation and/or should we replace a physical model by a more reliable one in terms of description of physics. At this point, it should be recalled that the distinction between numerical and modeling error is only valid for turbulence closures described by continuous partial differential equations. As soon as one deals with hybrid Large Eddy Simulation, such a classification is no more valid since the modeled turbulent structures depend on the size of the filter which is related with the size of the grid cell if no other specific measures are taken.

Compared to the results obtained in 2000 and 2005, the study of the flow around the KVLCC2 has shown that much progress has been made towards consistent and more reliable computations of after body flows for U shaped hulls. The intense bilge vortex and its related action on the velocity field is accurately reproduced by a majority of contributors employing very similar turbulence models implemented in different solvers and on various grids in terms of number of points or topology. The turbulence data confirm that the turbulence anisotropy is large in the propeller disk and more specifically in the core of the bilge vortex. For the first time, hybrid LES turbulence models have been introduced to compute model scale ship flows with a globally satisfactory performance on the mean flow-field. However, one has noticed that these models, in their current state of development, tend to predict ship wake composed of somewhat too intense longitudinal vortices. Explicit Algebraic Reynolds Stress Models reproduce satisfactorily the measured structure of the turbulence and appear to be the best answer in terms of robustness and computational cost for this specific flow field, compared to RSTM or DES based strategies, as long as one is interested in time-averaged quantities. However, difference persist in the total wake fraction distribution in the main vortical region indicating that progress in terms of turbulence models and/or control of the local discretization error are still necessary to improve the local quality of the flow field. It will be difficult to perform such a local flow assessment without the help of very reliable local flow measurements. Future studies should therefore be devoted to the enhancement of DES turbulence closures in order to improve the accuracy of the Reynolds stresses simulation. On the other hand, most of the grids are probably fine enough to capture the main longitudinal vortex when statistical turbulence closures are employed. However, there are some local structures

which cannot be captured without the use of a very fine grid or alternatively, locally refined grids. From that point of view, the results shown by IST-MARIN indicate that the grid convergence is not reached everywhere in the wake and it could be interesting to perform additional very fine grid studies to clarify also this issue and see if we can significantly improve the prediction of the total wake fraction at the propeller disk.

The study of the flow around the KCS gave us the opportunity to assess the best available methods to predict hull/propeller coupling in self propulsion conditions. Considering the complexity of this exercise, the results obtained by most of the participants are in good agreement with the experiments. This may be due to the use of very fine grids but the major factor explaining this observation is probably the accuracy of the propeller model. Surprisingly, computations based on RANSE everywhere do not appear significantly better than the best hybrid formulations based on simplified physics for the propeller. However, a simple body force formulation is not suited, which is not astonishing. In the same order of idea, the turbulence model does not seem to play a crucial role. It was also noticed that more care should be taken to the accurate description of the hull and particularly of the hub shape. Here again, hybrid LES computations have been presented for the first time in the framework of self-propelled model-scale flows. The performance of this unsteady turbulence modeling strategy is already very promising despite the fact that they do not outperform the best computations based on Reynolds-averaged statistical turbulence closures. These hybrid LES approaches are very expensive in terms of CPU time but they are the only ones able to provide reliable informations on unsteadiness, an output which is particularly useful in the framework of marine propulsion.

Compared to the results obtained during the last workshop held in 2005 in Tokyo, the level of agreement between computations and experiments for the flow around the DTMB5415 (case 3.1-a) has been much improved. This is probably due to a mix of several reasons involving modeling and discretization errors. Undoubtedly, the grids used in 2010 are finer, which reduce significantly the sources of discretization errors. It is also the first time that one can evaluate the time accurate LES or DES solution methods for these high Reynolds number flows. If one puts aside the penalties in terms of computational power needed (one to two orders of magnitude more in terms of grid size), LES and DES solution methods brought new answers to stimulate the discussion and clarify the complex topology of a flow for which experiments provided only very sparse informations.

Now, are we able to conclude that the use of DES or LES turbulence models is absolutely mandatory to get the right flow topology? Would it be possible to get a similar flow field on the sonar dome with statistical turbulence closures and grids locally fine enough? Once again, we have to reassess the respective role of discretization *vs.* modeling errors but this time for the computation of the flow at the bow of a ship, in a situation where the boundary layer is very thin. This is the reason why additional computations with statistical closures on very fine grids in the vicinity of the sonar dome will be presented in Chap. 7 with additional DES studies. These additional studies should help us to answer the following questions: (i) What is the plausible flow topology on the sonar dome? (ii) What is its downstream influence

on the development of the boundary layer along the hull? (iii) Is the flow at the sonar dome mainly influenced by modeling or discretization errors?

The cases 3.5 and 3.6 are devoted to unsteady flow configurations, either due to the diffraction in waves or to the roll decay. The test case 3.5 illustrates the far better behavior of the solution provided by IIHR/CFDShip-IowaV4. This clear superiority is probably due to the use of a very fine grid which is two orders of magnitude larger than the mesh used by the other participants. Although based on a theoretically more reliable turbulence model and a relatively fine grid, NMRI/SURF results are still polluted by too high a level of numerical diffusion. The innovative SWENSE defect correction employed by ECN/ICARE does not bring any improvement since their results are too much damped with a boundary layer thickness strongly over-estimated as it was already noticed in test case 3.1-a. Here again, the discretization errors are still very large, even if a modified viscous formulation is solved. SSRC/FLUENT12.1 results are in reasonable agreement with the experiments but the agreement is less good than what is demonstrated by IIHR. Although 100's M of grid points are not necessary to accurately predict such flows using URANS, more reliable turbulence models, such as anisotropic models, and a relatively finer grid than that used by the submissions would help reduce the numerical diffusion and dissipation, thereby improving numerical predictions. However, for advanced LES/DES models 100's M of grid points are required to achieve expected 80-90 % resolved turbulence levels. The same conclusions seem to hold for the test case 3.6 although the small number of participants preclude any general and consistent analysis on the reasons of disagreement between computations and experiments.

There are however some general conclusions which can be drawn from the local flow analysis described in this Chapter. The first one is the consistency of the simulations. When a reasonably fine grid is employed, similar turbulence models provide similar results, independently of the code used. This is a first very important observation which illustrates the state of maturity of modern CFD methodologies. The second conclusion concerns the promising unsteady turbulence closures like LES or hybrid LES (DES). It is crucial to recall that these models are supposed to be more physically consistent and reliable than the statistical turbulence closures. Therefore, it is mandatory to expect that these expensive and promising models provide first a better description of the turbulent structure, which will lead naturally to a better simulation of the mean flow field. It may be extremely misleading to evaluate the potential of LES or DES by assessing only the mean-flow quantities without checking the agreement on the turbulent Reynolds stresses.

Acknowledgements The author would like to thank Professor Lars Larsson, Professor Fred Stern and his team from the University of Iowa for their advices concerning this Chapter. Professor Shanti Bhushan (presently at Mississipi State University) should also be thanked for his personal contribution to the analysis of the test cases 3.5 and 3.6.

References

Bhushan S, Michael T, Yang J, Carrica P, Stern F (2010) Fixed sinkage and trim bare hull 5415 using CFDSHIP-IOWA. In: Gothenburg 2010: a workshop on CFD in ship hydrodynamics, Gothenburg, Sweden

Bingjie G, Steen S (2010) Added resistance of A VLCC in short waves. Proceedings of the 29th international conference on ocean, offshore and Arctic engineering, OMAE 2010

Deng G, Queutey P, Visonneau M (2005) Three-dimensional flow computation with Reynolds stress and algebraic stress models. In W Rodi, M Mulas (eds) Engineering turbulence modeling and experiments Vol 6, pp 389–398

Eça L, Vaz G, Hoekstra M (2010) Code verification, solution verification and validation in RANS solvers. Proceedings of ASME 29th international conference OMAE2010, Shanghai, China

Hino T (ed) (2005) Proceedings of CFD workshop Tokyo 2005. NMRI report 2005

Irvine M, Longo J, Stern F (2004) Towing tank tests for surface combatant for free roll decay and coupled pitch and heave motions. Proceedings 25th ONR symposium on naval hydrodynamics, St Johns, Canada

Kim WJ, Van DH, Kim DH (2001) Measurement of flows around modern commercial ship models. Exp Fluids 31:567–578

Lee S-J, Kim H-R, Kim W-J, Van S-H (2003) Wind tunnel tests on flow characteristics of the KRISO 3,600 TEU containership and 300 K VLCC double-deck ship models. J Ship Res 47(1):24–38

Longo J, Shao J, Irvine M, Stern F (2007) Phase-averaged PIV for the nominal wake of a surface ship in regular head waves. ASME J Fluids Eng 129:524–540

Olivieri A, Pistani F, Avanaini A, Stern F, Penna R (2001) Towing tank experiments of resistance, sinkage and trim, boundary layer, wake, and free surface flow around a naval combatant INSEAN 2340 model. Iowa Institute of Hydraulic Research, The University of Iowa, IIHR Report No. 421

Simonsen C, Otzen J, Stern F (2008) EFD and CFD for KCS heaving and pitching in regular head waves. Proceedings 27th Symposium Naval Hydrodynamics, Seoul, Korea

Van SH, Kim WJ, Yim DH, Kim GT, Lee CJ, Eom JY (1998a) Flow measurement around a 300 K VLCC model. Proceedings of the annual spring meeting, SNAK, Ulsan, pp 185–188

Van SH, Kim WJ, Yim GT, Kim DH, Lee CJ (1998b) Experimental investigation of the flow characteristics around practical hull forms. Proceedings 3rd Osaka colloquium on advanced CFD applications to ship flow and hull form design, Osaka, Japan

Xing T, Carrica P, Stern F (2010) Large-scale RANS and DDES computations of KVLCC2 at drift angle 0 degree. In: Gothenburg 2010: a workshop on CFD in ship hydrodynamics, Gothenburg, Sweden

Chapter 4
Evaluation of Seakeeping Predictions

Frederick Stern, Hamid Sadat-Hosseini, Maysam Mousaviraad and Shanti Bhushan

Abstract Test cases related to seakeeping are studied in this chapter including heave and pitch with or without surge motion in regular head waves for KVLCC2 and KCS and wave diffraction and roll-decay with forward speed for DTMB 5415. For seakeeping, the total average error is E = 23 %D, comparable to the average error for previous seakeeping predictions. For resistance, the largest error values are for the 1st harmonic amplitude and phase (34 %D), followed by 0th harmonic amplitude (18 %D) and steady (7 %D). For motions, the largest error values are for the 0th harmonic amplitudes (54 %D), followed by 1st harmonic amplitude and phase (13 %D) and steady (9 %D). The errors for the CFD predictions are similar for the different geometries and wavelengths, the small and large amplitude waves, and for the cases with and without surge motion. The errors are larger for the cases with zero forward speed. Compared with potential flow, CFD showed larger errors for motions for the medium and long wavelengths. For wave diffraction submissions, the large grid size DES simulation has achieved an average error value of less than 10 %D, while for the small grid size URANS simulations the average error is 28 %D. For roll decay submissions, the average error values are 10 %D for resistance and less than 1 %D for roll motions.

1 Introduction

Test cases for seakeeping are included in the G2010 CFD Workshop for ship hydrodynamics. Test cases 1.4a and b are regular head waves for KVLCC2 free to heave and pitch (FRzθ) measured at two different facilities. Test case 1.4c is regular head waves for KVLCC2 free to surge, heave, and pitch (FRxzθ). Test case 2.4 is regular head waves for KCS at free to heave and pitch (FRzθ). Test case 3.5 is forward speed diffraction for 5415 at fixed sinkage and trim (FXστ). Test case 3.6 is roll decay for 5415 at FXστ and free to roll only (FRϕ).

F. Stern (✉) · H. Sadat-Hosseini · M. Mousaviraad
University of Iowa and Iowa Institute of Hydraulic Research (IIHR),
Iowa City, IA, USA
e-mail: frstern@engineering.uiowa.edu

S. Bhushan
Mississippi State University, Starkville, MS, USA

L. Larsson et al. (eds.), *Numerical Ship Hydrodynamics,*
DOI 10.1007/978-94-007-7189-5_4, © Springer Science+Business Media Dordrecht 2014

These test cases have not been included in previous CFD Workshops, except test case 3.5, which was included at CFD Workshop Tokyo 2005 (Hino, 2005). CFD Workshop Tokyo 2005 included static drift, which was not included in the G2010 CFD Workshop since included in the SIMMAN 2008 (Stern et al. 2011) and forthcoming SIMMAN (2014) Workshops on Verification and Validation of Ship Maneuvering Simulation Methods.

Beck and Reed (2000) provided a review of computational methods for seakeeping of ships. Potential flow methods are widely used in seakeeping predictions. In potential flow, Laplace equation is solved along with the appropriate boundary conditions for the ship hull and free surface. Different potential flow methods are employed for seakeeping computations in which the nonlinearities in the hull and free surface boundary conditions are treated at different levels. These methods include linear potential flow, Froude-Krylov nonlinear method (weakly nonlinear method), body nonlinear method, body exact method (or weak scatter method), and fully nonlinear method. Unlike potential flow, only few simulations were available at that time using URANS methods in which the unsteady Navier-Stokes equations are solved. Significant progress has been made in the last ten years in URANS seakeeping computations as evident in the current G2010 workshop.

In linear potential flow, it is assumed that the oscillations of the boundaries (free surface and hull) are small and thus the boundary conditions are linearized and represented in terms of the mean free surface and wetted area. Since the governing equations and boundaries are linearized, the solution of the boundary value problem is assumed a linear superposition of several potential components including steady, wave, radiation, and diffraction potentials. The steady potential is found from the wave resistance problem. The wave potential is already known from the incident wave potential. The radiation and diffraction potentials are mainly obtained by either solving a two-dimensional (2D) boundary value problem based on strip theory or solving a three-dimensional (3D) boundary value problem based on panel methods. All the boundary value problems are solved in the equilibrium coordinate system (or hydrodynamic coordinates system) moving along the path of the ship at constant ship speed with xy plane parallel to the calm water surface (Fossen 2005; Fossen 2011). From each boundary value problem, the components of the hydrodynamic loads on the hull including steady, Froude-Krylov, radiation, and diffraction are computed using the linearized Bernoulli equation. The hydrostatic loads are also computed from the hydrostatic pressure integrated on the mean wetted area in the equilibrium coordinate system at no forward speed. To predict the ship motions, the loads on the hull are first transformed into the body fixed coordinate system and then applied to the linearized body fixed equations of motion in which the nonlinear Coriolis and centripetal terms are neglected (Fossen 2005; Fossen 2011). The computed radiation loads are usually represented in the form of linear functions of velocities and accelerations with wave frequency dependent coefficients called damping and added mass. The hydrostatic loads are also represented in the form of linear function of motions with constant restoring coefficients. Applying all the loads, the equations of motion are represented in the form of a system of linearly coupled equations, which can be solved in the frequency or time domain to predict

the motions. In the time domain, the added mass and damping terms are divided into an infinite frequency component that is constant and the convolution integral terms that account for the frequency dependence. In addition, the linear potential flow solvers require other techniques to take into account the higher order terms for the mean value computations such as the added resistance. These techniques are developed based on the pressure integration or mass conservation approaches.

The linear potential flow solvers do not give adequate results for many situations. To improve the linear potential flow, various potential flow approaches are developed in which the seakeeping boundary value problem is divided into several independent components similar to the linear potential flow. However, the nonlinearities are included to some extent for each component and the nonlinear Bernoulli equation and the fully nonlinear equations of motion are typically used in these methods. The approaches include Froude-Krylov nonlinear method (weakly nonlinear method), body nonlinear method and body exact method (or weak scatter method). In the Froude-Krylov nonlinear method, the nonlinear hydrostatic and the Froude-Krylov forces are found by integration of the pressure over the exact wetted surface under the actual wave profile. However, the radiation and diffraction boundary value problems are solved based on the mean wetted hull under the mean free surface, similar to the linear potential flow. This method is very popular since it can capture many important nonlinear effects without a significant computational cost. In the body-nonlinear method, the nonlinearities of hydrostatic and Froude-Krylov are treated as previous but the nonlinearities in radiation and diffraction are also included to some extent as the potentials are calculated for the wetted hull surface defined by the instantaneous position of the hull under the mean position of the free surface. This requires re-gridding and recalculation of the potential at every time step and thus the computational cost increases dramatically. The body exact approach is similar to the body-nonlinear method but the wetted area is defined by the instantaneous position of the hull under the actual wave profile. This method is also called "weak scatter method" as the disturbed waves generated by ships are disregarded when the radiation-diffraction value problem is set up.

In fully nonlinear potential flow methods, all the nonlinearities in the hull and free surface boundary conditions are considered and thus the fully nonlinear boundary value problem is solved to predict the velocity potential. Applying the nonlinear Bernoulli equation, the forces/moments on the ship are computed and transferred into the body fixed coordinate system to solve the equations of motion. The fully nonlinear potential flow can improve the seakeeping prediction for ships in large wave amplitude and steep waves. However, there can be difficulties associated with the stability of the free surface and wave breaking at the bow. Also, the viscous forces are not part of the solution and they must be obtained by other methods such as empirical formula when they are important.

To consider viscosity and complex free surface shape and wave breaking, URANS methods are developed which are similar to the fully nonlinear potential flow methods as both solve the fully nonlinear boundary value problem. For URANS methods, the unsteady Navier-Stokes equations for the flow with constant properties (viscosity and density) are solved in the inertial or relatively inertial coordinate systems. In addition,

the mass conservation is enforced through Poisson equation to solve the pressure. The solution of Poisson equation is achieved by the fractional step methods (predictor-corrector methods) or methods based on the SIMPLE algorithms (SIMPLEC, PISO, SIMPLER). The turbulence is often modeled (not resolved) as enormous number of grid points are required to resolve the turbulence and capture all the physics of the flow. The free surface is included in the computations using surface capturing or surface tracking methods. With appropriate initial and boundary conditions, the equations are solved and the velocity distribution, shear stresses and pressure are found in the computational domain. The total loads (hydrostatic and hydrodynamic) on the ship are computed from the shear stresses and pressure integrated on the exact wetted area and transferred into the ship fixed coordinate system. Applying the total loads to the right hand side of the equations of motion and retaining the nonlinearities such as Coriolis and centripetal terms, the ship motions are predicted by solving a system of coupled nonlinear equations.

Singh and Sen (2007) compared the predictions of potential flow with different levels of nonlinearities for seakeeping in regular and irregular head waves. The computations were conducted for two different geometries (Wigley hull and S175) at different wavelengths and ship speeds. The predictions were compared for linear computation, Froude-Krylov nonlinear computation (weakly nonlinear), body-nonlinear and body-exact nonlinear computations. The computations showed that the results could be considerably different depending on the level of the nonlinearities. The differences among the results can be as much as 30–40 %. The results showed that the improvement of the linear solution is not necessarily consistent with the level of nonlinearities included in the computation. It is shown that Froude-Krylov nonlinear computation is an efficient approach but may be inadequate for long waves. Also, the body-nonlinear and body-exact nonlinear computations influences the relative velocity more strongly than they do the relative displacement. In addition, the results showed that the effects of the nonlinearities depend on the geometry, speed and wavelength. The nonlinearities appear more pronounced for the S175 hull with flair compared to the Wigley hull with wall-sided upper body. Also, the nonlinearities are larger for higher speed and longer wavelength computations.

Bunnik et al. (2010) evaluated the predictions of the linear potential flow and CFD for seakeeping of a ferry and a containership in regular head waves, presumably with small wave amplitude. The linear potential flow computations were conducted using eight solvers from different institutes. The solvers used different techniques in a few aspects such as including and excluding the free surface (double body), treatments for the forward speed effects and linearized free surface boundary conditions with respect to either the calm water surface or steady wave field. The CFD computations were conducted by ISIS, COMET and the CFD code developed at Kyushu University, which all participated in G2010. The results showed that there are considerable differences between the potential flow predictions. It was shown that the differences between potential flow predictions are due to the differences in nearly all the hydrodynamic coefficients (restoring forces, the added mass and damping and the diffraction force). For heave motion, the best agreement with EFD data was achieved with average error $E = 2\,\%D$ for large wavelength ($\lambda/L \geq 1.4$), $E = 4\,\%D$ for mid-range

wave length ($0.8 < \lambda/L < 1.4$) and E = 18 %D for short wavelength ($\lambda/L \leq 0.8$). For pitch, the errors were similar to those for heave for mid-range and long wavelengths but better predictions were achieved at short wavelength (E = 14 %D). The added resistance was mostly under predicted with average error of 20 %D for mid-range and long wavelengths and 50 %D for short wavelengths. The CFD computations also showed some differences in the results due to the difference in the discretization schemes and numerical methods. For heave motion, CFD showed similar errors as potential flow but pitch motion was predicted better by CFD simulations for short wavelengths with E = 7 %D. The added resistance was also predicted better by CFD for mid-range and long wavelengths with E = 13 %D.

Belknap et al. (2010) evaluated the predictions for a nonlinear potential flow solver based on the body exact method with linearized free surface boundary conditions. The body exact method was employed by either using pre-computed frequency-domain hydrodynamic coefficients over the range of sectional drafts or solving the 2D body-nonlinear time-domain boundary value problem. Three different cases in calm water were considered; forced heave motion for a 2D cylinder; forced heave motion for a 2D ship section; and forced heave motion for a 3D hull form. The results for the first two cases were compared with CFD computations conducted by OpenFOAM or Fluent and the results for the third problem were compared with linear, nonlinear Froude-Krylov and fully nonlinear solutions of LAMP, a 3D panel method potential flow solver. Based on the results for the 2D cylinder, the potential flow could predict the nonlinearities for most of the conditions but showed differences with CFD for the computations at high frequency and large amplitude forced heave as the free surface nonlinearities were ignored in the potential flow. For the 2D ship section, the heave force for the two body exact potential flow approaches match of the CFD solution and the experiments very well for all forced heave frequency and amplitude conditions. In addition, it was shown that the hydrostatic heave force changes linearly with changing heave amplitude while the hydrodynamic heave force exhibits a noticeable degree of nonlinearity. For the 3D hull form, the computations for both potential flow methods were conducted at both zero speed and forward speed for only one heave frequency and amplitude. The fully nonlinear LAMP solver showed differences with the results from the linear and nonlinear Froude-Krylov solvers. The comparison with LAMP results showed that both the body exact methods could predict the nonlinearities in the surge, heave, and pitch loads for zero speed but not with forward speed, suggesting that the forward speed corrections could be critical.

Sadat-Hosseini et al. (2013) and Simonsen et al. (2012) also evaluated the potential flow approaches for the G2010 cases. Sadat-Hosseini et al. (2013) conducted the linear potential flow computations for case 1.4c but at more wavelength conditions and speeds and compared the predictions with URANS results. The potential flow solver was based on the enhanced unified theory, which is the same as strip theory at the high wave frequency but includes the 3D and forward speed effects and approaches to the slender-body theory at the low wave frequency to take into account the scattering wave generated near the ship bow (Kashiwagi 2009). The mean wave loads (added resistance) were computed based on the mass conservation approach (Maruo Method). It was shown that the linear potential flow predicts the overall trend of RAOs of surge amplitudes in head waves with the average error of 27 %D.

The average error for the heave and pitch RAO was 10 and 53 %D, respectively. The average error for both heave and pitch reduces to 3.7 %D by excluding the large errors for small motions at short wavelength ($\lambda/L \leq 0.8$). It should be noted that H/λ values were also large for short wavelengths. The errors for the phases were around 12 % for surge and pitch and about 5 % for heave. For added resistance, the linear potential flow showed large errors for all wavelengths with 24 %D on average. Overall, the average error for the motions and added resistance for the linear potential flow over a wide range of wavelengths was about 20 %D compared to 8 %D for the URANS predictions. The components of the wave forces/moments (radiation, diffraction, Froude-Krylov) are predicted with URANS and showed that the linear superposition of the 1st harmonic of the components can estimate the 1st harmonic of the total forces/moments with E = 4.5 %D. Unlike the linear potential flow, the URANS simulations could predict the higher order harmonics for the forces/moments components and it was shown that the linear superposition of higher order components could not estimate the higher order harmonics of the total forces/moments. Sadat-Hosseini et al. (2013) also investigated the condition for maximum responses. They showed that the peak for surge/pitch occurs at a wavelength near both $\lambda/L = 1.33$ and resonance conditions i.e. same encounter wave frequency and heave and pitch natural frequencies. For heave, the peak occurs in long waves and near the wavelength corresponding to the resonance condition for a given speed and variable wavelength. Simonsen et al. (2012) evaluated the linear potential flow computation for case 2.4 using AEGIR, which is a 3D potential flow solver developed by Joncquez (2009), and compared the results with EFD and URANS predictions. The added resistance is also computed using the momentum conservation approach. They showed that the potential flow computations overestimate both heave and pitch motions near the resonance condition. Also, the added resistance was over predicted at low speed and under predicted at high speeds. Unlike the potential flow, the URANS code could predict fairly well the motions and added resistance for all wavelengths and speeds. URANS predicts the heave and pitch amplitudes within ranges of 4.7–14.2 % and 1.2–23.2 %D, respectively. The added resistance is also predicted within a range of 4.4–50.9 % of the EFD data.

Assessment of CFD predictions for seakeeping should separate capability for 1st order vs. higher order terms similarly as done previously for calm water maneuvering (Stern et al. 2011). The considerations are given to the steady resistance, sinkage and trim in the calm water resistance test (X_*,σ,τ), the 0th harmonics (X_0, x_0, z_0, θ_0) and 1st harmonic amplitudes (X_1, x_1, z_1, θ_1) of the resistance (X), surge (x), heave (z), and pitch (θ) in waves, and the streaming parameters ($X_s = X_0 - X_*$, $z_s = z_0 - \sigma$,$\theta_s = \theta_0 - \tau$).

For the resistance problem in calm water, the steady resistance X_* is considered 1st order while sinkage and trim are 2nd order (Tarafder 2007; Tarafder and Khalil 2006) i.e. the contribution of sinkage and trim to the free surface elevation is 2nd order. For wave cases, X_0 and x_0 are considered 1st order and z_0/θ_0 are 2nd order using the same reasoning as in calm water. According to linear potential flow, X_1, x_1, z_1 and θ_1 are proportional to wave amplitude A and they are considered 1st order. However, RANS seakeeping studies in Sadat-Hosseini et al. (2013) and He et al. (2012) showed that X might have large higher order harmonics. Thus, the results are analyzed with both

including and separating X from 1st order terms. In addition, problems are reported for EFD measurement for X amplitude for case 1.4b and case 2.4 conducted in Force and NTNU, which supports studying the X amplitude separated from other 1st order terms. The problems in EFD measurement were associated with the fact that the EFD model was not fixed to the carriage in an ideal stiff setup and inertial force was included in the X amplitude measurement (Simonsen et al. 2012). For the streaming parameters, they are considered second order and are proportional to A^2 (Faltinsen 1990).

2 Post Processing Procedure for EFD and CFD Seakeeping Test Cases

2.1 Seakeeping Test Cases

The time history of the forces and motions are transferred into the frequency domain to obtain the amplitudes and phases. As a time reference, the incident wave height in the carriage coordinate system at a longitudinal position corresponding to the CG of the ship with fixed surge (or corresponding to the mean of longitudinal location of CG of the ship with free surge) is defined as:

$$\zeta(t) = A\cos(2\pi f_e t + \gamma_I) \tag{4.1}$$

where γ_I is the initial phase and is equal to zero at $t = 0$, A is incident wave amplitude, $f_e = f_w + U/\lambda$ is encounter frequency in Hz ($f_e = \omega_e/2\pi$ where ω_e is the encounter frequency in rad/s), $f_w = \sqrt{g/2\pi\lambda}$ is frequency of the incident wave in Hz ($f_w = \omega_w/2\pi$ where ω_w is the wave frequency in rad/s), U is carriage speed, and λ is the incident wavelength.

The mean, phase, and amplitude of the time history of the parameter $P(X, x, z, \theta, \xi)$ are determined by using a Fourier series as follows:

$$\begin{aligned}
P(t) &= \frac{P_0}{2} + \sum_{n=1}^{N} P_n \cos(2\pi f_e t + \Delta\gamma_n) \\
\Delta\gamma_n &= \gamma_n - \lambda_I \\
a_n &= \frac{2}{T}\int_0^T P(t)\cos(2\pi f_e t)\,dt \\
b_n &= \frac{2}{T}\int_0^T P(t)\sin(2\pi f_e t)\,dt \\
P_n &= \sqrt{a_n^2 + b_n^2} \\
\gamma_n &= \tan^{-1}\left(-\frac{b_n}{a_n}\right)
\end{aligned} \tag{4.2}$$

P_n is n-th harmonic amplitude and γ_n is the corresponding phase.

To plot the RAO, amplitudes of heave and surge are normalized by A, pitch is normalized by Ak, and added resistance ($X_s = X_0 - X_*$) is normalized by $\rho g A^2 B^2 / L$, where B is the ship breadth. For calm water cases, X_* is also normalized by $1/2\rho A_w U^2$ to compute the total resistance coefficient C_T.

The comparison error E (hereafter simply called the error) for global variables, i.e., forces, moment and motions, is defined as:

$$E\%D = 100 \times (D - S)/D \tag{4.3}$$

where, D is the EFD data and S is the CFD solution.

The average comparison error (hereafter simply called the average error) of N global variables is defined as:

$$Ave\ (E\%D) = \frac{1}{N} \sum_{i=1}^{N} 100 \times |D_i - S_i| / D_i \tag{4.4}$$

2.2 Forward Speed Diffraction Test Case

The post processing for EFD and CFD forces, moments and wave-elevation are similar to that described above. Also, the forward speed diffraction test case included the velocity measurements at the nominal wake plane which are discussed in Chap. 3.

2.3 Roll-Decay Test Case

The errors for the force C_T are obtained as discussed above. The errors for the roll angle are computed from the time history as below:

$$E_{RSS} = \frac{1}{N} \sqrt{\sum_{i=1}^{N} \left(\frac{D(t_i) - S(t_i)}{D(t_0)} \right)^2} \times 100 \tag{4.5}$$

where N is the total number of experimental data points at different time t_i instances and $D(t_0)$ is the initial roll angle of 10°.

3 Case 1.4a, b, c Seakeeping for KVLCC2 in Regular Head Waves

3.1 EFD Data

Model tests were conducted for KVLCC2, which is a modern commercial tanker ship with bulbous bow and stern bulb. The model has no appendages, rudders, and

Table 4.1 Summary of all EFD conditions for KVLCC2 seakeeping experiments

	INSEAN				NTNU				OU	
Case #	1.4a				1.4b				1.4c	
Model length	3.2 m				5.5172 m				3.2 m	
Appendages	No rudder				No rudder				No rudder	
DOF	2 (z,θ)				2 (z,θ)				3 (x,z,θ)	
λ/L	1.1	1.6	0.6364	0.6364	0.6364	0.9171	0.9171	0.6	1.1	1.6*
H/λ	1/59	1/85	1/118	1/23	1/23	1/34	1/34	1/32	1/59	1/85
Fr	0.142	0.142	0.142	0.142	0.182	0.0	0.142	0.142	0.142	0.142

*OU also has data at λ/L = 0.7, 0.9, 1, 1.2, 1.4, 1.8, 2 (H/λ = 1/37–1/106)

propellers. The test cases 1.4a and b are carried out for free to have and pitch condition (FRzθ) and test case 1.4c is performed for free to surge, heave, and pitch condition (FRxzθ). The FRxzθ tests are achieved by using a spring to attach the model to the towing carriage. The FRxzθ tests were conducted in the Osaka University (OU) towing tank for a 1/100 scaled model (L = 3.2 m). The FRzθ tests were conducted with the same model size in the Italian Maritime Research Center (INSEAN) 220 × 9 × 3.5 m towing tank and for a larger model (L = 5.5172 m) in the Norwegian University of Science and Technology (NTNU) 175 × 10.5 × 5.6 m towing tank. The tests for OU and INSEAN were conducted in calm water and regular head waves with (λ/L, H/λ) = (0.6,1/32), (1.1,1/59) and (1.6,1/85) for a model advancing at forward speed Fr = 0.142. The tests for NTNU were performed in calm water and regular head waves with (λ/L, H/λ) = (0.6364,1/118), (0.6364,1/23), and (0.9171,1/34) for a model advancing at forward speed Fr = 0.0, 0.142, 0.182. Note that the waves are quite steep for OU test condition at λ/L = 0.6 and most of NTNU test conditions. All EFD cases are summarized in Table 4.1.

3.1.1 Calm Water

Table 4.2 summarizes all available EFD data at Fr = 0.142 for C_T, σ and τ for calm water condition including data from MOERI for a model with L = 5.5172 m (Kim et al. 2001) and another data from INSEAN for a model with L = 7.0 m (Fabbri et al. 2011). The Reynolds numbers for OU, NTNU and INSEAN with smaller model size are reported from G2010 website, which imply the towing tank water temperature of T = 20 °C. The Reynolds number for INSEAN with larger model size is also computed assuming T = 20 °C. For MOERI, the Reynolds number is reported from Kim et al. (2001) which implies T = 10.2 °C. It should be noted that the MOERI calm water resistance data is used in Chap. 2 and 6. Also, Chap. 6 shows another set of OU data for calm water resistance test (OU_R) measured at T = 10.2 °C and different experimental setup, including data at Re = 1.9 × 10^6 and Fr = 0.142. The mount used for OU_R is usual resistance test apparatus with very strong spring. For the measurement of OU data in this Chapter, the added resistance mount is used which includes very weak spring with a light carriage on the rail. The difference in

Table 4.2 Comparison of KVLCC2 EFD data for resistance and motions in calm water at Fr = 0.142

	Surge motion	Model length (m)	Re × 10^6	Fr	Rudder	$10^3 \times C_T$		$1+k$		$10^3 \times (C_T - (1+k)C_F)$		$10^2 \times \sigma/L$ (−)		τ (deg)	
						D	Biases	D	Biases	D	Biases	D	Biases	D	Biases
OU	Free	3.2	2.546	0.142	No	5.093	10.374	1.180	1.027	0.534	9.949	− 0.099	5.930	− 0.129	0.310
INSEAN	Fixed	3.2	2.546		No	5.141	11.415	1.160	0.685	0.659	11.130	− 0.081	13.660	− 0.142	10.420
NTNU	Fixed	5.517	5.4		No	4.568	1.014	1.170[a]	0.171	0.650	9.612	− 0.116	24.170	− 0.130	1.090
MOERI (Kim et al. 2001)	Fixed	5.517	4.6		W/	4.110	10.929	1.160	0.685	0.108	81.788	− 0.079	15.500	− 0.132	2.640
INSEAN (Fabbri et al. 2011)	Fixed	7	8.240		No	4.160	9.845	1.170[a]	0.171	0.529	10.793	− 0.093	0.940	− 0.110	14.460
Average						4.614	8.714	1.168	0.548	0.593[b]	10.371[b]	− 0.094	12.040	− 0.129	5.784
Min.-max. facility biases							11.172		0.856		10.961[b]		19.836		12.442

[a] form factor is average of k from other facilities
[b] Excluded MOERI

the Reynolds number and the experimental setup causes 3 % lower total resistance at Fr = 0.142 for OU_R data compared to OU data reported in this Chapter.

The facility biases for the total resistance, form factor and residuary resistance for the data from different facilities are reported in Table 4.2. The residuary resistance is computed from the total resistance, form factor and the frictional resistance [Cr = $C_T - (1 + k)C_F$]. The frictional resistance component (C_F) is calculated based on ITTC 1957 friction line and the estimated form factors (k) by Prohaska method are used, which are reported in Chap. 6 and Larsson et al. (2010). For NTNU and INSEAN with larger model size, the form factor is estimated from the average k since they were not available. In Prohaska method, data sets of C_T/C_F versus Fr^4/C_F prepared from a series of low-speed resistance tests are fitted to the first order polynomial equation in form of a Fr^4/C_F+b, in which b is 1 + k.

The facility biases uncertainty for each facility (U_{FB}) and the facility biases uncertainty based on the dynamic range ($U_{FB_{DR}}$) for forces and motions are estimated from Eq. (4.6) as discussed in Stern et al. (2005):

$$\begin{cases} \bar{X} = \dfrac{1}{M}\sum_{i=1}^{M} X_i \\ U_{FB} = 100 \times \left|X_i - \bar{X}\right| \Big/ \bar{X} \\ U_{FB_{DR}} = \dfrac{1}{2}\left[\text{Max}\left(|X_i|\right) - \text{Min}\left(|X_i|\right)\right] / \bar{X}, \quad i = 1 \ldots M \end{cases} \tag{4.6}$$

where X_i is the data in ith facility and M is the number of facilities

For the total resistance, all facilities have larger resistance than MOERI data and show large facility biases ($U_{FB_{DR}} = 12$ %). The OU total resistance is larger than MOERI data partially due to the experimental setup and partly due to its lower Reynolds number (larger frictional resistance). Therefore, the total resistance for OU_R and MOERI would be similar by converting the OU_R Reynolds number to MOERI values based on Chap. 6 analysis. For INSEAN with smaller model size, the total resistance is similar to the OU data and thus it presumably agrees better with MOERI data by converting the data to MOERI test conditions. For INSEAN with larger model size and NTNU, the total resistance is surprisingly larger than MOERI data even though both have higher Reynolds number. Higher Reynolds number reduces the frictional resistance and consequently it should reduce the total resistance. Therefore, the large resistance for INSEAN with larger model size and NTNU is probably due to the experimental setup and should be investigated in future. The form factors are quite similar for different facilities with ($U_{FB_{DR}} = 0.86$ %). The values for residual resistance for most of the facilities are about 0.6×10^{-3} except for MOERI model with residual resistance of 0.1×10^{-3}. The large residual resistance is due to the larger total resistance because of the experimental setup. Therefore, the residual resistance for OU_R is similar to MOERI residual resistance, as shown in Chap. 6. The facility bias $U_{FB_{DR}}$ for the residual resistance excluding MOERI is about 11 %. It should be noted that MOERI model is appended with the rudder. Excluding the resistance of the rudder from the total resistance, the residual resistance for MOERI model would be about 0.08×10^{-3} (rudder resistance is about 0.76 %

of C_T according to Toxopeus et al. 2011). For motions, the surge is only available from OU and the facility biases cannot be studied. The sinkage is about 0.1 % of the ship length for OU model while it is smaller for INSEAN and MOERI models and larger for NTNU model. The trim is about $-0.13°$ for all of the facilities except for INSEAN. The facility biases $U_{FB_{DR}}$ for sinkage and trim are about 20 and 12 %, respectively. Overall, the average of facility biases of the resistance and motions is about 11.63 %D with the largest facility biases for sinkage. The overall uncertainty in the data should be calculated from RSS of the uncertainty (U_D) and facility biases of the data measured at same towing tank temperature among different facilities as discussed in Stern et al. (2005). Since uncertainty of the data (U_D) is not available and the temperatures of the towing tanks are not reported for all facilities, the overall uncertainty cannot be estimated for the calm water test case of KVLCC2. Thus, the available overall uncertainty for the calm water tests of DTMB 5512 is used for the validation purposes, as shown in Table 4.13.

3.1.2 Regular Head Waves

All EFD data for motions and added resistance are summarized in Figs. 4.1, 4.2, 4.3 and 4.4. There are some differences for the data provided from different facilities. INSEAN shows good agreement with OU data for 1st harmonic heave amplitude but indicates 37 % larger pitch value for $\lambda/L = 1.6$. There was no phase reference recorded for INSEAN EFD data and thus the INSEAN phases are not available for comparison with OU data. The INSEAN added resistance is 50 % larger than OU data at $\lambda/L = 1.6$. In addition, the time history of INSEAN resistance shows a nearly linear response at $\lambda/L = 1.1$ while OU time history shows nonlinearity. The NTNU amplitudes of motions at $Fr = 0.142$ show close agreement with OU and INSEAN while the phases are quite different. The NTNU added resistance at $Fr = 0.142$ is also different from OU data at very short wavelength ($\lambda/L = 0.6364$). Since NTNU surge motion is partially constrained by a spring system, the measured resistance amplitude might not be accurate as explained by NTNU and is not used for comparison (personal communication).

The motions and added resistance show expected trends for OU data. The OU heave amplitude is fairly small for short waves and reaches to about wave amplitude A for long waves with a small peak at $\lambda/L = 1.4$ corresponding to encounter frequency $f_e = 0.768$, near to heave natural frequency $f_n = 0.809$ Hz. The OU heave phase shows that there is no phase lag between heave response and wave for large wavelength suggesting that heave is synchronized with the incident wave. The OU pitch amplitude increases to about 1.0 at the long waves with a small peak near the pitch resonance condition. The ship reaches to an asymptotic behavior for long waves, where the pitch response leads 90° the incoming waves and is in phase with the wave slope. For both heave and pitch motions, the peaks are under resolved by the data such that additional wavelength conditions are required to capture the trend of the motions near the peak. The surge amplitude and phase are shown in Fig. 4.3. The maximum surge response is for the longest wave in which the surge amplitude

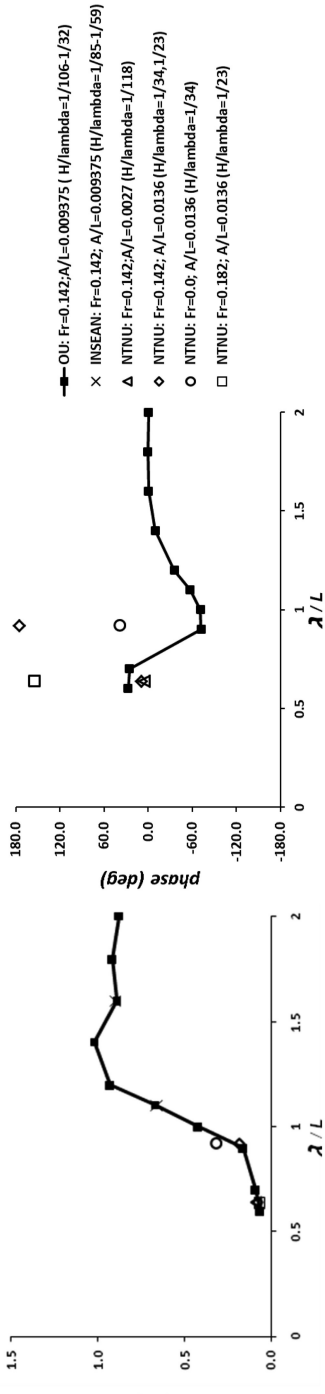


Fig. 4.1 Comparison of different EFD data for heave amplitude and phase for case 1.4a–c

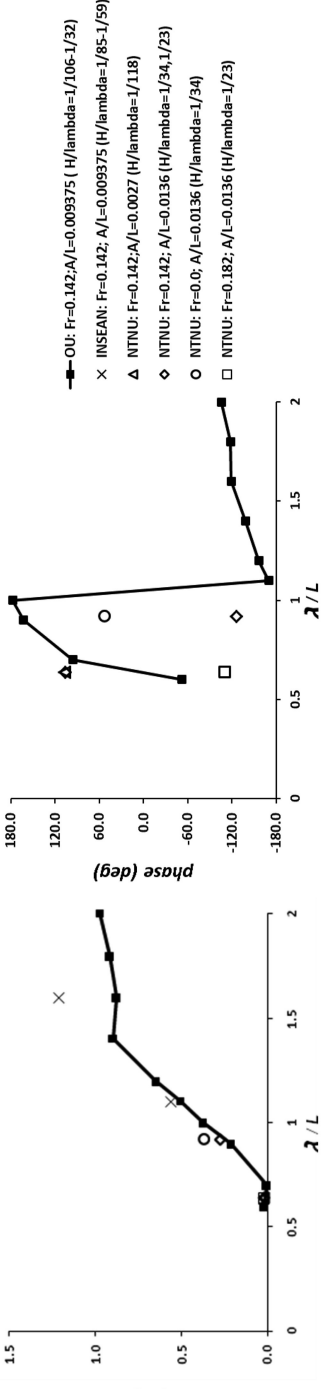


Fig. 4.2 Comparison of different EFD data for pitch amplitude and phase for case 1.4a–c

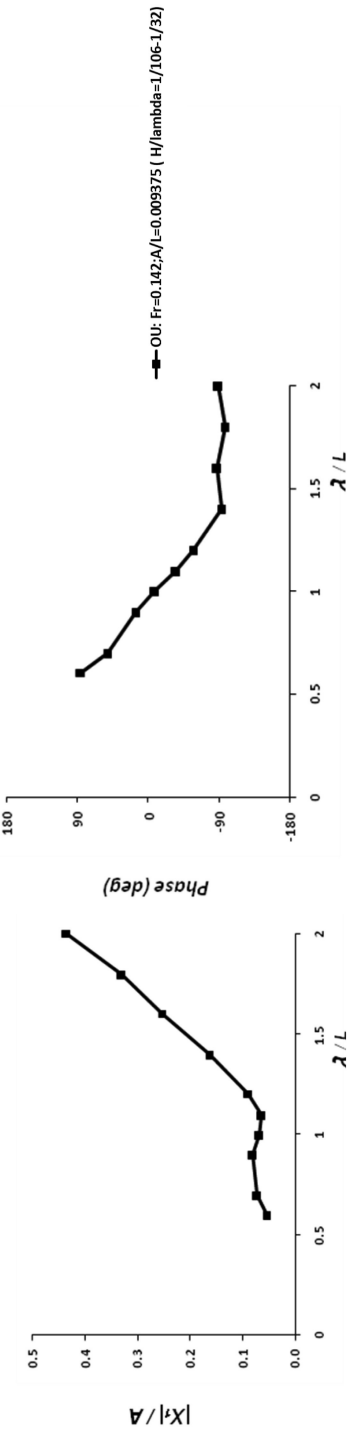


Fig. 4.3 OU data for surge amplitude and phase for case 1.4a–c

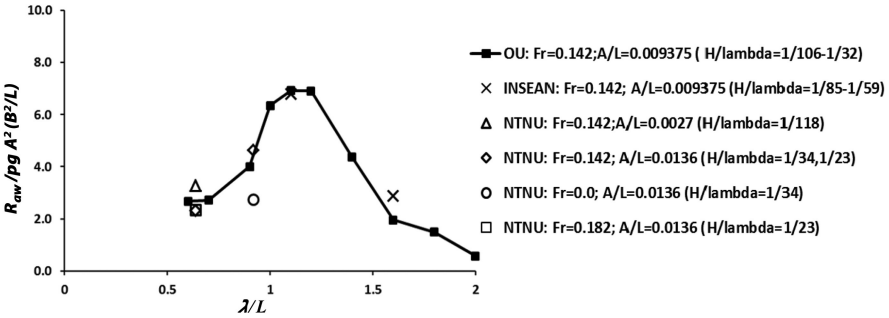


Fig. 4.4 Comparison of different EFD data for added resistance for case 1.4a-c

is about 50 % of the wave amplitude. The surge amplitude is largest when the ship is located on the wave downslope in long waves as shown by surge phase. The OU added resistance is maximum around $\lambda/L = 1.1$, as shown in Fig. 4.4. The INSEAN and NTNU data shows same trend as OU data for both motions and added resistance, suggesting that the effect of surge is neglegible on heave and pitch motions and added resistance. Although the motions for short wavelengths show agreement between different facilities, the values are very small and comparable with the sinkage and trim values at low Fr (see Chap. 2) such that the uncertainty of the data might be an issue for motions for short wavelengths. The NTNU data shows the effect of ship speed and wave slope on the data. It is shown that the ship speed effect is significant as it changes the encounter frequency. However, changing wave slope (wave amplitude) does not show noticeable impact on the results.

3.2 CFD Submissions

The submissions for the CFD simulation of KVLCC2 included 12 submissions from 5 institutions from 4 countries. Two institutions are from France (4 submissions), one institution from Germany (5 submissions), one institution from Japan (1 submission), and one institution from USA (2 submissions). Five different commercial/in-house URANS solvers and one DNS solver were used. Turbulence was modeled using 2-equation Reynolds-stress transport models. Free surface was mostly modeled by a surface capturing method (e.g. level-set, volume of fluid), and only two institutions utilized the surface tracking method. For numerical methods, spatial discretization was done by finite difference (2 solvers) or finite volume methods (4 solvers) with structured/unstructured grids with the number of grid points of 0.3–4.73M. The order of accuracy in time integration was mostly 2nd order or higher. The velocity/pressure coupling was achieved using different approaches including SIMPLE, PISO and Projection. All CFD submissions are summarized in Table 4.3.

Table 4.3 Summary of all CFD submissions for KVLCC2 seakeeping

Country	France	USA	France	Germany	Japan
Code	ECN/HOE (ICARE)	IIHR (CFDShip-Iowa V.4)	ECN/CNRS (ISISCFD)	GL&UDE/Univ. Duisburg (Comet/OpenFOAM)	Kyushu University (RIAM-CMEN)
Numerical methods	Finite difference, hybrid collocated/staggered URANS using 2 equation k-ω Non-linear surface tracking 2nd order upwind—convection Implicit, 2nd order—time Direct coupling of pressure-momentum	Finite difference, collocated URANS using 2 equation k-ω Level-set 4th order TVD for convection Implicit, 2nd order for time Pressure-correction—Projection	Finite volume, collocated URANS using 2 equation k-ω VOF 2nd order hybrid—convection 3 p. backward, 2nd order—time Pressure-correction—SIMPLE	Finite volume, collocated URANS using 2 equation k-ε VOF upwind and centered scheme-convection/TVD Implicit, 2nd order for time Pressure-correction—SIMPLE/PISO	Finite difference, staggered DNS Interface tracking 3rd order CIP for convection explicit, 1st order for time Pressure-correction
Test cases	1.4a, b	1.4a, c	1.4a, b	1.4a, b, c	1.4b

3.3 Verification

Only one submission (Deng et al. 2010) out of 12 submissions performed verification. For calm water, three different unstructured hexahedral meshes were generated for each case to assess the grid error. For calm water, the refinement ratios from the coarse grid to the medium grid and from the coarse grid to the fine grid were about 1.33 and 1.67 respectively. The background grid was refined near the free surface such that there is about 60 nodes in wavelength and 10 nodes in wave height for the coarse grid. The number of grid points for the coarse, medium, and fine grids was 0.43M, 0.82M, and 1.4M, respectively. The authors explained the calm water verification results as: "based on the extrapolated value, numerical uncertainty is about 1, 2 and 3 % respectively for the fine grid, the medium grid and the coarse grid without taking into account any safety factor." For waves, the verification study was performed for $\lambda/L = 0.6, 1.1, 1.6$ and the results were obtained for 0.8M, 1.3M, 1.9M grids. The authors explained the verification results in waves for $\lambda/L = 1.1$ using Fig. 4.5 as: "it can be seen that for a given time step, the relative error increases as we refine the grid. To reduce the error to an acceptable level ($< 4\,\%$), at least 250 time steps per period are needed."

Also, the effect of the grid size on the motions and resistance can be investigated from comparing the errors for different submissions for case 1.4a, b,c with different grid sizes. The analysis of the results indicates that increasing the grid size from 0.3 to 4.7M drops the errors for motions from 40–60 %D to 10 %D while the error for resistance is about 25–30 %D and changes slightly by increasing the grid size, as shown in Fig. 4.6.

A review of relevant verification studies in literature for seakeeping is presented in Sect. 4.

3.4 Error Analysis

To analyze the errors for seakeeping test cases, the errors for motions and resistance are reported in Tables 4.4, 4.6, 4.7 for test cases 1.4a, b, c and Tables 4.8 and 4.9 for test case 2.4. For each submission and test condition, the first row shows the errors for X_0, z_0 and θ_0, the second row shows the errors for X_1, z_1 and θ_1 amplitudes and the third row shows the errors for phases, if they are available. For each submission and test condition, the errors are averaged in different combinations. The errors for 0th and 1st harmonic amplitude and phase are averaged and reported in the fourth row. For z and θ, the errors are also averaged together to estimate the error of motions. In addition, the errors for X, z and θ are averaged together to estimate the total error for each submission and test case. The errors for each submission are averaged over different test conditions and reported for X, motions, 1st order quantities, 1st order quantities excluding X_1, and higher order terms. The 1st order quantities are resistance calm water, 0th and 1st harmonic of X, and 1st harmonic of z and θ. The

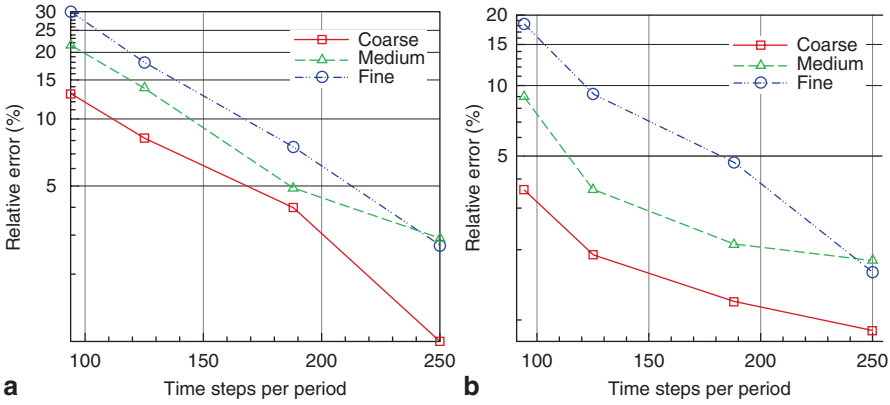


Fig. 4.5 Relative error for the case 1.4a with $\lambda/L = 1.1$. **a** 0th harmonic amplitude. **b** 1st harmonic amplitude

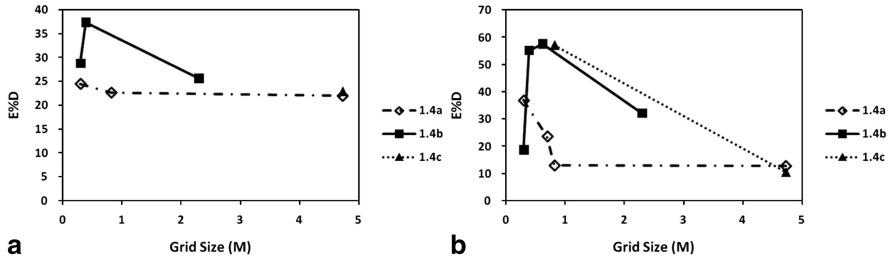


Fig. 4.6 Effects of the grid size on the error for case 1.4a, b,c for: **a** resistance; **b** motions

higher order quantities are calm water sinkage and trim and 0th harmonic of motions. Lastly, all the errors are averaged over all submissions to compute the overall error.

3.5 Discussion of Results for Test Case 1.4a

The summary of the results are shown in Table 4.4. The errors for phases could not be reported since the EFD phases are not used, as explained earlier.

3.5.1 Overall View

The error averaged over all five submissions and all three conditions is 17 %D, as shown in Table 4.4. The contribution of the errors for resistance and motions predictions are almost the same in the overall error. The average error for resistance is 23 %D with the largest error for 1st harmonic amplitude. For motions, the average

Table 4.4 Summary of submissions for test case 1.4a, *E%D*

Organization (Code)	Grids	λ/L_{pp}=1.1, H/ λ=1/59 (0th amp, 1st amp, 1st phase) E%D			λ/L_{pp}=1.6, H/ λ=1/85 (0th amp, 1st amp, 1st phase) E%D			*Calm water* (0th amp, 1st amp, 1st phase) E%D			Average Error				
		X	*z*	θ	*X*	*z*	θ	*X*	*z*	θ	*X*	*motions*	*1st order*	*1st order –X_1*	*higher*
ECN/ CNRS (ISISCFD)	Unstructured, 0.8M	-0.32 48.40 -	14.78 -4.73 -	24.63 -6.45 -	15.82 24.59 -	19.56 -5.22 -	18.03 13.08 -	9.93 - -	-23.9 - -	8.45 - -	8.69 36.5	18.23 7.37	14.28	7.94	18.23
		24.36	9.76 12.65	15.54	20.21	12.39 13.97	15.56	9.93	23.94 16.19	8.45	22.59	12.8			
		16.55			***16.05***			***14.11***			***17.7***				
ECN (ICARE)	Single block structured, 0.3M points	4.25 38.63 -	8.04 -23.7 -	13.16 -11.1 -	24.90 30.00 -	16.50 -9.31 -	17.06 11.12 -	-	-	-	14.58 34.32	13.82 13.83	19.13	14.06	13.69
		21.44	15.89 14.02	12.15	27.45	12.91 13.5	14.09	-	-	-	24.45	13.82			
		16.49			***18.15***			**-**			***17.32***				
GL&UDE (Comet)	Unstructured, 0.7 M	- - -	7.75 10.76 -	-33.3 17.06 -	- - -	10.23 -0.50 -	-56.2 21.65 -	-	-	-	- -	26.86 12.49	12.49	12.49	26.87
		-	9.26 17.21	25.17	-	5.37 22.15	38.93	-	- -	-	-	19.68			
		17.21			***22.15***						***19.68***				
GL&UDE (OpenFOAM)	Unstructured, 0.7 M	- - -	70.45 -9.01 -	33.91 -5.98 -	- - -	56.19 -3.14 -	27.71 12.33 -	-	-	-	- -	47.06 7.62	7.62	7.62	47.07
		-	39.73 29.84	19.95	-	29.67 24.84	20.02	-	-	-	-	27.34			
		29.84			***24.84***						***27.34***				
IIHR (CFDShip-Iowa V4)	Structured, overset, 4.73M	-5.04 36.65 -	7.24 0.85 -	22.43 6.33 -	-13.4 34.05 -	15.23 5.04 -	19.85 19.99 -	-6.8 - -	-25.3 - -	12.82 - -	8.42 35.35	17.15 8.05	14.24	8.21	17.15
		20.85	4.05 9.21	14.38	23.73	10.14 15.03	19.92	6.82	25.33 19.07	12.82	21.89	12.60			
		13.09			***17.93***			***14.99***			***17.24***				
Summary/ Average Error	**1.66M average (0.3M to 4.73M)**	3.2 41.23 -	21.66 9.82 -	25.48 9.39 -	18.04 29.55 -	23.54 4.64 -	27.77 15.63 -	8.38 - -	24.64 - -	10.64 - -	9.87 35.39	24.64 9.87	**15.54**	**9.87**	**22.29**
		22.22	**15.74** **16.59**	**17.44**	**23.79**	**14.09** **17.89**	**21.70**	**8.38**	**24.64** **17.64**	**10.64**	**22.63**	**17.25**			
		18.46			***19.03***			***14.55***			***<u>17.34</u>***				

error over all submission and test cases is 17 %D with the largest error for 0th harmonic. The average error for 1st order effect quantities is 16 and 10 %D including and excluding X_1, respectively. The average error for higher order quantities is 22 %D. Comparing the overall errors for calm water and different wavelength conditions indicates that the error averaged over all submissions is 14 %D for calm water compared to 19 %D for both mid-range and long wavelength cases. For all calm water and wave conditions, the same trend is observed for the errors i.e. larger errors for 1st harmonic of X and 0th harmonic of motions. The streaming quantities could be evaluated for two submissions (see Table 4.5). The streaming quantities and steady calm water sinkage and trim showed an average error of 20 %D.

3.5.2 Comparing Submissions

Overall, CFDShip-Iowa, ISISCFD, and ICARE show better agreement compared to the other submissions with the average error of 17 %D. For all submissions except ICARE, 1st harmonic of resistance and 0th harmonic of motions have the largest errors. The maximum error for resistance is observed for ICARE submission with the error of 24 %D.The maximum error form motions is for GL&UDE with the average of 27 %D. The errors for resistance and motions drop to 22 and 13 %D, respectively, for IIHR submission with grid size of 4.73M.

Table 4.5 Comparison of the error for terms including 1st and higher order effects for test case 1.4a, *E%D* (1st order terms are underlined)

Organization (Code)	Grids		λ/L_{PP}=1.1, H/ λ=1/59 *E%D*			λ/L_{PP}=1.6, H/ λ=1/85 *E%D*			*Averaged Error E%D*			Average Error E%D		
			X	*z*	θ	*X*	*z*	θ	*X*	*z*	θ	*1st order*	*1st order –X_1*	*higher*
ECN/ CNRS (ISISCFD)	Unstructured, 0.8M	steady	9.93	-23.9	8.45	9.93	-23.9	8.45	9.93	-23.9	8.45	14.28	7.94	19.66
		0th amp.	-0.32	14.78	24.63	15.82	19.56	18.03	8.07	17.17	21.33			
		added	9.93	28.10	26.04	18.68	30.88	19.91	14.30	29.49	22.97			
		1st amp.	48.40	-4.73	-6.45	24.59	-5.22	13.08	36.49	4.97	9.76			
		1st phase	-	-	-	-	-	-	-	-	-			
IIHR (CFDShip-Iowa V4)	Structured, overset, 4.73M	steady	-6.8	-25.3	12.82	-6.8	-25.3	12.82	-6.8	-25.3	12.82	14.24	8.21	19.27
		0th amp.	-5.04	7.24	22.43	-13.4	15.23	19.85	9.22	11.23	21.14			
		added	8.46	26.3	25.83	15.02	29.53	23.63	11.74	27.91	24.73			
		1st amp.	36.65	0.85	6.33	34.05	5.04	19.99	35.35	2.94	13.16			
		1st phase	-	-	-	-	-	-	-	-	-			
Summary/ Average Error	**2.76M average**	steady	**8.36**	**24.6**	**10.63**	**8.36**	**24.6**	**10.63**	**8.36**	**24.6**	**10.63**	**14.27**	**8.07**	**19.46**
		0th amp	**2.68**	**11.01**	**23.53**	**14.61**	**17.39**	**18.94**	**8.64**	**14.2**	**21.23**			
		added	**9.19**	**27.2**	**25.93**	**16.85**	**30.20**	**21.77**	**13.02**	**28.7**	**23.85**			
		1st amp.	**42.42**	**2.79**	**6.39**	**29.55**	**5.13**	**16.53**	**35.98**	**3.96**	**11.46**			
		1st phase	-	-	-	-	-	-	-	-	-	**14.81**		

3.6 Discussion of Results for Test Case 1.4b

3.6.1 Overall View

As shown in Table 4.6, the error averaged over all submissions and all conditions is 44 %D that drops to 22 %D by excluding the test condition with zero forward speed. The overall error for resistance and motions predictions are 28 %D/16 %D and 57 %D/24 %D including/excluding zero forward speed test case. The errors for the cases with forward speed are comparable with those seen for Test Case 1.4a. The large errors for motion are due to the 0th harmonic and the phase for 1st harmonic. The average error for quantities with 1st order effect is about 26 % for both with and without zero forward speed test case. However, the average error for higher order quantities drops from 83 to 20 % by excluding the zero forward speed test condition. Comparing overall errors for different wave conditions indicates that the error averaged over all submissions is minimum for $\lambda/L = 0.6364$ and $Fr = 0.182$ (18 %D) and maximum for $Fr = 0.0$ (111 %D). It should be mentioned that CFD showed good prediction for $\lambda/L = 0.6364$ even though the motions are quite small. In addition, it is shown that CFD predicted fairly well the resistance and motions for cases with fairly steep waves with the average error of 20 %D. In all wave conditions, the large errors belong to 0th harmonic of motions and/or 1st harmonic phase of motions.

Unlike Test Case 1.4a, there is no submission for calm water resistance and the streaming quantities cannot be evaluated.

3.6.2 Comparing Submissions

Overall, ICARE ($E = 23.14$ %D) and ISISCFD ($E = 23.21$ %D) show better agreement compared to the other submissions. Note that ICARE and ISISCFD grid sizes are dramatically different. ICARE predicts motions and ISISCFD predicts resistance force better than the other submissions. The errors for motions over all submissions are in the range of 22–103 %D while error for resistance is in the range of 19–42 %D. For all submissions, 0th harmonic of motions and/or phases of motions have the largest errors.

3.7 Discussion of Results for Test Case 1.4c

3.7.1 Overall View

The error averaged over all submissions and all conditions is 20 %D, as shown in Table 4.7. Therefore, the errors are comparable with those seen in test cases 1.4a, b and the effect of surge motion is not noticeable on the errors. The contribution of the errors for resistance and motions predictions are almost the same in the overall error. The average error for resistance is 21 %D with the largest error for 1st harmonic

Table 4.6 Summary of submissions for test case 1.4b

Organization (Code)	Grids	λ/L_{PP} = 0.9171; Fr=0.0; H/ λ=1/34 (0th amp, 1st amp, 1st phase) E%D for amp, E%360 for phase			λ/L_{PP} = 0.6364; Fr=0.142; H/ λ=1/118 (0th amp, 1st amp, 1st phase) E%D for amp, E%360 for phase			λ/L_{PP} = 0.6364; Fr=0.142; H/ λ=1/23 (0th amp, 1st amp, 1st phase) E%D for amp, E%360 for phase			λ/L_{PP} = 0.9171; Fr=0.142; H/ λ=1/34 (0th amp, 1st amp, 1st phase) E%D for amp, E%360 for phase			λ/L_{PP} = 0.6364; Fr=0.182, H/ λ=1/23 (0th amp, 1st amp, 1st phase) E%D for amp, E%360 for phase			Average Error excluding Fr=0.0						Average Error					
		X	z	θ	X	z	θ	X	z	θ	X	z	θ	X	z	θ	X	motions	1^{st}order	1^{st}order-X_1	higher	X	motions	1^{st}order	1^{st}order-X_1	higher
ECN/ CNRS (ISISCFD)	Unstructured, 2.3M	75.5	400	-4.35	5.37	13.5	-2.24	-3.79	7.80	3.41	-7.75	9.36	-0.44	1.00	11.93	5.10	4.48	6.72				18.68	45.81			
		-	19.75	6.59	-	-31.4	15.60	-	1.03	-5.44	-	-4.75	-7.87	-	1.51	2.44	-	8.76				-	9.67			
		-	-	-	-	-	-	-	-	-	-	-	-	-	-	-	-	-				-	-			
																	-	8.76	7.33	7.33	6.72	-	9.67	12.65	12.65	45.81
		75.5	209.9	5.47	5.37	22.43	8.92	3.79	4.42	4.43	7.75	7.06	4.16	1.00	6.72	3.77	4.48	7.74				18.68	27.74			
			107.69			15.67			4.425			5.61			5.245												
		96.96			***12.24***			***4.21***			***6.32***			***3.83***			***6.65***					***23.21***				
ECN (ICARE)	Single block structured, 0.3M points	68.2	60.78	28.3	-8.41	6.50	0.16	-11.5	6.4	2.6	-10.35	6.44	-5.84	-20.9	11.75	2.78	12.79	5.31				23.87	13.15			
		-	-14.57	4.76	-	11.02	18.7	-	2.65	-8.84	-	-13.62	-10.59	-	-5.06	2.44	-	9.12				-	9.23			
		-	37.91	43.6	-	-33.7	66.4	-	-30.5	68.2	-	18.24	-83.3	-	9.15	9.30	-	35.42				-	54.16			
																	-	22.27	22.15	22.15	5.31	-	31.7	24.48	24.48	13.16
		68.2	37.75	25.54	8.41	17.07	28.44	11.5	13.19	26.54	10.35	12.77	9.92	20.9	8.65	4.84	12.79	16.62				23.87	22.42			
			31.64			22.75			19.86			11.34			6.74												
		43.83			***17.98***			***17.08***			***11.01***			***11.46***			***14.38***					***23.14***				
GL&UDE (Comet)	Unstructured, 0.62 M	-	245.75	-296	-	5.61	-54.2	-	1.81	-46.92	-	6.44	-39.42	-	8.15	-24.5	-	23.38				-	72.84			
		-	6.94	5.92	-	33.98	25.00	-	14.49	15.65	-	1.17	2.72	-	12.56	13.82	-	14.92				-	13.22			
		-	45.84	49.51	-	-30.4	71.93	-	-30.2	71.14	-	21.47	-79.5	-	11.43	11.7	-	36.41	27.94	27.94	23.38	-	56.76	27.77	27.77	72.88
																	-	25.67				-	34.99			
		-	99.51	117.0	-	23.31	50.36	-	15.49	44.57	-	9.69	17.23	-	10.72	16.69	-	24.91				-	52.12			
			108.2			36.84			30.03			13.46			13.70												
		108.27			***36.84***			***30.03***			***13.46***			***13.70***			***23.51***					***52.12***				
GL&UDE (OpenFOAM)	Unstructured, 0.62 M	-	-1413	82.61	-	54.59	10.54	-	22.22	11.53	-	47.44	13.87	-	9.86	9.26	-	22.41				-	167.5			
		-	21.82	13.68	-	24.83	34.38	-	19.52	32.65	-	-3.56	0.15	-	18.93	32.52	-	20.82				-	20.19			
		-	44.08	47.37	-	-30.4	71.47	-	-31.3	73.47	-	19.51	-80.5	-	9.78	14.76	-	36.8	31.11	31.11	22.41	-	57.5	31.23	31.23	167.49
																	-	28.81				-	38.8			
		-	492.99	47.89	-	36.60	38.80	-	24.36	39.22	-	23.51	8.16	-	12.86	18.85	-	26.68				-	103			
			270.44			37.70			31.79			15.83			15.85												
		270.44			***37.70***			***31.79***			***15.83***			***15.85***			***25.29***					***97.6***				
Kyushu University (RIAM-CMEN)	Single block structured, 0.39M	81.35	-757.5	-20.9	-51.77	-22.67	-66.1	-24.35	-32.4	-57.72	-0.56	-30.35	-35.77	-49.63	-42.83	-60.2	31.58	43.51				41.53	112.65			
		-	-14.03	5.56	-	4.15	0.00	-	10.22	-41.5	-	21.39	2.65	-	19.54	0.00	-	12.43				-	11.9			
		-	44.92	47.88	-	-28.3	66.95	-	-29.7	72.17	-	22.02	-78.3	-	10.96	-72.5	-	42.32	30.33	30.33	43.51	-	67.56	32.02	32.02	112.64
																	-	27.38				-	39.73			
		81.35	272.16	24.77	51.77	18.37	44.36	24.35	24.14	57.13	0.56	24.59	15.59	49.63	24.44	44.23	31.58	32.75				41.53	76.19			
			148.46			31.36			40.63			20.09			34.33												
		126.09			***38.16***			***35.20***			***13.58***			***39.43***			***31.59***					***58.86***				
Summary/ Average Error	**0.846M average (0.39M to 2.6M)**	75.02	575.4	86.4	21.85	20.57	26.64	13.22	14.13	24.44	6.22	20.01	19.07	23.84	16.9	20.37	16.28	20.27				28.02	83.39			
		-	15.62	7.3	-	21.07	18.75	-	9.58	20.82	-	8.9	4.8	-	11.52	10.24	-	13.21				-	12.84			
		-	43.19	47.09	-	30.68	69.19	-	30.45	71.24	-	20.31	80.40	-	10.33	27.07	-	37.74	**25.52**	**25.52**	**20.27**	-	58.99	**27.95**	**27.95**	**82.39**
																	-	25.48				-	35.91			
		75.02	**211**	**46.93**	**21.85**	**23.56**	**34.18**	**13.22**	**16.32**	**34.38**	**6.22**	**15.52**	**42.6**	**23.84**	**12.68**	**17.68**	**16.28**	**23.74**				**28.02**	**56.65**			
			128.96			**28.87**			**25.35**			**29.06**			**15.18**												
		110.98			**26.53**			**21.31**			**21.44**			**18.07**			***21.84***					***43.83***				

Table 4.7 Summary of submissions for test case 1.4c

Organization (Code)	Grids	$\lambda/L_{PP} = 0.6$, H/λ=1/32 (0th amp, 1st amp, 1st phase) *E%D for amp, E%360 for phase*				$\lambda/L_{PP} = 1.1$, H/λ=1/59 (0th amp, 1st amp, 1st phase) *E%D for amp, E%360 for phase*				$\lambda/L_{PP} = 1.6$, H/λ=1/85 (0th amp, 1st amp, 1st phase) *E%D for amp, E%360 for phase*				*Calm water* (0th amp, 1st amp, 1st phase) *E%D for amp, E%360 for phase*				Average Error				
		X	*z*	θ	*x*	*X*	*z*	θ	*x*	*X*	*z*	θ	*x*	*X*	*z*	θ	*x*	*X*	*motions*	1st*order*	1st*order* $-X_1$	*higher*
GL&UDE (Comet)	Unstructured 0.7 M	-	-11.73	-94.35	-	-	-3.06	-81.34	-	-	-14.26	-67.59	-	-	-	-	-	-	45.38	25.26	25.26	45.39
		-	27.43	14.06	-13.87	-	11.30	8.34	-2.88	-	-1.60	-8.85	27.92	-	-	-	-	-	12.92			
		-	-20.27	82.77	-	-	-57.6	42.47	-	-	28.92	30.66	-	-	-	-	-	-	43.79			
																		-	28.35			
		-	19.81	63.73	13.87	-	24.00	44.05	2.88	-	14.92	35.70	27.92	-	-	-	-	-	36.86			
			32.47				23.64				26.18				-							
		32.47				***23.64***				***26.18***								***36.86***				
IIHR (CFDShip-Iowa V4)	Structured, overset, 4.73M	7.40	-5.28	7.18	-0.11	-3.40	-2.63	-2.92	0.38	-39.80	13.91	15.84	-2.22	-7.81	-2.13	4.04	-4.55	14.6	5.10	10.88	7.17	6.74
		54.29	10.76	-12.55	-0.11	28.33	1.71	-2.76	-8.77	59.66	3.95	-10.40	0.52	-	-	-	-	47.43	5.72			
		-6.20	16.75	18.85	16.175	-1.84	-1.47	2.82	0.55	-11.32	2.81	4.35	5.43	-	-	-	-	6.45	7.69			
																		26.94	6.71			
		22.63	10.93	12.86	5.47	11.19	1.94	2.83	3.23	36.92	6.89	10.20	2.72	7.81	2.13	4.04	4.55	20.77	5.90			
			9.75				2.66				6.60				3.57							
		12.97				***4.80***				***14.18***				***4.63***				***13.33***				
Summary/ Average Error	**5.43M average (0.7M to 4.73M)**	7.4	8.5	50.76	0.11	3.4	2.84	42.13	0.38	39.8	14.08	41.71	2.22	7.81	2.13	4.04	4.55	14.6	25.24	**15.26**	**12.56**	**20.77**
		54.29	19.1	13.3	6.99	28.3	6.5	5.55	5.82	59.66	2.77	9.62	14.22	-	-	-	-	47.43	9.32			
		6.20	18.51	50.82	16.17	1.84	29.56	22.65	0.55	11.32	15.86	17.5	5.43	-	-	-	-	6.45	19.64			
																		26.94	14.48			
		22.63	**15.37**	**38.30**	**7.76**	**11.19**	**12.97**	**23.44**	**2.25**	**36.92**	**10.90**	**22.95**	**7.29**	**7.81**	**2.13**	**4.04**	**4.55**	**20.77**	**19.86**			
			20.47				**12.88**				**13.71**				**3.57**							
		21.01				***12.46***				***25.31***				***4.63***				***20.31***				

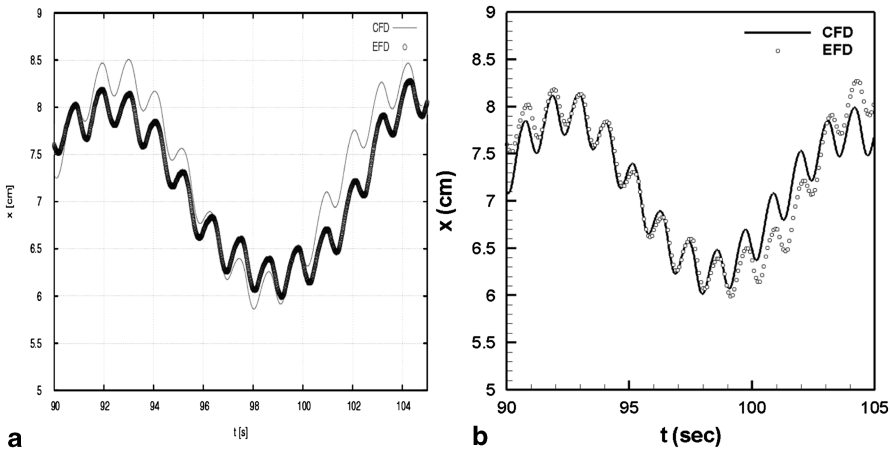


Fig. 4.7 Time histories of surge motion (x) at $\lambda/LPP = 1.1$ for case 1.4c. **a** GL&UDE (Comet). **b** IIHR (CFDShip-Iowa)

amplitude. For motions, the average error over all submission and test cases is 20 %D with the largest error for 0th harmonic and 1st harmonic phase. The average error for quantities with 1st order effect is 15 and 13 %D including and excluding X_1, respectively. The average error for higher order quantities is 21 %D. Comparing overall errors for calm water and different wavelength conditions indicates that the error averaged over all submissions is smallest for calm water (5 %D) and maximum for largest wavelength (25 %D). Similar to Case 1.4b, CFD showed good predictions for cases at short wavelengths in which the motions are quite small. The errors for steep wave condition ($\lambda/L = 0.6$) is comparable with the errors for other conditions. For all conditions, the 1st harmonic of X shows the largest errors. Figure 4.7 shows time history of surge motion predicted by GL&UDE (Comet) and IIHR (CFDShip-Iowa).

3.7.2 Comparing Submissions

Among the two submissions, CFDShip-Iowa shows better agreement with EFD data, with 13 %D error, which might be due to the advantage of close collaborations with OU to understand the EFD setup.

3.8 Conclusion

Five EFD data sets are available from different facilities for calm water condition, which show different values for resistance, sinkage, and trim. The largest facility bias was for sinkage, about 20 %D. Unfortunately, uncertainly of the measured data

were not available and the overall uncertainty could not be assessed. For waves, the data are provided from OU, INSEAN and NTNU. INSEAN shows good agreement with OU data for heave amplitude but indicates different pitch and added resistance for $\lambda/L = 1.6$. There was no phase reference recorded for INSEAN EFD data and thus the INSEAN phases are not available for comparison with OU data. The NTNU shows close agreement with OU and INSEAN while the phases for motions are quite different. The motions and added resistance show expected trends for OU data. However, the peaks are under resolved by the data such that additional wavelength conditions are required to capture the trend of the motions near the peak. The INSEAN and NTNU data shows same trend as OU data for both motions and added resistance, suggesting that the effect of surge is neglegible on heave and pitch motions and added resistance. Although the motions for short wavelengths show agreement between different facilities, the values are very small and comparable with the sinkage and trim values at low Fr (see Chap. 2) such that the uncertainty of the data might be an issue for motions for short wavelengths. The NTNU data also shows the ship speed effect is significant as it changes the encounter frequency. However, the quite large wave slope (wave amplitude) does not show noticeable impact on the results.

The submissions for the CFD simulation of cases1.4a–c included 12 submissions from 5 institutions from 4 countries with the number of grid points of 0.3–4.73M. Five different commercial/in-house URANS solvers and one DNS solver were used. Turbulence was modeled using 2-equation Reynolds-stress transport models. Free surface was mostly modeled by a surface capturing method and only two institutions utilized the surface tracking method. For numerical methods, spatial discretization was done by finite difference or finite volume methods with structured/unstructured grids with the number of grid points. The order of accuracy in time integration was mostly 2nd order or higher. The velocity/pressure coupling was achieved using different approaches including SIMPLE, PISO and Projection.

Verification studies are performed by one submission for case 1.4a in calm water and waves. Also, the analysis of the results indicates that increasing the grid size from 0.3 to 4.7M drops the errors for motions from 40–60 to 10 %D while the error for resistance is about 25–30 %D and changes slightly by increasing the grid size.

CFD has achieved the prediction of 1st order quantities for cases 1.4a, b, c with the average error of 19 %D and 14 %D including and excluding the error for X_1, respectively, as shown in Table 4.16 in Sect. 4. For higher order quantities, CFD overall error is 33 %D. For steady calm water and 0th harmonic of resistance, the average error is around 8 %D and 18 %, respectively, while the 1st harmonic amplitude and phase are predicted by 31 %D. For motions, the error is 10 %D for steady calm water and 33 %D for 0th harmonic while it is around 16 %D for 1st harmonic amplitude and phase. Therefore, for resistance, the largest error values are observed for the 1st harmonic amplitude and phase, followed by 0th harmonic amplitude and then steady. For both heave and pitch motions, the largest error values are observed for the 0th harmonic amplitudes followed by 1st harmonic amplitude and phase and then steady. Among different test conditions, the errors are similar for the different wavelengths, the linear and steep waves, and for the cases with and without surge motion (Tables 4.4, 4.6, 4.7). The errors are larger for the cases with zero forward

speed, possibly due to the measurement and/or URANS difficulties at zero forward speed. CFD showed same order error for all the test conditions with forward speed. In addition, CFD showed good prediction for test conditions with quite steep waves. An overall comparison of CFD seakeeping results including the KCS case 2.4, and previous studies in literature are presented in Sect. 4.

Comparing the errors for different submissions shows that the smallest error averaged over amplitudes and phase for resistance is 11.19 $\%D$ for case 1.4c with $\lambda/L = 1.1$ for CFDShip-Iowa with 4.73M grid points. Also the smallest error averaged over amplitudes and phase for motions is 2.66 $\%D$ for case 1.4c with $\lambda/L = 1.1$ for CFDShip-Iowa with 4.73M grid points.

4 Case 2.4 Seakeeping for KCS in Regular Head Waves

4.1 EFD Data for Test Case 2.4

Only one set of data is available for test case 2.4. Model tests are conducted for regular head waves at FORCE (Simonsen et al. 2008) for KCS containership appended with a rudder. The model was free to heave and pitch at $Fr = 0.26$ ($Re = 6.52 \times 10^6$), 0.33 ($Re = 8.27 \times 10^6$) and 0.40 ($Re = 1.002 \times 10^7$) for wavelength range of $\lambda/L = 0.5 - 2.0$ with constant wave steepness of $ak = 0.0525$ ($H/\lambda = 1/60$). $Fr = 0.26$ is the ship service speed, $Fr = 0.33$ is the coincidence Fr, and $Fr = 0.40$ was included to investigate the maximum response for higher Fr. The data include heave and pitch motions, as well as resistance force. UA studies were conducted for $Fr = 0.26$ and $\lambda/L = 1.15$ and the data uncertainties were found one order of magnitude larger than 5512 (See Table 4.12). It should be noted that during the tests, the model was mounted in two trim holders or posts. This system is normally used to measure heave and pitch motions, but was in this case used for force measurements as well. The system is not completely stiff, which means that it may allow small surge motions while the ship moves through the waves, so the system will act like being towed in a stiff spring. Therefore, it is believed that the 0th harmonic amplitude of resistance should work for comparison with CFD, but care should be taken when comparing the 1st harmonic amplitude and phase of resistance.

The EFD data for 1st harmonic amplitude and phase of heave and pitch motions, as well as added resistance versus λ/L are shown in Fig. 4.8. The results show the expected general trend, as also discussed for KVLCC2 in Sect. 3.1.2. For short wavelengths, both heave and pitch motions are small and comparable to the sinkage and trim values at low Fr reported in Chap. 2. For long waves, heave and pitch transfer functions approach 1.0 as the ship moves up and down with waves, and the phases approach 0° and − 90° for heave and pitch respectively, showing that for long waves the heave is synchronized with the wave height near the ship center of gravity and the pitch with the wave slope. The maximum response occurs at the coincidence Fr for added resistance, but for both heave and pitch the transfer functions increase with speed being maximum at $Fr = 0.4$. For heave, the maximum responses for all

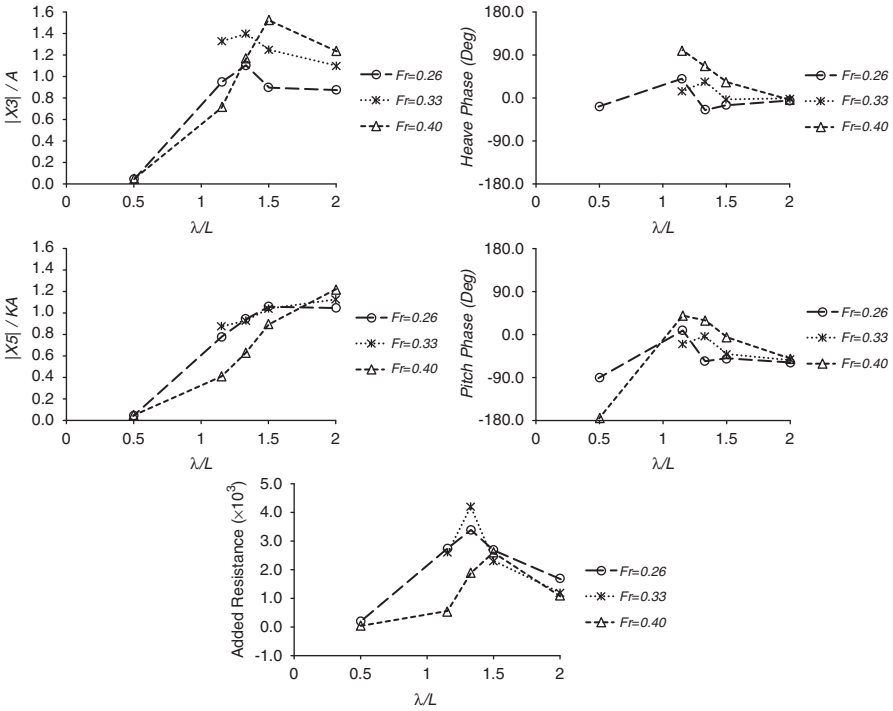


Fig. 4.8 EFD RAOs for heave, pitch, and added resistance for test case 2.4

three speeds occur at resonance, while for pitch they occur at different frequencies, all smaller than resonance. At fixed $\lambda/L_{PP} = 1.33$, local maximum heave response occurs for $f_e \sim f_n$, i.e. $Fr = 0.33$, but the maximum pitch response occurs at lowest $Fr = 0.26$.

The current G2010 test case 2.4 includes three conditions: $Fr = 0.26$ in wavelengths $\lambda/L_{PP} = 1.15$ and 2.00, and $Fr = 0.33$ in wavelength $\lambda/L_{PP} = 1.33$. $Fr = 0.26$ is the ship service speed at which $\lambda/L_{PP} = 1.15$ corresponds to natural frequency and $\lambda/L_{PP} = 2.00$ corresponds to largest wavelength (smallest encounter frequency) tested at this Fr, where heave and pitch transfer functions are close to 1.0 (see Fig. 4.8). At $Fr = 0.33$, $\lambda/L_{PP} = 1.33$ corresponds with the surge/pitch maximum excitation forces, as well as natural frequency. The EFD data are included in Table 4.8 based on data reduction by FORCE, approximating the time series with Fourier series expansions of third order. Later, Carrica et al. (2010) did an alternative data reduction using the time histories for EFD data provided at G2010 website, believing that reconstructed time series using the provided data reduction results do not match with the time histories of the data. The procedure included finding the encounter frequency from the data, making sure that the initial transient has passed, and then doing 1st order Fourier transform for motions and 3rd order for resistance. The results were similar for 1st harmonic amplitudes, but the differences were

Table 4.8 Summary of submissions for test case 2.4

Organization (Code)	Numerical Methods	Grids	HPC	λ/L_{PP}=1.15, H/λ=1/60, Fr=0.26 (0th amp, 1st amp, 1st phase) *E%D for amp, E%360 for phase*			λ/L_{PP}=2.00, H/λ=1/60, Fr=0.26 (0th amp, 1st amp, 1st phase) *E%D for amp, E%360 for phase*			λ/L_{PP}=1.33, H/λ=1/60, Fr=0.33 (0th amp, 1st amp, 1st phase) *E%D for amp, E%360 for phase*			Average Error				
				$C_T(\times 10^3)$	$z(mm)$	$\theta(deg)$	$C_T(\times 10^3)$	$z(mm)$	$\theta(deg)$	$C_T(\times 10^3)$	$z(mm)$	$\theta(deg)$	C_T	*motions*	*1st order*	*1st order-X_i*	*higher*
EFD (FORCE)	-	-	-	7.16 20.43 81.87	-5.44 39.54 -20.57	0.06 2.10 8.49	6.03 32.07 70.81	-6.57 67.33 -3.10	0.06 3.16 50.27	8.72 35.39 -260.21	-12.27 61.81 -18.28	-0.07 2.52 46.10	-				
FORCE (CFDship-Iowa V4)	Finite difference, collocated BKW (SST) Level-set 2nd order convection Implicit, 2nd order time Pressure-correct., Projection	Structured Overset 4.35M	2944 CPU-hours	5.57 82.33 1.10 *29.67*	-5.11 -10.11 -2.56 5.93 29.93	143.75 -14.03 -4.03 53.94	-	-	-	-	-	-	5.57 82.33 1.10 41.71 23.64	74.43 12.07 3.29 7.68 41.05	17.10	7.26	74.43
					29.80									**32.34**			
GL&UDE (Comet)	Finite volume, collocated k-epsilon with WF VOF 2nd order TVD - convection Implicit 2nd order time Pressure-correct., SIMPLE	Unstructured 1.2M	68 processors 1249 CPU-hours	-	-19.50 4.39 0.16 8.02 16.15	70.31 -1.29 -1.22 24.27	-	0.50 3.43 -0.54 1.49 28.13	159.68 0.86 -3.76 54.76	-	3.01 10.48 2.16 5.21 55.89	310.45 -0.99 8.24 106.56	-	93.91 3.57 2.68 3.13 48.52	3.13	3.13	93.91
GL&UDE (OpenFOAM)	Finite volume, collocated BKW with WF, VOF 2nd order TVD - convection Implicit – 2nd order time Pressure-correct., PISO	Unstructured 1.2M	Not Available	-	-7.97 1.83 -0.22 3.34 13.16	64.06 -3.34 -1.55 22.98	-	-7.62 3.33 -1.07 4.01 7.61	-29.03 0.48 -4.12 11.21	-	8.11 9.40 1.76 6.43 50.63	274.63 -1.98 7.90 94.84	-	65.24 3.39 2.77 3.08 34.16	3.08	3.08	65.24
IHI (WISDAM-UTokyo)	Finite volume, staggered Baldwin-Lomax and DSGS density function rho 3rd order convection Explicit – 2nd order time Pressure-correct., MAC	Overlapping Structured 553K	1 CPU (Desktop Workstation)	21.40 98.57 -1.49 *40.49*	-14.86 14.99 2.52 10.79 10.96	29.69 -0.62 -3.09 11.13	30.91 24.74 -3.75 *19.80*	-9.97 -36.12 1.51 15.86 16.38	43.55 1.24 -5.92 16.90	53.30 60.30 -50.80 *54.80*	46.23 8.89 -0.31 18.47 32.73	131.34 5.98 3.61 46.98	35.21 61.20 18.68 39.94 37.58	45.94 11.31 2.83 7.07 26.50	20.48	12.69	45.94
					25.73			**18.09**			**43.76**			**32.04**			
IIHR (CFDShip-Iowa V4)	Finite difference, collocated Hybird RANS/LES Level-set 2 to 4 order convection Implicit, 2nd order time Pressure-correct., Projection	Structured Overset 7.6M	48 processors 2880 CPU-hours	2.63 70.47 4.10 *25.73*	-17.22 14.11 -3.62 11.65 44.44	220.31 -5.44 -5.96 77.24	7.19 21.37 -3.19 *10.58*	1.26 7.28 -1.42 3.32 76.58	438.71 5.35 -5.48 149.85	6.05 85.63 -96.28 *62.65*	3.86 17.56 -1.19 7.54 32.00	159.70 -2.73 6.97 56.47	5.29 59.16 34.52 46.84 26.07	140.18 8.74 4.10 6.43 73.30	17.81	6.20	140.18
					35.09			**43.58**			**47.33**			**49.68**			
TUHH (FreSCo+)	Finite volume, collocated KW-Wilcox Turb. VOF 3rd order convect., QUICK Implicit, 1st order time Pressure-correct., SIMPLE	Unstructured, Adaptive, 830K	1 CPU 72 hours clock-time	-20.52 84.56 -9.99 *38.36*	-10.39 4.08 0.48 4.98 20.16	96.88 5.30 -3.85 35.34	-29.97 18.73 -0.54 *16.41*	3.42 -3.94 -0.30 2.55 13.81	59.68 -12.67 -2.85 25.07	-20.85 85.76 -10.06 *38.89*	-23.92 0.94 0.72 8.53 38.84	-201.5 2.58 3.42 69.16	23.78 63.02 6.86 34.94 29.36	65.97 4.91 1.93 3.43 34.70	15.34	7.50	65.97
					29.26			**15.11**			**38.87**			**32.03**			
Summary/ Average Error	4 FV and 2 FD (V4) One with LES, rest with 2-eq turb. Models 2-4 convect., 1-2 time order All with pressure correction	2.62M average (0.55M to 7.6M)	From 1 to 64 processors	12.53 83.98 4.17 *33.56*	12.51 8.25 1.59 7.45 22.47	104.17 5.00 3.28 37.48	22.69 21.61 2.49 *15.60*	4.55 10.82 0.97 5.45 28.50	146.13 4.12 4.43 51.56	26.73 77.23 52.38 *52.11*	17.03 9.45 1.23 9.24 42.02	215.52 2.85 6.03 74.80	**20.65** **60.94** **19.68** **40.31** **30.48**	**83.32** **6.75** **2.92** **4.84** **44.08**	**17.23**	**8.00**	**83.32**
					28.01			**22.05**			**47.07**			**37.28**			

significant for some 0th harmonic amplitudes and 1st harmonic phases. In this report, the submissions are evaluated based on FORCE data reduction, and then the differences are discussed considering the alternative data reduction. Future work should clarify the data reduction differences.

4.2 CFD Submissions for Test Case 2.4

CFD submissions for the KCS in regular head waves (test case 2.4) included 6 submissions from 5 institutions from 4 countries: FORCE from Denmark, GL&UDE (2 submissions) from Germany, IHI from Japan, IIHR from USA and TUHH from Germany. 5 different URANS solvers were used, 2 of which were commercial (Comet and OpenFoam) and 3 in-house research codes (CFDship-Iowa, WISDAM-UTokyo, FreSCo+), while one submission used DES (CFDShip-Iowa). Turbulence was modeled using 2-equation models in 4 of the solvers and using a 0-equation algebraic model (Baldwin-Lomax) in one solver. Free surface was modeled by surface capturing methods (e.g. level-set, volume of fluid) for all submissions. Other than CFDShip-Iowa (2 submissions, one URANS one DES) which is based on finite difference, other solvers were based on finite volume. Structured and unstructured grids with the number of grid points of 0.553M–7.6M were used. The order of accuracy for convection terms vary from 2nd order to 4th order. The order of accuracy in time integration was 1st order for one submission and 2nd order for the rest. All CFD submissions are summarized in Table 4.8.

4.3 Verification Studies for Test Case 2.4

Only one out of six submissions for test case 2.4 includes verification studies (Simonsen et al. 2008), as per Table 4.11. Grid studies are carried out for 1st harmonic amplitudes of resistance and motions which did not achieve monotonic convergence, perhaps due to small grid refinement ratio. Therefore, Richardson extrapolation could not be used; instead the uncertainties are obtained based on maximum differences between three solutions. The grid uncertainty is largest for heave (10.3 $\%S_1$) followed by pitch (2.6 $\%S_1$) and resistance (1.5 $\%S_1$).

Also, the effect of the grid size on the motions and resistance can be investigated by comparing the errors for different submissions for case 2.4 with different grid sizes. The analysis of the results indicates that increasing the grid size from 0.5 to 7.6M increases the average errors for motions from 20 to 50 %D, as shown in Fig. 4.9. The increasing of the error by increasing the grid size is because the computations are conducted by using different methods for discretization, velocity and pressure coupling, turbulence modeling and free surface as shown in Table 4.8. The error for resistance is about 30 %D and changes slightly by increasing the grid size.

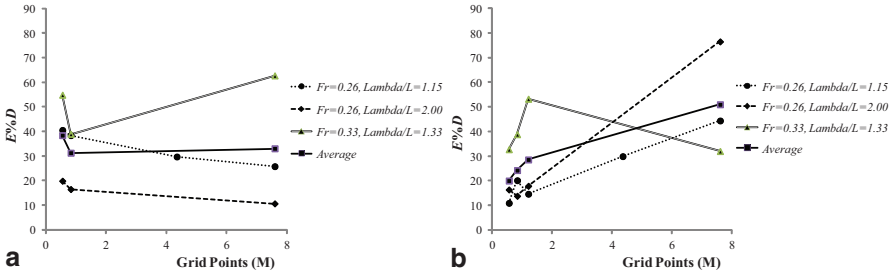


Fig. 4.9 Effects of the grid size on the error for test case 2.4 for: **a** resistance; **b** motions

Table 4.9 Comparison of 1st order vs. higher order effects for test case 2.4 (1st order terms are underlined)

Organization (Code)	Grids		λ/L_{PP}=1.15, H/λ=1/60, Fr=0.26 E%D for amp, E%δ360 for phase C_T	z	θ	Average Error E%D 1st order	1st order $-X_1$	higher order
FORCE (CFDship-Iowa V4)	Structured Overset 4.35M	steady	-5.6	-6.4	-4.0	15.67	6.98	26.61
		0th amp.	5.57	-5.11	143.75			
		added	3.0	6.0	18.0			
		1st amp.	82.33	-10.11	-14.03			
		1st phase	1.10	-2.56	-4.03	18.47		
Carrica et al. (2010) Data reduction								
FORCE (CFDship-Iowa V4)	Structured Overset 4.35M	steady	-5.6	-6.4	-4.0	15.51	6.78	15.14
		0th amp.	5.57	-16.85	51.72			
		added	3.0	6.0	18.0			
		1st amp.	82.32	-8.74	-13.22			
		1st phase	1.10	4.46	3.06	13.9		

4.4 Discussion of Results for Test Case 2.4

4.4.1 Overall View

The error averaged over all submissions and conditions is 37 %D, as shown in Table 4.8. The contribution of the error for resistance in the overall error is less than that for motions. The average error for resistance is 30 %D with the largest error for 1st harmonic amplitude. For motions, the average error over all submission and test cases is 44 %D with the largest error for 0th harmonic. The average error for quantities with 1st order effect is 17 and 8 %D including and excluding X_1, respectively. The average error for higher order quantities is 83 %D. Comparing overall errors for different wavelength conditions indicates that the error averaged over all submissions is smaller for the case at $\lambda/L = 2.0$. For all wave conditions, the same trend is observed for the errors i.e. larger errors for 1st harmonic of X and 0th harmonic of motions. The streaming quantities could be evaluated for one submission (see Table 4.9), showing the maximum error for added trim with E = 18 %D and minim error for added resistance with E = 3 %D.

4.4.2 Comparing Submissions

Overall, FreSCo+, WISDAM-UTokyo and CFDShip-Iowa URANS submissions show better agreement with average error of 32 %*D* compared to CFDShip-Iowa DES submission with average error of 50 %D. The maximum average error for resistance is 38 %D for the coarsest grid and the best resistance errors are for the two finest grids with average error of 25 %*D*. For motions, the best prediction is for coarse grid with E = 26.5 %D and the largest error is for the finest grid with E = 73 %D.

4.5 Evaluation of Test Case 2.4 Based on Carrica et al. (2010) Data Reduction

Table 4.10 and Fig. 4.11 show the results for the six submissions for test case 2.4 based on re-evaluation of data reduction explained in Sect. 4.1. Further investigations are needed to identify the better data reduction; the differences are just addressed here.

4.5.1 Overall View

The error averaged over all submissions and all conditions is 32 %D, as shown in Table 4.10. Total average error is smaller based on Carrica et al. (2010) data reduction, which is due to reduction in motion error since resistance is almost unchanged. The contribution of the error for resistance in the overall error is less than that for motions. The average error for resistance is 30 %D with the largest error for 1st harmonic amplitude. For motions, the average error over all submission and test cases is 35 %D with the largest error for 0th harmonic. The average error for quantities with 1st order effect is 18 and 8 %D including and excluding X_1, respectively. The average error for higher order quantities is 64 %D. Comparing overall errors for different wavelength conditions, the same trend is observed, but the error values are reduced for some conditions. The streaming quantities could be evaluated for one submission (see Table 4.9), showing the maximum error for added trim with E = 18 %D and minim error for added resistance with E = 3 %D.

4.5.2 Comparing Submissions

The overall ranking for the submissions are changed significantly. The two CFDShip-Iowa submissions show better agreement with average error of 20 %*D* compared to other submissions with average error of 37 %D. As seen in Fig. 4.11, the trend for resistance is not changed and it shows that the average error decreases as the grid size increases. For motions, a different trend is observed since for all conditions, the motion errors decrease by increasing the grid size. Looking at Table 4.10, three

Table 4.10 Summary of submissions for test case 2.4 based on re-evaluated data reduction

Organization (Code)	Numerical Methods	Grids	HPC	λ/L_{pp}=1.15, H/λ=1/60, Fr=0.26 (0th amp, 1st amp, 1st phase) E%D for amp, E%360 for phase			λ/L_{pp}=2.00, H/λ=1/60, Fr=0.26 (0th amp, 1st amp, 1st phase) E%D for amp, E%360 for phase			λ/L_{pp}=1.33, H/λ=1/60, Fr=0.33 (0th amp, 1st amp, 1st phase) E%D for amp, E%360 for phase			Average Error				
				$C_T(\times 10^3)$	$z(mm)$	$\theta(deg)$	$C_T(\times 10^3)$	$z(mm)$	$\theta(deg)$	$C_T(\times 10^3)$	$z(mm)$	$\theta(deg)$	C_T	*motions*	*1st order*	*1st order-X_1*	*higher*
EFD (FORCE)	-	-	-	7.159 20.42 82	-4.89 40.04 4.7	-0.058 2.11 34	6.033 32.07 70.8	-6.52 65.8 9	-0.13 3.12 61	8.716 35.4 99.8	-11.4 58.1 21	0.075 2.43 45	-				
FORCE (CFDship-Iowa V4)	Finite difference, collocated BKW (SST) Level-set 2nd order convection Implicit, 2nd order time Pressure-correct., Projection	Structured Overset 4.35M	2944 CPU-hours	5.57 82.32 1.14	-16.85 -8.74 4.46	51.72 -13.22 3.06	-	-	-	-	-	-	5.57 82.32 1.14 41.73	34.29 10.98 3.76 7.37	16.93	7.01	34.29
				29.68	10.02 16.34	22.67							23.65	20.83			
				20.79									**22.24**				
GL&UDE (Comet)	Finite volume, collocated k-epsilon with WF VOF 2nd order TVD - convection Implicit 2nd order time Pressure-correct., SIMPLE	Unstructured 1.2M	68 processors 1249 CPU-hours	-	-32.84 5.57 7.18	132.76 -0.57 5.86	-	-0.31 1.19 2.82	71.54 -0.29 -0.78	-	-4.43 4.76 13.07	-88.00 -4.86 7.93	-	54.98 2.87 6.27 4.57	4.57	4.57	54.98
					15.20 30.8	46.40		1.44 12.82	24.20		7.42 20.51	33.60		29.78			
GL&UDE (OpenFOAM)	Finite volume, collocated BKW with WF, VOF 2nd order TVD - convection Implicit – 2nd order time Pressure-correct., PISO	Unstructured 1.2M	Not Available	-	-20.02 3.05 6.80	139.66 -2.61 5.54	-	-8.50 1.08 2.29	161.54 -0.67 -1.14	-	1.07 3.62 12.67	-56.00 -5.88 7.59	-	64.46 2.81 6.0 4.41	4.41	4.41	64.47
					9.96 29.61	49.27		3.96 29.20	54.45		5.79 14.47	23.16		34.44			
IHI (WISDAM-UTokyo)	Finite volume, staggered Baldwin-Lomax and DSGS density function rho 3rd order convection Explicit – 2nd order time Pressure-correct., MAC	Overlapping Structured 553K	1 CPU (Desktop Workstation)	21.40 98.57 -1.46	-27.69 16.05 9.54	177.59 0.09 4.00	30.91 24.75 -3.75	-10.86 -39.28 4.87	126.92 0.10 -2.94	53.30 60.31 49.20	42.11 3.07 10.61	72.00 2.39 3.30	35.21 61.21 18.14 39.68	76.19 10.16 5.87 8.02	20.95	13.46	76.20
				40.48	17.76 39.16	60.56	*19.80*	18.34 30.83	43.32	*54.27*	18.59 22.24	25.90	37.44	42.10			
				39.60			**27.15**			**32.92**			**39.77**				
IIHR (CFDShip-Iowa V4)	Finite difference, collocated Hybird RANS/LES Level-set 2 to 4 order convection Implicit, 2nd order time Pressure-correct., Projection	Structured Overset 7.6M	48 processors 2880 CPU-hours	2.63 70.46 4.14	-30.31 15.17 3.40	-32.76 -4.69 1.12	7.19 21.38 -3.19	0.46 5.13 1.94	-61.54 4.26 -2.50	6.05 85.64 3.72	-3.51 12.29 9.72	46.67 -6.67 6.67	5.29 59.16 3.68 31.42	29.21 8.03 4.22 6.13	13.24	5.96	29.21
				25.74	16.29 14.57	12.86	*10.59*	2.51 12.64	22.77	*31.80*	8.51 14.25	20.00	18.36	17.67			
				18.30			**11.96**			**20.10**			**18.01**				
TUHH (FreSCo+)	Finite volume, collocated KW-Wilcox Turb. VOF 3rd order convect., QUICK Implicit, 1st order time Pressure-correct., SIMPLE	Unstructured, Adaptive, 830K	1 CPU 72 hours clock-time	-20.52 84.56 -9.96	-22.72 5.26 7.50	103.45 5.97 3.24	-29.97 18.73 -0.54	2.64 -6.35 3.06	119.23 -13.97 0.13	-20.85 85.76 89.95	-33.42 -5.39 11.63	369.33 -1.15 3.11	23.78 63.02 33.48 48.25	108.47 6.35 4.78 5.57	18.38	6.43	108.47
				38.35	11.83 24.69	37.55	*16.42*	4.02 24.23	44.44	*65.52*	16.81 70.67	124.53	36.02	57.02			
				29.24			**21.63**			**68.95**			**46.52**				
Summary/ Average Error	4 FV and 2 FD (V4) One with LES, rest with 2-eq turb. Models 2-4 convect., 1-2 time order All with pressure correction	2.62M average (0.55M to 7.6M)	From 1 to 64 processors	12.53 83.98 4.17	25.07 8.98 6.48	106.32 4.53 3.80	22.69 21.62 2.50	4.55 10.60 3.00	108.15 3.86 1.50	26.73 77.24 47.62	16.91 5.82 11.54	126.40 4.19 5.72	20.65 60.94 18.10 39.52	64.57 6.33 5.34 5.84	**17.58**	**8.80**	**64.57**
				33.56	13.51 25.86	38.22	*15.60*	6.05 21.94	37.84	*50.53*	11.42 28.43	45.44	30.09	35.20			
				28.43			**19.83**			**35.80**			**32.64**				

levels of grids can be identified: fine group includes two CFDShip-Iowa simulations with average grid points of 5.97M, medium group consists of Comet and OpenFoam submissions with 1.2M grid points, and coarse group is FreSCo+ and WISDAM-UTokyo with average 0.69M grid points. Note that resistance is not included for the medium group and this group is considered only for motions comparisons. Average resistance errors for the fine and coarse groups are 21 %D and 37 %*D*, respectively. Comparing motions, the average errors for the fine, medium, and coarse groups are 19 %D, 32 %D, and 50 %*D*, respectively. The total errors for the fine and coarse groups are 20 %D and 43 %D, respectively.

4.6 Discussion on Overall CFD Results for Seakeeping

Verification studies for seakeeping using CFDShip-Iowa are summarized in Table 4.11. The average of the fine grid points is 7M. Time step studies were included by 3 studies out of 5. Resistance was included in only one U_T study with relatively high uncertainty level ($U_T = 21$ %S) compared to average uncertainty of motions ($U_T = 2.5$ %S). Comparing motions, heave had generally higher U_T than pitch for almost all studies. For grid studies, three out of five studies considered resistance with average resistance uncertainty of $U_G = 2$ %S_1, which is smaller than the average time step uncertainty for resistance. Heave and pitch had similar grid uncertainties, with average uncertainty of $U_G = 3.75$ %S_1, which is slightly larger than that for time step studies. Overall, average simulation numerical uncertainties for seakeeping verification studies were $U_{SN} = 6.8$ %D for resistance and $U_{SN} = 4.7$ %D for motions.

The UA studies for EFD data for seakeeping are summarized in Table 4.12. Only two studies are conducted focusing mainly on heave and pitch transfer functions. 1st harmonic phases for motions were included only in one study. Neither study included 0th harmonics or resistance. The 1st harmonic amplitude motions are included in both studies, showing one order of magnitude larger U_D for KCS (12.3 %D) compared to 5512 (1.1 %D). The reason for the differences needs further investigations.

For calm water resistance, sinkage, and trim, the experimental UA studies are summarized in Table 4.13 from Stern et al. (2000) and Longo and Stern (2005) for individual facilities and from Stern et al. (2004) and Stern et al. (2005) for uncertainties including facility biases. Note that uncertainties at each *Fr* are normalized with the experimental results for individual facilities, and with the average results amongst all facilities for uncertainties including facility biases. Also note that U_D for C_T, C_{T15} and C_R are equivalent as U_k and U_{CF} are not considered. As the table shows, by including facility biases the average uncertainties increase from 1 to 8 %D for resistance and from 8 to 20 %D for trim, while for sinkage the difference is not significant. Note that the differences, especially for resistance, might be partly due to scale effects and not only facility biases since IIHR uses a smaller model.

CFD results for resistance, sinkage, and trim in calm water are summarized in Table 4.17 for CFDShip-Iowa V4/V4.5 studies, showing average error of 3 %, 8 %

Table 4.11 Summary of CFDShip-Iowa verification studies for seakeeping

Study	Geom.	Grid	Code	λ/L ak	Fr	V&V Method	U_T (%S_I) (0th amp, 1st amp, 1st phase)			U_G (%S_I) (0th amp, 1st amp, 1st phase)			U_{SN} (%D) (0th amp, 1st amp, 1st phase)			*Reported* U_T (%D) (0th amp, 1st amp, 1st phase)			*E%D* for amp, *E%360* for phase (0th amp, 1st amp, 1st phase)			
							C_T	z	θ	C_T	z	θ	C_T	z	θ	C_T	z	θ	C_T	z	θ	*motions*
Weymouth et al. (2005)	Wigley	0.11-0.29	CFDShip-Iowa V3	1.25 0.018	0.3	Correction Factor	- 21.44 -	- 5.97 -	- 0.68 -	- 2.84 -	- 0.73 -	- 1.32 -	- 21.63 -	- 6.02 -	- 1.48 -	- 21.77 -	- 6.52 -	- 2.91 -	- 0.84 -	- 6.56 -	- 2.28 -	- 4.42 -
								3.32			1.02			3.75			4.71		0.84	4.42		4.42
							12.38			1.93			12.69			13.24			**2.63**			
Carrica et al. (2007)	DTMB 5512	0.38-2.96	CFDShip-Iowa V4	1.50 0.025	0.28	Correction Factor	-			2.0 -	- -	- -	2.0 -	- -	- -	2.0 -	- -	- -	- -	21.25 2.8 0.3	3.33 2.7 1.2	12.29 2.75 0.75
																						1.75
																				7.45	2.41	7.02
																				4.93		
Simonsen et al. (2008)	KCS	1.8-3.8	CFDShip-Iowa V4	1.15 0.052	0.26	Correction Factor	-			- 1.5 -	- 10.3 -	- 2.6 -	- 1.5 -	- 10.3 -	- 2.6 -	- 10.52 -	- 10.3 -	- 2.6 -	5.57 82.32 1.14 41.71	-5.11 82.33 1.10	143.75 -10.11 -2.56	74.43 12.07 3.29 7.68
											6.45			6.45			6.45		*23.64*	5.93 29.93	53.94	41.05
										3.97			3.97			8.48			**32.34**			
Castiglione et al. (2011)	DELFT Cat.	0.7-5.4	CFDShip-Iowa V4	1.806 0.025	0.75	Correction Factor	-	- 1.54 -	- 0.45 -	- -	- 3.27 -	- 1.66 -	- -	- 3.6 -	- 1.72 -	- -	- 4.39 -	- 3.04 -	- -	- 9.38 -	- 0.12 -	- 4.75 -
								0.99			2.46			2.66			3.71			4.75		4.75
Mousaviraad et al. (2010)	DTMB 5512	2.8-22.1	CFDShip-Iowa V4	0.839-2.977 (*averaged Over frequencies*) 0.025	0.34	Factor of Safety	-	- 5.66 1.97	- 2.20 2.80	- -	- 4.94 2.77	- 4.89 4.81	- -	- 9.07 3.41	- 5.61 5.59	- -	- 9.17 9.12	- 5.77 14.10	- -	- 3.75 2.29	- 2.24 5.26	- 2.99 3.75
								3.81	2.5		3.85	4.85		6.24	5.6		9.14	9.93		3.02	3.75	3.38
								3.15			4.35			5.92			9.53			3.38		
Average (Average fine grid=7M)							- 21.44 -	- 4.39 1.97	- 1.11 2.80	2.0 2.17 -	- 4.81 2.77	- 2.62 4.81	2.0 11.56 -	- 7.25 3.41	- 2.85 5.59	2.0 16.14 -	- 7.59 9.12	- 3.58 14.10	5.57 41.58 1.14	15.44 5.53 7.00	25.98 3.89 3.73	20.71 4.71 5.36
																			21.36			5.03
								3.18	1.95	2.08	3.79	3.71	6.78	5.33	4.22	9.07	8.35	8.84	*13.46*	9.32	11.2	12.87
								2.56			3.75			4.77			8.59			10.26		
							12.0			2.91			5.77			8.83			**13.17**			

Table 4.12 Summary of previous experimental uncertainty studies for heave and pitch in waves

Study	Geom.	Fr	λ/L	$U_D\%D$					$U_D\%2\pi$		
				f	f_e	ζ	TF_{X3}	TF_{X5}	γ_ζ	γ_{X3}	γ_{X5}
Irvine et al. (2008)	DTMB 5512	0.28	1.501	0.6	0.4	0.6	1.02	1.17	3.3	4.6	4.6
							1.095			4.6	
Simonsen et al. (2008)	KCS	0.26	1.15	-	-	-	16.8	7.74	-	-	-
							12.27				
Average				0.6	0.4	0.6	8.91	4.45	3.3	4.6	4.6
							6.68				

Table 4.13 Summary of previous experimental uncertainty studies for calm water sinkage, trim, and resistance for DTMB 5512

Facility Model Size	Fr	$U_D\%D$ Stern et al., 2000 Longo & Stern, 2005			$U_D\%D$ with facility biases Stern et al., 2004 Stern et al., 2005		
		C_{T15}	σ	τ	C_R	σ	τ
DTMB L=5.72m	0.1	1.49	12.2	14.4	11.3	13.4	55.5
	0.28	0.33	5.6	2.8	2.8	5.5	5.5
	0.41	NA	2.5	1.5	NA	4.9	6.6
	Avg.	**0.91**	**6.77**	**6.23**	**7.05**	**7.93**	**22.53**
INSEAN L=5.72m	0.1	2.68	42	32	20.1	43.1	40.9
	0.28	0.64	4.71	4.7	2.1	4.7	8.8
	0.41	0.61	2.93	0.87	6.6	3.0	10.0
	Avg.	**1.31**	**16.55**	**12.52**	**9.60**	**16.93**	**19.9**
IIHR L=3.038m	0.1	1.46	8.72	10.22	14.5	7.6	25.9
	0.28	0.63	1.4	1.83	5.1	1.4	14.6
	0.41	0.6	0.61	1.76	6.5	1.2	16.6
	Avg.	**0.90**	**3.58**	**4.60**	**8.70**	**3.4**	**19.03**
Average	0.1	1.88	20.97	18.87	15.30	21.37	40.77
	0.28	0.53	3.90	3.11	3.33	3.87	9.63
	0.41	0.61	2.01	1.38	6.55	3.03	11.07
	Avg.	**1.04**	**8.96**	**7.79**	**8.45**	**9.42**	**20.49**

and 11 %D for resistance, sinkage and trim, respectively, for $Fr = 0.0 - 1.0$. It must be noted that Xing et al. (2008) and Sadat-Hosseini et al. (2010, 2011) used dynamic range of sinkage and trim to evaluate errors, thus the errors for lower Fr are small. Overall, the results show that the errors are large for smaller Fr compared to larger Fr. Delft catamaran studies (Castiglione et al. 2011; Zlatev et al. 2009) show sinkage and trim errors up to 26 %D for lower Fr. Verification studies using CFDShip-Iowa V4/V4.5 shows averaged $U_{SN} = 2\,\%$, 2 % and 9 %S for resistance, sinkage and trim, respectively. The validation uncertainty levels are 3 %, 11 % and 10 %D. The averaged errors are comparable to validation uncertainty levels. Table 4.15 summarizes the predictions of G2010 calm water submissions discussed in Chap. 2. As shown in Table 4.15, the average error for resistance for the entire Fr range and for both $FX_{\sigma\tau}$ and $FR_{z\theta}$ is about 2.25 %D for G2010 calm water submissions in Chap. 2, which is consistent with CFDShip-Iowa predictions. Note that the average errors shown in Table 4.15 are different with those reported in Chap. 2 as the absolute values for the

errors are used to calculate the averages reported in Table 4.15. For $Fr < 0.2$, the average errors for sinkage and trim are 40 % and 93 %D, respectively. The average errors for $Fr \geq 0.2$ are 8 % and 13 %D for sinkage and trim, respectively, which are consistent with CFDShip-Iowa predictions. The large errors for the motions at lower Fr could be both due to the measurement uncertainties at low speed model test and small absolute D values.

The overall validation of CFD for seakeeping is summarized in Table 4.16. U_T and U_G values for 1st harmonics are from Table 4.11. U_{SN} values for steady calm water and 0th harmonics are from Table 4.14, and for 1st harmonics are calculated from the corresponding U_G and U_T values. U_D values for steady calm water and 0th harmonics are from Table 4.13 including facility biases, and from Table 4.12 for 1st harmonics. U_V values are calculated from U_{SN} and U_D. Error values are included for the current G2010 workshop (test cases 1.4a–c and 2.4). U_T for 1st harmonic amplitude resistance is large (21 %D), which is only from one study using a coarse grid (0.3M). U_G values average about 3 %D. For U_{SN}, again 1st harmonic amplitude resistance is large, as per large U_T. In the view of the average grid size for U_{SN} studies (Table 4.11) being only about 7M, the solutions are likely far from the asymptotic range and therefore U_{SN} values are optimistic. U_D values are large for trim, which is due to large uncertainties at low Fr where the trim is small (Table 4.13). U_{SN}/U_D values show that almost for all variables, U_D is larger than U_{SN}, except for 1st harmonic phase of pitch (θ_{1p}) where they are comparable. Also it can be seen that U_{SN}/U_D values are generally larger for 1st harmonics than steady/0th harmonics. U_V is therefore dominated by U_D. U_V values seem large for trim due to large U_D. Average error values are very large for 0th harmonic motions and 1st harmonic resistance. For 1st harmonic resistance, the large error might be partly due to flexible mount used in the experiments. Validation is achieved for steady resistance at 9 %D interval, for pitch at 22 %D interval, and for 1st harmonic amplitude of heave (z_{1a}) at 11 %D interval.

4.7 Conclusion

Six submissions were available for test case 2.4, as summarized in Table 4.8, only one of which included verification studies (Simonsen et al. 2008 in Table 4.11). The mount used in the experiments allowed small surge motions, which might have affected 1st harmonic resistance. The average errors were larger for conditions where responses were larger, and the total average error was 37 %D as shown in Table 4.8. Average error was smaller for 1st order terms (17 and 8 %D including and excluding X_1) compared to higher order terms (83 %D). Steady simulations in calm water were not included in test case 2.4, except for one submission, and therefore streaming values could not be compared between submissions. The three better codes all had average error around 32 %D while the largest average error was about 50 %D. Increasing the number of grid points seemed to reduce only the resistance error. There was

Table 4.14 Summary of previous CFDShip-Iowa V4/V4.5 resistance, sinkage and trim studies for various geometries

Reference	Geometry	Fr	Grid	Resistance			Sinkage			Trim		
				$\|E_{CT}\|$%D	U_{SN}%S	U_D%D	E_σ%D	U_{SN}%S	U_D%D	$\|E_\tau\|$%D	U_{SN}%S	U_D%D
Carrica et al. (2007)	5415	0.28	3M	4.3		0.64	7.4		4.71	10.4		4.7
		0.41		1.5		0.61	1.5		2.93	1.11		0.87
Xing et al. (2011)	5415	0.28	1.3M	3.7		0.64	9.5		4.71	2.2		4.7
		0.41		4.5		0.61	4.5		2.93	19.3		0.87
Hyman, M. (2010)	5415	0.138	23M	2.5		1.32	13.6		6.57	3.8		7.64
		0.28		3.5		0.64	10.4		4.71	7.7		4.7
		0.41		4.5		0.61	14.4		2.93	6.4		0.87
Xing et al. (2008)	Bare hull Athena	0.2 - 1.0	1M	2.1	2.53	1.5	7.7	1.6	29.3	9.6	15.3	8.1
	Propelled Appended Athena	0.2 - 0.84	2.2M	4.5			8.1			5.0		
Sadat-Hosseini et al. (2010,2011)	ONR Tumble home	0 - 0.6, Roll $\phi = 10°$	3.3M	2.6	0.42		3.62	2.3		14.15	2.4	
		0 - 0.6, Roll $\phi = 20°$	3.3M	2.5			2.47			10.03		
Stern et al. (2007)	HSSL-Delft catamaran	0.2 - 0.65	-	8.0			23.0			17.0		
Castiglione et al. (2011); Zlatev et al. (2009)	Delft catamaran	0.18 - 0.75	5.4M	0.8 - 9.5			11 - 26			6 - 26		
Kandasamy et al. (2010)	DTMB 5594	0.511	1.8M	0.78			0.8			14.3		
	5594, Water Jet self propelled	0.511	1.8M	4.6			9.0			13.7		
Takai et al. (2011)	JHSS, Bare hull	0.34	29M	2.2	3.6	5.8	11.6			13.7		
	JHSS, Water Jet self propelled	0.34	13M	0.2	1.1	1.2	10.27			27.4		
Summary		**0 - 1.0**	**8.4M**	3.0	1.9	1.84	7.92	1.95	10.8	10.63	8.85	5.31

disagreement on EFD data reduction and the submissions were re-evaluated, which resulted in the same trends, but different error values and ranking between codes.

The overall verification and validation for seakeeping is summarized in Table 4.16. U_T is large for 1st harmonic amplitude of X (22 %D) which is only from one study with a coarse grid (0.3M). Without considering 1st harmonic amplitude of X, the average U_T value is about 3 %D. For U_G the average is about 3 %D. The average U_{SN} values are about 5 %D for motions and 9 %D for resistance. Almost for all variables, U_D is larger than U_{SN} and U_V is dominated by U_D. The average U_V is the same for resistance and motions, about 13 %D. Validation is achieved for steady calm water resistance, trim, and 1st harmonic amplitude heave at average intervals of 9 %, 22 % and 11 %D, respectively.

Considering the current workshop seakeeping submissions (test cases 1.4 and 2.4 in Table 4.16), total error is 23 %D. The errors of the CFD predictions are similar for the different geometries (KVLCC2 and KCS), different wavelengths, the linear and steep waves, and for the cases with and without surge motion. The errors are larger for the cases with zero forward speed, possibly due to the measurement and/or URANS difficulties at zero forward speed. Similar trend is observed for all cases, i.e. higher average errors for conditions where responses are larger (See Tables 4.4, 4.6, 4.7 and 4.8), and higher error values for higher order terms (31 %D) compared to 1st order terms (18 %D/13 %D for including/excluding 1st harmonic amplitude of X). Maximum error occurs for 0th harmonic motions (54 %D) followed by 1st harmonics resistance (34 %D) and minimum error occurs for steady calm water resistance (7 %D). For calm water, the error values for the current workshop with $Fr >$ 0.2 are comparable to previous studies (See Table 4.15), but for small $Fr < 0.2$ the errors are much larger. Comparing the average errors of the URANS predictions for the current workshop submissions with the errors for linear potential flow predictions reported in Sadat-Hosseini et al. (2013) and Simonsen et al. (2012) shows that the 1st harmonics of motions are predicted within 14 %D error for URANS while potential flow shows an average error of 20 %D. Also, the 0th harmonic of resistance (and added resistance) is predicted by 18 %D for URANS compared to 24 % for linear potential flow (Fig. 4.10).

5 Case 5.3 Wave Diffraction for DTMB 5415

5.1 EFD Data

The model tests for 1/46.6 scale bare hull 5415 at fixed sinkage and trim towed in head waves were conducted in the IIHR towing tank (Gui et al. 2002; Longo et al. 2007). The flow conditions were $Re = 4.86 \times 10^6$, $Fr = 0.28$, $\sigma = -1.92 \times 10^{-3}$, $\tau = -0.136°$, incident wavelength $\lambda = 1.5 L_{PP}$ and wave steepness $A_k = 0.025$. Data were procured for unsteady resistance, heave force, pitching moment using strain-gage load cell, unsteady free-surface elevations using longitudinal wave cut method with two wave probes, and phase-averaged organized oscillations velocities and

Table 4.15 Summary of current G2010 and previous CFDShip-Iowa V4/V4.5 studies for resistance, sinkage and trim for various geometries

Studies	Geometry	Fr	Grids	Resistance			Sinkage			Trim		
				$\|E_{CT}\|$%D	U_{SN}%S	U_D%D	E_σ%D	U_{SN}%S	U_D%D	$\|E_\tau\|$%D	U_{SN}%S	U_D%D
Gothenburg 2010	KVLCC2, $FX_{\sigma\tau}$	0.1423		1.7			-			-		
	KCS, $FX_{\sigma\tau}$	0.26		0.8±1.0			-			-		
	5415, $FX_{\sigma\tau}$	0.28		2.5±1.6			-			-		
	KVLCC2, $FR_{z\theta}$	< 0.2		2.1			33.3			7.5		
	KCS, $FR_{z\theta}$	< 0.2		1.64			55.6			30.5		
		≥0.2					7.5			3.62		
	5415, $FR_{z\theta}$	< 0.2		3.0			31.4			164.6		
		≥0.2					8.8			23.0		
Average G2010		< 0.2	2.43M	2.25			40.0			93.1		
		≥0.2					8.2			13.3		
CFDShip-Iowa Studies (Table 4-7)	Various, $FR_{z\theta}$	0 - 1.0	8.4M	3.0	1.9	1.84	7.92	1.95	10.8	10.63	8.85	5.31

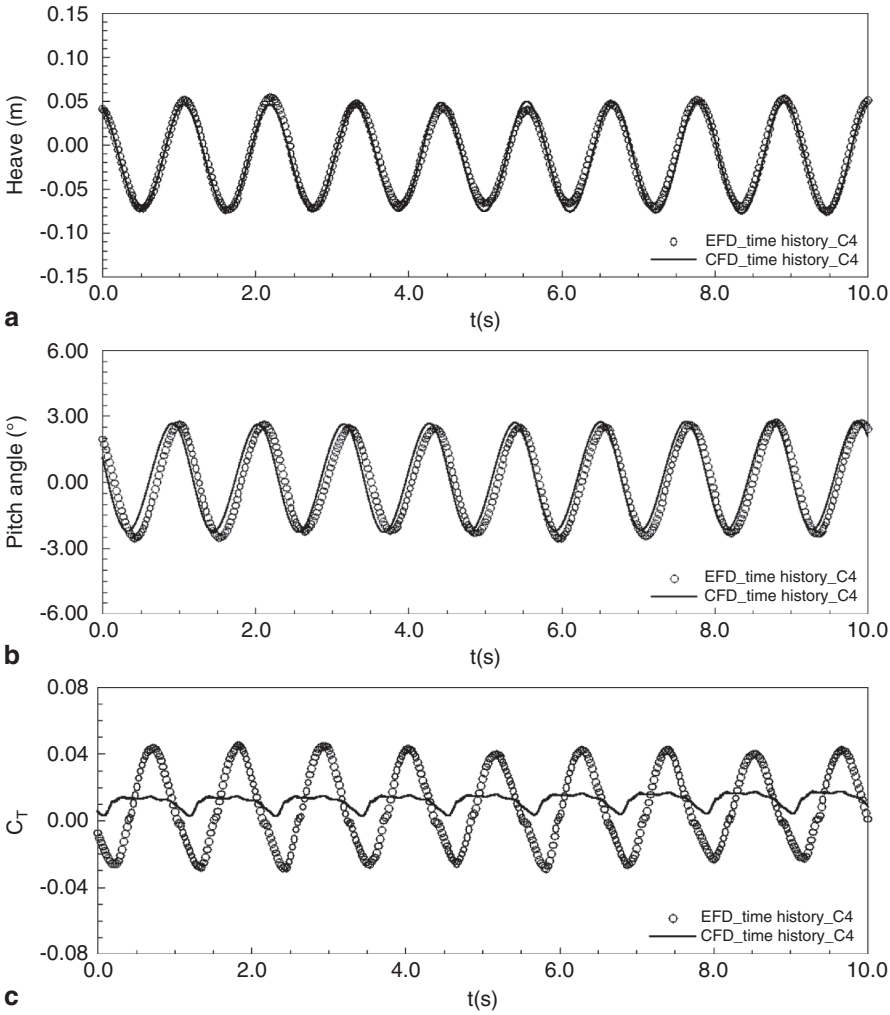


Fig. 4.10 Typical CFD results for test case 2.4 showing solutions from best code (FreSco+) for $Fr = 0.33$ condition. **a** Heave, **b** Pitch, **c** Total Resistance

random fluctuation Reynolds stresses at the nominal wake plane using 2D particle-image velocimetry (PIV). The Reynolds stress data at the nominal wake plane was not used for validation in this or previous workshops (Tokyo 2005 workshop).

Longo et al. (2007) reported experimental uncertainty $U_D = 4.23\,\%\mathrm{D}_1$, $9.76\,\%\mathrm{D}_1$ and $2.93\,\%\mathrm{D}_1$ for $\mathrm{C_T}$, $\mathrm{C_H}$ and $\mathrm{C_M}$, respectively, where D_1 is the first harmonic amplitude. The averaged $U_D = 3.7\,\%\mathrm{D}_1$ and $4.05\,\%\mathrm{D}_2\pi$ for the forces and moment 1st harmonic amplitudes and phases, respectively, where $\mathrm{D}_2\pi = 2\pi$. The averaged $U_D = 3.3\,\%\mathrm{D}_1$ for the free-surface measurements.

Table 4.16 Summary of G2010 seakeeping validation results; amplitudes are $\%D$ and phases are $\%2\pi$; X_s, σ, τ: steady calm water resistance, sinkage, and trim, respectively; X, z, θ, x: resistance, heave, pitch and surge, respectively; 0, 1a, 1p: 0th harmonic amplitude, 1st harmonic amplitude, and 1st harmonic phase, respectively

		U_T	U_G	U_{SN}	U_D	U_{SN}/U_D	U_V	E Case 1.4a Avg. Grid=1.7M	E Case 1.4b Avg. Grid=0.8M	E Case 1.4c Avg. Grid=5.4M	E Case 1.4 Avg. Grid=2.6M	E Case 2.4 Avg. Grid=2.6M	E_{avg} Avg. Grid=2.6M
X_s				1.9	8.45	0.22	8.66	8		8	8.00	6	7.33
σ				1.95	9.42	0.21	9.62	25		2	13.50	6	11.00
τ				8.85	20.49	0.43	22.32	11		4	7.50	4	6.33
X_0				1.9	8.45	0.22	8.66	10	28	15	17.67	21	18.50
z_0				1.95	9.42	0.21	9.62	25	83	25	44.33	83	54
θ_0				8.85	20.49	0.43	22.32	25	83	25	44.33	83	54
x_0										1.82	1.62		
X_{1a}		21.44	2.17	21.55			21.55	35		47	41.00	61	47.67
X_{1p}								35		6	20.50	20	20.33
z_{1a}		4.39	4.81	6.51	8.91	0.73	11.03	10	14	9	11.00	7	10.00
z_{1p}		1.97	2.77	3.4	4.6	0.74	5.72	10	36	20	22.00	3	17.25
θ_{1a}		1.11	2.62	2.85	4.45	0.64	5.28	10	14	9	11.00	7	10.00
θ_{1p}		2.8	4.81	5.57	4.6	1.21	7.22	10	36	20	22.00	3	17.25
x_{1a}										9.01	9.01		
x_{1p}										7.38	7.36		
1st order	*Steady calm water resistance*			1.90	8.45	0.22	*8.66*	8.00		8.00	8.00	6.00	*7.33*
	0th harmonic resistance			1.90	8.45	0.22	*8.66*	10.00	28.00	15.00	17.67	21.00	*18.50*
	1st harmonic resistance	21.44	2.17	21.55			*21.55*	35.00		26.50	30.75	40.50	*34.00*
	1st harmonic motions	2.57	3.75	4.58	5.64	0.83	*7.32*	10.00	25.00	14.50	16.50	5.00	*13.63*
	Average	12.01	2.96	7.48	7.51	0.42	**11.55**	15.75	26.50	16.00	19.42	18.13	**18.37**
Higher order	*Steady calm water motions*			5.40	14.96	0.32	*15.97*	18.00		3.00	10.50	5.00	*8.67*
	0th harmonic motions			5.40	14.96	0.32	*15.97*	25.00	83.00	25.00	44.33	83.00	*54*
	Average	`		5.40	14.96	0.32	**15.97**	21.50	83.00	14.00	33.50	44.00	**31.34**
Overall		12.00	2.96	6.79	11.23	0.37	**13.02**	17.67	54.75	18.13	30.18	26.75	**22.68**

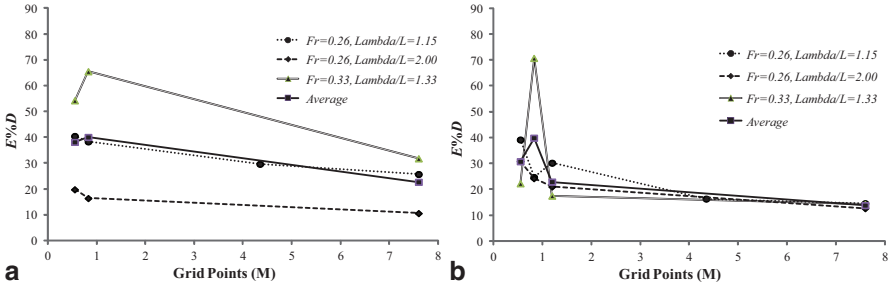


Fig. 4.11 Effects of the grid size on the error for test case 2.4 based on re-evaluated data reduction for: **a** resistance; **b** motions

The experimental data shows that the dominant frequencies of the forces and moment correspond to the imposed wave encounter frequency. The difference between the steady calm water and twice the 0th harmonic is 9 $\%C_T$. The first harmonic is 1.38 % of the steady C_T and the second harmonic is 2.7 % of the first harmonic. The phase angles for maximum C_T, C_H, and C_M correspond to wave crests at $x/L_{PP} = 0.1$, 0.39, and 0.003, respectively, i.e., crests on the fore body for the resistance and pitch moment and near the mid body for the heave force.

As shown in Fig. 4.12, the mean wave elevation displays Kelvin-type transverse and diverging wave patterns. The 1st harmonic amplitude shows a large amplitude crest line and low amplitude trough line diverging from the fore body shoulder ($x = 0.35$) and transom corner, respectively, with a 24.5° angle to the hull center plane. The peak amplitudes are 1.7 times the incident wave amplitude. The crest line leads and the trough line lags the incident wave by $\pi/3$.

5.2 CFD Submissions

Four organizations (ECN, ICARE, France; IIHR, CFDShip-Iowa V4, US; NMRI, SURF, Japan; and SSRC/Univ. of Strathclyde, Fluent 12.2, UK) contributed for this test case. Three of the submissions used in-house research solver, whereas SSRC/Univ. of Strathclyde used commercial software. The solvers are based on either finite-volume or finite-difference methods on collocated grids. Three of the submissions use URANS, whereas CFDShip-Iowa V4 use DES. Turbulence models included standard k-ω, blended k-ω/k-ε SST or explicit algebraic stress. SSRC/Univ. of Strathclyde, Fluent 12.2 also use wall-functions $y^+ = 30 - 50$ for wall-layer modeling. Level-set, VOF or non-linear surface tracking methods are used for free-surface modeling. The convection term discretization is performed using 2nd order upwind and 4th order TVD schemes for URANS and DES, respectively. Implicit 1st or 2nd order schemes were used for time stepping. The pressure equations are either coupled directly with the momentum equations using artificial incompressibility or solved using pressure-correction methods. The submissions use structured grids

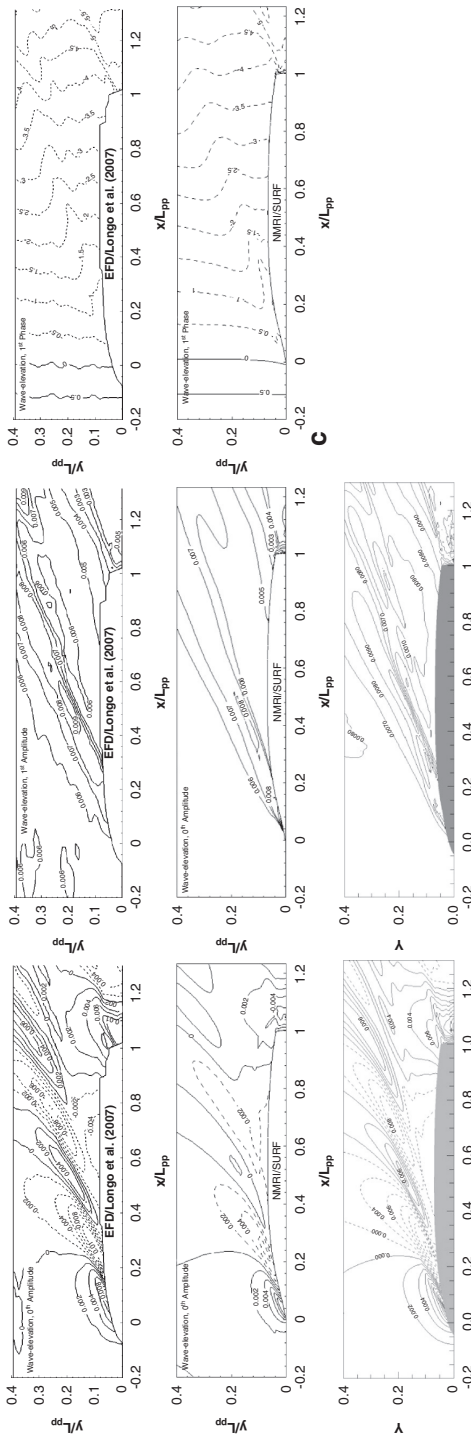


Fig. 4.12 Selected G2010 submissions compared against EFD wave elevation 0th harmonic amplitude (*left* panel), 1st harmonic amplitude (*middle* panel) and 1st harmonic phase (*right* panel) for test case 3.5. **a** EFD. **b** NMRI/SURF, 2.69M grid. **c** CFDShip-Iowa V4, 115M grid

consisting of 0.8–3M points for URANS and a 115M grid for DES. The coarse grid simulations are performed on 16 processors, which required about 500 CPU hours. The large grid simulation was performed on 500 processors, which required 180 K CPU hours. All the CFD submissions are summarized in Table 4.17.

In this chapter, the submissions are compared for forces and moment, and wave elevation predictions. The nominal wake predictions are discussed in Chap. 3.

5.3 Verification

None of the submissions performed verification study.

5.4 Discussion of Results for Test Case 3.5

5.4.1 Unsteady Forces and Moment

The averaged error for all the submissions is 25.7 %. The averaged errors are 28 % and 9.8 % on coarse (up to 3M) and fine grids (115M), respectively. The best predictions are obtained for the heave force followed by the resistance and pitch moment for which errors are 10.05, 23.36 and 47.27 %, respectively.

Overall, the mean values are predicted best, followed by the 1st harmonic amplitude and phases, except for the mean pitch moment for which errors are 88 %D due to small mean values. The coarse grid simulations predicts average $E = 6.4$ %D, 15.2 %D and 40.6 %D for the mean, 1st harmonic amplitudes and 1st harmonic phases, respectively. The large grid simulation shows significant improvements in the forces and pitch moment predictions, where $E = 1.54$ %D, 5.6 %D and 22.2 %D for the mean, 1st harmonic amplitudes and phases, respectively. The errors for the forces and moments mean and 1st harmonic amplitudes are smaller than the averaged experimental uncertainties of 5.6 %D.

Based on the coarse grid CFD predictions, Carrica et al. (2007) suggested that there may be an error in the EFD phases and should lag by 27°. To evaluate how a lag in EFD data affects the CFD errors, we look at $E\%2\pi$, which is a measure of the differences in EFD and CFD phase. When the EFD data lag is used the averaged errors of the CFD predictions for coarse grids for both Tokyo 2005 workshop (Hino, 2005) and Gothenburg 2010 workshop decrease from -10.0 to -2.5 %. However, for the large grid simulations the averaged error changes from -4.42 to $+3.08$ %. Thus, the large grid simulations do not support that EFD data should include a phase lag. Further, the grid resolution significantly improves the phase lag predictions. So, we cannot conclude with certainty whether the large errors for the phases are due to errors in the EFD data or accuracy of the CFD simulations.

Table 4.17 Summary of G2010 submissions for test case 3.5: forward speed diffraction

Submission (Code)	ECN/HOE (ICARE)	IIHR (CFDShip-Iowa) V.4	NMRI (SURF)	SSRC/University of Strathclyde (Fluent12.1),
Country	France	US	Japan	UK
Numerical methods	Finite difference, hybrid collocated/staggered URANS using 2 equation k-ω Non-linear surface tracking 2nd order upwind—convection Implicit, 2nd order—time Direct coupling of pressure-momentum	Finite difference, collocated DES-BKW Level-set 4th order TVD for convection Implicit, 2nd order for time Pressure-correction—Projection	Finite volume, collocated URANS, 2 equation explicit algebraic stress model Level-set 2nd order upwind—convection Implicit, 1st order—time Artificial incompressibility	Finite volume, collocated URANS, BKW, WF, $y^+ = 30\text{-}50$ VOF 2nd order upwind—Convection Implicit, 1st order—time Pressure-correction—SIMPLE
Grids	Single block structured, 800 K points	Structured, overset, 115M	Single block structured, 1.72M	Multi-block structured, 3M
HPC	16 processors, 1040 CPU hours	500 processors, 180 K CPU hours	16 processors, 320 CPU hours	16 processors, 480 CPU hours
Verification	None	None	None	None
Forces and moments mean, amplitude and phase	✓	✓	✓	✓
Wave-elevation ζ_T				
$t/T_e = 0$, 1/4, 1/2, 3/4	✓	✓	✓	Only $t/T_e = 1/2$
0th harmonic amplitude	✓	✓	✓	None
1st harmonic amplitude	✓	✓	✓	None
1st harmonic phase	✓	✓	✓	None

✓Results submitted

5.4.2 Unsteady Wave Elevations

Figure 4.12 compares some selected CFD submissions with EFD to represent the wave elevation predictions on coarse and large grids. The coarse grid submissions predict the Kelvin-type wave pattern near the hull well, but shows diffused and dissipated patterns away from the hull. ECN, ICARE predictions for 0.8M grid shows the worst prediction, where the 0th harmonic amplitude peak and trough are under predicted by up to 40 $\%D$ and fail to capture the 1st harmonic phase. NMRI, SURF on 2.69M grid performs better but predicts 10–20 % lower peaks than EFD.

The large grid IIHR, CFDShip-Iowa V4 simulation shows a significant improvement in the wave elevation pattern, where the Kelvin wave pattern is well defined and the 0th and 1st harmonic amplitudes compare within 2–3 $\%D$ of the experiment. The 1st harmonic phase was not reported, thus is not compared. However, good predictions of the quarter-phase wave elevation suggest that the phases are predicted accurately. The large grid simulation also predicts bow wave breaking and associated scars, which were not predicted by CFDShip-Iowa V4 on coarse grid.

5.4.3 Comparing Submissions

Among the coarse grid submissions, both ECN, ICARE on 0.8M grid and NMRI, SURF on 2.7M grid predictions for resistance and heave forces and pitch moment are comparable, i.e., $E = 26$–$29\,\%D$. The latter performs significantly better than the former in predicting wave elevation. The IIHR, CFDShip-Iowa V4 predictions on a 115M grid significantly improves the forces and moment predictions, and provide very detailed agreement of the wave elevation. The large grid predictions are best among the submissions.

5.5 Comparison with Previous CFD

In the previous Tokyo 2005 workshop (Hino, 2005) workshop, four organizations (ECN, ICARE, France; ECN/CNRS, ISIS, France; CFDShip-Iowa V4, IIHR, US and SVA, nep III, Germany) contributed for this test case. All the submissions used in-house research solvers based on either finite-volume or finite-difference methods on collocated grids. The submissions were for URANS using standard k-ω or blended k-ω/k-ε SST models. For the free-surface treatment level-set, interface tracking or multi-domain formulation based on concentration transport equations were used. Simulations were performed using 2nd order implicit schemes. The grid sized varied from 0.9 to 3M points. SVA, nep III used unstructured grid, whereas other submissions used structured grid.

Verification was performed only by IIHR, CFDShip-Iowa V4. They performed grid and time step verification studies for mean forces and moment and wave-cuts ($y/L_{PP} = 0.082$ and 0.262) following methodology and procedure proposed by Stern

et al. (2001, (2004). The verification studies were performed using refinement ratio $r = 2^{1/2}$. The time step size varied from 0.0366 to 0.00683 and the grid sizes from 0.42 to 3.3M. The time step uncertainties (U_T) were 0.23 %S_1, 1.16 %S_1 and 0.31 %S_1 for C_T, C_H, and C_M, respectively, where S_1 is the solution on the fine grid. The grid uncertainties (U_G) were 6.4 %S_1, 15.96 %S_1 and 1.98 %S_1 for C_T, C_H, and C_M, respectively. The numerical uncertainties ($\sqrt{U_{SN}^2+U_D^2}$) were 6.3 %S_1, 16 %S_1 and 2 %S_1 for C_T, C_H, and C_M, respectively. For the wave-cuts, $U_{SN} = 10$–15 % based on the peak wave elevation.

The submissions predicted the frequencies and amplitudes of the forces and moment reasonably well. As shown in Table 4.18, the averaged errors were $E = 5.8$ %D, 12.12 %D and 50.7 %D for forces and moment 0th and 1st harmonic amplitudes and 1st harmonic phase, respectively, except for C_M 0th harmonic amplitude for which $E = 87$ %D. It must be noted that the large errors for C_M 0th harmonic amplitude are due to small mean values. IIHR, CFDShip-Iowa V4 mean forces and moment were validated, $E \leq U_V = \sqrt{U_{SN}^2+U_D^2}$ at 9.92 %D interval.

Overall wave elevation pattern were predicted well. The mean wave elevation was predicted best by ECN/CNRS, ISIS using low discretization error GDS scheme for the free surface on 2.2M grid, but over predicted the peaks and troughs by 20 %D. The other submissions showed diffused and dissipated wave pattern away from the hull with 20–30 %D lower peaks and troughs. All the submissions predicted the 1st harmonic amplitude and phase contours well, but under predicted the peak amplitude by 10–20 %D.

The errors for the forces, moments and wave-elevations reported in this workshop are comparable to those reported in Tokyo 2005 workshop (Hino, 2005) on similar size grids, i.e., grid resolutions < 3.3M.

5.6 Conclusion

The wave diffraction for 5415, test case 3.5, was previously used in Tokyo 2005 workshop (Hino, 2005) workshop. The EFD data for this case was procured in the IIHR towing tank and the dataset includes forces and moments, unsteady wave elevation and unsteady nominal wake plane unsteady organized velocities and Reynolds stresses. The Reynolds stress data was not used for validation in the workshop, and the nominal wake predictions are discussed in Chap. 3.

The averaged experimental uncertainty $U_D = 5.39$ %D for the mean forces and moment and 1.7 %D for the unsteady velocities. None of the submissions performed V&V study. Previously, Carrica et al. (2006) performed V&V for the mean forces and moment using CFDShip-Iowa V4 in Tokyo 2005 workshop (Hino, 2005) workshop on 0.4–3.3M grids. The averaged numerical uncertainty the mean forces and moment were 8.13 %D and the CFD predictions were validated at $U_V = 9.92$ %D interval.

There are four submissions for the wave diffraction case, three using URANS on coarse grids (1–3M points) and one using DES on a large 115M grid. The averaged

Table 4.18 0th and 1st harmonic amplitudes and 1st harmonic phase of the resistance and moment coefficients for test case 3.5: forward speed diffraction

Submissions		Grids	E_{CT}%D			E_{CT}%2π	E_{CH}%D			E_{CH}%2π	E_{CM}%D			E_{CH}%2π	*Averaged E%D* **(U%)**		
			0th Amplitude	1st Amplitude	1st Phase	*1st Phase*	0th Amplitude	1st Phase	1st Phase	*1st Phase*	0th Amplitude	1st Amplitude	1st Phase	*1st Phase*	0th Amplitude	1st Amplitude	1st Phase
EFD (Longo et al, 2007) (U_D)			**(4.23%)**	**(3.83%)**	**(3.62%)**		**(9.76%)**	**(3.18%)**	**(6.24%)**		**(2.93%)**	**(4.25%)**	**(2.32%)**		**(5.67%)**	**(3.7%)**	**(4.05%)**
Tokyo 2005	ECN(ICARE)	Structured, 0.9M	-3.78	-16.97	67.22	*-11.1*	1.40	-16.70	27.16	*-10.55*	-77.97	-15.13	64.96	*-10.81*	-26.78	-16.27	53.11
															32.0		
	ECN/CNRS(ISIS)	Unstructured, 2.2M	-11.57	-5.11	-	-	7.28	1.29	-	-	-1.69	-9.56	-	-	-1.99	-4.46	-
															3.25		-
	IIHR (CFDShip-Iowa V4) (U_{SN})	Structured 0.4 - 3.3M	-0.32 **(6.4%)**	-7.91	70.21	*-11.7*	0.52 **(16.0%)**	29.98	13.60	*-5.24*	3.39 **(2.0%)**	-13.28	62.29	*-10.37*	1.19	2.93	48.70
															18.0 (8.13%)		
	SVA (nep III)	Structured, 1.4M	-7.14	-11.37	63.12	*-10.3*	14.17	-9.62	24.97	*-9.7*	-272.88	-20.61	62.94	*-10.48*	-88.61	-13.87	50.34
															50.87		
Gothenburg 2010	ECN (ICARE)	Structured, 0.8M	-2.81	-16.94	68.4	*-10.0*	17.66	-19.05	28.57	*-11.11*	-6.91	-25.93	69.39	*-11.33*	2.65	-20.64	55.45
															26.26		
	NMRI (SURF)	Structured, 2.69M	-2.38	-21.55	60.35	*-8.61*	5.99	-15.41	21.43	*-8.33*	-57.9	-26.85	61.39	*-10.02*	-18.10	-21.27	47.72
															28.96		
	SSRC (FLUENT12.1)	Structured, 3M	-12.55	-27.47	58.45	*-8.28*	-2.99	-20.73	13.57	*-11.11*	-205.92	-25.93	14.63	*-9.08*	-73.82	-24.71	28.88
															42.46		
Averaged Error		**1- 3M**	**-5.79**	**-15.33**	**55.39**	***-10.0***	**6.29**	**-7.18**	**18.47**	***-9.34***	**-88.55**	**-19.61**	**47.94**	***-10.5***	**-29.35**	**-14.04**	**40.60**
			25.3				**10.7**				**52.03**				**28.0**		
Gothenburg 2010	IIHR (CFDShip-Iowa V4)	**Structured, 115M**	**0.43**	**-2.3**	**26.54**	*-4.66*	**-1.2**	**-6.16**	**9.29**	*-3.61*	**2.96**	**-8.33**	**30.61**	*-5.0*	**0.73**	**-5.60**	**22.15**
			9.74				**5.53**				**13.96**				**9.78**		

$E\%D = (D\text{-}S)/D \times 100$

errors for the forces and moments are 28 % and 9.8 % on coarse and fine grids, respectively, where the resistance and heave forces are predicted better than the pitch moment. The mean values are predicted best, followed by the 1st harmonic amplitude and the phases, except for the mean moment for which errors are 88 %D due to small mean values. The errors for mean force predictions on coarse grids is validated at $E = 6.04\,\%\mathrm{D} < U_V = 9.92\,\%\mathrm{D}$ interval, and errors for the forces and moments on the large grid using CFDShip-Iowa V4 are validated at $E = 0.73\,\%\mathrm{D} < U_D = 5.39\,\%\mathrm{D}$ interval. Thus mean force predictions are validated at 9.92 %*D* and 5.4 %*D* interval on coarse and large grids, respectively. The coarse grid simulations predict diffused and dissipated Kelvin-type wave pattern with 10–20 % lower peaks than the experimental data. On the other hand, the large grid simulation predicts the unsteady wave elevation within 2–3 % of the EFD.

Overall, the large grid simulations significantly improve resistance and pitch moment predictions as observed in the seakeeping cases. The grid resolutions are also an important factor for improved wave elevation prediction. As pointed out in Chap. 3, hundreds of millions of grid points is not necessary to accurately predict such flows using URANS. Rather more reliable turbulence models, such as anisotropic models, and a relatively finer grid than that used by the submissions would help reduce the numerical diffusion and dissipation, thereby improving numerical predictions. However, for advanced LES/DES models hundreds of millions of grid points are required to achieve expected 80–90 % resolved turbulence levels.

6 Test Case 3.6 Roll-Decay with Forward Speed for 5415

6.1 EFD Data

The model-scale test for 1/46.6 scale 5415 bare hull with bilge keels free to roll-decay advancing in calm water was performed in the IIHR towing tank (Irvine et al. 2004). The flow conditions were $Re = 2.56 \times 10^6$, $Fr = 0.138$, $\sigma = 2.93 \times 10^{-4}$, $\tau = -3.47 \times 10^{-2\circ}$ and initial roll angle $\varphi = 10^\circ$. Data were procured for the forces and moments using strain gage load cell, the unsteady ship roll motion using a Krypton Motion Tracker, the unsteady wave elevation on the starboard side using four servo wave probes, and unsteady velocities at $x/L_{PP} = 0.675$ in a region near bilge keels using 2D PIV system.

Experimental uncertainties are $U_D \leq 2.1\,\%\mathrm{D_R}$ for resistance and pitch moment, but significantly higher $\mathrm{U_D} \geq 12.4\,\%\mathrm{D_R}$ for sway and heave force and yaw moment, where the dynamic range $\mathrm{D_R}$ is used to normalize the uncertainty. The higher uncertainties for the latter were due to restrained motions which results in small dynamic range. $U_D = 1.5\,\%\mathrm{D_R}$ for the roll motion. $U_D = 8\,\%\mathrm{D_1}$ for the wave elevation measurements, where $\mathrm{D_1}$ is the 1st harmonic amplitude. The uncertainties for the velocity measurements were not reported.

The experimental data shows that the roll-decay damping increases with the increase in *Fr* with a plateau for $0.19 \leq Fr \leq 0.34$ due the increase in lift damping with

increasing forward speed, i.e., roll-period decreases with the increase in *Fr*. The presence of bilge keels increases damping and roll period compared to the bare hull case. For $Fr = 0.138$, the bilge keel damps the roll amplitude by 11 % and increases the roll period by 3.7 % compared to the bare hull case. Overall, roll-decay exhibits non-linear damping for $Fr \leq 0.138$ for both with and without bilge keels, and linear damping for higher *Fr*. The time history of C_T shows large amplitude scatter. The averaged C_T tends to increase with the increase in roll angle for $Fr \leq 0.28$, but for higher *Fr* tends to collapse to zero roll angle value. For the present case, the averaged C_T is 7.1 % higher compared to the zero roll angle case.

The unsteady wave field in Fig. 4.14 resembles the steady wave pattern, i.e., Kelvin wave pattern generated by an advancing ship hull, with a superimposed oscillation radiating from the hull shoulder. As the model is rolled fully to the starboard side, a wave trough develops at the shoulder followed by a crest aft of the shoulder. As the model begins to roll to the port side the trough and crest move forward, and the crest is located at the shoulder when the model is rolled fully to the port side. The wave crests and troughs dissipate forward of the model as model rolls, and the amplitudes of the crests and troughs decay with the decay of roll motion.

6.2 CFD Submissions

Four organizations (ECN, ICARE, France; ECN, ISIS, France; GL&UDE/University of Duisburg, OpenFOAM, Gremany; and SSRC/Univ of Strathclyde, Fluent 12.2, UK) contributed for this test case. Three of the submissions use in-house research solver, whereas SSRC/Univ. of Strathclyde use commercial software. ECN, ICARE is based on finite-difference methods, whereas others are based on finite-volume methods on collocated grids. All the submissions are for URANS using standard k-ω or blended k-ω/k-ε SST turbulence models. GL&UDE/University of Duisburg, OpenFOAM and SSRC/Univ. of Strathclyde, Fluent 12.2 also use wall-functions $y^+ = 25$–50 for wall-layer modeling. ECN (ICARE) use non-linear surface tracking methods, whereas the other solvers use VOF for free-surface modeling. All the solvers use moving mesh with re-gridding to predict motions. The convection terms are discretized using 2nd order schemes, and time stepping is performed using implicit 1st or 2nd order schemes. The pressure equations are coupled directly with the momentum equations using artificial incompressibility in ECN (ICARE), but are solved using pressure-correction methods in rest of the submissions. The submissions use structured or unstructured grids consisting of 0.8–5M points. The simulations were performed on 16 to 32 CPU and the averaged CPU time was 700 h. All the CFD submissions are summarized in Table 4.19.

In this chapter, the submissions are compared for resistance, pitch moment, roll-decay motions, and wave elevation predictions. The wake predictions are discussed in Chap. 3.

Table 4.19 Summary of G2010 submissions for test case 3.6: roll-decay

Submission (Code)	ECN/BEC/HOE (ICARE)	ECN/CNRS (ISISCFD)	GL&UDE/Univ. Duisburg (OpenFOAM)	SSRC/University of Strathclyde (Fluent12.1),
Country	France	France	Germany	UK
Numerical methods	Finite difference, collocated URANS using 2 equation k-ω Non-linear surface tracking Moving mesh, regridding 2nd order upwind—convection Implicit, 2nd order—time Direct coupling of pressure-momentum	Finite volume, collocated URANS, BKW VOF Moving mesh, regridding 2nd order Upwind for convection Implicit, 2nd order for time Pressure-correction—SIMPLE	Finite volume, collocated URANS, BKW with WF, $y^+ = 25$–50 VOF Moving mesh, regridding 2nd order TVD—convection Implicit—1st order time Pressure-correction—PISO	Finite volume, collocated URANS, BKW, WF, $y^+ = 30$–50 VOF Moving mesh 2nd order upwind—convection Implicit, 1st order—time Pressure-correction—SIMPLE
Grids	Single block structured, 800 K	Unstructured, 4.9M	Single block unstructured, 1M	Multi-block structured, 3M
HPC	16 processors, 1040 CPU hours	32 processors, 750 CPU hours	16 processors, 320 CPU hours	16 processors, 640 CPU hours
E_{RSS} for force coefficients and roll angle	✓	✓	φ only	✓
Wave-elevation	✓	✓	None	Only at $t/T_e = 3/4$

✓Results submitted

6.3 Verification

None of the submissions performed verification study.

6.4 Discussion of Results for Test Case 3.6

6.4.1 Unsteady Force and Roll-Decay Motion

All the submissions show non-linear oscillations for C_T as observed in EFD. The mean C_T is predicted within 10 %D of the EFD as summarized in Table 4.20. The amplitude and period of the roll motions are predicted within 0.85 %D of the EFD as shown in Fig. 4.13.

6.4.2 Unsteady Wave Elevations

ECN (ICARE) simulation on 0.8M grid failed to predict the Kelvin wave pattern and the development of the wave troughs and crest due to roll motions. SSRC, Fluent 12.1 predictions on 3M grid also showed poor Kelvin wave predictions, and attributed the poor predictions to grid resolution issues. ECN, ISIS predictions on 4.9M grid points in Fig. 4.14 shows overall good agreement with the EFD for the Kelvin wave pattern and the development of wave troughs and crest at the shoulder, but the waves are located closer to the hull and dissipate faster away from the hull. Overall, the wave elevation predictions improve with grid resolution, but for such low *Fr* (which exhibits short Kelvin wave wavelength) even larger grids are required to predict accurately the wave elevation pattern.

6.4.3 Comparing Submissions

All the submissions agree well for C_T predictions. The roll-decay is predicted very well by all the solvers, except for SSRC, Fluent which show 2 % larger amplitudes and larger roll periods for the 4–6th rolls. ECN/CNRS, ISIS predictions on 4.9M grid shows better wave elevation and bilge-keel vortex predictions compared to other simulation on $<$ 3M grids. However, have deficiencies in wave elevation predictions and bilge keel vortex predictions at inception.

6.5 Comparison with Previous CFD

Wilson et al. (2006) performed URANS verification and validation studies using CFDShip-Iowa V3, which uses surface tracking method for free-surface modeling,

Table 4.20 Resistance coefficients and motions for test case 3.6: roll-decay

Submissions		Grids	*E%D*		*Averaged E%D* (**U%**)
			C_T	ϕ	
EFD (Irvine et al, 2004) (***U_D***)			**(1.4%)**	**(1.5%)**	
Wilson et al. (2006)	IIHR (CFDShip-Iowa V3) (***U_{SN}***)	Structured, 0.86 - 2.3M	**-**	0.87 **(0.83%)**	- **(0.83%)**
Gothenburg 2010	ECN (ICARE)	Structured, 0.8M	9.2	0.5	4.85
	ECN/CNRS (ISISCFD)	Unstructured, 4.9M	9.3	0.26	4.8
	GL&UDE/Univ. Duisburg (OpenFOAM)	Unstructured, 1M	-	0.17	-
	SSRC (FLUENT12.1)	Structured, 3M	11.6	2 - 3	7.05
Averaged Error		**1- 5M**	**10.0**	**0.85**	**5.45**

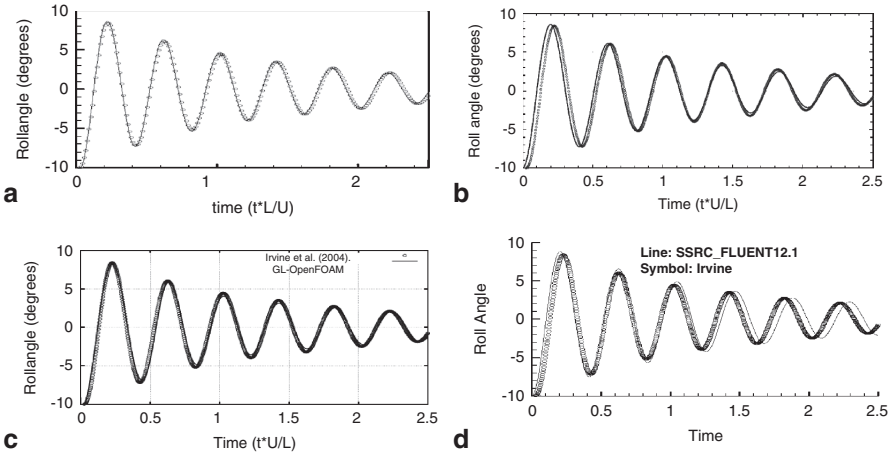


Fig. 4.13 Time histories of roll angle for G2010 submissions for test case 3.6; EFD: *Open circle*, CFD: *Solid line*. **a** ECN/BEC/HO-Icare **b** ECN_CNRS-ISISCFD **c** GL&UDE-OpenFOAM **d** SSRC-FLUENT12.1

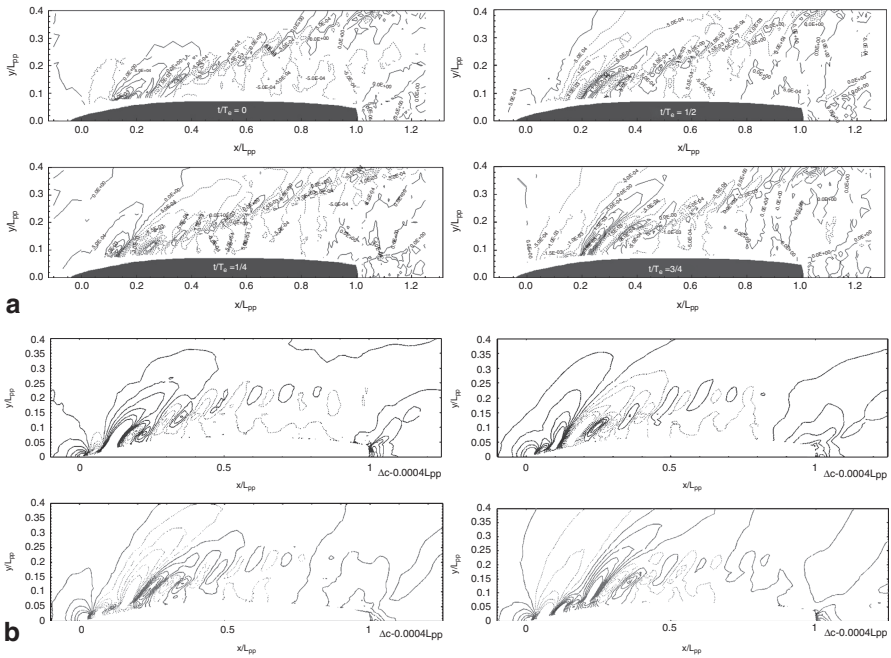


Fig. 4.14 ECN- CNRS, ISIS wave elevation predictions at quarter phases for test case 3.6 compared with EFD data. **a** EFD. **b** ECN- CNRS, ISIS

on 2.3M grid to understand the source of free oscillations and identify the vortical structures for this case. Time step and grid verification studies were performed for roll-decay motion using refinement ratio $r = 2^{1/4}$ following methodology and procedure proposed by Stern et al. (2001). The time step size varied from 0.00841 to 0.01189 and grid sizes from 0.86 to 2.3M. As summarized in Table 4.20, the uncertainties U_T, U_G and U_{SN} were predicted to be 0.63 %S_1, 0.54 %S_1 and 0.83 %S_1, respectively. The roll motion was validated at $U_V = 1.71\,\%D$ interval.

It was identified that the bilge keels do not affect the free-surface development. The viscous and pressure effects on the hull surface, induced by the the roll motion, generate and propagate the free-surface perturbations. During the roll motion, the viscous no-slip boundary conditions induce vertical velocity near the free surface, which induces crest or trough depending on the roll phase, whereas the pressure forces induce transverse velocity causing the oblique wave crest/trough to propagate upstream. The mean Kelvin wave pattern was not well resolved away from the hull, since their wavelength (for such low *Fr*) was quite small in comparison with the grid resolution. The overall agreement between the CFD and EFD predictions were good.

The roll-decay predictions reported in G2010 are comparable to IIHR, CFDShip-Iowa V3 predictions. ECN, ISIS wave elevation predictions on 4.9M grid are similar to IIHR, CFDShip-Iowa V3 predictions, where both show dissipated Kelvin waves away from the hull.

6.6 Conclusion

The EFD data used for this test case were procured in the IIHR towing tank for forces and moments, roll motion, unsteady wave elevation on the starboard side and unsteady velocities in a region close to the bilge keels. In this chapter, the prediction of unsteady forces, roll motion and wave elevation reported by the submissions are discussed. The wake predictions reported in the workshop are discussed in Chap. 3.

The experimental uncertainties $U_D = 1.5\,\%D$ for the resistance and roll motion. None of the submissions performed V&V for this test case. Previously, Wilson et al. (2006) performed by grid and time step verification study for the roll motion using CFDShip-Iowa V3 on 0.89–2.3M grids. The numerical uncertainty for the roll motions were reported to be $U_{SN} = 0.83\,\%$ and the CFD predictions were validated at $U_V = 1.71\,\%$D interval.

There are four URANS submissions on 0.8–4.9M grids for this test case. All the submissions predicted averaged C_T and roll motions within 10 %D and 0.85 %D of the EFD, respectively. The roll motion predictions are validated at $U_V = 1.71\,\%$D interval using the numerical uncertainty reported for CFDShip-Iowa V3 on similar size grids.

The simulations on up to 3M grids show poor predictions of the unsteady wave elevation pattern. ECN/CNRS, ISIS predictions on 4.9M grid, on the other hand, predict the wave pattern well. However, the diverging waves are closer to the hull and the wave elevations are dissipated away from the hull. Overall, the results show

that the force and roll motion predictions are not significantly affected by the large grid resolution, but the wave elevation and local flow predictions are significantly affected.

7 Conclusions

Test cases related to seakeeping are studied including heave and pitch with or without surge motions in regular head waves for KVLCC2 and KCS, wave diffraction for DTMB 5415, and roll-decay with forward speed for DTMB 5415. The EFD data are procured in one or multiple facilities and CFD submissions are compared against the data.

Assessment of CFD predictions for seakeeping in regular head waves separate capability for 1st order vs. higher order terms similarly as done previously for calm water maneuvering. For resistance problem in calm water, the steady resistance X_* is considered 1st order while sinkage and trim are considered 2nd order. For wave cases, X_0 is considered 1st order and z_0/θ_0 are 2nd order using the same reasoning as in calm water. According to linear potential flow, X_1, z_1 and θ_1 are proportional to wave amplitude A, thus they are considered 1st order. However, RANS seakeeping studies in Sadat-Hosseini et al. (2013) and He et al. (2012) showed that X might have large higher order harmonics. Thus, the results are analyzed with both including and separating X from 1st order terms. In addition, problems are reported for EFD measurement for X amplitude for case 1.4b and case 2.4 conducted in Force and NTNU, which supports studying the X amplitude separated from other 1st order terms. For the streaming parameters, they are considered second order and are proportional to A^2.

The average error for resistance for the entire *Fr* range and for both $FX_{\sigma\tau}$ and $FR_{z\theta}$ is about 2.25 %D for G2010 calm water submissions discussed in Chap. 2, which was comparable to previous studies. It should be noted that the average error is different with that reported in Chap. 2 as the absolute values for the errors are used to calculate the averages. For $Fr < 0.2$, the average errors for sinkage and trim are 40 % and 93 %D, respectively. The average errors for $Fr \geq 0.2$ are 8 % and 13 %D for sinkage and trim, respectively, which are consistent with previous studies. The large errors for the motions at lower *Fr* could be due to the measurement uncertainties for low speed model test as the absolute *D* values are small.

For the current G2010 submissions, the total average error for seakeeping in regular head waves is 23 %D, comparable to the average error for previous seakeeping predictions. The errors of the CFD predictions are similar for the different geometries (KVLCC2 and KCS), different wavelengths, the linear and steep waves, and for the cases with and without surge motion. The errors are larger for the cases with zero forward speed, possibly due to the measurement and/or URANS difficulties at zero forward speed. Similar trend is observed for all cases i.e., higher error values for higher order terms (31 %D) compared to 1st order terms (18 %D/13 %D for including/excluding 1st harmonic amplitude of X). For steady calm water resistance, the

average error is 7 %D for submissions corresponding to the seakeeping conditions, compared to 2.25 %D for submissions reported in Chap. 2 and 3 %D for previous studies. The larger errors are due to both the smaller number of calm water submissions in this Chapter and possibly the data since the seakeeping experimental setup is used to measure the calm water resistance. The 0th harmonic of resistance and the 1st harmonic amplitude and phase are predicted by 18 %D and 34 %D, respectively. For motions, the average error is 9 %D for steady calm water submissions corresponding to seakeeping conditions, comparable to the errors for G2010 Chap. 2 submissions and previous studies. The average error is 54 %D for 0th harmonic while it is around 13 %D for 1st harmonic amplitude and phase. Therefore, for resistance, the largest error values are observed for the 1st harmonic amplitude and phase, followed by 0th harmonic amplitude and then steady. For motions, the largest error values are observed for the 0th harmonic amplitudes followed by 1st harmonic amplitude and phase and then steady. For most conditions, the smallest errors are for the submissions with the largest number of grid points. The other submissions usually have higher errors depending on how coarse their grids are. Comparing the average errors of the URANS predictions with those for the potential flow shows that the 1st harmonics amplitude and phase of motions are predicted within 14 %D of the experiment for URANS, while the potential flow shows an average error of 20 %D. The URANS predictions of motions show similar order of error for short, mid-range and long wavelengths and small and large wave amplitudes, while for the potential flow the average error for both heave and pitch reduces to 3.7 %D by excluding the large errors for small motions at short wavelength ($\lambda/L \leq 0.8$). It should be noted that H/λ values were also large for short wavelengths. The 0th harmonic of the resistance (and added resistance) is predicted by about 18 %D for URANS compared to 24 % for potential flow for all the wavelengths. Therefore, URANS showed capability for a wide range of head wave conditions covering short, medium and long waves, small and large amplitude waves and including global and local flow variables; however, with larger errors compared to the potential flow for the motions for medium and long wavelengths and with larger computational cost.

An overall summary of CFD verification and validation for seakeeping in regular head waves is provided in this Chapter including the current G2010 submissions and the previous studies. Time-step uncertainty U_T is large for 1st harmonic amplitude of X (22 %D) which is only from one study with a coarse grid (0.3M). Without considering 1st harmonic amplitude of X, the average U_T value is about 3 %D. The averaged grid uncertainty U_G is also about 3 %D for both motions and resistance. The average numerical simulation uncertainty U_{SN} is about 5 %D for motions and 9 %D for resistance. For most variables, U_D is larger than U_{SN} ($U_{SN}/U_D = 0.4$) and thus U_V is dominated by U_D. The average U_V is the same for resistance and motions, about 13 %D. Validation is achieved for steady calm water resistance, trim, and 1st harmonic amplitude heave at average intervals of 9 %, 22 % and 11 %D, respectively. Both uncertainties and errors are higher for higher order versus 1st order terms. Maximum error occurs for 0th harmonic motions (54 %D) followed by 1st harmonics resistance (34 %D) and minimum error occurs for steady calm water resistance (7 %D). For steady calm water resistance (1st order) and steady calm

Table 4.21 Overall summary of current G2010 and previous CFD studies for different cases/conditions

Case/Condition	Average error (E%D)
Resistance, sinkage, and trim (G2010 and previous)	3.3 % for resistance 10.3 % for motions at Fr $\geq$ 0.2; 44.7 % for motions at Fr 0.2
Seakeeping in regular head waves (G2010 and previous)	18 % for 1st order terms 31 % for higher order terms
Test case 3.5: wave diffraction for DTMB 5415	9.8 % for large grids (115M) 28 % for small grid (1–3M)
Test case 3.6: roll decay with forward speed for DTMB 5415	10 % for resistance 0.9 % for roll motions

water motions (higher order) validation is achieved at average intervals of 9 %D and 16 %D, respectively.

The submissions for the wave diffraction case included coarse 1–3M grids and one 115M grid solution. None of the studies performed verification study. The averaged errors for the forces and moments are 28 and 9.8 % on coarse and fine grids, respectively, where the forces are predicted better than the moments. The mean values are predicted best, followed by the 1st harmonic amplitudes and the phases, except for the mean moment for which errors are 88 %D due to small mean values. The mean forces and moments predictions on coarse grids showed $E = 6.04$ %D and 1.12 %D, respectively. The forces and moments on the large grid showed $E = 0.73$ %D. To estimate the validation interval of the predictions on coarse grids, numerical uncertainties reported in previous workshop on similar size grids, $U_{SN} = 8.1$ %S, are used. For the large grids, only the experimental uncertainty $U_D = 5.39$ %D is considered. The mean forces predicted on coarse grid were validated at $U_V = 9.92$ %D, and the forces and moments on the large grid at 5.39 $\%D$ interval. The large grid calculations outperformed coarse grid in unsteady wave elevation predictions, where the results compared within 2–3 % of the data. Overall, the large grid simulations significantly improve resistance, moment and wave elevation predictions. For URANS simulations, anisotropic turbulence models and a relatively finer grid around 5M are found to be sufficient for good predictions. Whereas, advanced LES/DES models require hundreds of millions of grid points to achieve expected 80–90 % resolved turbulence levels.

The submissions for the roll-decay case used 0.8–4.9M grids, and none of the studies performed verification study. All the submissions predicted averaged C_T and roll motions within 10 %D and 0.85 %D of the EFD, respectively. To estimate the validation interval of the predictions, numerical uncertainties reported in previous workshop on similar size grids, $U_{SN} = 0.83$ $\%S$, are used. C_T is not validated, but the roll motions are validated at $U_V = 1.71$ %D interval. The wave elevation predictions improved with the increase in grid resolution, but the results did not agree very well with the data.

An overall summary of the G2010 submissions discussed in this Chapter and the related previous CFD studies is provided in Table 4.21. For calm water simulations, the average error for resistance (1st order) is about 3 %D for G2010 and previous

simulations. For low speed Fr < 0.2, the average error for motions are large (45 %D) perhaps due to the measurement uncertainties for low speed model test as the absolute D values are small, whereas for Fr ≥ 0.2 the average error for motions is about 10 %D. For seakeeping simulations in regular head waves, the total average error is 23 %D. The average error values are 18 and 31 %D for 1st order and higher order terms, respectively. For wave diffraction submissions, the large grid DES simulation predicts an average error value of less than 10 %D, while for the small grid size URANS simulations the average error is 28 %D. For roll decay submissions, the average error values are 10 %D for resistance and less than 1 %D for roll motions.

Several issues need to be resolved for further assessment of CFD predictions for seakeeping. (1) additional experimental uncertainty analysis is required, including multiple facilities; (2) consensuses are needed on the best normalization and averaging for the errors for small values such as sinkage and trim and motions in short waves, e.g., %D vs. %DR and mean error vs. E_{RSS}; (3) verification studies are needed to estimate numerical uncertainties, including comparisons between currently used verification procedures; (4) experimental measurements require additional care for the head wave resistance, small sinkage and trim values, and Fourier coefficient analysis; and (5) more studies are required for zero forward speed issues and under resolved peaks of motions. Also, the capability of URANS codes for seakeeping applications should be investigated in future for the self-propelled ship, irregular waves, oblique waves, large wave amplitudes, zero forward speed, and for more mid-range wavelength (frequency) conditions to better define the ship motions curve.

Acknowledgement The research at Iowa was sponsored by Office of Naval Research under Grant Nos. N00014-01-1-0073 and N00014-06-1-0420 administered by Dr. Patrick Purtell. The authors would like to thank Dr. Dave Kring, Dr. Arthur Reed and Prof. Bob Beck for their helpful comments, especially Prof. Beck who patiently went through several iterations, which clarified our analysis and conclusions.

References

Beck RF, Reed AM (2000) Modern computational methods for ships in a seaway. Proceedings of 23rd ONR Symposium on Naval Hydrodynamics, Val de Reuil, France

Belknap W, Bassler C, Hughes M (2010) Comparisons of body-exact force computations in large amplitude motion. 28th Symposium on Naval Hydrodynamics, Pasadena, California

Bunnik T, Daalen EV, Kapsenberg G, Shin Y, Huijsmans R, Deng G, Delhommeau G, Kashiwagi M, Beck B (2010) A – comparative study on state-of-the-art prediction tools for seakeeping. 28th Symposium on Naval Hydrodynamics, Pasadena, California

Carrica PM, Wilson RV, Stern F (2006) Unsteady RANS simulations of the ship forward speed diffraction problem. Comput Fluids 35(6):545–570

Carrica PM, Wilson RV, Noack RW, Stern F (2007) Ship motions using single-phase level set with dynamic overset grids. Comput Fluids 36(9):1415–1433

Carrica PM, Fu H, Stern F (2010) Self-propulsion free to sink and trim and pitch and heave in head waves of a Kcs model. Proceedings of Gothenburg 2010: A Workshop on CFD in Ship Hydrodynamics, Gothenburg, Sweden

Castiglione T, Stern F, Bova S, Kandasamy M, (2011) Numerical investigation of the seakeeping behavior of a catamaran advancing in regular head waves. Ocean Eng 38(16):1806–1822

Deng GB, Leroyer A, Guilmineau E, Queutey P, Visonneau M, Wackers J (2010) Verification and validation for unsteady computation. Proceedings of Gothenburg 2010: A Workshop on CFD in Ship Hydrodynamics, Gothenburg, Sweden

Fabbri L, Campana E, Simonsen C (2011) An experimental study of the water depth effects on the KVLCC2 tanker. AVT-189 Specialists Meeting on Assessment of Stability and Control Prediction Methods for NATO Air and Sea Vehicles, Portsdown West, UK

Faltinsen OM (1990) Sea loads on ships and offshore structures. Cambridge University press, Cambridge

Fossen TI (2005) A nonlinear unified state-space model for ship maneuvering and control in seaways. J Bifurcat Chaos. doi:10.1142/S0218127405013691

Fossen TI (2011) Handbook of marine craft hydrodynamics and motion control. John Wiley & Sons Ltd

Gui L, Longo L, Metcal B, Shao J, Stern F (2002) Forces, moment, and wave pattern for naval combatant in regular head waves-part 2: measurement results and discussions. Exp Fluids 32(1):27–36

He W, Diez M, Peri D, Campana EC, Tahara Y, Stern F (2012) URANS study of delft catamaran total/added resistance, motions and slamming loads in heading sea including irregular wave and uncertainty quantification for variable regular wave and geometry. 29th Symposium on Naval Hydrodynamics Gothenburg, Sweden, 26–31 August 2012

Hino T (ed.) (2005) Proceedings of CFD workshop, NMRI report, Tokyo 2005

Hyman M (2010) Gothenburg 2010 submission for Case 3.2 using CFDShip-Iowa V4. Proceedings of Gothenburg 2010: A Workshop on CFD in Ship Hydrodynamics, Gothenburg, Sweden

Irvine M, Longo J, Stern F (2004) Towing tank tests for surface combatant for free roll decay and coupled pitch and heave motions. Proceedings of 25th ONR Symposium on Naval Hydrodynamics, St Johns, Canada

Irvine M, Longo J, Stern F (2008) Pitch and heave tests and uncertainty assessment for a surface combatant in regular head waves. J Ship Res 52(2):146–163

Kandasamy M, Ooi SK, Carrica PM, Stern F (2010) Integral force/moment water-jet model for CFD simulations. J Fluid Eng 132:101103-1-9

Kashiwagi M (2009) Impact of hull design on added resistance in waves—application of the enhanced unified theory. Proceedings of the 10th International Marine Design Conference, Trondheim, Norway, pp 521–535

Joncquez SAG (2009) Second-Order Forces and Moments acting on Ships in Waves. PhD Thesis, Technical University of Denmark, Denmark

Kim WJ, Van SH, Kim DH (2001) Measurement of flows around modern commercial ship models. Exp Fluids 31:567–578

Larsson L, Stern F, Visonneau M (eds) (2010) Gothenburg 2010: a workshop on numerical ship hydrodynamics. Gothenburg, Sweden

Longo J, Stern F (2005) Uncertainty assessment for towing tank tests with example for surface combatant DTMB model 5415. J Ship Res 49(1):55–68

Longo J, Shao J, Irvine M, Stern F (2007) Phase-averaged PIV for the nominal wake of a surface ship in regular head waves. J Fluid Eng 129:524–540

Mousaviraad SM, Carrica PM, Stern F (2010) development and validation of harmonic wave group single-run procedure for RAO with comparison to regular wave and transient wave group procedures using URANS. Ocean Eng 37(8):653–666

Sadat-Hosseini H, Stern F, Olivieri A, Campana E, Hashimoto H, Umeda N, Bulian G, Francescutto A (2010) Head-waves parametric rolling of surface combatant. Ocean Eng 37(10):859–878

Sadat-Hosseini H, Carrica PM, Stern F, Umeda N, Hashimoto H, Yamamura S, Mastuda A (2011) CFD, system-based and EFD study of ship dynamic instability events: surf-riding, periodic motion, and broaching. Ocean Eng 38(1):88–110

Sadat-Hosseini H, Wu PC, Carrica PM, Kim H, Toda Y, Stern F (2013) CFD verification and validation of added resistance and motions of KVLCC2 with fixed and free surge in short and long head waves. Ocean Eng 59:240–273

Singh SP, Sen D (2007) A comparative linear and nonlinear ship motion study using 3-D time domain methods. Ocean Eng 34:1863–1881

Simonsen CD, Otzen JF, Stern F (2008) EFD and CFD for KCS heaving and pitching in regular head waves. Proceedings of 27th ONR Symposium on Naval Hydrodynamics, Seoul, Korea

Simonsen CD, Otzen JF, Joncquez S, Stern F (2012) EFD and CFD for KCS heaving and pitching in regular head waves. submitted to Ocean Engineering

SIMMAN (2014) http://www.simman2014.dk.

Stern F, Longo J, Penna R, Oliviera A, Ratcliffe T, Coleman H (2000) International collaboration on benchmark CFD validation data for naval surface combatant. Invited Paper: Proceedings of 23rd ONR Symposium on Naval Hydrodynamics, Val de Reuil, France

Stern F, Wilson RV, Coleman H, Paterson E (2001) Comprehensive approach to verification and validation of CFD simulations-part 1: methodology and procedures. J Fluid Eng 123(4):793–802

Stern F, Olivieri A, Shao J, Longo J, Ratcliffe T (2004) Statistical approach for estimating intervals of certification or biases of facilities or measurement systems including uncertainties. IIHR-Hydroscience & Engineering, The University of Iowa, IIHR Report No 442, pp 67

Stern F, Olivieri A, Shao J, Longo J, Ratcliffe T (2005) Statistical approach for estimating intervals of certification or biases of facilities or measurement systems including uncertainties. J Fluid Eng 127:604–610

Stern F, Carrica P, Kandasamy M, Gorski J, O'Dea J, Hughes M, Miller R, Kring D, Milewski W, Hoffman R, Cary C (2007) Computational hydrodynamic tools for high-speed sealift. Trans Soc Naval Archit Marine Eng 114:55–81

Stern F, Agdrup K, Kim SY, Hochbaum AC, Rhee KP, Quadvlieg F, Perdon P, Hino T, Broglia R, Gorski J (2011) Experience from SIMMAN 2008—the first workshop on verification and validation of ship maneuvering simulation methods. J Ship Res 55(2):135–147

Takai T, Kandasamy M, Stern F (2011) Verification and validation study of URANS simulations for an axial waterjet propelled large high-speed ship. J Mar Sci Technol 16(4):434–447

Tarafder S (2007) Third order contribution to the wave-making resistance of a ship at finite depth of water. Ocean Eng 34(1):32–44. (January 2007)

Tarafder S, Khalil G (2006) Calculation of ship sinkage and trim in deep water using a potential based panel method. Int J Appl Mech Eng 11(2):401–414

Toxopeus S, Simonsen C, Guilmineau E, Visonneauc M, Stern F (2011) Viscous-flow calculations for KVLCC2 in manoeuvring motion in deep and shallow water. AVT-189 Specialists Meeting on Assessment of Stability and Control Prediction Methods for NATO Air and Sea Vehicles, Portsdown West, UK

Weymouth G, Wilson R, Stern F (2005) RANS CFD predictions of pitch and heave ship motions in head seas. J Ship Res 49:80–97

Wilson RV, Carrica PM, Stern F (2006) Unsteady RANS method for ship motions with application to roll for a surface combatant. Comput Fluids 35(5):419–451

Xing T, Carrica P, Stern F (2008) Computational towing tank procedures for single run curves of resistance and propulsion. J Fluid Eng 130(10):1–14

Xing T, Carrica P, Stern F (2011) Developing streamlined version of CFDShip-Iowa-4.5. IIHR-Hydroscience & Engineering, The University of Iowa, IIHR Report No. 479, pp 63

Zlatev Z, Milanov E, Chotukova V, Sakamoto N, Stern F (2009) Combined model-scale EFD-CFD investigation of the maneuvering characteristics of a high speed catamaran. Proceedings of FAST 2009: The 10th International Conference on Fast Sea Transportation, Athens, Greece

Chapter 5
A Verification and Validation Study Based on Resistance Submissions

Lu Zou and Lars Larsson

Abstract In Chap. 5 the database of ship total resistances submitted to the workshop is used to evaluate the error and uncertainty by means of a systematic verification and validation (V&V) study along with statistical investigations. Three representative methods are applied for verification: Grid Convergence Index, Factor of Safety and Least Squares Root. Validation of the results is carried out by the ASME V&V 20-2009 Standard. It is found that the iterative convergence is an important aspect in the numerical computation due to its contribution to the numerical uncertainty and its influence on the determination of discretization uncertainty. A limit for the iterative error is proposed. In the grid convergence study, unstructured grids are shown to more seldom achieve monotonic convergence than the structured grids. 2 to 10 million grid points and a grid refinement ratio 1.2 are most common among the research groups. In the study of structured grids using different verification methods, most solutions achieve monotonic convergence and are in the vicinity of the asymptotic range. Similar uncertainties are then predicted by the three methods. For cases further from the asymptotic range the methods predict quite different uncertainties. The scatter in solutions is an issue which is shown to significantly affect the determination of the grid convergence and the order of accuracy. In the validation study, the numerical error is mostly larger than the experimental error. Most solutions are estimated to have a smaller comparison error than validation error, implying that the modeling error is buried in the numerical and experimental noise.

Acronyms

CD-adapco:	CD-adapco, Germany
CEHINAV:	Model Basin of Naval Architecture Department (CEHINAV) of the Universidad Politécnica de Madrid
CSSRC:	China Ship Scientific Research Center

L. Zou (✉) · L. Larsson
Chalmers University of Technology, Gothenburg, Sweden
e-mail: luzou@sjtu.edu.cn

L. Zou
Shanghai Jiao Tong University, Shanghai, China

L. Larsson
e-mail: lars.larsson@chalmers.se

L. Larsson et al. (eds.), *Numerical Ship Hydrodynamics,*
DOI 10.1007/978-94-007-7189-5_5, © Springer Science+Business Media Dordrecht 2014

HSVA:	Hamburg Ship Model Basin
MARIC:	Marine Design & Research Institute of China
MARIN:	Maritime Research Institute Netherlands
MOERI:	Maritime & Ocean Engineering Research Institute
NavyFOAM:	Naval Surface Warfare Center Carderock Division
NMRI:	National Maritime Research Institute
NTNU:	Norwegian University of Science and Technology
Southampton/QinetiQ:	University of Southampton, QinetiQ Ltd
SSPA:	SSPA Maritime Consulting AB
SVA:	Potsdam Model Basin
TUHH&ANSYS:	Hamburg University of Technology & ANSYS Germany
UoGe:	Marine CFD Group, University of Genova
VTT:	VTT Technical Research Centre of Finland

1 Introduction

In the ship hydrodynamics community, the series of international Workshops on Numerical Ship Hydrodynamics (1980, 1990, 2000 and 2010 in Gothenburg; 1994 and 2005 in Tokyo) is well known for its assessments of state-of-the-art Computational Fluid Dynamics (CFD) computations in ship hydrodynamics. The focus of such assessments is mainly on the level of accuracy in CFD computations, combined with a comparison of computational methods (e.g. governing equations, turbulence model, boundary conditions, grid resolution, numerical approach), as well as computing expense. In past workshops, the accuracy of a CFD computation was evaluated simply through a comparison between the numerical solution and the experimental data, as was commonly done in the community at the time. The detailed relationship between the computational method and accuracy was normally somewhat unclear, and the reason for such low accuracy was thus difficult to understand. The situation changed with the Gothenburg Workshop in 2000, at which errors and uncertainties were for the first time estimated through formal verification and validation (V&V) studies. Since that time formal V&V studies have been requested at the workshops.

Documentations indicate that each workshop attracted a great number of participants and submissions than prior workshops. With regard to the V&V for resistance predictions, the first three V&V test cases appeared at the 2000 Gothenburg CFD Workshop (Larsson et al. 2002) for three designated benchmark hull forms (KVLCC, KCS and DTMB 5415), with half of the 20 participants providing the numerical uncertainties; five years later at the Tokyo CFD Workshop (Hino 2005), involving 24 research groups, eleven submitted the uncertainties for five test cases; and at the most recent Gothenburg 2010 Workshop (Larsson et al. 2010), the number of V&V test cases reached nine, a total of 33 research groups attended and 16 of them submitted V&V results. Since the submissions differ in various ways and cover a huge amount of information, the many submissions in 2010 establish a valuable database for a V&V study. To better evaluate the computed results in terms of V&V and to help

understand the accuracy in CFD computations, it is worthwhile to make use of this database to dig more deeply into numerical solutions and evaluations of the accuracy by means of a comprehensive V&V study accompanied by a statistical analysis, on which this Chapter will report.

2 V&V Methods

The CFD technique has gradually become a powerful tool for dealing with real physical problems. In the past decade in particular, the rapidly developing computer technology has greatly facilitated the application of CFD techniques and extended it to more difficult and complicated problems. Since the real problem is not solved directly but through 'modeling' based on mathematical equations, the degree of accuracy, in other words the error and uncertainty (an interval within which the error probably falls), during the CFD computational process is therefore usually a significant concern. Currently, verification and validation tend to be useful for quantifying numerical and modeling errors in CFD computations, as well as for establishing the credibility of the CFD method and its solutions. The classical interpretation of V&V (Roache 1998) defines verification as 'solving the equations right' and validation as 'solving the right equations'. In more specific terms, verification consists of code verification followed by solution verification. The former determines that a CFD code solves the mathematical equations correctly, and enables the evaluations of errors to be controlled in the light of a known benchmark solution (e.g. manufactured solution). Solution verification estimates the numerical error and uncertainty in the computation of a particular problem, the solution to which is unknown. The interest in a verification process is very often concentrated on the solution verification, since it is normally assumed that the code has been developed correctly and that code verification has been made prior to the practical application of a CFD code. In practical applications, solution verification estimates the numerical error and uncertainty, in which the most important issue is determining the iterative and discretization error and uncertainty. Although several techniques are available (Roache 1998), a so-called grid convergence study is normally used. Preceded by verification, validation is a process that controlling the numerical solution against the appropriate experimental data, in order to reveal the error and uncertainty from both numerical and modeling deficiencies.

The development of a standard V&V method has been a topic of research for a long time. Several constructive V&V methods based on Richardson Extrapolation (RE) have been put forward in the past decade. Roache (1998) introduced a Grid Convergence Index (GCI) using a factor of safety to estimate numerical uncertainty; the International Towing Tank Conference (ITTC 1999, 2002, 2008) based on the approach by Stern et al. (2001) recommended an uncertainty assessment methodology, in which the error and uncertainty are estimated by means of a correction factor that takes the closeness to the asymptotic range into consideration; Eça and Hoekstra (2002, 2006a) developed a method based on RE and GCI, but employing a

Least Squares Root approach (denoted as the LSR method in this paper) to take the numerical scatter into account; following the previous work by Stern et al. (2001), Xing and Stern (2008, 2009, 2010, 2011) established a Factor of Safety (FS) method, which improves the measure of the distance from the asymptotic range and the error/uncertainty estimate. The American Society of Mechanical Engineers (ASME) V&V 20 Committee (2009) released an elaborate standard by introducing a definition of error and uncertainty, as well as the detailed concept of verification and validation, combined with specific examples. The objective is to specify standard verification and validation methods that quantify the degree of accuracy in computational fluid dynamics and computational heat transfer.

Apparently, existing V&V methods differ in features and performance, thus leading to a variety of V&V observations. The series of Lisbon Workshops on CFD Uncertainty Analysis (2004, 2006 and 2008) succeeded in applying the systematic V&V method to computations for a classical simple turbulent flow case: the flow over a backward-facing step. A promising performance of V&V to quantify accuracy in CFD computations was demonstrated. However, the application of V&V to complex turbulent flow or more practical fluid dynamics problems, e.g., ship hydrodynamics, is still limited. The comprehensive V&V test cases and submissions to the 2010 CFD Workshop make a systematic V&V study to evaluate practical ship resistance predictions feasible. The present study intends to adopt systematic V&V to investigate all CFD solutions of the workshop test cases. The three most well-known verification methods and a validation procedure are applied. The methods are described as follows:

2.1 Verification Methods

This section introduces the verification methods for estimating the numerical uncertainty U_{SN} in the computations of total ship resistance. Assuming that the round-off error is negligible so that the contribution to the numerical error mainly comes from the iteration and grid discretization, yields a numerical uncertainty of: $U_{SN}=\sqrt{U_I^2+U_G^2}$. U_I is the iterative uncertainty attributed to the lack of convergence in the iteration process, and U_G is the grid discretization uncertainty caused by the limited grid resolution. For a well-converged computation, the contribution of the former uncertainty U_I should approach a negligible level, and was already estimated by each individual participant. The emphasis of the present verification study is on the determination of the latter: the grid discretization uncertainty U_G investigated through a grid convergence study. The first method is the classical Grid Convergence Index (GCI) by Roache (1998), which also forms the basis of the FS and LSR methods. GCI starts with determining the grid convergence by RE after which the uncertainty estimate can be determined from the absolute value of the RE error δ_{RE} and a factor of safety F_S:

$$U_{SN} = F_S\,|\delta_{RE}| \tag{5.1}$$

F_S is an empirical value, Roache recommended $F_S = 3$ for two-grid studies and $F_S = 1.25$ for studies with at least three grids.

The second method is the updated FS method by Xing and Stern (2010); and the final one is the LSR method developed and revised by Eça et al. (2010a, b). All methods establish the numerical errors and uncertainties based on the computations of systematic grid refinement. The basic descriptions of the FS and LSR methods are given below, coupled with some RE details.

2.1.1 FS Method

This method assumes that iterative convergence has been achieved to make the iterative uncertainty at least one order-of-magnitude smaller than the grid discretization uncertainty. Thus, it will not influence the determination of the latter. In the convergence study, three systematic similar grids (to be used as a triplet) are computed and the uniform refinement ratio r_G defined as: $r_G = \frac{h_2}{h_1} = \frac{h_3}{h_2}$, where h_3, h_2, h_1 denote the grid spacing of the coarse, medium and fine grid, respectively (for non-uniform refinement $r_G^{12} = \frac{h_2}{h_1}, r_G^{23} = \frac{h_3}{h_2}$). The corresponding computed solutions are represented by S_3, S_2, S_1, and the solution changes of two successive grids are defined as: $\varepsilon_{12} = S_2 - S_1$, $\varepsilon_{23} = S_3 - S_2$. The convergence ratio R has the form: $R = \varepsilon_{12}/\varepsilon_{23}$.

Based on the R value, the state of discretization convergence can be classified as:

1. Monotonic convergence: $0 < R < 1$
2. Oscillatory convergence: $R < 0, |R| < 1$
3. Monotonic divergence: $R > 1$
4. Oscillatory divergence: $R < 0, |R| > 1$

Only for the monotonic convergence $0 < R < 1$, the generalized Richardson Extrapolation (RE) can be used to express the numerical solution with a form of power series, which results in (e.g., considering the leading term alone):

$$S_i = S_0 + \alpha h_i^p \tag{5.2}$$

where S_i is the solution to the ith grid ($i = 1, 2, 3$), S_0 is the extrapolated solution to zero step size, h_i represents the step size (grid spacing) of the ith grid, α is a constant, and p is the order of accuracy. From Eq. (5.2), the order of accuracy p and the error δ_{RE} in numerical solutions of systematically refined grids can be derived as:

$$p = \frac{\ln(\varepsilon_{23}/\varepsilon_{12})}{\ln(r_G)}, \quad \delta_{RE} = S_1 - S_0 = \frac{\varepsilon_{12}}{r_G^p - 1} \tag{5.3}$$

Theoretically, the converged solutions should be within the asymptotic range where the attained order of accuracy, p, equals the theoretical one designated in the numerical method, p_{th}, i.e., $p = p_{th}$. However, in practical applications, solutions are often out of the asymptotic range ($p > p_{th}$ or $p < p_{th}$). Stern et al. (2001) and Xing and Stern (2008, 2009, 2010) assumed this is due to the coarseness of the grid, and Xing and Stern (2010) used the distance metric P to define the distance of solutions

from the asymptotic range, where: $P = p/p_{th}$. Then, the error estimate is defined as: $\delta = P \cdot \delta_{RE}$

To estimate the numerical uncertainty U_{SN}, the FS method adopts the general form proposed by Roache (1998): $U_{SN} = F_S|\delta_{RE}|$, but considers three factors of safety according to the P value: F_{S0} ($P = 0.0$), F_{S1} ($P = 1.0$), F_{S2} ($P = 2.0$). The uncertainty estimate in the FS method is formulated below:

$$U_{SN}^{FS} = F_S(P)|\delta_{RE}| = \begin{cases} [F_{S1} \cdot P + F_{S0} \cdot (1 - P)]|\delta_{RE}|, & 0 < P \leq 1 \\ [F_{S1} \cdot P + F_{S2} \cdot (P - 1)]|\delta_{RE}|, & P > 1 \end{cases} \tag{5.4}$$

Based on statistical analysis (Xing and Stern 2010), $F_{S0} = 2.45$, $F_{S1} = 1.6$, $F_{S2} = 14.8$ are recommended in the method, produces the following:

$$U_{SN}^{FS} = F_S(P)|\delta_{RE}| = \begin{cases} (2.45 - 0.85P)|\delta_{RE}|, & 0 < P \leq 1 \\ (16.4P - 14.8)|\delta_{RE}|, & P > 1 \end{cases} \tag{5.5}$$

2.1.2 LSR Method

This method is characterized by including more than three grid densities, considering the scatter among numerical solutions and using a curve fit by the Least Squares Root approach to determine the order of accuracy and the numerical error. It is designed for computations with a theoretical second order of accuracy (assuming the theoretical order of accuracy $p_{th} = 2.0$). The procedure is based on the RE and the GCI.

In the LSR method, the discretization error is denoted by ε_{RE}, following the general RE form:

$$\varepsilon_{RE} \approx \delta_{RE} = S_i - S_0 = \alpha h_i^p \tag{5.6}$$

where $i = 1, 2 \ldots n_g$, n_g: available number of grids, $n_g > 3$.

To determine the three unknowns (S_0, α, p) in the equation above, at least three solutions are needed. For more than three solutions, the observed order of accuracy p can be estimated through the curve fit of the Least Squares Root approach minimizing the following function (Eça and Hoekstra 2006a):

$$f(S_0, \alpha, p) = \sqrt{\sum_{i=1}^{n_g} \left(S_i - \left(S_0 + \alpha {h_i}^p\right)\right)^2} \tag{5.7}$$

The convergence condition is then decided, following the rules below:

1. Monotonic divergence: $p < 0$
2. Monotonic convergence: $p > 0$
3. Oscillatory convergence: $n_{ch} \geq \text{INT}(n_g/3)$, where n_{ch} is the number of triplets with $(S_{i+1} - S_i)(S_i - S_{i-1}) < 0$
4. Otherwise, anomalous behavior

Considering the fact that the determination of p considerably depends on the scatter in the solutions, the estimation of the numerical error ε_{RE} in this method not only derives from δ_{RE}. Instead, three alternative error estimates are introduced (the first two estimators are obtained from a curve fit as well) (Eça et al. 2010a):

$$\delta_{RE}^{02} = S_i - S_0 = \alpha_{02} h^2 \tag{5.8}$$

$$\delta_{RE}^{12} = S_i - S_0 = \alpha_{11} h + \alpha_{12} h^2 \tag{5.9}$$

$$\begin{aligned} \delta_{\Delta_M} &= \frac{\Delta_M}{\left(h_{n_g} / h_1\right) - 1}, \text{ where } \Delta_M \text{ is the data range,} \\ \Delta_M &= \max(|S_i - S_j|) 1 \le i, j \le n_g \end{aligned} \tag{5.10}$$

The numerical uncertainty still follows the form used in Roache (1998): $U_{SN} = F_S\,|\varepsilon|$, but the safety factor and error estimate involved are quite dissimilar from those used by the FS method. Based on the convergence condition, the numerical uncertainty is formulated as follows:

1. Monotonic convergence:

   a. $0.95 \le p \le 2.05 : U_{SN} = 1.25\delta_{RE} + U_{SD}$ (5.11)

   b. $p \le 0.95 : U_{SN} = \min\left(1.25\delta_{RE} + U_{SD}, 3\delta_{RE}^{12} + U_{SD}^{12}\right)$ (5.12)

   c. $p \ge 2.05 : U_{SN} = \max\left(1.25\delta_{RE} + U_{SD}, 3\delta_{RE}^{02} + U_{SD}^{02}\right)$ (5.13)

2. Oscillatory convergence:

$$U_{SN} = 3\delta_{\Delta M} \tag{5.14}$$

3. Anomalous behavior:

$$U_{SN} = \min\left(3\delta_{\Delta_M}, 3\delta_{RE}^{12} + U_{SD}^{12}\right) \tag{5.15}$$

where $U_{SD}, U_{SD}^{02}, U_{SD}^{12}$ are standard deviations of the curve fit for equations (5.6, 5.8, 5.9), e.g.:

$$U_{SD} = \sqrt{\frac{\sum_{i=1}^{n_g} \left(S_i - \left(S_0 + \alpha {h_i}^p\right)\right)^2}{n_g - 3}} \tag{5.16}$$

2.2 Validation Procedure

Unlike the specific control of numerical accuracy during the process of verification, validation controls errors or uncertainties of CFD computations in a more fundamental and extensive sense. It determines the level of accuracy to which a numerical

model describes a real physical problem, in combination with a comparison with experimental data. The validation procedure adopted in this report is a simplified version of the above-mentioned ASME V&V 20-2009 Standard (2009). This simplified version was used at the 3rd Lisbon Workshop on CFD Uncertainty Analysis (2008) as well. Two parameters are introduced in this procedure: the validation comparison error, denoted as $E = S\text{-}D$ and the validation uncertainty (at 95 % confidence level) defined as $U_{val}^2 = U_{SN}^2 + U_{input}^2 + U_D^2$. In these equations S and D represent the simulated solution and experimental data, respectively. U_{SN} is the numerical uncertainty, U_{input} is the input parameter uncertainty (for a strong model concept, $U_{input} = 0$) and U_D represents the data uncertainty in the experiment. In this report, U_{val} is approximated as: $U_{val}^2 = U_{SN}^2 + U_D^2$. If $|E| \gg U_{val}$, the sign and magnitude of E might be used to improve the modeling, thereby reducing the comparison error or modeling error; but if $|E| \leq U_{val}$, the modeling error falls within the 'noise level' of U_{val} caused by numerical, input parameter and experimental data uncertainties; thus, there is little room to improve the modeling error.

3 V&V Submissions and Results: 2010 Gothenburg Workshop

Nine V&V test cases were used at the 2010 Gothenburg Workshop, including the V&V studies of CFD predictions regarding resistances and motions for three benchmark hull forms (KVLCC2, KCS and DTMB 5415) in various conditions, including low or high speeds, zero/fixed or dynamic/free sinkage and trim or self-propulsion. Although the complexity and difficulty of computations had increased, submissions of V&V test cases increased greatly at the 2010 Workshop. The iterative uncertainty during previous workshops was not always well-documented, which is why the 2010 Workshop requested participants to provide details of applied V&V methods and the determination of iterative uncertainty. This information was reported via either questionnaires or workshop submissions. The general distribution of V&V submissions versus case name is shown in Table 5.1, in which the determination of iterative convergence and its uncertainty is classified into the following categories:

I. Residuals
II. Iterative history of integral quantity
III. Number of iterations

A total of 43 submissions from 16 research groups contributed to the test cases of which 13 submissions applied more than three grids; in the present investigation, their solutions are split into several triplets with certain refinement ratios to be used in the FS method. For the determination of iterative convergence, criteria I and II are the most popular ones. Most submissions used more than one criterion and 88 % included a three-order drop in residuals, 88 % the iterative history of an integral quantity, while only 2.3 % included the number of iterations. However, no more than half of the submissions reported how U_I was estimated. As for the turbulence model, the major types presented here are: (one-equation) 1E Spalart-Allmaras, 1E Menter,

Table 5.1 Distribution of selected submissions

No.	Case name	Entries no.	Group	Code	Turbulence model	Determination of iterative convergence and uncertainty
1	1.2a	5	HSVA	FreSCo +	2E k-ω	III (U_I estimated from curve fit of an exponential function for the convergence target value)
			MARIC	FLUENT6.3	k-ω SST	II ($U_I = 0.5 \times (S_{upper}\text{-}S_{lower})$ for oscillatory iterative convergence)
			MOERI	WAVIS	Realizable k-ε	I (3 orders of magnitude drop in averaged pressure residual), II
			NTNU	FLUENT	k-ω SST	I, II
			VTT	FINFLO	k-ω SST	I (3∼4 orders of magnitude drop in averaged momentum residual), II (forces)
2	1.2b (six *Fr*)	6	MOERI	WAVIS	Realizable k-ε	I (3 orders of magnitude drop in averaged pressure residual), II
3	2.2a	6	CD-adapco	STARCCM +	Standard k-ε	I (3 orders of magnitude drop in averaged residual norms), II
			CSSRC	FLUENT6.3	k-ω SST	I (3 orders of magnitude drop in averaged pressure residual)
			MARIC	FLUENT6.3	Realizable k-ε	II ($U_I = 0.5 \times (S_{upper}\text{-}S_{lower})$ for oscillatory iterative convergence)
			MOERI	WAVIS	Realizable k-ε	I (3 orders of magnitude drop in averaged pressure residual), II
			SVA	CFX12	k-ω SST	I (max. residual 5E-03) ($U_I = 0.5 \times (S_{upper}\text{-}S_{lower})$)
			TUHH ANSYS	CFX12.1	k-ω SST	I (3 orders of magnitude drop in all residual & steady state resistance), II
4	2.2b (six *Fr*)	1	CD-adapco	STAR-CCM +	Standard k-ε	I (3 orders of magnitude drop in averaged residual norms), II
		6	MOERI	WAVIS	Realizable k-ε	I (3 orders of magnitude drop in averaged pressure residual), II
		6	Southampton QinetiQ	CFX12	k-ω SST	I (RMS residuals at 1E-6), II (U_I from standard deviation over last 200 iterations)
5	2.3a	5	MARIN	PARNASSOS (PROCAL)	1E Menter	I, II (U_I from extrapolation based on a geometric progression)
			MOERI	WAVIS	Realizable k-ε	I (3 orders of magnitude drop in averaged pressure residual), II

Table 5.1 (continued)

No.	Case name	Entries no.	Group	Code	Turbulence model	Determination of iterative convergence and uncertainty
			NMRI	SURF	1E Modified Spalart-Allmaras	II (U_I from maximum and minimum values of last 1000 steps)
			Southampton QinetiQ	CFX	k-ω SST	I (RMS residuals at 0.5E-4), II (U_I from standard deviation over last 200 iterations)
			SSPA	SHIPFLOW v4.3	EASM	I, II (U_I from relative variation in percentage compared with an average value of last 4000 iterations)
6	2.3b	2	MOERI	WAVIS	Realizable k-ε	I (3 orders of magnitude drop in averaged pressure residual), II
			SSPA	SHIPFLOW v4.3	EASM	I, II (U_I from relative variation in percentage compared with an average value of last 4000 iterations)
7	3.1a	4	CEHINAV	STAR-CCM +	k-ω SST	I (4 orders of magnitude drop in averaged pressure residual), II
			UoGe	STAR-CCM +	Realizable k-ε	–
			MARIC	FLUENT6.3	k-ω SST	I, II
			MARIN	PARNASSOS	1E Menter	I, II (U_I from extrapolation based on a geometric progression)
8	3.1b	1	NavyFOAM	NavyFOAM	Wilcox k-ω	I (drop by 3 orders)
9	3.2	1	MARIN	PARNASSOS	1E Menter	I, II (U_I from extrapolation based on a geometric progression)
SUM		43				* S_{upper} and S_{lower} refer to maximum and minimum values over last two oscillation periods

(two-equation) 2E k-ε, 2E k-ω and EASM (Explicit Algebraic Stress Model), among which the 2E k-ε and 2E k-ω models were mostly used.

In the following sub-sections, the results of various V&V methods (the one submitted by participants, the FS, GCI and LSR methods) are summarized on a case-by-case basis. To unify the investigation, this report only considers the submissions involving at least three grids and those with a uniform grid refinement ratio. Therefore, 40 submissions are finally selected, of which we obtain *80 triplets* of solutions for the FS method and *13 sets* of solutions for the LSR method. In the present study, the grid convergence in the GCI method is determined by the triplets, similar to the FS case, the only difference being the uncertainty estimates. In GCI, the uncertainties are estimated from Eq. (5.1). The results of the respective test cases are distributed via two types of tables. First, the 'a' table presents the basic information of the submitted V&V studies (e.g. grid type, grid numbers, maximum grid size (M, in million), the refinement ratio r_G, the iterative uncertainty U_I, experimental data uncertainty U_D), as well as the results of V&V methods submitted (reference (Ref.) of the method applied, P, U_G, U_{SN}). The definitions of grid type are: S (Single-block structured grid), MS (Multi-block structured grid), OS (Overlapping structured grid), U (Unstructured grid) and MU (Multi-block unstructured grid). Second, the 'b' table shows results based on the FS method (R, type of convergence; P, U_G, U_{SN} for monotonic convergence, U_{val} and $|E|$); results based on the GCI method (uncertainty results alone), as well as results from the LSR method (type of convergence, P; U_G, U_{SN}, U_{val} and $|E|$). Note that here the same definition $P = p/p_{th}$ is used in all methods to denote parallel comparison (assuming $p_{th} = 2.0$). Note that for $p = p_{th}$ $P = 1.0$, and that this P is denoted as P_{th}. As for the classification of convergence types from the V&V study, 'mon.' represents monotonic convergence, 'osc.' stands for oscillatory convergence, and 'div.' denotes divergence. Moreover, the number '1' in 'Tri.' represents the finest grid in triplets. $|E|$ denotes the comparison error, i.e., the difference between the CFD result (S) of the finest grid in each triplet (FS and GCI methods) or set (LSR method) and experimental data D. Furthermore, $|E|$, U_D and U_{val} values are normalized by D, while U_G and U_{SN} values are normalized by S in each triplet or set, while U_I is normalized by two parameters, S and the solution difference of the final two successively refined grids ε_{12}, for comparison purpose. Graphical results are presented through figures, including the LSR curve fit plots (where i th grid refinement ratio is represented by h_i/h_1, h_1 being the grid spacing of the finest grid1), the comparison of CFD results and experimental data, as well as the illustration of relevant numerical uncertainties and data uncertainties from the 'b' table. Note that in all uncertainty plots, only the FS and LSR results are presented.

3.1 Case 1.2a

The adopted grid convergence results for Case 1.2a include HSVA, MARIC, MOERI and VTT submissions, of which HSVA used five unstructured grids, while VTT used nine multi-block and overlapping structured grids, and every three grids adopted

Table 5.2 Submitted V&V results (Case 1.2a, $Fr = 0.142$)

Group (Code)	Basic information							Group submission				
	Grid type	Grid no.	Max. size (M)	r_G	U_I $\%\varepsilon_{12}$	U_I $\%S$	U_D $\%D$	Ref.	P	U_G $\%S$	U_{SN} $\%S$	U_{val} $\%D$
HSVA (FreSCo +)	U	5	10.2	2.0	1.0	0.01	1.0	Stern et al. 2001	0.847	0.16	0.16	1.01
MARIC (FLUENT6.3)	MS	3	2.9	1.414	12.5	0.19	1.0	ITTC 2002	1.354	2.01	2.02	2.31
MOERI (WAVIS)	MS	3	4.9	1.414	0.0	0.0	1.0	Stern et al. 2001	0.947	0.10	0.10	1.01
VTT (FINFLO)	MS OS	9	5.5	2.0	2.4	1.40	1.0	–	0.951	4.82	5.02	5.24

Table 5.3 V&V results from FS and GCI methods (Case 1.2a, $Fr = 0.142$)

Group (Code)	FS method (2010)							GCI (Roache)			$\|E\|$ $\%D$
	Tri.	R	Con. type	P	U_G $\%S$	U_{SN} $\%S$	U_{val} $\%D$	U_G $\%S$	U_{SN} $\%S$	U_{val} $\%D$	
HSVA (FreSCo +)	3-2-1	3.412	Div.	–	–	–	–	–	–	–	–
	4-3-2	1.545	Div.	–	–	–	–	–	–	–	–
	5-4-3	0.035	Mon.	2.415	0.24	0.24	1.03	0.01	0.02	1.00	2.55
	5-3-1	0.231	Mon.	0.528	1.09	1.09	1.49	0.68	0.68	1.21	0.73
MARIC (FLUENT6.3)	3-2-1	0.391	Mon.	1.354	7.06	7.06	7.37	1.19	1.21	1.60	3.43
MOERI (WAVIS)	3-2-1	0.515	Mon.	0.947	2.15	2.15	1.73	1.64	1.64	1.93	0.46
VTT (FINFLO)	7-4-1	0.455	Mon.	0.568	9.66	9.76	10.07	6.14	6.30	6.54	2.58
	8-5-2	0.278	Mon.	0.923	3.44	3.72	3.93	2.59	2.95	3.17	1.97
	9-6-3	0.363	Mon.	0.731	11.64	11.72	12.58	7.96	8.07	8.69	7.01

Table 5.4 V&V results from LSR method (Case 1.2a, $Fr = 0.142$)

Group (Code)	LSR method (2010)					
	Con. type	P	U_G $\%S$	U_{SN} $\%S$	U_{val} $\%D$	$\|E\|$ $\%D$
HSVA (FreSCo +)	Mon.	1.314	2.68	2.68	2.88	0.73
MARIC (FLUENT6.3)	–	–	–	–	–	–
MOERI (WAVIS)	–	–	–	–	–	–
VTT (FINFLO)	Osc.	0.951	24.65	24.69	25.34	2.58
	Mon.		5.12	5.31	5.54	

the same refinement ratio $r_G = 2.0$. The other two groups utilized three multi-block structured grids using the same grid refinement ratio: 1.414. Details of the results are provided in Tables 5.2, 5.3 and 5.4. From the FS and GCI methods, nine triplet combinations are investigated, while HSVA and VTT are the sole entries from the LSR method.

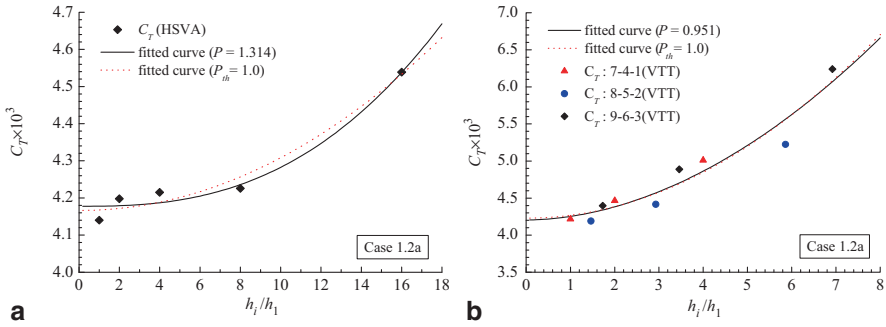


Fig. 5.1 Grid convergence of **a** HSVA solutions, **b** VTT solutions

The results yielded by the FS method indicate that with the same refinement ratio, the coarse grids (MARIC) give rise to a larger P value than the finer grids (MOERI), the latter obtaining a P value of 0.957, quite close to the theoretical value of $P_{th} = 1.0$. The coarse grids then lead to a higher grid discretization uncertainty. Splitting the five grid densities in the HSVA submission produces four triplets, of which (5-3-1) and (5-4-3) achieve monotonic convergence while the coarsest combination (5-4-3) produces a high order of accuracy ($P = 2.415$), implying that this triplet is so coarse that the solutions are distant from the asymptotic range, while its grid discretization uncertainty is surprisingly minor. However, the remaining two triplets diverge, especially the finest triplet (3-2-1) with a maximum grid size of around 10.2 million. With a special combination of triplets in terms of the uniform refinement ratio, the three triplets of the VTT submission all achieve monotonic convergence coupled with a different convergence rate, among which the (8-5-2) triplet obtains a fairly promising order of accuracy of $P = 0.923$, close to the asymptotic range and with only a minor numerical uncertainty, while the other two triplets have slightly smaller P values and thus larger uncertainties. In comparing the grid discretization uncertainty, the largest difference between FS and GCI with a high order of accuracy ($P = 2.415$) appears at the (5-4-3) triplet in the HSVA solution, as seen in Table 5.3. From the FS method, $U_G = 0.24\,\%S$, while the value is much smaller for the GCI, only $0.01\,\%S$. Similarly in MARIC submission ($P = 1.354$), the difference is also evident. However in the other submissions, the estimated uncertainties by FS and GCI are comparable and their corresponding P values are close to unity. Utilizing the LSR method, all the solutions from HSVA and VTT can be considered. As indicated in Table 5.4, this method yields a monotonic convergence for HSVA solutions with $P = 1.314$ a bit closer to the asymptotic range, as well as a larger U_G value compared to the result of the triplet (5-3-1) from the FS and GCI methods, while in the VTT submission, the P value obtained indicates that their solutions are closer to the asymptotic range. However, two types of convergence are observed from the solutions: oscillatory and monotonic. The former gives high grid discretization uncertainty, whereas the latter produces a very low value at only about 20 % of the uncertainty of the oscillatory convergence.

For a more detailed illustration, the grid convergence tendency and the Least Squares Root curve fit for the HSVA and VTT solutions are plotted in Fig. 5.1a and b,

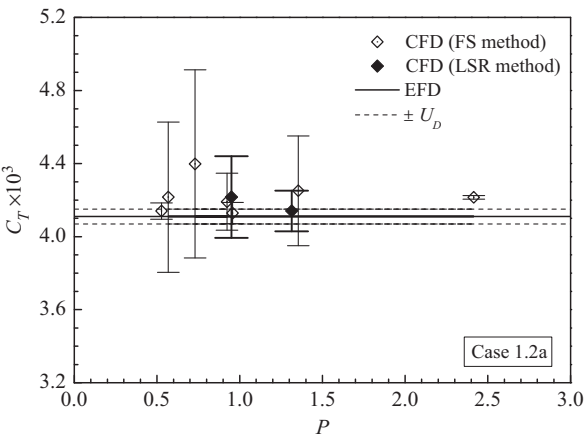


Fig. 5.2 V&V results in Case 1.2a

including for reference the curve fit from the theoretical order of accuracy, $P_{th} = 1.0$. The scatter around the fitted curve in numerical solutions is clearly displayed in both figures. In addition, as shown in Fig. 5.1a, the result of the coarsest grid5 from the HSVA submission is quite different from the others, further indicating this grid is too coarse to produce the appropriate solution. Combined with the observation from the FS method, the scatter is probably due to the fact that the HSVA applied unstructured grids have greater difficulty in ensuring the systematic refinement than the structured grids; concequently the grid similarity is not ideal, as is also the case with the grid convergence. Another explanation might be that the grid refinement step ($r_G = 2.0$) is too large, thereby affecting the curve fit and grid dependence by the solutions left out. The scatter is even more pronounced in the VTT solutions in Fig. 5.1b, the reason for the oscillatory convergence, something that is more probably attributed to the non-uniform refinement among the triplets. If each triplet (with a separate color in Fig. 5.1b) is a separate combination, it obviously exhibits monotonic convergence, thereby producing lower uncertainties.

Figure 5.2 presents the estimated numerical uncertainties at the finest grids (in triplets) from the FS method (the predicted resistances are represented by open diamonds) and from the LSR method (resistance solutions are denoted by solid diamonds) in comparison with the data uncertainty versus the P value obtained. For P less than 1.5, all numerical uncertainties overlap the data uncertainty, indicating that the modeling error is within the numerical and experimental data uncertainties, making it impossible to conclude anything about the modeling error without further investigation. For P larger than 1.5, only one triplet (5-4-3 from HSVA) exists with no overlap between the numerical and data uncertainty. Its comparison error is undoubtedly larger than the validation uncertainty, resulting in a modeling error comparable to the comparison error. The minor grid size might explain the large difference between solution and data (comparison error). However, the reason for the low numerical uncertainty is still not clear, illustrating the complexity of determining the numerical error and uncertainty when the solutions are distant from the asymptotic range.

Table 5.5 Submitted V&V results (Case 1.2b, MOERI (WAVIS))

Basic information								Group submission				
Fr	Grid type	Grid no.	Max. size (M)	r_G	U_I % ε_{12}	U_I %*S*	U_D %*D*	Ref.	*P*	U_G %*S*	U_{SN} %*S*	U_{val} %*D*
0.1010	MS	3	4.9	1.414	0.0	0.0	1.0	Stern et al. 2001	3.252	0.16	0.16	1.01
0.1194	MS	3	4.9	1.414	0.0	0.0	1.0		6.332	0.003	0.003	1.00
0.1377	MS	3	4.9	1.414	0.0	0.0	1.0		1.435	0.20	0.20	1.02
0.1423	MS	3	4.9	1.414	0.0	0.0	1.0		3.298	0.14	0.14	1.01
0.1469	MS	3	4.9	1.414	0.0	0.0	1.0		1.015	0.01	0.01	1.00
0.1515	MS	3	4.9	1.414	0.0	0.0	1.0		0.835	0.22	0.22	1.03

Table 5.6 V&V results from FS method (Case 1.2b, MOERI (WAVIS))

Fr	FS method (2010)							GCI (Roache)			|*E*| %*D*
	Tri.	*R*	Con. type	*P*	U_G %*S*	U_{SN} %*S*	U_{val} %*D*	U_G %*S*	U_{SN} %*S*	U_{val} %*D*	
0.1010	3-2-1	0.111	Mon.	3.171	0.88	0.88	1.33	0.03	0.03	1.00	0.35
0.1194	3-2-1	0.012	Mon.	6.369	0.004	0.004	1.00	0.0001	0.0001	1.00	1.29
0.1377	3-2-1	0.370	Mon.	1.434	2.46	2.46	2.71	0.35	0.35	1.06	2.28
0.1423	3-2-1	0.094	Mon.	3.417	0.61	0.61	1.18	0.02	0.02	1.00	2.93
0.1469	3-2-1	0.490	Mon.	1.029	1.20	1.20	1.59	0.72	0.72	1.25	2.74
0.1515	3-2-1	0.559	Mon.	0.839	1.75	1.75	2.06	1.26	1.26	1.64	2.75

3.2 Case 1.2b

In this test case, six conditions (Froude numbers $Fr = 0.1010$, 0.1194, 0.1377, 0.1423, 0.1469, 0.1515) must be computed, in order to examine the performance of resistance predictions at various speeds. As indicated in Table 5.5, only the MOERI group provided V&V results and the iterative uncertainty U_I was stated to be zero. This group adopted three multi-block structured grids, thereby only including the FS method in the investigation. Results for all conditions are given in Table 5.6. From the FS method, monotonic convergence is obtained for all six conditions, but more than half get very large *P* values. The numerical uncertainty versus Froude number is indicated in Table 5.6 and further illustrated in Fig. 5.3a and b together with the data uncertainty. The absolute values of numerical uncertainty are fairly minor based on the FS method but at some speeds they are slightly higher than the data uncertainty. This may imply that the resistance is more difficult to predict by numerical tools than by experimental techniques. Another observation from the numerical uncertainty is that the GCI computations with *P* close to $P_{th} = 1.0$ (e.g., $Fr = 0.1469$, 0.1515) yield results very similar to the FS results, while those with large *P* values ($Fr =$ 0.1010, 0.1194, 0.1423) all produce much smaller uncertainties than the FS method. Moreover, the comparison errors |*E*| generally increase from low speeds (0.35 %*D*

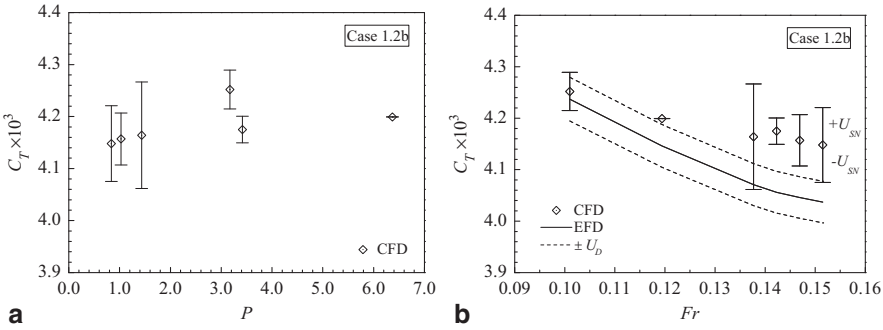


Fig. 5.3 V&V results in Case 1.2b

Table 5.7 Submitted V&V results (Case 2.2a, $Fr = 0.26$)

Group (Code)	Basic information							Group submission				
	Grid type	Grid no.	Max. size (M)	r_G	U_I $\%\varepsilon_{12}$	U_I $\%S$	U_D $\%D$	Ref.	P	U_G $\%S$	U_{SN} $\%S$	U_{val} $\%D$
CD-adapco (STARCCM+)	U	3	3.0	1.5	–	–	1.0	–	–	–	–	–
CSSRC (FLUENT6.3)	MS	3	1.3	1.414	2464	9.52	1.0	ITTC 2002	3.060	0.76	9.55	9.78
MARIC (FLUENT6.3)	MS	4	6.5	1.414	3.0	0.01	1.0	ITTC 2002	–	3.97	3.97	4.20
MOERI (WAVIS)	MS	3	4.3	1.414	0.0	0.0	1.0	Stern et al. 2001	2.758	0.87	0.87	1.33
TUHH&ANSYS (CFX12.1)	MS	3	16.4	1.5	0.1	0.0003	1.0	ITTC 2002	3.323	0.02	0.02	1.00

at $Fr = 0.1010$) to high speeds (2.75 $\%D$ at $Fr = 0.1515$), and in four conditions (the second and the final three conditions), the $|E|$ values exceed the numerical or experimental uncertainties, demonstrating that the pronounced free surface effect at high speed induces a difficulty in resistance prediction, with the consequence that a potential modeling error might exist in computation and/or experiment.

3.3 Case 2.2a

V&V results are shown in Tables 5.7, 5.8 and 5.9. Within five entries, only the CD-adapco group used unstructured grids, while all others used multi-block structured grids. From the FS method, CSSRC, MOERI and TUHH&ANSYS solutions achieved monotonic convergence with the P values obtained around twice the theoretical value of $P_{th} = 1.0$. The situation is not improved with much finer grids (maximum grid size of around 16.4 million) used by the TUHH&ANSYS group. With those

Table 5.8 V&V results from FS and GCI methods (Case 2.2a, $Fr = 0.26$)

Group (Code)	FS method (2010)							GCI (Roache)			$\|E\|$ %D
	Tri.	R	Con. type	P	U_G %S	U_{SN} %S	U_{val} %D	U_G %S	U_{SN} %S	U_{val} %D	
CD-adapco (STARCCM+)	3-2-1	−2.167	Osc.	–	–	–	–	–	–	–	–
CSSRC (FLUENT6.3)	3-2-1	0.120	Mon.	3.063	1.86	9.70	9.93	0.07	9.52	9.75	1.91
MARIC (FLUENT6.3)	3-2-1	−0.667	Osc.	–	–	–	–	–	–	–	–
	4-3-2	−0.052	Osc.	–	–	–	–	–	–	–	–
MOERI (WAVIS)	3-2-1	0.148	Mon.	2.758	2.52	2.52	2.71	0.10	0.10	1.01	0.20
TUHH&ANSYS (CFX12.1)	3-2-1	0.067	Mon.	3.339	0.95	0.95	1.39	0.03	0.03	1.00	1.27

Table 5.9 V&V results from LSR method (Case 2.2a, $Fr = 0.26$)

Group (Code)	LSR method (2010)					
	Con. type	P	U_G %S	U_{SN} %S	U_{val} %D	$\|E\|$ %D
CD-adapco (STARCCM+)	–	–	–	–	–	–
CSSRC (FLUENT6.3)	–	–	–	–	–	–
MARIC (FLUENT6.3)	Osc.	9.730	13.04	13.04	13.41	2.61
MOERI (WAVIS)	–	–	–	–	–	–
TUHH&ANSYS (CFX12.1)	–	–	–	–	–	–

high P values, results from the FS and GCI methods are rather different. In fact, the uncertainties from the GCI are at least one order of magnitude less than those from the FS. On the other hand, the CD-adapco and MARIC (two triplets) solutions achieve oscillatory convergence, making it impossible to estimate the error and uncertainty by the FS method. However, the LSR method has no such limitation; thus, the error and uncertainty can be obtained for the MARIC submission with four systematic grids. It turns out that oscillatory convergence is achieved by the LSR method as well, but the observed order of accuracy reaches a surprising $P = 9.730$. The grid convergence tendency and the LSR curve fit are presented in Fig. 5.4, illustrating the reason for the extremely large P value in the MARIC submission: grid 4 is too coarse to give a reasonable result, while the other three solutions are almost independent of grid density. Apart from grid size, the scatter in solutions might be a possible explanation. It would be helpful to apply more refined grids to further investigate grid dependence from the LSR method in particular, since there are only three grids left after dropping the coarsest grid4.

With regard to estimated uncertainties, it is surprising that the iterative uncertainty U_I provided by CSSRC is so substantial. U_I is around one order of magnitude higher than the solution change in the last two finest grid ε_{12} and grid discretization uncertainty U_G, such that the requirements in neither the FS nor the LSR methods are fulfilled. Obviously, with poor iterative convergence, it is not possible to estimate

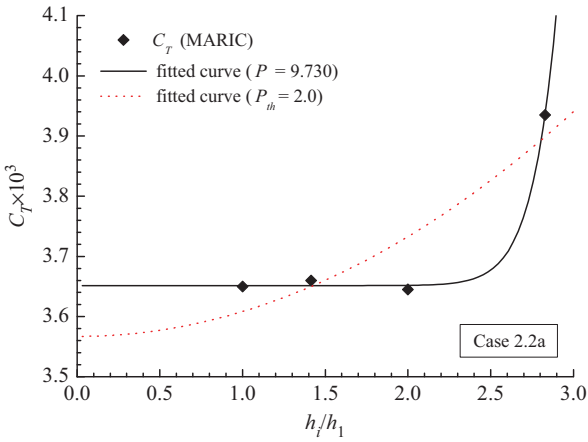


Fig. 5.4 Grid convergence of MARIC solutions

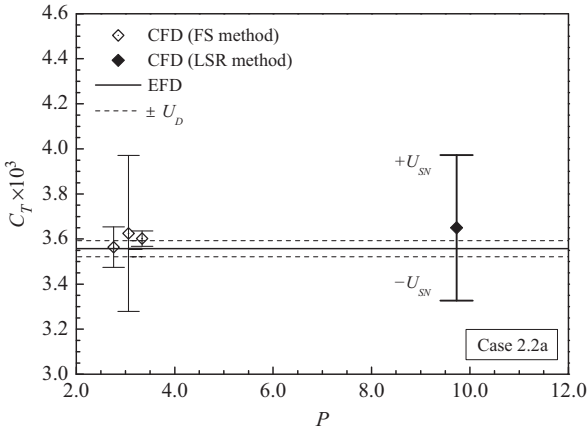


Fig. 5.5 V&V results in Case 2.2a

discretization uncertainty. Thus, a V&V study for this kind of solution using the FS (GCI) and LSR methods would be inappropriate.

The predicted numerical uncertainties U_{SN} and given data uncertainty U_D are plotted in Fig. 5.5, where U_{SN} in almost all solutions is higher than U_D. The largest P value (using the LSR method) in the MARIC submission gives considerable numerical uncertainty, while other results, based on the FS method produce lower P values and numerical uncertainties, excluding the high uncertainty of the CSSRC solution because of inappropriate iterative convergence. The high numerical uncertainty associated with the CSSRC solution may also be attributable to insufficient grid resolution (1.3 million points only).

3.4 Case 2.2b

This is the test case with the largest number of submissions. It includes six conditions (*Fr*) and more than one submission for each condition for a total of 13 submissions, the details of which are shown in Table 5.10. Three groups provided detailed computations: MOERI and Southampton/QinetiQ used multi-block structured grids for discretization; CD-adapco applied an unstructured grid and computed a single condition; however, no V&V result was presented as no monotonic convergence was observed. Comparing the submitted P values in Table 5.10, in the first three conditions, the solutions from MOERI with medium grid density ($\sim$4.3 million) are farther away from the asymptotic range than those of the Southampton/QinetiQ group with finer grids ($\sim$9.3 million), while the convergence rates are more comparable for the remaining three conditions.

The large amount of submissions leads to 43 triplets for the FS and GCI methods and six sets for the LSR method. The V&V results using these methods are available in Tables 5.11 and 5.12. In particular, with six systematically varied grids in the Southampton/QinetiQ submissions, the investigation can be made from several aspects. Firstly, the 43 triplets are investigated by the FS and GCI methods. Most triplets achieve monotonic convergence (37): three attain oscillatory convergence, and the other three reach divergence. In general, the observed order of accuracy in monotonic convergence is similar to the theoretical case of $P_{th} = 1.0$. Secondly, with the same P values close to the asymptotic range, numerical uncertainties produced by the FS and GCI methods are rather similar and within the same order; this is, however, not the situation involving two cases with large P: MOERI submission with $P = 2.929$ in No.1 *Fr* and with $P = 2.242$ in No.2 *Fr*, see Table 5.11. Thirdly, solutions should converge with grid refinement, and the same applies to the triplets, that is, the order of accuracy obtained from the triplets should approach the theoretical value as the asymptotic range is approached. However, if we compare the P values for a set of gradually refined triplets [$r_G = 1.2$: (6-5-4) $\rightarrow$ (5-4-3) $\rightarrow$ (4-3-2) $\rightarrow$ (3-2-1)] in six conditions, the tendency of P is unclear and neither monotonically decreasing nor increasing, as shown in Fig. 5.6. Nevertheless, the situation is different in the other set of triplets with another refinement ratio [$r_G = 1.44$: (6-4-2) $\rightarrow$ (5-3-1)], where the P values mostly increase against the grid refinement and approach the asymptotic range ($P \rightarrow 1$). Finally, it is also feasible to use the LSR method to obtain the observed order of accuracy and, thereafter, estimate the numerical uncertainties for Southampton/QinetiQ submissions. As in previous test cases, the grid convergence plots together with the curve fits are illustrated for all conditions in Figs. 5.7 to 5.12. The solutions for all conditions seem to indicate monotonic convergence: the fitted curves nearly go through all the solutions, and the solution changes between two successively refined grids are getting smaller.

The estimated P values, listed in Tables 5.11 and 5.12, are all within the range of [0.4, 0.8] implying a slightly lower observed order of accuracy p which indicates a slow rate of convergence. However, a comparison of the results from the FS and LSR methods indicates that the two methods give similar results. The P values and

Table 5.10 Submitted V&V results (Case 2.2b)

No.	*Fr*	Basic information								Group submission					
		Group (Code)	Grid type	Grid no.	Max. size (M)	r_G	U_I % ε_{12}	U_I %S	U_D %D	Ref.	P	U_G %S	U_{SN} %S	U_{val} %D
1	0.1083	MOERI (WAVIS)	MS	3	4.3	1.414	0.0	0.0	1.0	Stern et al. 2001	2.902	0.92	0.92	1.34
		Southampton/QinetiQ (CFX12)	MS	6	9.3	1.2	0.4	0.004	1.0	Eça and Hoekstra 2008	0.486	7.23	7.23	7.28
2	0.1516	MOERI (WAVIS)	MS	3	4.3	1.414	0.0	0.0	1.0	Stern et al. 2001	2.235	1.06	1.06	1.45
		Southampton/QinetiQ (CFX12)	MS	6	9.3	1.2	0.8	0.01	1.0	Eça and Hoekstra 2008	0.624	5.65	5.65	5.80
3	0.1949	MOERI (WAVIS)	MS	3	4.3	1.414	0.0	0.0	1.0	Stern et al. 2001	1.654	1.63	1.63	1.90
		Southampton/QinetiQ (CFX12)	MS	6	9.3	1.2	0.6	0.01	1.0	Eça and Hoekstra 2008	0.741	4.69	4.69	4.94
4	0.2274	MOERI (WAVIS)	MS	3	4.3	1.414	0.0	0.0	1.0	Stern et al. 2001	0.507	1.71	1.71	1.97
		Southampton/QinetiQ (CFX12)	MS	6	9.3	1.2	3.3	0.03	1.0	Eça and Hoekstra 2008	0.772	4.63	4.63	4.90
5	0.2599	CD-adapco (STAR-CCM +)	U	3	3	1.5	–	–	1.0	–	–	–	–	–
		MOERI (WAVIS)	MS	3	4.3	1.414	0.0	0.0	1.0	Stern et al. 2001	0.394	2.70	2.70	2.88
		Southampton/QinetiQ (CFX12)	MS	6	9.3	1.2	1.1	0.01	1.0	Eça and Hoekstra 2008	0.714	5.08	5.08	5.27
6	0.2816	MOERI (WAVIS)	MS	3	4.3	1.414	0.0	0.0	1.0	Stern et al. 2001	1.022	0.65	0.65	1.19
		Southampton/QinetiQ (CFX12)	MS	6	9.3	1.2	0.3	0.001	1.0	Eça and Hoekstra 2008	0.798	2.15	2.15	2.40

Table 5.11 V&V results from FS and GCI methods (Case 2.2b)

Fr No.	Group (Code)	FS method (2010)							GCI (Roache)			$\|E\|$ %*D*
		Tri.	*R*	Con. type	*P*	U_G %*S*	U_{SN} %*S*	U_{val} %*D*	U_G %*S*	U_{SN} %*S*	U_{val} %*D*	
1	MOERI (WAVIS)	3-2-1	0.131	Mon.	2.929	2.46	2.46	2.59	0.09	0.09	1.00	2.95
	Southampton/QinetiQ (CFX12)	3-2-1	1.056	Div.	–	–	–	–	–	–	–	0.26
		4-3-2	0.750	Mon.	0.789	5.03	5.03	5.16	3.53	3.53	3.69	0.74
		5-4-3	0.686	Mon.	1.035	5.88	5.88	6.07	3.39	3.39	3.59	1.69
		6-5-4	1.148	Div.	–	–	–	–	–	–	–	–
		5-3-1	0.627	Mon.	0.640	6.27	6.27	6.33	4.11	4.11	4.22	0.26
		6-4-2	0.641	Mon.	0.609	7.59	7.59	7.71	4.91	4.91	5.04	0.74
2	MOERI (WAVIS)	3-2-1	0.212	Mon.	2.242	3.59	3.59	3.70	0.20	0.20	1.02	0.93
	Southampton/QinetiQ (CFX12)	3-2-1	0.814	Mon.	0.565	8.19	8.19	8.35	5.20	5.20	5.35	1.18
		4-3-2	0.843	Mon.	0.468	12.75	12.75	13.07	7.77	7.77	8.00	2.14
		5-4-3	0.761	Mon.	0.748	7.84	7.84	8.16	5.40	5.40	5.67	3.32
		6-5-4	0.798	Mon.	0.620	13.32	13.32	13.98	8.66	8.66	9.12	4.72
		5-3-1	0.661	Mon.	0.568	8.12	8.12	8.28	5.16	5.16	5.32	1.18
		6-4-2	0.623	Mon.	0.650	7.91	7.91	8.14	5.21	5.21	5.42	2.14
3	MOERI (WAVIS)	3-2-1	−3.083	Osc.	–	–	–	–	–	–	–	–
	Southampton/QinetiQ (CFX12)	3-2-1	0.738	Mon.	0.833	4.25	4.25	4.49	3.05	3.05	3.30	3.11
		4-3-2	0.764	Mon.	0.740	6.84	6.84	7.18	4.69	4.69	4.98	4.00
		5-4-3	0.786	Mon.	0.661	10.41	10.41	11.00	6.90	6.90	7.32	5.21
		6-5-4	0.745	Mon.	0.808	9.70	9.70	10.41	6.88	6.88	7.41	6.79
		5-3-1	0.584	Mon.	0.738	5.21	5.21	5.47	3.58	3.58	3.82	3.11
		6-4-2	0.591	Mon.	0.720	7.14	7.14	7.49	4.86	4.86	5.15	4.00
4	MOERI (WAVIS)	3-2-1	0.714	Mon.	0.486	3.70	3.70	3.81	2.27	2.27	2.47	0.81
	Southampton/QinetiQ (CFX12)	3-2-1	0.698	Mon.	0.987	3.11	3.11	3.37	2.41	2.41	2.69	3.58
		4-3-2	0.717	Mon.	0.914	5.03	5.03	5.34	3.75	3.75	4.05	4.44
		5-4-3	0.870	Mon.	0.383	23.19	23.19	24.53	13.65	13.65	14.46	5.68
		6-5-4	0.676	Mon.	1.072	10.77	10.77	11.61	4.84	4.84	5.30	7.41
		5-3-1	0.566	Mon.	0.781	4.73	4.73	5.00	3.31	3.31	3.57	3.58
		6-4-2	0.602	Mon.	0.695	8.01	8.01	8.43	5.39	5.39	5.71	4.44

Table 5.11 (continued)

Fr No.	Group (Code)	FS method (2010)							GCI (Roache)			$\|E\|$ %*D*
		Tri.	*R*	Con. type	*P*	U_G %*S*	U_{SN} %*S*	U_{val} %*D*	U_G %*S*	U_{SN} %*S*	U_{val} %*D*	
5	CD-adapco (STAR-CCM +)	3-2-1	−0.370	Osc.	–	–	–	–	–	–	–	–
	MOERI (WAVIS)	3-2-1	0.738	Mon.	0.438	4.90	4.90	4.99	2.95	2.95	3.11	0.11
	Southampton/QinetiQ (CFX12)	3-2-1	0.696	Mon.	0.995	3.10	3.10	3.32	2.42	2.42	2.66	1.91
		4-3-2	0.754	Mon.	0.774	6.63	6.63	6.89	4.62	4.62	4.86	2.78
		5-4-3	0.824	Mon.	0.530	14.83	14.83	15.46	9.27	9.27	9.69	4.02
		6-5-4	0.755	Mon.	0.770	10.45	10.45	11.08	7.27	7.27	7.75	5.66
		5-3-1	0.578	Mon.	0.752	5.11	5.11	5.30	3.53	3.53	3.73	1.91
		6-4-2	0.622	Mon.	0.651	8.76	8.76	9.06	5.77	5.77	6.02	2.78
6	MOERI (WAVIS)	3-2-1	−0.483	Osc.	–	–	–	–	–	–	–	–
	Southampton/QinetiQ (CFX12)	3-2-1	0.760	Mon.	0.753	2.39	2.39	2.62	1.65	1.65	1.95	1.31
		4-3-2	0.625	Mon.	1.289	5.77	5.77	5.95	1.14	1.14	1.53	1.73
		5-4-3	1.026	Div.	–	–	–	–	–	–	–	–
		6-5-4	0.619	Mon.	1.315	9.24	9.24	9.58	1.52	1.52	1.83	0.143
		5-3-1	0.557	Mon.	0.803	2.14	2.14	2.39	3.12	3.12	3.33	1.31
		6-4-2	0.637	Mon.	0.618	4.80	4.80	4.98	1.71	1.71	2.02	1.73

Table 5.12 V&V results from LSR method (Case 2.2b)

Fr No.	Group (Code)	LSR method (2010)					
		Con. type	P	U_G %S	U_{SN} %S	U_{val} %D	$\|E\|$ %D
1	MOERI (WAVIS)	–	–	–	–	–	–
	Southampton/QinetiQ (CFX12)	Mon.	0.480	6.15	6.15	6.21	0.26
2	MOERI (WAVIS)	–	–	–	–	–	–
	Southampton/QinetiQ (CFX12)	Mon.	0.618	4.55	4.55	4.71	1.18
3	MOERI (WAVIS)	–	–	–	–	–	–
	Southampton/QinetiQ (CFX12)	Mon.	0.740	3.59	3.59	3.84	3.11
4	MOERI (WAVIS)	–	–	–	–	–	–
	Southampton/QinetiQ (CFX12)	Mon.	0.775	3.50	3.50	3.76	3.58
5	CD-adapco (STAR-CCM +)	–	–	–	–	–	–
	MOERI (WAVIS)	–	–	–	–	–	–
	Southampton/QinetiQ (CFX12)	Mon.	0.708	4.00	4.00	4.20	1.91
6	MOERI (WAVIS)	–	–	–	–	–	–
	Southampton/QinetiQ (CFX12)	Mon.	0.753	1.81	1.81	2.08	1.31

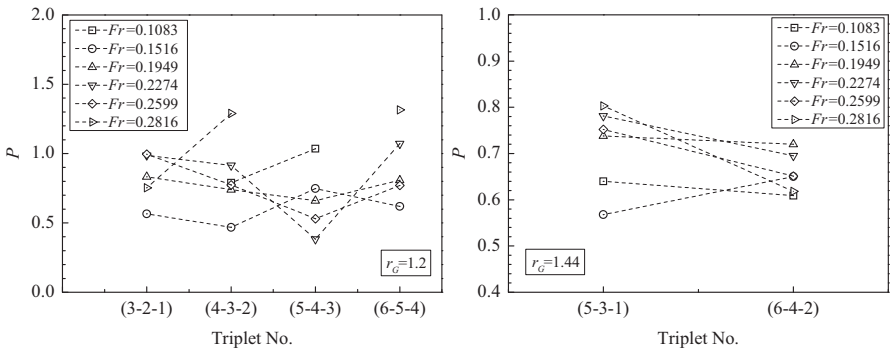


Fig. 5.6 Tendencies of P value in triplets (all Fr): $r_G = 1.2$ (*left*) and 1.44 (*right*)

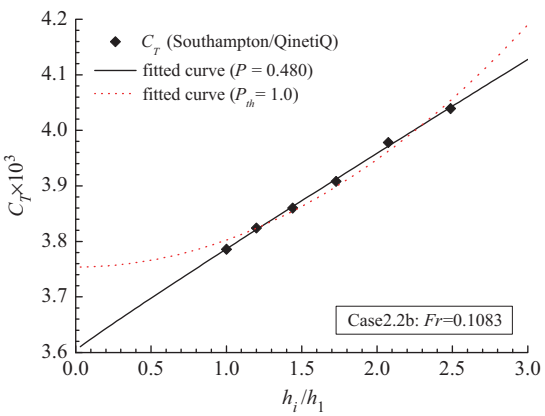


Fig. 5.7 Grid convergence in Case 2.2b ($Fr = 0.1083$)

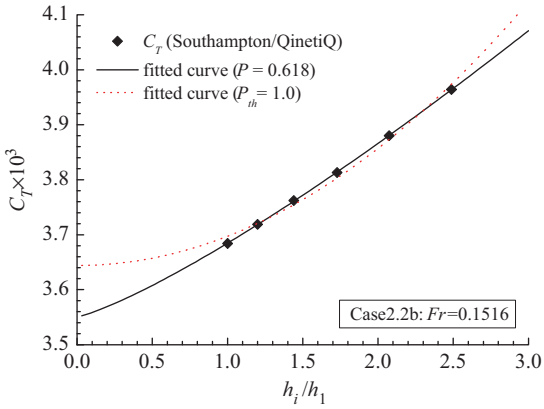


Fig. 5.8 Grid convergence in Case 2.2b ($Fr = 0.1516$)

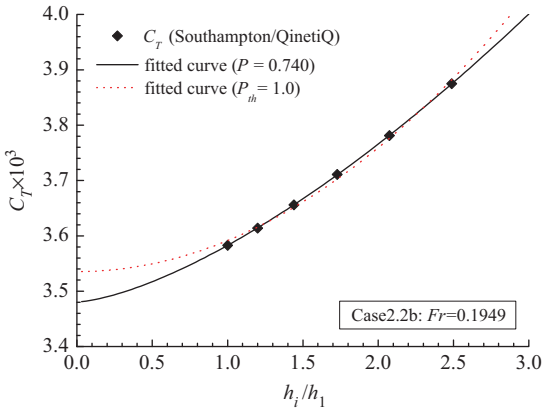


Fig. 5.9 Grid convergence in Case 2.2b ($Fr = 0.1949$)

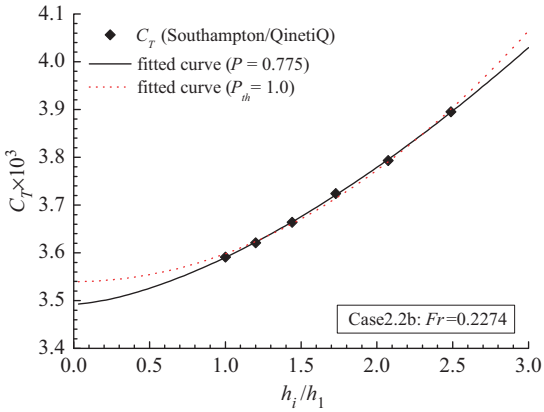


Fig. 5.10 Grid convergence in Case 2.2b ($Fr = 0.2274$)

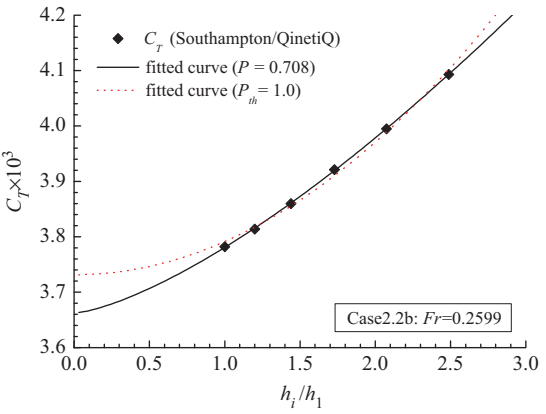


Fig. 5.11 Grid convergence in Case 2.2b ($Fr = 0.2599$)

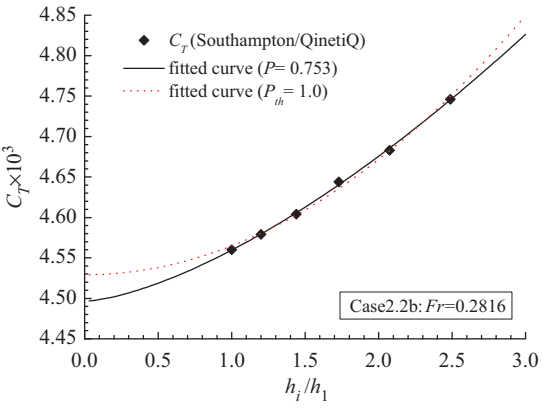


Fig. 5.12 Grid convergence in Case 2.2b ($Fr = 0.2816$)

the estimated uncertainties are of the same order. In the last condition, the FS and LSR methods typically obtain the same P value with a finest grid combination, i.e., grid triplet 3-2-1 in the FS and grid set 6 to 1 in the LSR. Their uncertainty results are also comparable, but if taking the GCI results into account, the LSR results more closely approximate the GCI results.

Graphical illustrations of the comparison between CFD solutions and experimental data, as well as numerical and data uncertainties, are presented in Figs. 5.13 to 5.18. Referring to the quantitative value in Tables 5.11 and 5.12, the numerical uncertainties from using the FS and LSR methods are similar, displaying an agreement between the two methods. As for the validation part, it is evident that almost all numerical uncertainties are larger than data uncertainties showing that predicting ship resistance by numerical tools in free conditions (heave and pitch) is more difficult and complicated than experimental processes. In addition, the situation $U_{SN} \gg |E|$ in most solutions implies that modeling errors are concealed in the numerical uncertainty, indicating that further investigations are required before arriving at any findings about the modeling error.

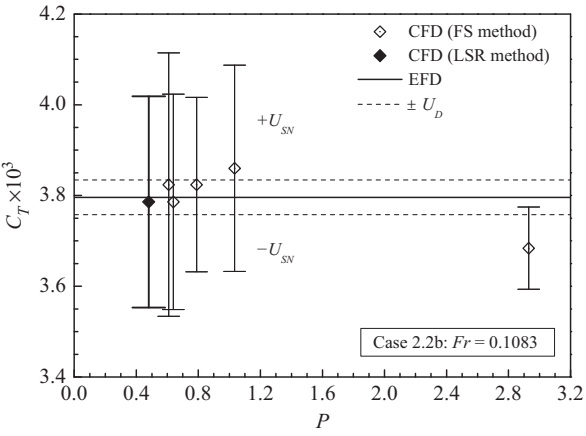


Fig. 5.13 V&V results in Case 2.2b ($Fr = 0.1083$)

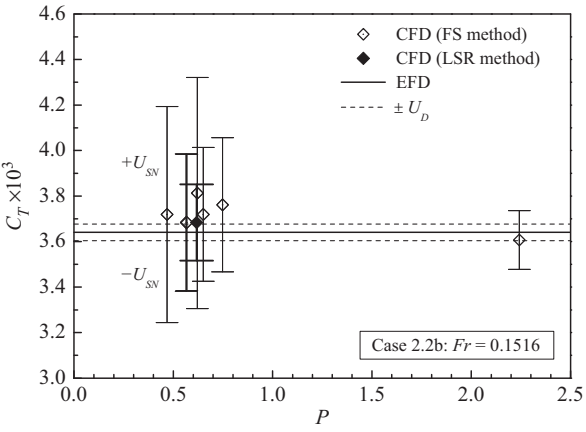


Fig. 5.14 V&V results in Case 2.2b ($Fr = 0.1516$)

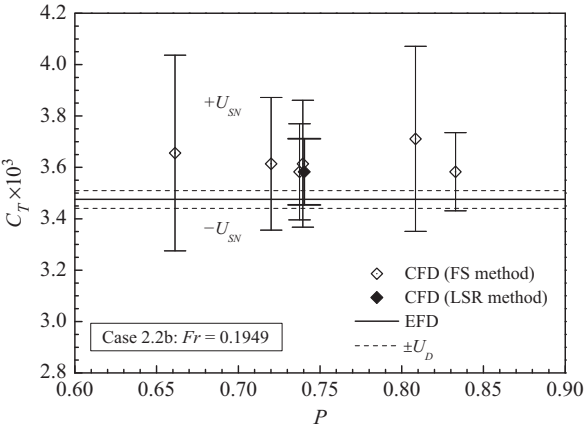


Fig. 5.15 V&V results in Case 2.2b ($Fr = 0.1949$)

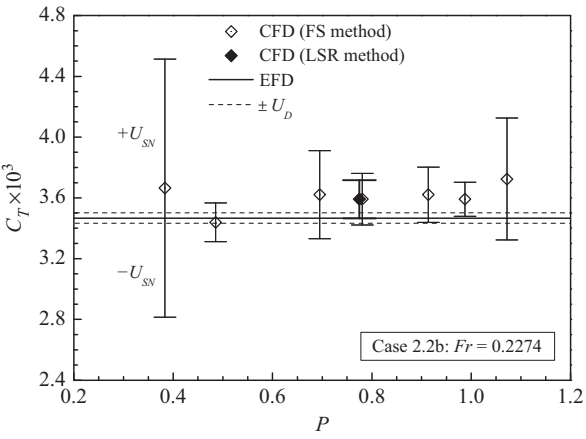


Fig. 5.16 V&V results in Case 2.2b ($Fr = 0.2274$)

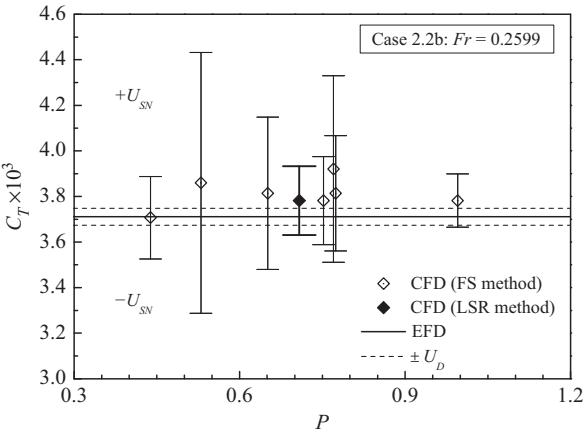


Fig. 5.17 V&V results in Case 2.2b ($Fr = 0.2599$)

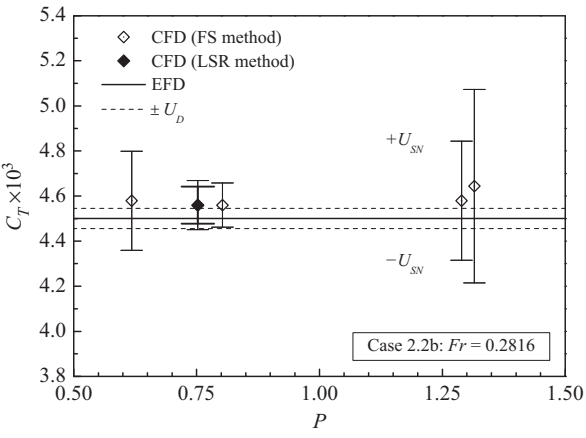


Fig. 5.18 V&V results in Case 2.2b ($Fr = 0.2816$)

Table 5.13 Submitted V&V results (Case 2.3a, $Fr = 0.26$)

Group (Code)	Basic information						Group submission			
	Grid type	Grid no.	Max. size (M)	r_G	U_I % ε_{12}	U_I %S	Ref.	P	U_G %S	U_{SN} %S
MARIN (PARNASSOS-PROCAL)	MS	3	6.2	2.0	0.6	0.003	Xing and Stern 2010	–	–	–
MOERI (WAVIS)	MS	3	8.6	1.414	0.0	0.0	Stern et al. 2001	2.088	1.78	1.78
NMRI (SURF)	S	3	3.8	1.414	24.5	0.17	ITTC 2002	2.730	0.13	0.22
Southampton/ QinetiQ (CFX)	MS	3	9.0	1.414	–	–	Eça and Hoekstra 2008	–	–	–
SSPA (SHIPFLOWv4.3)	OS	4	9.2	1.3195	0.6	0.001	Eça and Hoekstra 2006a	1.295	1.20	1.20

3.5 Case 2.3a

Two self-propulsion cases (for KCS hull) were specified at the workshop, Cases 2.3a and 2.3b. The V&V submissions for Case 2.3a are introduced in Table 5.13, including in total five groups with structured grids. In the results submitted, MARIN and Southampton/QinetiQ did not produce estimated uncertainties, implying that monotonic convergence was not attained in their studies, while the other three research groups, MOERI, NMRI and SSPA, observed $P > 1.0$. Note that NMRI has a relatively large iterative uncertainty: U_I is 24.5 % ε_{12} and comparable to the discretization uncertainty U_G submitted. Although the contribution of the iterative uncertainty to the numerical uncertainty appears negligible, since $U_{SN} \approx U_G$, the influence of a large U_I on the determination of U_G is considerable. A further investigation of this influence will be introduced later in this report.

From the FS method, as shown in Table 5.14, in agreement with their original observation the only divergence state is observed from the solutions of the Southampton/QinetiQ group. The others have a monotonic type of convergence and all obtain $P > 1.0$. NMRI has the largest order of accuracy ($P = 2.730$), perhaps as a result of applying fewer grid points. In this case, the estimated uncertainties depend mainly on the P value, that is, the closer P is to one, the lower the numerical uncertainty, e.g., $P = 1.161$ yields $U_{SN}\%S = 0.54$ while $P = 2.076$ yields $U_{SN}\%S = 6.34$. The GCI method still yields lower uncertainties (e.g., 0.41 %S with $P = 2.076$ and 0.16 %S with $P = 2.730$) than the FS (6.34 %S and 3.76 %S respectively). The two triplets based on the SSPA solutions produce slightly different results: from (4-3-2) to (3-2-1), the P value increases and lies farther away from the asymptotic range, whereas numerical uncertainties are reduced. Obviously, the result from the LSR method

Table 5.14 V&V results from FS and GCI methods (Case 2.3a, $Fr = 0.26$)

Group (Code)	FS method (2010)						GCI (Roache)		$\|E\|$ $\%D$
	Tri.	R	Con. type	P	U_G $\%S$	U_{SN} $\%S$	U_G $\%S$	U_{SN} $\%S$	
MARIN (PARNASSOS-PROCAL)	3-2-1	0.200	Mon.	1.161	0.54	0.54	0.16	0.16	0.40
MOERI (WAVIS)	3-2-1	0.237	Mon.	2.076	6.34	6.34	0.41	0.41	0.03
NMRI (SURF)	3-2-1	0.151	Mon.	2.730	3.76	3.76	0.16	0.23	3.56
Southampton/QinetiQ (CFX)	3-2-1	1.522	Div.	–	–	–	–	–	–
SSPA (SHIPFLOWv4.3)	3-2-1	0.400	Mon.	1.652	1.64	1.64	0.17	0.17	0.71
	4-3-2	0.513	Mon.	1.204	2.60	2.60	0.66	0.66	0.91

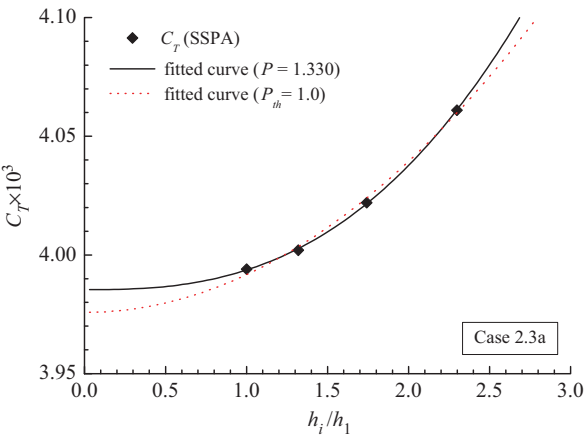


Fig. 5.19 Grid convergence of SSPA solutions

is available only for the SSPA group. The grid convergence tendency is presented in Fig. 5.19 together with the fitted curves in which the solutions are fitted well with the Least Squares Root curve. Similarly, monotonic convergence is observed from the LSR method (Table 5.15), and the estimated P value and uncertainties correspond fairly well with the results obtained by using the FS method.

Since it was not available from the experiments, the data uncertainty is absent in this case. Shown in Fig. 5.20, the estimated P values from both the FS and LSR methods are all larger than 1.0, and the two triplets (NMRI and MOERI) with $P > 2$ give large numerical uncertainties. As explained above, the large uncertainty of the NMRI submission is comprehensible as the grids may be too coarse to yield accurate results. However, the reason for the large uncertainty in the MOERI submission is not as clear, especially since the grids were not coarse (with finest grid size being 8.6M).

Table 5.15 V&V results from LSR method (Case 2.3a, $Fr = 0.26$)

Group (Code)	LSR method (2010)				
	Con. type	P	U_G %S	U_{SN} %S	$\|E\|$ %D
MARIN (PARNASSOS-PROCAL)	–	–	–	–	–
MOERI (WAVIS)	–	–	–	–	–
NMRI (SURF)	–	–	–	–	–
Southampton/QinetiQ (CFX)	–	–	–	–	–
SSPA (SHIPFLOWv4.3)	Mon.	1.330	1.43	1.43	0.71

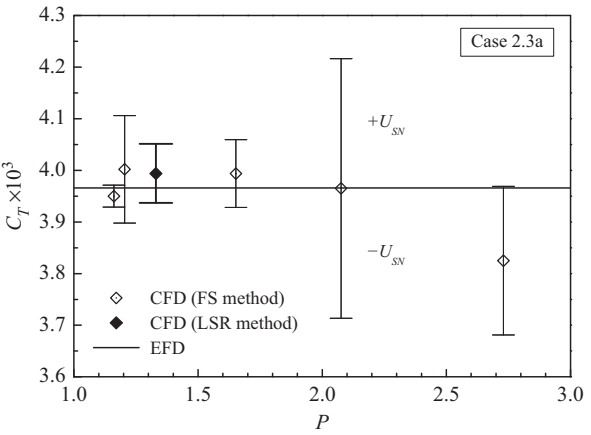


Fig. 5.20 V&V results in Case 2.3a

3.6 Case 2.3b

This case is similar to 2.3a, except that in Case 2.3b the KCS hull is free to heave and pitch. Only MOERI and SSPA participated in this test case. As indicated in Table 5.16, MOERI used three multi-block structured grids, while SSPA used four overlapping structured grids as in Case 2.3a. The maximum grid size and grid refinement ratio are very similar in the two submissions. However, the P values obtained are quite different: one is very high ($P = 2.347$) while the other is small ($P = 0.088$). In comparison with ε_{12}, U_I in the SSPA computations exhibits a non-negligible magnitude 32.5 %; however, compared to the submitted U_G, it is two orders of magnitude smaller. The influence of U_I on U_G will be discussed below.

The FS method yields the monotonic convergence for the MOERI solutions and the (3-2-1) triplet in the SSPA solutions, leading to $P > 2.0$ in both cases. In particular, the SSPA value is quite high (4.041); see Table 5.17. It might be suspected that a coarse grid induces this remoteness from the asymptotic range, but since the maximum grid size is around 9.2 million, it is most likely due to the scatter in the solutions—as displayed in Fig. 5.21, the grid convergence plotting from the LSR method. Also, the results from the FS, GCI and LSR methods are very dissimilar from one another: a large P value yields a relatively low uncertainty in the FS method, even lower uncertainty in the GCI, while a small P value from the LSR produces high

Table 5.16 Submitted V&V results (Case 2.3b, $Fr = 0.26$)

Group (Code)	Basic information						Group submission			
	Grid type	Grid no.	Max. size (M)	r_G	U_I % ε_{12}	U_I %S	Ref.	P	U_G %S	U_{SN} %S
MOERI (WAVIS)	MS	3	8.6	1.414	0.0	0.0	Stern et al. 2001	2.347	1.80	1.80
SSPA (SHIPFLOWv4.3)	OS	4	9.2	1.3195	32.5	0.03	Eça and Hoekstra 2006a	0.088	1.61	1.61

Table 5.17 V&V results from FS and GCI methods (Case 2.3b, $Fr = 0.26$)

Group (Code)	FS method (2010)						GCI (Roache)		
	Tri.	R	Con. type	P	U_G %S	U_{SN} %S	U_G %S	U_{SN} %S	$\|E\|$ %D
MOERI (WAVIS)	3-2-1	0.199	Mon.	2.329	5.86	5.86	0.31	0.31	6.89
SSPA (SHIPFLOWv4.3)	3-2-1	0.106	Mon.	4.041	0.66	0.66	0.02	0.04	10.70
	4-3-2	5.875	Div.	–	–	–	–	–	–

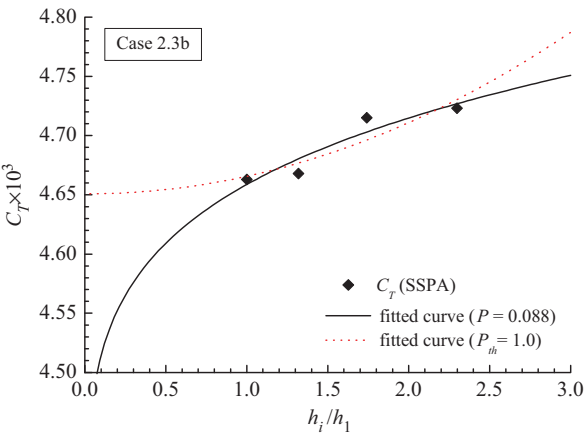


Fig. 5.21 Grid convergence of SSPA solutions

uncertainty. Such inconsistency is inevitable, as in this case the scatter in solutions is significant. Even with the Least Squares Root approach, the determination of the grid convergence and/or uncertainty is difficult. To obtain more information on grid dependence, investigating additional solutions would be essential.

The comparison of CFD solutions and measured data is shown in Fig. 5.22. Although the data uncertainty is missing, large numerical uncertainties from both methods are observed. The differences between solutions and data are considerable (refer to $|E|\%D$ values in Tables 5.17 and 5.18), leading to suspicious of a modeling error in computations and/or experiment.

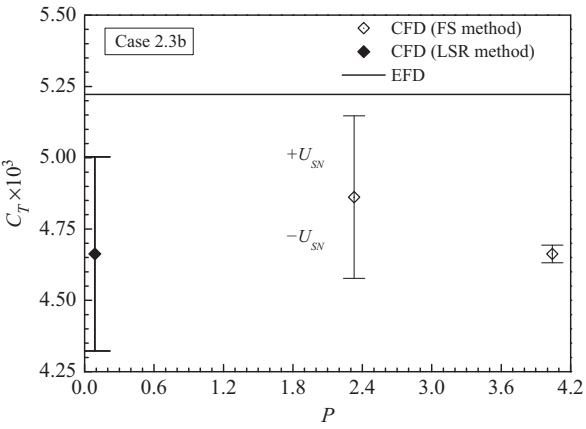


Fig. 5.22 V&V results in Case 2.3b

Table 5.18 V&V results from LSR method (Case 2.3b, $Fr = 0.26$)

Group (Code)	LSR method (2010)				
	Con. type	P	U_G %S	U_{SN} %S	$\|E\|$%D
MOERI (WAVIS)	–	–	–	–	–
SSPA (SHIPFLOWv4.3)	Mon.	0.088	7.30	7.30	10.70

Table 5.19 Submitted V&V results (Case 3.1a, $Fr = 0.28$)

Group (Code)	Basic information							Group submission				
	Grid type	Grid no.	Max. size (M)	r_G	U_I % ε_{12}	U_I %S	U_D %D	Ref.	P	U_G %S	U_{SN} %S	U_{val} %D
MARIC (FLUENT6.3)	MS	3	2.2	1.414	0.2	0.59	0.64	ITTC 2002	1.036	2.97	3.03	3.10
MARIN (PARNASSOS)	MS	4	7.4	2.0	20.8	2.84 E-05	0.64	Xing and Stern 2010	–	1.40	1.40	1.54
UoGe (STAR-CCM+)	U	3	2.1	1.5	0.01	0.002	0.64	–	–	–	–	–

3.7 Case 3.1a

Three research groups contributed results to this case: unlike the other two groups, MARIC, MARIN and UoGe, and UoGe used unstructured grids. MARIC and UoGe used fewer grid points (∼2 million), while MARIN used 7.4 million grid points, as indicated in Table 5.19. In their own grid dependency study, the UoGe group did not attain monotonic convergence with their unstructured grids, so that no uncertainty was reported; and based on the FS method applied here, neither was any monotonic convergence achieved. Only MARIN submitted results based on more than three grids. Comparing its results using the FS method (monotonic convergence for triplet

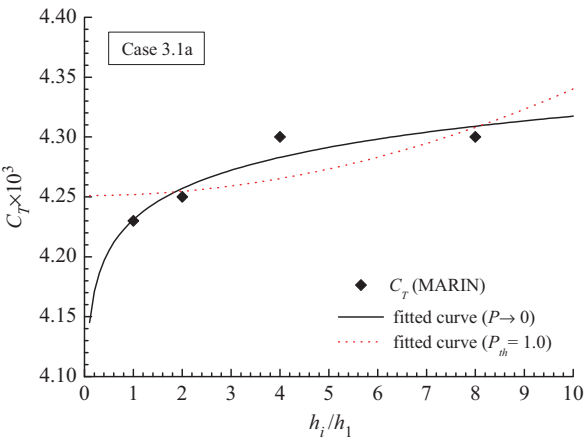


Fig. 5.23 Grid convergence of MARIN solutions

Table 5.20 V&V results from FS and GCI methods (Case 3.1a, $Fr = 0.28$)

Group (Code)	FS method (2010)							GCI (Roache)			$\|E\|$
	Tri.	R	Con. type	P	U_G %S	U_{SN} %S	U_{val} %D	U_G %S	U_{SN} %S	U_{val} %D	%D
MARIC (FLUENT6.3)	3-2-1	0.488	Mon.	1.036	5.94	5.98	5.91	3.37	3.42	3.49	0.17
MARIN (PARNASSOS)	3-2-1	0.400	Mon.	0.661	0.60	0.60	0.87	0.39	0.39	0.75	0.00
	4-3-2	∞	Div.	–	–	–	–	–	–	–	–
UoGe (STAR-CCM+)	3-2-1	−0.031	Osc.	–	–	–	–	–	–	–	–

3-2-1 only) and the LSR method (monotonic convergence), the difference lies mainly in the P value: the LSR method yields a much lower order of accuracy, close to zero. As shown in the grid convergence plot, Fig. 5.23, the scatter in the solutions providing a likely explanation, the grid refinement step ($r_G = 2.0$) might be too large, or grid4 may be too coarse. Consequently, to improve the grid convergence such measures as neglecting grid4, adding more refined grids or changing grid refinement ratio should be considered. Although the P values from the FS and LSR methods differ greatly, the uncertainties estimated agree with one another. Moreover, the order of accuracy from the triplets (MARIC and MARIN) by the FS and GCI methods are reasonably close to the theoretical $P_{th} = 1.0$, and the uncertainties from these two methods are also comparable (Tables 5.20 and 5.21).

The estimated numerical uncertainties and data uncertainty are presented in Fig. 5.24. The P value of the MARIC solutions is almost identical to the theoretical value ($P_{th} = 1.0$), but its numerical error interval is surprisingly large, most likely owing to its small grid size (2.2M).

Table 5.21 V&V results from LSR method (Case 3.1a, $Fr = 0.28$)

Group (Code)	LSR method (2010)					
	Con. type	P	U_G %S	U_{SN} %S	U_{val} %D	$\|E\|$ %D
MARIC (FLUENT6.3)	–	–	–	–	–	–
MARIN (PARNASSOS)	Mon.	0.0003	0.71	0.71	0.96	0.00
UoGe (STAR-CCM+)	–	–	–	–	–	–

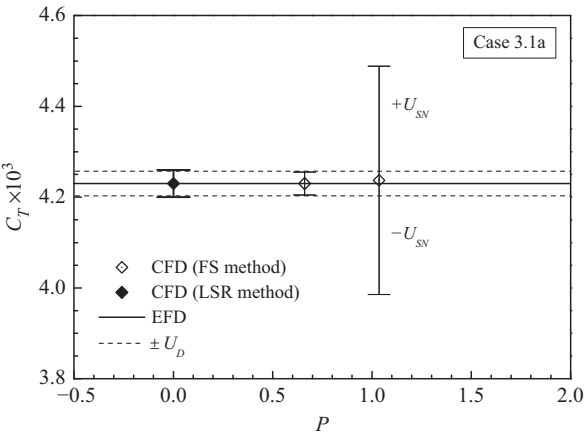


Fig. 5.24 V&V results in Case 3.1a

Table 5.22 Submitted V&V results (Case 3.1b, $Fr = 0.28$)

Group (Code)	Basic information						
	Grid type	Grid no.	Max. size (M)	r_G	U_I % ε_{12}	U_I %S	U_D %D
NavyFOAM (NavyFOAM)	U	3	13.0	1.41	–	–	0.63

3.8 Case 3.1b

Since no monotonic convergence was obtained, with three unstructured grids but without V&V result, the NavyFOAM group is the only entry in this test case. Therefore, only basic information is presented in Table 5.22. In the FS method, the solutions still diverge with grid refinement, producing no V&V result either. It should be noted that this group applied a larger grid size, with the grid convergence problem probably attributed to unstructured grids. This again illustrates the difficulty of applying grid convergence studies to this type of grid.

3.9 Case 3.2

In this test case, V&V results at three speeds (Fr) in the free (heave and pitch) condition were requested; however, there was only one submission, in which for $Fr = 0.28$ from the MARIN group (Table 5.23). The submission was almost the same as in Case 3.1a in which the computation was set up at the same speed but at fixed

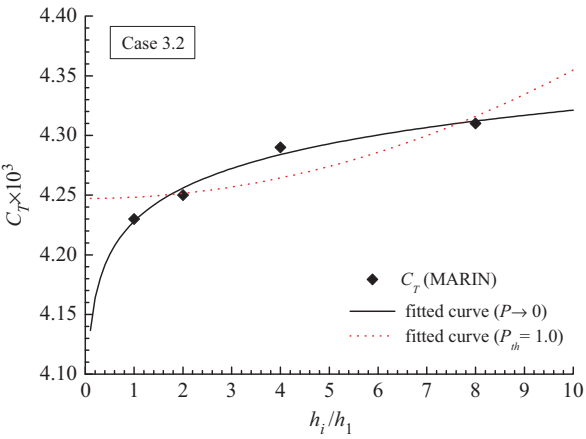


Fig. 5.25 Grid convergence of MARIN solutions

Table 5.23 Submitted V&V results (Case 3.2, $Fr = 0.28$)

Group (Code)	Basic information							Group submission				
	Grid type	Grid no.	Max. size (M)	r_G	U_I % ε_{12}	U_I %S	U_D %D	Ref.	P	U_G %S	U_{SN} %S	U_{val} %D
MARIN (PARNASSOS)	MS	4	7.4	2.0	0.01	4.73 E-05	0.64	Xing and Stern 2010	–	1.40	1.40	1.54

Table 5.24 V&V results from FS and GCI methods (Case 3.2, $Fr = 0.28$)

Group (Code)	FS method (2010)							GCI (Roache)			|E| %D
	Tri.	R	Con. type	P	U_G %S	U_{SN} %S	U_{val} %D	U_G %S	U_{SN} %S	U_{val} %D	
MARIN (PARNASSOS)	3-2-1	0.500	Mon.	0.500	0.96	0.96	1.15	0.59	0.59	0.87	0.00
	4-3-2	2.000	Div.	–	–	–	–	–	–	–	–

Table 5.25 V&V results from LSR method (Case 3.2, $Fr = 0.28$)

Group (Code)	LSR method (2010)					
	Con. type	P	U_G %S	U_{SN} %S	U_{val} %D	|E| %D
MARIN (PARNASSOS)	Mon.	0.003	0.81	0.81	1.03	0.00

dynamic sinkage and trim. Small P values are estimated from both the FS and LSR methods. In particular, the value from the LSR method is close to zero. Figure 5.25 illustrates that the grid refinement ratio is too large and grid 4 too coarse, as explained in Case 3.1a. The uncertainties from the FS and LSR methods and data uncertainty are available in Tables 5.24 and 5.25 and in Fig. 5.26, in which the finest solution well matches experimental data.

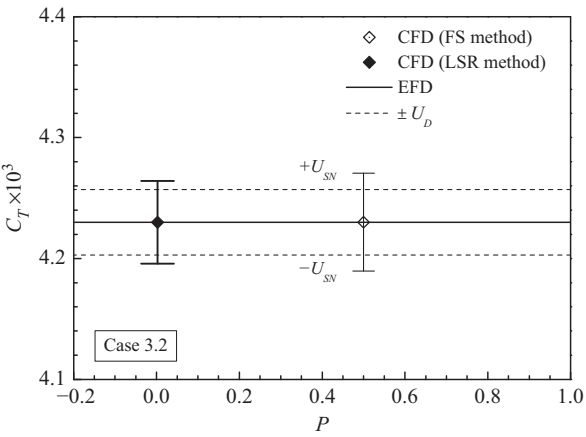


Fig. 5.26 V&V results of MARIN submission

4 Discussions of the V&V Study

In this section, some observations from the investigations and/or statistical analysis presented are discussed.

4.1 V&V Credibility

As mentioned above, the accuracy (coupled with computing expense) of the CFD computation is one of the most important issues in solving physical problems by computational/numerical techniques. Assessing accuracy by comparing numerical solutions and experimental data has a long tradition, while the concept of V&V and its application have not attracted enough attention, especially for complex turbulent flows, involving ship hydrodynamics. The reason, apart from the complicated and time-consuming procedure, might be traced to doubts regarding the reliability and usefulness of V&V.

Certainly, only if the error and uncertainty are quantified appropriately, V&V would be able to provide valuable information in CFD computations and thus demonstrate the credibility required. Verification addresses the numerical error and uncertainty in the process of iteration and discretization, which are inevitable issues in numerical computation. If the estimation was reliable, it could be used to balance the numerical accuracy against the computing expense. Validation, on the other hand, not only highlights the level of agreement with available experimental data, but also hints at the possible interval within which the modeling error falls in a CFD computation. However, V&V is indeed a complicated subject and the determination of a reliable error and uncertainty is challenging, as implied by the fact that several V&V methods exist, but that a commonly accepted standard is still missing.

Considering the above, the three most well-known verification methods, FS, GCI and LSR, are presented in this report and used to estimate the numerical error and uncertainty. If it could be demonstrated that these three methods produce similar results, it would strengthen their credibility. Such a comparison will now be made by taking the 12 entries to which the three methods can be applied, 12 triplets (3-2-1) for the FS and GCI methods, and 12 sets (more than three solutions) for the LSR method from the same test case submissions. The results are summarized in Table 5.26.

First, considering the grid convergence, the same type is obtained in 10 out of the 12 entries, as shown in Table 5.26. No. 1 and 3 differ, for which the LSR method produces monotonic convergence while the FS method shows divergence. The difference is likely to be attributable to scatter in the solutions, which is smoothed out in the LSR method but may create divergence in the FS method.

Turning next to the observed order of accuracy p (represented by P), a comparison between the FS/GCI and LSR methods is made in Table 5.26 and Fig. 5.27 (P is the same for the FS and GCI methods). Note that P can only be estimated for the nine monotonically convergent cases in the FS/GCI method. Out of these nine cases, three exhibit completely different P values compared with the LSR method. For No. 4 to No. 9 the correspondence is good, but for $10 \sim 12$ the LSR method produces a significantly lower P. The reason for this discrepancy is the large scatter in the solutions involving this case (SSPA contribution in Case2.3b). This scatter is smoothed out in the LSR but not in the FS/GCI method. Another reason is that the coarse grid (MARIN contribution in Case 3.1a and 3.2) strongly affects the curve fit in the LSR method, as seen in Figs. 5.23, 5.25. Concerning the error estimate δ_{RE}, a good correspondence for No. 4 to No. 9 is observed as well.

Another interesting quantity is the numerical uncertainty, U_{SN}. Comparing the values in Table 5.26 and the solid and dashed curves of Fig. 5.27, a decent correspondence between FS and LSR is noted. The exception is No. 10, for which the P value varies. As for the comparison between the FS and GCI methods, uncertainties from the GCI (even with a large P value in No. 10) are generally comparable to those of the FS but with smaller values, as the uncertainty results in Section 3 for all test cases have presented. Another observation is that using the GCI method, the estimated uncertainties for $p > p_{th}$ are smaller than those for $p < p_{th}$. One reason is that the error estimate δ_{RE} in the GCI is much smaller than that in the FS method. This issue is also mentioned and illustrated by Xing and Stern (2010) in their statistical analysis. As for validation, finally, the FS and LSR methods provide the same result, $|E| < U_{val}$ in almost all cases, except No.6 where U_{val} is very close to $|E|$ in both methods. The GCI provides similar U_{val} as FS, albeit with smaller values.

Considering the general difficulties in conducting a V&V study as revealed in the previous section of this report, and the fact that the FS and LSR methods were developed based on entirely different benchmark data, the correspondence attained between results is surprising and lends significant credibility to both methods. This is particularly the case when the solutions are close to the asymptotic range. Further away from this range, the differences become larger, which is not surprising since the formulas used are based on data close to the range (In the FS method $P = 2.0$ is stated as the upper limit of validity). It should be stressed, however, that the number

Table 5.26 Summary of V&V results (from FS, GCI and LSR methods) for 12 entries

No.	Case name	Group name	Con. type		P		$\delta_{RE}\%S_1$		$U_{SN}\%S$			$U_{val}\%D$			$\|E\|\%D$
			FS & GCI (3-2-1)	LSR	FS & GCI (3-2-1)	LSR	FS & GCI (3-2-1)	LSR	FS (3-2-1)	GCI (3-2-1)	LSR	FS (3-2-1)	GCI (3-2-1)	LSR	
1	1.2a	HSVA	Div.	Mon.	–	1.314	–	−0.91	–	–	2.68	–	–	2.88	0.73
2	2.2a	MARIC	Osc.	Osc.	–	9.730	–	−0.04	–	–	13.04	–	–	13.41	2.61
3	2.2b-*Fr*1	Southampton/QinetiQ	Div.	Mon.	–	0.480	–	4.80	–	–	6.15	–	–	6.21	0.26
4	2.2b-*Fr*2	Southampton/QinetiQ	Mon.	Mon.	0.565	0.618	4.16	3.62	8.19	5.20	4.55	8.35	5.35	4.71	1.18
5	2.2b-*Fr*3	Southampton/QinetiQ	Mon.	Mon.	0.833	0.740	2.44	2.86	4.25	3.05	3.59	4.49	3.30	3.84	3.11
6	2.2b-*Fr*4	Southampton/QinetiQ	Mon.	Mon.	0.987	0.775	1.93	2.74	3.11	2.41	3.50	3.37	2.69	3.76	3.58
7	2.2b-*Fr*5	Southampton/QinetiQ	Mon.	Mon.	0.995	0.708	1.93	3.17	3.10	2.42	4.00	3.32	2.66	4.20	1.91
8	2.2b-*Fr*6	Southampton/QinetiQ	Mon.	Mon.	0.753	0.753	1.32	1.39	2.39	1.65	1.81	2.62	1.95	2.08	1.31
9	2.3a	SSPA	Mon.	Mon.	1.652	1.330	0.13	0.22	1.64	0.17	1.43	–	–	–	0.71
10	2.3b	SSPA	Mon.	Mon.	4.041	0.088	0.01	9.37	0.66	0.04	7.30	–	–	–	10.70
11	3.1a	MARIN	Mon.	Mon.	0.661	0.0003	0.32	>100	0.60	0.39	0.71	0.87	0.75	0.96	0.00
12	3.2	MARIN	Mon.	Mon.	0.500	0.003	0.47	>100	0.96	0.59	0.81	1.15	0.87	1.03	0.00

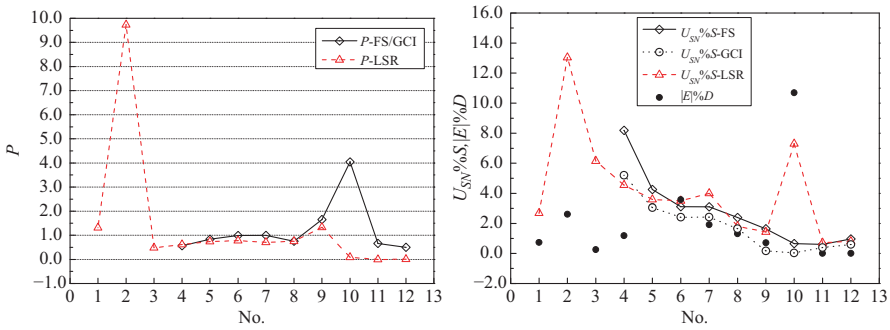


Fig. 5.27 V&V results from FS/GCI and LSR method for 12 entries

of cases used by this study is very limited. Since in most verification methods U_{SN} is quantified on the basis of experience or statistical analysis to ensure a 95 % level of confidence, more practical or complicated applications are necessary to test the V&V methods.

4.2 Verification Investigation

Verification is a process for estimating the numerical error or uncertainty in CFD computations, caused by the iteration and grid discretization errors in the present steady-state investigation. As mentioned previously, the iterative error or uncertainty is usually obtained from the iterative history of a CFD computation, while the latter is estimated by means of a grid convergence study. From this point of view, several questions of significance for a verification investigation should be paid attention to.

4.2.1 Influence of U_I on U_G

Prior to the estimation of a discretization error, iterative convergence should be achieved. In principle, any computation should be converged to machine accuracy to ensure a negligible iterative error. However, in practical applications, especially for complex flows, this requirement is seldom satisfied and there is no uniform way to control the iterative convergence, because of the fact that computing expense or CPU time is so important. Eça and Hoekstra (2006b, 2009) pointed out that the iterative and discretization errors are not independent of each other—the former may affect the determination of the latter. When balancing iterative accuracy against computing expense, however, the solutions need not be converged to machine accuracy to attain a negligible contribution from the iterative error. Instead, it was suggested to minimize such an influence by requesting the iterative error to be two to three orders of magnitude below the discretization error. Stern et al. and Xing and Stern (2001,

2010) made a similar proposal to require an iterative error of at least one order of magnitude smaller in their methods. Since the control of iterative convergence and its influence on the determination of the discretization error are so important, it is worthwhile to look into the available material from the 2010 workshop to investigate these issues in practice.

As reported above, almost all participants at the workshop provided their iterative convergence criteria, among which the residuals and the iterative history of an integral quantity were the most common. As for the quantification of U_I, the reported methods are mainly: the average of the maximum and minimum values over the last two oscillation periods for oscillatory iterative convergence (ITTC 1999, 2002, 2008; Stern et al. 2001); relative variation (standard deviation) of the last iterations; and/or extrapolation of norms of the changes in the solution based on a geometric progression (Eça and Hoekstra 2006b, 2009). In the respective submissions, the closeness of the iterative convergence to the machine accuracy is unknown, and the quantification methods for U_I are also complex to evaluate. Nevertheless, the influence of the iterative error on the determination of the discretization error leads itself to investigation.

Before any grid convergence study is made, U_G is unknown, so the magnitude of U_I cannot be expressed in percentage of U_G. It seems reasonable to instead base the acceptable level of U_I on the solution change between the two finest grids, ε_{12}, since the determination of p and thereby U_G is based on this quantity (and ε_{23}, see equation (5.3)). In this chapter we will investigate the effect on U_G by varying the finest solution S_1 by $\pm U_I$, i.e., and then compare the original U_G against that obtained with S_1 changed to $S_1 + U_I$ and $S_1 - U_I$. This should provide an indication of the effect of the U_I uncertainty. For a more exact evaluation U_I should be considered for all three solutions (i.e., S_1, S_2 and S_3) used to determine p. The solutions should then be considered independent. The variations will be made for all converged triplets in the FS method.

The computed changes in grid discretization uncertainty (ΔU_G) due to increased ($+U_I$) or decreased ($-U_I$) S_1 are illustrated in Table 5.27, in which U_I is also expressed in percentage of U_G for comparison purpose. The table shows that the extremely large iterative error in the finest solution S_1 ($U_I \,\%\, \varepsilon_{12} = 2464$) for No. 11 entirely changes the grid convergence tendency from being monotonically convergent to being divergent ($+U_I$) or oscillatory ($-U_I$). To help understand the influence of U_I on U_G, graphical results are presented in Figs. 5.28 and 5.29, in which the computed ΔU_G are plotted versus the increase or decrease of S_1 (i.e. $+/-U_I$). Expressing U_I in percentage of both ε_{12} and U_G in these two figures makes it possible to compare the different references (ε_{12} and U_G). In Fig. 5.28 U_G changes a great deal (at least 50 %) towards the positive $U_I \,\%\, \varepsilon_{12} > 12.5$ (Fig. 5.28a) and towards the negative $U_I \,\%\, \varepsilon_{12} > 1.1$ (Fig. 5.28b). On the other hand in Fig. 5.29, U_G presents a large variation when the positive $U_I \,\%\, U_G > 4.602$ (Fig. 5.29a) and the negative $U_I \,\%\, U_G > 0.888$ (Fig. 5.29b). Note that for $U_I \,\%\, \varepsilon_{12} \leq 1.1$ or $U_I \,\%\, U_G \leq 0.888$, ΔU_G from positive U_I and negative U_I have similar magnitudes with opposite signs—but when the U_I value is larger, the magnitudes of ΔU_G from positive U_I

Table 5.27 Variation of U_G with U_I

No.	Case name	Group name	Tri.	U_I % U_G	U_I % ε_{12}	$\Delta U_G \% U_G$ $(+U_I)$	$\Delta U_G \% U_G$ $(-U_I)$
1	Case 1.2a	HSVA	5-3-1	5.835	1.000	1.910	−1.886
2		MARIC	3-2-1	2.624	12.500	−14.163	1.099
3		MOERI[a]	3-2-1	0.001	0.001	0.004	−0.004
4		VTT	7-4-1	14.556	237	104.659	−55.850
5	Case 1.2b	MOERI	3-2-1	0.0002	0.001	−0.001	0.001
6		MOERI	3-2-1	0.001	0.001	0.002	−0.002
7		MOERI	3-2-1	0.0002	0.001	−0.0001	0.0001
8		MOERI	3-2-1	0.0002	0.001	0.002	−0.002
9		MOERI	3-2-1	0.001	0.001	−0.008	0.008
10		MOERI	3-2-1	0.0005	0.001	0.004	−0.004
11	Case 2.2a	CSSRC	3-2-1	512	2464	Div.	Osc.
12		MOERI	3-2-1	0.0002	0.001	0.066	0.063
13		TUHH&ANSYS	3-2-1	0.035	0.100	−0.157	0.157
14	Case 2.2b	MOERI	3-2-1	0.0002	0.001	−0.001	0.001
15	($Fr = 0.1083$)	Southampton/ QinetiQ	5-3-1	0.064	0.400	0.886	−0.878
16	Case 2.2b	MOERI	3-2-1	0.0002	0.001	−0.001	0.001
17	($Fr = 0.1516$)	Southampton/ QinetiQ	3-2-1	0.093	0.800	6.284	−5.825
18	Case 2.2b ($Fr = 0.1949$)	Southampton/ QinetiQ	3-2-1	0.001	0.600	3.768	−3.622
19	Case 2.2b	MOERI	3-2-1	0.020	0.001	0.005	−0.005
20	($Fr = 0.2274$)	Southampton/ QinetiQ	3-2-1	0.888	3.300	20.932	56.462
21	Case 2.2b	MOERI	3-2-1	0.0002	0.001	0.005	−0.005
22	($Fr = 0.2599$)	Southampton/ QinetiQ	3-2-1	0.300	1.100	6.515	20.115
23	Case 2.2b ($Fr = 0.2816$)	Southampton/ QinetiQ	3-2-1	0.052	0.300	1.958	−1.915
24	Case 2.3a	MARIN	3-2-1	0.566	0.600	−0.336	0.312
25		MOERI	3-2-1	0.0002	0.001	0.001	−0.001
26		NMRI	3-2-1	4.602	24.500	34.011	−33.251
27		SSPA	3-2-1	0.073	0.600	0.148	−0.166
28	Case 2.3b	MOERI	3-2-1	0.0002	0.001	0.001	−0.001
29		SSPA	3-2-1	5.304	32.500	53.097	−46.228
30	Case 3.1a	MARIC	3-2-1	9.965	20.800	49.553	84.216
31		MARIN	3-2-1	0.005	0.006	0.018	−0.018
32	Case 3.2	MARIN	3-2-1	0.003	0.010	0.020	0.020

[a]The MOERI group reported zero U_I in all submissions. To investigate the influence of U_I, we here assume a negligible $U_I \% \varepsilon_{12} = 0.001\,\%$

and negative U_I are quite different, indicating the strongly non-linear dependence of U_I on U_G. From Figs. 5.28 and 5.29, the interesting conclusion may be drawn that, at least based on this extremely limited material, controlling the iterative error U_I with the reference to either the discretization error U_G or the solution change in two successive grids ε_{12} leads to similar results. As to the maximum permissible value of U_I, it can be derived only if the acceptable level of accuracy of U_G was defined, but

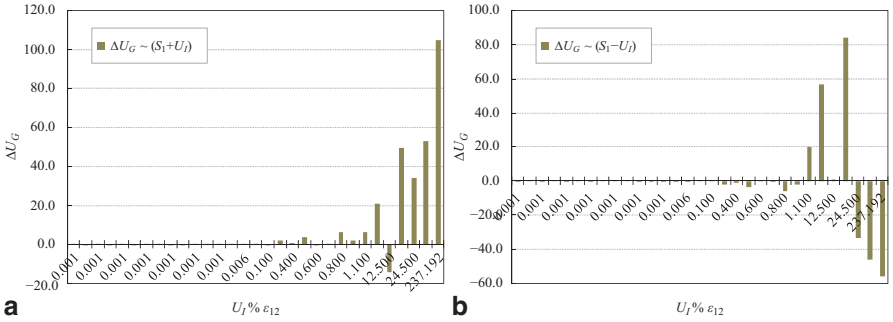


Fig. 5.28 $\Delta U_G \% U_G$ versus increased and decreased S_1 ($\pm U_I$) [U_I denoted as U_I % ε_{12}]

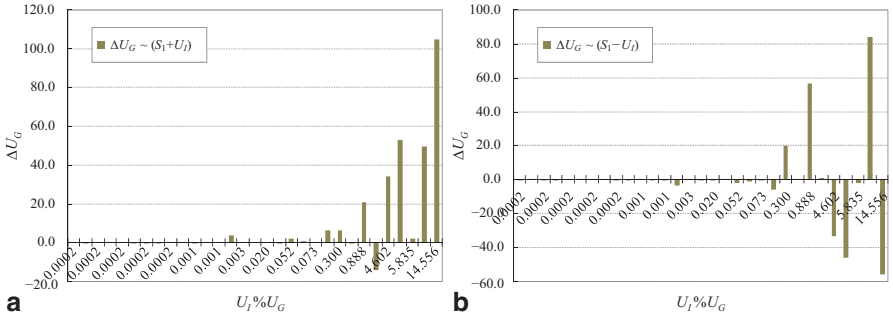


Fig. 5.29 $\Delta U_G \% U_G$ versus increased and decreased S_1 ($\pm U_I$) [U_I denoted as U_I %U_G]

the plots clearly indicate that the requirement is quite strong. For instance, $U_I \% \varepsilon_{12}$ (or $U_I \% U_G$) < 1 does not guarantee an error in U_G smaller than 10 %. For this to remain the case, the present results indicate that $U_I \% \varepsilon_{12}$ (or $U_I \% U_G$) < 0.1 is required. Since the number of entries is low (only 32), there is no guarantee that even this requirement be sufficient in all cases. However, it is consistent with the statement by Eça et al. that U_I must be reduced to two or three orders of magnitude below U_G. Consequently, exercising the grid convergence study (by the FS/GCI or LSR methods) for submissions with large iterative uncertainties is meaningless, which means that these submissions will be excluded from the discussions in the following sections.

Two final comments on the effect of U_I on U_G: First, as mentioned above, the effect was estimated by varying S_1 alone. This will underestimate the requirement on U_I, since variations in S_2 and S_3 should be considered as well. It is unlikely, however, that this will change the order of magnitude of the requirement. Second, the effect may be estimated without access to the computed data by assuming P and δ_{RE} (or ε_{12} and ε_{23}). In the present study, these values have been obtained on the basis of realistic computations.

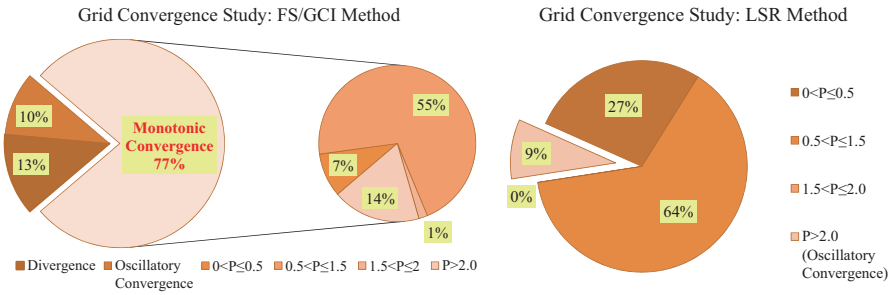


Fig. 5.30 Convergence type and P value in the FS/GCI method and the LSR method

4.2.2 Convergence Type and Observed Order of Accuracy

In principle with increasing number of grid points, the discretization error should tend towards zero, i.e., the solutions should converge to a certain value (the solution to the differential equation); however, this is not always the case, and how to quantify the error or uncertainty in the grid discretization is a common concern. The general convergence conditions are classified as (monotonic or oscillatory) convergence and (monotonic or oscillatory) divergence, the ideal situation being that the solutions converge monotonically. As mentioned above, solutions with large U_I should be omitted, and *71 triplets* in the FS/GCI method and *11 sets* in the LSR method are finally obtained. Using the FS/GCI method, three types of convergence are attained: 55 triplets (77 %) have monotonic convergence, 7 (10 %) have oscillatory convergence, while 9 (13 %) exhibit divergence. In the FS/GCI method, only monotonic convergence can be used to apply RE to estimate the convergence rate p and the discretization error δ_{RE}. The classification of determined order of accuracy P for the 77 % of the triplets with monotonic convergence is presented in a pie chart (see Fig. 5.30): 7 % have a P in the range $0 < P \leq 0.5$, 55 % in $0.5 < P \leq 1.5$, 1 % in $1.5 < P \leq 2.0$ and 14 % in $P > 2.0$. Most solutions (55 %) are thus close to the asymptotic range, but the remaining 22 % get either larger or smaller P values and those with large P value are in a majority (14 % with $P > 2.0$).

In the LSR method, the estimation of P is not restricted to monotonic convergence. Therefore, all 11 sets of solutions have obtained P values. Three sets (27 %) fall within in the range $0 < P \leq 0.5$, seven (64 %) in $0.5 < P \leq 1.5$, and these ten sets all achieve monotonic convergence. No submission is in the range of $1.5 < P \leq 2.0$ and only one set (9 %) has $P > 2.0$ and appears to have oscillatory convergence. As shown in Fig. 5.30, overall 64 % P values from the LSR method are in the vicinity ($0.5 < P \leq 1.5$) of the theoretical one, which is comparable to the 55 % in the FS/GCI method. The proportion of those having low accuracy within $0 < P \leq 0.5$ (27 %) is larger than in the FS/GCI method (7 %), however. The scatter in numerical solutions is a possible explanation for the excessive or low level of accuracy (P), as suggested by the developers of the LSR method. As shown in the curve fits, the scatter is clearly present in most submissions. The Least Squares Root curve fit works well in

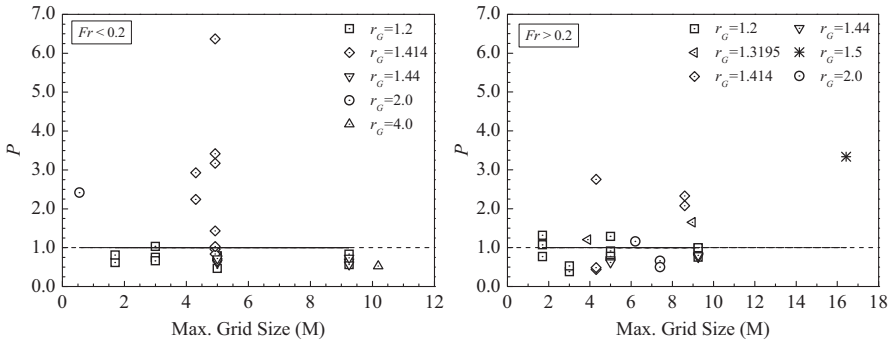


Fig. 5.31 P value versus maximum grid size at $Fr < 0.2$ and $Fr > 0.2$

smoothing it out. However, since the number of entries that can be used in the LSR method is very limited, it is difficult to draw reliable statistical conclusions.

4.2.3 Convergence State Versus Grid Type

In the grid convergence study, the level of accuracy obtained is always associated with the form of grid discretization, e.g., the adopted grid type, the grid sizes and the refinement ratio used to create systematic similar grids. First and foremost is the grid type. Classifying it as structured or unstructured, in the FS/GCI method, 63 triplets used structured grids, of which 53 achieved monotonic convergence (84 %); the other eight triplets used unstructured grids and two of them achieved monotonic convergence (25 %). However, in the LSR method, of the 11 sets of submissions, only one used an unstructured grid and it attained monotonic convergence. Nine of the other ten sets with structured grids attained monotonic convergence and the remaining one featured oscillatory convergence. These observations imply that structured grids clearly are more prevalent and attain monotonic convergence more easily than unstructured grids. However, since the number of entries applying unstructured grids is only eight, it is difficult to draw statistically sound conclusions.

4.2.4 Observed Order of Accuracy Versus Grid Step and Grid Size

To better understand the relationship between the grid resolution and the obtained order of accuracy, estimated P values are plotted in Fig. 5.31 against their relevant maximum grid sizes (in millions) and grid refinement ratio r_G for the 55 monotonically converged triplets in the FS/GCI method. The maximum grid size refers to the finest grid in each triplet. Note that results are split in low speed ($Fr < 0.2$) and high speed ($Fr > 0.2$) computations. r_G is classified by seven values, from 1.2 to 4.0, each represented by a symbol. The theoretical order of accuracy ($P_{th} = 1.0$) is indicated by a dashed line in the figure as well for reference.

Figure 5.31 shows that the maximum grid sizes of 2∼10 million are the most common in the grid refinement study; in particular, 3∼5 million are mostly used for low speed, but for high speed the grid size is more scattered between 2 and 10 million. Most P values are located around the $P = 1.0$ line. However, it is not possible to infer any dependence of P on grid size from the present investigation. The reason is that large or small P values are not entirely dependent upon the lack of grid discretization points; for instance, the P values estimated from about 4 million grid points vary between 0.5 and 6.5, and even with a 16.5 million grid size the P value reaches 3.5. Further, combining the P value with the refinement ratio r_G, the figure indicates that the problematic P values (far away from 1.0) are associated not only with the grid refinement ratio, but also with the grid size. A typical example is $r_G = 2.0$; at low speed ($Fr < 0.2$) this ratio coupled with a small grid size (only about 0.5 million) causes the P to be larger than 2.0, while in the high-speed case, this r_G with a grid size of more than 6 million yields P close to 1.0. Moreover, with respect to the grid refinement ratio, $r_G = 1.2$ is the most common one and its P values are all located in the vicinity of the asymptotic range. There are also other grid refinement ratios with P close to 1.0, such as $r_G = 1.3195, 1.44$. In view of the insufficiency of submissions for these refinement ratios, no comment on their relation to the estimated P will be made.

4.2.5 Numerical Uncertainty Versus Order of Accuracy and Grid Size

The numerical uncertainty primarily derives from the grid discretization, as for a well-converged computation the iterative uncertainty U_I should be tiny compared to the grid discretization uncertainty U_G. In fact, with the requirements of both V&V methods as specified above, U_I is negligible in the computation of U_{SN}. The estimated numerical uncertainties U_{SN} based on the FS and LSR methods against the obtained order of accuracy p (P) are presented in Fig. 5.32, in which the relevant uncertainty bars are plotted. Open symbols represent the finest solutions in the triplets (FS), while solid symbols represent the finest solutions in sets (LSR). In the figure, results are grouped by three grid sizes: small size (≤ 3 million grid points), medium size (between 3 and 8 million) and large size (> 8 million), and thereafter split by low-speed ($Fr < 0.2$) and high-speed ($Fr > 0.2$) computations. The medium size is widely used in the low-speed computations, while in high-speed computations the medium and large sizes are more frequent. In both low- and high-speed computations, the less frequently used smaller grid sizes always produce larger numerical uncertainty. And if we compare the global U_{SN} at $Fr < 0.2$ and $Fr > 0.2$, it is seen that the magnitudes in the high-speed computations are larger than those in the low-speed computations, especially with small grid sizes. Furthermore, for medium and large grid sizes in low- and high-speed computations, the relationship between U_{SN} and P indicates that when the solutions are far from the asymptotic range, the estimated uncertainties from the FS method are either huge or minor, revealing the difficulties in quantifying the error or uncertainty in such situations.

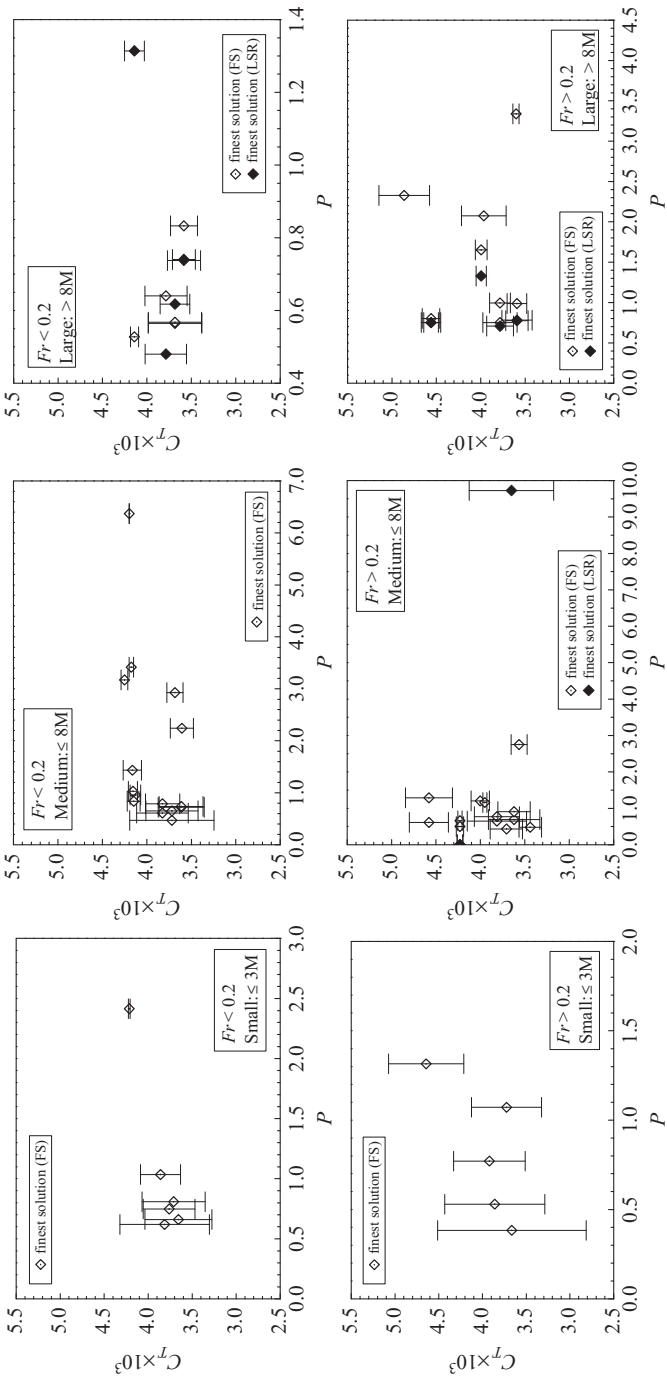


Fig. 5.32 Numerical uncertainties versus grid size and P value for $Fr < 0.2$ and $Fr > 0.2$

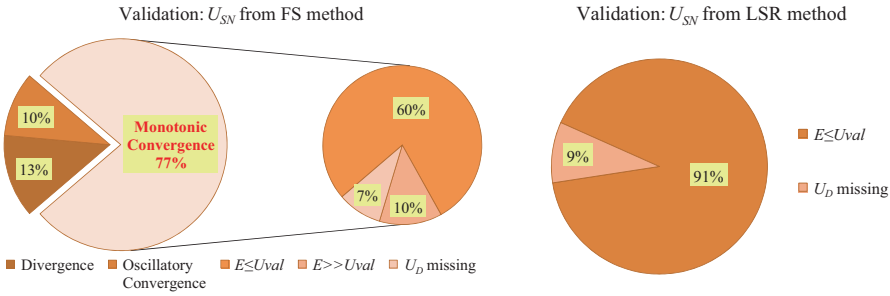


Fig. 5.33 Validation results (based on U_{SN} from the FS method and the LSR method)

4.3 Validation

4.3.1 Assessment of Validation: U_{val} Versus $|E|$

As far as validation is concerned, the traditional procedure has been to consider it to be a success or a failure simply by comparing it with experimental data, and always for a specific application alone. However, what is 'validated' in this case, as the V&V 20 standard (ASME 2009) points out, is 'not a quality of the code/model but an involved process'. Following the suggestion of the V&V 20 standard, the present work is focused on the quantitative assessment of the validation (within $E \pm U_{val}$) instead of making any judgment of success or failure.

For validation, experimental data are always necessary. More available data and their uncertainties at the 2010 Workshop have improved the prospects for conducting a systematic validation study for the various submissions compared with earlier workshops. To evaluate the overall accuracy of the numerical computations, the procedure followed in this study is to compare the comparison error E against validation uncertainty U_{val}. U_{val} is composed of numerical uncertainty $U_{SN}=\sqrt{U_I^2+U_G^2}$ and data uncertainty U_D, i.e., the modeling errors or uncertainties from both computations and experiments are involved. From the FS method, U_G is only estimated for monotonic convergence, so that 55 monotonically converged triplets (77 % as in the verification section) have the predicted U_G, from which a comparison between E and U_{val} is feasible. The results are illustrated in Fig. 5.33. The classification in the FS method is: 60 % $E \leq U_{val}$, 10 % $E \gg U_{val}$. For 7 % U_D are missing (the self-propulsion Case 2.3a&b) so that no comparison can be made. From the LSR method, except for one submission with the missing U_D in Case 2.3a, all the others (91 %) yield $E \leq U_{val}$, indicating a relatively small comparison error and, accordingly unclear deficiency in the numerical computations. Note that only an overview of the summarized results from the FS and LSR methods is presented in Fig. 5.33. The correspondence between the two methods for the same submissions is illustrated in Table 5.26 and Fig. 5.27.

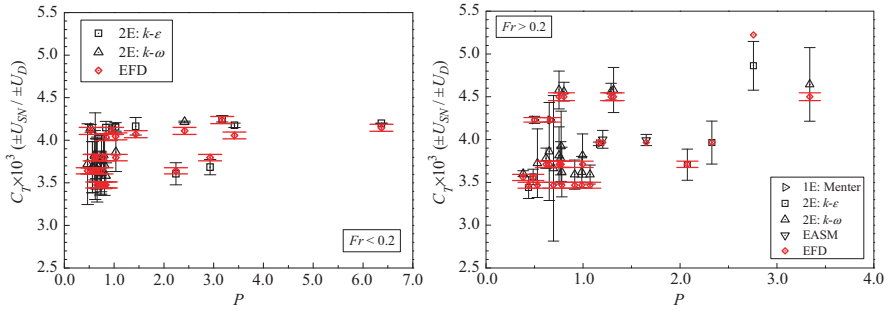


Fig. 5.34 Comparison of U_{SN} (from the FS method) and U_D versus P at $Fr < 0.2$ and $Fr > 0.2$

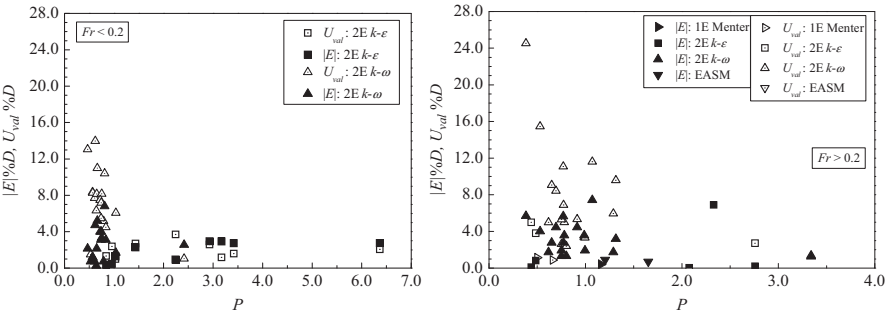


Fig. 5.35 U_{val} (from the FS method) and $|E|$ versus P at $Fr < 0.2$ and $Fr > 0.2$

4.3.2 Modeling Error Versus Turbulence Modeling

The modeling error in CFD computations is related to many aspects, for example the turbulence model, boundary conditions, the simulation of the free surface and the propeller model in the self-propulsion condition. Considering the diversity in CFD codes at this workshop, it is difficult to cover all modeling aspects in an individual CFD code. In the present investigation, the turbulence model is considered to be the most important and is thus undergoing the closest examination. The dependence of the error on the turbulence model is discussed in Chap. 2, showing that a more advanced model is not a guarantee for a good result, even with a large number of grid points. In this section, a further evaluation of the turbulence modeling is made from both verification and validation aspects. Figure 5.34 shows the comparison of numerical uncertainty U_{SN} (horizontal short bars) estimated by the FS method and data uncertainty U_D (horizontal long bars) for different turbulence models in the low- and high-speed conditions. Both uncertainties are presented against the order of accuracy P. Figure 5.34 is essentially also a collection of U_{SN} in Fig. 5.32 for low- and high-speed computations, respectively, but with a classification based on the turbulence model. Figure 5.35 then gives the validation uncertainties U_{val} $\%D$ (open symbols) and the comparison errors $|E|\%D$ (solid symbols) for all predicted

resistances. Thus U_{val} and $|E|$ can be easily compared and validation can be evaluated following ASME 2009 or Eça et al. (2010a, b).

Two types of models are used in the low-speed computations, and both are two-equation models: the k-ε and k-ω models. On the other hand, four turbulence models are applied in the high-speed computations: the one-equation (1E), two-equation (2E k-ε and 2E k-ω) and EASM models. Both Figs. 5.34 and 5.35 indicate that two-equation models are the most common, as seen in Chap. 2. The estimated P values mostly cluster around the vicinity of the theoretical one $P_{th} = 1.0$. However, the corresponding U_{SN} varies considerably with most entries, especially for the k-ω model. The reason for the variation in U_{SN} is not fully clear from the current investigation. One possibility is that some of the grid sizes are so small that the solutions do not converge very well, resulting in large numerical uncertainties. Moreover, because a large numerical uncertainty often yields $U_{val} > |E|$, the uncertainty induced 'noise' will make it difficult to identify the modeling error, further polluting the validation. As for the other turbulence models, the entries are few which makes it hard to draw any conclusions.

Comparing the values of U_{val} and $|E|$ in Fig. 5.35, a general observation is that the results in the low- and high-speed computations are comparable; most U_{val} $\%D$ are below 16 % and $|E|\%D$ below 8 %, excluding the largest value (with 2E k-ω model) in the high-speed computations. Regarding the comparison between U_{val} and $|E|$, in both low- and high-speed computations, the majority of U_{val} is larger than the relevant $|E|$, implying difficulties in clarifying the modeling error. As for the individual turbulence models, in the low-speed cases it is indicated that the k-ω model with $|E| < U_{val}$ is in the majority, while the rarely used k-ε model generates more distinct $|E| > U_{val}$, thereby implying a possible modeling deficiency. In the high-speed computations, the widely used k-ω model presents larger validation uncertainties and comparison errors than other turbulence models. However, apart from a few missing U_{val} (U_D), almost all the turbulence models produce $|E| < U_{val}$ in the high-speed computations, especially the k-ε model (refer to the results at $Fr < 0.2$ for contrast). It appears that the 1E, k-ε or EASM turbulence models generate lower uncertainty and comparison error in the present investigation, but considering the fact that the entries for the turbulence models are unequal in number, more results from each turbulence model are needed to enable reliable observations and statistical analyses to be performed.

5 Concluding Remarks

Based on the database of ship resistance predictions in the 2010 Gothenburg Workshop on Numerical Ship Hydrodynamics, this report presents a survey of V&V applications in practical complex turbulent flow, together with statistical investigations. With the difficulty and complexity in mind, the quantification of accuracy in CFD solutions is analyzed from various aspects, making use of systematic V&V methodology and, in particular, three representative verification methods: FS, GCI

and LSR. Although the present investigations are limited to available submissions, several general conclusions about V&V can be drawn for practical applications:

1) V&V appears to be able to give a relatively reliable error and uncertainty estimation, as implied by the corresponding results (P, δ_{RE} and U_{SN} or U_{val}) from the V&V study by the three different verification methods: FS, GCI and LSR. However, this is only true for solutions in the vicinity of the asymptotic range. A typical problem involving the GCI method is that it estimates much lower uncertainties than the FS and LSR methods. Furthermore, improving the accuracy quantification for solutions far away from the asymptotic range is still an issue.
2) The iterative convergence is an important aspect in the numerical computation due to its contribution to the numerical uncertainty and influence on the determination of discretization uncertainty. The level of iterative uncertainty U_I is normally measured by referring to the grid discretization uncertainty U_G, but before a grid convergence study has been made, such a comparison will be difficult to carry out. The investigation in this report introduces another parameter ε_{12}, the solution change between two successive fine grids, for a more direct comparison. Computed results indicate that U_I may have a significant influence on U_G for $U_I \,\%\, \varepsilon_{12} > 0.1$. The same holds if $U_I \,\%U_G > 0.1$. U_I can thus be compared with either ε_{12} or U_G.
3) The grid convergence study is complicated by several aspects: grid type, grid size, grid refinement ratio, convergence state, convergence rate (order of accuracy), etc., to which the grid discretization error is always related. From present investigations, the following conclusions can be arrived at:
   a. Grid type: unstructured grids more seldom achieve monotonic convergence than the structured grids.
   b. Grid size and refinement ratio: an observed tendency from the statistical analysis is that 2 to 10 million grid points and a refinement ratio $r_G = 1.2$ were most common among the research groups (low and high speed). However, the observed order of accuracy indicates no clear dependence on the grid size or refinement ratio. This is understandable as in addition to these two factors, the detailed grid distribution must have a considerable effect on the degree of accuracy in a solution.
   c. Convergence state and observed order of accuracy: in this report, most submissions achieved monotonic convergence (77 % from the FS/GCI method, 91 % from the LSR method). Most of the solutions are in the vicinity of the asymptotic range ($0.5 < P < 1.5$) for both the FS/GCI (55 % of 77 %) and LSR (64 % of 91 %) methods. Such correspondence between the FS/GCI and LSR methods is promising. However, the observations for solutions far away from the asymptotic range vary a great deal between the two methods, indicating the complexity of determining the grid convergence and numerical error for that case. Another typical issue in the grid convergence study is the scatter in solutions, which complicates the study and has been shown to significantly affect the determination of the grid convergence and the order of accuracy.

Although the LSR method takes the scatter into consideration, more investigations are needed to further improve the determination of grid convergence for solutions with scatter.

4) The validation uncertainty U_{val} is a combination of the numerical and experimental deficiencies: the numerical uncertainty U_{SN} and the experimental uncertainty U_D. A common observation in the resistance predictions at the workshop is that the numerical deficiency exceeds the experimental one, indicating the greater difficulty in predicting the resistance by CFD techniques.
5) Most resistance solutions are estimated to have a lower comparison error than validation error, i.e. $|E| < U_{val}$ burying the modeling error in the numerical and experimental noise. On the other hand, for the fewer cases with $|E| > U_{val}$, modeling errors are significant, and reducing the E value is an objective of the model improvement. A potential source of modeling error, the turbulence model, is investigated in the report. Two-equation models (k-ε and k-ω) were widely used in the resistance predictions (low and high speed) and were shown to produce larger $|E|$ and U_{val} than the other models (1E and EASM), especially the k-ω model. The tiny number of entries with models other than the two-equation models makes it, however, difficult to draw firm conclusions.

Acknowledgements The authors thank Professors Fred Stern and Tao Xing and Dr Luis Eça for their valuable comments on this Chapter.

References

Analysis (2008) Workshops on CFD uncertainty analysis (Lisbon 2004, 2006, 2008) http://maretec.ist.utl.pt/html_files/CFD_Workshops.htm

ASME V & V 20-2009 (2009) Standard for verification and validation in computational fluid dynamics and heat transfer

Eça L, Hoekstra M (2002) An evaluation of verification procedures for CFD applications, 24th symposium on naval hydrodynamics. Fukuoka, Japan

Eça L, Hoekstra M (2006a) Discretization uncertainty estimation based on a least squares version of the grid convergence index, 2nd workshop on CFD uncertainty analysis. Lisbon, Portugal

Eça L, Hoekstra M (2006b) On the influence of the iterative error in the numerical uncertainty of ship viscous flow calculations, 26th symposium on naval hydrodynamics. Rome, Italy

Eça L, Hoekstra M (2008) Testing uncertainty estimation and validation procedures in the flow around a backward facing step, 3rd workshop on CFD uncertainty analysis. Lisbon

Eça L, Hoekstra M (2009) Evaluation of numerical error estimation based on grid refinement studies with the method of the manufactured solutions. Computers and Fluids 38(8):1580–1591

Eça L, Vaz G, Hoekstra M (2010a) Code verification, solution verification and validation in RANS solvers, Proceedings of ASME 29th international conference OMAE2010. Shanghai, China

Eça L, Vaz G, Hoekstra M (2010b) A verification and validation exercise for the flow over a backward facing step, V European conference on computational fluid dynamics, ECCOMAS CFD 2010, (eds) Pereira JCF, Sequeira A. Lisbon

Hino T (ed) (2005) Proceedings of CFD workshop Tokyo 2005. NMRI report

ITTC Quality Manual, 4.9-04-01-01, (1999) CFD general: Uncertainty analysis in CFD-Uncertainty assessment methodology

ITTC Quality Manual, 7.5-03-01-01, (2002) CFD General: Uncertainty analysis in CFD-Verification and validation methodology and procedures
ITTC Recommended Procedures and Guidelines, 7.5-03-01-01, (2008) Uncertainty analysis in CFD-Verification and validation methodology and procedures
Larsson L, Stern F, Bertram V (2002) Gothenburg 2000-A workshop on numerical hydrodynamics, department of naval architecture and ocean engineering. Chalmers University of Technology, Gothenburg
Larsson L, Stern F, Visonneau M (2010) Proceedings of a workshop on numerical hydrodynamics. Gothenburg, Sweden
Roache PJ (1998) Verification and validation in computational science and engineering. Hermosa Publishers, Albuquerque
Stern F, Wilson RV, Coleman HW, Paterson EG (2001) Comprehensive approach to verification and validation of CFD simulations – Part I: Methodology and procedures. ASME J Fluids Eng 123:793–802
Xing T, Stern F (2008) Factors of safety for Richardson extrapolation for industrial applications. IIHR Report No. 466
Xing T, Stern F (2009) Factors of safety for Richardson extrapolation. IIHR Report No. 469
Xing T, Stern F (2010) Factors of safety for Richardson extrapolation. J Fluids Eng 132(6):061403-061403-13. doi:10.1115/1.4001771
Xing T, Stern F (2011) Closure to Discussion of 'Factors of safety for Richardson extrapolation' J Fluids Eng 133(11):115502-115502-6. doi: 10.1115/1.4005030 (2011, ASME J. Fluids Eng., 133, p. 115501)

Chapter 6
Additional Data for Resistance, Sinkage and Trim

Lu Zou and Lars Larsson

Abstract In this Chapter, additional resistance, sinkage and trim data are presented against Froude number for KVLCC2, KCS and DTMB 5415. Comparisons are made with the original data used at the Workshop. The purpose is to provide additional information useful for future validation of CFD results and to estimate the uncertainty in the data from the different facilities. However, due to lack of information about precision in most measurements only bias errors are estimated. For KVLCC2 and KCS one additional set of data is added to that used at the Workshop. The estimated bias errors in residuary resistance are very small, around 0.2 % of the mean total resistance, while those of sinkage and trim are considerably larger: 6–11 % of the mean values across the Froude number range. For 5415 new data from three organizations are presented. Bias errors in residuary resistance are 0.9–1.6 % of the mean total resistance. Sinkage errors are in the range 3–6 % of the mean value and trim errors around 0.01°.

In this Chapter, additional resistance, sinkage and trim data are presented against Froude number for KVLCC2, KCS and DTMB 5415. Comparisons are made with the original data used at the Gothenburg 2010 Workshop. The purpose is to provide additional information useful for future validation of CFD results and to estimate the uncertainty in the data from the different facilities. However, due to lack of information about precision in most of the measurements only facility bias errors will be estimated.

1 Definitions

The resistance data include the total resistance coefficient $C_T^{15^\circ}$ and the residuary resistance coefficient C_R.

L. Zou (✉) · L. Larsson
Chalmers University of Technology, Gothenburg, Sweden
e-mail: luzou@sjtu.edu.cn

L. Zou
Shanghai Jiao Tong University, Shanghai, China

L. Larsson
e-mail: lars.larsson@chalmers.se

L. Larsson et al. (eds.), *Numerical Ship Hydrodynamics,*
DOI 10.1007/978-94-007-7189-5_6, © Springer Science+Business Media Dordrecht 2014

$C_T^{15^\circ}$ is converted from the measured model temperature to a nominal temperature of 15 degrees as follows:

$$C_T^{15^\circ} = C_R + (1+k) \cdot C_F^{15^\circ}$$

$$C_F^{15^\circ} = \frac{0.075}{(\log_{10} Re - 2)^2} \quad \text{(ITTC-1957 model-ship correlation line)}$$

where Re is the Reynolds number. The water density ρ and kinematic viscosity ν are linearly interpolated using fresh water values as recommended by the ITTC Quality Manual Procedure 4.9-03-01-03, Density and Viscosity of Water. The form factor $(1+k)$ is determined by the Prohaska method, recommended by the ITTC Quality Manual Procedure 4.9-03-03-01.2, ITTC Performance Prediction Method.

The sinkage, σ, and trim, τ, are defined as:

$$\sigma = \frac{\Delta_{AP} + \Delta_{FP}}{2L_{PP}}, \quad \tau = \frac{180}{\pi} \cdot \arctan\left(\frac{\Delta_{FP} - \Delta_{AP}}{L_{PP}}\right)(^\circ)$$

where Δ_{FP} and Δ_{AP} are the changes in vertical position (positive upwards) of the hull at the fore and aft perpendiculars relative to the zero speed case.

2 KVLCC2

Measurements from two facilities are available for KVLCC2. Results from MOERI were used at the workshop, while data from the University of Osaka (Toda, private communication) have been obtained after the workshop. Since none of the tests were made with the nominal temperature, the temperature correction has been applied. As the tests were repeated around certain Froude number and there is scatter in the data, mean values of the measurements are calculated and indicated in the figures.

Measurements of global forces, wave pattern, and mean velocity components were carried out in the MOERI (formerly KRISO) towing tank. The size of the tank is 200 m × 16 m × 7 m (length × width × depth) and the towing carriage can run up to 6 m/s. The blockage coefficient, defined as the ratio of the sectional area of the model and the towing tank, was less than 0.35 %, allowing the blockage effect to be ignored. The water temperature in the test was 13.9° C. Hull data are given in Table 6.1.

The test basin at the University of Osaka's Graduate School of Engineering is 100 m × 7.8 m × 4.35 m (length × width × depth), making it a mid-sized experimental basin. Towing carriage is 7.4 m in length, 7.8 m in width, 6.4 m wheel base. Its running speed ranges from 0.01 to 3.5 m/s. The water temperature in the test was 10.2° C.

The scale ratio used in the Osaka test was 100, giving rise to a ship model length: $L_{PP} = 3.2$ m. The corresponding blockage ratio was 0.36 %.

In Figs. 6.1, 6.2, 6.3 and 6.4 results for $C_T^{15^\circ}$, C_R, sinkage and trim are given versus Froude number, Fr. Mean lines are given for each facility and for all data. The form

Table 6.1 KVLCC2 geometry data in MOERI test

Scale Ratio = 58.0	Ship	Model
L_{PP} (m)	320.0	5.5172
B (m)	58.0	1.0000
T (m)	20.8	0.3586
Volume (m^3)	312621.7	1.6023
S w/o rudder (m^2)	27194.0	8.0838
S of rudder (m^2)	273.3	0.0812
C_b	0.8098	
C_m	0.9980	
LCB(%), fwd+	3.5	

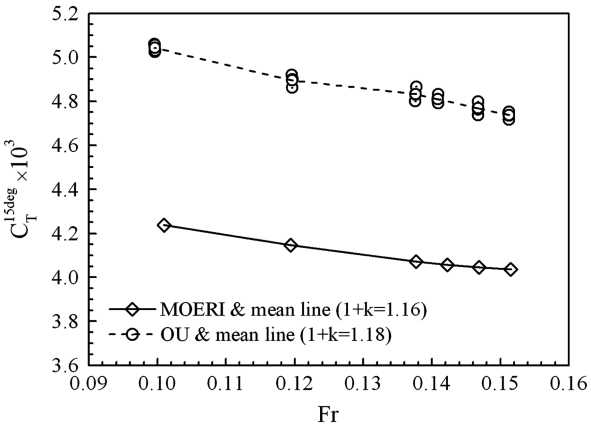


Fig. 6.1 Total resistance coefficient against *Fr* (Note: different *Re*)

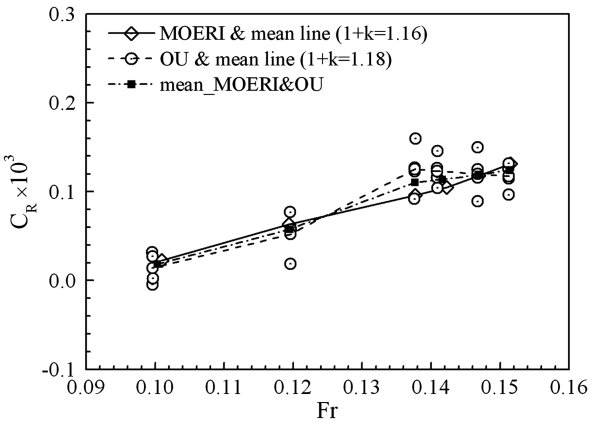


Fig. 6.2 Residuary resistance coefficient against *Fr*

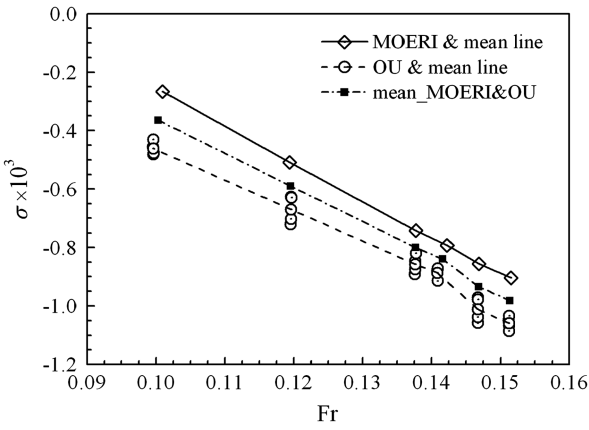


Fig. 6.3 Sinkage against *Fr*

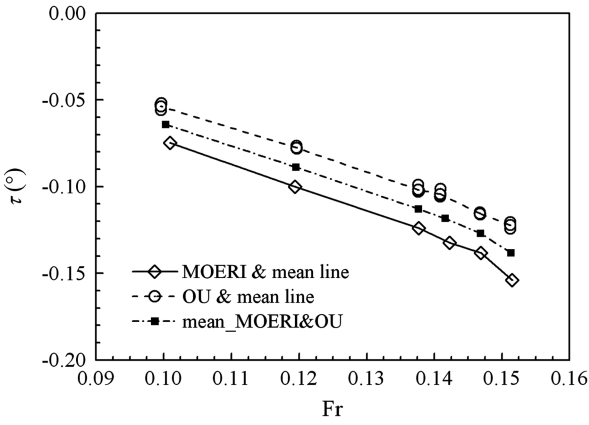


Fig. 6.4 Trim against *Fr*

factor, obtained using the Prohaska method, is slightly different between the two facilities.

Since the models are at different scales the total resistance coefficient should be different, but the residuary resistance should be independent of scale. The average deviation from the mean of the two facilities may be used as an estimate of the facility bias error. Since there are only two facilities they will have the same bias. For C_R the bias is 0.0069×10^{-3}, corresponding to 0.2 % of the mean C_T across the Froude number range.

The facility bias for sinkage may be estimated to 0.073×10^{-3}, or 9.7 %, while that for trim is 0.012°, or 11.4 %.

Table 6.2 KCS geometry data in MOERI and NMRI tests

Scale Ratio = 31.6	Ship	Model
L_{PP} (m)	230	7.2786
B (m)	32.2	1.0190
T (m)	10.8	0.3418
Volume (m^3)	52030	1.6490
S w/o rudder (m^2)	9420.0	9.4379
S of rudder (m^2)	74.0	0.0741
C_b	0.6505	
C_m	0.9849	
LCB(%), fwd+	-1.48	

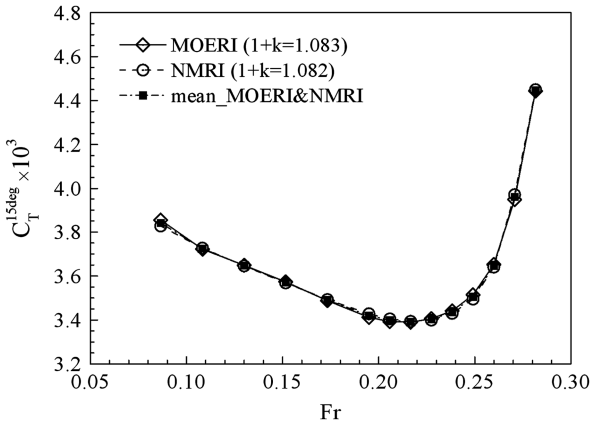


Fig. 6.5 Total resistance coefficient against *Fr*

3 KCS

Two sets of measurements are included for KCS. Again, the MOERI results are those used at the workshop, while new results are reported from NMRI (Hirata, private communication). The same scale was used in both facilities and the temperature of the water was the same, 10.9°. The hull data are given in Table 6.2.

The dimensions of the NMRI towing tank are 400 m × 18 m × 8 m (length × width × depth). It is used for various model tests ranging from very large crude oil carriers to super high speed vessels. There is a very small blockage ratio in both tanks; 0.31 % and 0.24 % for MOERI and NMRI, respectively.

In Figs. 6.5, 6.6, 6.7 and 6.8 the same quantities as for KVLCC2 are presented. The scale factor was the same in the two facilities, and the correspondence between the resistance data is remarkable. No mean lines are plotted in the first two figures, since the trend lines for the two facilities almost coincide.

The mean facility biases, computed like for KVLCC2, of $C_T^{15^\circ}$, C_R, σ and τ, are 0.0056×10^{-3} (0.2 %), 0.0056×10^{-3} (0.2 %), 0.0696×10^{-3} (6.0 %) and 0.0058° (5.9 %) respectively.

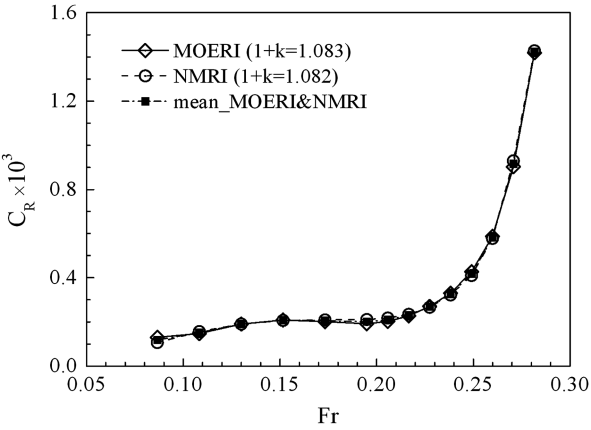


Fig. 6.6 Residuary resistance coefficient against *Fr*

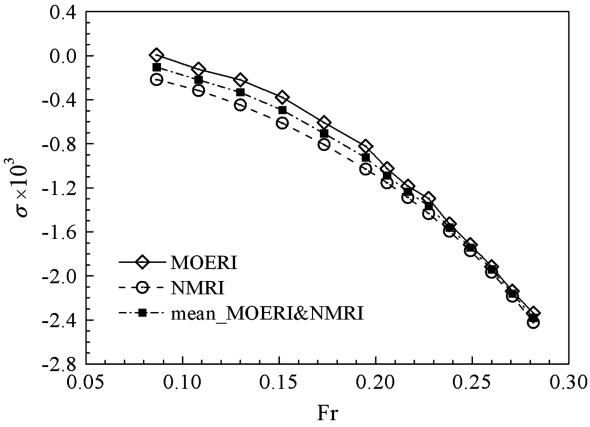


Fig. 6.7 Sinkage against *Fr*

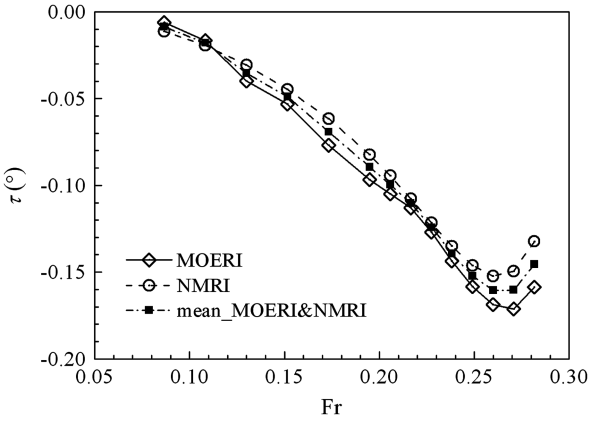


Fig. 6.8 Trim against *Fr*

Table 6.3 5415 geometry data

	Ship	DTMB	INSEAN	IIHR
Scale Ratio	1.0	24.824	24.824	46.59
L_{PP} (m)	142.0	5.720	5.720	3.038
B (m)	19.06	0.768	0.768	0.409
T (m)	6.15	0.248	0.248	0.132
Volume (m^3)	8424.4	0.5507	0.5507	0.0833
S w/o rudder (m^2)	2972.6	4.8238	4.8238	1.3695
S of rudder (m^2)	30.8	0.0500	0.0500	0.0142
C_b	0.507			
C_m	0.821			
LCB(%), fwd+	-0.683			

4 5415

Three facilities: DTMB, INSEAN and IIHR contributed data for this hull (Stern et al. 2000, 2005). Geometry data are given in Table 6.3. The towing tank water temperature was measured daily at the model mid draft using a digital thermometer. The form factor $k = 0.15$ has been calculated using the Prohaska method, and is the same for all tests.

The experiments at DTMB were performed in basin no. 2, with dimensions 575 m × 15.5 m × 6.7 m (length × width × depth). Basin no. 2 is equipped with an electro-hydraulically operated drive carriage and capable of speeds of 10.3 m/s. Sidewall and end wall beaches enable 20-minute intervals between carriage runs. The blockage ratio was 0.18 % and the temperature 17.8°.

At INSEAN the experiments were carried out in towing tank no. 2 (220 m × 9 m × 3.6 m). This tank has a single drive carriage with a maximum speed of 10 m/s. Sidewall and end wall beaches enable 20-minute intervals between carriage runs. The blockage was 0.59 % and the temperature was 22.1°.

The tests at IIHR were made in the IIHR towing tank (100 m × 3.048 m × 3.048 m), which has an electric-motor operated drive carriage capable of speeds of 3 m/s. Sidewall and end wall beaches enable twelve-minute intervals between carriage runs. The blockage was 0.58 % and the temperature was 25.1° in the resistance tests.

The total resistance is plotted in Fig. 6.9 and the residuary resistance in Fig. 6.10. Due to the much smaller scale for the IIHR model the total resistance coefficient is much higher than for the DTMB and INSEAN models. There is however a very good correspondence between the latter two. In Fig. 6.10 a mean line is presented, but it is mostly hidden behind the data points. If the deviation from the mean line is taken as the bias error for the three institutes, the average is 0.0453×10^{-3} (0.9 %), 0.0749×10^{-3} (1.5 %) and 0.0788×10^{-3} (1.6 %), respectively for DTMB, INSEAN and IIHR. The values within brackets are the errors in percent of the total resistance

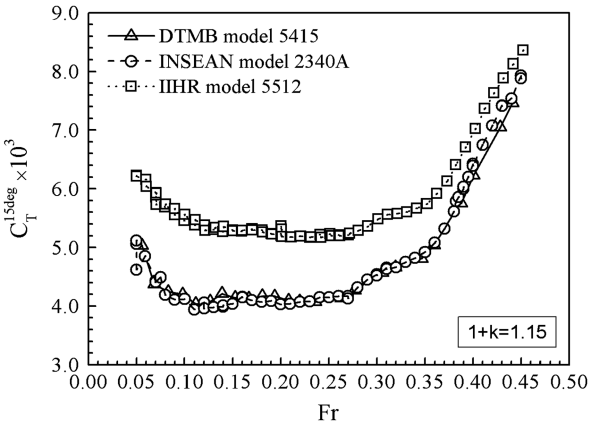


Fig. 6.9 Total resistance coefficient against *Fr*

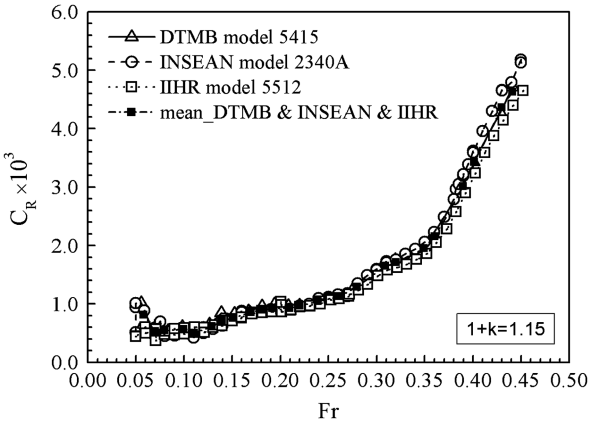


Fig. 6.10 Residuary resistance coefficient against *Fr*

averaged across the Froude number range. A more complete analysis of the uncertainty may be found in Stern et al. (2005). Since precision limits were available in these tests they could be included in an estimated total uncertainty for resistance.

Sinkage and trim are presented in Figs. 6.11 and 6.12. Mean lines would be completely hidden by the symbols due to the very good correspondence between the facilities. The estimated bias error in sinkage is 0.100×10^{-3} (5.6 %), 0.086×10^{-3} (4.8 %) and 0.061×10^{-3} (3.4 %) for the three institutes. In trim the corresponding errors are 0.010° (29.5 %), 0.010° (27.9 %) and 0.014° (39.9 %). The latter percentages are somewhat misleading, since the average trim angle across the Froude number range is close to zero. Errors of the order on 0.01° are obviously very small.

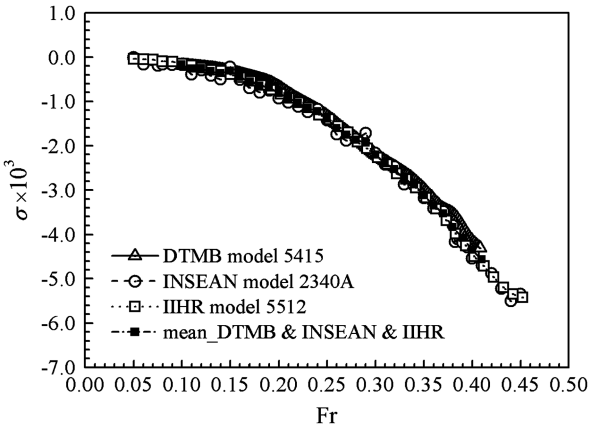


Fig. 6.11 Sinkage against *Fr*

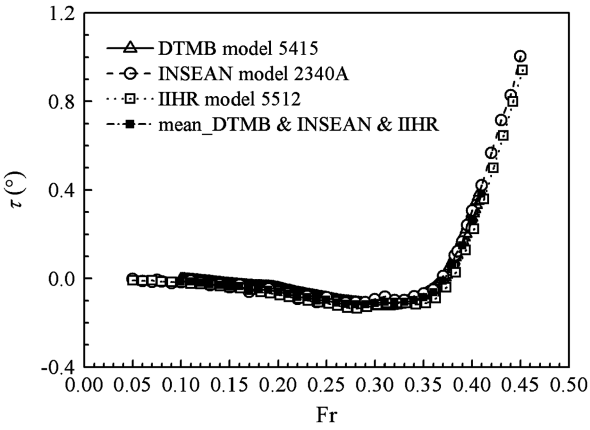


Fig. 6.12 Trim against *Fr*

5 Conclusions

In this Chapter, additional resistance, sinkage and trim data for the three Workshop hulls have been presented and compared with data used at the workshop. The comparison has enabled an estimate of facility bias errors.

For KVLCC2 and KCS one additional set of data was added to that used at the Workshop. The estimated bias errors in residuary resistance were very small, around 0.2 % of the mean total resistance, while those of sinkage and trim were considerably larger: 6–11 % of the mean values across the Froude number range.

For 5415 new data from three organizations were presented. Bias errors in residuary resistance were here 0.9–1.6 % of the mean total resistance. Sinkage errors were in the range 3–6 % of the mean value and trim errors were around 0.01°.

Acknowledgements The authors wish to thank the University of Osaka, NMRI and IIHR for providing the new experimental data.

References

Stern F, Longo J, Penna R et al (2000) International collaboration on benchmark CFD validation data for surface combatant DTMB model 5415. Proceedings of 23rd symposium on naval hydrodynamics, Val de Reuil, France

Stern F, Olivieri A, Shao J et al (2005) Statistical approach for estimating intervals of certification or biases of facilities or measurement systems including uncertainties. Trans ASME 127(5)

Chapter 7
Post Workshop Computations and Analysis for KVLCC2 and 5415

Shanti Bhushan, Tao Xing, Michel Visonneau, Jeroen Wackers, Ganbo Deng, Frederick Stern and Lars Larsson

Abstract The Workshop submissions for the local flow predictions for straight ahead KVLCC2 and 5415 were on large disparate grids ranging from 0.6M to 300M, which made it difficult to draw concrete conclusions regarding the most reliable turbulence model, appropriate numerical method and grid resolution requirements. In this chapter, additional analysis including grid verification study is performed on intermediate grids to shed more light on these issues. Second order TVD or bounded central difference schemes are found to be sufficient for URANS, whereas fourth or higher order schemes are required for hybrid RANS/LES (HRLES). Resistance predictions show grid uncertainties $\leq 2.2\,\%$ for URANS on 50M grid and HRLES on 300M grid, which suggests that these grids are approaching asymptotic range. URANS with anisotropic turbulence model perform better than URANS with isotropic turbulence model. Grid with 3M points are found to be sufficient for resistance predictions, however, grids with up to 10s M points are required for local flow predictions. Adaptive grid refinement is helpful in generating optimal grids; however available grid refinement technique based on the Hessian of pressure, fails to refine the grid further downstream along the hull. HRLES simulations are promising in providing the details of the flow topology. However, they show limitations such as grid induced separation for bluff body KVLCC2 and inability to trigger turbulence for slender body 5415. Implementation of improved delayed DES and/or physics based RANS/LES

F. Stern (✉)
University of Iowa and Iowa Institute of Hydraulic Research (IIHR),
Iowa City, IA, USA
e-mail: frstern@engineering.uiowa.edu

S. Bhushan
Mississippi State University, Starkville, MS, USA
e-mail: sbhushan@cavs.msstate.edu

T. Xing
University of Idaho, Moscow, ID, USA
e-mail: xing@uidaho.edu

M. Visonneau · J. Wackers · G. Deng
CNRS/Centrale Nantes, Nantes, France
e-mail: michel.visonneau@ec-nantes.fr

L. Larsson
Chalmers University of Technology, Gothenburg, Sweden
e-mail: lars.larsson@chalmers.se

L. Larsson et al. (eds.), *Numerical Ship Hydrodynamics,*
DOI 10.1007/978-94-007-7189-5_7, © Springer Science+Business Media Dordrecht 2014

transition is required to address these limitations. Grid resolution of 300M shows resolved turbulence levels of $> 95\,\%$ for bluff body, thus such grids seem sufficiently fine for HRLES. The free-surface predictions do not show significant dependence on boundary layer predictions, and accurate prediction for 5415 at $Fr = 0.28$ is obtained using just 2M grid points. The free-surface reduces pressure gradients on the sonar dome, causing weaker vortical structures than single phase. Flow over 5415 shows three primary vortices, and all of them originate from the sonar dome surface. Onset analysis shows that all the three vortices have open-type separation, and separate from the surface due to cross flow. Further investigation of the cause of differences in KVLCC2 CFD submissions and experimental data suggests that it could be due to differences in the sharpness of the stern.

1 Introduction

In Chap. 3, analysis of the local flow characteristics for KVLCC2 (case 1.1a), 5415 (cases 3.1-a&b, 3.5 and 3.6) and KCS (cases 2.1 and 2.3-a) predicted by the submissions were performed. Analysis for KVLCC2 and 5415 case 3.1-a&b focused on the influence of discretization and turbulence modeling errors in the wake predictions along the hull and turbulence structure predictions at propeller plane. Analysis for 5415 cases 3.5 and 3.6 focused on the influence of the waves and roll motion on the local flow. Analysis for KCS cases with and without propeller focused on the comparison at the propeller modeling and recommendations were made for future studies. The chapter also outlined the progress achieved since the Gothenburg 2000 (Larsson et al. 2003) and Tokyo 2005 (Hino 2005) workshops, conclusions were drawn to establish the performances of the computational and modeling strategies, and some issues were raised regarding the grid size and turbulence modeling.

Submissions showed significant improvements in the after-body flow, and vortical and turbulent structures compared to the previous workshops. The improved predictions were due to reduction in modeling and discretization errors. The grids used in the workshop were significantly finer (ranged from 615K to 305M) than those in the previous workshops (< 3M). The finer grids helped in reducing discretization errors, and mostly performed better than coarser grids for the prediction of vortical and turbulence structures. The submissions also used a wide range of turbulence models including unsteady Reynolds Averaged turbulence model (URANS) with isotropic and anisotropic turbulence models, hybrid RANS/LES (HRLES) with detached eddy simulation (DES) and Large Eddy Simulation (LES) with Smagorinsky model.

URANS with anisotropic turbulence models performed better than URANS with isotropic models for the prediction of turbulence quantities. HRLES with DES model somewhat over predicted mean axial velocity, over predicted longitudinal vortices and higher levels of resolved turbulence for KVLCC2. In addition, the 305M grid cases showed grid induced separation and modeled stress depletion issues in the boundary layer. For 5415 cases 3.1a&b, HRLES with DES and LES with Smagorinsky model predictions provided a plausible description of the progression and interaction of the vortical structure reported in the sparse experimental data. This

also initiated further discussions regarding the flow topology on the sonar dome. However, HRLES with DES predicted low levels of resolved turbulence, thus their predictions could not be validated. Further, LES study did not report turbulence predictions, so they could not be judged thoroughly. The need for detailed experiments were also emphasized. For the 5415 case 3.5, HRLES with DES calculations showed significantly better resistance, moments and wave elevation predictions than those using URANS, which was primarily due to finer grid resolution. Self-propelled HRLES with DES were performed for the first time for KCS. The HRLES predictions compared well with the experiments for the mean flow, and they outperformed URANS calculations for the turbulence predictions. Considering the computational expense required for the HRLES, it was concluded that URANS with anisotropic turbulence model is the most economical approach for the prediction of time-averaged quantities.

The issues raised by the analysis were: 1) grid verification studies need to be performed to evaluate the grid convergence of the solutions and validate the predictions; 2) what is the optimal grid resolution and/or numerical method to reduce discretization error to achieve benchmark URANS predictions; 3) the grid resolution for HRLES were one or two orders of magnitude larger than URANS, so it was difficult to get a direct comparison between the two approaches; 4) local flow assessment could also be affected by the poor resolution of the experimental measurements. Additional issue was raised regarding onset and progression of the vortices.

In this chapter, additional analysis is presented to address some of the concerns raised by the submissions, particularly regarding the effect of grid resolution and turbulence modeling. For the KVLCC2 case 1.1a, Xing et al. (2012) performed a total of nine CFDShip-Iowa V4 (henceforth V4) simulations on systematically refined grids ranging from 600K to 13M points and an extremely fine 305M grid. Simulations were also performed using URANS with isotropic (BKW) and anisotropic (ARS) turbulence model and HRLES with ARS based DES and delayed DES (DDES) models, and 2nd and 4th order convective schemes. In the workshop, only the best results using HRLES with anisotropic DES on a 13 million grid and URANS with ARS on a 305 million grid were submitted, and the additional results were discussed in the accompanying paper and supplemental material. The additional results were not discussed in Chap. 3, as it only focused on the submitted results. Hence, they are presented herein to discuss the effect of numerical schemes, turbulence model anisotropy, URANS and HRLES computations, and grid resolution.

For 5415, additional CFDShip-Iowa V4, ISIS-CFD and Fluent (Version 14, refer to FLUENT 6.3 manual for details) simulation are performed using multi-block overset, adaptively refined and single-block O-type grids with resolutions varying from 2M to 50M, including verification and validation (V&V) for resistance predictions using URANS with isotropic BKW and anisotropic ARS models, and HRLES with BKW or ARS based DES models. V&V study is included because HRLES is relatively new to ship hydrodynamics, and such studies for their integral variable predictions help gain confidence in their capability. The wide range of grid resolutions including those submitted in the workshop, from 615K to 300M, helps to study the effect of grid resolution and topology on the prediction of vortical structures. Simulations are performed using URANS with isotropic and anisotropic models, and HRLES with DES models to study the effect of turbulence modeling on flow



Fig. 7.1 KVLCC2 geometry

predictions. Simulations are also performed for single-phase flow to study the effect of free-surface, and the predictions from different solvers are compared to study the effect of numerical methods. Additional analysis is also performed for the V4 HRLES with DES predictions on 300M helps in identification of additional vortices on the sonar dome, as reported by ISIS-CFD predictions, and study the onset and progression of vortices.

Herein, the discussions are presented in terms of turbulence closure models. URANS mathematical model with BKW or ARS turbulence models are referred to as BKW or ARS, respectively. Similarly, HRLES mathematical model with BKW based DES and ARS based DES are referred as BKW-DES and ARS-DES, respectively. DES is used to discuss the general nature of DES turbulence modeling approach. In addition, HRLES mathematical model with BKW based DDES and DHRL are referred to as DDES and DHRL, respectively. Further, to draw general conclusions for mathematical models, URANS and HRLES are used.

In Chap. 3, a significant blockage of KVLCC2 in the wind tunnel was pointed out, and it was conjectured that this effect could be significant for the detailed distribution of the wake contours in the propeller plane. Reference was made to post-workshop computations of the blockage effect at ECN/CNRS and Chalmers. These computations are presented here.

In Chap. 2, the difficulty of accurately measuring the sinkage and trim at very small Froude numbers was pointed out. Measurement errors were reported as the main reason for the large differences between the computations and the data. Additional computations are performed by ECN/CNRS and Chalmers to further investigate the issue.

2 KVLCC2– CASE 1.1-A

A side view of the KVLCC2 geometry is shown in Fig. 7.1. The geometry is a double model for KVLCC2 without rudder in straight ahead condition. KVLCC2 is the second variant of the MOERI tanker with more U-shaped stern frame-lines (Van et al. 1998). The length between perpendiculars is $Lpp = 320\,\mathrm{m}$. The ship is fixed at zero sinkage and trim. Reynolds number is $Re = 4.6 \times 10^6$. Simulations are compared with the experimental data (EFD) by Van et al. (1998) and Lee et al. (2003).

2.1 Review of the New Contributions

There were nine simulations for case 1.1-a conducted by IIHR/CFDShip-IowaV4 using various turbulence models, grids, and numerical schemes as summarized in

Table 7.1 Simulation matrix for Case 1.1a by IIHR/CFDShip-IowaV4

Case No.	Case	Turbulence model	Wall model/Flow	Discretization characteristics	Grid (M)	Resolved TKE (%)
1	ARS-DES-G4	ARS-DES	Near wall	TVD 2nd order	0.59	0
2	ARS-DES-G3		+ no slip	with super bee	1.6	0
3	ARS-DES-G2		Steady	limitation	4.6	0
4	ARS-DES-G1				13	87
5	ARS-G1	ARS	Near wall	TVD 2nd order	13	0
6	ARS- G0		+ no slip	with super bee	305	0
			Steady	limitation		
7	ARS-FD4-G0			Hhybrid 2nd/ 4th order	305	0
8	BKW-DES-FD4-G0	BKW-DES	Near wall	Hybrid 2nd/	305	95
			+ no slip	4th order		
9	BKW-DDES-FD4-G0	BKW-DDES	Unsteady		305	95

Table 7.1. For detailed dimensions for all the grids, the readers can refer to Xing et al. (2007, 2012). These simulations were completed and submitted to the Gothenburg 2010 CFD Workshop. However, only the best results for ARS (Case 5) and DES (Case 4) were presented in Volume II of the proceedings (downloadable from the website SpringerExtras, see the book cover for address) and discussed in Chap. 3. Verification and validation for integral variables using ARS-DES were conducted using four systematically refined overset multi-block grids (Cases 1 to 4). The results were summarized in Table 3 of Xing et al. (2012). Herein, Case 6 (ARS-FD4-G0) is compared to Case 5 (ARS-G0) to evaluate the effect of numerical scheme on ARS on the 305M grid. Case 7 (ARS-G1) is compared with Case 5 (ARS-G0) to evaluate sensitivity of grid on ARS. The effect of turbulence models are evaluated by comparing Case 8 with Case 6 for ARS vs. DES and Case 9 with Case 8 for DDES vs. DES.

2.2 Effect of Convection Scheme, RANS Model Anisotropy, Grid Sensitivity Studies for RANS (ARS)

Ismail et al. (2010) identified that the TVD scheme is better than the FD4 and 2nd order upwind scheme on a 1.6 M grid (Grid 3). Herein, differences between the results of Case 5 (ARS-G0) and Case 6 (ARS-FD4-G0) are negligible on the grid with 305 M points for which both cases predict steady flows. This suggests that the difference of truncation errors between numerical schemes may be negligible on very fine grids for the ARS turbulence models. Although it cannot be ascertained that a similar conclusion can be drawn for BKW and other RANS models, but one should expect a behavior similar to that for ARS.

By comparing these new results with those already published, it is suggested that URANS with isotropic turbulence models are insufficient to capture the two vortical structures in the propeller plane. ARS model improve the predictions, but the two

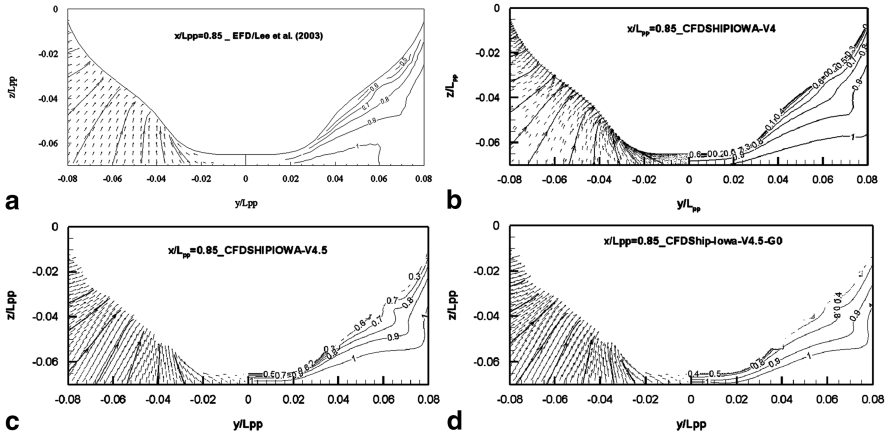


Fig. 7.2 *U* contours (*right panel*), cross flow vectors and streamlines (*left panel*) at $x/L_{pp} = 0.85$. **a** EFD, **b** ARS-Grid1, **c** BKW-DES-FD4-Grid0, **d** BKW-DDES-FD4-Grid0

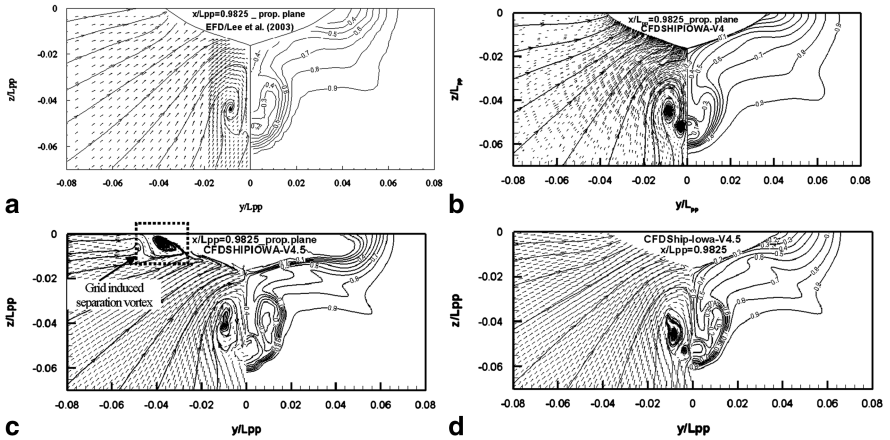


Fig. 7.3 *U* contours (*right panel*), cross flow vectors and streamlines (*left panel*) at $x/L_{pp} = 0.9825$. **a** EFD, **b** ARS-Grid1, **c** BKW-DES-FD4-Grid0, **d** BKW-DDES-FD4-Grid0

vortices in the propeller plane are still too weak compared to EFD. The results do not improve significantly on finer grid, which suggests that it is caused by the model deficiency instead of grid resolution. Comparison between ARS-G1 and ARS-G0 in Figs. 7.1–7.4 (Fig. 1.1a-2 in Proceedings volume II) shows that grid refinement has little effects on the axial velocity contour for ARS. Nonetheless, compared with ARS-G1 (Fig. 7.5a), total wake fraction on the propeller plane predicted by ARS-G0 (Fig. 1.1a-4 in Proceedings volume II) agrees much better with the data at all the four radial locations, especially for φ values between 90° and 270°. As shown in Fig. 7.6, effect of convection scheme and grid refinement has negligible effect on the lateral evolution of the local velocity profiles at $z/L_{pp} = -0.05075$.

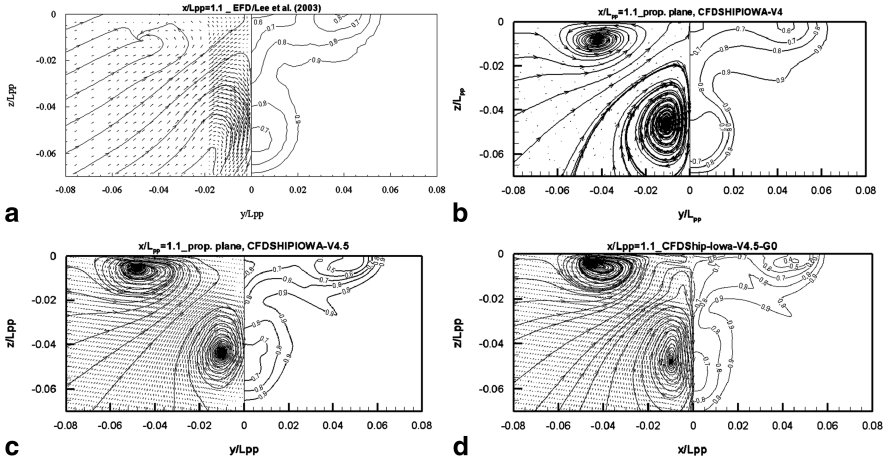


Fig. 7.4 *U* contours (*right panel*), cross flow vectors and streamlines (*left panel*) at $x/L_{pp} = 1.1$. **a** EFD, **b** ARS-Grid1, **c** BKW-DES-FD4-Grid0, **d** BKW-DDES-FD4-Grid0

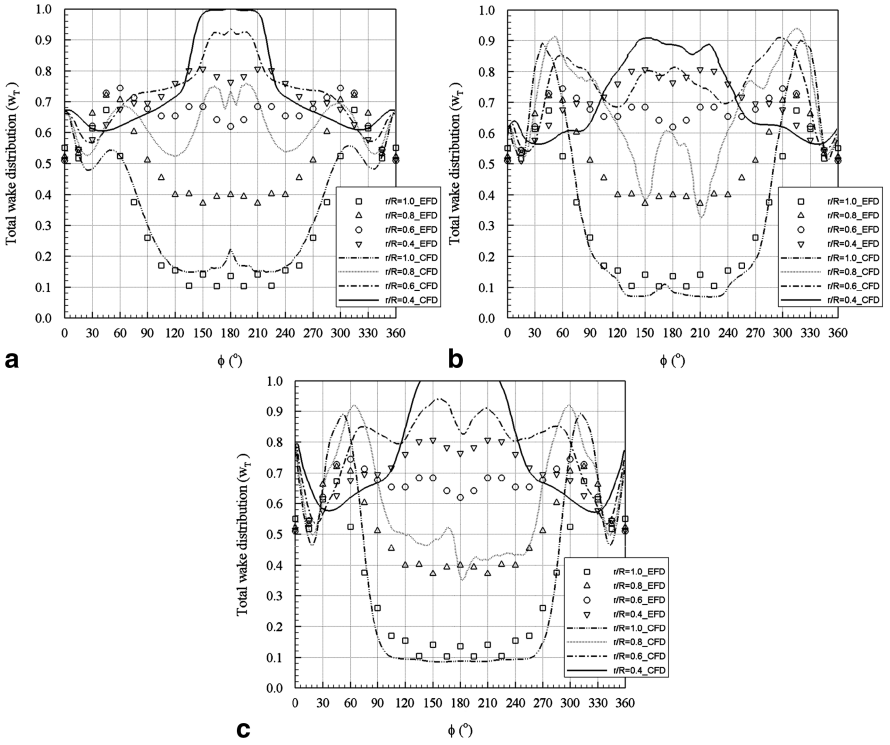


Fig. 7.5 Total wake fraction (w_T) on the propeller plane ($x/L_{pp} = 0.9825$). **a** ARS-Grid1, **b** BKW-DES-FD4-Grid0, **c** BKW-DDES-FD4-Grid0

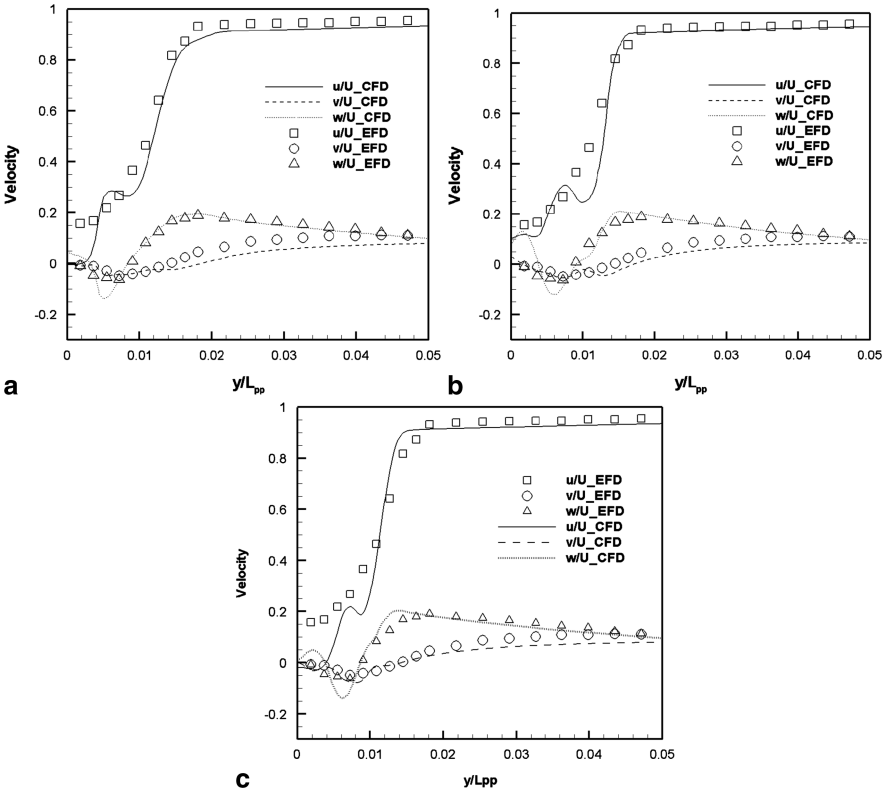


Fig. 7.6 Velocity on the propeller plane ($x/L_{pp} = 0.9825$) at ($z/L_{pp} = -0.05075$). **a** ARS-Grid1, **b** BKW-DES-FD4-Grid0, **c** BKW-DDES-FD4-Grid0

Similar to ARS-G0, ARS-G1 predicts accurately the circumferential variation of the total wake fraction at r/R = 1.0 except for $30° < \phi < 60°$ and $300° < \phi < 330°$, where ARS under predicts the total wake fraction (Fig. 7.5). At r/R = 0.6 and 0.4, ARS-G1 over-estimates w_T by about 15 to 50 % in the vicinity of the plane of symmetry.

2.3 Grid Sensitivity Studies for ARS-DES, and Comparison Between ARS, BKW/ARS-DES and DDES

As shown by Table 3 of Xing et al. (2012) for ARS-DES, monotonic convergence is only achieved on grid set (1,2,3) for total resistance coefficient C_t and on grid set (1,2,3) and (2,3,4) for frictional resistance coefficient C_f. The estimated orders of accuracy show large oscillations as P_G has values from 1.16 to 4.09. Pressure resistance coefficient *Cp* shows oscillatory divergence on the two grid triplets. ARS flow predictions shows less dependence on grids than ARS-DES. This is expected

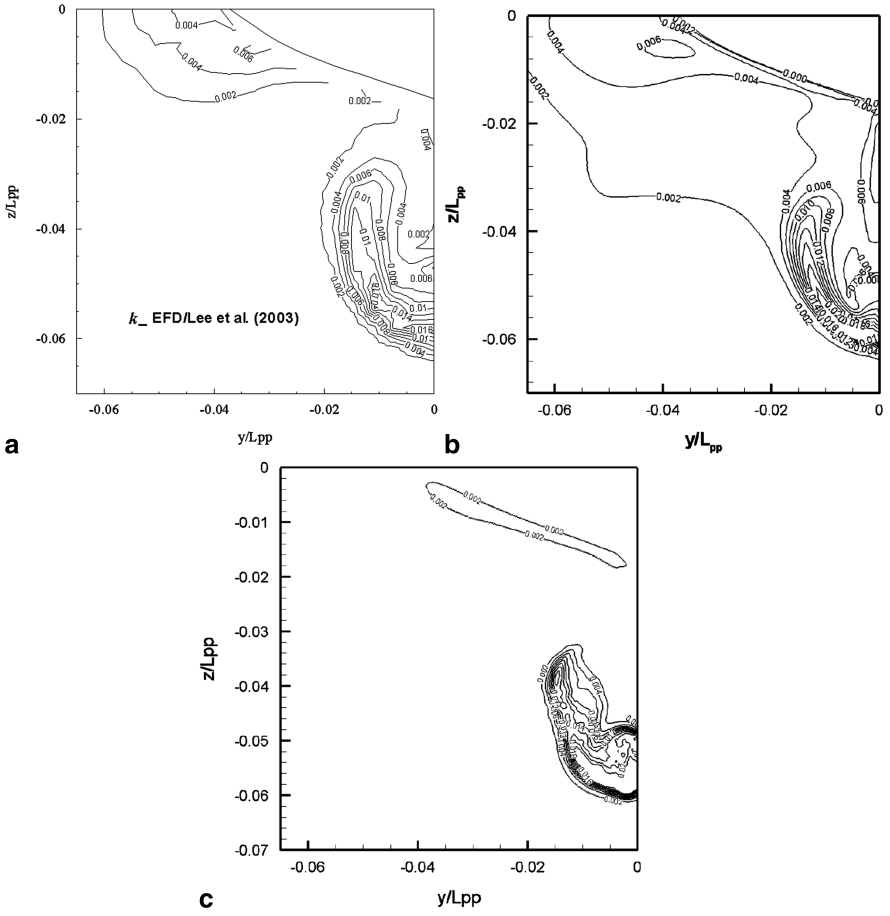


Fig. 7.7 Turbulent kinetic energy (k) contours at ($x/L_{pp} = 0.9825$). **a** EFD, **b** ARS-Grid1, **c** BKW-DDES-FD4-Grid0

as ARS-DES models are functions of grid spacing and can resolve more turbulent structures when the grid is refined.

BKW or ARS predicts steady flows for Case 1.1-a. DES predicts unsteady flows unless the grid is too coarse (e.g. Grids 2-4). Compared to BKW or ARS solutions on the same grid, DES improve the prediction of the total resistance (Table 6 in Xing et al. 2012) and velocity distribution for most regions at the propeller plane (Fig. 5 in Xing et al. 2012); however, DES tends to over-predict the velocity near the symmetry plane (Fig. 1.1a-5 in proceedings volume II and Fig. 5b in Xing et al. 2012) and the Reynolds stresses at the propeller plane (Fig. 1.1a-6-11 in proceedings volume II and Fig. 7.12). For the axial velocity contours at the propeller plane ($X/L_{pp} = 0.9825$), ARS-DES-G1 (Fig. 1.1a-2 in Proceedings volume II) shows more vortical structures

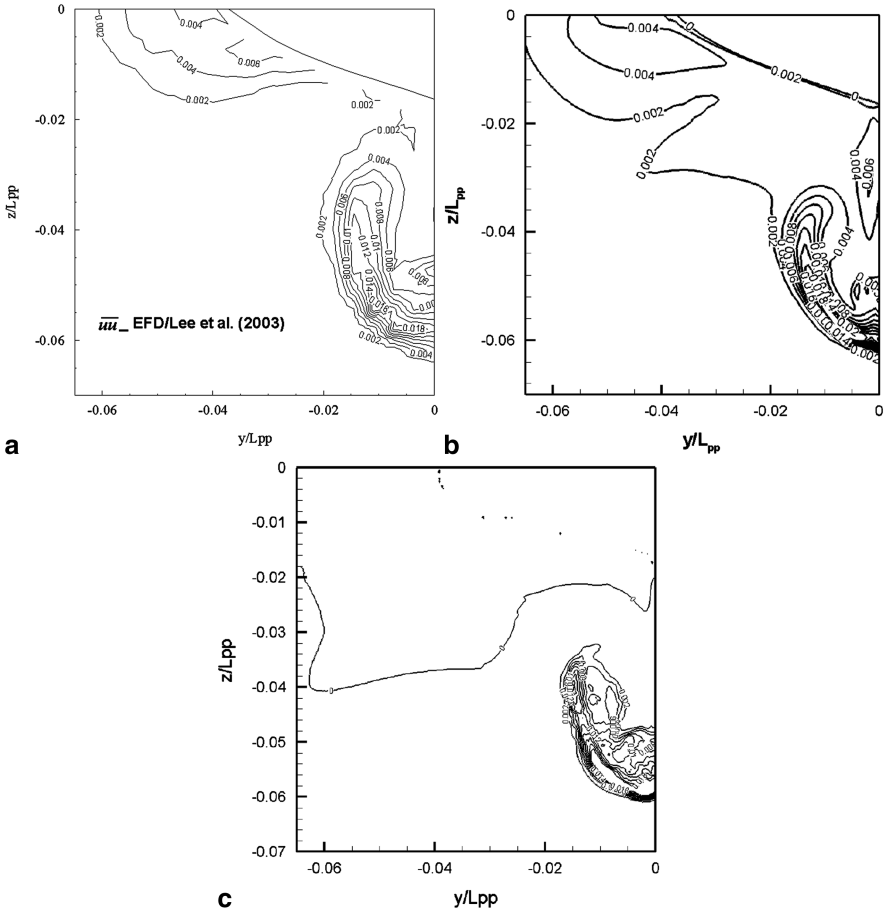


Fig. 7.8 $\overline{uu}$ contours at ($x/L_{pp} = 0.9825$). **a** EFD, **b** ARS-Grid1, **c** BKW-DDES-FD4-Grid0

than ARS-G1 (Fig. 7.3b) and agrees better with EFD. As shown in Fig. 7.6, ARS-DES model shows results similar to ARS on the lateral evolution of the local velocity profiles at $z/L_{pp} = -0.05075$. Similar to ARS-G0 and ARS-DES-G1, BKW/ARS-DES and DDES predicts accurately the circumferential variation of the total wake fraction at r/R = 1.0 except for $30° < \phi < 60°$ and $300° < \phi < 330°$, where DES/DDES over-predicts the total wake fraction (Fig. 7.5).

BKW-DES-FD4-G0 shows grid induced separation in the boundary layer, which induces unsteadiness in the cross-plane. Thus, it requires longer sampling time to obtain statistically converged turbulence quantities. However, the averaging period was found to be sufficient to obtain statistically converged mean and RMS of integral quantities and local mean flow variable, as shown by Xing et al. (2012). Local turbulent variables were also mostly converged, except in the regions of grid induced separation. In addition, the objective of presenting BKW-DES-FD4-G0 results is to

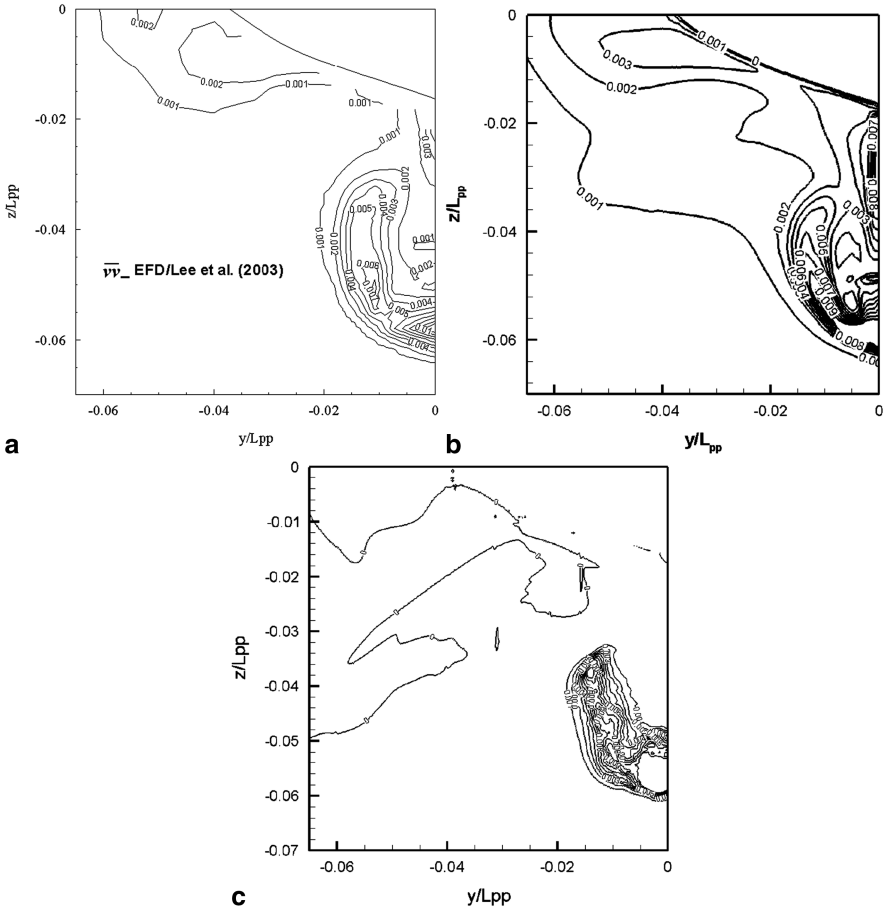


Fig. 7.9 $\overline{vv}$ contours at ($x/L_{pp} = 0.9825$). **a** EFD, **b** ARS-Grid1, **c** BKW-DDES-FD4-Grid0

highlight the grid induced separation issue in DES. Thus, their turbulence predictions are not reported. At r/R = 0.8, BKW-DES-FD4-G0 over-predicts the total wake fraction for almost all ϕ. BKW-DDES-FD4-FD4-G0 significantly improves the prediction and agrees much better with EFD. At r/R = 0.6 and 0.4, BKW-DES-FD4-G0 and BKW-DDES-FD4-G0 over-estimate w_T by about 15 to 50 % in the vicinity of the plane of symmetry.

Turbulence data at the propeller plane are presented for ARS-G1 and BKW-DDES-FD4-G0. The two-extreme configuration as observed by EFD for the turbulent normal stresses is well captured by BKW-DDES-FD4-G0 (Figs. 7.7c, 7.8c, 7.9c, 7.10c) but with higher magnitude, which is contrary to the under estimation by ARS-DES-G1 (Figs. 1.1a-7, 8, 9 in Proceedings volume II). The agreement of all the computations with EFD is reasonable for the turbulent shear stresses $\overline{uv}$ for ARS-G1 (Fig. 7.11b). For $\overline{uw}$, ARS-G1 finds a zone of $\overline{uw} > 0.002$ which is consistently smaller than what

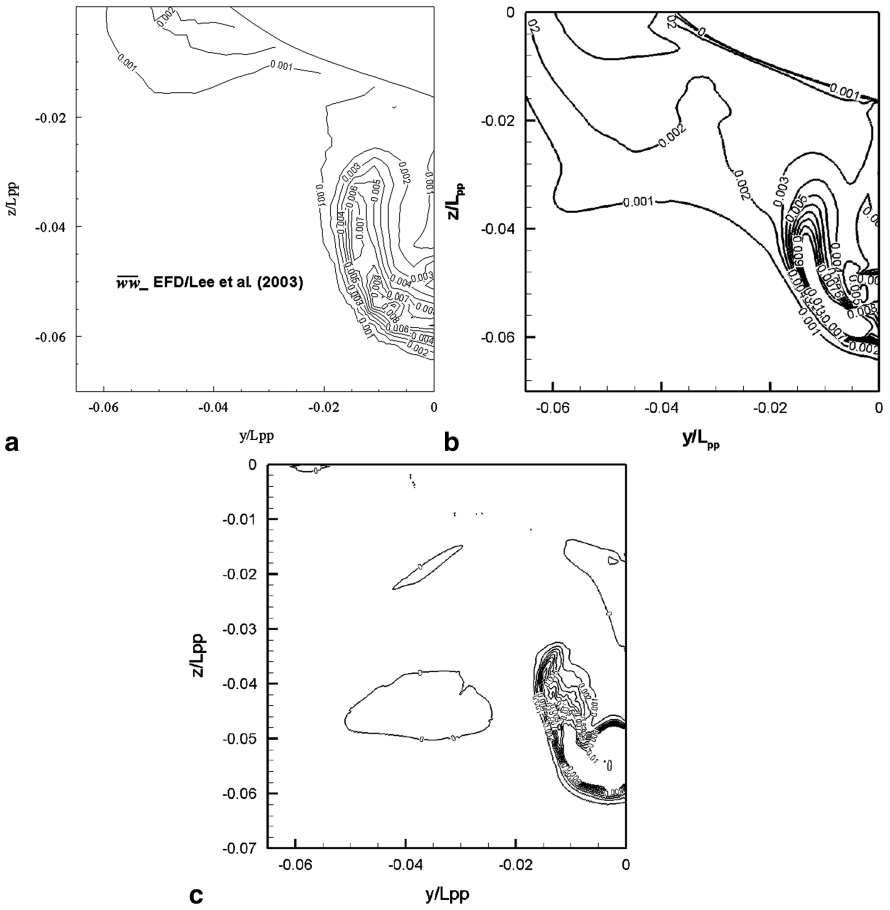


Fig. 7.10 $\overline{ww}$ contours at ($x/L_{pp} = 0.9825$). **a** EFD, **b** ARS-Grid1, **c** BKW-DDES-FD4-Grid0

is observed in the experiments. Only ARS-G1 (Fig. 7.12b) and ARS-G0 (Fig. 1.1a-11 in Proceedings volume II) predict the region near the vertical symmetry plane where $\overline{uw}$ of EFD shows negative value at -0.002, which is more apparent on ARS-G0, likely due to the use of a much finer grid. The global agreement on $\overline{uw}$ is far better when the ARS-DES (Fig. 1.1a-11 in Proceedings volume II) or BKW-DDES-FD4-G0 (Fig. 7.12c) is used, compared to the results of the computations performed with ARS.

The wall pressure and limiting streamlines (Figs. 7.13, 7.14, 7.15, and 7.16) for ARS-G1 and BKW-DDES-FD4-G0 show global similarity to ARS-G0 and ARS-DES-G1. The difference is observed in regions near the propeller plane where BKW-DDES-FD4-G0 predicts longer line of convergence for streamlines, which indicates that the longitudinal vortex is more intense. This is also consistent with the over-predicted Reynolds stresses due to the usage of a much finer grid.

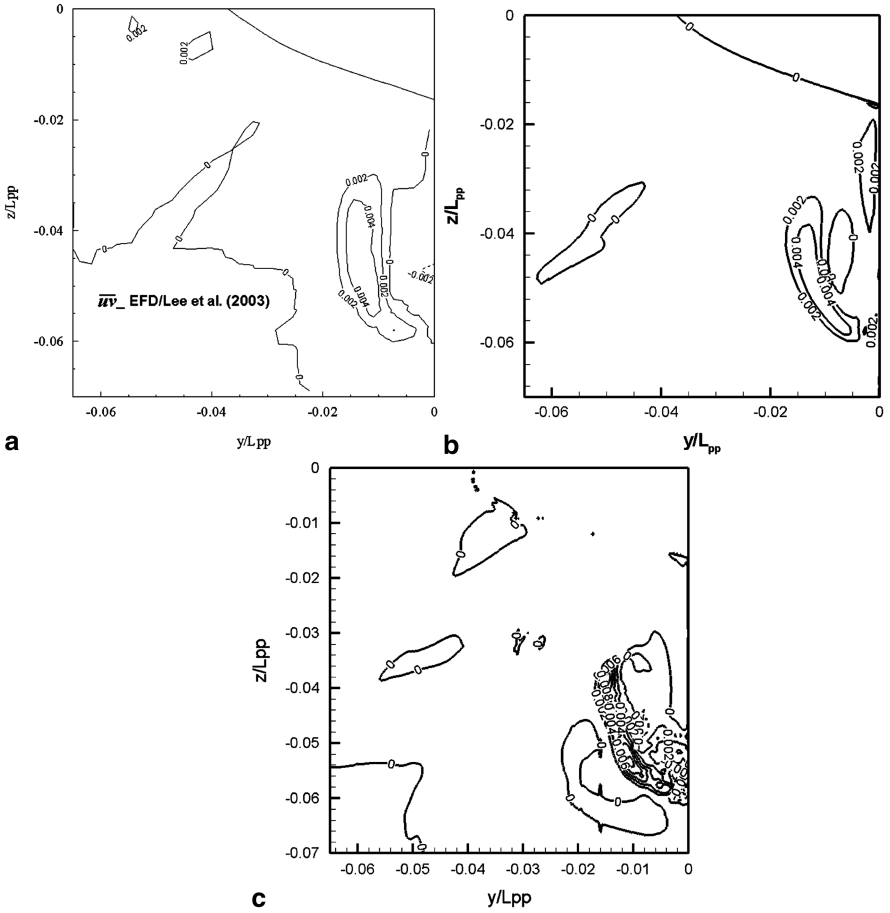


Fig. 7.11 $\overline{uv}$ contours at ($x/L_{pp} = 0.9825$). **a** EFD, **b** ARS-Grid1, **c** BKW-DDES-FD4-Grid0

2.4 Influence of Grid-Induced Separation and Modeled Stress Depletion Issues

BKW-DES on 305M grid (BKW-DES-FD4-G0) shows an additional vortex in the boundary layer due to grid induced separation, as shown by Fig. 7.3c. The grid induced separation is due to the activation of LES inside the boundary layer, and is resolved using DDES on the same grid (BKW-DDES-FD4-G0; Fig. 7.3d). Figure 7.3c and 7.3d show that BKW-DES and DDES on the 305M grid predict much stronger vortices than EFD, which is consistent with ARS-DES-G1. However, compared to ARS, both DES and DDES shows modeled-stresses depletion, i.e., modeled Reynolds stress inside the boundary layer is very small due to a very low value of

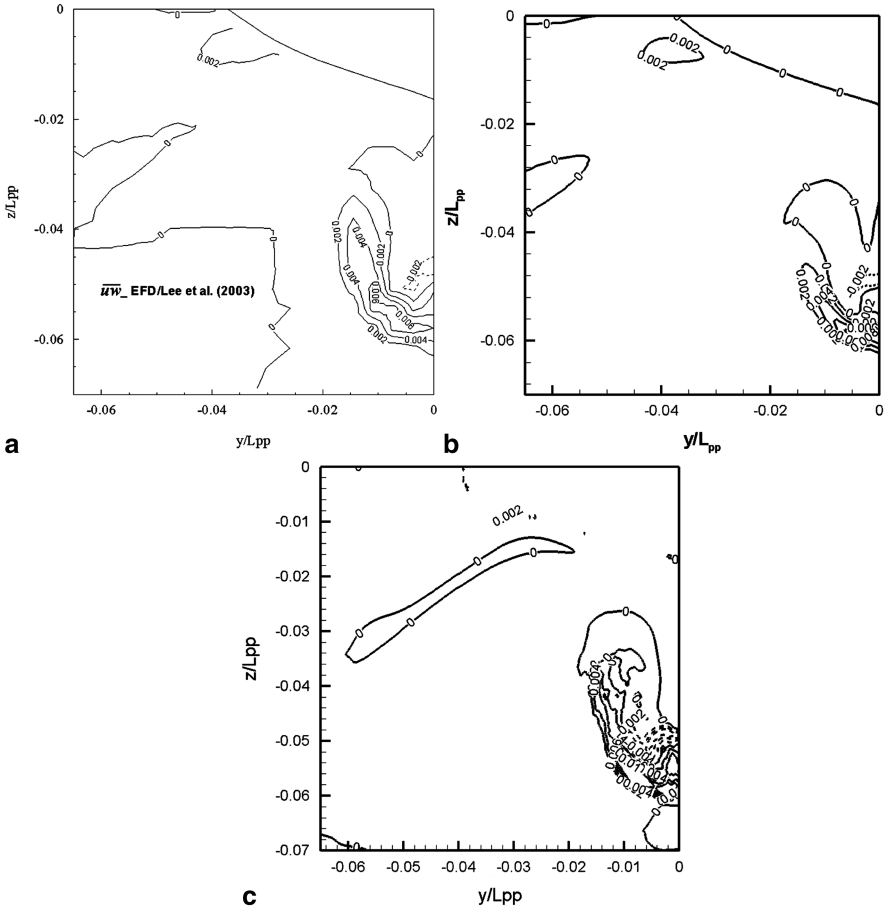


Fig. 7.12 $\overline{uw}$ contours at ($x/L_{pp} = 0.9825$). **a** EFD, **b** ARS-Grid1, **c** BKW-DDES-FD4-Grid0

turbulent eddy viscosity. These can be clearly seen in Fig. 7.12. The modeled-stresses depletion is less apparent for a coarser grid (ARS-DES-Grid 1).

2.5 Conclusions and Perspective of Future Work

The TVD numerical scheme is found to be more accurate than upwind schemes for URANS simulations on coarser grids (with resolution of the order of millions). However, for finer grids (with resolution of the order of 10s millions) effect of numerical schemes are negligible. Higher order schemes are required for HRLES, and 4th order scheme is found to be sufficient in the present study.

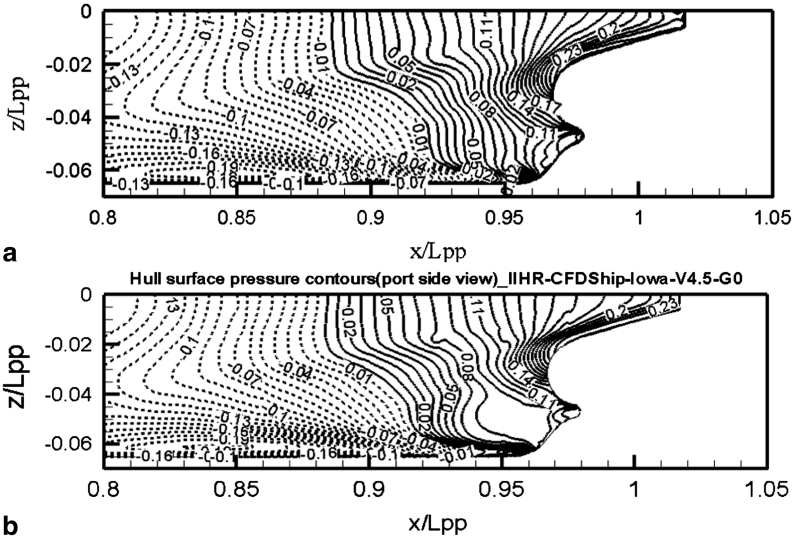


Fig. 7.13 Hull surface pressure contours (*port side view*). **a** ARS-Grid1, **b** BKW-DDES-FD4-Grid0

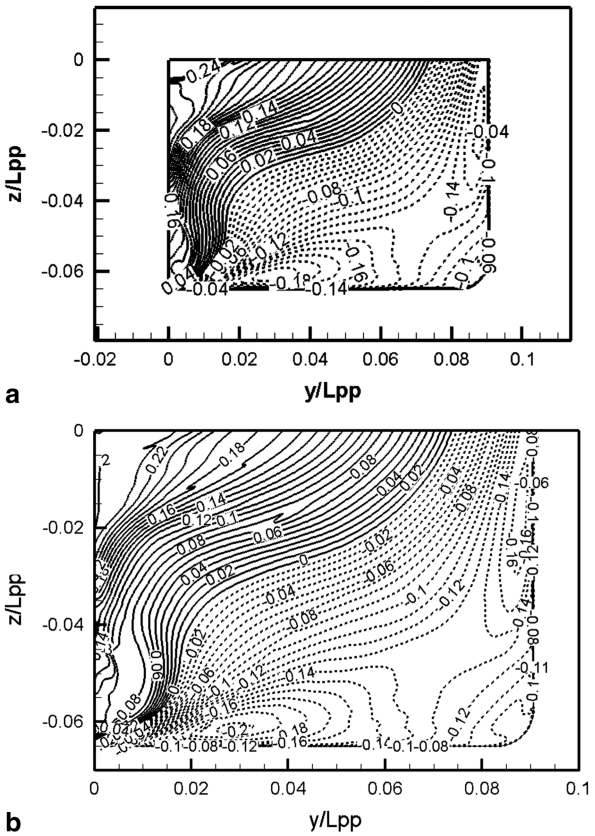


Fig. 7.14 Hull surface pressure contours (*back view*). **a** ARS-Grid1, **b** BKW-DDES-FD4-Grid0

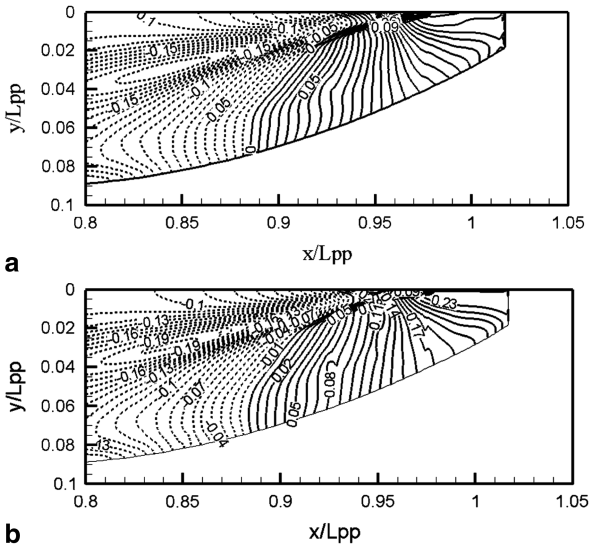


Fig. 7.15 Hull surface pressure contours (*bottom view*).**a** ARS-Grid1, **b** BKW-DDES-FD4-Grid0

ARS shows advantages over BKW in regions where anisotropic effect is dominant, i.e., at the propeller plane. ARS mean flow and turbulence predictions improve with grid refinement from < 1M to 13M, but do not show significant improvement from 13M to 305M. Further, on the finer two grids, the sizes of the main and secondary vortices are under predicted, and turbulent kinetic energy (TKE) is over predicted. Thus, these deficiencies are identified due to modeling errors and not due to grid. Due to the complexity of various grid types, grid resolution, turbulence models, and numerical schemes used in the study, no general conclusion can be drawn regarding the grid size that is sufficient for RANS computations.

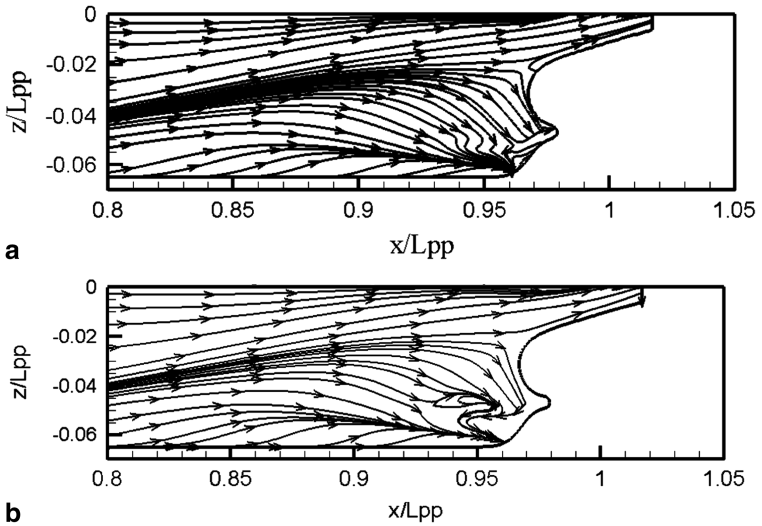


Fig. 7.16 Limiting streamlines (*port side view*). **a** ARS-Grid1, **b** BKW-DDES-FD4-Grid0



Fig. 7.17 DTMB5415 hull geometry

ARS-DES results are much more sensitive to grid refinements compared to BKW or ARS. The resolved turbulence levels improve with grid refinement, and are up to 95 % for 305M grids. The predictions improve with grid refinement up to 13M grid, but on 305M grid the mean flow velocity and turbulence quantities are over predicted.

ARS-DES predicts unsteady vortices, whereas BKW or ARS predict steady vortices. When compared with the experimental data, HRLES computation using ARS-DES on 13M grid are the best among the HRLES computations on both coarser and finer grids. However, both axial velocity, and vortical and turbulent structures are over predicted. Overall, best HRLES predictions are comparable to best URANS predictions, as the latter is equally under predictive for axial velocity and vortical structures and equally over predictive for turbulent structures.

DES shows grid induced separation inside the boundary layer and modeled stress depletion on the 305M grid. The grid induced separation issue was resolved by using DDES approach, but it did not address modeled stress depletion issue. It is expected that the modeled-stress depletion could be resolved using the improved DDES (IDDES) model.

No general conclusions can be drawn regarding the appropriate grid requirements for DES, due to modeling issue. In order to determine the grid sufficiency, systematic grid refinement and verification and validation (V&V) studies need to be performed for local quantities. Additionally, one must note that the available V&V methodology and procedures such as the factor of safety method (Xing and Stern 2010) is only applicable to URANS. It cannot be applied directly for HRLES due to the coupling of modeling and numerical errors.

Future work includes, investigation of the correlation between mean flow and turbulent structures to provide feedback for better turbulence model development. Advanced turbulence models for URANS such as the full Reynolds stress models should be investigated to improve stress anisotropy formulation. Advanced models are required for HRLES to address the modeled stress depletion issue. In addition, the effect of numerical scheme on HRLES predictions needs to be evaluated. Except the IIHR submissions, all other submissions used relative coarser grids (≤ 8 million). It is recommended that systematic refined grids with the finest grid up to 100s M points should be generated to perform grid sensitivity and validation studies. New V&V methodology and procedures need to be developed for HRLES.

3 DTMB 5415: CASES 3.1-A & B

The model DTMB 5415 shown in Fig. 7.17, was conceived as a preliminary design of a Navy Surface combatant, which was actually never built. The hull geometry includes both a sonar dome and transom stern. In the cases 3.1-a & b, only the

bare hull in calm water conditions is considered. The froude number (Fr) for the computations is 0.28 and the hull is positioned in the basin at its dynamic sinkage and trim. Two series of experiments are available for this test case. The first one was performed at INSEAN by Olivieri et al. (2001) for a model of 5.82 m long ($Re = 1.19 \times 10^7$, sinkage $= -1.82 \times 10^{-3}\ L_{pp}$, trim $= -0.108°$). A second set of experiments was performed at IIHR by Longo et al. (2007) at the same $Fr = 0.28$ with a smaller model of 3.048 m long ($Re = 5.13 \times 10^6$, sinkage $= -1.92 \times 10^{-3}$ L_{pp}, trim $= -0.136°$).

These two experiments provide complementary information on the local flow. Measurements made at INSEAN give the contours of the longitudinal component of the velocity, cross-flow vectors and secondary streamlines in the several transversal, while those performed at IIHR provide streamwise velocity contours, turbulent kinetic energy and Reynolds stresses (uu, vv, ww, uv and uw) at the propeller plane $x/L_{pp} = 0.9346$.

3.1 Review of New Contributions

Table 7.2 summarizes post-workshop simulations using CFDShip-Iowa V4, ISIS-CFD and Fluent, including V4 workshop submissions on 615K and 300M grids. The nomenclature used for the simulations is Solver—Grid Type—Grid Number—Turbulence Model—Flow Phase. For solver tags V4, ISIS and F are used for CFDShip- Iowa, ISIS-CFD and Fluent runs, respectively. Tags B, A and O are used for multi-block overset grid, adaptively refined grid and single-block O-type grids respectively. The grids B0 (300M), B1 (50M), B2 (10M) and B3 (2M grid) are systematically coarsened using $r_G = 3^{1/2}$. The adaptive grid A consists of 6M points, and is generated by automatic adaptive mesh refinement, wherein the cell sizes are based on the second spatial derivatives of the pressure. O2 consists of 615K points and is refined using grid refinement ratio $r_G = 2$ to obtain O1 consisting of 5M points. The nomenclature for the turbulence model is No-model (NM), BKW for blended k-ε/k-ω, ARS for algebraic Reynolds stress, EASM for explicit algebraic stress model, SA/DES for Spalart-Allmaras based DES (Spalart et al. 2006), BKW/DES for DES based on BKW, ARS/DES for DES based on ARS, and DHRL for dynamic Hybrid RANS/LES (Bhushan and Walters 2012). Tag S is used to indicate single-phase simulation, whereas no tag is used for semi-coupled two-phase simulations.

Simulations on B1, B2 and B3 using both BKW and ARS are used for grid verification of resistance predictions. Simulations B0-BKW/DES, B1-ARS/DES and B2-ARS/DES are used for grid verification study for HRLES resistance predictions. High-resolution sonar dome predictions using V4-B0-BKW/DES and ISIS-A-EASM are used to study the onset and progression of the vortical structures. V4 simulations on wide range of grids help evaluate the effect of grid refinement on URANS predictions on up to 50M grids, and DES predictions on up to 300M grids. ARS and BKW simulations help evaluate the effect of isotropic and anisotropic turbulence

Table 7.2 Summary of post-workshop simulations using CFDShip-Iowa V4, fluent and ISIS-CFD, including resolved TKE levels for DES simulations. V4 workshop submissions on 615K and 300M grids (*shaded*) are also presented for comparison purposes

Simulations	Grid	Solver	Turbulence Model	Total Resistance♣		Resolved TKE level	Vortex extent*				Objective
				$C_T \times 10^3$	*E%D*		SDV	SDTEV	SDSV	FBKV	
V4-O2-BKW (Xing et al., 2010)	615K – O Grid	CFDShip-Iowa V4	BKW	5.01	-8.68	-	0.28	-	-	0.53	• G2010 Submission • Compared BKW and ARS predictions
V4-O2-ARS (Bhushan et al., 2012)			ARS	4.97	-7.81		0.29	-	-	0.53	
V4-O1-BKW	5M – O Grid	CFDShip-Iowa V4	BKW	4.81	-4.33	-	0.44	-	-	0.64	• Study effect of grid topology and wave elevation on vortical structures • Study effect of numerical methods
V4-O1-ARS			ARS	4.75	-3.04		0.45	-	-	0.64	
V4-O1-ARS-S			ARS	-			0.98	-	-	0.92	
F-O1-BKW-S	5M – O Grid	Fluent	BKW	-		-	>1	-	-	>1	
F-O1-SA/DES-S			DES			0.1%	>1	-	-	>1	
F-O1-DHRL-S			DHRL			65%	>1	-	-	> 1	
ISIS-O1-BKW-S	5M – O Grid	ISIS-CFD	BKW	-		-	>1	-	-	>1	
ISIS-A-EASM-S	6M Adaptive		EASM				0.85	0.25	-	0.85	• Effect of adaptive mesh refinement
V4-B3-BKW	2M – Overset multi-block	CFDShip-Iowa V4	BKW	4.72	-2.38	-	0.29	-	-	0.53	• Verification study for BKW and ARS using 10M and 50M results
V4-B3-ARS			ARS	4.68	-1.52		0.3	-	-	0.55	
V4-B2-NM	10M – Overset multi-block	CFDShip-Iowa V4	No-Model	2.46	35.6	-	>1	-	-	>1	• Compare isotropic and anisotropic turbulence models for URANS • Verify resolved turbulence issue in DES • Estimate effect of numerical dissipation
V4-B2-BKW			BKW	4.94	-7.15		0.44	-	-	0.64	
V4-B2-ARS			ARS	4.88	-5.85		0.45	-	-	0.64	
V4-B2-BKW/DES			BKW-DES	4.79	-3.90	0.3%	0.47	-	-	0.68	
V4-B2-ARS/DES			ARS-DES	4.77	-3.43	0.3%	0.47	-	-	0.68	
V4-B1-BKW	50M – Overset multi block	CFDShip-Iowa V4	BKW	4.83	-4.77	-	0.66	-	-	0.67	• Compare isotropic and anisotropic turbulence models for URANS Verify resolved turbulence issue in DES
V4-B1-ARS			ARS	4.77	-3.40		0.68	-	-	0.68	
V4-B1-ARS/DES			ARS-DES	4.78	-3.52	1%	0.71	-	-	> 1	
V4-B0-BKW/DES (G2010)	300M– Overset Multi-block	CFDShip-Iowa V4	BKW-DES	4.73	-2.60	2.5%	> 1	0.32	0.27	>1	

♣C_T (EFD) = 4.61×10^3

*Based on $Q = 10$

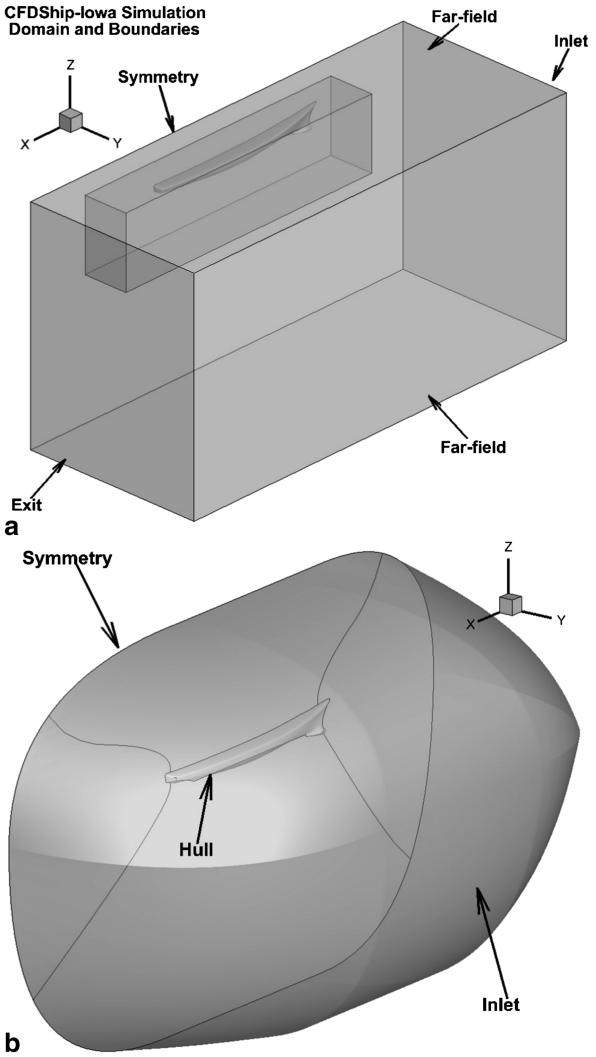


Fig. 7.18 Domain and boundary condition for CFDShip-Iowa V4 simulations using **a** B-grid and **b** O-grid

models on nominal wake predictions. The ISIS-A grid simulation is performed to obtain very high grid resolution in the regions of vortex onset, in order to assess the URANS modeling errors. Simulation B2-NM is performed to identify the cause of the BKW-DES resolved turbulence issues from either numerical dissipation or DES model limitation. Predictions using O grids are compared with those using B grids to study the effect of grid topology on the vortical structures. Single-phase simulations on O1-S using different solvers help in evaluating the effect of free-surface on the vortical structures and study the effect of numerical methods.

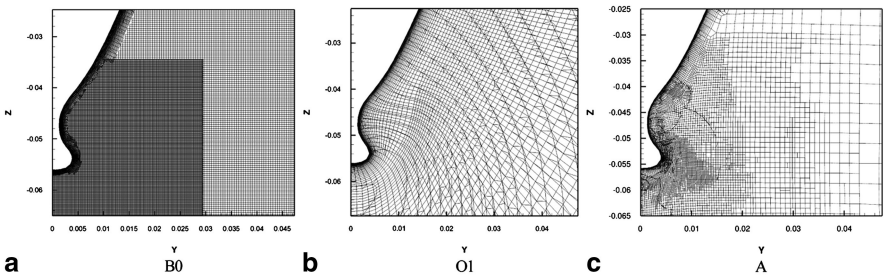


Fig. 7.19 Grid resolution for **a** B0, **b** O1, and **c** A grids and at $x/L_{pp} = 0.1$

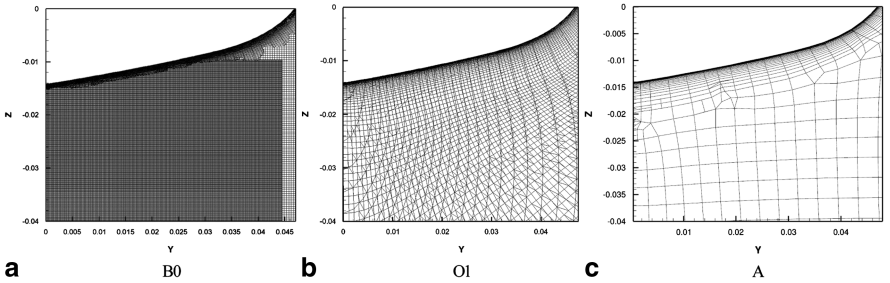


Fig. 7.20 Grid resolution for **a** B0, **b** O1, and **c** A grids at $x/L_{pp} = 0.9346$

CFDShip-Iowa V4 Numerical Methods and Turbulence Models V4 solves for the semi-coupled two-phase URANS/HRLES flows. The governing equations are discretized using node-centered finite difference schemes on body-fitted curvilinear grids and solved using a predictor-corrector method. The time marching is done using a second-order backward difference scheme, the convection terms are discretized using a hybrid second/fourth-order linear scheme, and level-set equations are discretized using a hybrid first/second-order TVD scheme. The equations are solved using implicit schemes. The pressure Poisson equation is solved using the PETSc toolkit and projection algorithms are used to satisfy continuity (Carrica et al. 2007). Simulations are performed using no-model (or implicit LES), isotropic BKW, anisotropic ARS models, and BKW- and ARS- based DES models.

ISIS-CFD Numerical Methods ISIS-CFD solves for the incompressible URANS equations (Queutey and Visonneau 2007). The solver uses 2nd order finite volume method to build the spatial discretization of the transport equations. The solver uses a generalized face-based method for three-dimensional unstructured meshes for which non-overlapping control volumes are bounded by an arbitrary number of constitutive faces. The velocity field is obtained from the momentum conservation equations and the pressure field is extracted from the mass conservation constraint transformed into a pressure equation. Turbulence modeling is performed using explicit algebraic stress model (EASM) and BKW. The additional transport equations for modeled variables are discretized and solved using the same principles as the momentum equation. The

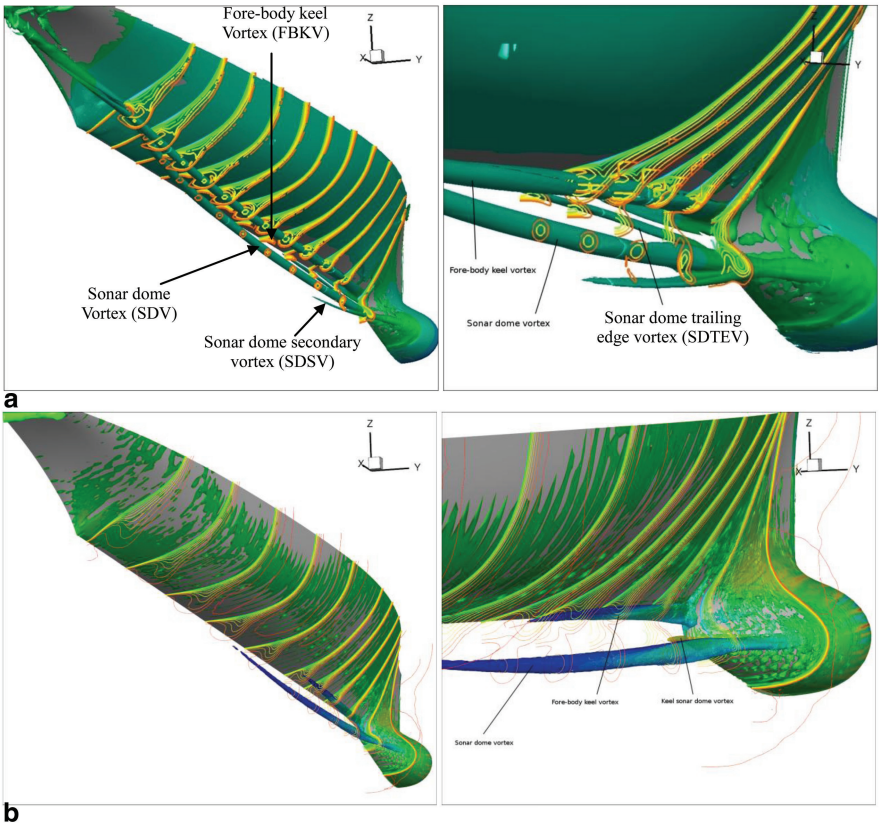


Fig. 7.21 Global view of the DTMB5415 vortices predicted by **a** V4-B0-BKW/DES and **b** ISIS-A-EASM-S are shown using the isosurface Q = 500. Isosurface are colored using axial velocity contours

solver has free-surface capability, wherein immiscible fluids are modeled through the use of conservation equations for each volume fraction of phase/fluid. However, only single-phase simulations are performed herein.

Fluent Numerical Methods Single-phase simulations are performed using 2nd order bounded central difference scheme for momentum equation convection term, and 2nd order upwind scheme for turbulence equation convection term. The diffusion terms are discretized using 2nd order central difference scheme for both the momentum and turbulence equations. Pressure-velocity coupling is performed using SIMPLE (Semi Implicit Method for Pressure Linked Equations) scheme (Patankar 1980). Time stepping is performed using 2nd order implicit scheme. Simulations are performed using NM, BKW, SA-DES, and DHRL which couples BKW and Implicit LES (Bhushan and Walters 2012; Bhushan et al. 2012a).

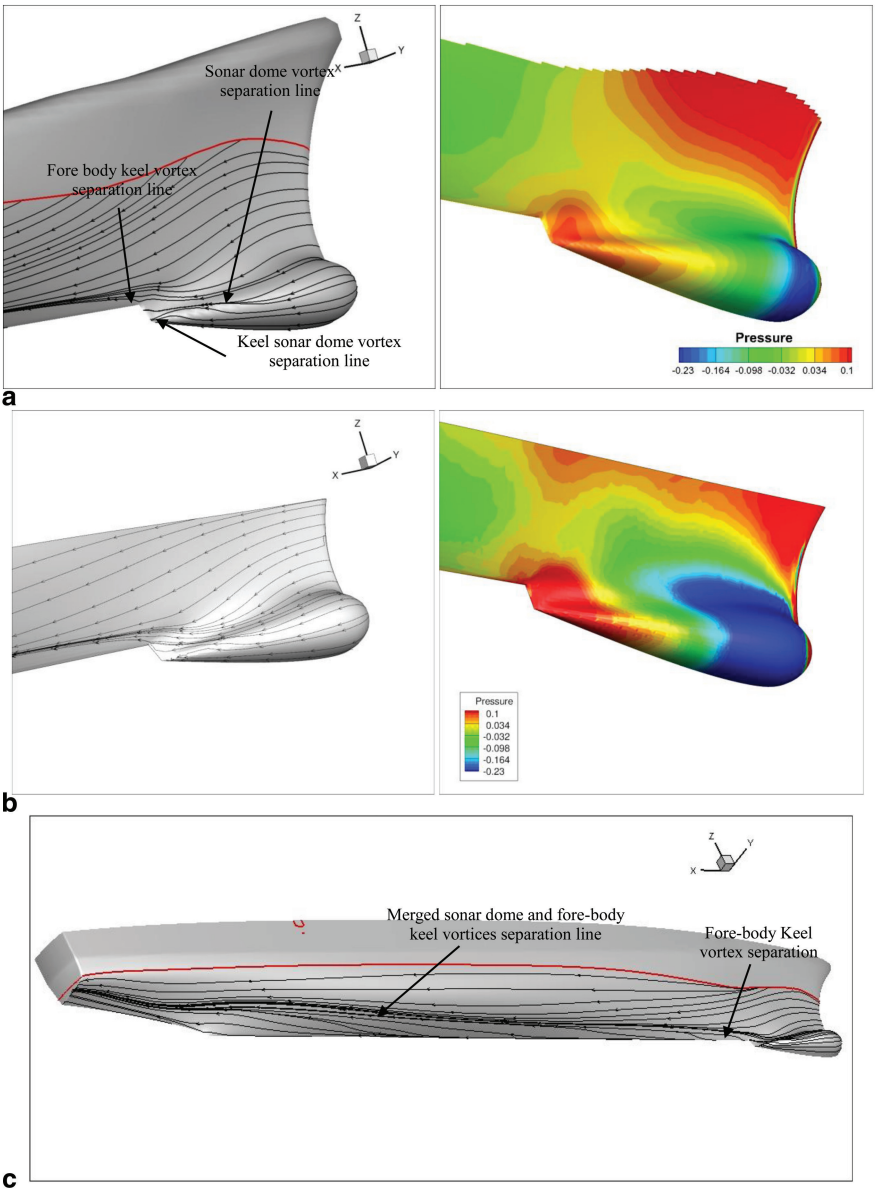


Fig. 7.22 Vortex onset and separation pattern are shown using surface streamline and pressure distribution on sonar dome using **a** V4 –B0 BKW/DES predictions and **b** ISIS-A-EASM-S predictions, and **c** surface streamline all along the hull using V4 –B0-BKW/DES predictions show the vortex progression

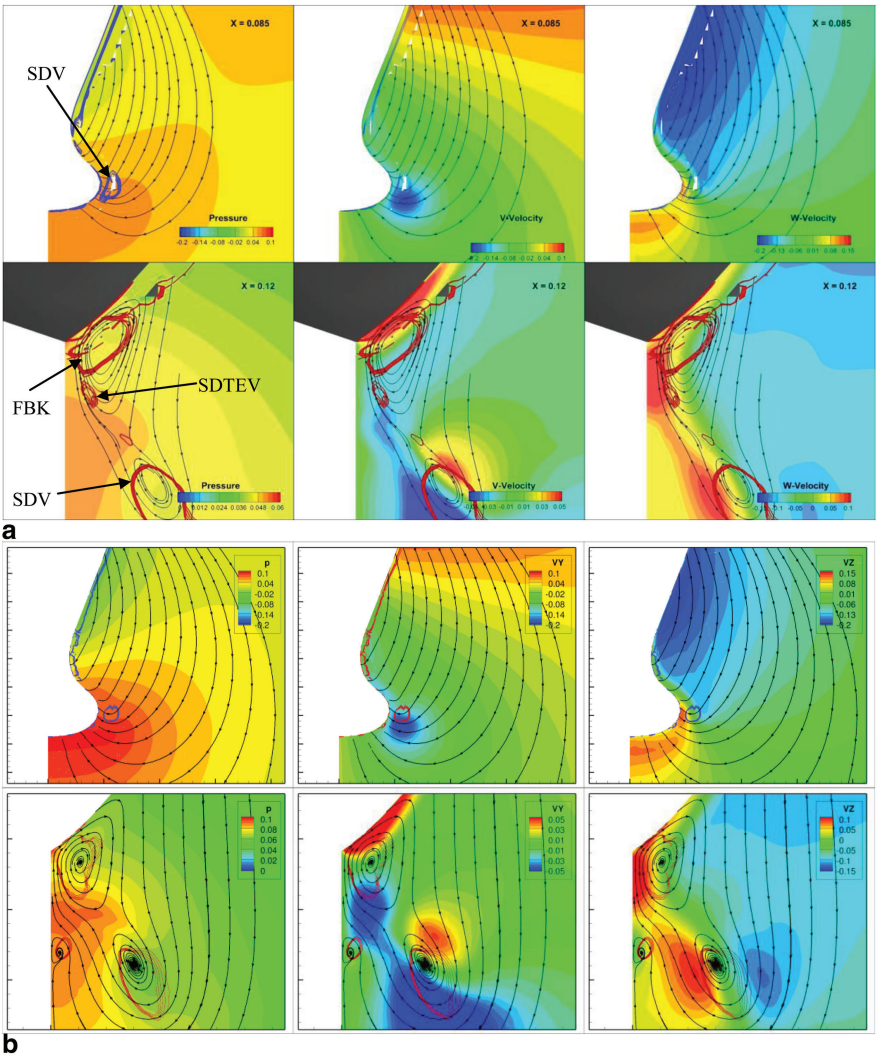


Fig. 7.23 Flow streamlines, pressure, cross flow contours and contour lines of Q for slices at X = 0.085 (*top*) and 0.12 (*bottom*) obtained using **a** V4 –B0-BKW/DES and **b** ISIS-A-EASM-S. The Q contours are for 5 levels Q = 500 − 1000, and the SDV, FBKV and SDTEV votices are labeled

Grids, Domains and Boundary Conditions The domain and boundary conditions used for B and O grids are shown in Fig. 7.18. All the simulations are performed using half domain hull with symmetry boundary conditions at Y = 0. For the B grid simulations, a uniform inlet and convective exit boundary conditions are applied at the X-Min and X-Max planes, respectively. A symmetry boundary condition is applied at $Y/L_{PP} = 0$, no-slip boundary conditions at the wall, and far-field

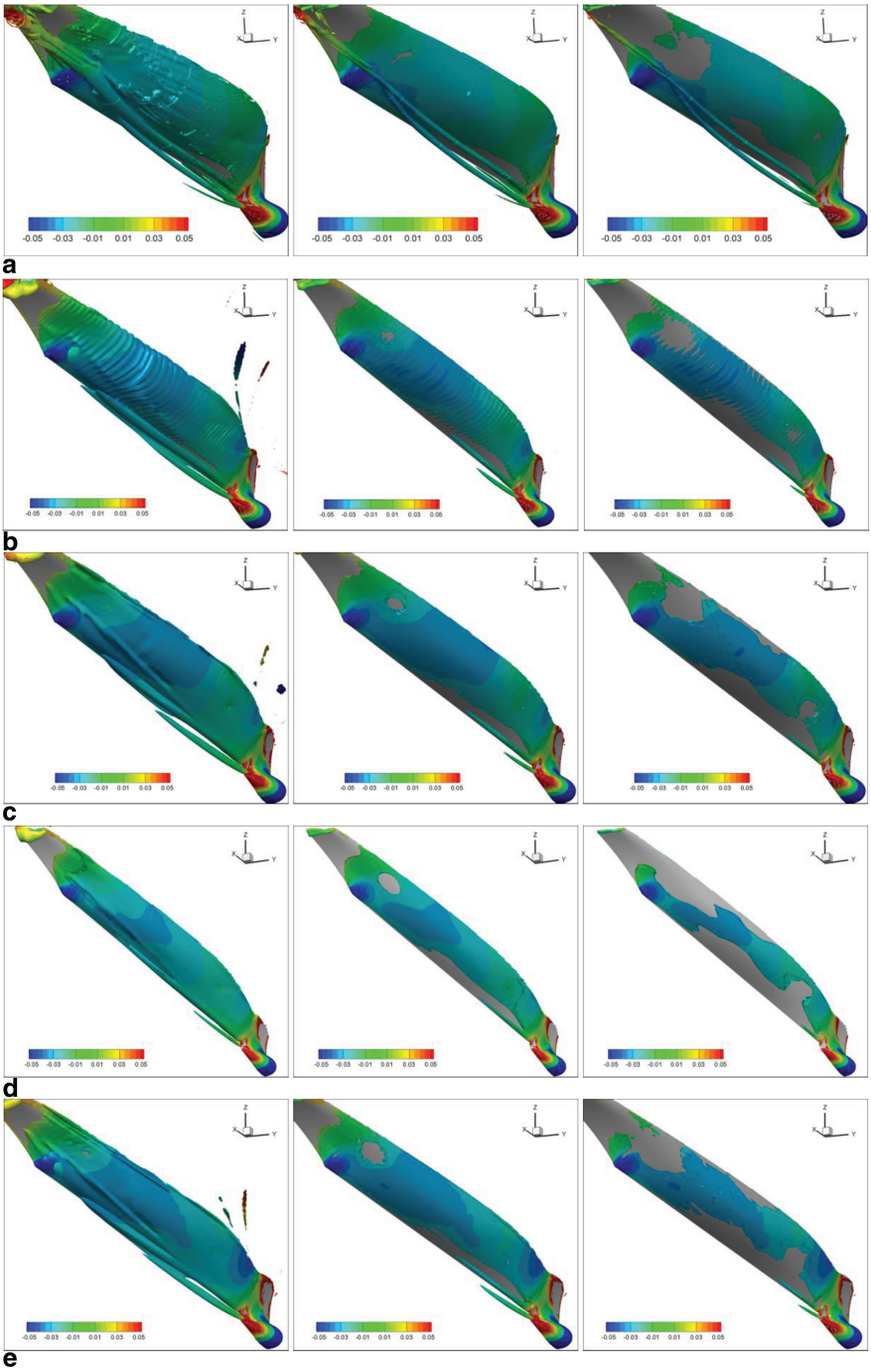


Fig. 7.24 Vortical structures are shown using isosurface of normalized helicity Q = 10 (*Left*), 100 (*Middle*) and 300 (*Right*) for selected two-phase CFDShip-Iowa V4- ARS and ARS/DES simulations on B and O grids. Q isosurfaces are colored using pressure. **a** V4-B0-BKW/DES. **b** V4-B1-ARS. **c** V4-B2-ARS. **d** V4-B3-ARS. **e** V4-O1-ARS

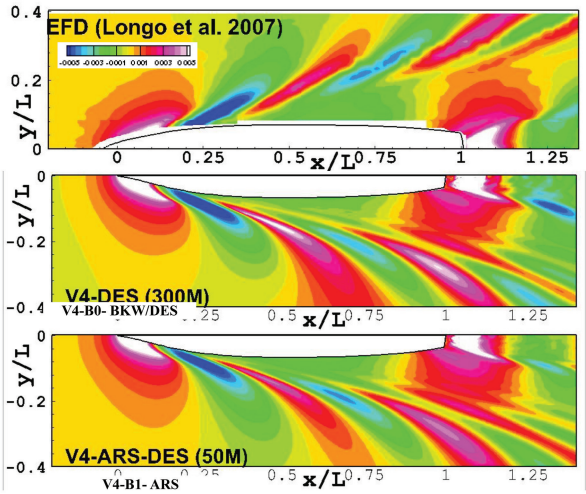


Fig. 7.25 Wave-elevation pattern is shown for selected V4-B-grid predictions using NM, ARS and DES. Free-surface is colored using wave elevation $z/L_{PP} = [-0.005, 0.005]$ using 21 levels

conditions for rest of the boundaries. O grid simulations are performed using inlet for far-field. ISIS-CFD single-phase simulations are performed using double-body, i.e., symmetry plane ay Z = 0 plane, thus deck vortices are not predicted. The grid resolution for the B0, O1 and A grids are shown in Figs. 7.19 and 7.20 at $x/L_{PP} = 0.1$ and 0.935, respectively. The simulations are performed for case 3.1b conditions, i.e., $Re = 5.13 \times 10^6$, sinkage $= 1.92 \times 10^{-3}$ and trim $= 0.136°$, and $Fr = 0.28$ for two-phase and $Fr = 0$ for single phase.

3.2 *Verification and Validation Studies for BKW, ARS and DES Resistance Predictions*

Verification studies are performed for resistance coefficients following the quantitative methodology and procedures proposed by Stern et al. (2006) and Xing and Stern (2010) to estimate numerical uncertainties and validation interval. Uncertainties due to the numerical iteration (U_I) are estimated from the dynamic range of the running mean oscillations. Validation is performed by comparing the error $|E|$ in total resistance (C_T) predictions, i.e., difference from the experimental data, with the validation interval.

As summarized in Table 7.3, BKW and ARS shows averaged $U_I \sim 0.04\,\%S_I$ and averaged ratio of U_I and the relative change between the two fine grid solutions (U_I/ε_{12}) =0.04. DES shows $U_I \sim 0.1\,\%S_I$ and $U_I/\varepsilon_{12} = 0.08$. URANS resistance predictions show mostly oscillatory convergence with averaged convergence ratio R_G around -0.042. DES predictions show monotonic convergence with averaged R_G around 0.61, and the ratio of predicted to theoretical order of accuracy p_{re}/p_{Gth} varies in the range 0.8–1.3. The averaged grid uncertainty (U_G) for C_T is predicted to be $2.3\,\%S_I$ and $2.1\,\%S_I$ and $1.25\,\%S_I$ for BKW, ARS and DES, respectively. U_G for

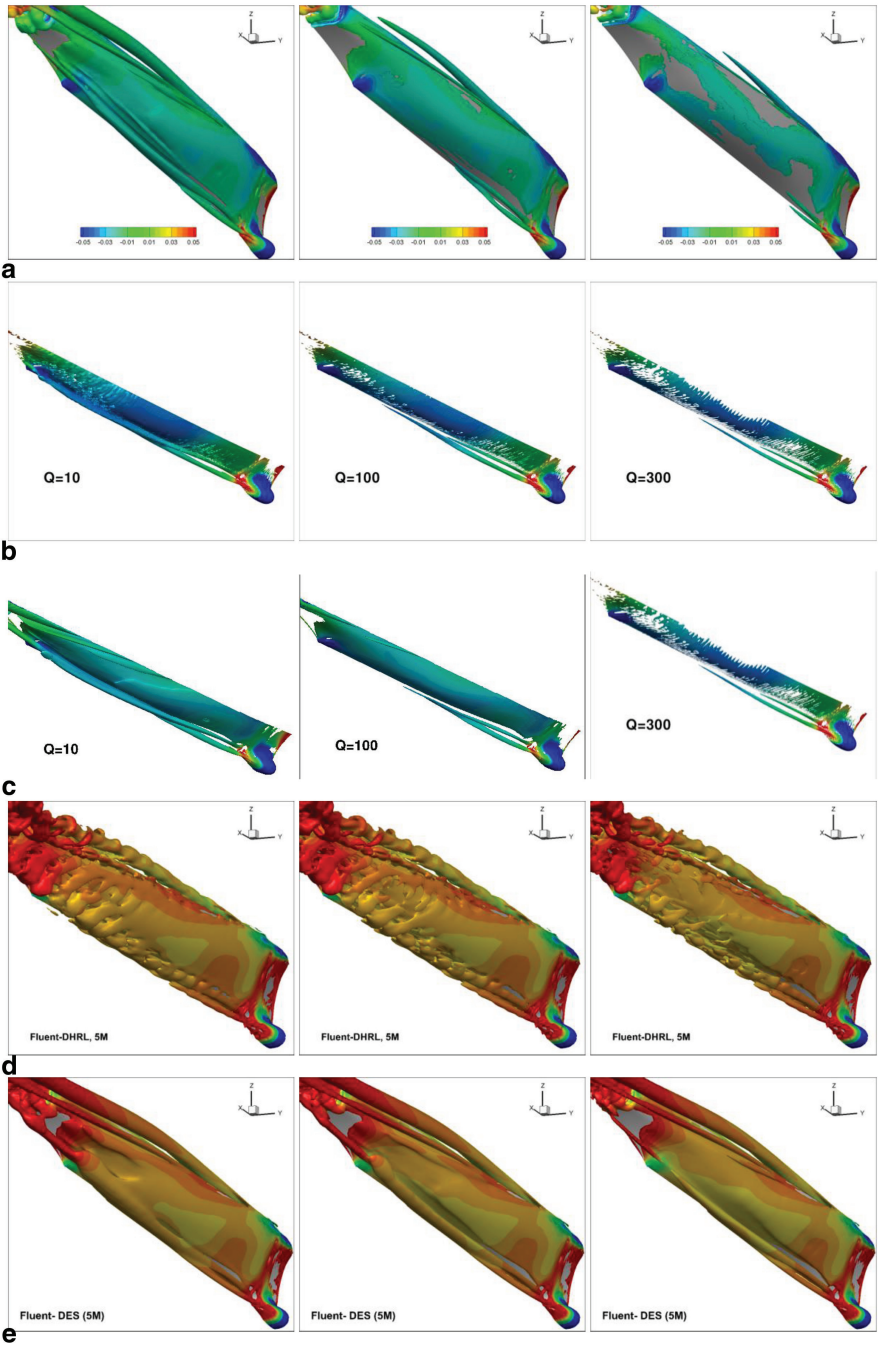


Fig. 7.26 Vortical structures are shown using isosurface of normalized helicity Q = 10 (*Left*), 100 (*Middle*) and 300 (*Right*) for single-phase V4-O1-ARS-S, ISIS-CFD predictions on A using EASM and O1 grids using BKW, and Fluent on O1 grid using DHRL and SA/DES. Q isosurfaces are colored using pressure. **a** V4-O1-ARS-S. **b** ISIS-A-EASM-S. **c** ISIS-O1-BKW-S. **d** F-O1-DHRL-S. **e** F-O1-SA/DES-S

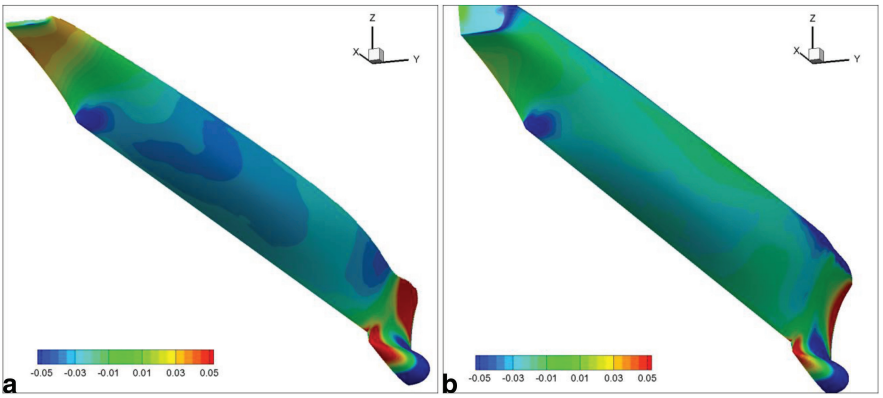


Fig. 7.27 Surface pressure distribution for **a** V4-O1-ARS and **b** V4-O1-ARS-S are compared to study the effect of wave elevation on vortical structures

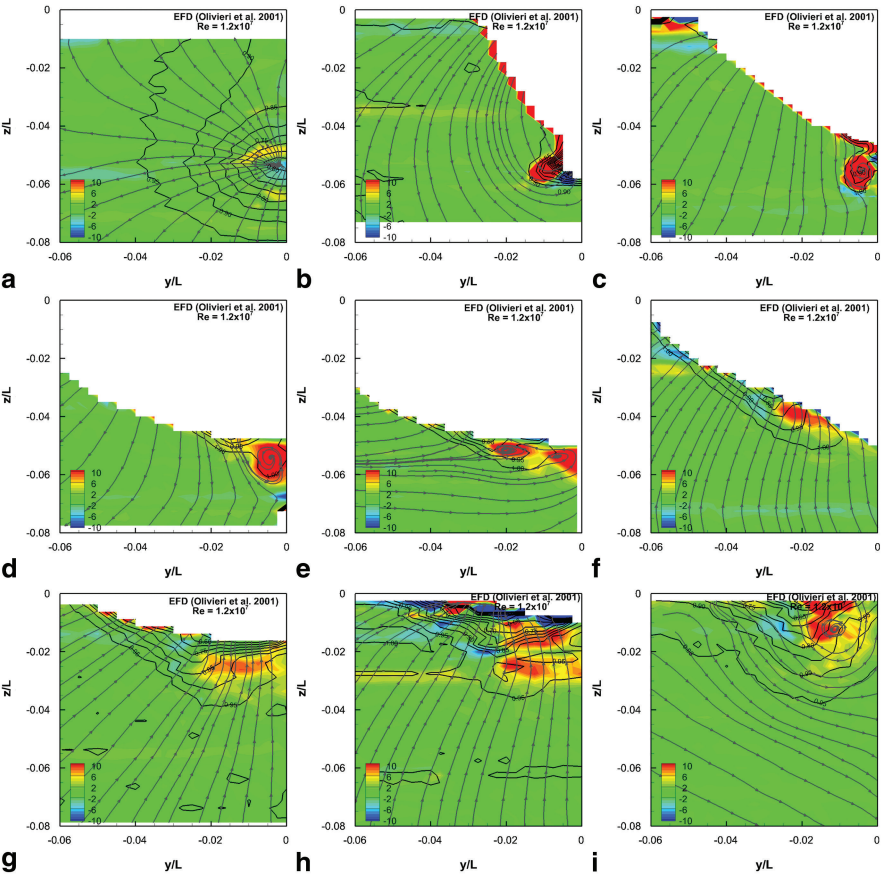


Fig. 7.28 Experimental measurements of (Olivieri et al. 2001) streamwise vorticity (*flooded contours*), streamwise velocity (*black lines*) and cross flow streamline (*grey lines*) at several streamwise locations x/L = −0.00524 to 1.1 are shown. **a** x/L = −0.00524. **b** x/L = 0.1. **c** x/L = 0.2. **d** x/L = 0.4. **e** x/L = 0.6. **f** x/L = 0.8. **g** x/L = 0.935. **h** x/L = 1.0. **i** x/L = 1.1

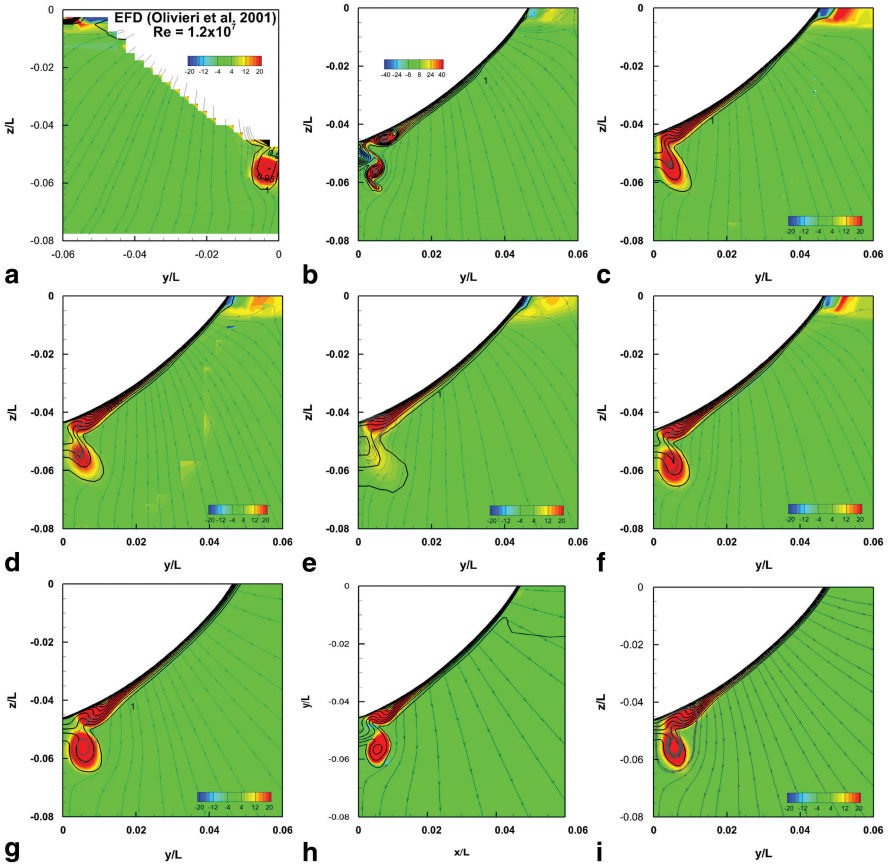


Fig. 7.29 Contour of streamwise vorticity (*flooded contours*), streamwise velocity (*lines*) and cross flow streamlines (*lines with arrows*) at x/L = 0.2 obtained using V4-B0-BKW/DES, V4 with ARS on B1, B2, B3 and O1grids, ISIS-A-EASM-S and F-O1-DHRL-S are compared with EFD data (Olivieri et al. 2001). **a** EFD. **b** V4-B0-BKW/DES. **c** V4-B1-ARS. **d** V4-B2-ARS. **e** V4-B3-ARS. **f** V4-O1-ARS. **g** V4-O1-ARS -S. **h** ISIS-A-EASM -S. **i** F-O1-DHRL -S

frictional resistance (C_F) is smaller $< 1.62\,\%S_1$ for BKW and ARS, and $0.44\,\%S_1$ for DES. U_G is largest for pressure resistance (C_R), about $11.31\,\%S_1$ for BKW and ARS, and $3.5\,\%S_1$ for DES.

As summarized in Table 7.2, $|E|$ for C_T decreases with the grid refinement, i.e., averaged $|E| = 8.3\,\%$ for 615K grid, 5.5 % for 10M grid, 3.6 % for 50M grid and 2.6 % for 300M grid, except for 2M grid for which shows averaged $|E| = 1.95\,\%$. ARS shows 1.5 % better predictions than BKW. DES predictions show $< 0.5\,\%$ variation on BKW and ARS basis models. DES shows 2.5 % better predictions than BKW or ARS on 10M grid, but is comparable to BKW or ARS on 50M grid. As expected, NM simulations shows 35 % lower predictions as frictional resistance is under predicted. As summarized in Table 7.3, C_F predictions also improve with grid resolution and

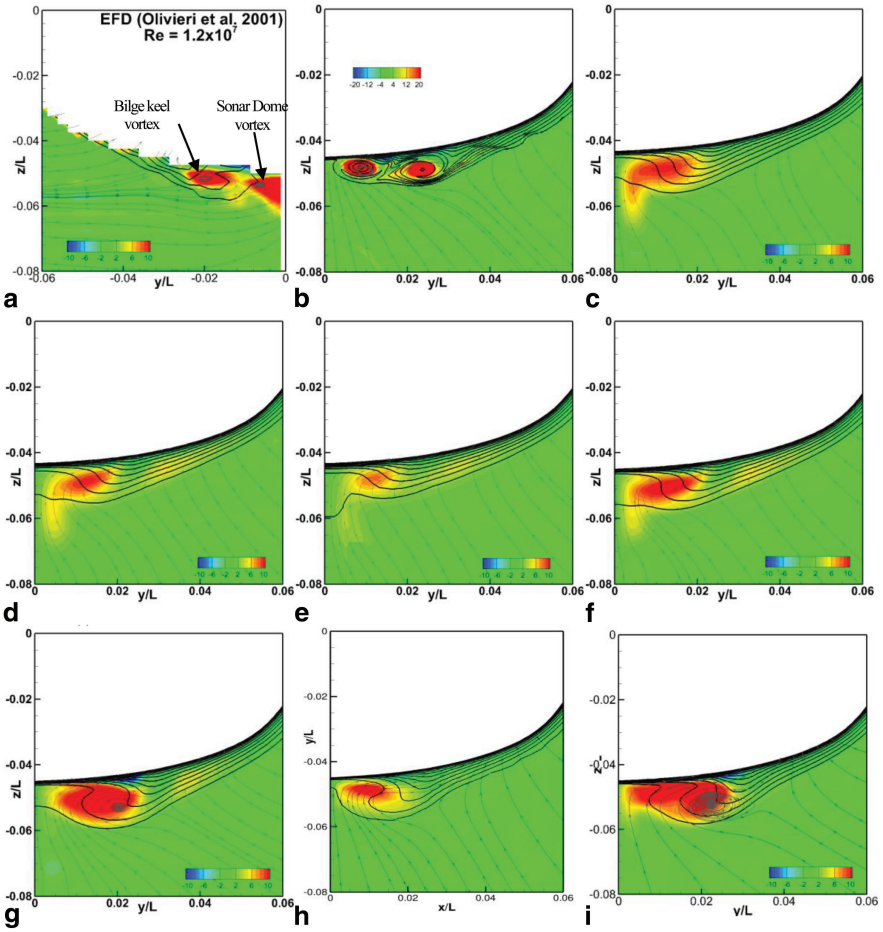


Fig. 7.30 Contour of streamwise vorticity (*flooded contours*), streamwise velocity (*lines*) and cross flow streamlines (*lines with arrows*) at x/L = 0.6 obtained using V4-B0-BKW/DES, V4 with ARS on B1, B2, B3 and O1grids, ISIS-A-EASM-S and F-O1-DHRL-S are compared with EFD data (Olivieri et al. 2001). **a** EFD. **b** V4-B0-BKW/DES. **c** V4-B1-ARS. **d** V4-B2-ARS. **e** V4-B3-ARS. **f** V4-O1-ARS. **g** V4-O1-ARS -S. **h** ISIS-A-EASM -S. **i** F-O1-DHRL -S

compare within 3 % of ITTC for 10M and finer grids. C_R predictions show the largest $|E|$, which are up to 10 % for URANS and 7.5 % for DES. Validation uncertainty (U_V) for C_T is predicted to be $U_V = 4.77\,\%\mathrm{D}$, $3.4\,\%D$ and $1.4\,\%D$ for BKW, ARS and DES, respectively, using experimental uncertainty of $U_D = 0.61\,\%D$. C_T predictions for both URANS and DES are not validated, even though the errors are $|E| < 4.8\,\%D$, due to small uncertainty interval $U_V < 2.5\,\%D$.

As discussed in Chap. 2, averaged comparison errors for G2010 submission for 5415 cases 3.1a &b were below 3 % and standard deviations around 4 %. It was concluded that 3M grid are sufficient to obtain comparison errors < 3 %. Herein, the

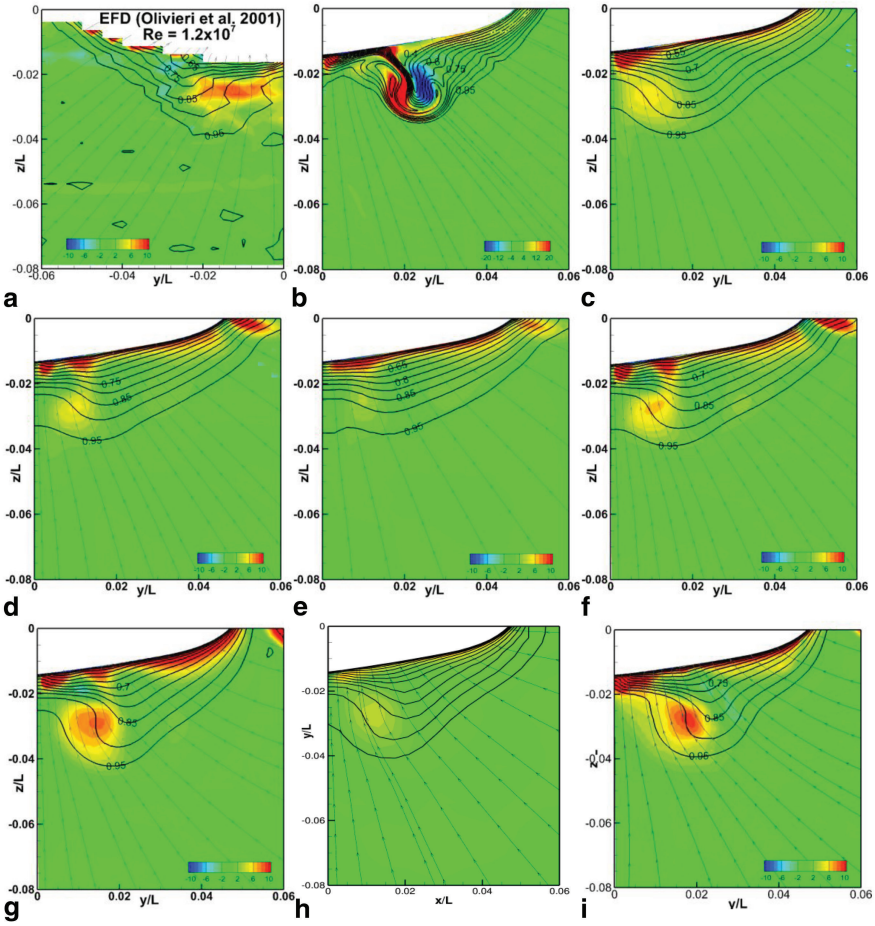


Fig. 7.31 Contour of streamwise vorticity (*flooded contours*), streamwise velocity (*lines*) and cross flow streamlines (*lines with arrows*) at x/L = 0.935 obtained using V4-B0-BKW/DES, V4 with ARS on B1, B2, B3 and O1grids, ISIS-A-EASM-S and F-O1-DHRL-S are compared with EFD data (Olivieri et al. 2001). **a** EFD. **b** V4-B0-BKW/DES. **c** V4-B1-ARS. **d** V4-B2-ARS. **e** V4-B3-ARS. **f** V4-O1-ARS. **g** V4-O1-ARS -S. **h** ISIS-A-EASM -S. **i** F-O1-DHRL -SS

averaged |E| for all the grids is 4.2 %D. Neglecting the predictions for the coarsest 0.6M grid, the averaged |E| drops to 3.54 %D. The averaged errors |E| for 2M to 10M grids is 3.56 %D, and those on > 10M grids is 3.55 %D. This suggests that grids with 2M to 10M points are sufficient to provide the best prediction of resistance, which is consistent with Chap. 2 conclusions. However, the averaged errors are 0.5 % higher.

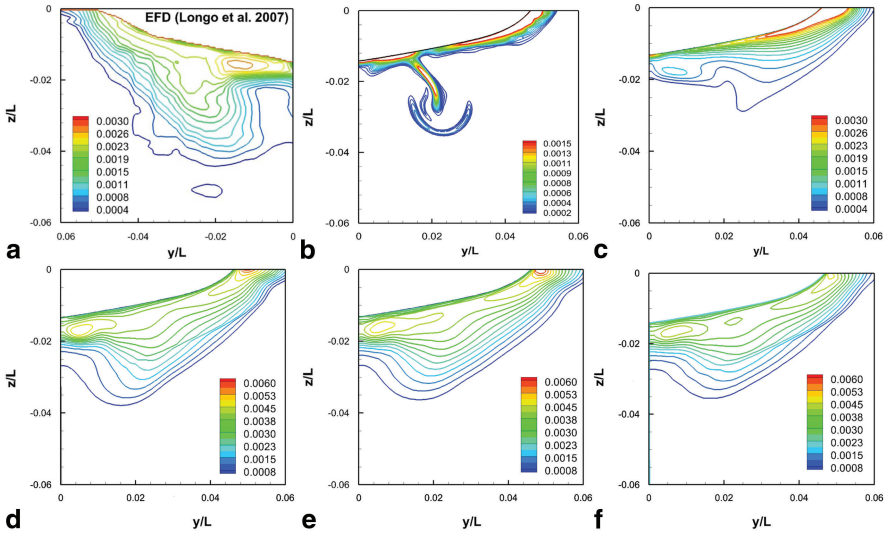


Fig. 7.32 CFDShip-Iowa V4 TKE predictions at nominal wake plane obtained using different models and grids are compared with EFD (Longo et al. 2007). **a** EFD. **b** V4-B0-BKW/DES. **c** V4-B1-ARS/DES. **d** V4-B1-ARS. **e** V4-B2-ARS. **f** V4-B3-ARS

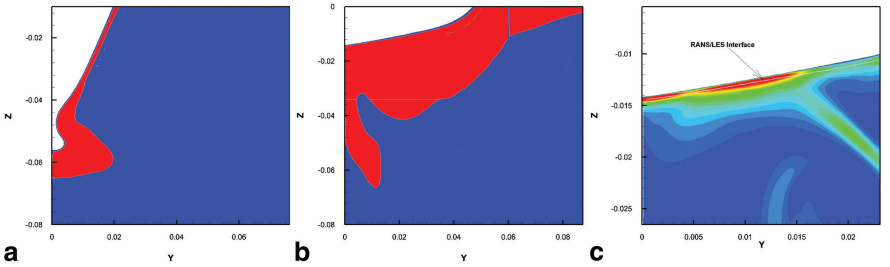


Fig. 7.33 LES-zones (*red flooded region*) for the B0 grid at **a** x/L = 0.1, **b** x/L = 0.935, and **c** TKE and RANS/LES interface zone at x/L = 0.935

3.3 Onset and Progression of Vortical Structures

Surana et al. (2006) identified that three-dimensional steady separation or reattachment can be categorized as closed separation, open separation and open-closed-separation. The separation pattern is identified from the surface streamline patterns and the presence of saddle point and nodes. The closed separation is more-or-less well understood (D'elery 2001). Whereas the concepts of open separation, such as how it starts and separates from the surface are debatable (Chapman 1986; Kenwright 1988). The open-closed separation has received less attention compared to the other types (Surana et al. 2006). The above studies discuss only the onset of separation from surface streamline, but do not discuss the progression of the vortices.

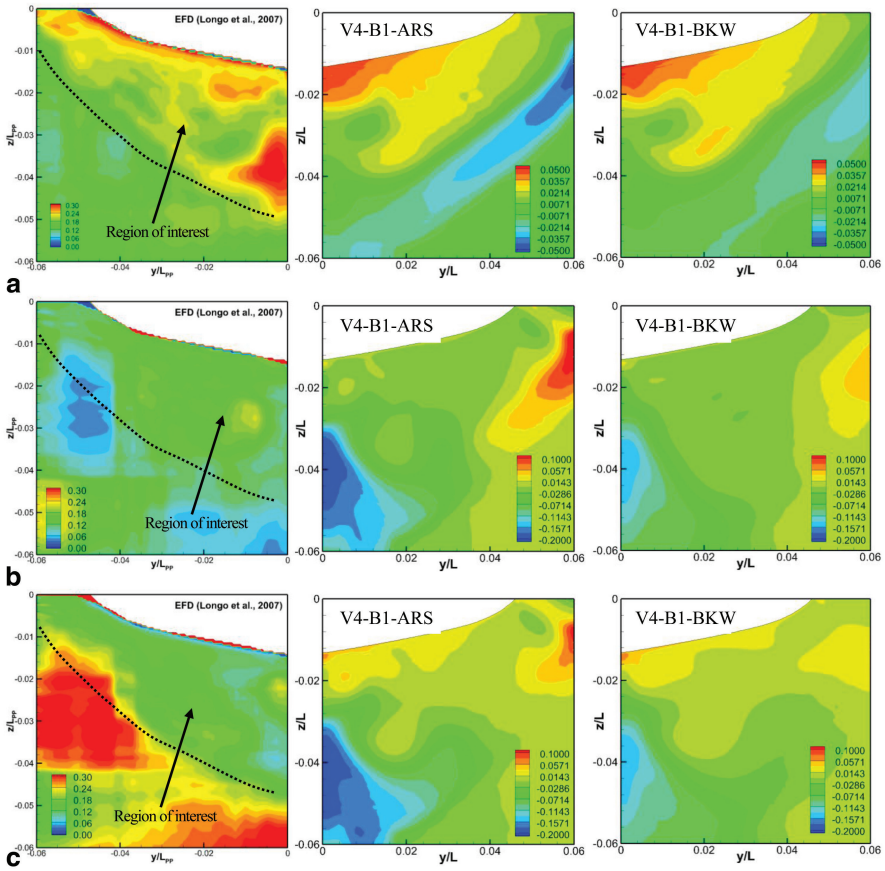


Fig. 7.34 CFDShip-Iowa V4 anisotropic stress (**a**) b_{11}, (**b**) b_{22} and (**c**) b_{33} profile at nominal wake plane obtained using V4-B1-BKW and -ARS are compared with EFD (Longo et al. 2007). The region of intest is in between the hull and the dotted line

Closed separation is identified by the presence of saddle points and nodes in the surface streamline pattern. The separation line is the surface streamline passing through a saddle point. Convergence of the surface streamlines when approaching the separation line results in a vertical dilatation of the stream tube, which causes the flow to detach. Similarly, divergence of the surface streamlines when streaming away from the separation line results in a vertical contraction of the streamtube, which causes the flow to attach. The closed separation vortices detach or attach on the surface at a node.

Open separation also known as cross-flow separation are identified by the converging surface streamline patterns. Such separation occur without skin-friction zeros at either end of the separation line. The separation line does terminate at a critical point, but does not originate from one. Open-closed separations are identified when the

Table 7.3 Verification and validation study for V4 resistance predictions using BKW, ARS and DES

Parameters	EFD (D)	ITTC	S_3	S_2	S_1	r_G	R_G	$e_{12}\%S_1$	U_I/e_{12}	$p_{re}/p_{G,th}$	$U_G\%S_1$	$U_D\%D$	$U_v\%D$	E%D
BKW Verification			**B3**	**B2**	**B1**									
$C_T\times10^3$**(E%*D*)**	**4.61**		4.72 **(2.38)**	4.94 **(7.15)**	4.83 **(4.77)**	$3^{1/2}$	-0.5	2.28	0.03	-	2.30	**0.63**	**2.36**	**4.77**
$C_F\times10^3$**(E%*ITTC*)**		**3.38**	3.32 **(1.77)**	3.50 **(3.55)**	3.51 **(3.84)**		0.06	-0.29	0.007	1.31	0.78	-	-	-
$C_R\times10^3$**(E%*D*)**	**1.23**		1.40 **(13.82)**	1.44 **(17.07)**	1.33 **(8.13)**		-2.75	8.27	0.05	-	-	-	-	-
ARS Verification			**B3**	**B2**	**B1**									
$C_T\times10^3$**(E%*D*)**	**4.61**		4.68 **(1.52)**	4.88 **(5.85)**	4.77 **(3.40)**	$3^{1/2}$	-0.55	2.31	0.03	-	2.10	**0.63**	**2.19**	**3.40**
$C_F\times10^3$**(E%*ITTC*)**		**3.38**	3.49 **(3.25)**	3.38 **(0.1)**	3.40 **(0.59)**		-0.18	-0.59	0.007	-	1.62	-	-	-
$C_R\times10^3$**(E%*D*)**	**1.23**		1.19 **(3.25)**	1.50 **(21.95)**	1.37 **(11.38)**		-0.42	4.75	0.05	-	11.31	-	-	-
DES Verification			**B2**	**B1**	**B0**									
$C_T\times10^3$**(E%*D*)**	**4.61**		4.785 **(3.43)**	4.753 **(3.02)**	4.732 **(2.60)**	$3^{1/2}$	0.656	0.44	0.06	0.78	1.25	**0.63**	**1.39**	**2.60**
$C_F\times10^3$**(E%*ITTC*)**		**3.38**	3.535 **(4.43)**	3.456 **(2.24)**	3.412 **(1.17)**		0.594	1.29	0.01	0.946	0.44	-	-	-
$C_R\times10^3$**(E%*D*)**	**1.23**		1.25 **(1.62)**	1.297 **(5.40)**	1.32 **(7.34)**		0.489	-1.74	0.10	1.30	3.45	-	-	-

S_1: Solution of finegrid; S_2: Solution of middle grid; and S_3: Solution of coarse grid.

surface streamline pattern shows converging streamlines originating from a saddle point, but do not terminate in a node.

Herein, preliminary onset and progression analysis of high-resolution CFD predictions, in particular V4-B0-BKW/DES and ISIS-A-EASM-S, are performed. The dominant vortical structures in the flow are shown using isosurface of normalized helicity (Q) = 500 and velocity profiles along the hull in Fig. 7.21 for two-phase V4-B0-BKW/DES and single-phase ISIS-A-EASM-S solutions. As discussed in Chap. 3, V4-B0-BKW/DES provided a detailed description of the progression of the vortical structures. The predictions show two main vortices: the sonar dome (SDV) and fore-body keel (FBKV) vortices. An additional vortex between the SDV and FBKV vortices was identified from post workshop ISIS-A-EASM-S simulation. A closer look at the V4-B0-BKW/DES confirmed the presence of this vortex. This vortex is generated from the trailing edge of the sonar dome, hence is identified as sonar dome trailing edge vortex (SDTEV). V4-B0-BKW/DES also predicts a secondary vortex, which breaks from the sonar dome vortex. This vortex is called sonar dome secondary vortex (SDSV). In this section, the onset and progression of the vortices up to $x/L_{PP} = 0.12$ are discussed, and their progression further downstream are discussed in the next section. V4-B0-BKW/DES and ISIS-A-EASM-S simulations are used for the analysis, as they provide the most detailed description of the vortical structures near the sonar dome. Nonetheless, surface streamline pattern and cross flow predictions on coarser V4 grid are similar to B0 grid predictions, thus other grids are expected to show similar onset and progression. The onset and progression of the SDV, SDTEV and FBKV vortices are discussed below and summarized in Table 7.4.

Sonar Dome Vortex (SDV) The sonar dome surface streamline shows that the vortex separation occurs as the flow streamlines converge along a dividing streamline as shown in Fig. 7.22. Thus, it is an open-type separation. The separation occurs at $x/L_{PP} = 0.065$, $z/L_{PP} = -0.055$. Inspection of the streamwise velocity in the sonar dome sub-layer shows that the boundary layer remains attached, even though the vortex separates from the surface.

Contours of pressure and cross flow velocity at selected slices are shown in Fig. 7.23. The slices show that the vortex is generated due to the development of a cross flow pattern, which results in streamwise vorticity. The cross flow pattern is generated as the high pressure on the bow combined with the suction on the forward part of the sonar dome induces a downward flow (negative vertical velocity) and the high pressure aft on the bottom of the sonar dome induces an upward flow (positive vertical velocity). The high pressure at the sonar dome bottom is generated as the flow in the boundary layer decelerates due to flow expansion induced by the tapering sonar dome. The vortex separates from the surface as positive wall normal velocity is generated at the core of the vortex. The positive wall normal velocity can be explained from the continuity equation, i.e., at the separation point $\partial w/\partial z < 0$, $\partial u/\partial x < 0$, which results in $\partial v/\partial y > 0$. The strong v-velocity gradient causes the vortex to move away from the sonar dome surface downstream of the separation. The pressure gradients are stronger in the ISIS-A-EASM-S computation than in the

Table 7.4 Summary of onset, separation and pregression characteristics for vortices for straight ahead barehull 5415 at $Re = 5.13 \times 10^6$, $Fr = 0.28$ predicted by V4-B0-BKW/DES and ISIS-A-EASM-S simulations

Vortex	Onset	Separation	Progression
Sonar dome (SDV)	Side of sonar dome surface	Open-type	Advected by streamwise velocity
Counter clockwise rotating	X = 0.065, Z = −0.055	Without BL separation	away from the sonar dome
	Free-surface induced downward flow and sonar dome geometry induced upward flow	Induced by high wall normal velocity at separation	
Sonar dome trailing vortex (SDTEV)	Convex section of the sonar dome keel	Open-type	Advected in sonar dome wake
	X = 0.109, Z = −0.054	Separates at the sonar dome keel	towards the hull
Clockwise rotating	Flow deceletaion in the concave portion of the sonar dome		
Fore body keel (FBKV)	Concave section of the sonar dome close to the keel	Open-type	Advected by streamwise velocity
Counter clockwise rotating	X = 0.107, Z = −0.0461	Boundary layer separation at the	Moves upwards of the keel due to
	Free-surface induced downward flow and upward flow from the concave portion of sonar dome	sonar dome-keel intersection	high pressure in sonar dome wake

V4-B0-BKW/DES computation, which are probably due to the absence of free-surface. The vortex is primarily advected by the streamwise velocity. At the inception, the vortex strength $\omega_x = 120U/L$, which strengthens after separation up to $\omega_x = 180$ U/L by $x/L_{PP} = 0.2$ and dissipates after that.

Sonar Dome Trailing Edge Vortex (SDTEV) The sonar dome surface streamline shows that the vortex separation occurs as the flow streamlines converge along a dividing streamline towards the sonar dome keel. Thus, it is an open-type separation. The vortex separates from the edge of the sonar dome keel around $x/L_{PP} = 0.109$, $z/L_{PP} = -0.054$. The vortex is generated slightly upstream of the edge and has an opposite rotation to the sonar dome vortex, i.e., counter-rotating. The counter-rotating axial vortex is generated due to the high pressure in the concave portion of the sonar dome due to flow deceleration.

The vortex is advected downstream in the wake of the SDV and lies below and inboard of the FBKV vortex, as shown in Fig. 7.23. The presence of the strong SDV and FBKV vortices creates a positive vertical velocity, which causes the SDTEV to move towards the keel. The vortex strength at inception is $\omega_x = -80$ U/L, which dissipates very quickly after separation to $\omega_x = -40$ U/L by $x/L_{PP} = 0.2$. This vortex dissipation is caused by the presence of these two stronger counter-rotating vortices.

Fore-body Keel Vortex The sonar dome surface streamlines close to the sonar dome—keel intersection in Fig. 7.22 shows streamline convergence in the concave section, where the vortex is initiated. Therefore, this is also an open-type separation. The vortex separates from the surface at $x/L_{PP} = 0.107$, $z/L_{PP} = -0.0461$, and is strengthened by the boundary layer separation at the sonar dome—keel intersection. The streamlines converge due to downward flow generated by the flared bow and the upward flow generated by the high pressure in the concave region (due to flow deceleration). These two gradients generate strong cross-flow slightly above the concave region. The vortex has the same rotation as the sonar dome vortex.

As shown in Fig. 7.23, the vortex is advected by the axial velocity away (upwards) from the keel and away from the hull. The vortex moves away from the wall as high wall normal velocity is predicted between the core and sonar dome surface, as explained for the separation of SDV. The vortex is pushed upwards of the keel because of the high pressure in the wake of the sonar dome, which induces flow in the vertical direction. Further downstream, SDV and FBKV wrap around each other and eventually merge (refer to Chap. 3 for more detailed discussions). At the vortex inception, the strength of the vortex is $\omega_x = 80$ U/L. The vortex gains strength after separation and shows $\omega_x = 160$ U/L at $x/L_{PP} = 0.2$. The vortex dissipated thereafter as discussed in previous section.

3.4 Effect of Turbulence Models, Grids, Free-Surface and Numerical Methods

Vortical Structures and Free-Surface Predictions using CFDShip-Iowa V4 The vortical structures predicted by V4-B and -O grid simulations are discussed in this

section. Due to space limitations, vortical structures for only the key DES and ARS simulations are shown in Fig. 7.24. The discussions are organized by turbulence model, i.e., discussions of DES predictions followed by ARS, BKW and NM. Effect of grid topology is studied for the ARS model. For DES, only the B0 grid result is shown as it provides the best prediction, and the predictions on coarser grids are similar to those on ARS. ARS results are shown on B1, B2, B3 and O1which display the effect of grid resolution and topology. The figure shows the vortical structures using $Q = 10$,100 and 300, and the discussions focus on the strength of the vortical structures and how far they extend along the hull. The extent of the vortices are summarized in Table 7.2. As expected, the vortices are visible up to a larger extent along the hull when smaller Q value is used. However, the vortices are not well defined for smaller values. In the following discussion the extent of the vortices are reported based on $Q = 10$ prediction.

In DES, the resolved TKE levels are 0.5 %, 1 % and 2.5 % for B1, B1 and B0 grids, respectively, as shown in Table 7.2. The resolved TKE levels are far below desired values. SDV extends up to $x/L_{PP} = 0.47$, 0.71 and > 1 on B2, B1 and B0, respectively. FBKV extends up to $x/L_{PP} = 0.68$ for B2 and up to $x/L_{PP} > 1$ for B1 and B0. The extent of vortical structures are similar for both BKW/DES and ARS/DES. SDTEV vortex is predicted only on the B0 grid. This vortex is much weaker compared to the SDV and FBKV vortices and survives only up to $x/L_{PP} = 0.32$. SDSV is predicted only on the B0 grid, which breaks away from the SDV around $x/L_{PP} = 0.13$. This vortex is weaker than other vortices and extends only up to $x/L_{PP} = 0.27$.

In ARS simulations, SDV extends up to $x/L_{PP} = 0.3$, 0.45 and 0.68 on B3, B2 and B1, respectively. FBKV shows smaller variation with grid resolution, and its extent increases from $x/L_{PP} = 0.55$, 0.64 and 0.68 on B3, B2 and B1, respectively. Predictions on O2 and O1 grids are similar to those predicted by B3 and B2, respectively; this is because O2 and B3, and O1 and B2 have similar grid resolution close to the hull. BKW predicts around 2–5 % smaller extent for SDV than ARS, whereas FBKV vortex shows negligible variation compared to ARS.

In NM simulation, both SDV and FBKV extend up to $x/L_{PP} > 1$, but are much closer to the hull compared to the turbulence simulations. The vortices start to breakdown around $x/L_{PP} = 0.4$ and small structures are generated.

As shown in Fig. 7.25, the measured wave elevation displays the so-called Kelvin wave pattern consisting of diverging and transverse waves within a half envelope angle $\alpha = 19°$. The free-surface predictions do not show dependence on URANS or HRLES solutions. The NM predictions, which have significantly thin boundary layer compared to the turbulence simulations, are similar to turbulence predictions. The wave elevation predictions do not show significant improvement on grid refinement for the B grids, this is because the overset grids have additional refinement near the free-surface. The wave elevations compare within 3 to 4 % of the experiments. The O-grid predictions show diffused wave elevation compared to B grids, as they do have sufficient refinement near the free-surface. The averaged errors are up to 6 %D and 8 %D for O1 and O2 grids, respectively.

Vortical Structure Predictions for Single-Phase Simulations The vortical structures predicted by V4, ISIS and Fluent- single-phase simulations on O1 grid and ISIS-A-EASM predictions, are discussed in this section. Due to space limitations only key results are shown in Fig. 7.26. The discussions are organized by solver, i.e., discussions of V4 predictions followed by ISIS and Fluent. Effect of free-surface is discussed for V4 predictions. Effect of adaptive mesh refinement is studied for ISIS predictions. Predictive capability of DHRL, DES and BKW turbulence models are assessed using Fluent simulations. Figure 7.26 shows the vortical structures using $Q = 10{,}100$ and 300, and the discussions focus on the strength and extent of the vortical structures, as in previous section.

All the simulations show dominant SDV and FBKV vortices from the bottom hull, similar to the two-phase simulation, and also shows deck vortices on O1 grid. SDTEV is not predicted on O1 grid simulations, but are predicted for ISIS-A grid simulation, as discussed earlier. None of the simulations predict the SDSV. Similar to the two-phase simulations, the vortices are visible up to a larger extent along the hull when smaller Q value is used.

V4-O1-ARS-S predicts the extent of SDV up to $x/L_{PP} = 0.98$ and FBKV up to $x/L_{PP} = 0.92$. Comparing with the two-phase simulation, the vortices are stronger and extends up to a longer distance along the hull. As shown in Fig. 7.27, the single-phase simulation has higher surface pressure than that in the two-phase. Thus, the vortices in the single-phase are further away from the hull compared to the two-phase, and encounter less dissipation. Further, the pressure gradients at the vortex separation are stronger for the single-phase flow. The above two factors cause higher strength vortex in single-phase compared to that in two-phase.

ISIS-A predicts extent of SDV up to $x/L_{PP} = 0.85$ and FBKV up to $x/L_{PP} = 0.85$. Whereas in ISIS-O1 simulation, the vortices extend up to $x/L_{PP} > 1$. The extent of vortices are slightly lower for adapted ISIS-A grid, because the grid becomes progressively coarser moving downstream. This is in return caused by the refinement criterion, which reacts less to the weakening vortices. The grid refinement is limited only to the sonar dome region due to the excessive damping of vortices by URANS, which resulted in lower pressure gradients.

In F-O1-DHRL simulation, the resolved TKE level is around 70 %, as shown in Table 7.2. The vortices SDV and FBKV extend all along the hull, and shows breakdown starting from $x/L_{PP} = 0.3$. In F-O1-SA/DES simulation, the resolved TKE level is around 0.1 %. The vortical structures are almost steady and extend all along the hull. F-O1-BKW simulation also predicts steady vortical structures extending all along the hull.

F-O1-SA/DES also fails to trigger resolved turbulence, similar to V4-DES predictions. This confirms the limitation of DES model in triggering resolved turbulence for such flows. The DHRL model predicts significant vortex break-up, and is expected to be a promising alternative for DES models.

Fluent predictions shows significantly stronger vortex than the other solvers. This suggests that the central difference discretization of the convective term leads to stronger vortices than the upwind schemes. However, additional simulations need to be performed using different available convective schemes to arrive at concrete conclusions.

3.5 Validation

Experimental data (Olivieri et al. 2001) are available for the streamwise and cross flow velocities at cross-sections $x/L_{PP} = -0.00524$, 0.1, 0.2, 0.4, 0.6, 0.8, 0.9346, 1.0 and 1.1. Longo et al. (2007) experimental data provides the details of the turbulent structures at $x/L_{PP} = 0.9346$, including TKE, normal and shear stresses. The sparse experimental data fails to explain the generation, convection and dissipation of the vortices. Furthermore, the experimental data does not provide enough resolution near the hull, where the vortices are generated and convected, and so several key features may be missing. As discussed in Chap. 3, fine-grid V4-B0 simulation, even though did not predict turbulent structures well, provided for first time plausible description overall vortex structures, and helped in understanding the sparse experimental data.

The objective herein is to assess the accuracy of the simulations by comparing the predictions with experimental data at selected cross-section. For this purpose, boundary layer and wake predictions are compared with Olivieri et al. (2001) data at three cross-sections $x/L_{PP} = 0.2$, 0.6 and 0.935. TKE, normal stress anisotropy and shear stress predictions are compared with Longo et al. (2007) data focusing mainly on the accuracy of URANS with isotropic and anisotropic turbulence models.

Boundary Layer and Wake Predictions The vortical structure and boundary layer wake observed in the experiment are shown in Fig. 7.28 using streamwise vorticity flooded contours, streamwise velocity lines contour and cross flow streamlines. The experimental data shows a diverging flow pattern upstream of the bow due the presence of stagnation point at the bow leading edge. A dominant vortex starts from the side of the sonar dome at $x/L_{PP} = 0.1$, which gains strength and aligns along the center plane by $x/L_{PP} = 0.2$. The vortex size grows and strength dissipates by $x/L_{PP} = 0.4$, but are still aligned with the center plane. At $x/L_{PP} = 0.6$, two co-rotating vortices are observed one aligned with the center plane and other outboard located close to the hull. At $x/L_{PP} = 0.8$, a weak vortex is observed away from the center plane and close to the hull, and the cross-flow does not show any closed cross-flow streamlines. The vortex dissipates further downstream, as observed at $x/L_{PP} = 0.935$ and 1.0. Closed cross-flow streamlines are again predicted at $x/L_{PP} = 1.1$.

Selected results are shown in Figs. 7.29, 7.30 and 7.31 for: V4-B0-BKW/DES, which are the best predictions of DES in terms of description of the vortical structures; V4 with ARS predictions on B1, B2,B3 and O1 which displays the effect of grid refinement and topology; V4-O1-ARS-S is presented to discuss the effect of free-surface; ISIS-A-EASM-S is presented to evaluate the effect of adaptive mesh refinement; and F-O1-DHRL-S to evaluate the capability of DHRL. The results are discussed based on turbulence model, i.e., discussions of DES followed by DHRL and ARS.

V4-B0-BKW/DES predictions at $x/L_{PP} = 0.2$ shows closed cross-flow streamlines due to SDV, FBKV and SDTEV vortices. SDV is aligned with the centerline, but is up to two-times stronger than the experiment. SDSV is visible breaking away from the SDV, and moving away from the center plane. SDTEV has negative vorticity, as it is counter-rotating with respect to SDV. FBKV vortex is located deep in

the boundary layer, and is co-rotating with respect to SDV. The experiment does not show SDTEV and SDSV, but hints at the presence of FBKV near the hull. SDSV seems unphysical, and is probably generated due to under-resolved turbulence. At $x/L_{PP} = 0.6$, both the co-rotating vortices are predicted, but the axial velocity defects are more pronounced than the experiments. At $x/L_{PP} = 0.935$, simulations shows the presence of a counter-rotating vortex pair compared to a single vortex in the experiment, and again the axial velocity defects are more pronounced than the experiments.

F-O1-DHRL-S predicts SDV and FBKV at $x/L_{PP} = 0.2$. The magnitude of SDV compares well with experiment, and its alignment with center plane is better than DES. At $x/L_{PP} = 0.2$, the co-rotating vortices are not predicted and the vorticity strength is over predicted compared to experiment. However, the boundary layer profile compares well with the experiment. At $x/L_{PP} = 0.935$, vorticity magnitude is over predicted and the boundary layer bulge is sharper compared to the experiment.

V4 with ARS simulations, vorticity magnitude and boundary layer predictions improve with grid refinement, for both B- and O-grids. The best predictions are obtained using B1 grid, which shows the presence of SDV and FBKV at $x/L_{PP} = 0.2$. However, SDV is not aligned with the center plane and tends to move outwards. FBKV is predicted deep in the boundary layer as in DES predictions. The co-rotating vortices are not predicted at $x/L_{PP} = 0.6$, and the vortices are weaker and boundary layer bulge is smoother compared to the experiment at $x/L_{PP} = 0.935$. Predictions using O2 and O1 are similar to those predicted by B3 and B2, respectively; as they have similar grid resolution close to the hull.

V4-O1-ARS-S predicts SDV and FBKV at $x/L_{PP} = 0.2$. SDV is 20 % stronger than the experiment, but aligns very well with the center plane. At $x/L_{PP} = 0.6$, a closed cross-flow streamlines is predicted, but again the vorticity magnitude is stronger. A similar over prediction of vorticity magnitude and boundary layer bulge is predicted at $x/L_{PP} = 0.935$. Compared to the two-phase simulation, the single-phase simulation predicts better alignment of SDV, but predicts 40 % stronger vortices.

ISIS-A-EASM-S predicts SDV, SDTEV and FBKV at $x/L_{PP} = 0.2$. SDV is aligned well with the center plane, but its strength is stronger compared to the experiment. Counter-rotating SDTEV is predicted in between the SDV and FBKV, similar to V4-B0-BKW/DES predictions. The simulation also predicts a closed cross-flow streamlines at $x/L_{PP} = 0.6$, which is stronger than the experiment, and predicts sharper hook shape at $x/L_{PP} = 0.935$. The stronger vortex strength and sharper hook shape predictions are similar to V4 single-phase simulation.

Turbulent Structures at Nominal Wake Plane Experimental TKE data in Fig. 7.32 shows high TKE region close to the hull slightly outboard of the center plane. TKE profile away from the boundary layer shows a hook shape similar to the streamwise velocity profile.

DES simulations significantly under predict TKE in the region away from the wall, where LES is active, due to low resolved turbulence predictions. TKE is under predicted more-and-more as the grid is refined, and the averaged TKE values are < 10 % of the experiment on B0. No significant differences are observed between

ARS and BKW based DES models. The results also show under predictions of normal and shear stresses due to resolved turbulence issues, thus are not discussed below. As shown in Fig. 7.33, the low resolved TKE predictions in DES is due to the activation of LES in lower log-layer, around $y^+ = 60$, where there is no background fluctuation to trigger resolved turbulence. Thus, there is a significant drop in TKE across the RANS/LES interface.

For ARS simulations, TKE profile predictions improve with the grid refinement, but the magnitude is over predicted by up to 30 % compared to the experiment. BKW also over predicts the TKE peak by 30 %. But, ARS performed better than BKW in predicting the TKE core shape, thus predicts the TKE profile better.

The normal stress anisotropy from experiment is shown in Fig. 7.34, where anisotropy is defined as:

$$b_{ij} = 1/3 - \overline{u_i{}' u_j{}'}/2TKE, i = j = 1,2,3$$

The region of interest is within the hook shape of the TKE or streamwise velocity profile, as marked on the figure. In the region of interest, the experimental data shows two main areas of anisotropy one close to the center plane and $z/L_{PP} = -0.04$, and other close to the boundary layer. As observed b_{22} and b_{33} have similar nature in this region, both show low values near the center plane and slightly higher values in the boundary layer. Overall, b_{33} has lower magnitude than b_{22}. The behavior of b_{11} is quite different from b_{22} and b_{33} and has higher values. Averaged b_{11}: b_{22}: $b_{33} \approx 1$: 0.5: 0.42 in the region of interest.

Both ARS and BKW capture the high b_{11} values close to the boundary layer, but the second peak is predicted farther away from the center plane compared to the experiment. For the b_{22} profile, both models show large variations compared to the experiment. For b_{33} profile, both the models predict the high and low peaks near the center plane, but the magnitudes are much larger than the experiment. ARS predicts peak b_{11}: b_{22}: $b_{33} \approx 1$: 1.3: 1.1. BKW shows peak b_{11}: b_{22}: $b_{33} \approx 1$: 0.2: 0.2, i.e., b_{11} dominates over other components. The anisotropy predictions using ARS are not as good as expected, which needs to be investigated.

The experimental $\overline{u'v'}$ shear stress profile in Fig. 7.35, shows negative values towards the center plane, and positive values outboard. The $\overline{u'w'}$ shear stress profile shows high value in the core of the TKE, and its profile shows the hook shape similar to TKE. ARS simulations predict the shear stress magnitude well compared to the data, and the profile predictions improve with the grid refinement. The simulation also predicts multiple positive/negative stress pockets near the center plane and the hull, which are not observed in the experiment. The best predictions of the stress magnitude are obtained using B1 grid, for which the results compare within 5 % of the data. BKW predicts diffused profiles, and over predicts peak values by 10 % compared to the experimental data.

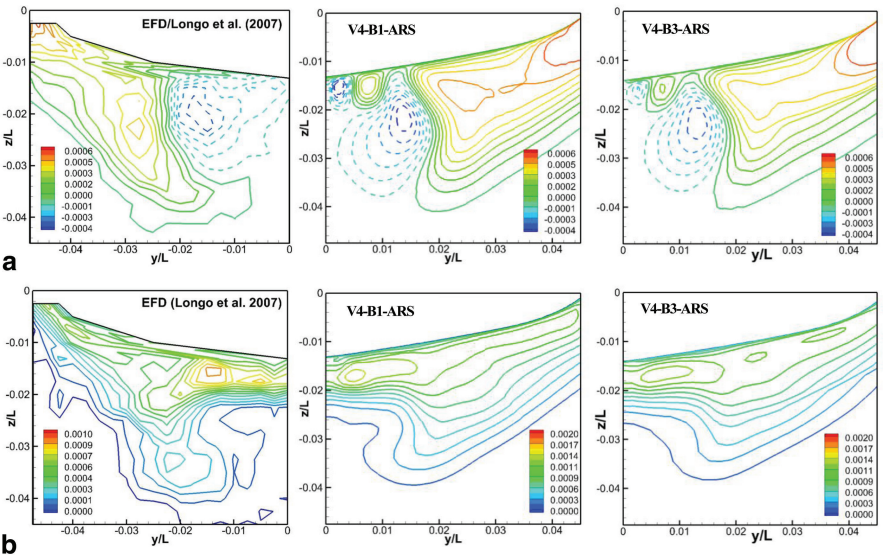


Fig. 7.35 Shear stress (**a**) u'v' and (**b**) u'w' profiles at nominal wake plane (x/L = 0.935) using V4-B1-ARS and V4-B2-ARS are compared with EFD (Longo et al. 2007)

3.6 Conclusions and Perspective of Future Work

Experimental data available for straight ahead 5415 includes, streamwise and cross flow velocities at several cross-sections along the hull $x/L_{PP} = -0.00524$ to 1.1 (Olivieri et al. 2001) for $Re = 1.2 \times 10^7$; and TKE, normal and shear stresses at nominal wake plane $x/L_{PP} = 0.935$ for $Re = 5.13 \times 10^6$. The sparse experimental data fails to explain the generation, convection and dissipation of the vortices, and do not have enough resolution near the hull to capture key features.

CFDShip-Iowa V4 grid verification studies are performed for resistance predictions using DES on up to 300M grids and for URANS on up to 50M grid. The studies show significantly small iterative errors, suggesting that they do not contaminate grid uncertainty estimates. C_T grid uncertainties are small $< 1.25\,\%S_1$ for DES and $< 2.2\,\%S_1$ for URANS. The order of accuracy ratio is close to 1 for DES study, suggesting that the 300M grids are approaching asymptotic range. The DES grid uncertainties are slightly higher than 5415 static drift $\beta = 20°$ DES study on up to 250M grids, for which averaged U_G was $0.5\,\%S_1$ (Bhushan et al. 2011). The larger uncertainties herein are due to poor convergence of pressure coefficients. C_T predictions on 50M grids for URANS and 300M grid for DES are not validated, even though the errors $|E| = 3.4\,\%$ for ARS and 2.6 % for DES are reasonably small. The averaged error for grids with 2M to 10M points is around 3.5 %D, which does not show significant decrease with further grid refinement. Thus, the results agree with conclusion drawn in Chap. 2 that 3M grid point is sufficient for resistance predictions.

Four vortices have been identified, i.e., SDV, SDTEV, FBKV and SDSV, where SDV, FBKV and SDSV are co-rotating and SDTEV is counter-rotating. The presence of SDV is well recognized from both experiments and CFD simulations. FBKV was recognized in the experiments only at mid-girth. Most CFD simulations have predicted this vortex at $x/L_{PP} = 0.2$, but did not show its presences at mid-girth. This vortex was predicted at mid-girth for the first time in V4-B0-BKW/DES and FOI-LES studies. SDTEV is reported for the first time from V4-B0-BKW/DES and ISIS-A-EASM high sonar-dome resolution studies, and is located in between the SDV and SDTEV. SDSV is also predicted for the first time from V4-B0-BKW/DES, and is formed due to the break-up of SDV. SDSV seems unphysical, and is probably generated due to under-resolved turbulence in the simulation.

SDV, SDTEV and FBKV originate from the sonar dome surface, and all of them have open-type separation, i.e. the onset is characterized by converging streamlines, without any originating critical point. SDV is initiated due to bow-flare/free-surface induced downward flow and sonar dome geometry induced upward flow patterns. SDLEV is initiated due to flow deceleration in the concave portion of the sonar dome. FBKV is initiated due to free-surface induced downward flow and upward flow from the concave portion of sonar dome. All the three vortices separate from the surface due to cross flow and are not associated with boundary layer separation. The cross-flows are induced either by the geometry, which generate high normal wall velocity between the vortex core the wall causing the vortex to separate. SDV is advected by the streamwise velocity, and moves away from the sonar dome. SDTEV is advected in the sonar dome wake towards the keel. FBKV moves upwards of the keel due to high pressure in the sonar dome wake, and away from the hull due to high wall normal velocity in between the vortex core and the wall.

A plausible description of the convection of the vortices are predicted by V4-B0-BKW/DES, where the SDV and FBKV extend all along the hull and wrap around each other beyond mid-girth. On the other hand, SDTEV and SDSV dissipate before mid-girth. The vortices dissipated faster in URANS compared to HRLES, and BKW predicts 2–4 % higher dissipation of vortices than ARS. The best predictions for the two-phase URANS shows SDV and FBKV up to $x/L_{PP} = 0.7$. The free-surface reduces hull pressure and leads to weaker pressure gradients on the sonar dome, thus single-phase simulations predict stronger vortices than the two-phase simulations. SDV and FBKV are predicted at least up to $x/L_{PP} > 0.85$ in all the single-phase simulations. The adaptive grid refinement in ISIS simulation gives very good resolution of the vortex inception, and the refined grid becomes coarser downstream when the vortices damp out. The refinement is based on the second-order spatial derivatives of the pressure, which decrease when the vortex is damped out, thus increasing the grid size. This may be a contributing factor to the disappearance of the vortices towards the stern. Prediction of vortical structures does not show dependence on grid topology. Comparison of V4, ISIS and Fluent predictions suggests that central difference scheme results in stronger and better defined vortical structures than the upwind schemes.

The free-surface predictions improve with the grid refinement, especially near the free-surface, but does not show dependence on boundary layer predictions. Predictions on grids with just 2M points, with sufficient resolution near the free-surface, agree within 3–4 % of the experiments.

V4 with DES on 300M grid is the only solution, which captures the co-rotating vortices at mid-girth as observed in the experiment. However, it over predicts the vorticity strength and causes more pronounces axial velocity defect at nominal wake plane. The stronger vortex predictions were due to low levels of resolved turbulence. Fluent with DES also shows similar low resolved turbulence predictions. The low resolved turbulence predictions by DES were due to its inability to trigger turbulence, as LES was activated in the boundary layer where resolved turbulent fluctuations were not sufficient to match the RANS stresses. This in return leads to modeled stress depletion in the boundary layer. Fluent predictions using recently developed DHRL model suggest that the above limitations of DES can be addressed by implementing RANS/LES transition based on turbulence production.

BKW and ARS predictions improve with grid, when compared to the experimental data. However, even on the 50M grid, they under predicts the vorticity magnitude, fails to predict co-rotating vortices at mid-girth, and under-predicts boundary layer bulge at nominal wake plane. ARS performs better than the BKW for the prediction of turbulent structures. ARS predict the correct shape for TKE and shear stress, and the peak values correspond reasonably well. However, the turbulent kinetic energy and Reynolds stresses are over predicted by about 25 % and 50 %, respectively. In addition, the stress anisotropy predicted by V4 with ARS does not compare very well with the experiments, compared to those predicted by NMRI explicit ARS model as discussed in Chap. 3.

Future work should focus on extending the onset and progression analysis for unsteady flows following Surana et al. (2008). Implementation of DHRL model in ship hydrodynamics solver to validate its ability to address the limitation of DES model for free-surface simulations. Compare different anisotropic turbulence models for URANS to identify the best model that represents turbulence anisotropy. Adaptive grid refinement are helpful in generating optimal grids, however better refinement metric are required, since refinement based on pressure gradient or vortical structures on the background grid fails to refine grid all along the hull. The effect of numerical methods on flow predictions need to be studied, especially comparing the central difference and upwind schemes. In addition, high-resolution experimental data are required to validate the progression of the vortices predicted by the simulations. One key issue for disagreement is the existence of the co-rotating vortices at the mid-girth. Some researchers believe that this may in fact be due to measurement errors in the very small cross-flow velocities, and the prediction of the co-rotating vortices in V4-B0-BKW/DES or FOI-LES could be due to turbulence modeling errors. Tomographic PIV data are being procured at IIHR for this purpose. The data will provide high-resolution datasets for onset and progression of the vortices including Q contours.

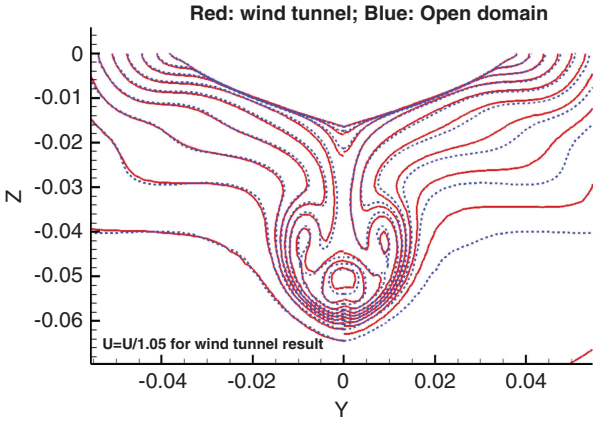


Fig. 7.36 ECN/CNRS computations of wake contours in the propeller plane. Contours shown are: 0.1(0.1)0.9. *Blue*: open domain, *red*: wind tunnel. *Left*: velocities normalized by 1.05 times free stream velocity. *Right*: normalized by free stream velocity

4 Blockage Effects on the Wake Data for KVLCC2

In Chap. 3 the significant blockage of KVLCC2 in the wind tunnel was pointed out, and it was conjectured that this effect could be significant for the detailed distribution of the wake contours in the propeller plane. Reference was made to post-workshop computations of the blockage effect at ECN/CNRS and Chalmers. These computations will be presented here.

The solid blockage, defined as the maximum cross-section of the (double model) hull divided by the tunnel cross-sectional area was 6.6 % in the tunnel. However, at the plane of interest—the propeller plane—the hull occupied only 0.3 % of the tunnel cross-section. Figure 7.36 shows computations of the wake contours in this plane. The right half of the figure shows velocity contours for an "open" computational domain (outer edge of domain located at 1.5Lpp with uniform flow boundary conditions) and for the real case with no-slip boundary conditions on the tunnel walls. As expected, there is a considerable difference between the two cases. However, in the left half of the figure the computed tunnel velocities have been reduced by 5 %, through normalization by 1.05 times the undisturbed velocity, and the large discrepancy in the outer contours has disappeared completely. The blockage effect at the propeller plane thus corresponds to an increase in undisturbed flow of 5 %.

Similar computations were carried out by Chalmers, however with slip conditions applied on the tunnel walls. Then the blockage effect was much smaller, and to match the outer wake contours with and without tunnel the tunnel velocities had to be normalized by 1.01–1.02 times the undisturbed velocity. The different behavior may be explained with reference to Fig. 7.37. Here the velocity contours from ECN/CNRS in the entire cross-section of the tunnel are displayed. It is seen that there is a very

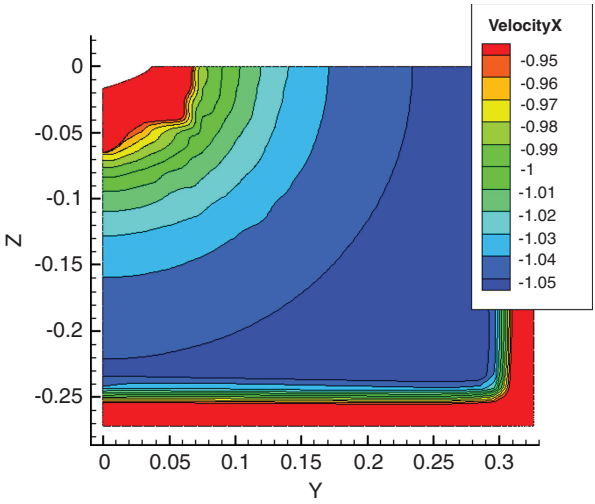


Fig. 7.37 Velocity contours in the tunnel cross-plane at the position of the propeller

thick boundary layer on the tunnel wall. The side wall boundary layer thickness is about 10 % of the tunnel half-width and the bottom boundary layer about 13 % of the tunnel half-height. Adopting flat plate relations, the displacement thickness is 1/8 of the total thickness, i.e. 1.3 % of the half-width and 1.6 % of the half-height, respectively. This corresponds to a reduction in cross-sectional area of about 3 %. Of the 5 % velocity increase seen by ECN/CNRS, about 3 % thus comes from the wall boundary layer (assumed starting at the inlet to the measuring section) and the rest from the "inviscid" restrictions to the flow caused by the tunnel wall. This rest, about 2 %, may seem large, as the area ratio at this station is only 0.3 %, but there is also a significant effect of the hull boundary layer. The displacement surface, surrounding the hull section, should be several times the area of this section itself, so the effective area ratio could be significantly larger than the geometric one.

The 5 % velocity increase discussed so far holds for the flow in the outer part of the viscous wake. However in the inner part, from velocity contour 0.4 and inwards (see Fig. 7.36), there seems to be practically no effect of the blockage. This might be explained by the variation of the blockage along the hull. On the parallel middle body the blockage is largest, and it is reduced towards the stern where the hull cross-section (including the boundary layer displacement thickness) is reduced. The excess velocity in the outer flow is thus reduced and the positive longitudinal pressure gradient always found in this region is increased. This is known as the "diffuser effect", and may cause separation of the flow in certain cases (see i.e. Zou and Larsson 2013). The low-momentum flow in the inner part of the boundary layer is more sensitive to this increase in pressure gradient than the outer high-momentum flow and the velocity is reduced in the inner part. This effect seems to balance the general increase in velocity due to the blockage.

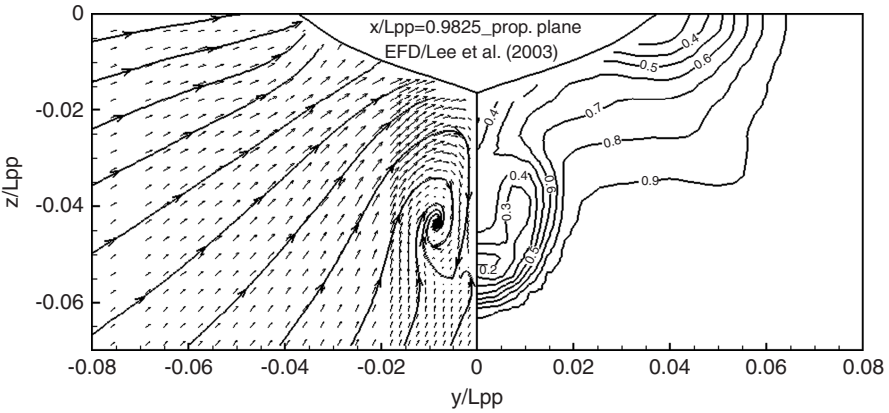


Fig. 7.38 Measured velocity contours (*right*) and velocity vectors (*left*) in the propeller plane. (Same as 3.4a)

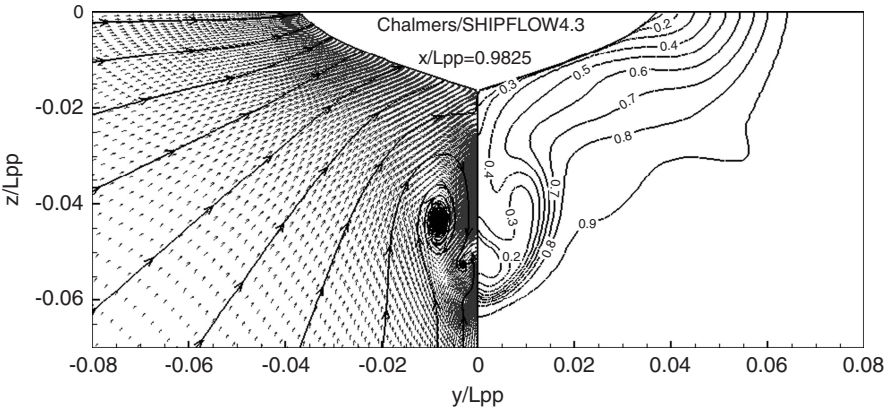


Fig. 7.39 Results computed by Chalmers. (Same as 3-4c)

Figures 7.38 and 7.39 are imported from Chap. 3 (Fig. 3.4a and c). The first one shows the measured wake contours in the tunnel, while the second one is a representative of the better predictions (without blockage). In general, there is a good correspondence between the wake contours in the propeller disk, but there is one significant difference that was pointed out in Chap. 3: the different behavior of the 0.4 contour. In the experiment it is split into an upper and a lower branch, while in the computations it is continuous from top to bottom. This is a feature shared with all five submissions in Fig. 3.4 of Chap. 3. As we have just concluded, there is no blockage effect on this contour, so the difference must be due to other effects.

Figure 7.40 displays the difference between the contours obtained in the wind tunnel and the towing tank (solid blockage 0.2 %). The displacement outwards of the outer tunnel contours is an effect of the blockage, as we have seen in Fig. 7.36.

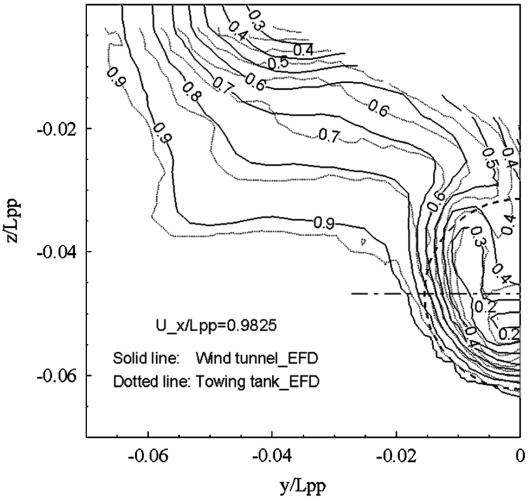


Fig. 7.40 Wake contours in the propeller plane. Comparison between wind tunnel and towing tank data. (Same as Fig. 3.2)

However, further in there is a relatively good correspondence between the two sets of results, with one notable exception: the 0.4 contour. In fact the towing tank results correspond very well with the computed ones. This leads to the suspicion that there was a difference in stern geometry between the two models tested. Such a difference is not out of the question, since a number of different IGES files exist for this hull, and it is not possible, at present, to say how they are related to the two models tested. One possibility that can be ruled out, however, is an influence of different boss endings. Both the tunnel model and the IGES file used in the computations had a hemispherical cap attached to the ending. If there was a difference in geometry it must have been further forward, perhaps in the sharpness of the very end of the stern just in front of the upper part of the propeller disk. Other possible differences between the tunnel and the towing tank may be upstream turbulence, flow non-uniformity or different turbulence stimulation. Unfortunately, there is no way to clarify this further.

5 Additional Sinkage and Trim Calculations for KVLCC2

The difficulty of accurately measuring the sinkage and trim at very small Froude numbers was pointed out in Chap. 2 and its Appendix. Measurement errors were thus stated as the main reason for the large differences between the computations (only MOERI) and the measured sinkage data in the Froude number range 0.10–0.15. To further investigate the accuracy of the numerical predictions additional computations were carried out by ECN/CNRS and Chalmers. ECN/CNRS carried out the computations in the same way as MOERI, i.e. using free surface boundary

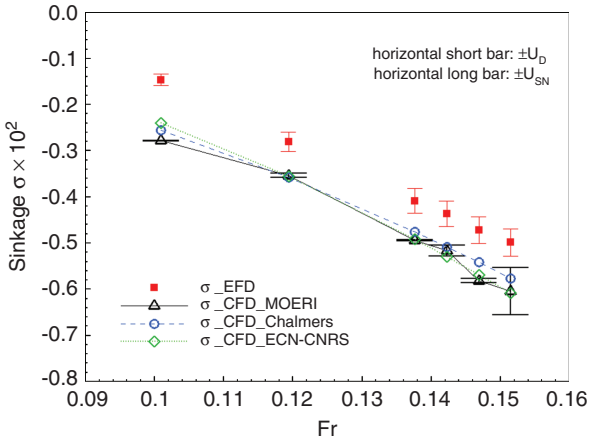


Fig. 7.41 Sinkage (σ) versus Froude number (Fr), Case 1.2b. Error bars from MOERI computations (U_{SN}) and measurements (U_D). Cf. Figure 2.1!

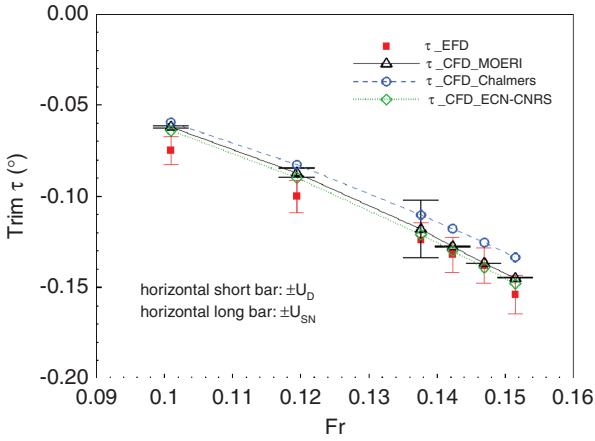


Fig. 7.42 Trim (τ) versus Froude number (Fr), Case 1.2b. Error bars from MOERI computations (U_{SN}) and measurements (U_D). Cf. Figure 2.5!

conditions and a VOF technique. Chalmers, on the other hand, obtained the sinking force and trimming moment from the double model pressure distribution and applied zero speed hydrostatic data to obtain the sinkage and trim. As seen in Fig. 7.41 there is an excellent agreement between the three computed sinkages, but a constant shift from the measured data. This supports the conjecture that the large comparison errors for small Froude numbers are due to measurement difficulties. There is also a rather good correspondence between the three computations of the trim in Fig. 7.42, even though the Chalmers results deviate slightly from the other two. In this case, the comparison errors are smaller at the high speeds, but rather large for the lowest speeds.

6 Overall Conclusions

As discussed in Chap. 3, the submissions in G2010 for the local flow predictions for KVLCC2 and 5415 ranged from URANS on 615K to 305M grids, and HRLES using DES on 13M to 305M grids. The large disparity in the grid sizes made it difficult to draw concrete conclusions regarding the most reliable turbulence model and appropriate grid resolution requirements. In this chapter, additional analysis is performed to shed more light on these issues. For KVLCC2, CFDShip-Iowa V4 predictions submitted as supplemental material in the workshop are discussed. The simulations included URANS with BKW and ARS and HRLES with DES and DDES, on 13M and 305M grids. For 5415, additional simulation have been performed using V4, ISIS-CFD and Fluent solvers. The simulations included, two-phase URANS with isotropic BKW and anisotropic ARS turbulence model and HRLES with DES model using CFDShip-Iowa V4 on 2M to 50M grids; single phase URANS with EASM model using ISIS-CFD on 5-6M grids, including an adaptively refined grid; and single-phase URANS with BKW model, and HRLES with DES and DHRL models using Fluent on a 5M grid.

The numerical method study showed that the TVD schemes are better than the upwind schemes. Limited results suggest that the central-difference scheme perform better than the upwind schemes in the prediction of vortical structures. 2nd order schemes are sufficient for URANS simulations even on finer grids consisting of 10s M points. HRLES are expected to require higher order numerical schemes, such as 4th order or higher.

Grid verification studies for V4 resistance predictions have been performed using DES on up to 300M grids, and BKW and ARS on up to 50M grid. The study showed small grid uncertainties $< 1.25\,\% S_1$ for DES and $< 2.2\,\%$ for BKW and ARS, suggesting that the grids are approaching asymptotic range.

URANS with anisotropic turbulence model provide better resistance and local flow predictions than URANS with isotropic turbulence model for both KVLCC2 and 5415. URANS predictions improve significantly with the increase in the grid resolution from $\sim$ 1M to $\sim$ 10M, but no significant improvements were predicted for larger grids. The adaptive grid refinement approach provided a 6M grid for the single-phase 5415. However, the grids were refined only in the sonar dome region, and not along the entire hull. One should have expected a significantly larger grid, of the order of 10s M, if the adaptive refinement would have continued all along the hull. The averaged error for resistance predictions on grids with 2M to 10M points is around 3.5 %D, which does not show significant decrease with further grid refinement. Thus, the results agree with conclusion drawn in Chap. 2 that 3M grid points are sufficient for resistance predictions. However, finer grid with up to 10s M points are required for local flow predictions. Overall, URANS with anisotropic turbulence model on 10s M grid are recommended for industrial applications considering the relative low cost compared to HRLES.

Hybrid RANS/LES with DES performs better than URANS with BKW or ARS for resistance predictions for both the geometries. For KVLCC2, DES solution on 13M

grid with sufficient resolved turbulence levels (i.e., $> 80\,\%$) show best comparison with data among the HRLES computation. Overall, best HRLES predictions are comparable to best URANS predictions, as the former is over predictive for both mean and turbulent quantities, whereas the latter is equally under predictive for mean quantities and over predictive for turbulent quantities. For 5415, DES solution on 300M grid is the only solution that captures the co-rotating vortices at mid-girth.

DES models have been primarily developed for massively separate flows, and have provided good predictions with $> 95\,\%$ resolved turbulence for slender and bluff bodies at static drift and with appendages, such as KVLCC2 at static drift (Xing et al. 2012), 5415 at static drift (Bhushan et al. 2011) and appended Athena transom flow (Bhushan et al. 2012b). However, they show limitations for straight ahead simulations for both bluff and slender bodies, as they have limited separation. For KVLCC2 bluff body, they suffer from either grid-induced separation or modeled-stress depletion issues in the boundary layer. For 5415 slender body, when the expected turbulence levels are an order of magnitude lower than the bluff bodies, they fail to trigger resolved turbulence. This limitation is identified due to the activation of LES in lower log-layer around $y^+ = 60$, where there is no background fluctuation to trigger resolved turbulence. The grid induced separation and modeled stress depletion issues for DES have been reported by several studies in the literature (Fu et al. 2007; Spalart 2009; Coronado et al. 2010). It is caused by the activation of LES in the boundary layer region where the turbulent fluctuations are absent. DDES helps in alleviating the grid induced separation issue, and improved DDES (IDDES) is expected to help in addressing the modeled stress depletion issue (Lyons et al. 2009; Shur et al. 2008). However, they do not address their inability to trigger turbulence issue. The models inability to trigger turbulence can be addressed by implementing physics based RANS/LES transition (Menter et al. 2003; Menter and Egorov (2010); Travin et al. 2004) along with coupling of RANS model with well validated LES model such as dynamic Smagorinsky model (Lilly 1992). Such a model has been recently developed by Bhushan and Walters (2012), which shows encouraging results for single-phase 5415 study.

Hybrid RANS/LES models are promising in providing the details of the flow topology, if the modeling issues are resolved. Grid resolution of the order of 300M show resolved turbulence levels of $> 95\,\%$ for straight ahead bluff bodies, static drift or appended bodies, thus these grids seem sufficiently fine. Nonetheless appropriate grid resolution requirements cannot be ascertained yet, due to modeling issues.

Onset analysis is performed for 5415 vortex separation. Study showed that the SDV, SDTEV and FBKV originate from the sonar dome surface and have open-type separation. All the three vortices separate from the surface due to cross flow and are not associated with boundary layer separation. Experimental data are required to validate the CFD predictions.

The free-surface predictions show improvements with the grid refinement, especially near the free-surface, but does not show dependence on boundary layer predictions. The predictions compare within 3–4 % of the experiment for just 2M grids. The free-surface reduces hull pressure and leads to weaker pressure gradients on the sonar dome, causing weaker vortical structures compared to the single-phase case.

In Chap. 3, a significant blockage of KVLCC2 in the wind tunnel was pointed out, and it was conjectured that this could have affected the CFD validations. Further study concludes that the differences are not caused by blockage. It is pointed out that the difference could be due to stern geometry used in CFD and experiments, in particular sharpness of the very end of the stern just in front of the upper part of the propeller disk.

Future work should focus on: 1) investigation of the correlation between mean flow and turbulent structures to provide feedback for better turbulence mode development; 2) comparison of different anisotropic turbulence models for URANS to identify the best model that represents turbulence anisotropy; 3) implementation of advanced turbulence models for hybrid RANS/LES in ship hydrodynamics solvers; 4) identification of better refinement metric for adaptive grid refinement; 5) development of V&V methodologies for hybrid RANS/LES; and 6) procurement of high-resolution experimental data to validate the onset and progression of the vortices predicted by the simulations and support turbulence model development.

Acknowledgements The research at Iowa was sponsored by Office of Naval Research under Grant Nos. N00014-01-1-0073 and N00014-06-1-0420 administered by Dr. Patrick Purtell. CFDShip-Iowa V4 simulations were performed on NAVY HPCMP machines Babbage IBM P5 and DaVinci IBM P6. Iowa research group would also like to acknowledge contributions of Dr. Pablo Carrica for generation of large grids for KVLCC2 and 5415 simulations using CFDShip-Iowa V4.

References

Bhushan S, Walters DK (2012) A dynamic hybrid RANS/LES modeling framework. Phys Fluids 24:015103

Bhushan S, Michael T, Yang J, Carrica P, Stern F (8-10 Dec 2010) Fixed sinkage and trim bare hull 5415 simulations using CFDShip-Iowa. Gothenburg 2010: A workshop on CFD in ship hydromechanics, Gothenburg, Sweden

Bhushan S, Carrica P, Yang J, Stern F (2011) Scalability and validation study for large scale surface combatant computations using CFDShip-Iowa. Int J High Perform C 25(4):466–487

Bhushan S, Alam F, Walters DK (2012a) Application of dynamic hybrid RANS/LES model for straight ahead surface combatant vortical and turbulent structure predictions. ParCFD 2012, Atlanta (22–26 May)

Bhushan S, Xing T, Stern F (2012b) Vortical structures and instability analysis for athena wetted transom flow with full-scale validation. J Fluids Eng 134:031201

Carrica PM, Wilson RV, Stern F (2007) An unsteady single-phase level set method for viscous free surface flows. Int J Numer Meth Fl 53(2):229–256

Chapman GT (1986) Topological classification of flow separation on three-dimensional bodies. AIAA-86-0485, AIAA 24th Aerospace Sciences Meeting, Reno

Coronado P, Wang B, Zha G-C (2010) Delayed detached eddy simulation of shock wave/turbulent boundary layer interaction. 48th AIAA Aerospace Sciences Meeting, Orlando (4–7 January)

D'elery JM (2001) Robert Legendre and Henri Werl'e: Toward the elucidation of three-dimensional separation. Annu Rev Fluid Mech 33:129–154

FLUENT 6.3, User Guide FLUENT 6.3, FLUENT Inc., Centerra Resource Park, 10 Cavendish Court, Lebanon, NH 03766, USA

Fu S, Xiao Z, Xhen H, Zhang Y, Huang J (2007) Simulation of wing-body junction with hybrid RANS/LES methods. Int J Heat Fluid Fl 28:1379–1390

Hino T (ed.) (2005) Proceedings of CFD workshop, NMRI report, Tokyo 2005
Ismail F, Carrica PM, Xing T, Stern F (2010) Evaluation of linear and nonlinear convection schemes on multidimensional non-orthogonal grids with applications to KVLCC2 tanker. Int J Numer Meth Fl 64:850–886
Kenwright DN (1998) Automatic detection of open and closed separation and attachment lines. In Proceeding Visualization '98, pp. 151–158
Larsson L, Stern F, Bertram V (2003) Benchmarking of computational fluid dynamics for ship flow: the Gothenburg 2000 Workshop. J Ship Res 47:63–81
Lee S-J, Kim H-R, Kim W-J, Van S-H, (2003) Wind tunnel tests on flow characteristics of the KRISO 3,600 TEU containership and 300K VLCC double-deck ship models. J Ship Res 47(1):24–38
Lilly DK (1992) A proposed modification of the germano subgrid-scale closure method. Phys Fluids 4(3):633–634
Longo J, Shao J, Irvine M, Stern F (2007) Phase-averaged PIV for the nominal wake of a surface ship in regular head waves. J Fluid Eng 129(5):524–540
Lyons DC, Peltier LJ, Zajaczkowski FJ, Paterson EG (2009) Assessment of DES models for separated flow from a hump in a turbulent boundary layer. J Fluid Eng 131(11):111203
Menter FR, Egorov Y (2010) The scale-adaptive simulation method for unsteady turbulent flow predictions. Part 1: Theory and model description flow, turbulence and combustion. 85:113–126
Menter FR, Kuntz M, Bender R (2003) A scale-adaptive simulation model for turbulent flow predictions. AIAA Paper No. 2003–0767
Olivieri A, Pistani F, Avanzini A, Stern F, Penna R (2001) Towing tank experiments of resistance, sinkage and trim, boundary layer, wake, and free surface flow around a naval combatant INSEAN 2340 model. IIHR technical report: 421
Patankar SV (1980) Numerical heat transfer and fluid flow (14. printing. ed.). Bristol, PA: Taylor & Francis. ISBN9780891165224
Queutey P, Visonneau M (2007) An interface capturing method for free-surface hydrodynamic flows. Comput Fluids 36(9):1481–1510
Shur M, Spalart PR, Strelets MKh, Travin A (2008) A hybrid RANS-LES approach with delayed-DES and wall-modeled LES capabilities. Int J Heat Fluid Flow 29:1638–1649
Spalart PR (2009) Detached-eddy simulation. Annu Rev Fluid Mech 4:181–193
Spalart PR, Deck S, Shur ML, Squires KD, Strelets MKh, Travin A (2006) A new version of detached-eddy simulation, resistant to ambiguous grid densities. Theor Comput Fluid Dyn 20:181–191
Stern F, Wilson R, Shao J (2006) Quantitative approach to V & V of CFD simulations and certification of CFD codes. Int J Numer Method Fluids 50:1335–1355
Surana A, Grunberg O, Haller G (2006) Exact theory of three-dimensional flow separation. Part I: Steady separation. J Fluid Mech 564:57–103
Surana A, Gustaaf BJ, Grunberg O, Haller G (2008) An exact theory of three-dimensional fixed separation in unsteady flows. Phys Fluids 20:107101
Travin A, Shur M, Spalart PR, Strelets M (2004) On URANS solutions with LES-like behavior. Congress on computational methods in applied sciences and engineering, ECCOMAS
Van SH, Kim WJ, Yim GT, Kim DH, Lee CJ (1998) Experimental investigation of the flow characteristics around practical hull forms. Proceedings 3rd Osaka colloquium on advanced CFD applications to ship flow and hull form design, Osaka
Xing T, Stern F (2010) Factors of safety for Richardson extrapolation. J Fluids Eng 132(6):061403-061403-13. doi:10.1115/1.4001771
Xing T, Shao J, Stern F (2007) BKW- RS-DES of unsteady vortical flow for KVLCC2 at Large drift angles, the 9th international conference on numerical ship hydrodynamics, Ann Arbor
Xing T, Bhushan S, Stern F (2012) Unsteady vortical flow and turbulent structures for a tanker hull form at large drift angles. Ocean Eng 55:23–43
Zou L, Larsson L (2013) Computational Fluid Dynamics (CFD) prediction of bank effects including verification and validation. J Mar Sci Tech. doi:10.1007/s00773-012-0209-7